NASA TECHNICAL TRANSLATION

NASA TT F-15,407

INTERPLANETARY FLIGHT PREDICTION

Ts.V. Solov'yev and Ye.V. Tarasov

Translation of "Prognozirovaniye Mezhplanetnykh Poletov, "Mashinostroyeniye" Press, Moscow, 1973, 400 pp.

(NASA-TT-F-15407) INTERPLANETARY FLIGHT PREDICTION (Scientific Translation Service) 494 p HC $27.75 CSCL 22A

N74-28312

Unclas
G3/30 43141

NATIONAL AERONAUTICS AND SPACE ADMINISTRATION
WASHINGTON, D.C. 20546 JUNE 1974

STANDARD TITLE PAGE

1. Report No.	2. Government Accession No.	3. Recipient's Catalog No.
NASA TT F-15,407		

4. Title and Subtitle	5. Report Date
INTERPLANETARY FLIGHT PREDICTION	June, 1974
	6. Performing Organization Code

7. Author(s)	8. Performing Organization Report No.
Ts.V. Solov'yev and E.V. Tarasov	10. Work Unit No.

9. Performing Organization Name and Address	11. Contract or Grant No.
SCITRAN Box 5456 Santa Barbara, CA 93108	NASw-2483
	13. Type of Report and Period Covered Translation
12. Sponsoring Agency Name and Address National Aeronautics and Space Administration Washington, D.C. 20546	14. Sponsoring Agency Code

15. Supplementary Notes

Translation of "Prognozirovaniye Mezhplanetnykh Poletov, "Mashinostroyeniye" Press, Moscow, 1973, 400 pages.

16. Abstract

This volume covers methods for calculating the ballistic design characteristics of interplanetary vehicles and determining the most favorable launch dates for flights to the planets. We examine possible schemes of spacecraft flight to other planets both with and without return of the vehicles to the Earth. We also consider special schemes of spacecraft flight to the Sun and planets when the gravitational fields of other planets, specifically Venus and Jupiter, are used to improve the ballistic characteristics.

17. Key Words (Selected by Author(s))	18. Distribution Statement
	Unclassified - Unlimited

19. Security Classif. (of this report)	20. Security Classif. (of this page)	21. No. of Pages	22. Price
Unclassified	Unclassified	492	

ANNOTATION

This volume covers methods for calculating the ballistic design characteristics of interplanetary vehicles and determining the most favorable launch dates for flights to the planets. We examine possible schemes of spacecraft flight to other planets both with and without return of the vehicles to the Earth. We also consider special schemes of spacecraft flight to the Sun and planets when the gravitational fields of other planets, specifically Venus and Jupiter, are used to improve the ballistic characteristics.

Optimal solution search methods based on patched conic approximation of the interplanetary trajectories are constructed with account for both impulsive velocity change and finite powered segment duration. Approximate solutions are given for the differential equations of spacecraft motion which permit finding optimal spacecraft design solutions with good accuracy and considerable reduction of the digital computer time.

Extensive calculations are presented of the various characteristics of interplanetary vehicles which can perform flights to the solar system planets in the foreseeable future.

The book is intended for scientists, engineers, and specialists in several branches of industry. It will also be useful to college students.

Reviewer: Prof. M.K. Tikhonravov, Doctor of Technical Sciences

FOREWORD

Modern cosmonautics is developing along three basic directions.

The first is use of spacecraft for the national economy, for example, for communications, weather prediction, marine and aerial navigation, Earth resource studies, and other purposes.

The second is exploration of cosmic space with the aid of piloted vehicles. By exploration of cosmic space we mean actions directed toward learning to live and work in space, to become a permanent resident rather than a traveler in interplanetary space. In the near future long-lived piloted orbital stations, the prototype of which is the Soviet Salyut orbital station, will be assembled and function in near-Earth space.

The orbital stations can also perform tasks characteristic of the first and, as will be seen later, third directions. These stations will initiate the long-term settlements in space which Tsiolkovskiy and his successors dreamed of. Various scientific laboratories, for example, space biology and medicine, geophysics and astrophysics will function aboard these stations and astronomical observatories will be set up. These stations will become the starting points for flights to the other planets.

The third direction includes systematic scientific studies and experiments in space with the aid of automatic vehicles and piloted spacecraft.

Specialized interplanetary vehicle scientific systems have been developed in a comparatively short period. The outstanding

advances in cosmonautics have stimulated the development of several new natural science fields: space biology and medicine, physics of the planets and interplanetary space. Many branches of engineering have acquired the label space: space engine construction, space electronics, space material science. The rocket and space industry and cosmonautics are intimately associated with the scientific and technical revolution which mankind is living through, acting as both the initiator and stimulator of this revolution.

We need to introduce division of the tasks facing science and cosmonautics into two groups: studies in near space, space near the Earth, and studies of more distant objects of the solar system such as the planets.

In the first group, the Moon and near-lunar space have become a unique scientific-engineering testing ground. Here various scientific studies are carried out and integrated hardware check-out is performed. Both fixed and mobile automatic equipment can operate successfully on the Moon as aids to expeditions organized with the participation of scientists. The hardware intended for future study of Venus, Mars, Mercury, and the other planets can be investigated on the Moon.

The second group includes studies primarily of the nearby planets such as Venus and Mars and also the asteroids, the planets Mercury and Jupiter and the more distant planets. Broad possibilities for study of the other celestial bodies of the solar system such as comets and planetary satellites will open up in the future.

The present volume is devoted to solving the problems of the second group.

One can scarcely find today any skeptics who would deny the tremendous importance of and urgent necessity for study of the Sun,

planets, and other celestial bodies and interplanetary space itself. Direct study of the solar system is a prerequisite for its exploration by man. Among the more important and interesting scientific problems whose solution is the purpose of interplanetary flights we can include: study of the geological development of the planets, search for unknown forms of living matter on the other planets, determining the possibility of the origin of life under ambient conditions which differ radically from those on Earth, study of solar system origin and evolution, study of the nature of gravity, studies of the problem of providing for autonomous existence of man, terrestrial plants, and animals beyond the Earth. Many secrets of the Earth may be discovered more easily on the Moon, Venus, Mars, and other celestial bodies of the solar system. Who can be so bold as to predict even the beginning of the end of these investigations?

The results of space studies may alter radically our views and established concepts. In this connection it is difficult to foresee in advance exactly which directions will have the maximal scientific and practical effect. The sequence for studying the bodies of the solar system is determined by technological capabilities and scientific interests.

In the solution of scientific problems interplanetary vehicles are only a tool. However, the scientific goals of solar system study impose requirements for the improvement of the technical hardware for studying space. It is not possible to determine the study capabilities without clarifying the capabilities of the space tools for studying and exploring cosmic space.

At the present time automatic equipment for studying space is widely used.

The dimensions and weight of the automatic vehicles depend basically on the experimental tasks and booster capabilities; the

automatic equipment can operate and provide information under extremely varied conditions.

The scientific effectiveness of the studies performed aboard such vehicles and the information acquisition rate depend not only on the choice of scientific objective, but also on the methods and sequence of carrying out the studies.

Analysis of the development of space-borne equipment and preliminary results of study of the Moon and circumlunar space, Venus, and Mars have shown that the planetary study program can be represented approximately as consisting of the following stages.

Preliminary studies are first made using interplanetary vehicles flying along flyby trajectories. They make it possible to obtain preliminary information on the general characteristics of the planets such as, for example, structure of the planetary surface, presence of magnetic field and radiation belts, and the necessary data on the atmosphere.

Then orbital flights are made by vehicles which permit more detailed and thorough studies, including mapping, comparison of various regions of the planet, more profound study of the atmosphere, and so on.

Then descent and landing of vehicles at specified points of the planetary surface are accomplished in accordance with the scientific importance of these regions, determined on the basis of orbital observations. After successful resolution of the landing problem automated vehicles can be landed with equipment for moving over the surface of the planet, whose movement can be corrected remotely from the Earth.

Finally, the problems of automated equipment return to the Earth are resolved. We hardly need say that this is a qualitatively new stage and its resolution is the triumph of space automation. This operation requires automated launch from the planet, injection into orbit around the planet and, if nesessary, docking with the primary spacecraft, launch from orbit and injection into the return trajectory for encounter with the Earth; return trajectory corrections must be made at the required times and tne Earth's atmosphere is used to reduce the hyperbolic entry velocity and land the vehicle in the desired region of the Earth.

This sequence may be altered. Certain stages may be eliminated, depending on the design of the automatic control equipment and the space vehicles themselves.

However, automatic vehicles cannot support all scientific studies in cosmic space. Automatic vehicles operate in accordance with a program specified by man in advance and record the magnitude and nature of parameters which are determined in advance. Automatic vehicles can acquire all sorts of data but only those data which have been planned in advance. The program can obviously be altered by radio but we need to know how to alter the program, what new information the automatic vehicle is to record, and how to do this. And in order to know this we need to be on the spot, which is impossible if only automatic vehicles fly in space for study purposes.

Therefore we need piloted flights during which man can participate actively in carrying out the studies, perceive and sense completely new phenomena which were not suspected in advance, when man himself can direct the work of the automatic instruments to record the most important parameters and newly encountered and possibly previously unknown manifestations of the nature of space.

Strictly speaking, the need for piloted flights does not require any proof. Automatic spacecraft will assist in carrying out scientific studies to the degree they are capable of doing this, and to a greater degree the more extensively and profoundly man understands nature. Moreover, automatic vehicles will always have priority in visiting places which are inaccessible to man. Piloted vehicles with scientific personnel aboard are capable of more thorough and faster study of space and, most important, they will be called on to explore interplanetary space, which is an urgent problem for the future of mankind.

The mutual positioning of the planets changes with time as a consequence of their motion. Depending on the position of the planets at the time of launch and arrival, the trajectory of the interplanetary trip of a spacecraft from one planet to another will be different and the energy expenditures required for the trip change. Therefore the results of interplanetary flight vehicle ballistic design depend to a considerable degree on the launch and arrival times. Today one of the primary limiting factors in interplanetary spacecraft launch time selection is the limited range of powerplant specific thrust. Search for the most economical flight methods to reach the assigned objective is becoming very important. Such methods include, for example, flights utilizing the gravitational fields of Jupiter, Venus, and the other planets.

The comparative rarity of favorable launch windows — the range of optimal launch dates for flight to the planets — imposes limitations on the problem of direct study of the planets using spacecraft. Prediction of the ballistic design characteristics is based on optimal flight trajectory search methods and finding the optimal design parameters of the interplanetary flight vehicle. The approximate solution of the differential equations of controlled spacecraft motion described in the present work is original and fruitful. It permits finding optimal spacecraft design solutions

with good accuracy and significant reduction of the digital computer time required for the calculations.

In the book we examine various schemes of interplanetary vehicle flight to various planets, both with and without vehicle return to the Earth and evaluate these schemes. Special schemes of spacecraft flight to the planets and Sun are studied in which the gravitational fields of the other planets are used to improve the ballistic characteristics. Extensive results are presented of calculations of the various characteristics of interplanetary vehicles which may in the future make flights to the planets of the solar system.

The book is based on original material obtained by the authors in the field of spacecraft ballistic design and using publications in the foreign and Soviet press. This book differs from other works in this field in that the entire complex of interplanetary flight vehicle design problems is examined from the same scientific viewpoint with account for energy expenditures, launch windows, and sensitivity of the trajectories to deviations from the theoretical values.

M.K. Tikhonravov

FROM THE AUTHORS

The rapid development of cosmonautics has confronted science with several very complex problems in carrying out spacecraft interplanetary flights. The planning of new spacecraft flights to the planets of the solar system leads to the necessity for further study of the possible flight schemes, energy expenditures, and other interplanetary vehicle characteristics.

Studies have recently appeared in the periodic press in the Soviet Union and abroad in which the ballistic problems of spacecraft injection into circumplanetary orbit and descent of landers to the planet, the problems of spacecraft return from the destination planet to the Earth, and so on have been examined. In several publications the problems of using the gravitational fields of the planets to improve the ballistic characteristics of the interplanetary vehicle have been discussed extensively. These analyses have included, for example, flights to Mercury and Mars using the gravitational field of Venus, and flights to the Sun and other planets using the gravitational field of Jupiter. Attention has been devoted to the importance of reducing the velocity of recoverable vehicle entry into the Earth's atmosphere, which can be achieved, for example, by special maneuvers in the heliocentric segment of the return spacecraft flight. Serious problems arise in solving the problems of interplanetary flight optimization.

The objective of the present book is to systematize the problems of interplanetary vehicle ballistic design and present some methods for the solution of these problems; special attention is devoted to patched conic approximation of the interplanetary trajectory and approximate solution of the differential equations

of controlled motion in the form of finite analytic expressions. The classification of interplanetary flight schemes used in the book made it possible to systematize the solution of the previously known and new problems of spacecraft ballistic design under the traditional assumption, when the planets are considered to be non-gravitating centers in calculating the heliocentric trajectory segments. The optimal design solution search methods presented are constructed with account for both impulsive flight velocity change and finite duration of the powered segments.

The problem of "mating" the heliocentric trajectory segment with the planetocentric segments is examined in a new fashion in the book and optimization of the spacecraft ballistic characteristics and basic design parameters is carried out jointly.

Accounting for the gravisphere dimensions of certain planets becomes necessary in practice in several problems of cosmonautics. Therefore we examine here the optimal spacecraft ballistic design methods, accounting for the influence of planetary gravitation on the heliocentric segment.

Chapters 1, 2 (§ 1, 3), 3, 4 (§ 1) and 7, 9 (§ 3, 4) were written by Ye.V. Tarasov and Chapters 2 (§ 2, 4), 4 (§ 2, 3) 5, 6, 8, 9 (§ 1, 2) and 10 by Ts.V. Solov'yev.

The authors wish to thank all their coworkers who assisted in writing and publishing this volume.

The authors are deeply indebted to the reviewer Prof. M.K. Tikhonravov, Doctor of Tech. Sci., for several valuable suggestions which made it possible to improve the content of the book.

The authors are particularly grateful to A.V. Leshchinko, A.M. Potapov, and N.F. Shmakova for their assistance in developing some of the methods and carrying out the calculations.

NOTATIONS

a - orbit semimajor axis

b - orbit semiminor axis

C_{uf}, C_0 - constants of integration

C - orbit chord

c_x - aerodynamic drag coefficient

c_y - aerodynamic lift coefficient

E - eccentric anomaly

e - orbit eccentricity

F - force; auxiliary variable

f - gravity constant

G - weight (gravity force)

g - gravitational acceleration

h, H - flight height

H - argument of hyperbola

i - orbit plane inclination to reference plane

K - aerodynamic efficiency

L, l - flight range (angular or linear)

M - trajectory angle; instantaneous spacecraft mass; mean anomaly

m - mass of material point; planetary mass

n - load factor

n_x - axial load factor

n_0 - initial spacecraft thrust-weight ratio

P - spacecraft powerplant thrust force

P_{sp} - engine specific thrust

p - orbit focal parameter; auxiliary angle

Q - integral thermal flux

q - specific thermal flux

R - distance from Sun to material point

r - distance from center of planet to spacecraft

T_s - synodic period

T - Artificial Planet Satellite (APS) revolution period; temperature

t - flight time

Δt, $\Delta t_{1, 2}$ - spacecraft flight time from initial to final point of orbit (conic section curve)

U - force function

u - angular distance from orbit node (argument of latitude)

V - velocity; velocity of body relative to the Sun

V_∞ - hyperbolic excess velocity

V_Σ, $V_{X\,\Sigma}$ - total characteristic velocity

W - discharge velocity of working fluid products from engine nozzle

X - aerodynamic drag force

Y - aerodynamic lift force

x, y, z - Cartesian coordinates of material point

α - angle between velocity vector and thrust vector; angle of attack; auxiliary angle in Lambert equation for hyperbolic motion; right ascension

β - central angle of injection segment; auxiliary angle in Lambert equation for hyperbolic motion; logarithmic gradient of density

δ - declination

ε - inclination of Earth's equatorial plane to the plane of the ecliptic; constant of planetary flattening

Θ - trajectory angle

ϑ - pitch angle

λ - longitude of projection of point on base plane; Lagrange variable coefficient

μ - spacecraft relative instantaneous mass; gravitational constant

τ - constant of integration characterizing time of spacecraft passage through orbital pericenter

Φ - angular range of spacecraft flight along conic section curve

φ - angle of hyperbolic orbit asymptote

ν - true anomaly

Ω - ascending node longitude

ω - angular distance of orbit pericenter from line of ascending node

CHAPTER 1. FUNDAMENTALS OF SPACECRAFT MOTION THEORY

§ 1. ELEMENTS OF ATTRACTION THEORY

The cosmos (interplanetary space) is a medium in which of all /11* the forces of nature acting on a flight vehicle the primary force is that of attraction of celestial bodies. The theory of attraction, the cornerstone of which is Newton's law of universal gravitation, permits quantitative evaluation of the force of attraction of different material bodies. Knowledge of the fundamental viewpoints of this theory and its basic results is necessary for understanding the fundamentals of the spacecraft motion theory.

MATERIAL POINT. NEWTON'S LAW OF UNIVERSAL GRAVITATION

We shall examine the concept of the material point, since in gravity theory and in mechanics every material body is considered in the form of either a material point or an ensemble of material points. A material point is a portion of matter of infinitesimally small dimensions which, however, may have finite mass. Therefore, we can take a geometric point of finite mass as a material point. From the actual viewpoint this concept is purely fictitious, however, in the mechanical sense there exist points having identical meaning with the material point of finite mass. Actually, if a body moves under the action of a force applied to the center of mass the motion will be completely independent of the density and disposition of the material and body shape and will depend only on the amount of matter in the body, i.e., the center of mass moves as if the mass of the entire body were concentrated at this point. In this we see the realization of the material point concept.

* Numbers in the margin indicate pagination in original foreign text.

Material points attract one another. In accord with Newton's law of universal gravity any two material points attract one another with a force directly proportional to the product of the masses of these points and inversely proportional to the square of their relative distance. The magnitude of the force of attraction is found from the formula /12

$$F = f\frac{m_1 m_2}{\Delta^2}, \qquad (1.1.1)$$

where m_1 is the mass of one material point;
m_2 is the mass of the other material point;
Δ is the distance between the material points;
f is a constant of proportionality, termed the attraction constant or gravity constant.

The numerical value of the attraction constant f, whose dimensions are defined by the equality

$$[f] = m^{-1}l^3t^{-2},$$

depends on the choice of the basic units of mass, length, and time.

If we take the astronomical system of measurement units, in which the mass of the Sun is taken as the mass unit, the length unit is the mean distance between the Sun and the center of mass of the Earth + Moon system, and the time unit is the mean solar day, then the constant $f=k^2$ [30, p. 34], where

$$k = 0.01720209895.$$

In this case the coefficient k is called the Gaussian gravity constant.

In the CGS (centimeter, gram, second) system the attraction constant, determined from the calculations, is

$$f = 6.669 \cdot 10^{-8}.$$

The coefficient f is usually determined experimentally, which yields

$$f=6.673\cdot10^{-8}\ \text{cm}^3/(\text{g}\cdot\text{s})\ [30,\ \text{p. } 34].$$

In the solution of cosmonautic problems, in which the Sun or some planet is taken as the central celestial body, it is convenient to use the so-called heliocentric gravitational constant $GS=fm_\odot$ or the planetocentric gravitational constant $GM_{пл}=fm_{пл}$. Only the heliocentric and geocentric gravitational constants are included in the new system of astronomical constants and their numerical values are taken to be [30, p. 34]

$$GS=132718\cdot10^{15}\ \text{m}^3/\text{s}^2$$
$$GE=398603\cdot10^{9}\ \text{m}^3/\text{s}^2.$$

The value of the planetocentric gravitational constant for the remaining planets can be determined by multiplying f by the mass m_{pl} of the corresponding planet. /13

Formula (1.1.1) is symmetric relative to the points M_1 and M_2 and is independent of the choice of coordinate system. However, in the problems of spacecraft flight mechanics and celestial mechanics we examine the components of the attraction force along certain coordinates.

We select the Cartesian coordinate system Oxyz (Figure 1.1.1). The magnitude of the force vector $\bar{F}$ with which the material point $M_1(x_1, y_1, z_1)$ attracts the material point $M_2(x_2, y_2, z_2)$ is determined by the Formula (1.1.1). The distance Δ between the points is by convention always considered to be directed from the attracting point to the attracted point. Therefore the direction of the force $\bar{F}$ is opposite the direction of the vector Δ and we have the equality

$$\bar{F}=-f\frac{m_1m_2}{\Delta^2}\frac{\bar{\Delta}}{\Delta},\qquad(1.1.2)$$

and

$$\bar{F}=F_x\bar{i}+F_y\bar{j}+F_z\bar{k}.$$

The force field caused by mutual attraction of the material points M_1 and M_2 corresponds to the force function

$$U=f\frac{m_1m_2}{\Delta}, \qquad (1.1.3)$$

which is a function of all six coordinates of these points. In this connection the attraction force vector can be defined by the formula

$$\bar{F}=\frac{\partial U}{\partial x}\bar{i}+\frac{\partial U}{\partial y}\bar{j}+\frac{\partial U}{\partial z}\bar{k}, \qquad (1.1.4)$$

i.e.,

$$F_x=\frac{\partial U}{\partial x},\ F_y=\frac{\partial U}{\partial y},\ F_z=\frac{\partial U}{\partial z}. \qquad (1.1.5.)$$

The derivative of the force function with respect to an arbitrary direction has the form

$$\frac{\partial U}{\partial l}=|\bar{F}|\cos(\widehat{\bar{F},\bar{l}}).$$

The force function U is always positive, finite, continuous, and single-valued for any noncoinciding locations of the points M_1 and M_2. If these points approach the same point M of space, so that $M_1 \to M$ and $M_2 \to M$, the function U increases without bound and its limit approaches infinity. If the points M_1 and M_2 separate from one another to infinity the function's derivatives with respect to the coordinates approach zero. The force function U is analytic, i.e., it has continuous derivatives of all orders and is regular at infinity. /14

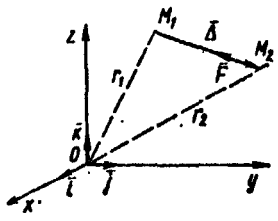

Figure 1.1.1. Diagram of effective material forces

The force function U has a definite physical meaning. If we judge by its dimension, we see from (1.1.3) that the dimension of the force function

coincides with the dimension of energy and work. The value of the force function U coincides with the value of the work which must be expended to overcome the attraction of the attracting mass m_1 and remove the attracted mass m_2 to an infinitely great distance from the mass m_1. The quantity U(x, y, z) is called the field potential energy at the point (x, y, z).

ATTRACTION OF MATERIAL POINT BY A BODY

In studying the motion of a spacecraft it is usually taken to be a material point. In most cases the planets must be considered as material bodies, having quite extensive geometric dimensions and definite shapes with specific mass distribution. In this case we cannot apply directly the law of universal gravity to calculate the attraction of the spacecraft by a celestial body, since it (the body) is now an attracting system consisting of an infinite set of material points.

In order to determine the magnitude of the attraction force with which a celestial body (material point) P acts on the spacecraft (material point) A and to determine the force field caused by the presence of the body P we break it down into a large number of very small elements of mass dm_j, concentrated at the points P_j. These material points attract the material point A with a force which can be determined from the law of universal gravity.

Passing to the limit of the sum of the attraction forces with unbounded increase of the number of elementary masses and unbounded reduction of their volumes, we obtain a definite integral taken over the entire attracting mass m in the form

$$F = fM \int_{(m)} \frac{dm}{\Delta_j^2} \qquad (1.1.6)$$

and thereby we find the body force function

$$U=fM\int_{(m)}\frac{dm}{\Delta}, \tag{1.1.7}$$

where the integration extends over the entire attracting mass and /15 Δ_j is the distance of the attracted material point spacecraft A from the attracting mass element dm, which is equal to the product of the density by the volume element, expressed in the corresponding coordinates. The expression for the force function of the celestial body P at the point A(x, y, z), which defines the spacecraft position, depends on the shape of the body, its internal structure, and the position of the celestial body relative to the adopted coordinate system. However, the total mass of the attracting body is defined in all cases by the formula

$$m=\int_{(m)}dm. \tag{1.1.8}$$

Moreover, the partial derivatives of the force function with respect to the coordinates coincide with the projections of the attractive force on the corresponding axes. Thus, for the x, y, z Cartesian coordinate system we have

$$F_x=\frac{\partial U}{\partial x},\quad F_y=\frac{\partial U}{\partial y},\quad F_z=\frac{\partial U}{\partial z}. \tag{1.1.9}$$

The form and analytic structure of the force function U, expressed by the definite integral (1.1.7), in which the spacecraft and celestial body coordinates play the role of parameters, may be very complex and varied and it can be calculated in elementary functions only in certain exceptional cases and is in general completely noncalculable [12]. The subject matter of attraction theory is study of the properties and nature of force functions defined by integrals of the form (1.1.7) and development of methods for their approximate representation and calculation [12, 18]. Utilizing the results of attraction theory, we turn

directly to discussion of the properties of the force function U, defined by the integral form (1.1.7), in outer space.

The force function is unique, bounded, and continuous in all space and is analytic outside of the attracting masses. The components of the attractive force acting on the spacecraft (point A (x, y, z)), considered as a funciton of the coordinates of the point A, are finite, continuous, and single-valued.

Let Δ be the distance between the material point A and a point constantly associated with the body P. Then with unbounded increase of the distance Δ the product ΔU approaches a definite limit equal to fMm. It follows from this property that when the distance Δ is sufficiently large in comparison with the linear dimensions of the celestial body P the approximate equalities hold /16

$$U = f\frac{Mm}{\Delta}, \quad \frac{\partial U}{\partial \Delta} = -f\frac{Mm}{\Delta^2}. \qquad (1.1.10)$$

This result is understanable: for distances between the material point A and the celestial body P considerably greater than the linear dimensions of the body P, in the integrand of (1.17) Δ can be averaged and in connection with (1.1.9) we obtain the relation (1.1.10).

Corollary 1. A celestial body P of any shape and any structure attracts a spacecraft (material point A) very distant from it as if the entire mass of the body were concentrated at a single point*.

A spacecraft may perform maneuvers near a planet. In this case the force function and the attractive force of the planet

* For celestial bodies we can show analogously that two celestial bodies, completely arbitrary in shape and structure, which are sufficiently distant from one another are mutually attracted nearly as two material points with the corresponding masses [12].

will depend not only on the distance from the spacecraft to the center of the planet but also on the shape, dimensions, and mass distribution of the planet. In the first approximation planets can be taken to be spheres with spherical * or uniform density distribution. This permits taking the integral in formula (1.1.7) in explicit form and obtaining

$$U = f\frac{Mm}{\Delta}$$

and

$$F_x = \frac{\partial U}{\partial x},\quad F_y = \frac{\partial U}{\partial y},\quad F_z = \frac{\partial U}{\partial z},$$

where Δ is the distance from the center of the sphere to the material point.

Corollary 2. A planet (material point) having the shape of a sphere with spherical or uniform density distribution attracts a spacecraft (external material point) as if all the mass of the planet were concentrated at its center.

These results are widely used in spacecraft flight mechanics and permit calculation of celestial body attractive force in convenient and simple form. The assumptions adopted here satisfy completely the accuracies which are necessary in studying spacecraft ballistic design characteristics in the preliminary design stage.

In studying and predicting the motion of artificial planetary /17 satellites, particularly those traveling in low orbits, more exact information on the gravitational field of the planet is necessary and the assumptions adopted previously on planet mass distribution and shape may be too approximate. For example, even direct optical observations show that the flattening of the planets Jupiter and Saturn is an order of magnitude greater than that of the Earth.

* Spherical density distribution is density variation as a function of the distance to the center of a sphere.

At the present time complete information on the shape and dimensions of the Earth as a geoid and of the other planets is not available. However, we can suggest physical models of the planets which approximate with practically any degree of accuracy the planet shape and potential as a function of the order of smallness of the discarded and retained terms. In addition to the spherical potential, we can consider as planetary potential models the potentials of a spheroid, triaxial ellipsoid, asymmetric spheroid, triaxial asymmetric ellipsoid, and so on. The selected model is usually termed the normal gravitational potential and its deviations from the actual potential are termed gravity anomalies. The choice of the normal potential is determined by the posed problem and the required level of solution accuracy.

For the problems of ballistic design and long-term prediction of circumplanetary orbits the assumption on axial symmetry of the bodies, i.e., on symmetric mass distribution relative to the planet's axis of rotation, is valid and yields good results. In this case, as a result of expansion of the planetary potential in spherical functions the gravity potential U can be represented, retaining two terms of the expansion, in the form [1]

$$U=\frac{fm_{pl}}{r}\left[1-\frac{2}{3}J\left(\frac{R_{pl}}{r}\right)^2 P_2(\sin\delta)-\ldots\right]= \\ =\frac{fm_{pl}}{r}\left[1-J\left(\frac{R_{pl}}{r}\right)^2\left(\sin^2\delta-\frac{1}{3}\right)-\ldots\right], \tag{1.1.11}$$

where R_{pl} is the mean equatorial radius of the planet;

r, δ are the spacecraft planetocentric radius vector and inclination;

$P_2=\frac{3\sin^2\delta-1}{2}$ is the second-order Legendre polynomial;

J is a dimensionless constant characterizing the shape of the planet*.

* For the Earth $J_2=\frac{2}{3}J=0.0010827$ [30], Mars J=0.002920, Jupiter J=0.02206, Saturn J=0.02501 [10].

ATTRACTION OF MATERIAL POINT BY A FINITE NUMBER OF MATERIAL BODIES /18

During spacecraft flight in the solar system it is acted on by the attractive force of not one but many celestial bodies. It is important to be able to calculate the resultant of these forces and its components along the coordinate axes. If we consider estimating the resultant of the attractive forces of many celestial bodies we can speak of large spacecraft distance from them. Otherwise we can with good approximation consider only the attractive force of the planet near which the spacecraft is located. Then, denoting by

$$\bar{\varrho}_a = x_a\bar{i} + y_a\bar{j} + z_a\bar{k},\quad \bar{\varrho}_j = x_j\bar{j} + y_j\bar{j} + z_j\bar{k}$$

the radius vector of the spacecraft and the radius vector of the i-th celestial body in the inertial Cartesian coordinate system, in accord with Corollary 1 the resultant of the attractive forces is represented in the form

$$\bar{F} = \frac{\partial U_a}{\partial x_a}\bar{i} + \frac{\partial U_a}{\partial y_a}\bar{j} + \frac{\partial U_a}{\partial z_a}\bar{k}, \qquad (1.1.12)$$

where $U_a = M\sum_{j=1}^{n} f\frac{m_j}{\Delta_{aj}}$

is the force function of the system of material bodies *;

$$\Delta_{aj} = |\bar{\varrho}_a - \bar{\varrho}_j| = [(\bar{\varrho}_a - \bar{\varrho}_j)(\bar{\varrho}_a - \bar{\varrho}_j)]^{1/2};$$

n is the number of material bodies of the system. There $\bar{F}$ and its components can be written as

$$\bar{F} = -fM\sum_{j=1}^{n}\frac{m_j}{\Delta_{aj}^3}(\bar{\varrho}_a - \bar{\varrho}_j), \qquad (1.1.13)$$

---

* The force function of a system of free material points, which celestial bodies are taken to be, differs fundamentally from U_a and is equal to

$$U = \frac{1}{2}f\sum_{i=1}^{n}\sum_{j=1}^{n}\frac{m_i m_j}{\Delta_{ij}},\ \text{where } i \neq j\ [12]. \qquad (1.1.12a)$$

$$\left.\begin{aligned} F_x &= \frac{\partial U_a}{\partial x_a} = -fM \sum_{j=1}^{n} \frac{m_j}{\Delta_{aj}^3}(x_a - x_j), \\ F_y &= \frac{\partial U_a}{\partial y_a} = -fM \sum_{j=1}^{n} \frac{m_j}{\Delta_{aj}^3}(y_a - y_j), \\ F_z &= \frac{\partial U_a}{\partial z_a} = -fM \sum_{j=1}^{n} \frac{m_j}{\Delta_{aj}^3}(z_a - z_j). \end{aligned}\right\} \qquad (1.1.14)$$

§ 2. SPACECRAFT RELATIVE MOTION IN GRAVITY FIELD OF THE SUN AND PLANETARY SYSTEMS. PLANETARY GRAVISPHERES

/19

Spacecraft motion takes place under the influence of forces of various nature; certain forces whose nature and character of action are known can be evaluated quantitatively, others can be evaluated either very approximately or are not amenable to quantitative estimation at all. In the general case the forces acting on a spacecraft can be represented as consisting of the thrust force P, celestial body attractive force F, and external medium* resistance force Q, whose components are not always amenable to quantitative estimation, since the laws and nature of their manifestation have been poorly studied or are not known at all. The differential equation of spacecraft motion in vector form is written as

$$M\ddot{\bar{\rho}}_a = \bar{P} + \bar{F} + \bar{Q}, \qquad (1.2.1)$$

where M is the spacecraft mass;

$\bar{\rho}_a$ is the spacecraft vector.

In studying interplanetary spacecraft flights the external medium resistance force is frequently neglected, since spacecraft motion takes place basically outside the atmosphere and the other

* The forces of resistance of the external medium include, for example, the planetary atmosphere resistance force, the solar ray pressure force, the electromagnetic forces which arise as a result of the presence of various electromagnetic fields in interplanetary space, and so on.

components of the force Q have very little influence on the flight * (and their quantitative evaluation is practically impossible). Therefore, the differential equation of spacecraft motion in vector form will be written as

$$M\ddot{\bar{\varrho}}_a=\bar{P}+\bar{F}. \tag{1.2.2}$$

Spacecraft motion described by (1.2.2) is termed controlled motion, since it can be altered by controlling the rocket engine thrust force vector. With powerplant off spacecraft motion is described by the differential equation

$$M\ddot{\bar{\varrho}}=\bar{F}. \tag{1.2.3}$$

This motion is called ballistic (uncontrolled) spacecraft motion. /20

If we take the Sun and planet systems as material points, then

$$\bar{F}=\frac{\partial U_a}{\partial \varrho_a}=-fM\sum_{j=0}^{n}\frac{m_j}{\Delta_{aj}^3}(\bar{\varrho}_a-\bar{\varrho}_j)$$

(see (1.1.12) and (1.1.13), where $\bar{\rho}_j$ is the radius vector of the j-th celestial body (j=0, 1, ..., 9); $\Delta_{aj}=|\bar{\rho}_a-\bar{\rho}_j|$ is the distance between the j-th celestial body and the spacecraft.

The controlled motion or the active acceleration and deceleration segments on which the energy level required for the vehicle to perform the specified maneuver is reached has a definite influence on selection of the ballistic design characteristics for interplanetary flights. However, the duration of the active segments

* For example, for conventional satellites traveling along quite high circular orbits with values of the coefficient A, expressing the ratio of satellite characteristic area to mass, in the range 0.003-0.3 $m^3/kg\cdot s^2$ the disturbances from light pressure are equal with respect to revolution period to $\Delta P=5\cdot10^{-7}-5\cdot10^{-5}$ sec and with respect to radius change for a single revolution $\Delta r_{max}=0.02-0.2$ m [50].

of the interplanetary flight trajectory may be quite different, depending on spacecraft powerplant type. Spacecraft with liquid rocket engine powerplants have large thrust accelerations, and therefore the required energy level is reached in a few minutes near the departure or arrival planet. However, ballistic flight may last several months or even years, depending on the destination planet. Spacecraft with electrorocket [ERE] powerplants have very small thrust accelerations, and therefore the active acceleration (deceleration) segment is commensurate with the ballistic segment. The methods for solution of the differential equation of controlled motion (1.2.2) are determined to a considerable degree by the duration of the active segments. We shall examine spacecraft with liquid rocket engines in the present volume. This makes it possible to demonstrate and evaluate specific methods for determining the active segments as a function of the required computational accuracy.

In order to find the solution of the differential equation of controlled (1.2.2) or ballistic (1.2.3) motion we need to have information on variation of the planet radius vector $\bar{\rho}_j$ as a function of the flight time t. This information can be obtained in various ways. The simplest technique involves the assumption of Keplerian motion of the planets around the Sun (i.e., motion of the planets under the action of the Sun's attractive force) and on isolatedness of the solar system (i.e., rectilinear and uniform motion of the solar system mass center). For more exact calculations the Equations (1.2.2) and (1.2.3) should be considered together with the differential equations of motion of the planets and the Sun.

However, study of spacecraft motion with account for the influence of the attraction forces of several celestial bodies in the absolute coordinate system is inconvenient and difficult, since astronomical observations yield only the relative positions /21

and velocities of the celestial bodies. Proposals have been made in texts on celestial mechanics [13, 48] that motion of the celestial bodies (planets) be studied in the relative (for example, heliocentric) coordinate system, when the coordinate origin is located at the mass center of one of the celestial bodies (the Sun, for example). Therefore it is better to convert to the differential equations of spacecraft relative motion, when the mass center of the central body * is taken as the coordinate origin.

In order to obtain the differential equation of the controlled relative motion we subtract from the left and right sides of (1.2.2), respectively, the left and right sides of the differential equation of motion of the central body

$$m_0\ddot{\bar{\varrho}}_0=\bar{F}_0,$$

which yields

$$\ddot{\bar{\varrho}}_a-\ddot{\bar{\varrho}}_0=\frac{\bar{P}}{M}+\frac{\bar{F}}{M}-\frac{\bar{F}_0}{m_0}.$$

Hence the differential equation of controlled spacecraft relative motion takes the form

$$\ddot{\bar{R}}_a=\frac{\bar{P}}{M}-\frac{fm_0}{R_a^3}\bar{R}_a-\sum_{j=1}^{n}fm_j\left(\frac{\bar{\Delta}_{aj}}{\Delta_{aj}^3}+\frac{\bar{R}_j}{R_j^3}\right),$$

where

$$\bar{R}_a=\bar{\varrho}_a-\bar{\varrho}_0,\quad \bar{R}_j=\bar{\varrho}_j-\bar{\varrho}_c\quad (j=1,\ldots,n),$$
$$\bar{\Delta}_{aj}=\bar{R}_a-\bar{R}_j.$$

As a consequence of validity of the relation

$$\frac{\bar{\Delta}_{aj}}{\Delta_{aj}^3}+\frac{\bar{R}_j}{R_j^3}=-\bar{\nabla}\left(\frac{1}{\Delta_{aj}}-\frac{\bar{R}_a\bar{R}_j}{R_j^3}\right),$$

where $\bar{\nabla}$ is the gradient operator with respect to the components

* The central body is a celestial body relative to which the motion is examined.

of the vector $\bar{R}_a$, we obtain

$$\ddot{\bar{R}}_a = \frac{\bar{P}}{M} - \frac{fm_0}{R_a^3}\bar{R}_a + \bar{\nabla}R_p. \qquad (1.2.4)$$

The scalar function

$$R_p = \sum_{j=1}^{n} fm_j\left(\frac{1}{\Delta_{aj}} - \frac{\bar{R}_a\bar{R}_j}{R_j^3}\right)$$

characterizes the attractions of the celestial bodies except for the central body and therefore it may be called the perturbing function, since the central body attractive force is dominant. This name is given R_p by analogy with the perturbing functions which arise in celestial mechanics in studying relative motion of the planets [13, p. 110]. The differential Equation (1.2.4) defines the controlled relative motion. The ballistic relative motion is described by the differential equation /22

$$\ddot{\bar{R}}_a = -\frac{fm_0}{R_a^3}\bar{R}_a + \bar{\nabla}R_p, \qquad (1.2.5)$$

obtained from (1.2.4). If the central body is selected properly, in the right sides of (1.2.4) and (1.2.5) $\left|\frac{fm_0}{R_a^3}\bar{R}_a\right| \gg |\bar{\nabla}R_p|$ and the term $|\bar{\nabla}R_p|$ can be treated as the perturbing acceleration arising from the perturbing forces — the attractive forces of the celestial bodies except for the central body. On the basis of this treatment of the attractive forces of the celestial bodies (except for the central body) the relative motion described by (1.2.4) and (1.2.5) is frequently considered as the perturbed relative spacecraft motion. This makes it possible to apply specific analytic and numerical methods to solve (1.2.4) and (1.2.5), which are examined in perturbed motion theory, (see, for example [13, Part 3, Chapters 7-9]).

The differential equations of relative spacecraft motion (1.2.4) and (1.2.5) cannot be integrated in finite form. Various numerical integration techniques, analytic and qualitative methods

of celestial mechanics are used to obtain the solution and spacecraft motion characteristics. In many cases the analytic methods make it possible to find the general or particular solution of the basic differential equation of motion (1.2.5) in infinite converging series form, which permits finding the numerical values of the required characteristics of the motion with any degree of accuracy. The qualitative methods made it possible to establish the general properties of spacecraft motion characteristics without knowledge of the general solution of the differential equation of motion. The distinctive feature of the numerical integration methods is their universality. While application of the analytic methods has definite limitations caused by smallness of the perturbations, limits in the values of spacecraft orbit parameters and so on, in numerical integration of the differential equations of motion no question arises concerning the nature of the spacecraft orbits or magnitude of the perturbations. However, the systematic accumulation of error in the integration process may in certain cases limit the possibilities of the numerical methods in comparison with the analytic methods, which are free of this drawback. When solving specific interplanetary spacecraft flight problems all the methods (analytic, numerical, and qualitative) should be used in conjunction in order to obtain more information on the motion characteristics. When obtaining the solutions of the differential equations of spacecraft relative motion (1.2.4) and (1.2.5) we must not forget that they are approximate. The approximations are caused by two different factors associated with the physical and mathematical nature of the problem solution. The physical reasons for the approximation are due to our level of knowledge of the forces acting and neglect (or impossibility of taking into account) of some of them. The mathematical reasons for the approximations are caused by the methods used to solve the equations of motion. If all these approximations are represented clearly and properly understood, we can avoid excessive accuracy and unnecessary

/23

difficulties in the process of finding the engineering solutions and analysis of the ballistic design characteristics of interplanetary spacecraft.

The way to improvement and simplification of the numerical integration of the differential equations of relative spacecraft motion lies in determining the region of dominant influence on the spacecraft of the attractive force of the celestial body, which should then be considered the central body. This body may be the Sun or any planet. Such a problem has previously arisen in celestial mechanics in studying the motion of comets. Its solution has been reduced to determining the planet sphere of action *.

PLANET SPHERE OF ACTION

The region of space in which, when calculating perturbations, it is advisable to take the planet as the central body and the Sun as the perturbing body is called the planet sphere of action. Quantitative evaluation of this region depends on the estimate of the perturbing acceleration ratio to the central body attractive force acceleration when reducing the general problem to the problem of three-bodies: spacecraft (or celestial body of very small mass), planet, and Sun. Let δS be the perturbing acceleration created by the attractive force of the Sun, and let F be the acceleration from the attractive force of the planet when regarded as the central body; δF is the perturbing acceleration created by the attractive force of the planet and S is the acceleration from the attractive force of the Sun when taken as the central body.

---

* The concept of planet "sphere of action" was introduced into celestial mechanics by Laplace in connection with study of the motion of comets as they approach Jupiter.

The bounding surface of the sphere of action is expressed by the equality

$$\frac{\delta S}{F} = \frac{\delta F}{S}.$$

The surface defined by this equation is very close to a sphere with center at the center of the planet and radius /24

$$\Delta_L = R \left(\frac{m_{pl}}{m_\odot}\right)^{2/5}, \qquad (1.2.6)$$

where R is the mean radius of the planet's orbit. The values of Δ_L for the planets are given in Table 1.1.

TABLE 1.1. PLANETARY GRAVISPHERE RADII*

Planet	Gravisphere radius in $10^6 \cdot$km			
	Δ_L	Δ_H	Δ_K	$\Delta_0=\Delta_{ea}$
Mercury	0,113	0,221	0,367	0,320
Venus	0,616	1,01	1,68	1,46
Earth	0,925	1,49	2,48	2,16
Mars	0,578	1,08	1,80	1,56
Jupiter	48,2	51,9	88,1	76,6
Saturn	54,6	64,3	108,3	94,1
Uranus	51,9	69,6	116 4	101,2
Neptune	87,0	115,4	193,1	167,9
Pluto	37,6	57,4	95,4	83,0

* Translator's note: Commas in numbers represent decimal points.

It should be noted that the introduction of the sphere of action concept in celestial mechanics was directed toward achieving more exact numerical integration results, since this makes it possible to avoid excessively large values of the terms in the right side of the differential equations of motion of the comets.

In cosmonautics improvement of the methods for numerical integration of the differential equations of motion, corresponds

to the requirement for flight trajectory calculation accuracy improvement in the final spacecraft design stage. Improvement of the spacecraft ballistic design methods involves search for simpler techniques for obtaining the required solution with accuracy requirements corresponding to the initial design stage. The solutions of the differential equations of spacecraft ballistic motion can be obtained in closed form, i.e., we can find all six first integrals if we neglect the perturbations and examine spacecraft motion under the influence of only the central body attractive force. The question arises of how accurate is this solution and under what conditions is it necessary when studying the interplanetary trajectory to change over from the planet as the central body to the Sun as the central body, and vice versa. The answer to this question is of considerable interest, since use of the closed solution of the two-body (space- /25
craft-celestial body) problem is very appealing and convenient in engineering practice. It is obvious that this solution will also be acceptable with regard to accuracy in the case of small influence of the perturbations on the exact solution. Thus the problem arises of how to minimize the deviations from the exact solution while remaining within the framework of the two-body problem solutions. We are talking about representing the solar system gravitational field in the form of the gravitational field of the Sun, bounded by the heliogravisurface, and the individual gravitational fields of the planets, each of which is bounded by the gravitational surface of the planet (planetogravisurface). Correct description of the gravisphere boundary surface means finding the minimum of the deviations from the exact solution for the adopted solar system gravitational field model. Here the fundamental factor is the question of the criterion used to evaluate such deviation.

Until recently the planet sphere of action defined by Laplace was widely used as the gravisphere surface boundary in spacecraft

REPRODUCIBILITY OF THE ORIGINAL PAGE IS POOR.

ballistic design practice. In this case it was claimed that the deviations from the exact solution lie within limits which are acceptable for ballistic design. However, as was mentioned previously, the introduction of the concept of planet sphere of action or Laplace gravisphere * was not really intended for solution of problems of this sort — evaluating the two-body problem problem solution. Therefore uncritical use of the Laplace gravisphere in spacecraft ballistic design practice can lead in the future to undesirable systematic errors, particularly in connection with increased requirements on preliminary analysis accuracy. It is true that the question of optimal (correct) planet gravitational surface geometric description still remains an open question. Kislik [26] examined this question in 1964.

KISLIK GRAVISPHERE**

Kislik made use of the capabilities resulting from the existence of the generalized energy integral (Jacobi integral) in the restricted circular three-body problem. The error of the approximate calculation of the generalized energy integral constant (Jacobi constant) was taken as the optimality criterion, the minimum of which was determined. Thereby an attempt was made to approach as closely as possible the solution of the previously formulated general problem. In fact, comparison of the exact and approximate trajectories showed that the calculation errors of the other trajectory parameters (Δa, Δe and so on) at the Kislik gravisphere boundary became on the average minimal for flight from one planet to another. /26

* This name for the planet's sphere of action permits clearer terminological differentiation between this and other planet gravisphere definitions.

** Kislik termed the gravisphere which he defined the "sphere of influence". However, the sphere of action (Laplace gravisphere) is sometimes called by this name in the literature. The names introduced here permit more clear-cut identification of gravispheres defined in various ways.

Without going into the details of the derivation [26], we note that the Kislik gravisphere boundary can be represented as a sphere whose center coincides with the planet and radius Δ_K is defined by the expression

$$\Delta_K = 1.15R\left(\frac{m_{pl}}{m_\odot}\right)^{1/3}. \qquad (1.2.7)$$

The values of Δ_K are given in Table 1.1. The relationship between Δ_L and Δ_K is expressed by the equality

$$\Delta_K = \frac{1,15}{\sqrt[15]{m_{pl}}}\,\Delta_L.$$

Comparison of the Δ_K and Δ_L values shows that the dimensions of the Kislik gravisphere exceed those of the Laplace gravisphere by 2-3 times.

Becuase of the absence of a solution of the general problem on approximate solution accuracy, the region of the space around the planet which is treated as the theoretical satellite existence planet boundary is of interest.

HILL GRAVISPHERE

As a result of study of the solution of the restricted circular three-body problem (spacecraft-planet-Sun) there are found five singular points, the so-called libration points, at which in the case of zero spacecraft flight velocity its acceleration is also zero. Such a singular point (point L_1) also exists on the straight line joining the Sun with the planet, between the Sun and the planet.

The distance of the libration point L_1 from the planet is determined by the following formula [48, p. 312]

$$\Delta_H = R\left(\nu - \frac{1}{3}\nu^2 - \frac{1}{9}\nu^3\right) \approx R\left(\frac{m_{pl}}{3m_\odot}\right)^{1/3}, \qquad (1.2.8)$$

where

$$\nu = \left(\frac{m_{pl}}{3m_\odot}\right)^{1/3}.$$

The numerical values of Δ_H are given in Table 1.1. We term the region of space with center in the planet and radius Δ_H the Hill gravisphere.

The surface of the sphere is a surface of zero velocity. It has several other interesting properties. Let the Jacobi constant — generalized energy integral constant in the three-body problem — on the Hill gravisphere surface be equal to C_1. If the Jacobi constant of the spacecraft ballistic motion is larger than the constant C_1, we can state that it always remains inside the Hill gravisphere. Such stability is termed Hill stability. The surface of the Hill gravisphere can be considered the theoretical boundary of planet satellite existence *. /27

For points located on the Laplace, Hill, and Kislik gravispheres surfaces the maximal values of the ratio $\delta S/F$ are equal to, respectively,

$$\left(\frac{\delta S}{F}\right)_L = 2\left(\frac{m_{pl}}{m_\odot}\right)^{1/5}; \quad \left(\frac{\delta S}{F}\right)_H = \frac{2}{3}; \quad \left(\frac{\delta S}{F}\right)_K = \sqrt{10}. \qquad (1.2.9)$$

In connection with these values of the ratio $\delta S/F$, the region of space around the planet bounded by the surface on which the perturbing acceleration δS caused by the attractive force of the

* It is remarkable that all the natural satellites of the planets in the solar system, except for the four satellites of Jupiter with retrograde motion (VIII, IX, XI, XII), are Hill stable.

Sun is equal to the acceleration F from the attractive force of the planet, when it is taken as the central body is of interest. From the equality $\delta S=F$ we find [48] that this region differs very little from a sphere with center at the center of the planet and radius equal to

$$\Delta_{ea} = R\left(\frac{m_{pl}}{m_\odot}\right)^{1/3}. \qquad (1.2.10)$$

By convention we call the sphere with radius Δ_{ea} the gravisphere of equal gravitational actions or the equal-action gravisphere.

MINIMAL DEVIATION GRAVISPHERE

Of interest is the fact that in spite of somewhat different basic assumptions the Kislik, Hill, and equal-action gravispheres in the first approximation are described with regard to shape by the same expression of the form [see (1.2.7), (1.2.8), (1.2.10)]

$$\Delta_l = k_l R\left(\frac{m_{pl}}{m_\odot}\right)^{1/3}, \qquad (1.2.11)$$

where k_1 are equal to $k_K=1.15$, $k_H=0.7$, $k_{ea}=1.0$, respectively. Therefore, the assumption is valid that the planet gravitational surface corresponding to the solution of the previously formulated general minimal deviation problem can also be represented in the first approximation by a sphere whose radius is expressed by a relation of the form (1.2.11). We shall call this the minimal deviation gravisphere. /28

We shall make several remakks concerning the possible quantitative estimate of the coefficient $k_1=k_0$ for determining the minimal deviation gravisphere radius. We first note that the coefficients k_1 change quite slowly in the following sequence: 0.7, 1.0, 1.15 and lie in a narrow range, the maximal values of the ratios $\left(\frac{\delta S}{F}\right)_{max}$ at the Hill, equal-action, and Kislik gravisphere

surfaces increase markedly in the following sequence: 2/3, 1.0, 3.3. Thus the values of the coefficients change by only a factor of 1.5, while the values of $\left(\frac{\delta S}{F}\right)_{max}$ change by a factor of five. This narrow range of the coefficient k_1 values with large spread of the $\left(\frac{\delta S}{F}\right)_{max}$ values makes it possible to assume that the value of k_0 also lies in the limits $0.7 \leq k_0 \leq 1.2$. However if we take into consideration the absence of a solution of the previously formulated general minimum deviation problem, and the assumptions made in determining the Kislik gravisphere radius [26] and take into account the fundamental role of the influence of the magnitude of the ratio $\delta S/F$ on the onset of approximate solution deviation from the exact solution, then it is reasonable to select the value of the coefficient k_0 as the quadratic mean of k_H, k_{ea}, k_K. Then we obtain

$$k_0 = \left(\frac{k_H^2 + k_{ea}^2 + k_K^2}{3}\right)^{1/2} = 1.$$

Consequently, in the first approximation the minimal deviation gravisphere is quite close to the equal-action gravisphere and its radius is defined by the expression

$$\Delta_0 = \left(\frac{m_{pl}}{m_\odot}\right)^{1/3}. \qquad (1.2.12)$$

§ 3. CONTROLLED AND BALLISTIC SPACECRAFT MOTION IN GRAVITY FIELD OF A SINGLE CELESTIAL BODY

Thus, solution of the differential equations (1.2.4) and (1.2.5) of controlled and ballistic perturbed motion makes it possible to obtain essentially exact information on interplanetary flight trajectory characteristics. If we ignore the errors of control law hardware realization on the active flight segments, the actual flight trajectory will differ very little from the theoretical trajectory. This is evidence not only of the objectivity of our knowledge but also correct evaluation of the external forces

acting on the spacecraft and, specifically, the dominant role of the attractive forces. However we should examine the exact solutions only after at least the preliminary design work has been completed. /29

During spacecraft preliminary design studies it is not really necessary to have information on the motion characteristics more exact than the accuracy of the spacecraft design weight characteristics and the data on constructional materials, fuel, and so on. The problem arises of obtaining approximate solutions of the differential equations of spacecraft motion which permit evaluation of the interplanetary flight characteristics quite simply but with the accuracy necessary for preliminary analyses and determining spacecraft requirements. This can be accomplished by simplifying the right sides of the differential equations of motion (1.2.4) and (1.2.5), if we do not take into account the attractive forces of those celestial bodies (planets, Sun) which for one reason or another (large distances, smaller masses, and so on) have a weak influence on spacecraft motion. Of all the admissible solutions the simplest is achieved in the case when we neglect the perturbing acceleration, setting $R_p=0$. In this case we have fictitious spacecraft motion arising under the influence of the thrust force and the central body attractive force, which we call the unperturbed motion. It approximates in the first approximation the actual motion. There exist definite boundaries (see § 2) within the limits of which it is possible to speak of good approximation of the unperturbed motion characteristics to the actual motion.

In accord with (1.2.4) the controlled unperturbed spacecraft motion is described by the following differential equation

$$\ddot{\bar{R}} = \frac{\bar{P}}{M} - \frac{fm_0}{R^3}\bar{R}, \qquad (1.3.1)$$

where $\bar{R}$ is the spacecraft radius vector;
M is the instantaneous spacecraft mass.

Solutions of the differential equation of controlled unperturbed motion (1.3.1) can be found only if the initial flight conditions and thrust vector variation with time are specified. Unfortunately there are no exact analytic solutions of this equation. However if we examine the differential equation of ballistic unperturbed motion

$$\ddot{\bar{R}} = -\frac{fm_0}{R^3}\bar{R}, \qquad (1.3.2)$$

we can obtain all the necessary first integrals, which describe completely the motion. In finding the first integrals of the ballistic unperturbed motion we usually use the two-body problem solution methods, see for example, [13, Chapter 4, 5], which have been well developed in celestial mechanics. Here the difference is that one of the bodies (the spacecraft) is taken as a body of infinitesimally small mass. The ballistic unperturbed spacecraft motion is also sometimes termed Keplerian motion. /30

In solving interplanetary flight problems it is procedurally more convenient to consider the ballistic motion as the particular controlled motion case with which the interplanetary flight begins. Therefore it would be desirable to find an approach to the solution of the differential equation of controlled unperturbed motion in which the controlled and ballistic motions are compatible and the first integrals of the ballistic motion are determined as a particular case of the general solution.

Let us examine (1.3.1). Taking $\dot{\bar{R}}=\bar{V}$, we write it in the form

$$\dot{\bar{V}} = \frac{\bar{P}}{M} - \frac{fm_0}{R^3}\bar{R}, \qquad (1.3.3)$$

where $\bar{V}$ is the spacecraft velocity vector.

ENERGY INTEGRAL

Multiplying scalarly the left and right sides of (1.3.3) by $2\bar{V}$, we find

$$2\bar{V}\cdot\dot{\bar{V}}=-\frac{2fm_0}{R^3}(\bar{R}\cdot\dot{\bar{R}})+\frac{2(\bar{P}\cdot\bar{V})}{M}.$$

After integration we find

$$V^2-\frac{2fm_0}{R}=h_0+2\int_{t_0}^{t}\frac{(\bar{P}\cdot\bar{V})}{M}\,dt, \qquad (1.3.4)$$

where h_0 is a constant of integration.

Converting to relative mass $\mu=\frac{M}{M_0}$ and taking into account the equality $\bar{P}=-\bar{p}W\dot{M}$, where $\bar{p}$ is the thrust unit vector, we obtain

$$V^2-\frac{2fm_0}{R}=h_0-2W\int_1^{\mu}\frac{(\bar{p}\cdot\bar{V})}{\mu}\,d\mu=h_0-2W\int_1^{\mu}(\bar{p}\cdot\bar{V})\,d\ln\mu, \qquad (1.3.5)$$

since $M(t_0)=M_0$ and therefore $\mu(t_0)=1$. Taking

$$h_u=h_0-2W\int_1^{\mu}(\bar{p}\cdot\bar{V})\,d\ln\mu, \qquad (1.3.6a)$$

we have

$$V^2-\frac{2fm_0}{R}=h_u. \qquad (1.3.7a)$$

We shall call (1.3.7a) the controlled motion energy integral, /31 showing that the total energy (sum of the kinetic and potential energies) per unit spacecraft mass changes in the active segment from h_0 to

$$h_{uf}=h_0-2W\int_1^{\mu_f}(\bar{p}\bar{V})\,d\ln\mu \qquad (1.3.6b)$$

(μ_f is the relative final spacecraft mass), while on the ballistic flight segment it remains constant and equal to h_{uf}. The change of the total energy per unit spacecraft mass during controlled motion takes place as a result of the work performed by the rocket engine thrust force. If the thrust force is always normal to

the velocity vector, since $(\bar{P}\cdot\bar{V}) = 0$ the engine thrust force work will be equal to zero and the total energy per unit spacecraft mass will not change during the entire flight. In order to obtain maximal total energy at the end of the active spacecraft flight segment it is necessary to control the thrust vector so that at each moment of controlled flight time $\frac{(\bar{P}\cdot\bar{V})}{M}=\max$ *.

In the ballistic motion case we represent the energy integral in the form

$$V^2-\frac{2fm_0}{R}=h_{uf}. \qquad (1.3.7b)$$

MOMENT OF MOMENTUM VECTOR INTEGRAL

After multiplying the left and right sides of (1.3.3) vectorially by $\bar{R}$ we have

$$\bar{R}\times\dot{\bar{V}}=\frac{\bar{R}\times\bar{P}}{M}-\frac{fm_0}{R^3}(\bar{R}\times\bar{R}),$$

and as a result of integration we obtain

$$\bar{R}\times\bar{V}=\bar{C}_0+\int_{t_0}^{t}\frac{\bar{R}\times\bar{P}}{M}\,dt=\bar{C}_0-\int_{t_0}^{t}\frac{\bar{R}\times\bar{W}}{M}\,\dot{M}dt, \qquad (1.3.8)$$

where $\bar{C}_0$ is a constant of integration.

By analogy with the transformations performed previousl, we reduce this equation to the form /32

$$\bar{R}\times\bar{V}=\bar{C}_0-W\int_{1}^{\mu}(\bar{R}\times\bar{p})\,d\ln\mu. \qquad (1.3.9)$$

Denoting

$$\bar{C}_\mu=\bar{C}_0-W\int_{1}^{\mu}(\bar{R}\times\bar{p})\,d\ln\mu, \qquad (1.3.10)$$

* It is a mistake to assume that $\max(\bar{P}\cdot\bar{V})=PV(t)$ for $\cos(\hat{\bar{P}\bar{V}})=1$. In this case the flight velocity $V(t)$ will be less than the flight velocity $V_{opt}(t)$ with optimal thrust vector control and $V_{opt}(t)\cos(\hat{\bar{P}\bar{V}})_{opt}>V(t)$.

we write (1.3.9) as

$$\bar{R} \times \bar{V} = \bar{C}_u. \tag{1.3.11a}$$

We shall call this equation the controlled flight moment of momentum vector integral * per unit spacecraft mass. It shows that the moment of momentum vector per unit spacecraft mass changes for controlled motion from $\bar{C}_0$ to $\bar{C}_{uf} = \bar{C}_0 - W\int_0^{\dot{\mu}_f} (\bar{R}\cdot\bar{p})\cdot d \ln \mu$ and after engine cutoff (on the ballistic motion segment) is constant and equal to $\bar{C}_{uf}$. On the controlled motion segment the moment of momentum vector changes because of change of the moment of momentum vector of the discharging rocket engine working fluid particles. If the thrust control law is such that the thrust force vector is always parallel to the spacecraft radius vector, the moment of momentum vector per unit spacecraft mass does not change and will be equal to $\bar{C}_0$ throughout the entire flight.

For ballistic motion the moment of momentum vector integral is expressed in the form

$$\bar{R}\cdot\bar{V} = \bar{C}_{uf}. \tag{1.3.11b}$$

EQUATION OF THE INSTANTANEOUS PLANE

If we multiply the right and left sides of (1.3.1a) scalarly by $\bar{R}$ and by $\bar{V}$ we obtain

$$\bar{R}\cdot\bar{C}_u = 0, \tag{1.3.12}$$

$$\bar{V}\cdot\bar{C}_u = 0. \tag{1.3.13}$$

Consequently the moment of momentum vector $\bar{C}_u$ per unit spacecraft mass is always normal to the instantaneous plane passing

* By analogy with the two-body celestial mechanics problem integrals (1.3.8) can be called the vector area integral.

through the central body center of mass, so that both the spacecraft radius vector $\bar{R}$ and the velocity vector $\bar{V}$ lie in this plane /33 (Figure 1.3.1). The ballistic unperturbed motion takes place in a single plane, which is the instantaneous plane of the end of the active segment and is defined by the equation

$$\bar{R}_a \cdot \bar{C}_{uf} = 0, \qquad (1.3.14)$$

where $\bar{R}_a$ is the radius vector of the end of the active segment.

The cosine of the instantaneous plane inclination to the initial orbit plane is (see Figure 1.3.1)

$$\cos\eta = \frac{\bar{C}_0 \cdot \bar{C}_u}{C_0 \cdot C_u} = \frac{C_0^2 + (\bar{C}_0 \cdot \bar{I}_c)}{C_0^2 + C_0 I_c}, \qquad (1.3.15)$$

where

$$\bar{I}_c = -W \int_1^{\mu} (\bar{R} \times \bar{p})\, d \ln \mu.$$

Therefore, in accord with (1.3.15) the ballistic motion orbital plane inclination to the initial orbital plane will be

$$\eta_f = \arccos \frac{\bar{C}_0 \cdot \bar{C}_{uf}}{C_0 \cdot C_{uf}}. \qquad (1.3.16)$$

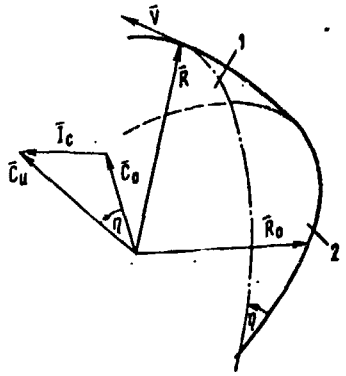

Figure 1.3.1. Determination of instantaneous plane and the vector variable $\bar{C}_u$:
1- instantaneous plane; 2- initial plane

If the thrust vector is controlled so that the vector $\bar{I}_c$ is parallel to the initial moment of momentum vector $\bar{C}_0$, in accord with (1.3.15) $\eta=0$ and the controlled and ballistic motions take place in a single plane — in the initial orbital plane. In this case we have

$$\bar{R}\cdot\bar{C}_0=0 \text{ and } \bar{R}\cdot\bar{I}_c=0.$$

This equation corresponds to the condition $\bar{C}_0\cdot\bar{I}_c = 0$ and therefore $\bar{C}_0\cdot\bar{p} = 0$.

LAPLACE VECTOR INTEGRAL

After multiplying the right and left sides of (1.3.3) vectorially by $\bar{C}_u$ and in view of the equality

$$\bar{R}\times\bar{C}_u=\bar{R}\times(\bar{R}\times\dot{\bar{R}})$$

we obtain

$$\dot{\bar{V}}\times\bar{C}_u=-\frac{fm_0}{R^3}[\bar{R}\times(\bar{R}\times\dot{\bar{R}})]+\frac{\bar{P}\times\bar{C}_u}{M}.$$

Since /34

$$\frac{1}{R^3}[\bar{R}\times(\bar{R}\times\dot{\bar{R}})]=\frac{1}{R^3}[\bar{R}(\bar{R}\cdot\dot{\bar{R}})-\dot{\bar{R}}(\bar{R}\cdot\bar{R})]=$$
$$=-(\dot{\bar{R}}R-\bar{R}\dot{R})/R^2=-\frac{d}{dt}\frac{\bar{R}}{R},$$

after integrating and considering the equality

$$\int(\dot{\bar{V}}\times\bar{C}_u)\,dt=-\int\bar{C}_u\times d\bar{V}=\bar{V}\times\bar{C}_u-\int\bar{V}\times d\bar{C}_u,$$

we have

$$\bar{V}\times\bar{C}_u=fm_0\frac{\bar{R}}{R}+\int_{t_0}^{t}\left(\bar{V}\times\dot{\bar{C}}_u+\frac{\bar{P}\times\bar{C}_u}{M}\right)dt+fm_0\bar{e}_0,$$

where $\bar{e}_0$ is a vector constant of integration.

Denoting

$$fm_0\bar{e}_u = fm_0\bar{e}_0 + \int_{t_0}^{t}\left(\bar{V}\times\dot{\bar{C}}_u + \frac{\bar{P}\times\bar{C}_u}{M}\right)dt,$$

we transform the last equation to the form

$$\bar{V}\times\bar{C}_u = fm_0\frac{\bar{R}}{R} + fm_0\bar{e}_u \qquad (1.3.17)$$

and by analogy with the solution of the two-body problem of celestial mechanics we call it the vector Laplace integral and we call the variable vector $\bar{f}_u = fm_0\bar{e}_u$ the variable Laplace vector of the controlled unperturbed motion. Taking into account in accord with (1.3.8) and (1.3.11) the expressions for the variable vectors $\dot{\bar{C}}_u$ and $\bar{C}_u$, we represent the vector $\bar{e}_u$ as

$$\bar{e}_u = \bar{e}_0 + \frac{1}{fm_0}\int_{t_0}^{t}[\bar{V}\times(\bar{R}\times\bar{P}) + \bar{P}\times(\bar{R}\times\bar{V})]\frac{dt}{M}.$$

Expanding the expression for the triple product, we obtain

$$\bar{e}_u = \bar{e}_0 + \frac{1}{fm_0}\int_{t_0}^{t}[2(\bar{P}\cdot\bar{V})\bar{R} - (\bar{P}\cdot\bar{R})\bar{V} - (\bar{V}\cdot\bar{R})\bar{P}]\frac{dt}{M} \qquad (1.3.18)$$

or, considering the value of the vector $\bar{P}$, we have

$$\bar{e}_u = \bar{e}_0 - \frac{W}{fm_0}\int_{1}^{\mu}[2(\bar{p}\cdot\bar{V})\bar{R} - (\bar{p}\cdot\bar{R})\bar{V} - (\bar{V}\cdot\bar{R})\bar{p}]\,d\ln\mu. \qquad (1.3.19a)$$

For unperturbed ballistic flight the vector $\bar{e}_u$ becomes constant and equal to /35

$$\bar{e}_{uf} = \bar{e}_0 - \frac{W}{fm_0}\int_{1}^{\mu_f}[2(\bar{p}\cdot\bar{V})\bar{R} - (\bar{p}\cdot\bar{R})\bar{V} - (\bar{V}\cdot\bar{R})\bar{p}]\,d\ln\mu, \qquad (1.3.19b)$$

and the Laplace integral has the form

$$\bar{V}\times\bar{C}_{uf} = fm_0\frac{\bar{R}}{R} + fm_0\bar{e}_{uf}. \qquad (1.3.20)$$

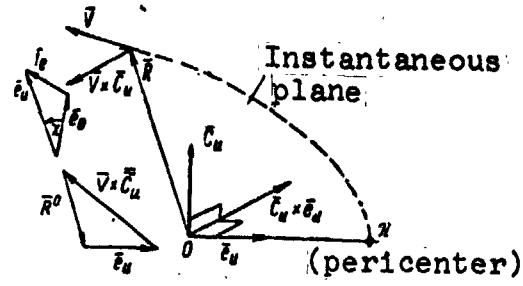

Figure 1.3.2. Scheme of vector relations:
$\bar{R}^0=\frac{\bar{R}}{R}$; $\bar{C}_u=\frac{\bar{C}_u}{fm_0}$

The position of the vector $\bar{e}_u$ in space can be determined by multiphying the left and right sides of (1.3.17) scalarly by $\bar{C}_u$, which leads to the condition

$$\bar{C}_u\cdot\bar{e}_u=0. \tag{1.3.21}$$

Thus the Laplace vector $\bar{e}_u$* is orthogonal to the variable moment of momentum integral $\bar{C}_u$. Therefore the Laplace vector $\bar{e}_u$ always lies in the instantaneous plane (Figure 1.3.2) defined by (1.3.12).

ORBIT EQUATION

Multiplying the right and left sides of (1.3.17) scalarly by $\bar{R}$ and bearing in mind the equality

$$(\bar{V}\times\bar{C}_u)\cdot\bar{R}=(\bar{R}\times\bar{V})\bar{C}_u=\bar{C}_u\cdot\bar{C}_u=C_u^2,$$

we find

$$R+(\bar{R}\cdot\bar{e}_u)=\frac{C_u^2}{fm_0}. \tag{1.3.22}$$

This is the equation of the instantaneous surface at one point of which the spacecraft is located at the given instant

* In the following we shall also call the vector $\bar{e}_u$ the Laplace vector to simplify the terminology.

of time. Together with the equation of the instantaneous plane (1.3.12), the equation of the instantaneous surface (1.3.22) defines the instantaneous controlled motion orbit. Therefore the /36 two equations (1.3.12) and (1.3.22) represent the general equation of the instantaneous orbit, at one point of which the spacecraft is located at the given moment. Equation (1.3.22) defines at each moment of time a second-order surface. Let us examine the form of the surface. The family of planes perpendicular to the instantaneous direction of the variable Laplace vector $\bar{e}_u$ is defined by the equation

$$\bar{R}\cdot\bar{e}_u=d, \tag{1.3.23}$$

where d is the parameter of the family. Then in accord with (1.3.22) we obtain

$$R=\frac{C_u^2}{fm_0}-d, \tag{1.3.24}$$

i.e., the sections of the instantaneous second-order surface (1.3.22) by the family of planes perpendicular to the straight line directed along the instantaneous Laplace vector $\bar{e}_u$ are circles. Consequently, the instantaneous surface (1.3.22) is a second-order surface of revolution around an axis directed along $\bar{e}_u$ and is either an ellipsoid, paraboloid, or hyperboloid of revolution. One focus of this surface coincides with the central body center of mass. Since the instantaneous plane (1.3.12) passes through the axis of rotation of the surface, the instantaneous controlled spacecraft motion orbit is a plane second-order curve, one focus of which coincides with the central body center of mass and the line of apsides (principal or focal axis) of which coincides with the direction of the instantaneous Laplace vector.

The instantaneous Laplace vector $\bar{e}_u$ is always directed toward the orbit instantaneous pericenter — toward the point on the instantaneous orbit located closest to the central body center of mass, taken as the right-hand orbit focus. Taking

the angle between the instantaneous spacecraft radius vector and the instantaneous Laplace vector equal to ν, we write the equation of the instantaneous orbit in the instantaneous plane in accord with (1.3.22) in the form

$$R=\frac{C_u^2/fm_0}{1+e_u\cos\upsilon}. \qquad (1.3.25)$$

This equation is the polar equation of a conic section if we take $p_u = C_u^2/fm_0$ to be the instantaneous orbit focal parameter, e_u the instantaneous orbit eccentricity, ν the instantaneous orbit true anomaly.

Thus the family of three-dimensional controlled motion flight trajectories is located on a surface which is the envelope of the instantaneous ellipsoids, paraboloids, and hyperboloids defined by (1.3.22); in the two-dimensional controlled motion case the flight trajectory is the envelope of the instantaneous ellipses, parabolas, /37 and hyperbolas expressed by (1.3.25).

Therefore the instantaneous conic section of the end of the active segment is the unperturbed ballistic motion orbit expressed by the equation

$$R=\frac{C_{uf}^2/fm_0}{1+e_{uf}\cos\upsilon}=\frac{p_{uf}}{1+e_{uf}\cos\upsilon}. \qquad (1.3.26)$$

The orbit is located in the plane defined by (1.3.14).

The angle χ between the initial and instantaneous Laplace vectors can be found from the equation

$$\cos\chi=\frac{\bar{e}_0\cdot\bar{e}_u}{e_0e_u}=\frac{e_0^2+(\bar{e}_0\cdot\bar{I}_e)}{e_0^2+e_0I_e}, \qquad (1.3.27)$$

where

$$\bar{I}_e=-\frac{W}{fm_0}\int_1^{\mu}[2(\bar{\rho}\cdot\bar{V})\bar{R}-(\bar{\rho}\cdot\bar{R})\bar{V}-(\bar{V}\cdot\bar{R})\bar{\rho}]\,d\ln\mu. \qquad (1.3.28)$$

Then the inclination of the unperturbed ballistic orbit motion Laplace vector to the initial vector $\bar{e}_0$ is

$$\chi_f = \arccos \frac{\bar{e}_0 \cdot \bar{e}_{uf}}{e_0 e_{uf}} = \arccos \frac{e_0^2 + (\bar{e}_0 \cdot \bar{l}_{ef})}{e_0^2 + e_0 l_{ef}}. \qquad (1.3.29)$$

The instantaneous Laplace vector $\bar{e}_u$ will always be parallel to the initial vector if the thrust vector control law is such that the equality is satisfied

$$\bar{e}_0 \times \bar{e}_u = \bar{e}_0 \times \bar{l}_e = 0,$$

which is satisfied when the condition is met

$$2(\bar{p} \cdot \bar{V})(\bar{e}_0 \times \bar{R}) - (\bar{p} \cdot \bar{R})(\bar{e}_0 \times \bar{V}) - (\bar{V} \cdot \bar{R})(\bar{e}_0 \times \bar{p}) = 0. \qquad (1.3.30)$$

The relation obtained can be satisfied for two different thrust vector control laws. If the thrust vector and the velocity vector are both always parallel to the radius vector directed along the line of apsides of the initial orbit, then in view of $\bar{e}_0 \times \bar{R} = \bar{e}_0 \times \bar{V} = \bar{e}_0 \times p = 0$ the relation (1.3.30) is satisfied and $\bar{e}_u = \bar{e}_0$. If the thrust vector $\bar{P}$ is parallel to the velocity vector $\bar{V}$, which is orthogonal to the radius vector $\bar{R}$ directed toward the initial orbit pericenter, the relation (1.3.30) will be satisfied in view of $\bar{e}_0 \times \bar{R} = 0$ and $(\bar{p} \cdot \bar{R}) = (\bar{V} \cdot \bar{R}) = 0$. This is possible with location of the thrust vector in the orbit plane and with impulsive thrust change (i.e., impulsive flight velocity change) at the instantaneous orbit pericenter.

For unperturbed ballistic flight we may be interested in the spacecraft velocity vector $\bar{V}$ dependence on the radius vector, which /38 can be obtained after vector multiplication of the left and right sides of (1.3.20) by $\bar{C}_{uf}$ and several transformations in the form

$$\bar{V} = \frac{f m_0}{C_{uf}} e_{uf} \bar{C}^0_{uf} \times \bar{e}^0_{uf} + \frac{f m_0}{C_{uf}} \bar{C}^0_{uf} \times \bar{R}^0.$$

It is remarkable that the velocity vector $\bar{V}$ is expressed as the sum of two components, constant in magnitude, one of which is perpendicular to the radius vector and equal to fm_0/C_{uf} while the other is perpendicular to the line of apsides and equal to $\frac{fm_0}{c_{uf}} e_{uf}$. Further, considering in accordance with the definition of true anomaly the expression

$$\bar{R}^0 = \bar{e}^0_{uf}\cos \upsilon + (\bar{C}^0_{uf} \cdot \bar{e}^0_{uf}) \sin \upsilon, \qquad (1.3.31a)$$

the preceding equation may be written in the form

$$\bar{V} = \frac{fm_0}{\bar{C}_{uf}} [(e_{uf} + \cos \upsilon)\bar{C}^0_{uf} \cdot \bar{e}^0_{uf} - \bar{e}^0_{uf} \sin \upsilon], \quad (1.3.31b)$$

which shows the dependence of the spacecraft velocity vector $\bar{V}$ for unperturbed ballistic motion on the true anomaly and the vector constants of integration $\bar{C}_{uf}$ and $\bar{e}_{uf}$.

INTERDEPENDENCE OF THE VECTOR VARIABLES $\bar{C}_u$, $\bar{e}_u$, h_u

There is an interdependence between the vector variables $\bar{C}_u$, $\bar{e}_u$ and the variable h_u. Let us find it. After multiplying the right and left sides of (1.3.17) scalarly by $\bar{e}_u$ we have

$$fm_0(\bar{e}_u \cdot \bar{e}_u) = (\bar{V} \times \bar{C}_u) \cdot \bar{e}_u - \frac{fm_0}{R}(\bar{R} \cdot \bar{e}_u).$$

Substituting into this equation the values of $\bar{e}_u$ and $(\bar{R} \cdot \bar{e}_u)$ in accord with (1.3.17) and (1.3.22) and considering the equalities

$$(\bar{V} \times \bar{C}_u) \cdot (\bar{V} \times \bar{C}_u) = (\bar{C}_u \cdot \bar{C}_u) V^2,$$
$$(\bar{V} \times \bar{C}_u) \cdot \bar{R} = (\bar{C}_u \cdot \bar{C}_u),$$

we obtain

$$(\bar{e}_u \cdot \bar{e}_u) = 1 + \frac{(\bar{C}_u \cdot \bar{C}_u)}{(fm_0)^2} h_u$$

or

$$e_u^2 = 1 + \left(\frac{C_u}{fm_0}\right)^2 h_u. \qquad (1.3.32a)$$

Hence we have the equality

$$h_u=(fm_0)^2\frac{(\bar{e}_u\cdot\bar{e}_u)-1}{(\bar{C}_u\cdot\bar{C}_u)}. \qquad (1.3.32b)$$

BALLISTIC MOTION

/39

It is advisable to become more familiar with the characteristics of the ballistic motion, since it encompasses the longest interplanetary flight time interval. The unperturbed ballistic motion is described by the first integrals (1.3.7b), (1.3.11b), (1.3.20). The constants of integration h_{uf}, $\bar{C}_{uf}$, f_{uf} determine completely the orbital plane position, orbit orientation in the plane of motion, and orbit shape and dimensions. It is clear that of the seven scalar quantities h_{uf}, C^i_{uf}, $f^i_{uf}(i=1, 2, 3)$ only five are independent, since, in accord with (1.3.21) and (1.3.32), they are connected by the following relations

$$\bar{C}_{uf}\bar{f}_{uf}=0,\ h_{uf}=\frac{(\bar{f}_{uf}\bar{f}_{uf})-(fm_0)^2}{(\bar{C}_{uf}\bar{C}_{uf})}. \qquad (1.3.33)$$

Therefore in order to form the general integral of the vector equation of motion (1.3.2) we need to find the sixth integral, which contains time explicitly. The condition (1.3.14), characterizing planar ballistic motion, makes it possible to represent the moment of momentum integral (1.3.11b) in the orbit plane in the form $R^2\frac{d\upsilon}{dt}=C_{uf}$, which makes it possible with account for the orbit polar equation (1.3.26) to write the missing (sixth) independent first integral in the form

$$\bar{C}_{uf}\bar{f}_{uf}=0,\ h_{uf}=\frac{(\bar{f}_{uf}\bar{f}_{uf})-(fm_0)^2}{(\bar{C}_{uf}\bar{C}_{uf})}. \qquad (1.3.34a)$$

or

$$t-t_a=\frac{C^3_{uf}}{(fm_0)^2}\int_{\upsilon_a}^{\upsilon}\frac{1}{(1+e\cos\upsilon)^2}\,d\upsilon \qquad (1.3.34b)$$

where $e = |\bar{e}_{uf}| = \frac{|\bar{r}_{uf}|}{fm_0}$ is the ballistic motion orbit eccentricity;

τ is the time of spacecraft passage through the orbit pericenter;

t_a is the powerplant cutoff time or the initial ballistic motion time termed the initial epoch;

υ_a is the spacecraft instantaneous orbit true anomaly at powerplant cutoff.

The integral (1.3.34) is tabulated. However, it is taken differently depending on the type of ballistic motion.

In the elliptic motion case [13, § 2 Chapter 5] (when $V_a^2 < \frac{2fm_0}{R_a}$ and $e < 1$), we obtain /40

$$n(t-t_a)=E-E_a-e(\sin E-\sin E_a) \qquad (1.3.35a)$$

or

$$n(t-\tau)=E-e\sin E, \qquad (1.3.35b)$$

where E is the eccentric anomaly, whose geometric interpretation is given in Figure 1.3.3;

$$n=\sqrt{\frac{fm_0}{a^3}};$$

a is the orbit semimajor axis.

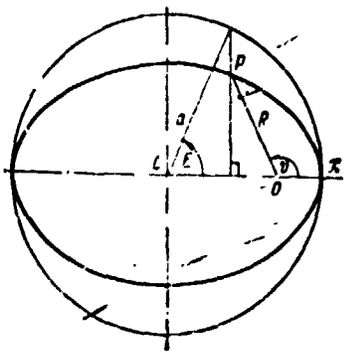

Figure 1.3.3. Geometric interpretation of true anomaly υ and eccentric anomaly E of elliptic orbit

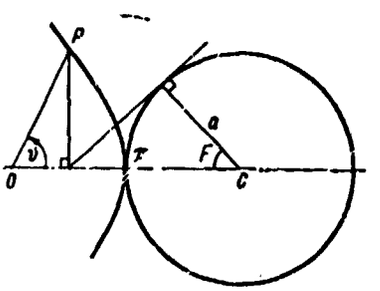

Figure 1.3.4. Geometric interpretation of true anomaly υ and auxiliary variable F of hyperbolic orbit

For <u>hyperbolic motion</u> [13, § 2 Chapter 5] (when $V_a^2 > \frac{2fm_0}{R_a}$ and e > 1) we have

$$n(t-t_a)=e(\operatorname{tg}F-\operatorname{tg}F_a)-\ln\left[\operatorname{tg}\left(\frac{F}{2}+45^\circ\right)\Big/\operatorname{tg}\left(\frac{F_a}{2}+45^\circ\right)\right] \qquad (1.3.36a)$$

or

$$n(t-\tau)=e\operatorname{tg}F-\ln\operatorname{tg}\left(\frac{F}{2}+45^\circ\right), \qquad (1.3.36b)$$

where F is an auxiliary variable whose geometric interpretation is shown in Figure 1.3.4.

If we introduce a new auxiliary variable H, connected with F by the relation /41

$$\operatorname{sh}H=\operatorname{tg}F,$$

we have

$$n(t-t_a)=e(\operatorname{sh}H-\operatorname{sh}H_a)-(H-H_a) \qquad (1.3.37a)$$

or

$$n(t-\tau)=e\operatorname{sh}H-H. \qquad (1.3.37b)$$

In addition to elliptic and hyperbolic spacecraft motion it is possible in principle to examine circular $\left(e=0,\ V_a=\sqrt{\frac{fm_0}{R_a}}\right)$, parabolic $\left(e=1,\ V_a=\sqrt{2\frac{fm_0}{R_a}}\right)$, and rectilinear motion as unperturbed motion. While the last motion (rectilinear) can be treated as degenerate, we must approach the circular and parabolic motions as limiting cases of cases of Keplerian motion. If the elliptic orbit eccentricity is amall (for example, e < 0.02 for R_{av} < 10,000 km) it is convenient to utilize the relations of circular motion theory, considering the circular motion as the first approximation to the elliptic motion, which permits representing the spacecraft coordinates (and velocity components) in the form of an explicit dependence on time [50]

$$v=M+2e\sin M, \qquad (1.3.38)$$

$$R=a(1-e\cos M), \qquad (1.3.39)$$

where $M = \frac{\sqrt{fm_0}}{a^{3/2}}(t-\tau)$. In this case, the approximate estimates for the spacecraft position determination linear errors ΔR in the radial direction and ΔN along the normal to the radius (lying in the orbital plane) may be calculated from the relations [50]

$$|\Delta R| \leqslant e^2 R_{av}, \quad |\Delta N| \leqslant \frac{5}{4} e^2 R_{av}. \qquad (1.3.40)$$

The changeover from the exact elliptic motion formulas to nearly circular motion theory can be considered completely justified for ΔR and ΔN values not exceeding 5-10 km, since the errors arising from the unperturbed motion assumption (neglect of the influence of gravity force field noncentrality, aerodynamic drag, attractive force of the sun, and so on) may reach magnitudes on the order of tens and even hundreds of kilometers. It is clear that circular and nearly circular motion theory can be used in studying ballistic motion characteristics only for artificial satellites of the planets.

Parabolic spacecraft motion is the limiting case of elliptic /42 or hyperbolic motion. In reality parabolic motion can exist as a type of motion only a single instant, transforming under the influence of even very small perturbations into a different type: elliptic or hyperbolic. However the parabolic motion and parabolic velocity, determined from $V_a = \sqrt{\frac{2fm_0}{R_a}}$, are of definite theoretical interest and make it possible to find the limiting artificial planetary satellite motion characteristics and the minimal interplanetary flights energy possibilities. In the parabolic motion case, since $V_a = \sqrt{\frac{2fm_0}{R_a}}$ and $e = 1$ we obtain in accord with (1.3.34)

$$2n(t-t_a) = \left(\operatorname{tg}\frac{v}{2} - \operatorname{tg}\frac{v_a}{2}\right) + \frac{1}{3}\left(\operatorname{tg}^3\frac{v}{2} - \operatorname{tg}^3\frac{v_a}{2}\right) \qquad (1.3.41a)$$

or

$$2n(t-\tau)=\operatorname{tg}\frac{\upsilon}{2}+\frac{1}{3}\operatorname{tg}^3\frac{\upsilon}{2}, \qquad (1.3.41b)$$

which makes it possible to reduce the problem of determining the true anomaly υ for a given moment of time t to solution of the cubic equation

$$\sigma^3+3\sigma-M=0, \qquad (1.3.42)$$

which has a single real solution. Here $\sigma = \operatorname{tg}\frac{\upsilon}{2}$, $M = 6n(t-t_a)$ or $M = 6n(t-\tau)$.

Thus the relations (1.3.7b), (1.3.11b), (1.3.20), (1.3.34) [or in place of (1.3.34) the equations (1.3.35), (1.3.36), (1.3.41)] permit one to determine with account for (1.3.33) the six independent first integrals, and thereby form the general integral of the vector equation of motion (1.3.2). Knowledge of the seven independent constants h_{uf}, C^i_{uf}, f^i_{uf} (i = 1, 2, 3) and t_a or τ makes it possible to determine uniquely spacecraft position in space and at a given moment of time. The six constants of integration which make it possible to determine spacecraft position uniquely at any instant of time during unperturbed ballistic motion are called the spacecraft orbital elements. The subject system of spacecraft orbital elements is complete. Other than this system, it is possible to introduce many other complete spacecraft orbital element systems [50, § 5.4, 5.6], [7, § 1.8], [52, § 3.7, 3.8], defining them in various ways. For the solution of several problems presented in the subsequent chapters it is important to represent the ballistic orbit and motion characteristics as functions of the kinematic parameters at the end of the active segment and t_a.

SYSTEM OF ELEMENTS $\bar{R}_a$, $\bar{V}_a$, t_a /43

Assume that we use as orbital elements the radius vector $\bar{R}_a$ and velocity vector $\bar{V}_a$ at the moment t_a of powerplant cutoff. From the

integral relations (1.3.11) and (1.3.20) and the expression (1.3.32) we find the constants of integration in the form

$$\left.\begin{aligned} \bar{C}_{uf} &= \bar{R}_a \times \bar{V}_a, \\ \bar{f}_{uf} &= \bar{V}_a \times \bar{C}_{uf} - fm_0 \frac{\bar{R}_a}{R_a}, \\ h_{uf} &= \frac{f_{uf}^2 - (fm_0)^2}{C_{uf}^2}. \end{aligned}\right\} \qquad (1.3.43)$$

Then we can find the Keplerian orbital elements (see, for example [13, § 3 Chapter 4]): focal parameter p, eccentricity e, and orbital semimajor axis a from the following relations

$$e = e_{uf} = \left\{\left[\frac{(\bar{R}_a \times \bar{V}_a)^2}{fm_0 R_a} - 1\right]^2 + \left[\frac{|\bar{R}_a \times \bar{V}_a|}{fm_0 R_a}(\bar{R}_a \cdot \bar{V}_a)\right]^2\right\}^{1/2}, \qquad (1.3.44)$$

$$p = p_{uf} = \frac{(\bar{R}_a \times \bar{V}_a)^2}{fm_0}, \quad a = \frac{fm_0}{2\frac{fm_0}{R_a} - V_a^2}, \qquad (1.3.45)$$

where

$$|\bar{R}_a \times \bar{V}_a| = R_a \cdot V_a \cdot \cos\theta_a = \sqrt{(R_a V_a)^2 - (\bar{R}_a \cdot \bar{V}_a)^2} \qquad (1.3.46)$$

and $-\frac{\pi}{2} \leq \theta \leq \frac{\pi}{2}$ (Figure 1.3.5). The elements p, e, a characterize the shape and dimensions of the orbit. Considering the definition of true anomaly, we find

$$\left.\begin{aligned} \cos v_a &= \frac{1}{fm_0 e}\left[\frac{(\bar{R}_a \times \bar{V}_a)^2}{R_a} - fm_0\right], \\ \sin v_a &= \frac{|\bar{R}_a \times \bar{V}_a|}{fm_0 e R_a}(\bar{R}_a \cdot \bar{V}_a). \end{aligned}\right\} \qquad (1.3.47)$$

* The value a < 0 corresponds to the hyperbolic orbit, arbitrarily represented in the form of an imaginary elliptic orbit (ellipse with negative semimajor axis and imaginary semiminor axis), which permits formal application to the hyperbolic orbit of all the relations obtained for motion in elliptic orbit.

Solving (1.3.3.a) and (1.3.31b) for the unit vectors $\bar{e}^0_{uf}$ and $\bar{I}^0 = \bar{C}^0_{uf} \cdot \bar{e}^0_{uf}$ for given $\bar{R}_a$, $\bar{V}_a$, υ_a, we obtain /44

$$\bar{e}^0_{uf} = \frac{e+\cos\upsilon_a}{p}\bar{R}_a - \frac{R_a}{\sqrt{fm_0 p}}\sin\upsilon_a \bar{V}_a, \qquad (1.3.48)$$

$$\bar{l}^0 = \frac{\sin\upsilon_a}{p}\bar{R}_a + \frac{R_a}{\sqrt{fm_0 p}}\cos\upsilon_a \bar{V}_a. \qquad (1.3.49)$$

Here we must bear in mind that the vector $\bar{e}^0_{uf}$ is directed from the center of the celestial body toward the orbit pericenter and the vector $\bar{I}^0$ is perpendicular to it in the orbital plane for a right-hand coordinate system (Figure 1.3.6). It is interesting to note that the orbit pericenter radius vector $\bar{R}_\pi$ is expressed by the formula

$$\bar{R}_\pi = \frac{e+\cos\upsilon_a}{1+e}\bar{R}_a - \sqrt{\frac{p}{fm_0}}\frac{R_a\sin\upsilon_a}{(1+e)}\bar{V}_a, \qquad (1.3.50)$$

easily obtained from (1.3.48) after multiplying its left and right sides by R_π with account for the equality $p=R_\pi(1+e)$.

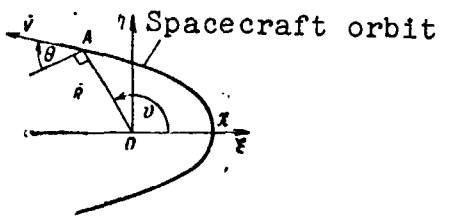

Figure 1.3.5. Orbital polar coordinate system:

υ- is the true anomaly; $\bar{R}$- is the distance from the center of the celestial body to the spacecraft (point A)

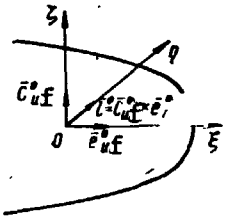

Figure 1.3.6. Orbital coordinate system and its unit vectors

Turning again to (1.3.31a) and (1.3.31b), we can with account for the relations obtained (1.3.48) and (1.3.49) represent the dependence of the instantaneous radius vector $\bar{R}$ and velocity vector $\bar{V}$ on $\bar{R}_a$, $\bar{V}_a$ and the difference $(\upsilon-\upsilon_a)$ in the form

$$\overline{R}=\left\{1-\frac{R}{p}[1-\cos(\upsilon-\upsilon_a)]\right\}\overline{R}_a+\frac{R\cdot R_a}{\sqrt{fm_0p}}\sin(\upsilon-\upsilon_a)\overline{V}_a, \qquad (1.3.51)$$

$$\overline{V}=\left\{\frac{(\overline{R}_a\cdot\overline{V}_a)}{pR_a}[1-\cos(\upsilon-\upsilon_a)]-\frac{1}{R_a}\sqrt{\frac{fm_0}{p}}\sin(\upsilon-\upsilon_a)\right\}\overline{R}_a+ \qquad (1.3.52)$$

$$+\left\{1-\frac{R_a}{p}[1-\cos(\upsilon-\upsilon_a)]\right\}\overline{V}_a. \qquad /45$$

Expressing $\cos\upsilon = \cos[(\upsilon-\upsilon_a)+\upsilon_a]$ and considering the relation

$$(\overline{V}\cdot\overline{R}^0)=\dot{R}=\sqrt{\frac{fm_0}{p}}\,e\sin\upsilon, \qquad (1.3.53)$$

for convenience in calculating the radius R we write the polar equation of the orbit in the form

$$R=\frac{p}{1+\left(\frac{p}{R_a}-1\right)\cos(\upsilon-\upsilon_a)-\frac{1}{R_a}\sqrt{\frac{p}{fm_0}}(\overline{R}_a\cdot\overline{V}_a)\sin(\upsilon-\upsilon_a)}. \qquad (1.3.54)$$

In order to determine the dependence of the instantaneous values of $\overline{R}$, R, $\overline{V}$ on the flight time t for given $\overline{R}_a$, $\overline{V}_a$, t_a it is necessary to utilize the equations (1.3.35a), (1.3.37a) - (1.3.39) and (1.3.41), depending on motion type. However we can obtain other dependences of R and V on t for given $\overline{R}_a$, $\overline{V}_a$, t_a, which are more convenient for calculations but will be directly associated with the specific motion type.

ELLIPTIC MOTION

Bearing in mind the definition of the eccentric anomaly E (see Figure 1.3.3), we obtain

$$R=a(1-e\cos E), \qquad (1.3.55)$$

$$\cos\upsilon=\frac{\cos E-e}{1-e\cos E},\quad \sin\upsilon=\frac{\sqrt{1-e^2}\sin E}{1-e\cos E}, \qquad (1.3.56)$$

$$\cos E=\frac{e+\cos\upsilon}{1+e\cos\upsilon},\quad \sin E=\frac{\sqrt{1-e^2}\sin\upsilon}{1+e\cos\upsilon}, \qquad (1.3.57)$$

Therefore we can write

$$\cos E=\frac{1}{e}\left(1-\frac{R}{a}\right),\quad \sin E=\frac{\overline{R}\cdot\overline{V}}{e\sqrt{fm_0a}}. \qquad (1.3.58)$$

These relations permit representing (1.3.35a) in the following form [7, § 2.6] after several transformations

$$n(t-t_a)=(E-E_a)+\frac{\overline{R}_a\cdot\overline{V}_a}{\sqrt{fm_0a}}[1-\cos(E-E_a)]-\\-\left(1-\frac{R_a}{a}\right)\sin(E-E_a). \tag{1.3.59}$$

Substituting into (1.3.31) and (1.3.48), (1.3.49) the values of cos υ and sin υ from (1.3.56), after some transformations we write (1.3.31) in the form /46

$$\overline{R}=\left\{1-\frac{a}{R_a}[1-\cos(E-E_a)]\right\}\overline{R}_a+\\+\left\{(t-t_a)-\frac{1}{n}[(E-E_a)-\sin(E-E_a)]\right\}\overline{V}_a, \tag{1.3.60}$$

$$\overline{V}=-\frac{\sqrt{fm_0a}}{R\cdot R_a}\sin(E-E_a)\,\overline{R}_a+\left\{1-\frac{a}{R}[1-\cos(E-E_a)]\right\}\overline{V}_a. \tag{1.3.61}$$

HYPERBOLIC MOTION

Similarly, considering the equations

$$R=a(e\operatorname{ch}H-1), \tag{1.3.62}$$

$$\cos\upsilon=\frac{e-\operatorname{ch}H}{e\operatorname{ch}H-1},\quad \sin\upsilon=\frac{\sqrt{e^2-1}\operatorname{sh}H}{e\operatorname{ch}H-1}, \tag{1.3.63}$$

$$\operatorname{ch}H=\frac{e+\cos\upsilon}{1+e\cos\upsilon},\quad \operatorname{sh}H=\frac{\sqrt{e^2-1}\sin\upsilon}{1+e\cos\upsilon}, \tag{1.3.64}$$

we transform (1.3.31) and (1.3.37a) to the form

$$n(t-t_a)=\frac{(\overline{R}_a\cdot\overline{V}_a)}{\sqrt{fm_0a}}[\operatorname{ch}(H-H_a)-1]+\\+\left(1+\frac{R_a}{a}\right)\operatorname{sh}(H-H_a)-(H-H_a), \tag{1.3.65}$$

$$\overline{R}=\left\{1-\frac{a}{R_a}[\operatorname{ch}(H-H_a)-1]\right\}\overline{R}_a+\\+\left\{(t-t_a)-\frac{1}{n}[\operatorname{sh}(H-H_a)-(H-H_a)]\right\}\overline{V}_a, \tag{1.3.66}$$

$$\overline{V}=-\frac{\sqrt{fm_0a}}{R\cdot R_a}\operatorname{sh}(H-H_a)\,\overline{R}_a+\left\{1-\frac{a}{R}[\operatorname{ch}(H-H_a)-1]\right\}\overline{V}_a. \tag{1.3.67}$$

Thus we can determine spacecraft position, its velocity, and velocity components at every instant of time from the values of the

kinematic parameters at the end of the active segment. There is one-to-one correspondence between the sets of kinematic parameters at the end of the active segment and the constants of integration and Keplerian elements.

SPACECRAFT MOTION ALONG CIRCUMPLANETARY ORBITS IN NORMAL GRAVITY FIELD

/47

In many interplanetary flight problems the spacecraft must enter (or leave) an elliptic or circular circumplanetary orbit. The selection of spacecraft characteristics is inseparably linked with calculation of the interplanetary flight trajectory. Moreover, in the case of requirement for definite spacecraft stay time in orbit the problem arises of predicting its motion, since the orbital elements change with time under the influence of the actual gravity field of the planet. Therefore prediction of spacecraft motion in circumplanetary orbit is an inseparable part of the interplanetary flight trajectory calculation problem.

For the motion prediction accuracy level required for orbit design problems we can represent the normal potential of the planet in the form (1.1.11). Then in vector form the differential equation of relative spacecraft ballistic motion in the normal planetary gravity field in accord with (1.2.3) is represented as follows

$$\ddot{\bar{R}} = -\frac{fm_{pl}}{R^3}\bar{R} - \bar{\nabla}U_1, \qquad (1.3.68)$$

where

$$U_1 = \frac{fm_{pl}}{R} J\left(\frac{R_{pl}}{R}\right)^2\left(\frac{1}{3} - \sin^2\delta\right),$$

and

$$\sin\delta = \bar{R}^0 \times \bar{i}_z; \quad \bar{\nabla}(\bar{R}^0\cdot\bar{i}_z) = \frac{1}{R}[\bar{i}_z - (\bar{R}^0\cdot\bar{i}_z)\bar{R}^0]; \quad \bar{\nabla}R = \bar{R}^0; \qquad (1.3.69)$$

$\bar{I}_z$ is the unit vector along the axis of symmetry.

Studies by Kislik [24, 25] led to obtaining an exact solution of this equation of motion,* which is the next approximation in comparison with Keplerian motion theory in describing the actual circumplanetary spacecraft motion in a space without atmosphere.

Using the first integrals obtained by Kislik we can predict spacecraft motion qutie exactly, excluding the influence of gravity force anomalies and solar perturbations. For circumplanetary orbit calculation problems the primary prediction factor is the change of the motion characteristics during the revolution period. Therefore, considering the orbit tc be elliptic through each revolution period (periods), we compare its elements with the reference elliptic orbit constructed using the initial conditions of spacecraft insertion into orbit around the planet. The orbital element variations during the revolution period are called <u>secular variations</u> (perturbations). Analysis of the indicated integrals of the equations of motion showed the absence of secular perturbations of the initial spacecraft orbit elements p, e, i and the existence of secular variations of the elements Ω, ω, τ, obeying the following conditions (see [25], Formulas (111), (120), (130)

/48

$$\frac{d\Omega}{dN} = -2J\frac{\pi R_{\text{pl}}^2}{p^2}\cos i, \tag{1.3.70}$$

$$\frac{d\omega}{dN} = \frac{\pi R_{\text{pl}}^2}{p^2}(5\cos^2 i - 1), \tag{1.3.71}$$

$$\frac{d\tau}{dN} = -J\frac{\pi R_{\text{pl}}^2}{p^2}\sqrt{\frac{p^3}{fm_{\text{pl}}}}(1+5\cos^2 i), \tag{1.3.72}$$

where $\frac{d\Omega}{dN}$, $\frac{d\omega}{dN}$, $\frac{d\tau}{dN}$ are the changes of the elements Ω, ω, τ during a single spacecraft revolution.

---

* The system of differential equations of perturbed APS motion in the general case cannot be integrated in closed form. However, there are various ways to obtain approximate solutions describing satellite motion in a noncentral gravity field. Many such approximate techniques are known at the present time. For example, see [10, 17].

The error of (1.3.71) increases with decrease of e and reaches a maximal value (magnitude of order $\varepsilon^2=JR_{pl}^2/p^2$) for $e(\varepsilon^2)$. Formula (1.3.71) cannot be applied to such orbits, since the error reaches the same order as the quantity $\frac{d\omega}{dN}$ itself. For $e\approx 1$ this error is on the order of ε^4.

Equation (1.3.70) shows that under the influence of the normal planetary gravity field attractive forces the initial ascending node angle changes in the direction opposite spacecraft revolution. The change takes place the more rapidly the lower the orbital plane inclination to the plane of the equator. Under the influence of these same forces the initial elliptic orbit pericenter and its angular distance (1.3.71) change during the period. The pericenter angular distance increases if $(5\cos^2 i - 1) > 0$, i.e., $i < 63.4°$, and decrease if $(5\cos^2 i - 1) < 0$. For the value $i=63.4°$ the pericenter essentially does not alter its position. Thus, under the influence of the attractive forces of a spheroidal planet the position of the original elliptic orbit changes both as a result of orbital plane rotation and as a result of line-of-apsides rotation, i.e., rotation of the orbit itself in the plane, and the orbit shape and dimensions do not experience secular variations. However, the time of spacecraft passage through the ascending node changes during the revolution period.

The spacecraft period of revolution in orbit in the normal /49

planetary gravity field with an error of order $\varepsilon^2 e^2\sqrt{\frac{p^3}{fm_{pl}}}$ is

$$T=2\pi\sqrt{\frac{a^3}{fm_{pl}}}\left\{1-\frac{1}{2}\varepsilon^2\left[(1+5\cos^2 i)+6e\cos\omega+\right.\right.$$
$$\left.\left.+2e\cos(\zeta-\omega)(1-5\cos^2 i)\right]\right\}, \qquad (1.3.73)$$

where

$$\varepsilon=J\frac{R_{pl}^2}{p^2},$$

$$\sin\zeta\approx\frac{\sin\delta}{\sin i}.$$

The draconic period T_d of spacecraft revolution in the normal planetary gravity field (interval of time between two successive spacecraft passages through the ascending node) may be represented in the form

$$T_d = 2\pi \sqrt{\frac{a^3}{fm_{pl}}} \left\{1 - \frac{1}{2} e^2 [(1+5\cos^2 i) - 2e\cos\omega\ (1-5\sin^2 i)]\right\}. \quad (1.3.74)$$

The relations presented above make it possible to predict initial spacecraft orbit evolution near a planet whose normal potential is described by (1.1.11).

CHAPTER 2. INTERPLANETARY TRAJECTORY SEGMENT CALCULATION METHODS /50

§ 1. ORBIT DETERMINATION FROM TWO SPACECRAFT POSITIONS

There are various ways to calculate interplanetary spacecraft flight orbits in the heliosphere. The difference in the methods is caused primarily by the different initial conditions defining the interplanetary flight requirements and mission. In many many cases we can consider the initial conditions to be the spacecraft positions at the beginning and end of the flight, specified by the radii vectors $\bar{R}_1$ and $\bar{R}_2$ (Figure 2.1.1), the launch time t_1, and the flight time $\Delta t_{1,\,2}$. Specification of $\bar{R}_1$, $\bar{R}_2$, t_1, $\Delta t_{1,\,2}$ permits complete determination of the orbit shape and dimensions, position of its plane in space, and its Keplerian elements. However, this involves solving a system of six transcendental equations in six orbital parameters. We shall describe the equations of the subject system and methods for its solution.

LAMBERT METHOD

Lambert equation. Since the modulus $|\bar{C}_{uf}|$ of the vector constant of the vector moment of momentum integral is equal to twice the sectoral velocity, then twice the sector area

$$S_{1,\,2} = C_{uf}(t_2 - t_1) = C_{uf}\Delta t_{1,\,2}.$$

Considering the relation $C_{uf} = \sqrt{fm_0 p}$, we find /51

$$\Delta t_{1,2} = \frac{S_{1,2}}{\sqrt{fm_0 p}} = \frac{a^{3/2}}{\sqrt{fm_0}} \frac{S_{1,2}}{a\sqrt{ap}}. \qquad (2.1.1)$$

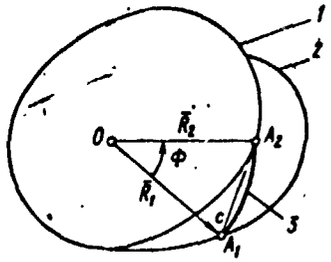

Figure 2.1.1. Interplanetary spacecraft flight orbit:

1- destination planet orbit;
2- departure planet orbit;
3- spacecraft interplanetary flight orbit

We find that the right side of (2.1.1) can be represented as a function of a, R_1, R_2 and c or Φ (see Figure 2.1.1), whose structure is associated with the motion type and the resulting ambiguity in definition of the conic section curve, since the position of the free focus is not fixed [41, Chapter 5]. The reason is that for unknown free focus position (the celestial body is located at the principal focus) through two specified points in space there may pass two specific orbit types with the same value of the total energy h_{uf} per unit spacecraft mass, i.e., for the same value of the semimajor axis a. Therefore the sector area depends not only on the angle Φ but also on the free focus position relative to the chord A_1A_2 (for an elliptic orbit see Figure 2.1.2).

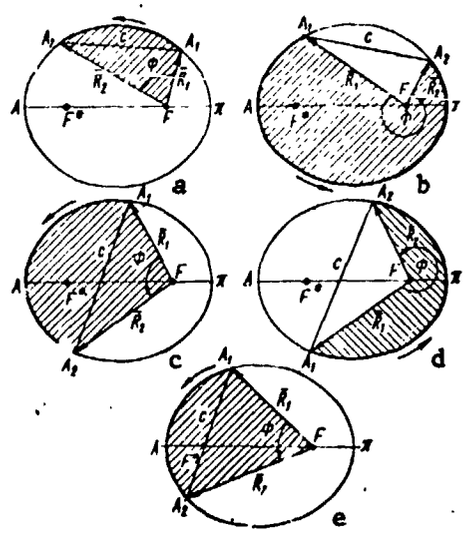

Figure 2.1.2. Elliptic trajectories:

a- $\Phi<\pi$, the chord A_1A_2 does not cross line of apsides between the foci FF*; b- $\Phi>\pi$, $\Phi=2\pi-\Phi_a$, the chord A_1A_2 does not cross the line of apsides between foci FF*; c- $\Phi<\pi$, the chord A_1A_2 crosses the line of apsides between the foci FF*; d- $\Phi>\pi$, $\Phi=2\pi-\Phi_b$, the chord A_1A_2 crosses the line of apsides between the foci FF*; e- the free focus F* lies on the chord A_1A_2

We shall obtain the Lambert equation for elliptic orbits, /52
since interorbital transfers are characterized basically by such orbits. In the general case we have

$$\frac{S_{1,2}}{a\sqrt{ap}} = (\bar{\varepsilon} - \sin\bar{\varepsilon}) - (\bar{\delta} - \sin\bar{\delta}), \qquad (2.1.2)$$

where the values of the angles ε and δ are determined ambiguously from the relations

$$\sin\frac{\bar{\varepsilon}}{2} = \pm\sqrt{\frac{R_1 + R_2 + c}{4a}}, \quad \sin\frac{\bar{\delta}}{2} = \pm\sqrt{\frac{R + R_2 - c}{4a}}. \qquad (2.1.3)$$

However we can calculate the sectoral area using a more definite formula if the values of $\bar{\varepsilon}/2$ and $\bar{\delta}/2$ are selected in the range from zero to $\pi/2$, considering the possible transfer trajectory conditions (see Figure 2.1.2). On the basis of this figure we find

$$(S_1, {}_2)_b = S - (S_1, {}_2)_a,$$
$$(S_1, {}_2)_d = S - (S_1, {}_2)_c,$$

where S is twice the area of the ellipse.

For Figure 2.1.2 a and c we have, respectively, [41]

$$\left.\begin{aligned}\frac{(S_{1,2})_a}{a\sqrt{ap}} &= (\varepsilon - \sin\varepsilon) - (\delta - \sin\delta),\\ \frac{(S_{1,2})_c}{a\sqrt{ap}} &= 2\pi - (\varepsilon - \sin\varepsilon) - (\delta - \sin\delta),\end{aligned}\right\} \qquad (2.1.4)$$

where $0 \leqslant \varepsilon \leqslant \pi$, $0 \leqslant \delta < \pi$ and are expressed by (2.1.3). Then we obtain for Figure 2.1.2 b and d

$$\left.\begin{aligned}\frac{(S_{1,2})_b}{a\sqrt{ap}} &= 2\pi - (\varepsilon - \sin\varepsilon) + (\delta - \sin\delta),\\ \frac{(S_{1,2})_d}{a\sqrt{ap}} &= (\varepsilon - \sin\varepsilon) + (\delta - \sin\delta).\end{aligned}\right\} \qquad (2.1.5)$$

Generalizing these sectoral area calculation cases and considering (2.1.1), we write the Lambert equation in the form

$$\Delta t_{1,2}=\frac{\pi a^{3/2}}{\sqrt{f m_0}}\left\{1+\frac{\operatorname{sign}(\sin\Phi)}{\pi}\left[\pm(\varepsilon-\sin\varepsilon-\pi)-(\delta-\sin\delta)\right]\right\}, \qquad (2.1.6)$$

where the upper sign corresponds to cases a and b, when the chord A_1A_2 does not cross the line of apsides between the foci*. Here sign (sin Φ) is defined as +1, 0, -1, depending on the sign of the argument sin Φ, i.e., /53

$$\operatorname{sign}(\sin\Phi)=\begin{cases}+1 & \sin\Phi>0\\ 0 & \sin\Phi=0\\ -1 & \sin\Phi<0\end{cases}$$

If the spacecraft performs several revolutions in the transfer orbit prior to encounter with the destination planet the flight time will be

$$\Delta t=NT+\Delta t_{1,2},$$

where $T=\frac{2\pi a^{3/2}}{\sqrt{f m_0}}$ is the revolution period in the elliptic transfer orbit;

N is the number of revolutions in the transfer orbit (N=0, 1, ...).

In this case the generalized Lambert equation (2.1.6) reduces to the form

$$\Delta t_{1,2}=\frac{\pi a^{3/2}}{\sqrt{f m_0}}\left\{2N+1+\frac{\operatorname{sign}(\sin\Phi)}{\pi}\left[\pm(\varepsilon-\sin\varepsilon-\pi)-(\delta-\sin\delta)\right]\right\}. \qquad (2.1.7)$$

Consequently, solving the transcendental equation (2.1.7) for known number N of spacecraft revolutions prior to encounter with the destination planet and for given Δt, $\bar{R}_1$, $\bar{R}_2$ we can calculate the transfer orbit semimajor axis a.

---

* Another orbit classification may be encountered. The elliptic trajectories for which the orbit free focus lies outside the segment (area between the trajectory and the straight line A_1A_2) are called elliptic trajectories (orbits) of the first kind (cases a and d). The elliptic trajectories for which the orbit free focus lies within the segment (cases b and c) are called elliptic trajectories (orbits) of the second kind. The elliptic trajectories for which the free focus lies on the chord A_1A_2 are called limit elliptic trajectories (see Figure 2.1.2e).

Equations (2.1.2) and (2.1.7) make it possible to represent the relationship between the difference of the angles (ε-δ) and ($\bar{\varepsilon}$-$\bar{\delta}$) in the form

$$\Delta=\bar{\varepsilon}-\bar{\delta}=(2N+1)\pi+\operatorname{sign}(\sin\Phi)[\pm(\varepsilon-\pi)-\delta]. \qquad (2.1.8)$$

Moreover, determination of the angles $\bar{\varepsilon}$ and $\bar{\delta}$ involves the equality

$$E_2-E_1=\bar{\varepsilon}-\bar{\delta}=\Delta. \qquad (2.1.9)$$

Note. For the hyperbolic orbit the analog of the generalized Lambert equation is the equation

$$\Delta t_{1,2}=\frac{\sqrt{-a^3}}{\sqrt{f m_0}}[(\operatorname{sh}\alpha-\alpha)-(\operatorname{sh}\beta-\beta)\operatorname{sign}(\sin\Phi)], \qquad (2.1.10)$$

which follows from (2.1.1) with account for the possible trajectories (Figure 2.1.3). Here /54

$$\operatorname{sh}\frac{\alpha}{2}=\sqrt{\frac{R_1+R_2+c}{-4a}},\quad \operatorname{sh}\frac{\beta}{2}=\sqrt{\frac{R_1+R_2-c}{-4a}},\quad \alpha\geqslant\beta>0. \qquad (2.1.11)$$

The flight time from point R_1 to point R_2 along the parabolic trajectory (possible cases in Figure 2.1.4) in accord with (2.1.1) is expressed by the Euler equation

$$\Delta t_{\text{par}}=\frac{1}{6\sqrt{f m_0}}[(R_1+R_2+c)^{3/2}-(R_1+R_2-c)^{3/2}\operatorname{sign}(\sin\Phi)]. \qquad (2.1.12)$$

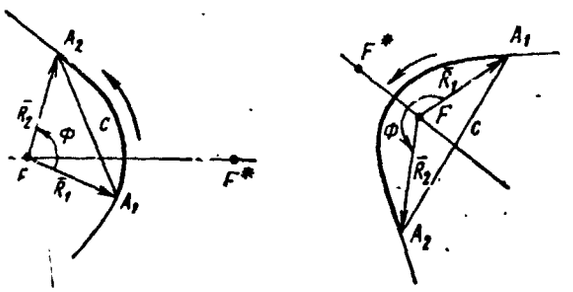

Figure 2.1.3. Hyperbolic trajectories

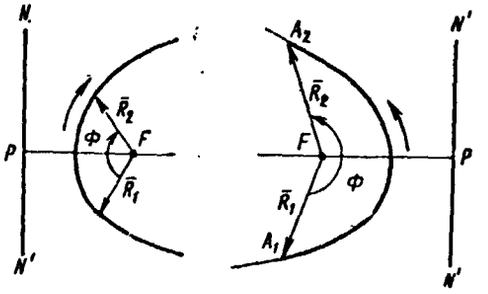

Figure 2.1.4. Parabolic trajectories: NN') directrix; FP) line of apsides

Determination of trajectory type. The solution of the transcendental equations (2.1.7), (2.1.10), (2.1.12) for the semimajor axis a can be carried out by known numerical methods if the motion type, free focus location relative to the chord, and the number N of revolutions in the elliptic orbit case are known in advance. Preliminary determination of these conditions simplifies and facilitates the iteration process. For the same boundary conditions $\bar{R}_1$ and $\bar{R}_2$ satisfaction of the inequality $\Delta t_h < \Delta t_{par} < \Delta t_{el}$ is quite natural. Therefore it is only necessary to calculate Δt_{par} using (2.1.12) in order to determine the orbit type. If the given $\Delta t_{1,2}$ satisfies the inequality

$$\Delta t_{1,2} < \Delta t_{par}, \qquad (2.1.13)$$

transfer from point $\bar{R}_1$ to point $\bar{R}_2$ can be made only along a hyperbolic orbit; however if /55

$$\Delta t_{1,2} > \Delta t_{par}, \qquad (2.1.14)$$

transfer can be realized only along an elliptic orbit.

The limiting elliptic orbit (see Figure 2.1.1e) is characterized by location of the free focus F* on the chord connecting the points $\bar{R}_1$ and $\bar{R}_2$. The focal property of an ellipse permits writing

$$R_1 + F^*A_1 + R_2 + F^*A_2 = 4a$$

and thereby in view $F^*A_1 + F^*A_2 = c$ we can find the limiting elliptic orbit semimajor axis

$$a_m = \frac{1}{4}(R_1 + R_2 + c). \qquad (2.1.15)$$

We note that a_m is the smallest value of the semimajor axis for which an elliptic trajectory is still possible for the given $\bar{R}_1$ and $\bar{R}_2$. According to (2.1.7) and (2.1.3) the flight time for the limiting trajectory is expressed by the formula

$$\Delta t_m = \frac{a_m^{3/2}}{\sqrt{f m_0}}[(2N+1)\pi - \operatorname{sign}(\sin\Phi)(\delta - \sin\delta)], \qquad (2.1.16)$$

where $\sin\frac{\delta}{2}=\sqrt{\frac{R_1+R_2-C}{R_1+R_2+C}}$, $\frac{\delta}{2}<\frac{\pi}{2}$.

The value of Δt_m with satisfaction of the inequality (2.1.14) permits finding the form of the elliptic trajectory. Studies [50, § 8.6, 8.7] for N = 0 show that if the given $\Delta t_{1,2}$ satisfies the inequality

$$\Delta t_{1,2}<\Delta t_m \tag{2.1.17}$$

spacecraft transfer can be accomplished only along an elliptic trajectory of the first kind; nowever if

$$\Delta t_{1,2}>\Delta t_m, \tag{2.1.18}$$

realization of the transfer is possible only along an elliptic trajectory of the second kind.

Thus the Lambert equation (2.1.6) can be written as

$$\Delta t_{1,2}=\frac{a^{3/2}}{\sqrt{fm_0}}[\pi+\operatorname{sign}(\Delta t_m-\Delta t_{1,2})(\varepsilon-\sin\varepsilon-\pi)- -\operatorname{sign}(\sin\Phi)(\delta-\sin\delta)]. \tag{2.1.19}$$

For N ≥ 1 the solution of the generalized Lambert equation (2.1.7) is not unique. However, for $\Delta t_{1,2} < \Delta t_m$ and given N elliptic trajectories of the second kind cannot be realized. Moreover it can be shown that if for given values of $\bar{R}_1$, $\bar{R}_2$, $\Delta t_{1,2}$ solution is possible for some $N=N_k$ then it is also possible for any $N<N_k$. Let k be the maximal value of N for which problem solution is still possible. It is determined from the condition /56

$$\Delta t_k\leqslant\Delta t_{1,2},\quad \Delta t_{k+1}>\Delta t_{1,2},$$

where Δt_k is the minimal possible Δt for N=k. Then the number of possible solutions of (2.1.7) is 2k [50, § 8.7].

Determination of the velocity vectors $\bar{V}_1$ and $\bar{V}_2$. As a result of solution of the Lambert equation we calculate the orbital semi-major axis a. The remaining elements of the orbit and its position in space are now determined considerably more simply. For the solution of this problem it is sufficient to find the velocity vector $\bar{V}_1$ at the initial point. i.e., reduce the problem to determining the orbit from the initial values $\bar{R}_1$ and $\bar{V}_1$, which was solved earlier in § 3 of Chapter 1. It is also useful to have the dependence of the velocity vector $\bar{V}_2$ at the final point on $\bar{R}_1$ and $\bar{R}_2$.

Let us examine (1.3.60) and (1.3.61). Bearing in mind the equality (2.1.9) and the new notations, we represent them in the form

$$\bar{R}_2=\left[1-\frac{a}{R_1}(1-\cos\Delta)\right]\bar{R}_1+\left[\Delta t_{1,2}-\frac{a^{3/2}}{\sqrt{fm_0}}(\Delta-\sin\Delta)\right]\bar{V}_1,$$

$$\bar{V}_2=-\frac{\sqrt{fm_0a}}{R_1R_2}\sin\Delta\,\bar{R}_1+\left[1-\frac{a}{R_2}(1-\cos\Delta)\right]\bar{V}_1,$$

and in accordance with the previous analysis we have for N=0

$$\Delta=\pi+\operatorname{sign}(\Delta t_m-\Delta t_{1,2})(\varepsilon-\pi)-\operatorname{sign}(\sin\Phi)\delta. \qquad (2.1.20)$$

After transformation we obtain

$$\bar{V}_1=A\bar{R}_2- \qquad (2.1.21)$$

$$\bar{V}_2=B_2\bar{R}_2-CR_1, \qquad (2.1.22)$$

where

$$\left.\begin{aligned} A&=\left[\Delta t_{1,2}-\frac{a^{3/2}}{\sqrt{fm_0}}(\Delta-\sin\Delta)\right]^{-1},\\ B_1&=A\left[1-\frac{a}{R_1}(1-\cos\Delta)\right],\quad B_2=A\left[1-\frac{a}{R_2}(1-\cos\Delta)\right],\\ C&=\frac{\sqrt{fm_0a}}{R_1R_2}\sin\Delta+B_1\left[1-\frac{a}{R_2}(1-\cos\Delta)\right]. \end{aligned}\right\} \qquad (2.1.23a)$$

If we consider (2.1.8) and the relation /57

$$\sqrt{R_1R_2}\cos\frac{\Phi}{2}=2a\sin\frac{\bar{\varepsilon}}{2}\sin\frac{\bar{\delta}}{2},$$

the values of the coefficients A, B, C can be also represented in the form

$$\left.\begin{aligned} A&=\frac{\sqrt{fm_0}\sqrt{aR_1R_2}}{2\sin\frac{\Delta}{2}\cos\frac{\Phi}{2}},\quad B_1=A\left(1-\frac{2a}{R_1}\sin^2\frac{\Delta}{2}\right),\\ B_2&=A\left(1-\frac{2a}{R_2}\sin^2\frac{\Delta}{2}\right),\\ C&=\frac{\sqrt{fm_0a}}{R_1R_2}\sin\Delta+B_1\left(1-\frac{2a}{R_2}\sin^2\frac{\Delta}{2}\right).\end{aligned}\right\}\qquad(2.1.23b)$$

Note. For the hyperbolic orbit the values of the coefficients A, B, C are expressed by the relations

$$\left.\begin{aligned} A&=\left[\Delta t_{1,2}-\frac{a^{3/2}}{\sqrt{fm_0}}(\operatorname{sh}\Delta-\Delta)\right]^{-1};\\ B_1&=A\left[1-\frac{a}{R_1}(\operatorname{ch}\Delta-1)\right],\ B_2=A\left[1-\frac{a}{R_2}(\operatorname{ch}\Delta-1)\right];\\ C&=\frac{\sqrt{fm_0a}\sin\Delta}{R_1R_2}+B_1\left[1-\frac{a}{R_2}(\operatorname{ch}\Delta-1)\right],\end{aligned}\right\}\qquad(2.1.24)$$

where $\Delta=\alpha-\beta\operatorname{sign}(\sin\Phi)$.

On the basis of the fact that the tangents to the orbit at the points A_1 and A_2 and the bisector of the central angle Φ have a common point of intersection we can obtain the relation

$$\left.\begin{aligned} \operatorname{tg}\theta_1&=\operatorname{ctg}\frac{\Phi}{2}-\sqrt{\frac{R_1}{R_2}}\cos\frac{\Delta}{2}\operatorname{cosec}\frac{\Phi}{2};\\ \operatorname{tg}\theta_2&=\sqrt{\frac{R_2}{R_1}}\cos\frac{\Delta}{2}\operatorname{cosec}\frac{\Phi}{2}-\operatorname{ctg}\frac{\Phi}{2},\end{aligned}\right\}\qquad(2.1.25)$$

expressing the values of the trajectory angle at the points A_1 and A_2.

Determination of focal parameter p. In many cases a different algorithm for determining the orbit may be more convenient, when after solving the Lambert equation (calculating a) we turn directly to the relations defining the focal parameter p. Using the relations between the true and eccentric anomalies we have

$$\sqrt{R_1R_2}\sin\frac{\Phi}{2}=\sqrt{ap}\sin\frac{1}{2}(E_2-E_1). \qquad (2.1.26)$$

Further, using the equality /58

$$C^2=(\overline{R}_2-\overline{R}_1)^2=2a\sin\frac{E_2-E_1}{2}\sqrt{1-e^2\cos^2\frac{E_2+E_1}{2}}$$

and defining ε and δ in the limits from zero to π with account for the inequalities (2.1.17) and (2.1.18), we find

$$p=\frac{R_1R_2\sin^2\frac{\Phi}{2}}{a\sin^2\frac{\varepsilon-\gamma}{2}} \qquad (2.1.27a)$$

or

$$p=\frac{4aR_1R_2\sin^2\frac{\Phi}{2}}{c^2}\sin^2\frac{\varepsilon+\gamma}{2}, \qquad (2.1.27b)$$

where

$$\gamma=\delta\,[\operatorname{sign}(\Delta t_m-\Delta t_{1,2})\operatorname{sign}(\sin\Phi)].$$

Using (1.3.51) with account for the new notations we obtain the formula defining the velocity vector at the initial point

$$\overline{V}_1=\frac{\sqrt{fm_0p}}{R_1R_2\sin\Phi}\left\{\overline{R}_2-\left[1-\frac{R_2}{p}(1-\cos\Phi)\right]\overline{R}_1\right\}. \qquad (2.1.28)$$

Thus the problem is reduced to finding the orbit from the initial conditions $\overline{R}_1$ and $\overline{V}_1$, which was solved in § 3 of Chapter 1.

Note. For the hyperbolic orbit the focal parameter p is found from the formula

$$p = -\frac{4aR_1R_2\sin^2\frac{\Phi}{2}}{e^2}\,\mathrm{sh}\,\frac{\alpha+\gamma}{2}, \qquad (2.1.29)$$

where

$$\gamma = \beta\,\mathrm{sign}\,(\sin\Phi).$$

In determining the orbit plane position in space we may encounter several solution singularities, when $\Phi=\pi$ and the given spacecraft location points lie on opposite sides of the straight line passing through the attracting center. Geometrically this means that the orbit position is not defined — it may be located in any plane passing through the straight line A_1A_2. In order to determine the orbit we must first specify the position of its plane and direction of motion. Moreover, in this case we may run into difficulties in calculating the other orbital elements, since the denominator vanishes in several of the relations presented above.

υ-ITERATION METHOD

/59

In order to avoid these singularities in the calculation of the elements characterizing orbital shape and dimensions it is well to use iteration with respect to the true anomaly (υ-iteration method). Studies have shown that this method is very convenient and permits determining the orbit quite quickly from two positions and the transfer time interval [52, § 6.5 Chapter 6].

The υ-iteration method involves prespecification of the initial true anomaly υ_1. We then can calculate the orbit eccentricity using the formula

$$e = \left|\frac{R_2 - R_1}{(R_1 - R_2\cos\Phi)\cos\upsilon_1 + R_2\sin\Phi\sin\upsilon_1}\right|, \qquad (2.1.30)$$

obtained from the polar equation of the orbit with account for the two given spacecraft positions. If $\Delta t_{1,\,2} < \Delta t_{par}$ the initial value υ_{10} must satisfy the condition $e \geq 1$, which may be achieved

if it is determined from (2.1.30) for e = 1, i.e., from the equation

$$\cos \upsilon_{10} + \frac{R_2 \sin \Phi}{R_1 - R_2 \cos \Phi} \sin \upsilon_{10} - \frac{R_2 - R_1}{R_1 - R_2 \cos \Phi} = 0. \qquad (2.1.31)$$

In the case $\Delta t_{1,\ 2} > \Delta t_{par}$ the value of υ_{10} must be selected in the range from zero to the value of υ determined from (2.1.31).

The focal parameter p and the orbit semimajor axis are calculated from the relations

$$p = R_1 (1 + e \cos \upsilon_1), \quad a = \frac{p}{1 - e^2}. \qquad (2.1.32)$$

Now we can check the correctness of the selection of υ_{1j} (j = 0, 1, ..., n is the iteration number), using in the relation for e and the relations (2.1.17) and (2.1.18) the equation (2.1.7). or (2.1.10). After satisfying the specified problem solution accuracy, verified by the value of the difference $[\Delta t_{1,2} - (\Delta t)_{\upsilon_j}]$, we use (2.1.8) to calculate the angle Δ. Use of the relations (2.1.21) — (2.1.23) makes it possible to find $\bar{V}_1$ and $\bar{V}_2$ and thereby determine the orbit position from the initial conditions.

In addition to the methods described there are other methods for determining the orbit from two spacecraft positions $\bar{R}_1$, $\bar{R}_2$ and the transfer time $\Delta t_{1,\ 2}$, which have their advantages and disadvantages. The methods discussed are most convenient for analysis of the ballistic design characteristics of spacecraft making interplanetary flights and are characterized by good convergence of the iteration process.

§ 2. "IMPACTING TRAJECTORY" METHOD

The use of the Lambert method to construct the interplanetary flight trajectory characteristic isoline field requires an interpolation program, which increases digitial computer operating time. Therefore a direct method, called the "impacting trajectory" method, was developed to calculate the isoline field. The idea of this method reduces to a boundary value problem in which for the specified launch date t_0, we select those parameters of the Earth sphere of action departure velocity vector $\bar{V}_{\infty 0}$ which ensure spacecraft impact on the destination planet.

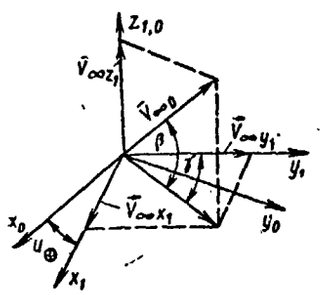

Figure 2.2.1. Kinematic diagram of spacecraft and Earth velocity vector components

Let us examine the case of isoline calculation for specified vector modulus magnitude $|\bar{V}_{\infty 0}|$. We introduce a moving coordinate system whose origin is located at the center of the Earth or planet (Figure 2.2.1). We direct the x_1 axis along the radius vector toward the Sun, the y_1 axis is perpendicular to the x_1 axis and pointed in the direction of motion of the Earth. The x_1 and y_1 axes lie in the ecliptic plane. The z_1 axis completes the right-hand system.

We specify the direction of the vector $\bar{V}_{\infty 0}$ by two angles: the angle β formed by the projection of the vector $\bar{V}_{\infty 0}$ on the x_1, y_1 plane with the vector $\bar{V}_{\infty 0}$; the angle γ between the projection of the vector $\bar{V}_{\infty 0}$ on the plane x_1, y_1 and the y_1 axis. The projections of the vector $\bar{V}_{\infty 0}$ on the axes of this coordinate system (x_1, y_1, x_1) will be

$$\left.\begin{aligned} V_{\infty x_1} &= V_{\infty 0}\cos\beta\sin\gamma;\\ V_{\infty y_1} &= V_{\infty 0}\cos\beta\cos\gamma;\\ V_{\infty z_1} &= V_{\infty 0}\sin\beta. \end{aligned}\right\} \qquad (2.2.1)$$

The projections of the vector $\bar{V}_{\infty 0}$ on the axes of the ecliptic heliocentric coordinate system (x_0, y_0, z_0) are:

$$\left.\begin{aligned} V_{\infty x_0} &= V_{\infty x_1}\cos u_\oplus - V_{\infty y_1}\sin u_\oplus;\\ V_{\infty y_0} &= V_{\infty x_1}\sin u_\oplus + V_{\infty y_1}\cos u_\oplus;\\ V_{\infty z_0} &= V_{\infty z_1}. \end{aligned}\right\} \qquad (2.2.2)$$

Combining the components of the Earth velocity vector and spacecraft velocity vector $\bar{V}_{\infty 0}$ on the sphere of action [Equations (2.2.2)], we obtain the components of the vehicle velocity vector $\bar{V}_0$ in the heliocentric coordinate system at the initial instant of time (launch time) /61

$$\left.\begin{aligned} V_{x_0} &= V_{\oplus x_0} + V_{\infty x_0};\\ V_{y_0} &= V_{\oplus y_0} + V_{\infty y_0};\\ V_{z_0} &= V_{\oplus z_0} + V_{\infty z_0}. \end{aligned}\right\} \qquad (2.2.3)$$

Knowing the initial conditions x_0, y_0, z_0, V_{x_0}, V_{y_0}, V_{z_0}, using well-known formulas we find the spacecraft transfer orbit elements: a, e, Ω, i, ω, which makes it possible to find the spacecraft coordinates x_f, y_f, z_f at the final moment as a function of transfer time Δt and determine the distance between the spacecraft and the target planet from the formula

$$\Delta R = \sqrt{(x_{pl}-x_f)^2 + (y_{pl}-y_f)^2 + (z_{pl}-z_f)^2}. \qquad (2.2.4)$$

With increase of the flight time (from $\Delta t_0 = 0$) the miss distance ΔR for fixed values of β and γ will have a minimum for some value $\Delta t = \Delta t_m$. By altering in a definite fashion the values of β and γ we can reduce the miss distance ΔR to the specified encounter accuracy ΔR_{per} (Figure 2.2.2).

Thus the problem reduces to finding the unknown quantities Δt_m, β_m, γ_m. There are several methods for solving problems of this sort. Studies have shown that search convergence improves

if we use a combination of the steepest descent gradient method with respect to the parameters β and γ and variation of Δt. The essence of the algorithm is as follows.

If $\Delta R=\Delta R(\beta, \gamma)$ is the function being optimized and

$$\operatorname{grad}\Delta R=\left\{\frac{\partial\Delta R}{\partial\beta},\ \frac{\partial\Delta R}{\partial\gamma}\right\},$$

then to find the minimum we must move along the direction opposite the gradient.

The step in the parameters β and γ is found from the formulas

$$\Delta\beta=\frac{\partial\Delta R/\partial\beta}{\frac{\partial\Delta R}{\partial\gamma}\sqrt{\left(\frac{\partial\Delta R/\partial\gamma}{\partial\Delta R/\partial\beta}\right)^2+\left(\frac{\partial\Delta R/\partial\beta}{\partial\Delta R/\partial\gamma}\right)^2}};$$

$$\Delta\gamma=\frac{\partial\Delta R/\partial\gamma}{\frac{\partial\Delta R}{\partial\beta}\sqrt{\left(\frac{\partial\Delta R/\partial\gamma}{\partial\Delta R/\partial\beta}\right)^2+\left(\frac{\partial\Delta R/\partial\beta}{\partial\Delta R/\partial\gamma}\right)^2}}.$$

This step is regulated automatically as the solution is approached. After 5-6 steps the process usually converges to the specified accuracy with respect to ΔR (ΔR_{per}=1,000 km). Thus for given launch date t_0 and $V_{\infty 0}$ values of t_m, β_m, γ_m are determined, which form an impacting trajectory. The computation time is reduced when approximating the function being optimized by a three-point parabola. /62

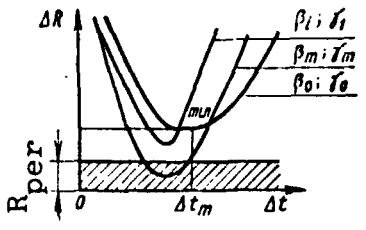

Figure 2.2.2. Schematic of impacting trajectory method computation process

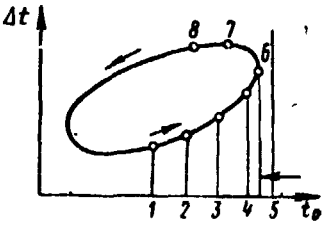

Figure 2.2.3. Schematic of computational process for constructing flight trajectory characteristic isolines

By varying the launch date t_0 we can determine the quantities Δt, β, γ corresponding to the specified velocity vector modulus isolines (Figure 2.2.3).

W en constructing a closed isoline, from the moment 5 for t_0 with the given $V_{\infty 0}$ impact will not be obtaine'l (the search process converges to $\Delta R > \Delta R_{per}$). In this case we seek the point 6 (see Figure 2.2.3) lying on the vertical tangent (return with fractional step δt_0). After this the sign of the step change δt_0 is reversed and points 7, 8, and so on are calculated. The search process at subsequent points is abbreviated considerably if we take as the zero approximations the parameters Δt_m, β_m, γ_m of the preceding point. This isoline construction algorithm ensures unimodality of the gradient search region. The flight trajectory isoline field can be calculated in this fashion along the first semiorbit (transfer angle $\Phi \geq \pi$).

In order to calculate the second semiorbit ($\Phi \geq \pi$) isoline field the value of Δt_0 in the isoline point search process must be selected so that the first trajectory obviously lies in the second semi-orbit trajectory region.

The isolines of the other parameters (β and γ) can be constructed similarly without altering the method logic.

Use of the impacting trajectory metnod also makes it possible to determine the initial kinematic parameters of the heliocentric trajectory segment in the exact formulation with account for finite planet sphere of action dimensions and the influence of various perturbations.

§ 3. APPROXIMATE METHOD FOR SOLVING THE DIFFERENTIAL EQUATIONS OF CONTROLLED SPACECRAFT MOTION

/63

If we take the integrals in the right sides of (1.3.6), (1.3.10), (1.3.19), i.e., if we determine h_u, $\bar{C}_u$, $\bar{e}_u$ as functions of the kinematic parameters, relative instantaneous weight μ, and initial spacecraft thrust-weight ratio n_0, the relations (1.3.7a), (1.3.11a), (1.3.17) become the basis for analysis of the spacecraft ballistic design characteristics. For a given thrust vector control law such solutions can be obtained exactly only by one of the numerical methods and the results will depend on the initial thrust-weight ratio n_0 and final relative weight μ_f. All this make makes analysis of the spacecraft ballistic design characteristics difficult.

In order to find the optimal spacecraft ballistic design characteristics it is necessary to use optimal flight vehicle design theory [43, Chapter 3], based on variational calculus and numerical methods for solving boundary value problems.

Particularly marked in the initial design stage is the numerical method weakness associated with the fact that while yielding quite exact answers they do little to expose the essence of the problem. In the stage of preliminary spacecraft design and initial interplanetary flight trajectory calculations it is most important that the designers and mathematicians study the essential approximate solution aspects which will aid them in identifying the determining elements and parameters and finding rational ways to realize the general project concept. Here an important role will be played by the approximate methods for solution of the differential equations of the controlled motion, whose degree of accuracy must satisfy the preliminary design requirements.

The preliminary analysis of spacecraft interplanetary flight trajectories is sometimes based on the impulsive approximation, which does not take into account the finite duration of the active segments in the planet's sphere of action and replaces the finite thrust applied in the course of a definite time by a thrust impulse of zero duration which leads to stepwise change of the flight velocity.

However, the impulsive approximation does not always meet the accuracy requirements and does not permit identifying the influence of such an important basic spacecraft parameter as the initial thrust-weight ratio n_0 on the ballistic design characteristics. The methods based on approximate definite integral calculating techniques are more fruitful and encompass a wide range of requirements.

ACTIVE SPACECRAFT ACCELERATION SEGMENT /64

According to (1.3.6b) the value of h_{uf} at the final point of the active flight segment is

$$h_{uf} = h_0 - 2W \int_0^{\mu_f} (\bar{p}\cdot\bar{v})\, d\ln\mu.$$

After integration by parts we find

$$h_{uf} = h_0 - 2W\left[(\bar{p}\cdot\bar{v})_a \ln\mu_f - \int_{(\bar{p}\cdot\bar{v})_0}^{(\bar{p}\cdot\bar{v})_a} \ln\mu\, d(\bar{p}\cdot\bar{v})\right].$$

In the case of continuous increase (decrease) of the scalar quantity $(p\cdot\bar{v})$ with time, using the mean value theorem *, we obtain

$$h_{uf} = h_0 - 2W\left[(\bar{p}\cdot\bar{v})_a \ln\mu_f - a_e \ln\mu_f\left[(\bar{p}\cdot\bar{v})_a - (\bar{p}\cdot\bar{v})_0\right]\right], \qquad (2.3.1)$$

* See, for example, G.M. Fikhtengol'ts, Osnovy Matematicheskogo Analiza (Fundamentals of Mathematical Analysis), Vol. 1, GITTL, 1956 (§ 2, Chapter 11).

where

$$a_e = \frac{(\ln \mu)_e}{\ln \mu_f};$$

$(\ln\mu)_e$ is the intermediate value of $\ln\mu$ on the interval $[(\bar{p}\cdot\bar{v})_0, (\bar{p}\cdot\bar{v})_a]$.

Then the controlled motion energy integral (1.3.7a) for the moment of active segment termination is written in the form

$$v_a^2 - \frac{2fm_0}{r_a} = h_0 - 2\left[(1-a_e)(\bar{p}\cdot\bar{v})_a + a_e(\bar{p}\cdot\bar{v})_0\right] W \ln\mu_f. \qquad (2.3.2)$$

We transform the moment of momentum vector integral (1.3.11a) similarily. As a result of integrating the right side of (1.3.10) we find

$$\bar{C}_{uf} = \bar{C}_0 - W\left[(\bar{r}\times\bar{p})_a \ln\mu_f - a_m \ln\mu_f\right](\bar{r}\times\bar{p})_a - (\bar{r}\times\bar{p})_0, \qquad (2.3.3)$$

where

$$a_m = \frac{(\ln\mu)_m}{\ln\mu_f},$$

$(\ln\mu)_m$ is the intermediate value of $\ln\mu$ on the integration interval $[(\bar{r}\times\bar{p})_0, (\bar{r}\times\bar{p})_a]$.

Considering (2.3.3), we represent the moment of momentum vector integral (1.3.11a) for the time t_a by the formula

$$(\bar{r}\times\bar{v})_a = \bar{C}_0 - \left[(1-a_m)(\bar{r}\times\bar{p})_a + a_m(\bar{r}\times\bar{p})_0\right] W \ln\mu_f. \qquad (2.3.4)$$

Since the intermediate values $(\ln\mu)_e$ and $(\ln\mu)_m$ are determined in the region /65

$$0 \leqslant (-\ln\mu)_e < (-\ln\mu_f), \quad 0 \leqslant (-\ln\mu)_m < (-\ln\mu_f),$$

the functions a_e and a_m can vary in the limits

$$0 < a_e < 1, \quad 0 < a_m < 1. \qquad (2.3.5)$$

In the case of exact representation of a_e and a_m as functions of $\ln \mu_f$ (or $\ln \mu$) the relations (2.3.2) and (2.3.4) are exact *. Unfortunately the acquisition of this information involves only calculation of the integrals (1.3.7a) and (1.3.11a), which is equivalent to numerical integration of the system. However, another approach is possible: construction of the approximate dependences of a_e and a_m on μ_f and n_0 for different thrust vector variation laws. In this case the relations (2.3.2) and (2.3.4) will now be approximate and their accuracy is influenced in a definite fashion by the accuracy of construction of the a_e and a_m relations. Studies have shown that for the commonly used thrust vector variation laws the accuracy of the construction of the dependences of a_e and a_m on μ_f and n_0 in the range of their realistic values for spacecraft with liquid rocket engines has very little influence on the accuracy of the solution of the energy integral and the moment of momentum vector integral, represented in the form of the relations (2.3.2) and (2.3.4). Therefore, this method for approximate solution of the differential equations of controlled spacecraft motion is convenient and easily visualized and permits achieving quite simply the spacecraft ballistic design characteristic determination accuracy required for preliminary design purposes. Let us examine the approximate solutions of the relations (2.3.2) and (2.3.4) for known thrust vector control laws.

FLIGHT IN INITIAL ORBIT PLANE

Let us assume controlled spacecraft acceleration (deceleration) in a circumplanetary orbit plane. The initial orbit is specified by the constants h_0, $\bar{c}_0$, $\bar{e}_0$. Since the motion is planar the angle between the thrust vector $\bar{p}$ and the velocity vector $\bar{v}$ is expressed by the angle of attack α, and the angle between the

* The solution accuracy is limited by the conditions of satisfaction of the mean value theorem.

thrust vector $\bar{p}$ and the radius vector $\bar{r}$ is expressed by the angle $\gamma = \frac{\pi}{2} - (\theta + \alpha)$ (Figure 2.3.1).

Determination of v_a. We write the energy integral (2.3.2) in the form

$$v_a^2 - \frac{2fm_0}{r_a} + 2v_a(1-a_e)W\cos\alpha_a \ln\mu_f - \\ -(h_0 - 2v_0 a_e W\cos\alpha_0 \ln\mu_f) = 0. \tag{2.3.6}$$

Taking /66

$$\left.\begin{aligned} &v_{id\,a} = 1 - w\cos\alpha_a \ln\mu_f;\ v_{ea} = 1 - a_e w\cos\alpha_a \ln\mu_f; \\ &\tilde{v}_a = \frac{v_a}{v_0};\ \tilde{v}^2_{cir.o} = \frac{fm_0/r_0}{v_0^2}; \\ &w = \frac{W}{v_0};\quad \tilde{r}_a = \frac{r_a}{r_0}, \end{aligned}\right\} \tag{2.3.7}$$

we transform the energy integral (2.3.6) for planar controlled motion to the form

$$\tilde{v}_a = (v_{id\,a} - v_{ea}) + v_{ea}\left\{1 - \frac{2}{v_{ea}^2}\left[\tilde{v}^2_{cir.o}\left(1 - \frac{1}{\tilde{r}_a}\right) - \right.\right. \\ \left.\left. - [(\cos\alpha_a - \cos\alpha_0)a_e + (0.5 - a_e)w\cos^2\alpha_a \ln\mu_f]w\ln\mu_f\right]\right\}^{1/2}. \tag{2.3.8}$$

Expanding the radical into a series and retaining only the first term of the expansion, we obtain

$$\tilde{v}_a = v_{id\,a} - \frac{\tilde{v}^2_{cir.o}\left(1 - \frac{1}{\tilde{r}_a}\right) - [(\cos\alpha_a - \cos\alpha_0)a_e + (0.5 - a_e)w\cos^2\alpha_a \ln\mu_f]w\ln\mu_f}{v_{ea}}. \tag{2.3.9}$$

Studies have shown that regardless of the known $\alpha(t)$ laws* variation the values of a_e are close to 0.5. Therefore (2.3.9) can be represented in the $n_0 \geqslant 0.1$ and $\mu_f \geqslant 0.05$ approximate form

$$\tilde{v}_a = v_{id\,a} - \frac{1}{v_{ea}}\left[\tilde{v}^2_{cir.o}\left(1 - \frac{1}{r_a}\right) - (\cos\alpha_a - \cos\alpha_0)a_e w\ln\mu_f\right]. \tag{2.3.10}$$

* The calculations were made for tangential, transversal, and optimal (providing max h_{uf}) $\alpha(t)$ variation laws.

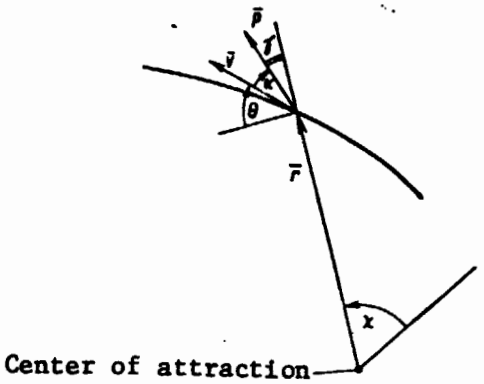

Figure 2.3.1. Kinematics of active segment

In many cases $\cos \alpha_a \approx \cos \alpha_0$, which makes it possible to obtain a new approximation in the form /67

$$\tilde{v}_a = v_{ida} - \frac{\tilde{v}^2_{cir.o}}{v_{ea}}\left(1 - \frac{1}{r_a}\right). \qquad (2.3.11)$$

Considering that in the first approximation for $n_0 > 0.1$ the values of $\tilde{r}_a$ are close to unity, we can calculate $\tilde{v}_a$ for determining the zero approximation from the formula

$$\tilde{v}_a = v_{ida} = 1 - \omega \cos \alpha_a \ln \mu_f, \qquad (2.3.12)$$

where the true velocity lies in the limits

$$(1 - w \cos \alpha \ln \mu_f) - \frac{v^2_{cir.o}}{v_{ea}}(1 - 1/r_a) < \tilde{v}_a < (1 - w \cos \alpha_a \ln \mu_f). \qquad (2.3.13)$$

Thus the relations (2.3.8) - (2.3.12) for known $\alpha(t)$ variation law define with different degree of approximation the dependence of v_a on $\tilde{r}_a$, μ_f, n_0, where the dependence on n_0 is manifested through a_e and $\tilde{r}_a$.

Determination of θ_a. We represent the moment of momentum vector integral (2.3.4) for planar controlled motion in the form

$$r_a v_a \cos \theta_a = C_v - [(1 - a_m) r_a \cos(\theta_a + \alpha_a) + a_m r_0 \cos(\theta_0 + \alpha_0)] W \ln \mu_f. \qquad (2.3.14)$$

Converting to relative quantities, after simple transformations we obtain

$$\cos\theta_a = \frac{\cos\theta_0 - [a_m \cos(\theta_0 + \alpha_0) - \tilde{r}_a(1 - a_m)\sin\theta_a \sin\alpha_a]\, w \ln\mu_f}{\tilde{r}_a[\tilde{v}_a + (1 - a_m)\, w \cos\alpha_a \ln\mu_f]}. \qquad (2.3.15)$$

For a given $\alpha(t)$ variation law (2.3.15) expresses the dependence of θ_a on $\tilde{r}_a$, μ_f, n_0, the dependence on n_0 being manifested through $\tilde{r}_a$, a_e and a_m. Consequently, in order to determine the dependence of $\tilde{v}_a$ and θ_a on μ_f and n_0 it is necessary to find the dependence of $\tilde{r}_a$ on these parameters. It can be found by various methods appropriate to the specific $\alpha(t)$ variation law.

We note first of all that the method for deriving the equations (2.3.8) and (2.3.15) can be used to calculate the instantaneous values of v and θ along the spacecraft flight trajectory if a_e and a_m correspond to those $(\ln\mu)_e$ and $(\ln\mu)_m$ which satisfy the inequalities

$$0 < (\ln\mu)_e < \ln\mu, \quad 0 < (\ln\mu)_m < \ln\mu,$$

where μ is the instantaneous relative weight.

With this in mind we find /68

$$\tilde{v} = (v_{id} - v_e) + v_e\left\{1 - \frac{2}{v_e}\left[\tilde{v}^2_{cir.o}\left(1 - \frac{1}{\tilde{n}}\right) - [(\cos\alpha - \cos\alpha_0)a_e + (0.5 - a_e)\, w \cos^2\alpha \ln\mu]\, w \ln\mu\right]\right\}^{1/2}; \qquad (2.3.16)$$

$$\cos\theta = \frac{\cos\theta_0 - [a_m \cos(\theta_0 + \alpha_0) - \tilde{r}(1 - a_m)\sin\theta \sin\alpha]\, w \ln\mu}{\tilde{r}[\tilde{v} + (1 - a_m)\, w \cos\alpha \ln\mu]}, \qquad (2.1.17)$$

where $v_{id} = 1 - w\cos\alpha\ln\mu$, $v_e = 1 - a_e w\cos\alpha\ln\mu$; $\tilde{v}$, θ, α, are the instantaneous velocity, trajectory angle, and angle of attack.

Formulas (2.3.16) and (2.3.17) express for known thrust vector control law $\alpha(t)$ the dependence of the instantaneous flight velocity $\tilde{v}$ and trajectory angle θ on the instantaneous radius $\tilde{r}$ and relative weight μ. Thus the active segment will be defined if the depen-

dence of the instantaneous radius r on the instantaneous relative weight μ is found. The solution of this problem with any particular degree of approximation is associated with the specific thrust vector control law α(t).

TANGENTIAL CONTROL LAW

The tangential thrust vector control law [$\alpha(t)=0$] is of interest in that with respect to results it is quite close to the optimal law, for which the overall energy per unit spacecraft mass at the end of the active flight segment (the quantity h_{uf}) reaches the maximal value for given μ_f. Usually the launch orbit (parking orbit) is circular $\left(v_0=\sqrt{\frac{fm_0}{r_0}},\ \theta_0=0\right)$.

Determination of $\tilde{v}_a$ and $\tilde{v}$. Equation (2.3.8) simplifies and takes the form

$$\tilde{v}_a=(\tilde{v}_{id\,a}-v_{ea})+v_{ea}\left\{1-\frac{2}{v_{ea}^2}\left[\left(1-\frac{1}{\tilde{r}_a}\right)-(0{,}5-a_e)(w\ln\mu_f)^2\right]\right\}^{1/2}. \qquad (2.3.18)$$

Retaining only the first term of the series expansion of the radical and considering that $a_e \approx 0.5$, we obtain

$$\tilde{v}_a=(1-w\ln\mu_f)-\frac{1-\frac{1}{\tilde{r}_a}}{1-a_e w\ln\mu_f}. \qquad (2.3.19)$$

Using similar simplifications, we reduce (2.3.16) to the form /69

$$\tilde{v}=(1-w\ln\mu)-\frac{1-\frac{1}{\tilde{r}}}{1-a_e w\ln\mu}. \qquad (2.3.20)$$

Determination of θ_a and θ. We transform (2.3.15) and (2.3.17) to the form

$$\cos\theta_a=\frac{1-a_m w\ln\mu_f}{\tilde{r}_a\left[\tilde{v}_a+(1-a_m)w\ln\mu_f\right]}; \qquad (2.3.21)$$

$$\cos\theta = \frac{1 - a_m w \ln\mu}{\tilde{r}\left[\tilde{v} + (1 - a_m) w \ln\mu\right]}. \qquad (2.3.22)$$

Substituting into (2.3.21) and (2.3.22) the values of v_a and v from (2.3.19) and (2.3.20), respectively, we obtain

$$\cos\theta_a = \frac{v_{ea} v_{ma}}{\tilde{r}_a\left[v_{ea} v_{ma} - \left(1 - \frac{1}{\tilde{r}_a}\right)\right]}; \qquad (2.3.23)$$

$$\cos\theta = \frac{v_e v_m}{\tilde{r}\left[v_e v_m - \left(1 - \frac{1}{\tilde{r}}\right)\right]}, \qquad (2.3.24)$$

where $v_m = 1 - a_m w \ln\mu$, $v_{ma} = 1 - a_m w \ln\mu_f$;

$v_e = 1 - a_e w \ln\mu$, $v_{ea} = 1 - a_e w \ln\mu_f$.

Determination of $\tilde{r}_a$ and $\tilde{r}$. The active segments of spacecraft with high-thrust engines (liquid and solid rocket engines) have short duration. Calculations show that for $n_0 \geq 0.1$ and $\mu_f \geq 0.05$ the inequalities hold

$$h_a = \frac{r_a - r_0}{r_0} < 1 \quad \text{and} \quad \theta_a < \frac{\pi}{4}.$$

In this connection, expanding the right side of (2.3.14) into a series in h and neglecting terms of higher than second order of smallness we obtain

$$\frac{v_e v_m}{\tilde{r}\left[v_e v_m - \left(1 - \frac{1}{\tilde{r}}\right)\right]} = 1 - \frac{v_e v_m - 1}{v_e v_m}(h - h^2).$$

With account for the expansion of cos θ into a series in θ and retaining only the first term, we transform (2.3.24) to the form

$$\theta = \left[2\,\frac{v_e v_m - 1}{v_e v_m}(h - h^2)\right]^{1/2}. \qquad (2.3.25)$$

Since the kinematic relation /70

$$\dot{r} = v \sin \theta,$$

holds and the relative mass variation rate

$$\dot{\mu} = -\frac{n_0}{P_{sp}},$$

we can write

$$\frac{dh}{d\mu} = -\frac{w}{n_0 \tilde{r}_0^2} \tilde{v} \sin \theta$$

or, with account for the assumptions made on the angle θ we obtain

$$\frac{dh}{d\mu} = -\frac{w}{n_0 \tilde{r}_0^2} \tilde{v}\theta,$$

where

$$\tilde{r}_0 = \frac{r_0}{R_e}.$$

Substituting into this equation the value of θ from (2.3.25), we have

$$\frac{dh}{d\mu} = -\sqrt{2}\frac{d \cdot v}{n_0}\left[\left(1 - \frac{1}{v_e v_m}\right)(h - h^2)\right]^{1/2},$$

where

$$d = \frac{w}{\tilde{r}_0^2}.$$

Considering that the errors introduced decrease upon integration, we substitute into the right side of this equation in place of $\tilde{v}$ its first approximation. Then we obtain

$$\int_0^h \frac{dh}{\sqrt{h(1-h)}} = -\sqrt{2}\frac{d}{n_0}\int_1^\mu (1 - w \ln \mu) \times$$

$$\times \sqrt{1 - \frac{1}{(1 - a_e w \ln \mu)(1 - a_m w \ln \mu)}}\, d\mu.$$

Taking into account the equality *

$$\int_0^h \frac{dh}{\sqrt{h(1-h)}} = -\arcsin(1-2h)\Big|_0^h = \arccos(1-2h),$$

we find /71

$$h = \frac{1 - \cos\left(\sqrt{2}\frac{d}{n_0} I_r\right)}{2}$$

* I.S. Gradshteyn and I.M. Ryzhik, Tablitsy Integralov, Summ, Ryadov i Proizvedeniy (Tables of Integrals, Sums, Series, and Products), Fizmatgiz Press, No. 2261, 1963.

or

$$\tilde{r} = 1 + \frac{1 - \cos\left(\frac{\sqrt{2}\,d}{n_0} I_r\right)}{2} = 1 + \sin^2\left(\frac{\sigma}{n_0} I_r\right), \qquad (2.3.26)$$

where $\sigma = \frac{1}{\sqrt{2}} d$,

$$I_r = -\int_1^{\mu} (1 - w \ln \mu) \sqrt{1 - \frac{1}{(1 - a_e w \ln \mu)(1 - a_m w \ln \mu)}}\, d\mu. \qquad (2.3.27)$$

For the final point of the active segment we obtain

$$\tilde{r}_a = 1 + \sin^2\left(\frac{\sigma}{n_0} I_{ra}\right), \qquad (2.3.28)$$

where

$$I_{ra} = -\int_1^{\mu_f} (1 - w \ln \mu) \sqrt{1 - \frac{1}{(1 - a_e w \ln \mu)(1 - a_m w \ln \mu)}}\, d\mu. \qquad (2.3.29)$$

Thus determination of the instantaneous radius $\tilde{r}$ and its final value $\tilde{r}_a$ and its final value $\tilde{r}_a$ as a function of μ is reduced to calculating the quadratures (2.3.27) and (2.3.29), numerical methods for calculating which are simple and well known. It is true that these quadratures may also be expressed analytically with any degree of approximation. A very important property of (2.3.26) and (2.3.28) is the weak influence of deviations of a_e and a_m from their "average" values, taken to be constant for the range $\mu_f \le \mu \le 1$, on the accuracy of the $\tilde{r}$ and $\tilde{r}_a$ calculation. Table 2.1 shows the errors $\left(\Delta r = \left|\frac{\tilde{r}_{a\,ex} - \tilde{r}_a}{\tilde{r}_{a\,ex}}\right| \cdot 100\%\right)$ of r_a calculation using the approximate formula (2.3.28) corresponding to $\mu_f = 0.1$ and $n_0 = 0.2$ for different and characteristic values of a_e and a_m, taken to be constant in the range $0.1 \le \mu_f \le 1$ *. Thanks to this property we can select those values of

* The calculations were made for the following initial conditions: circular launch orbit radius R_0=6571 km, specific thrust P_{sp}=350 s.

a_e and a_m, constant for any μ_f in the range $0.1 \leq \mu_f \leq 1$ and in view of the weak dependence of a_e and a_m on n_0 for any value of n_0 for any value of n_0 in the range $n_0 \geq 0.2$, for which the $\tilde{v}_a$, θ_a, $\tilde{r}_a$ (or $\tilde{v}$, θ, $\tilde{r}$) calculation errors are minimal and quite acceptable for ballistic design calculations. The studies made permit recommending the following values /72

$$a_e=0.5,\ a_m=0.64. \tag{2.3.30}$$

Incidentally, removing the ambiguity using the L'Hôpital rule, we can show that for $\mu = 1$ from (2.3.19) $a_e = 0.5$ and a_e changes very little with decrease of μ.

TABLE 2.1

a_e \ a_m	0.6	0.62	0.64	0.68
0.48	0.92	0.57	0.23	0.43
0.5	0.50	0.22	0.12	0.77

Tables 2.2 and 2.3 show the errors *

$$\left(\Delta v_a=\left|\frac{\tilde{v}_a\text{ex}-\tilde{v}_a}{\tilde{v}_a\text{ex}}\right|\cdot 100\%;\quad \Delta\cos\theta_a=\left|\frac{\cos\theta_a\text{ex}-\cos\theta_a}{\cos\theta_a\text{ex}}\right|\cdot 100\%;\right.$$

$$\left.\Delta r=\left|\frac{\tilde{r}_a\text{ex}-\tilde{r}_a}{\tilde{r}_a\text{ex}}\right|\cdot 100\%\right)$$

of the $\tilde{v}_a$, $\cos\theta_a$, $\tilde{r}_a$ calculations using the approximate formulas (2.3.18), (2.3.19), (2.3.21), (2.3.23), (2.3.28) for selected constant values of a_e and a_m in comparison with the exact $\tilde{v}_{a\text{ex}}$, $\cos\theta_{a\text{ ex}}$ and $\tilde{r}_{a\text{ ex}}$ calculations for different values of n_0 and μ_f. We see good accuracy of the subject approximate calculation method, satisfying completely the requirements imposed on ballistic

* The calculations were made for Table 2.2 with P_{sp}=350 s and form Table 2.3 with P_{sp}=450 s. The upper values in the boxes apply to calculations using formulas (2.3.18) and (2.3.21).

TABLE 2.2

/73

n_0	μ_f	Δr_a,%	$\Delta \cos \theta_a$,%	Δr_α,%
0.2	0.5	0.43 / 0.60	0.67 / 0.49	1.07
	0.4	0.21 / 0.65	0.99 / 0.5	1.18
	0.3	0.23 / 0.66	0.96 / 0.06	0.87
	0.2	0.47 / 0 89	0.05 / 1.7	0.2
	0.1	0.3 / 1.73	2.99 / 4.5	0.12
0.4	0.5	0.19 / 0.21	0.22 / 0.21	0.41
	0.4	0.23 / 0.28	0.41 / 0.41	0.64
	0.3	0.21 / 0.28	0.6 / 0.52	0.85
	0.2	0.13 / 0.27	0.64 / 0.16	0.96
	0.1	0.12 / 0.32	0.01 / 0.24	0.80
0.8	0.5	0.06 / 0.06	0.06 / 0.06	0.11
	0.4	0.07 / 0.19	0.12 / 0.11	0.19
	0.3	0.08 / 0.46	0.19 / 0.18	0.29
	0.2	0.08 / 0.96	0.26 / 0.24	0.39
	0.1	0.08 / 1.9	0.2 / 0.16	0.46

TABLE 2.3

/74

n_0	μ_f	Δv_a, %	$\Delta \cos \vartheta_a$, %	ΔJ_a, %
0,2	0,5	0,14 / 0,74	1,21 / 0,54	0,27
	0,4	0,53 / 0,81	1,34 / 0,21	0,80
	0,3	0,87 / 1,25	0,54 / 2,02	0,19
	0,2	0,15 / 2,55	1,23 / 4,12	1,14
	0,1	3,06 / 4,75	1,84 / 3,31	7,15
0,4	0,5	0,27 / 0,31	0,51 / 0,46	0,76
	0,4	0,22 / 0,34	0,64 / 0,70	1,06
	0,3	0,06 / 0,31	1,03 / 0,75	1,19
	0,2	0,092 / 0,31	0,66 / 0,17	1,02
	0,1	0,13 / 0,60	1,11 / ,70	1,57
0,8	0,5	0,09 / 0,09	0 / .4	0,23
	0,4	0,1 / 0,11	0,27 /	,38
	0,3	0,1 / 0,12	0,42 / 0,40	0,54
	0,2	0,07 / 0,11	0,5 / 0,47	0,68
	0,1	0,071 / 0,13	0,24 / 0,19	0,70

design calculation accuracy in the spacecraft preliminary design stage. The results obtained permit tabulation of the quadrature I_r as a function of μ for the selected values n_0 and μ_f, which facilitates and simplifies considerably the calculations.

Determination of polar angle χ_a. The kinematic equation /75

$$\frac{d\chi}{dt} = \frac{v}{r}\cos\theta$$

is represented in the form

$$\frac{d\chi}{d\mu} = -\frac{d}{n_0}\frac{\tilde{v}\cos\theta}{\tilde{r}}.$$

Substituting into this equation the values of $\tilde{v}$, $\cos\theta$, $\tilde{r}$ from (2.3.20), (2.3.22), (2.3.26), we obtain

$$\frac{d\chi}{d\mu} = -\frac{d}{n_0}\frac{\left[1+\left(1-\frac{1}{v_e v_{id}}\right)\sin^2\frac{\sigma}{n_0}I_r\right]v_{id}}{\left[1+\left(1-\frac{1}{v_e v_m}\right)\sin^2\frac{\sigma}{n_0}I_r\right]\left(1+\sin^2\frac{\sigma}{n_0}I_r\right)^2}.$$

Thus the calculation of χ_a reduces to calculating the quadrature

$$\chi_a = -\frac{d}{n_0}\int_1^{\mu_f}\frac{\left[1+\left(1-\frac{1}{v_e v_{id}}\right)\sin^2\frac{\sigma}{n_0}I_r\right]v_{id}}{\left[1+\left(1-\frac{1}{v_e v_m}\right)\sin^2\frac{\sigma}{n_0}I_r\right]\left(1+\sin^2\frac{\sigma}{n_0}I_r\right)^2}d\mu. \qquad (2.3.31)$$

with good degree of accuracy it can be represented in the form

$$\chi_a = -\frac{d}{n_0}\int_1^{\mu_f}\frac{v_{id}}{\left(1+\sin^2\frac{\sigma}{n_0}I_r\right)^2}d\mu. \qquad (2.3.32)$$

After expanding the integrand into a series we find

$$\chi_a = -\frac{d}{n_0}\int_1^{\mu_f} v_{id}\left[1-2\left(\frac{\sigma}{n_0}I_r\right)^2+3\left(\frac{\sigma}{n_0}I_r\right)^4-4\left(\frac{\sigma}{n_0}I_r\right)^6-\ldots\right]d\mu.$$

As a result we have

$$\chi_a = \frac{d}{n_0}\left[(1+w)(1-\mu_f)+\mu_f w\ln\mu_f-2\left(\frac{\sigma}{n_0}\right)^2 I_{\chi 2}+\right.$$
$$\left.+3\left(\frac{\sigma}{n_0}\right)^4 I_{\chi 4}-4\left(\frac{\sigma}{n_0}\right)^6 I_{\chi 6}+5\left(\frac{\sigma}{n_0}\right)^8 I_{\chi 8}\right], \qquad (2.3.33)$$

where

$$I_{\chi 2}=-\int_{f}^{\mu_f} v_{1d} I_r^2 d\mu; \quad I_{\chi 4}=-\int_{f}^{\mu_f} v_{1d} I_r^4 d\mu;$$
$$I_{\chi 6}=-\int_{f}^{\mu_f} v_{1d} I_r^6 d\mu; \quad I_{\chi 8}=-\int_{s}^{\mu_f} v_{1d} I_r^8 d\mu. \qquad (2.3.34)$$

Formulas (2.3.31) - (2.3.33) permit calculating with varying degree of accuracy the values of the polar angle χ at the end of controlled spacecraft flight as a function of μ_f and n_0. The expression (2.3.31) yields relatively better accuracy. More convenient for operational calculations and analysis of the ballistic design characteristics is the formula (2.3.33), since the values of the integrals (2.3.34) depend (for the same values of w) only on μ_f, which permits them to be tabulated. The calculation errors for P_{sp}=350 s arising when calculating χ_a using this formula are shown in Table 2.4. /76

TABLE 2.4

n_0 \ μ_e	0,5	0,4	0,3	0,2	0,1
0,2	0,55	0,56	0,14	0,26	0,30
0,4	0,20	0,32	0,41	0,43	0,26

Thus the method used in the present section to solve the controlled motion integrals has made it possible to find for the tangential thrust vector control law an acceptable approximation to the analytic dependences of $\tilde{v}_a$, θ_a, $\tilde{r}_a$, γ_a on the basic spacecraft design parameters μ_f and n_0.

Determination of h_{uf}, C_{uf}, e_{uf}. The results obtained make it possible to find directly the dependence of the constants of integration h_{uf}, C_{uf}, e_{uf} on μ_f and n_0. Since for the case of controlled motion in a stationary plane

$$h_{uf}=v_a^2-\frac{2fm_0}{r_a};$$

$$C_{uf}=v_a r_a\cos\theta_a,$$

after substituting into these equations the values of v_a, r_a, $\cos\theta_a$ from (2.3.19), (2.3.23), (2.3.28) and simple transformations we obtain

$$\frac{h_{uf}}{h_0}=\frac{\left[1+\left(1-\frac{1}{v_{ea}v_{ida}}\right)\sin^2\frac{a}{n_0}I_{ra}\right]^2 v_{ida}^2}{\left(1+\sin^2\frac{a}{n_0}I_{ra}\right)^2}-\frac{2}{1+\sin^2\frac{a}{n_0}I_{ra}}; \qquad (2.3.35)$$

$$\frac{C_{uf}}{C_0}=\frac{1+\left(1-\frac{1}{v_{ea}v_{ida}}\right)\sin^2\frac{a}{n_0}I_{ra}}{1+\left(1-\frac{1}{v_{ea}v_{ma}}\right)\sin^2\frac{a}{n_0}I_{ra}}v_{ida}\left(1+\sin^2\frac{a}{n_0}I_{ra}\right). \qquad (2.3.36)$$

We note that in the first approximation we can determine /77
C_{uf} from the formula

$$\frac{C_{uf}}{C_0}=v_{ida} \qquad (2.3.37)$$

with a calculation error not exceeding 5-8%.

According to (1.3.32a) the constant e_{uf} is defined by the relation

$$e_{uf}=\sqrt{1+\left(\frac{C_{uf}}{fm_0}\right)^2 h_{uf}}. \qquad (2.3.38)$$

ACTIVE SPACECRAFT DECELERATION SEGMENT

Up till now, in deriving the approximate formulas we had in mind spacecraft acceleration from the departure planet launch orbit to an escape orbit characterized by the constants h_{uf}, $\bar{C}_{uf}$, $\bar{e}_{uf}$.

C-2

In many cases interplanetary spacecraft flight is terminated by entry into a planned orbit (we call it the final orbit) around the destination planet. An active deceleration segment, in which the controlled motion problem is velocity reduction after which spacecraft flight will take place in the specified final orbit around the planet, is necessary for spacecraft insertion into this orbit. If spacecraft deceleration takes place in a single plane with tangential thrust vector control [$\alpha(t) = \pi$] we can utilize the preceding results by using the motion inversion principle. In so doing we must consider the well-known fact [51] that deceleration will be most economical in regard to energy expenditures if the active segment terminates at the pericenter of the final orbit, i.e., with $r_f = r_{f\pi}$ and $\theta_f = \theta_{f\pi}$. Using (2.3.19), (2.3.23), (2.3.28), (2.3.29) and (2.3.31) or (2.3.33) and (2.3.34) we represent the expressions for the velocity $\tilde{v}_t$, trajectory angle θ_t, radius $\tilde{r}_t$, and polar angle χ_t at the beginning of the active deceleration segment (Figure 2.3.2) in the form

$$\tilde{v}_t = v_{cir.t} - \frac{\left(1 - \frac{1}{\tilde{r}_t}\right)\tilde{v}^2_{cir.f}}{v_{et}}; \tag{2.3.39}$$

$$\cos\theta_t = \frac{v_{mt}v_{et}}{\tilde{r}_t\left[v_{mt}v_{et} - \tilde{v}^2_{cir.f}\left(1 - \frac{1}{\tilde{r}_t}\right)\right]}; \tag{2.3.40}$$

$$\tilde{r}_t = 1 + \sin^2\frac{\sigma_\tau}{n_0^*} I_{rt}; \tag{2.3.41}$$

$$\chi_h = -\frac{d}{n_0^*}\int_1^{\mu_f} \frac{\left[1 + \left(1 - \frac{\tilde{v}^2_{cir.f}}{v_e v_{id}}\right)\sin^2\frac{\sigma}{n_0^*} I_r\right] v_{id}}{\left[1 + \left(1 - \frac{\tilde{v}^2_{cir.f}}{v_e v_m}\right)\sin^2\frac{\sigma}{n_0^*} I_r\right]\left(1 + \sin^2\frac{\sigma}{n_0^*} I_r\right)^2} d\mu \tag{2.3.42}$$

or

$$\chi_t = \frac{d}{n_0^*}\left[(1+w)(1-\mu_f) + \mu_f \ln\mu_f - 2\left(\frac{\sigma}{n_0^*}\right)^2 I_{\chi 2} + \right.$$
$$\left. + 3\left(\frac{\sigma}{n_0^*}\right)^4 I_{\chi 4} - 4\left(\frac{\sigma}{n_0^*}\right)^6 I_{\chi 6} + 5\left(\frac{\sigma}{n_0^*}\right)^8 I_{\chi 8}\right]. \tag{2.3.43}$$

Here $n_0^* = \frac{g_{0\oplus}}{g_{0\,pl}} n_0$,

$$\tilde{v}_t=\frac{v_t}{v_{h\,x}},\quad \tilde{w}=\frac{w}{v_{h\,x}},\quad \tilde{v}^2_{\text{cir.e}}=\frac{\frac{fm_{\text{pl}}}{r_{\text{pl}}}}{v^2_{h\,x}},\quad \tilde{r}_t=\frac{r_t}{r_{\text{pl}}},$$

$$d=\frac{w}{\tilde{v}^2_{\text{cir.e}}},\quad \tilde{r}_e=\frac{R_{\text{sp}}}{R_{\text{pl}}},\quad \sigma=\frac{1}{\sqrt{2}}d_t,$$

$$v_{\text{id.t}}=1-w\ln\mu_e,\quad v_{et}=1-a_e w\ln\mu_e,\quad v_{mt}=1-a_m\ln\mu_e \tag{2.3.44}$$

$$I_{rt}=-\int_1^{\mu_e} v_{\text{id}}\left(1-\frac{\tilde{v}^2_{\text{cir.e}}}{v_e v_m}\right)^{1/2}d\mu;$$

$$I_r=-\int_1^{\mu_e} v_{\text{id}}\left(1-\frac{\tilde{v}^2_{\text{cir.e}}}{v_e v_m}\right)^{1/2}d\mu; \tag{2.3.45}$$

$$I_{\chi 2}=-\int_1^{\mu_e} v_{\text{id}}I_r^2 d\mu,\quad I_{\chi 4}=-\int_1^{\mu_e} v_{\text{id}}I_r^4 d\mu,$$

$$I_{\chi 6}=-\int_1^{\mu_e} v_{\text{id}}I_r^6 d\mu,\quad I_{\chi 8}=-\int_1^{\mu_e} v_{\text{id}}I_r^8 d\mu. \tag{2.3.46}$$

The expressions (2.3.39) - (2.3.43) define the dependence of the kinematic parameters of the initial point of the active deceleration segment of the basic spacecraft design parameters μ_f and n_0, realization of which is necessary for spacecraft insertion into the final orbit around the destination planet with tangential thrust vector control in the deceleration segment.

The transversal law, when $\alpha(t) = -\theta(t)$, is one of the known thrust vector control laws for spacecraft acceleration and deceleration segments in a given stationary plane. However this law is energetically uneconomical, since for the same values of the basic design parameters μ_f and n_0 the acceleration (deceleration) energy level, characterized by the value h_{uf}, is lower for transversal than for tangential control. Figure 2.3.3 shows the quantity $\Delta h_{ue}=\frac{(h_{ue})_{\alpha=0}-(h_{ue})_{\alpha=-\theta}}{(h_{uf})_{\alpha=0}}$, characterizing the acceleration energy level decrease when using transversal control in comparison with tangential control, as a function of μ_f for various n_0. We

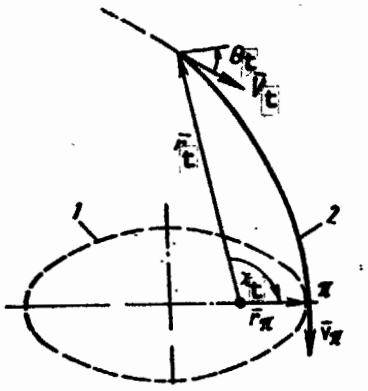

Figure 2.3.2. Kinematics of active deceleration segment:
1- final orbit; 2- active deceleration segment

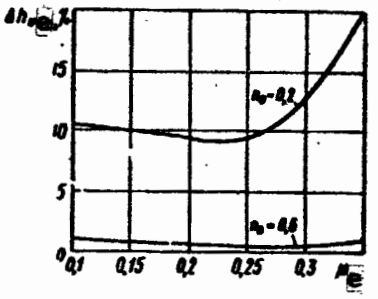

Figure 2.3.3. Energy losses for transversal control

also examined a "mixed" thrust vector control law which combines two control laws: up to the parabolic velocity the acceleration is performed with the transversal law $\alpha(t) = -\theta(t)$, after this the tangential law $\alpha(t) = 0$.is used. Figure 2.3.4 shows the quantity $\Delta h_{uf} = \frac{(h_{uf})_{a=0} - (h_{uf})_{cm}}{(h_{uf})_{a=0}}$ as a function of μ_f for various n_0. We see that the "mixed" law for small values of μ_f leads to considerably smaller losses than the transversal law. Comparison of tangential control with optimal control, in which for the same μ_f and n_0 maximum h_{uf} is reached, shows that the difference in the values of h_{uf} does not exceed one percent over a wide range of μ_f and n_0 values. Therefore, within the framework of the assumptions adopted and the approximations corresponding to ballistic design calculation requirements the tangential thrust vector control law can be considered an optimal law. This increases the importance and validity of the obtained approximate solutions of the differential equations of controlled spacecraft motion. /80

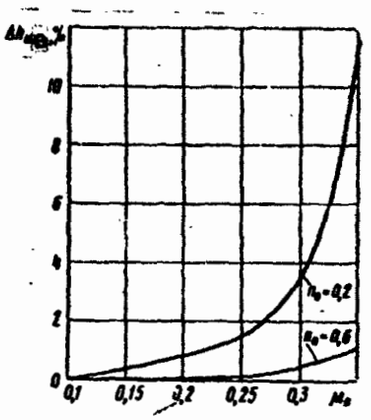

Figure 2.3.4. Energy losses for mixed control

§ 4. CALCULATION OF TRAJECTORIES WITH INTERMEDIATE IMPULSE

Impulsive transfer trajectories between two planets are planar trajectories of the conic section class. In this case the transfer trajectory plane is defined in terms of three points (Figure 2.4.1): I is the launch point from the first planet, II is the arrival point at the second planet; ⊙ is the center of attraction (Sun).

The angle i between the planet orbit planes is not large, therefore the transfer orbit plane usually has small inclination to the planet orbit planes (or to the ecliptic plane). However, in special cases when the transfer angle L approaches π (or $k\pi$, where k=1, 2, ...) there is sharp increase of the transfer orbit inclination to values of $\pm \frac{\pi}{2}$. This leads to increase of the relative launch velocity (the departure velocity V_∞ from the planet gravisphere) from the first planet and the relative velocity of approach to the second planet and consequently to increase of /81 the transfer energy expenditures. An "energy ridge" appears on the characteristic velocity (or velocity V_∞) isoline fields (see Figure 5.2.1). The band of launch dates and arrival dates adjacent to this ridge cannot be realized. It is obvious that the energy

expenditures for transfer trajectories in the "energy ridge" region may be decreased with changeover to a trajectory consisting of two (or more) planar segments [52, 60]. In this case an additional impulse is applied at point 1, causing a break in the transfer trajectory. In many cases it is advisable to use a transfer trajectory with intermediate impulse (or several impulses), even for transfers in a single plane [82]. Thus, for large transfer angles $L > \pi$ between planets I and II (Figure 2.4.2) the maneuver with insertion into orbit of planet I and application of an additional impulse at point 1 (the impulse does not after significantly the transfer plane) and transfer along two conic section trajectories will be energetically advantageous. The time and location of point 1 must be selected to minimize the overall energy expenditures in the transfer segment between planets I and II. The parameters to be optimized will be the three coordinates defining the intermediate impulse application point position and impulse application time.

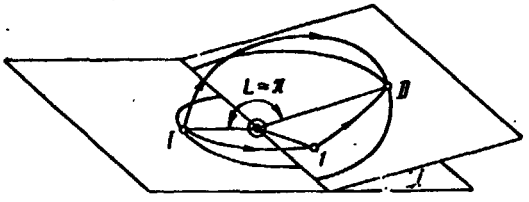

Figure 2.4.1. Schematic of nonplanar transfer with intermediate impulse

Thus for given times of launch t_I from planet I and arrival t_{II} at planet II the transfer trajectory optimization problem with a single intermediate impulse is four-parameter. In the general case, when the number of intermediate impulses is equal to n, the number of parameters to be optimized is $N = 4N$.

Let us examine such a case of transfer between planets I and II with application of intermediate impulses (Figure 2.4.3).

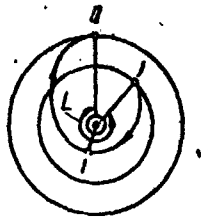

Figure 2.4.2. Schematic of planar transfer with intermediate impulse

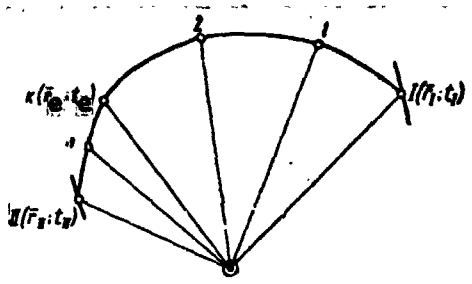

Figure 2.4.3. Schematic of transfer with intermediate impulses

Specification of the departure time t_I from planet I and arrival time t_{II} at planet II determines the position of the planet radii vectors $\tilde{r}_I$ and $\tilde{r}_{II}$ and planet velocity vectors $\bar{V}_I$ and $\bar{V}_{II}$. The /82 coordinates of the intermediate points (radius vector $\bar{r}_k$) and point passage times (intermediate impulse application times t_k) are selected to minimize the total characteristic velocity. For the sake of generality we examine the transfer trajectory between planets with launch impulse application at planet I and deceleration impulse application at planet II. In this case the total characteristic velocity

$$V_\Sigma = \Delta V_I + \Delta V_{II} + \sum_{k=1}^{n} |\bar{V}^b_{k+1} - \bar{V}^e_k|,$$

where ΔV_I and ΔV_{II} are the characteristic velocities of launch from planet I and deceleration at planet II, respectively;

$\bar{V}^b_{k+1}$ is the spacecraft velocity vector at the beginning of the (k+1)th transfer segment;

$\bar{V}^e_k$ is the spacecraft velocity vector at the end of the k-th transfer segment.

The characteristic launch velocity from planet I (Earth) is approximately equal to the velocity increment

$$\Delta V_I \approx V^{st}_{\pi h} - V^{\oplus}_{cir},$$

where $V_{cir}^{\oplus} = \sqrt{\frac{\mu_{\oplus}}{(R^{\oplus}+h)}}$ is the circular velocity in AES launch orbit (h = 200 km);

$V_{\pi h}^{st} = \sqrt{(V_{par}^{\oplus})^2+(V_{\infty}^{\oplus})^2}$ is the velocity at the launch hyperbola pericenter;

V_{par} is the parabolic velocity at height h;

$V_{\infty}^{\oplus}$ is the departure velocity from the Earth's sphere of action.

The characteristic deceleration velocity in artificial planet satellite (APS) orbit is similarly

$$\Delta V_{II} = V_{\pi h}^{pl} - V_{\pi el}^{pl},$$

where $V_{\pi h}^{pl} = \sqrt{(V_{par}^{pl})^2+(V_{\infty}^{pl})^2}$; $V_{\pi el}^{pl}$ is the velocity at the APS orbit pericenter.

For flyby and landing flight trajectories (without active deceleration into APS orbit) the component $\Delta V_{II} = 0$. For given intermediate impulse application point parameters the trajectory determination in each segment reduces to orbit determination on the basis of two positions. This problem can be solved by the Lambert or other methods. Optimization of the intermediate impulse application point parameters is made by the gradient method. The problem is solved by successive variation of the number of impulses. /83 The trajectory is first found without the intermediate impulse, then with a single intermediate impulse, two, and so on. The total velocity V_{Σ} is determined for each case. The optimal number of intermediate impulses is determined from the condition of minimum $V_{x\Sigma}$. If we limit the overall transfer angle $L < 2\pi$ (trajectories of the first or second semiorbit in the case of transfer without an intermediate impulse) the transfer angle in each segment $L_f < \pi$ (trajectory of the first semiorbit). In this case the V_{Σ} extremum search region even for a single intermediate impulse will

be unimodal (region with a single extremum), which ensures convergence of the gradient methods. For successive optimization of the number of impulses it is advisable to use the following strategy in selecting the zero approximations for the intermediate impulse parameters. For trajectory optimization with a single intermediate impulse the impulse application time for the zero approximation is defined as

$$t_1^0 = \frac{t_I + t_{II}}{2}.$$

The vector $\bar{r}_1^0$ is selected equal to the radius vector of the planar transfer trajectory at the time t_1^0. For a trajectory with two intermediate impulses /84

$$t_1^0 = t_I + \frac{t_{II} - t_I}{3};$$

$$t_2^0 = t_{II} - \frac{t_{II} - t_I}{3}.$$

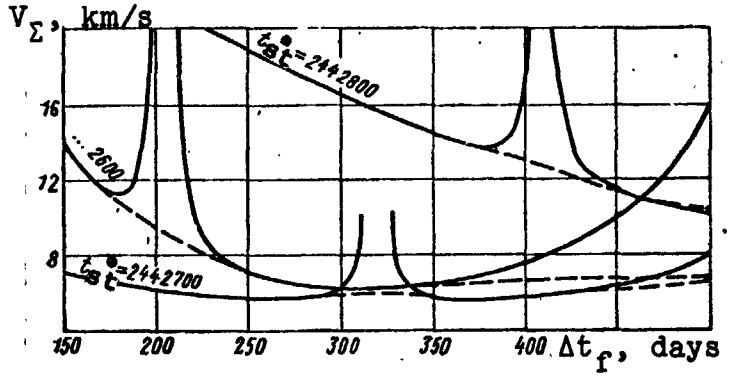

Figure 2.4.4. Transfer from AES orbit to artificial Mars satellite (AMS) orbit ($h_{cir}^{\oplus}$ = 300 km, $h_\pi^\sigma = 1000$ км, $h_\pi^\sigma = 20000$ км)
—— conventional trajectories; - - - with intermediate impulse

The vectors $\bar{r}_1^0$ and $\bar{r}_2^0$ correspond to the positions at times t_1^0 and t_2^0 on the planar transfer trajectory. In order to shorten the computation time when making massive calculations to construct the isoline fields, it is advisable to take the parameters of the

preceding point as the zero approximations. Calculations show that the "energy ridge" on the characteristic velocity isoline fields is cut down with application of additional impulses (Figures 5). Moreover, when using intermediate impulses the energy expenditures decrease for flights along the second semiorbit trajectories with long flight time. For flight trajectories from AES orbit to AMS orbit the characteristic feature is quite complete "cutoff of the energy ridge" separating the 1st and 2nd semiorbit trajectories. Some "energy ridge traces" remain for flight trajectories from AMS orbit to the Earth.

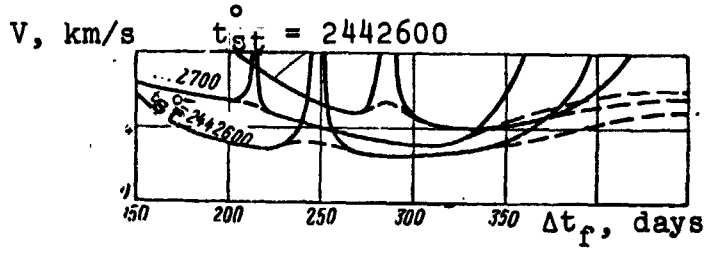

Figure 2.4.5. Transfer from artificial Mars satellite orbit to the Earth

CHAPTER 3. INTERPLANETARY VEHICLE FLIGHT SCHEMES AND TRAJECTORIES

/85

§ 1. INTERPLANETARY FLIGHT TRAJECTORY CHARACTERISTICS

The problem of useful load delivery to a target planet involves several stages, among which the primary influence on the flight energy expenditures is that of:

— spacecraft insertion into parking orbit by the rocket booster;

— departure from the parking orbit and acceleration to the energy level required to overcome the Earth's gravity field;

— ballistic flight to the target planet, which includes the energy expenditures associated with solution of the navigational problems which maintain the actual trajectory close to the nominal trajectory;

— spacecraft deceleration upon approach to the target planet, which makes it possible to enter circumplanetary orbit;

— spacecraft departure from circumplanetary orbit and touchdown on the surface of the target planet *;

— return, including the energy expenditures in performing the tasks of spacecraft return to the Earth and consisting of stages analogous to those examined previously (during flight to the target planet).

It is difficult to evaluate the degree of individual stage influence on the ballistic design characteristics and spacecraft useful load magnitude — all the stages are inter-related. However

* If direct spacecraft landing is planned we can examine in place of the last two stages a single deceleration stage (active or passive) and spacecraft landing on the planet.

each stage has a specific nature associated with maneuver realization, thrust vector control, and satisfaction of the flight stage final conditions. Therefore, for preliminary spacecraft design analyses we can find approximate problem solution methods which take into account the specific nature of each stage. Patching of /86 all the individually obtained solutions can be performed using the successive approximation method. This approach is convenient and fruitful because of the fact that it permits full utilization of the known method for approximating the actual interplanetary spacecraft flight trajectory by conic section segments (see § 2 of Chapter 1). The patched conic approximation permits determining a patched interplanetary trajectory which represents for design analyses a good approximation to the exact trajectory. In addition it is convenient to view this patched curve as the first approximation for the corresponding iterative process which is used in determining the final interplanetary trajectory with account for various perturbations.

Representation of the actual continuous interplanetary trajectory in conic section form is based on the assumption that only the central body attractive force acts during spacecraft motion in the planet's gravisphere or outside (in the heliosphere). In this case the active spacecraft acceleration segment in the Earth's gravisphere is followed by a hyperbolic departure orbit and the active spacecraft deceleration segment in the planet's gravisphere is preceded by a hyperbolic arrival orbit. Outside the gravispheres of the planets (in the heliosphere) we examine primarily ballistic spacecraft flight, taking place by assumption under the action of the attractive force of only the central body — the Sun. Here the orbits considered are basically elliptic transfer orbits.

In order to improve transfer energy effectiveness it is advisable in many cases to introduce additional active segments in the heliosphere (see § 4, Chapter 2).

The active segment of spacecraft injection into an intermediate orbit, which is usually taken to be circular with altitude 150 - 200 km, is determined by the ballistic design characteristics of the booster rocket. In planning interplanetary flights usually only the spacecraft are redisigned or modified and their parameters, configuration, and structure are selected with account for the specific nature of the mission being performed in studying the planets and interplanetary space. Spacecraft launch is usually accomplished by the rocket booster which is most economical for carrying the specified useful load (spacecraft weight) from a series of standard booster rocket types which constitute a multipurpose space rocket system. It is true that in many cases modification of the final rocket stage is carried out to achieve more rational use of rocket booster and spacecraft capabilities.

The departure from the circular parking orbit and acceleration to the required energy level, ballistic flight to the target planet, deceleration near the planet for entry into circumplanetary orbit, /87 and return to the Earth define the task of selecting the spacecraft ballistic design characteristics and the magnitude of the useful load which can be delivered to the target planet and returned to the Earth. Depending on the required accuracy and the number of selectable parameters this problem can be solved by various methods, the basis of which is patched conic approximation of the ballistic flight trajectory. These methods can be divided fundamentally into two types: the impulsive approximation method and the methods accounting for the duration and continuity of the active spacecraft acceleration and deceleration segments, which we by convention term finite thrust methods.

In the impulsive approximation method the active segment is represented in the form of instantaneous velocity change with unchanged spacecraft position. Thus we assume that as a consequence of the impulsive change the spacecraft instantaneously

transitions at the departure point on the circular parking orbit to the hyperbolic departure orbit, and at some point (departure point) of the hyperbolic arrival orbit the spacecraft transitions to the planned final circumplanetary orbit *. As a result of this impulsive approximation of the active segments the entire interplanetary trajectory consists of three conic sections (Figure 3.1.1): hyperbolic departure orbit (from the Earth's gravisphere), heliocentric (elliptic of hyperbolic) interorbital transfer segment (Earth orbit to target orbit), and the hyperbolic arrival orbit (target planet gravisphere). The heliocentric interorbital transfer segment may in turn consist of several Keplerian orbits, if the gravity fields of other planets are used to accelerate or decelerate the spacecraft or there are intermediate active segments. Patching of the indicated conic sections is satisfied when the asymptote of the hyperbolic departure orbit is parallel to the hyperbolic excess velocity vector $\bar{V}_{\infty f}$, determined from the equality /88

$$\bar{V}_{\infty 0}=\bar{V}_0-\bar{V}_\oplus, \qquad (3.1.1)$$

and the asymptote of the hyperbolic arrival orbit is parallel to the hyperbolic excess arrival velocity vector $\bar{V}_{\infty f}$, determined from the equality

$$\bar{V}_{\infty f} = \bar{V}_f-\bar{V}_{pl}. \qquad (3.1.2)$$

Here $\bar{V}_0$, $\bar{V}_f$ are the initial and final flight velocity vectors in the heliocentric segment; $\bar{V}_\oplus$ is the Earth's velocity vector at the initial moment of spacecraft flight in the heliosphere; $\bar{V}_{pl}$ is the target planet velocity vector at the final instant of spacecraft flight in the heliosphere. We therefore assume that the moment of spacecraft departure from the Earth's gravisphere and the instant of its entry into the target planet gravisphere coincide, respectively, with the points of intersection of the elliptic

* In the case of absence of intermediate passive segments during acceleration or deceleration. This approximation is admissible for a continuous active segment.

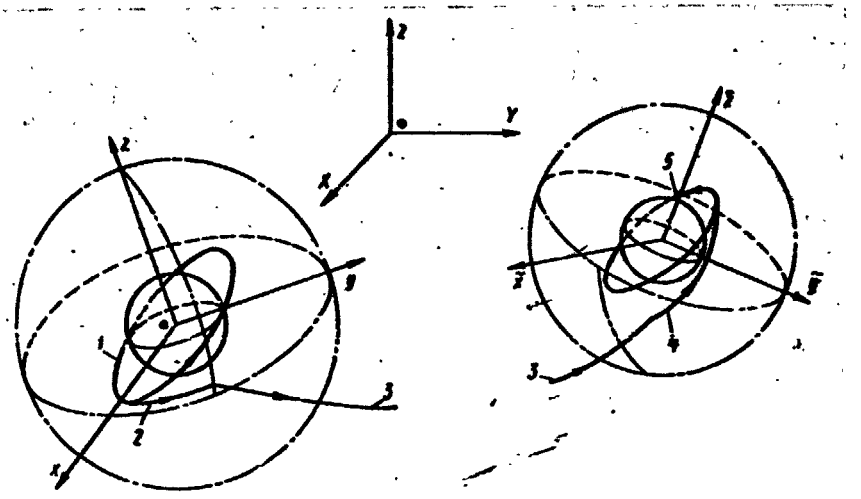

Figure 3.1.1. Patched conic approximation of interplanetary flight trajectory with impulsive velocity change:

1- parking orbit; 2- hyperbolic departure orbit; 3- heliocentric interorbital transfer segment; 4- hyperbolic arrival orbit; 5- final orbit

transfer orbit with the Earth and target planet orbits. From the physical viewpoint this means that the planets are considered non-gravitating centers and from the geometric viewpoint this is a consequence of neglecting the dimensions of the planetary gravi-spheres.

However this approach to evaluating patching of the heliocentric segment with the planetocentric segments is not always justified. For certain flight schemes, particularly when we examine flights to planets having large gravisphere dimensions, the heliocentric segment should be determined with account for the planetary gravi-sphere dimensions in order to obtain the required calculation accuracy. In this case patching is achieved as a result of combined computation of the heliocentric and planetocentric segments.

The impulsive approximation method is based on the assumptions examined above, which although they lead to definite idealization

of the actual interplanetary flight picture, do permit in the first approximation quite simple determination of the energy expenditures required for realization of interplanetary flight.

The use of the impulsive approximation method makes it possible to construct the following structural scheme for solving the problem of determining spacecraft ballistic design characteristics. We first solve the problem of determining the heliocentric interplanetary flight segment, one result of which is finding $\bar{V}_{\infty 0}$ and $\bar{V}_{\infty f}$. We then turn to the algorithms for seeking the hyperbolic departure and arrival orbits, the corresponding asymptotes of which will be parallel to $\bar{V}_{\infty 0}$ and $\bar{V}_{\infty f}$ and the energy integral constants are equal to $\bar{V}^2_{\infty 0}$ and $\bar{V}^2_{\infty f}$, respectively. /89

An important part of these algorithms are the blocks for calculating the minimal values of the characteristic acceleration $V^a_{x\Sigma}$ and deceleration $V^d_{x\Sigma}$ segment velocities, which express the relative final weights of the spacecraft accelerating μ_{f1} and decelerating μ_{f2} modules as follows

$$\mu_{e1}=\exp\left(-\frac{V^a_{x\Sigma}}{g_0 P_{sp1}}\right); \qquad (3.1.3)$$

$$\mu_{e2}=\exp\left(-\frac{V^t_{x\Sigma}}{g_0 P_{sp2}}\right), \qquad (3.1.4)$$

where P_{sp1}, P_{sp2} are the specific powerplant thrusts of the acceleration and deceleration modules respectively;

g_0 is the Earth's gravity acceleration.

The reason is that under the assumption of possible intermediate passive segments during spacecraft acceleration and deceleration, on the basis of the impulsive approximation the acceleration and deceleration trajectories can be represented in the form of several conic section pieces. In this case minimization of the total characteristic acceleration and deceleration segment

velocities becomes very important. The use of a large number of impulses makes it possible to select a trajectory which not only satisfies the boundary conditions but also optimizes the required value of the total characteristic velocity.

The impulsive approximation method, which is attractive from the viewpoint of relative simplicity and visualizability of the algorithm for calculating the interplanetary flight trajectory and the energy expenditures in realizing this trajectory, leads to an approximate estimate of transfer energy expenditures and does not permit complete determination of the spacecraft ballistic design characteristics.

The errors caused by the impulsive approximation are the result of ignoring the gravitational losses and thrust vector orientation change in the active segment, neglecting the parallax effect (extent of the planetary gravisphere) in calculating the heliocentric interorbital transfer segment and the length of the active segment.

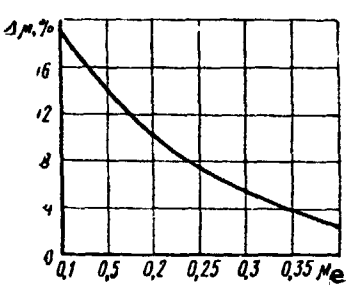

Figure 3.1.2. Gravitational losses of relative final spacecraft weight in the acceleration segment ($n_0 = 0.2$; $P_{sp} = 350$ s, $r_0 = 6571$ km)

Figure 3.1.2 shows the relative magnitude of the gravitational losses which are not taken into account in the impulsive approximation in the acceleration segment from a circular parking orbit for $n_0 = 0.2$ as a function of μ_f. /90

This method does not permit determination of the initial thrust-weight ratios of the spacecraft stages required for maneuvering.

However the impulsive approximation method is widely used in spacecraft design analyses, since the solutions obtained with the aid of this method can very well be used as the first approximation *.

The finite thrust method is not characterized by many of the deficiencies of the impulsive approximation method. The gravitational losses and time variation of the thrust vector are taken into account quite adequately in this method; this method makes it possible to determine the optimal values of the initial thrust-weight ratios of the spacecraft stages. The finite thrust method is based on approximate solutions of the system of differential equations of controlled spacecraft motion. Therefore the determination of the kinematic parameters of the end of the active acceleration or deceleration segments is not exact and leads to errors, which however are significantly less than the errors in the impulsive approximation and satisfy fully the requirements of preliminary spacecraft design analyses.

§ 2. CLASSIFICATION OF INTERPLANETARY VEHICLE FLIGHT SCHEMES

The selection of interplanetary vehicle ballistic design characteristics involves the evaluation of several criteria: energy expenditures, total flight time, launch window size, sensitivity of nominal trajectory to possible deviations, and so on. The optimal ballistic design characteristics correspond to the extremal value of one of the criteria with constraints on the others. However the analytic relations used, the nature of the search for the optimal ballistic design characteristics, and the solution results depend significantly on the interplanetary vehicle flight scheme. Selection of the flight scheme, expressing (without excessive details) the interplanetary trajectory profile, /91

* A detailed survey of studies devoted to the impulsive approximation method is presented in [64].

permits finding fundamental ways to solve the specific interplanetary flight problem. Classification of the flight schemes may become a component element of the algorithm for optimizing the interplanetary vehicle ballistic design characteristics, is algorithmic closeness of the flight schemes and ballistic requirements on the final maneuver and on the maneuver during intermediate planet flyby based on the ultimate flight objective are used as the classification basis.

The great variety of heliocentric flight segments to the planets may lead in the future to considerable increase of the number of possible flight profiles, which are usually formed from various combinations of known heliocentric flight orbit types. All this makes it useful to classify the interplanetary vehicle flight schemes.

The possible flight schemes to the planets can be divided into two types: the first are the flight schemes to the target planet without spacecraft return to the Earth, the second are the flight schemes to the target planet with spacecraft return to the Earth. Each type is divided in turn into two classes: the class of direct flight schemes to the target planet and the class of flight schemes with account for maneuver during intermediate planet flyby. For further definition of the specific flight scheme the classes are broken down into groups.

FIRST TYPE — FLIGHT SCHEMES TO TARGET PLANET WITHOUT RETURN TO THE EARTH

Flights to target planets without return to the Earth occupy and will continue to occupy an important position in order to gather information on the solar system planets. Such flight schemes are characteristic only of the automatic interplanetary vehicles, whose

primary mission is to deliver their payload to the target planet region in order to obtain the required information. Although there are many specific schemes of such flights they can be divided into two fundamentally different classes.

The first class is the direct flight schemes to the target planet (without return to the Earth). The direct flight scheme to the target planet is designed for a direct spacecraft trajectory from the Earth to the target planet without utilization of perturbation effects. Formal systematization of all heliocentric segments of direct spacecraft interplanetary flight trajectories to the target planet permits representing them by 13 orbit types [51, V. II, P. 2, § 9.2]: nine elliptic, one parabolic, and three hyperbolic (Figures 3.2.1 and 3.2.2). However classification of the direct flight schemes to the target planet with account for the previously indicated requirements, without disrupting formal systematization of the heliocentric segments, reduces the possible /92 flight schemes to four groups.

The first group includes the flight schemes along flyby-impact trajectories (see Figure 3.2.3). Flight begins from a parking orbit around the Earth and terminates either in flyby near the planet along a hyperbolic planetocentric trajectory or "direct" impact of the vehicle (vehicles) in a given region (regions) of the planet, where velocity reduction may be achieved by braking in the planet's atmosphere. A system for automatic guidance and /93 trajectory correction in the segment near the planet is necessary to ensure vehicle impact in the specified regions.

The second group is the flight schemes with entry into final orbit around the target planet (Figure 3.2.4). As in the preceding case, the flight begins from a parking orbit around the Earth and terminates in entry into the final orbit around the target planet. Entry into the specified final orbit around the planet can be

achieved in various ways. There are two fundamentally different braking techniques: active braking, when the velocity is reduced by means of retrothrust, and passive, when the velocity is reduced by vehicle braking in the planet's atmosphere. Combination of these techniques is possible. The selection of the particular braking technique depends on the problem formulation and final orbit specification.

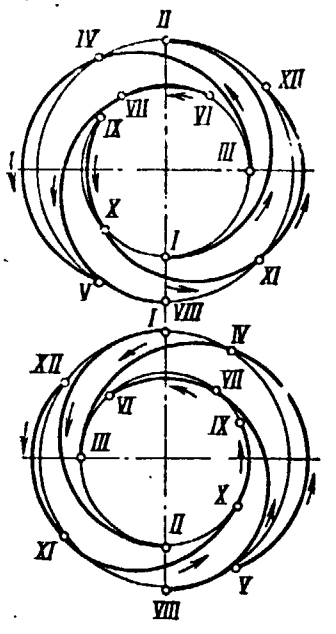

Figure 3.2.1. Nine basic elliptic heliocentric transfer segment types. Extreme points:

$$I \rightleftarrows II, III \rightleftarrows IV, \quad III \rightleftarrows V, \quad VI \rightleftarrows VIII,$$
$$VII \rightleftarrows VIII, \quad IX \rightleftarrows XI, \quad IX \rightleftarrows XII, \quad X \rightleftarrows XI,$$
$$X \rightleftarrows XII$$

The third group is the flight schemes with approach to the planet and descent vehicle landing (Figure 3.2.5). The salient feature of this flight scheme is that after launch from a parking orbit around the Earth and approach to the planet the scheme provides for landing of a descent vehicle (descent vehicles) on the surface of the planet. Soft touchdown of the descent vehicles can be accomplished in various ways: by braking using retrothrust and combination of this technique with braking in the planet's atmos-

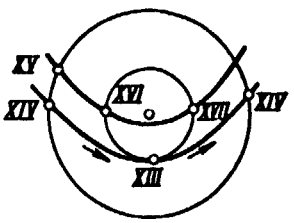

Figure 3.2.2. Three basic hyperbolic heliocentric segment types. Extreme points:
$XIII \rightleftarrows XIV$, $XV \rightleftarrows XVI$, $XV \rightleftarrows XVII$

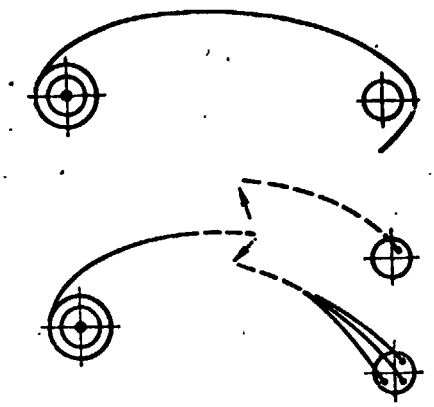

Figure 3.2.3. Scheme of automatic interplanetary vehicle flight along flyby-impact trajectory

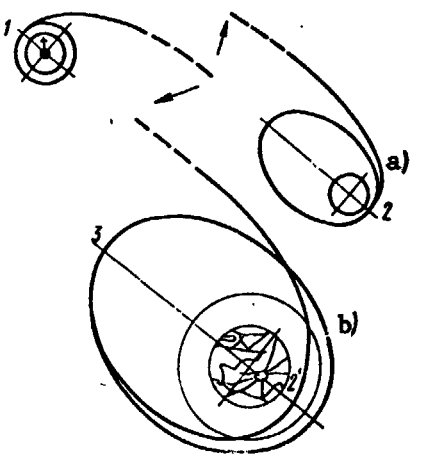

Figure 3.2.4. Scheme of automatic interplanetary vehicle flight with entry into orbit around target planet:

a- scheme with active braking; b- scheme with aerodynamic braking; 1- start from parking orbit; 2- active braking for entry into final orbit; 2'- braking in the planet's atmosphere; 3- correction for entry into final orbit

phere (ballistic descent, lifting descent). This flight scheme /94
provides for landing on the planet of either the entire vehicle or successive landing of its individual modules (descent vehicles).

The fourth group is the combined flight schemes (Figure 3.2.6). The combined schemes include those interplanetary flight schemes

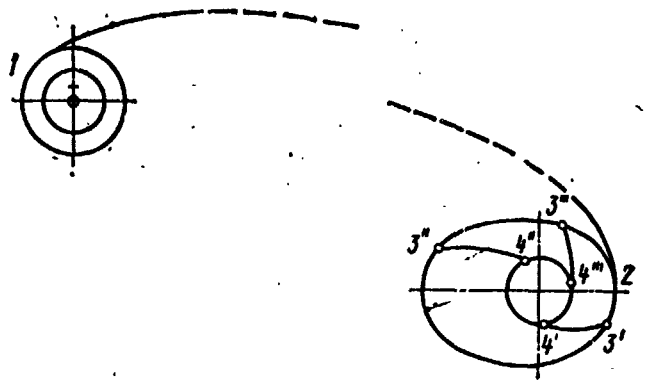

Figure 3.2.5. Automatic interplanetary vehicle flight with entry into circumplanetary orbit and descent vehicle landing on the surface of the planet:

1- launch from parking orbit; 2- entry into circumplanetary orbit; 3-4- descent segment to surface of the planet (3'-4'; 3"-4"; 3'"-4'")

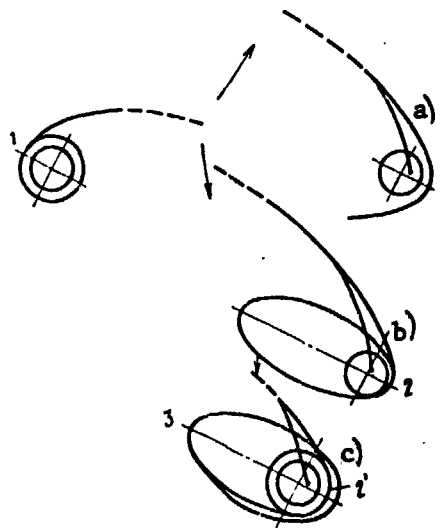

Figure 3.2.6. Combined interplanetary vehicle flight scheme:

a- flyby-landing scheme; b- orbital-landing scheme with active braking for entry into final orbit; c- orbital-landing scheme with aerodynamic braking for entry into final orbit; (1- launch from parking orbit; 2- braking for entry into final orbit; 2'- braking in the atmosphere; 3- correction for entry into final orbit)

in which during the approach segment to the planet the interplanetary vehicle separates into modules with some of the modules intended for planet flyby (flyby-landing scheme, Figure 3.2.6a) or entry into orbit around the planet (orbital-landing scheme Figure 3.2.6b and c), while the others are designed for descent to the surface of the planet (Figure 3.2.6). Another possible scheme is that in which one module enters orbit around the planet and another flys by the planet.

The second class is the flight schemes to the target planet with use of the perturbing effect of an intermediate planet. Utilization of the gravity fields of other planets for flight to the target planet is a very promising idea. In many cases this permits achieving greater interplanetary flight efficiency. The reason is that as a result of spacecraft flyby near the intermediate planet the heliocentric segment of the interplanetary trajectory is altered as a consequence of the action of its gravity field. Planning of the corresponding change and its proper utilization may lead to positive results: reduction of the overall energy expenditures, broadening of the launch window, and so on. Another very intriguing aspect is that a single interplanetary /95
vehicle can carry out studies of several planets. It is true that the requirements on spacecraft navigation are more stringent in this case, but today's technical capabilities make it possible to meet these requirements.

The maneuvers both near the intermediate planet and in the final stage of flight around the target planet influence the classification of such flight schemes. In this connection the flight schemes of this second class can be reduced to a few groups.

The first group is the flight schemes along swingby-flyby trajectories with utilization of the perturbation effect (Figure 3.2.7). After launch the interplanetary vehicle passes near the

intermediate planet along a hyperbolic (relative to the planet) trajectory and as a result of the corresponding heliocentric segment change reaches the target planet. Change of the interplanetary trajectory heliocentric segment takes place basically from the perturbation effect. However, in many cases thrust impulses are also used to increase the effect of the maneuver near the intermediate planet. At the end of the flight plans are made for either spacecraft flyby near the target planet or "direct" impact on a specified region of the planet.

In many cases flight schemes may be examined, in which prior to reaching the target planet the spacecraft flys by several planets, whose gravity fields alter correspondingly each time the interplanetary trajectory heliocentric segment.

The second group is the flight schemes utilizing the perturbing effect of an intermediate planet and entry into final orbit around the target planet. /96 The difference between this group of flight schemes and the preceding group lies in the final maneuver, which is designed for interplanetary vehicle entry into orbit around the planet.

The third group is the flight schemes utilizing the perturbing effect of an intermediate planet, approach to the planet, and landing of a descent vehicle.

The difference between this group of flight schemes and the analogous group of the preceding class lies in planning for flyby around the intermediate planet and utilization of its gravity field.

The fourth group is the combined flight schemes with utilization of the perturbing effect of an intermediate planet. This group of flight schemes includes those in which intermediate planet

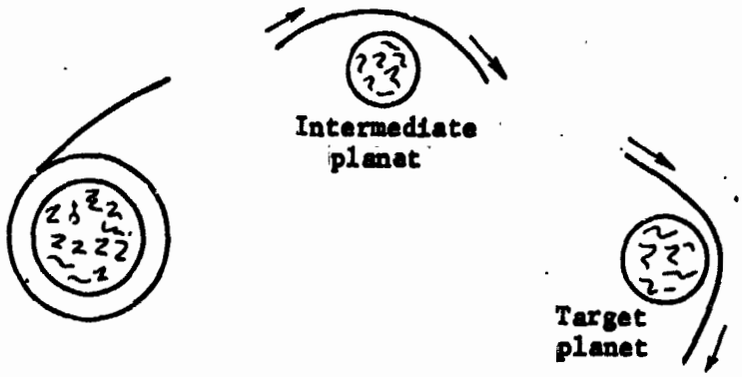

Figure 3.2.7. Flight along swingby-flyby interplanetary trajectories

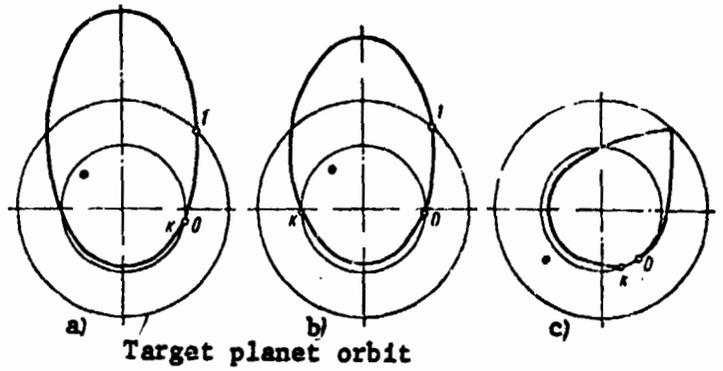

Figure 3.2.8. Flight along flyby-return trajectories:
a- flight with return to the Earth after whole number of sidereal years and without account for perturbing effect of target planet; b- flight with return to the Earth after fractional number of sidereal years and without account for perturbing effect of target planet; c- flight with return to the Earth with account for perturbing effect of target planet

flyby can be combined with landing of a descent vehicle on its surface; in the final flight stage near the target planet the interplanetary vehicle separates into modules with the mission of certain modules being flyby near the planet or entry into orbit around the planet while the mission of the others is to perform soft landing on the surface of the planet, and so on.

SECOND TYPE — FLIGHT SCHEMES TO TARGET PLANET WITH RETURN TO THE EARTH

Return to the Earth is the primary requirement for piloted interplanetary vehicles. This same requirement may also be advanced when planning flights of automatic interplanetary vehicles. Further accumulation of knowledge about the solar system is not feasible without the realization of such flight schemes. All these flight schemes can be broken down into two classes. The common feature /97 of these classes is vehicle entry into the Earth's atmosphere with velocity exceeding the escape speed. The possibility of using thrust impulses at points of the return trajectory heliocentric segment is assumed. In many cases the thrust impulses permit marked reduction of spacecraft entry velocity into the Earth's atmosphere.

The first class is the direct flight schemes to the target planet with return to the Earth. This class includes the direct trajectories from the Earth to the target planet and from the planet to the Earth. Here no provision is made for utilization of the perturbing effects of other planets either during flight to the target planet or during return to Earth. The direct flight schemes of the subject class can be broken down into groups.

The first group is the flight schemes along flyby-return trajectories (Figure 3.2.8). This group includes the flight schemes which involve interplanetary vehicle flyby near the target planet and vehicle return to the Earth. Return is provided for in various ways: selection of suitable heliocentric segment and launch date; use of the perturbing effect of the target planet; introduction of additional thrust impulses to alter the heliocentric segment of the interplanetary return trajectory.

The second group is the flight schemes with entry into parking orbit around the target planet and return to the Earth. This group of flight schemes differs from the preceding group in entry /98 into the parking orbit around the target planet, definite stay time in this orbit, and deorbiting for return to the Earth. All this requires large additional energy expenditures.

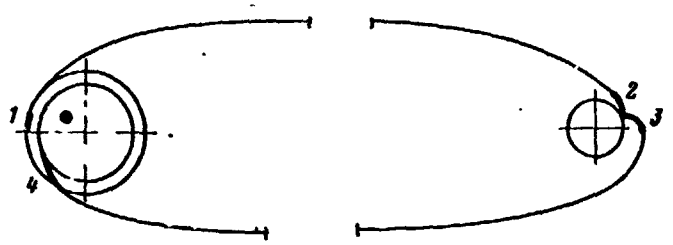

Figure 3.2.9. Interplanetary vehicle flight with descent module landing on target planet and return to the Earth:

1- launch from parking orbit; 2- landing on target planet; 3- launch from surface of the planet; 4- landing on the Earth

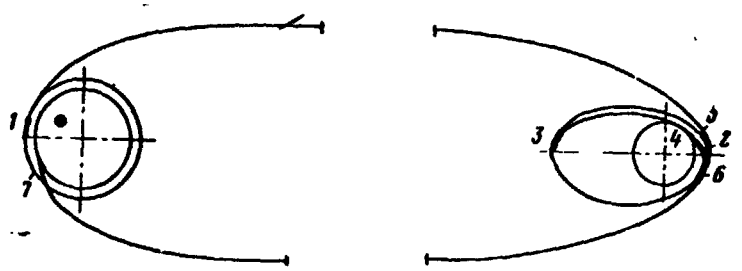

Figure 3.2.10. Earth-return interplanetary vehicle flight with entry into orbit and landing on target planet:

1- launch from parking orbit; 2- braking for entry into holding orbit; 3,4- descent from orbit to planet; 5- launch from surface of planet and entry into orbit; 6- launch from orbit; 7- landing on the Earth

The third group is the flight schemes with descent vehicle landing on the surface of the target planet and return to the Earth (Figures 3.2.9, 3.2.10). This group includes the flight schemes in which provision is made for descent module landing on the surface of the target plaret. Landing of the descent module can be provided

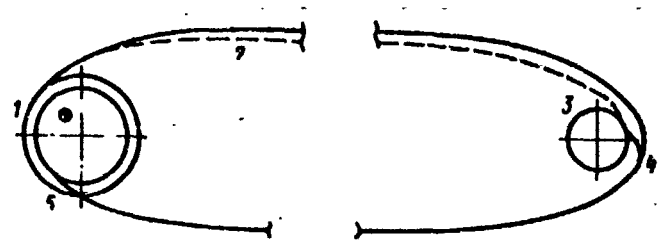

Figure 3.2.11. Combined flight scheme of Earth-return interplanetary vehicle with flyby and landing on the target planet:

1- launch from parking orbit; 2- correction of interplanetary trajectory; 3- landing of descent module; 4- launch from surface of Mars and rendezvous with flyby vehicle; 5- landing on the Earth

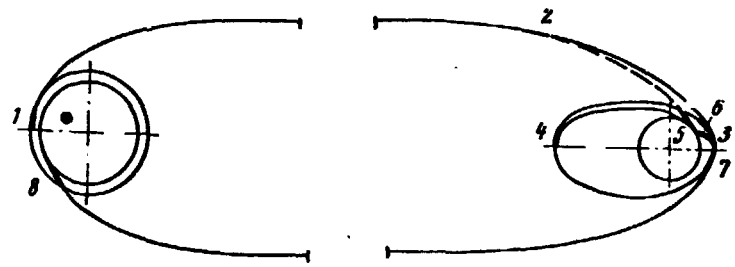

Figure 3.2.12. Combined flight scheme of Earth-return interplanetary vehicle with entry into orbit and landing on the target planet:

1- launch from parking orbit; 2,5- variant with direct landing of planetary station; 3- braking for entry into final orbit; 4- landing vehicle descent from orbit to planet; 6- launch from surface and entry into orbit; 7- launch from orbit; 8- landing on the Earth

by "direct" spacecraft landing, in which the hyperbolic arrival orbit mates directly with the descent trajectory, or by descent from a circumplanetary orbit which the spacecraft first enters. For return to the Earth provisions are made for launch from the planet, active segment of injection into circumplanetary orbit, and then departure from this orbit. The realization of such interplanetary flight schemes imposes special requirements on the powerplants and control systems and on space technology in general.

The fourth group is the combined flight schemes with return to the Earth (Figures 3.2.11, 3.2.12). /99 In the combined flight schemes the problem of interplanetary vehicle flyby near the target planet or entry into orbit around the planet is combined with descent of the spacecraft landing module (modules) to the planet surface, which may be accomplished using the scheme of the preceding group. Return to the Earth is provided for in various ways. For example, this may be accomplished by mating the module launched from the surface of the planet with the flyby vehicle (see Figure 3.2.11). Another solution of the return problem is obtained by mating the module launched from the planet with an orbital vehicle, after which the resulting complex departs from orbit around the planet and enters the return trajectory (see Figure 3.2.12).

The second class is the flight schemes to the target planet with return to the Earth and utilization of the perturbing effect of an intermediate planet. /100 In such flight schemes the influence of the perturbing effect from the intermediate planet may show up either during flight to the target planet or during the return stage. Use of the perturbing effect makes it possible to reduce the overall energy expenditures, broaden the Earth launch and target planet launch windows, and reduce the Earth atmosphere entry velocity.

We represent this class by the following groups.

The first group is the flight schemes along flyby-return trajectories with account for the perturbing effect of an intermediate planet. This group of flight schemes differs from the same group of the preceding class in that as a result of utilization of the gravity field of the planet past which spacecraft flight is planned there is change of either the heliocentric segment of the flight to the target planet or of the heliocentric segment of the return trajectory.

The second group is the flight schemes with account for the perturbing effect of an intermediate planet, entry into a parking orbit around the target planet, and return to the Earth. The difference between this group and the preceding group lies in the maneuvers of entry into and deorbit from the parking orbit.

The third group is the flight schemes with account for the perturbing effect of an intermediate planet, descent module landing on the surface of the target planet, and return to Earth. This group differs from the third group, of the preceding class only in planned variation of the heliocentric flight segment after spacecraft contact with the intermediate planet, either during the flight stage to the target planet or during return.

The fourth group is the combined flight schemes with return to the Earth and utilization of the perturbing effect of an intermediate planet. The combined flight schemes include those schemes in which target planet flyby is combined with descent of a landing module (modules). In addition provision is made for descent of a landing module during spacecraft contact with the intermediate planet during the flight segment to the target planet.

CHAPTER 4. PLANETOCENTRIC FLIGHT SEGMENTS

§ 1. KINEMATIC PARAMETERS INJECTION SEGMENT FROM PARKING ORBIT INTO EARTH ESCAPE HYPERBOLA

The flight trajectory from the launch point to the instant /101
when the SC velocity vector acquires the required direction is termed the injection segment. The purpose of the injection segment is to ensure SC motion during departure from the gravisphere with velocity vector equal to the hyperbolic excess velocity vector $\bar{V}_{\infty 0}$, determined from solution of the outer problem.

The injection segment consists of the controlled flight trajectory (active injection segment) and the passive flight trajectory (passive injection segment). The passive segment which terminates the injection is the hyperbolic escape orbit with $h_{u\,f} = V_{\infty 0}^2$.

The active injection segment may be of two types: the first is the continuous ascent active segment, in which the engines operate practically continuously and their intermediate shutdown is not associated with injection mission performance, the second is the active segment with parking orbit, in which intermediate engine shutdown is planned to provide passive vehicle motion along a preselected parking orbit, which leads to better solution of the injection problems. If we evaluate the active segments on the basis of solution of the correct launch time problem and the navigation problem with minimal energy expenditures, then preference must be given to the active segment with parking orbit (Figure 4.1.1), which is widely used in solving injection problems.

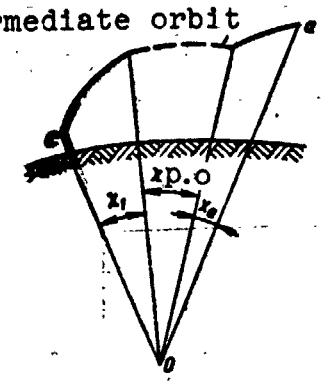

Figure 4.1.1. Active injection segment with parking orbit: C- launch point; a- end of active injection segment

Let us evaluate the geometric characteristics of the injection segment and their interrelationships, considering that the escape orbit semimajor axis and asymptote direction are predetermined by specification of $V_{\infty 0}$ and $\bar{V}^0_{\infty 0}$. For solution of the problem of hyperbolic escape orbit asymptote parallelism to the unit vector /102 $\bar{V}^0_{\infty 0}$, it is necessary that the asymptote lie in the plane of the vector. If $\bar{N}$ is the normal to the escape orbit plane, this condition corresponds to the vector equation of the plane

$$\bar{N} \cdot \bar{V}^0_{\infty 0} = 0.$$

RELATION BETWEEN ORBIT PLANE INCLINATION i AND TARGET VECTOR DECLINATION δ_0

Let the target vector $\bar{W}$, drawn from the coordinate origin parallel to $\bar{V}^0_{\infty 0}$ and equal to the latter, be defined in the second equatorial geocentric coordinate system by the right ascension α_0 and declination δ_0 (Figure 4.1.2). Then, considering the kinematic equation $\bar{N} \cdot \bar{N} = 1$, the solution of the vector equation of the plane N_x and N_y can be represented in the form

$$\left.\begin{aligned} N_y &= \frac{-\cos i \sin \delta_0 \sin \alpha_0 \pm \cos \alpha_0 (1 - \sin^2 \delta_0 - \cos^2 i)^{1/2}}{\cos \delta_0}; \\ N_x &= -\frac{N_y \sin \alpha_0 \cos \delta_0 + \cos i \sin \delta_0}{\cos \alpha_0 \cos \delta_0}, \end{aligned}\right\} \qquad (4.1.1)$$

since $N_z = \cos i$, $W_x = \cos \alpha_0 \cos \delta_0$, $W_y = \sin \alpha_0 \cos \delta_0$, $W_z = \sin \delta_0$. Consequently, the escape orbit plane position must

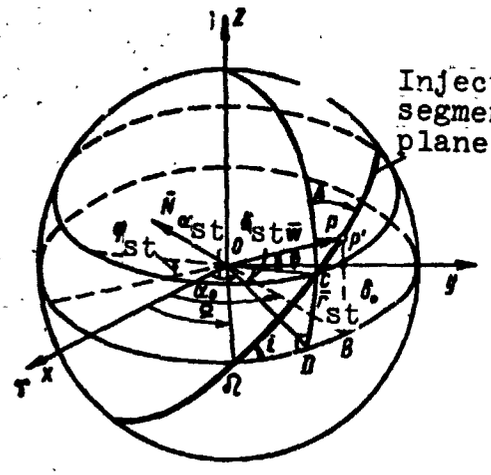

Figure 4.1.2. Kinematics of injection segment

satisfy the inequality

$$\cos^2 i \leqslant \cos^2 \delta_0 \text{ or } \pm \cos i \leqslant \cos \delta_0, \quad (4.1.2)$$

which reduces to the condition for launch:

in the northeast direction $\left(0 \leqslant i \leqslant \frac{\pi}{2}\right)$

$$i \geqslant |\delta_0|. \quad (4.1.3a)$$

in the southeast direction $\left(\frac{\pi}{2} \leqslant i \leqslant \pi\right)$

$$(\pi - i) \geqslant |\delta_0|. \quad (4.1.3b)$$

Thus the hyperbolic escape orbit plane position must be such that its inclination i (or π - i) to the equator can be only greater than or equal to the target declination vector $|\delta_0|$, i.e., /103

$$|\delta_0| \leqslant i \leqslant \pi - |\delta_0|. \quad (4.1.3c)$$

RELATION BETWEEN ANGLE i AND LAUNCH POINT DECLINATION δ_{st}

The injection energy expenditures will be smaller if the active segment lies in the escape orbit plane — absence of expenditures in a nonplaner maneuver. Therefore, if $\bar{r}^0_{st}$ is the unit radius vector of the launch point C, this requirement corresponds to tne vector equation of the plane

$$\bar{N} \cdot \bar{r}^0_{st} = 0$$

whose solution with account for $\bar{N} \cdot \bar{N} = 1$ is possible with

satisfaction of the inequality

$$\pm \cos i \leq \cos \delta_{st} \qquad (4.1.4)$$

which reduces to the condition:

for launch in the northeast direction $\left(0 \leqslant i \leqslant \frac{\pi}{2}\right)$

$$i \geq |\delta_{st}| \qquad (4.1.5a)$$

for launch in the southeast direction $\left(\frac{\pi}{2} \leqslant i \leqslant \pi\right)$

$$(\pi - i) \geq |\delta_{st}|. \qquad (4.1.5b)$$

Thus, the hyperbolic escape orbit plane position must be such that its inclination i (or $\pi - i$) to the equator can be only greater than or equal to the launch point geographic latitude $|\varphi_{st}|$ (or the declination $|\delta_{st}|$ at the instant of launch), i.e., /104

$$|\varphi_{st}| \leq i \leq \pi - |\varphi_{st}|. \qquad (4.1.5c)$$

When solving the problem of selecting the parking orbit plane (escape orbit plane) inclination i, the target vector declination δ_0 and launch point geographic latitude φ_{st} are quantities which are specified in advance. The boundaries of possible i values are to be determined in accordance with the value of the quantities δ_0 and φ_{st} in accord with the conditions (4.1.3) and (4.1.5). If the launch point latitude φ_{st} is greater than or equal to the target vector declination δ_0 ($\varphi_{st} \geq \delta_0$), the choice of inclination angle i is determined by the inequalities (4.1.5) and is independent of δ_0. However, if the target vector declination δ_0 is greater than or equal to the launch point latitude ($\varphi_{st} \leq \delta_0$), the choice of inclination angle is determined by the inequalities (4.1.3) and is independent of the launch point latitude.

OPTIMIZATION OF INCLINATION ANGLE i FOR MINIMAL ENERGY EXPENDITURES

The relations (4.1.3) and (4.1.5) provide some freedom in selection of the injection trajectory plane inclination to the equator. However, this angle has a definite influence on the active segment energy expenditures. Therefore, it is desirable to reduce the injection energy expenditures by suitable selection of the inclination angle i. The basis for this is proper utilization of the Earth rotation energy. We shall assume impulsive velocity change. Then the energy expenditures of injection into the parking orbit will be expressed by the characteristic velocity, equal to (Figure 4.1.3):

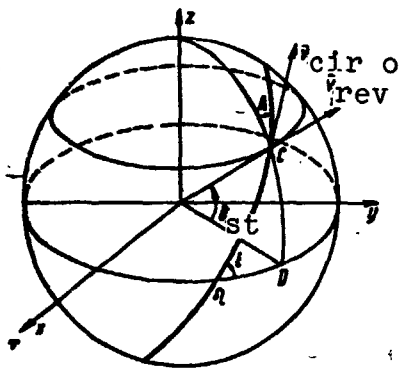

Figure 4.1.3. Illustration for optimizing the inclination angle i

$$V_{x\ inj} = v_{cir\ o} - v_{rev} \cos(\bar{v}_{cir\ o}, \hat{\bar{v}}_{rev}) =$$

$$v_{cir\ o} - \omega_E R_E \cos\delta_{st} \cos\left(\frac{\pi}{2} - A\right),$$

where $v_{cir\ o}$ is the circular velocity of the rocket in the parking orbit; ω_E is the Earth angular velocity of rotation; R_E is the radius of the Earth; $\bar{v}_{rev}$ is the Earth rotation velocity vector at the point C; A is the launch azimuth and is the angle between the meridional plane of the launch point and the injection trajectory plane, positive toward the east from the exact north direction (see Figure 4.1.3). /105

From the right spherical triangle ΩCD, we find

$$\sin A = \frac{\pm \cos i}{\cos \delta_{st}},* \qquad (4.1.6)$$

where the minus sign corresponds to $\pi/2 < i \leq \pi$.

Hence, we obtain

$$V_{X\ inj} = V_{cir\ o} - \omega_E R_E (\pm \cos i).$$

Thus, the energy expenditures during rocket injection into the parking orbit will be minimal for the maximal possible values of $(\pm \cos i)$. Now, depending on the relationship of the angles δ_0 and φ_{st}, we can determine the optimal values of the inclination angle i. If $\varphi_{st} \geq \delta_0$, then during launch:

in the northeast direction

$$i = \varphi_{st}; \qquad (4.1.7a)$$

in the southeast direction

$$i = \pi - |\varphi_{st}|. \qquad (4.1.7b)$$

If $\varphi_{st} \leq \delta_0$, then during launch:

in the northeast direction

$$i = \delta_0; \qquad (4.1.8a)$$

in the southeast direction

$$i = \pi - |\delta_0|. \qquad (4.1.8b)$$

*We assume launch in the easterly direction only.

LIMITATIONS ON CHOICE OF LAUNCH AZIMUTH A

The influence of launch azimuth A on injection segment geometry shows up through the inclination angle i. With change of the launch azimuth A, the injection trajectory plane rotates relative to the launch point radius vector. However, such rotation can take place only under definite limitations, since the target vector $\bar{W}$ must also be located in the injection trajectory plane. Using the condition (4.1.2) and Equation (4.1.6), we write

$$\sin A \leq \frac{\cos \delta_0}{\cos \varphi_{st}}. \qquad (4.1.9)$$

Consequently, if the target vector declination δ_0 is greater than the launch point latitude φ_{st} ($\varphi_{st} < \delta_0$), there is a range arc $\sin \frac{\cos \delta_0}{\cos \delta_{st}} = A_1 < A < A_2 = \pi - \text{arc} \sin \frac{\cos \delta_0}{\cos \delta_{st}}$ of launch azimuths (symmetric about the east direction) in which launch is impossible from the specified launch point. However, if the target vector declination δ_0 is smaller than or equal to the launch point latitude φ_{st} ($\varphi_{st} \geq \delta_0$), launch can be accomplished for all permissible azimuths (within the safety limits). /106

ASCENDING NODE LONGITUDE Ω

The parking orbit (hyperbolic escape orbit) ascending node longitude is determined from the right spherical triangle ΩPB (see Figure 4.1.2). We have

$$\operatorname{tg} \delta_0 = \sin(\alpha_0 - \Omega) \operatorname{tg} i \qquad (4.1.10a)$$

or

$$\Omega = \alpha_0 - \text{arc} \sin \frac{\operatorname{tg} \delta_0}{\operatorname{tg} i}. \qquad (4.1.10b)$$

RELATIONS BETWEEN CENTRAL INJECTION ANGLE β AND DECLINATIONS δ_0, δ_{st} AND LAUNCH AZIMUTH A

The injection segment central angle β is the angle between the launch point radius vector and the target vector (direction of the asymptote) (see Figure 4.1.2). It is the total angular distance which the rocket must travel from the instant of launch to the moment when the SC velocity vector is parallel to the vector $\bar{V}_{\infty 0}$. For known launch point location (φ_{st}) and specified target declination δ_0, the angle β depends on the launch azimuth A.

From the right spherical triangle CPP' (see Figure 4.1.2), we obtain

$$\cos\beta = \operatorname{ctg} P \cdot \operatorname{tg} A,$$

and from the right spherical triangle ΩPB, we find

$$\sin P = \frac{\cos i}{\cos \delta_0}$$

or with account for (4.1.6),

$$\sin P = \frac{\cos \delta_{st} \sin A}{\cos \delta_0}.$$

Then we will have

$$\cos\beta = \pm \sqrt{\left(\frac{\cos \delta_0}{\cos \delta_{st} \sin A}\right)^2 - 1}\ \operatorname{tg} A. \qquad (4.1.11)$$

The ambiguity in determination of the angle β corresponds to two possible launch times in the day for a definite launch azimuth. /107

The asymptote inclination φ to the line of apsides of the hyperbolic escape orbit is found from the equation

$$\cos\varphi = -\frac{1}{e} \quad \left(\frac{\pi}{2} < \varphi < \pi\right).$$

In the case of impulsive acceleration from a parking orbit, its radius is equal to the escape orbit perigee radius. Therefore, the equality holds

$$e=\frac{r_0}{a}+1$$

or, excluding $a=\frac{fm_\oplus}{V_{\infty 0}^2}$, we obtain

$$e=1+\frac{V_{\infty 0}^2}{v_{\text{cir o}}^2}. \qquad (4.1.12)$$

Consequently,

$$\cos\varphi=-\frac{1}{1+V_{\infty 0}^2/v_{\text{cir o}}^2}. \qquad (4.1.13)$$

Knowledge of the asymptote inclination φ to the hyperbolic escape orbit line of apsides permits for known asymptote direction, defined by the target vector $\bar{W}$, finding the point of departure from the parking orbit for impulsive acceleration.

The relations (4.1.7) - (4.1.13) characterize the injection segment geometry, determining the injection trajectory plane location and the orientation, dimensions, and shape of the hyperbolic escape orbit.

PROBLEM OF LAUNCH AT CORRECT MOMENT OF TIME

The strict dependence between launch azimuth and launch time forms the basis for solution of the problem of launch at the correct moment of time. Thus, if the launch time of day is specified in advance, the launch azimuth must be selected so that the injection trajectory plane will contain the target vector $\bar{W}$. On the other hand, if the launch azimuth is fixed in advance, the launch must be accomplished at the instant of time when the launch point crosses the injection trajectory plane.

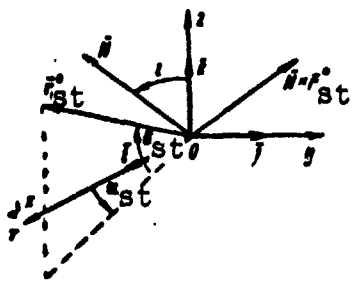

Figure 4.1.4. Vector diagram at launch time.

The following equations must be satisfied at the instant of launch point alignment with the injection trajectory plane fixed in space (Figure 4.1.4) /108

$$\bar{N} \cdot \bar{r}^0_{st} = 0;$$

$$(\bar{N} \times \bar{r}^0_{st}) \cdot \bar{k} = \sin i.$$

Solving these equations for the launch point right ascension α_{st}, we obtain

$$\left.\begin{aligned} \cos \alpha_{st} &= -\frac{N_x \cos i \sin \delta_{st} + N_y \sin i}{\sin^2 i \cos \delta_{st}}; \\ \sin \alpha_{st} &= -\frac{N_y \cos i \sin \delta_{st} - N_x \sin i}{\sin^2 i \cos \delta_{st}}. \end{aligned}\right\} \quad (4.1.14)$$

Here we used the fact that $\bar{r}^0_{st} = \cos \alpha_{st} \cos \delta_{st} \bar{I} + \sin \alpha_{st} \cos \delta_{st} \bar{J} + \sin \delta_{st} \bar{k}$.

Expressions (4.1.14) with account for (4.1.1) permit determining the launch point right ascension α_{st} as a function of launch azimuth. Moreover, the launch point right ascension α_{st} is related with the launch time t_{st}, measured from midnight of the launch day, by the following relation

$$\alpha_{st} = -\mathrm{GHA} + \lambda_{st} + \omega_E t_{st} \quad (4.1.15a)$$

or

$$t_{st} = \frac{1}{\omega_E}(\alpha_{st} - \mathrm{GHA} - \lambda_{st}), \quad (4.1.15b)$$

where GHA is the Greenwich hour angle at midnight of the launch

day; λ_{st} is the launch point geographic longitude.

The relations (4.1.15) make it possible for selected launch azimuth A and given target declination δ_s and launch point declination δ_{st} to determine using the relations (4.1.1) and (4.1.14), the launch time of day on a known launch date.

Thus, we have obtained an analytic solution of the injection problem which permits for given and constant vector $\bar{V}_{\infty 0}$ calculation of the geometric characteristics of the injection segment and determination of the launch time of day t_{st}. /109

SELECTION OF INCLINATION i TO INCREASE LAUNCH WINDOW WITH ACCOUNT FOR PERTURBATIONS

So far, we have examined the problem of selecting the injection segment kinematic parameters without account for noncentrality of the Earth's gravity field and variation of the hyperbolic excess velocity vector $\bar{V}_{\infty 0}$ as a function of time. However, if we take into account the possibility of launch time deviation from the nominal date, such simplifications may lead to significant errors.

In actuality, noncentrality of the Earth's field leads to variation of the parking orbit plane position as a function of time. In the first approximation (see § 3 of Chapter 1), its ascending node longitude change can be estimated as

$$\Delta\Omega = -\omega_s \Delta t_s, \qquad (4.1.16)$$

where $\Delta\Omega = \Omega_s - \Omega_0$; Ω_0, Ω_s are the parking orbit ascending node longitudes for the nominal and actual launch dates $t_s = t_0 + \Delta t_s$; ω_s is the orbit plane model regression rate.

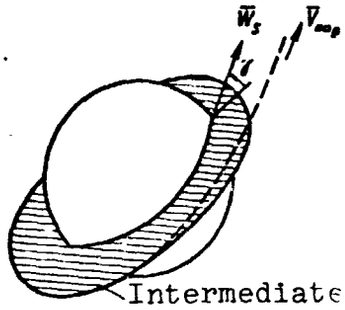

Figure 4.1.5. Deviation of hyperbolic excess velocity vector (target vector) from parking orbit plane for actual launch date

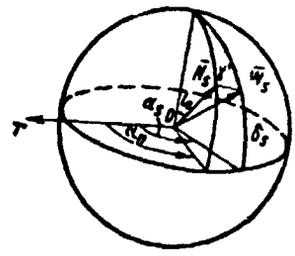

Figure 4.1.6. Kinematics of vectors for actual launch date and geometric interpretation of the angle γ:

$$\alpha_n = \frac{3}{2}\pi + \Omega_s;\ \gamma' = \gamma \pm \frac{\pi}{2}$$

In addition, the hyperbolic excess velocity vector $\bar{V}_{\infty 0}$ also changes with time in magnitude and direction, forming with the parking orbit plane the angle γ (Figure 4.1.5), which is found from the equation (Figure 4.1.6): /110

$$\sin\gamma = \cos i \sin\delta_s + \sin i \cos\delta_s \cos(\alpha_s - \alpha_n),$$

where α_n, α_s are the right ascensions of the vectors $\bar{N}_s$, $\bar{W}_s$; $\bar{N}_s$, $\bar{W}_s$ are the vector normal to the parking orbit plane and the target vector for the actual launch date.

Since by the definition of the angles we have

$$\alpha_n = \frac{3}{2}\pi + \Omega_s = \frac{3}{2}\pi + \Omega_0 + \Delta\Omega,$$

with account for (4.1.10) and (4.1.16), we obtain

$$\alpha_n = \frac{3}{2}\pi + \alpha_0 - \arcsin(\operatorname{ctg} i \operatorname{tg}\delta_0) - \omega_s \Delta t_s.$$

Substituting this value of α_n into the preceding equation, after some transformations, we find

$$\sin\gamma = \cos i\,[\sin\delta_s - \cos(\alpha_0 - \alpha_s - \omega_s\Delta t_s)\cos\delta_s \operatorname{tg}\delta_0] \pm \pm \sqrt{\sin^2 i - \sin^2\delta_0}\sec\delta_0 \sin(\alpha_0 - \alpha_s - \omega_s\Delta t_s)\cos\delta_s, \qquad (4.1.17)$$

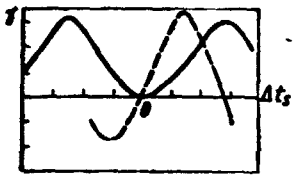

Figure 4.1.7. Variation of angle γ with deviation from nominal launch date

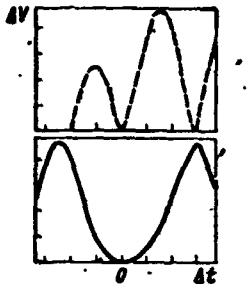

Figure 4.1.8. Characteristic velocity losses in nonplanar maneuver

where, in the prograde motion case, we take the sign "+" for $0 \leq (\alpha_0 - \Omega_0) \leq \pi/2$ and the sign "-" for $(\alpha_0 - \Omega_0) > \pi/2$.

Consequently, with deviation of the launch time from the nominal launch date as a consequence of parking orbit precession and escape orbit hyperbolic excess velocity vector change, conditions may arise in which the hyperbolic excess velocity vector will now not be located in the parking orbit plane. Such a situation leads to the necessity for a nonplanar SC module acceleration maneuver, which involves additional boost energy expenditures (in comparison with coplanar flight). Figure 4.1.7 shows typical variations of the angle γ from Δt_s, and Figure 4.1.8 shows the corresponding characteristic boost velocity increment variations. We note marked increase of the characteristic boost velocity as a consequence of appearance of the angle γ with deviation from the nominal launch date. /111

The subject process reduces markedly the launch window size and, thereby has a fundamental influence on parking orbit inclination angle selection. We find that, by selecting i in the range defined by the conditions (4.1.3), we can for certain values of Δt_s reduce somewhat the characteristic boost velocity increase in comparison with coplanar acceleration (Figure 4.1.9),

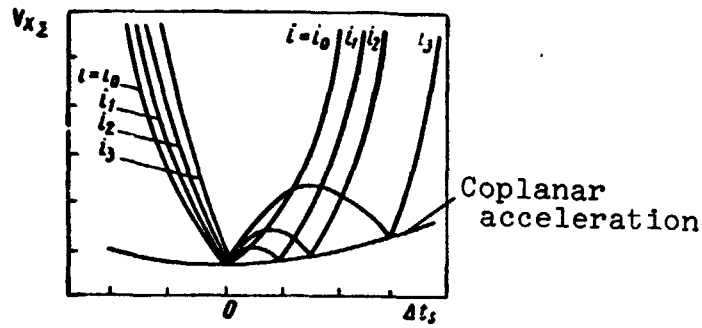

Figure 4.1.9. Required values of characteristic acceleration velocity versus deviation from nominal launch date as function of parking orbit inclination angle

which makes possible considerable broadening of the launch window. In this sense, the parking orbit inclination angle i selected in this fashion will be optimal. When constructing the algorithm for this process, the relation (4.1.17), which makes it possible to determine the dependence of γ on i for given Δt_s, should be used.

§ 2. IMPULSIVE SC MANEUVERS IN PLANETARY GRAVISPHERE

In the ballistic analysis of schemes for SC flight to the planets, the question of SC maneuvers in planetary gravispheres is essential. The approximate problem is usually examined in the impulsive formulation, which is quite adequate in the preliminary design stage.

In the following, we examine the basic forms of maneuvers used in various interplanetary SC flight schemes.

PERICENTRAL TRANSFER BETWEEN COPLANAR ELLIPTIC AND HYPERBOLIC ORBITS

The transfer of this type is used for SC braking in APS orbit /112 or launch from such an orbit. The required velocity increment

for transfer from elliptic orbit to hyperbolic (or vice versa) will be

$$\Delta V = V_{\pi h} - V_{\pi el}$$

where $V_{\pi h} = \sqrt{2V_{cir\pi}^2 + V_\infty^2}$ is the velocity at the pericenter of the hyperbola with hyperbolic excess velocity V_∞; $V_{cir\pi} = \sqrt{\mu_{pl}/r_\pi}$ is the circular velocity corresponding to the transfer point pericenter radius r_π; $V_{\pi el} = \sqrt{\mu[(2/r_\pi) - (1/a)]}$ is the velocity at the elliptic orbit pericenter; $a = r_\pi/(1 - e)$ is the semimajor axis of the ellipse with eccentricity $e = (r_\alpha - r_\pi)/(r_\alpha + r_\pi)$. Then

$$\Delta V = \sqrt{\frac{2\mu}{r_\pi} + V_\infty^2} - \sqrt{\frac{\mu(1+e)}{r_\pi}}.$$

If we take a circular orbit with $r_{cir} = r_\pi$ as the reference orbit, then /113

$$\Delta\tilde{V} = \sqrt{2 + \tilde{V}_\infty^2} - \sqrt{1+e},$$

where

$$\tilde{V} = V/(V_{cir},\ \tilde{r} = \frac{r}{2\pi}).$$

For transfers from circular orbit to hyperbolic (or vice versa)

$$\Delta\tilde{V} = \sqrt{2 + \tilde{V}_\infty^2} - 1.$$

The characteristics of coplanar pericentral ellipse-hyperbola transfers for $r_\pi = 1$ are shown in Figure 4.2.1 and ellipse-hyperbola transfers for various $\tilde{r}_\pi$ are shown in Figure 4.2.2.

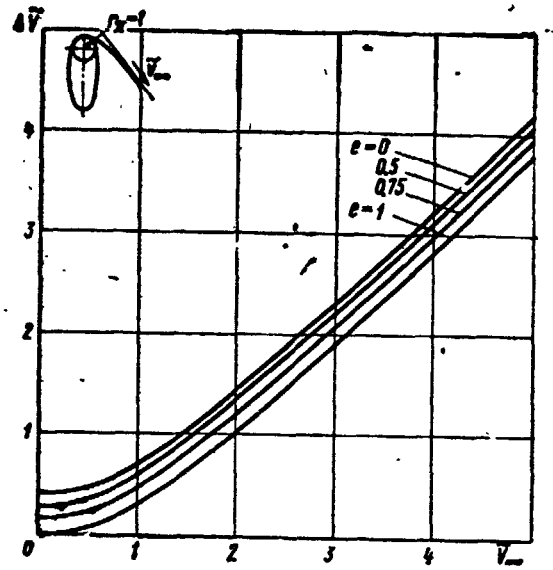

Figure 4.2.1. Characteristics of ellipse-hyperbola transfer for $\tilde{r}_{\pi} = 1$

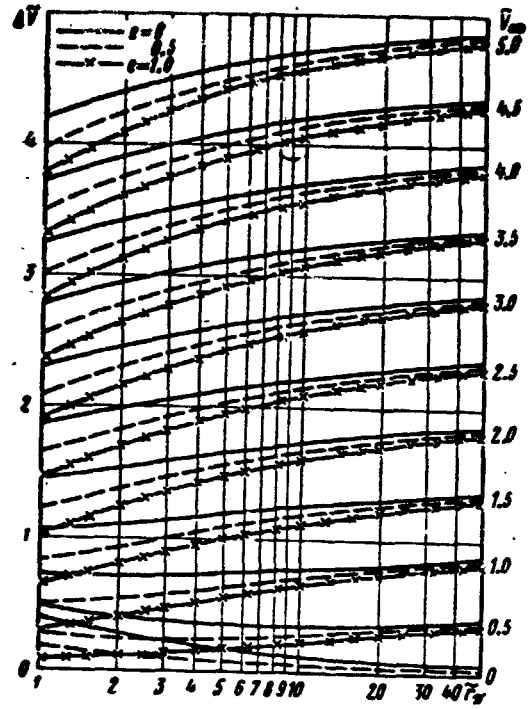

Figure 4.2.2. Characteristics of pericentral ellipse-hyperbola transfer

NONPERICENTRAL TRANSFER BETWEEN COPLANAR ELLIPTIC AND HYPERBOLIC ORBITS

This transfer can be used to form parking orbits around a planet.

The elliptic orbit is specified by the following parameters: /114 $r_{\pi el}$ is the pericenter radius and $r_{\alpha el}$ is the apocenter radius.

The point M of transfer from the ellipse to the hyperbola is specified by the true anomaly ν_{el} (Figure 4.2.3). The modulus of the hyperbolic excess velocity V_{∞} for the hyperbola is known. A family of hyperbolas can be drawn through the point M with given modulus V_{∞}. As the parameter of this family, we take the hyperbola pericenter radius $r_{\pi h}$. It is necessary to

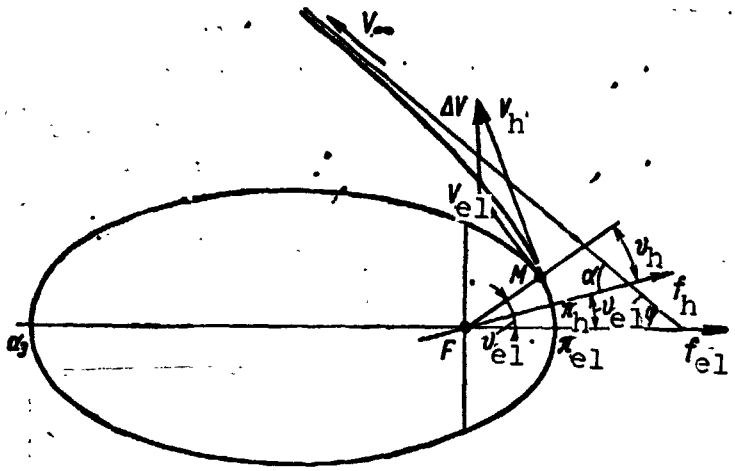

Figure 4.2.3. Schematic of nonpericentral ellipse-hyperbola transfer

find that value of $r_{\pi h}$ which minimizes the modulus of the vector $\Delta\tilde{V} = \tilde{V}_h - \tilde{V}_{el}$, providing transfer from the ellipse to the hyperbola (or vice versa). The modulus of the vector $|\Delta\tilde{V}|$ (dimensionless velocity referred to the circular velocity of an orbit with $r_{cir} = r_{\pi el}$) is

$$\Delta\tilde{V} = \sqrt{\Delta\tilde{V}_n^2 + \Delta\tilde{V}_r^2},$$

where

$$\Delta\tilde{V}_n = \tilde{V}_{nh} - \tilde{V}_{n\,el};\quad \Delta\tilde{V}_r = \tilde{V}_{rh} - \tilde{V}_{r\,el};$$

$\tilde{V}_{n\,el}$, $\tilde{V}_{n\,h}$ are the normal velocity components of the hyperbola and ellipse at point M; $\tilde{V}_{r\,el}$; $\tilde{V}_{r\,h}$ are the radial velocity components at point M.

These velocity components at point M of the ellipse are

$$V_{n\,el} = \sqrt{\mu_{pl}/p_{el}}\,(1 + e_{el}\cos v_{el});$$

$$V_{r\,el} = \sqrt{\mu_{pl}/p_{el}}\,e_{el}\sin v_{el}.$$

Referring the velocities to $V^{el}_{cir\ \pi} = \sqrt{\mu_{pl}/r_{\pi el}}$ and distances to $r_{\pi el}$, we obtain

$$\tilde{V}_{n\ el} = \frac{1 + e_{el} \cos \nu_{el}}{\sqrt{\tilde{p}_{el}}};\quad \tilde{V}_{r\ el} = \frac{e_{el} \sin \nu_{el}}{\sqrt{\tilde{p}_{el}}},$$

where

$$\tilde{p}_{el} = \frac{2\tilde{r}_{\alpha el}}{\tilde{r}_{\alpha el} + 1};\quad e_{el} = \frac{\tilde{r}_{\alpha el} - 1}{r_{\alpha el} + 1},$$

are the parameter and eccentricity of the elliptic orbit.

The components of the relative velocity at point M of the hyperbola are

$$\tilde{V}_{n\ h} = \frac{1 + e_h \cos \nu_h}{\sqrt{\tilde{p}_h}};\quad \tilde{V}_{r\ h} = \frac{e_h \sin \nu_h}{\sqrt{\tilde{p}_h}},$$

where

$$\tilde{p}_h = \tilde{a}_h(e_h^2 - 1) = \tilde{r}_{\pi h}(2 + \tilde{V}_\infty^2 \tilde{r}_{\pi h});$$

$$e_h = 1 + \frac{\tilde{r}_{\pi h}}{\tilde{a}_h} = 1 + \tilde{r}_{\pi h}\tilde{V}_\infty^2;\quad \tilde{a}_h = \frac{1}{\tilde{V}_\infty^2}.$$

The true anomaly of the hyperbola at point M is found from the condition

$$\tilde{r}_h = \tilde{r}_{el} \text{ or } \frac{\tilde{p}_h}{1 + e_h \cos \nu_h} = \frac{\tilde{p}_{el}}{1 + e_{el} \cos \nu_{el}}.$$

Hence,

$$\cos \nu_h = \frac{1}{e_h}\left[\frac{\tilde{p}_h}{\tilde{p}_{el}}(1 + e_{el} \cos \nu_{el}) - 1\right].$$

For given true anomaly ν_{el} of the transfer point M and V_∞, the volocity modulus $\tilde{\Delta V} = f(\tilde{r}_{\pi h})$. The limiting value of the hyperbola pericenter radius which ensures intersection with the ellipse at the point M is equal to $r_{\pi h} = r_{el}$ at the transfer point. Calculations show that the values of $r_{\pi h\ opt}$ which minimize $\tilde{\Delta V}$ correspond basically to the limiting values. For small values of the ellipse eccentricity and small ν_{el}, the values of $r_{\pi h\ opt}$ are somewhat larger than the limiting values. However, because of the flatness of the $\tilde{\Delta V} = f(\tilde{r}_{\pi h})$ optimum, the $\tilde{\Delta V}$ values corresponding to the $r_{\pi h}$ limiting values differ very little from the minimal values. Figure 4.2.4 shows curves of the minimal $\tilde{\Delta V} = f(\nu_{el})$ for various $\tilde{V}_\infty$ and $\tilde{r}_{\alpha el} = 5$. Also shown /116 are the values of the inclination of the impulse vector $\Delta\bar{V}$ to the local horizon

$$\operatorname{tg}\theta_* = \frac{\Delta V_r}{\Delta V_\tau}.$$

The angle between the ellipse axis of apsides and the hyperbola asymptote is

$$\varphi = \pi - [v + (\pi - \alpha)] = \alpha - v,$$

where

$$\cos\alpha = \frac{1}{e_h};\ \nu = \nu_{el} - \nu_h.$$

ROTATION OF ELLIPTIC ORBIT PLANE

This maneuver can be used to vary APS orbit inclination and form a parking orbit around a planet. Rotation of the elliptic orbit plane through the angle κ with minimal energy expenditures will be accomplished by rotating the velocity vector through the angle κ at the orbit apocenter where the flight velocity along the orbit is minimal. In this case, the required velocity impulse ΔV is

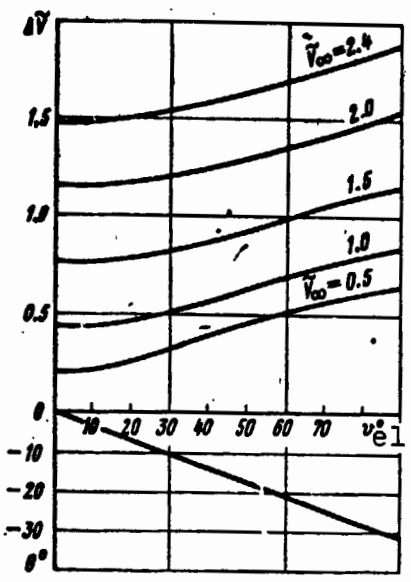

Figure 4.2.4. Characteristics of nonpericentral transfer for $\tilde{r}_{\alpha el} = 5$

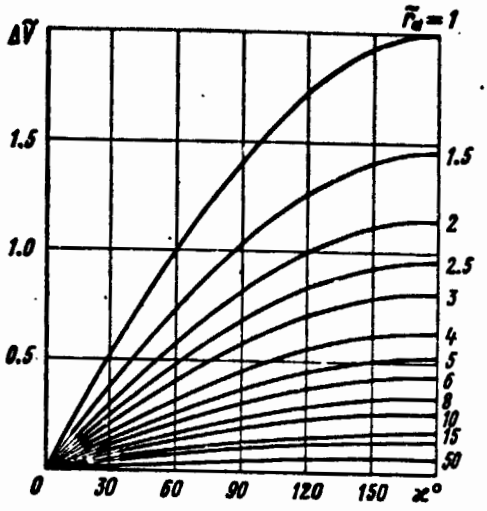

Figure 4.2.5. Characteristics of elliptic orbit plane rotation maneuver

$$\Delta V = V_a \sqrt{2(1-\cos\varkappa)} = 2V_a \sin\frac{\varkappa}{2}.$$

We find the velocity at the elliptic orbit apocenter from the relation /117

$$V_a^2 = \mu_{pl}\left(\frac{2}{r_a} - \frac{1}{a}\right).$$

Replacing $\mu_{pl} = V_{cir\pi}^2 r_\pi$ and $a = (r_\alpha + r_\pi)/2$, we obtain

$$V_\alpha = V_{cir\pi}\sqrt{\frac{2r_a^2}{r_a(r_a+r_a)}},$$

where V_{cir} is the circular velocity for $r = r_\pi$.

We convert to dimensionless variables, referring r to r_π and V_α to $V_{cir\pi}$. Then

$$\tilde{V}_a = \sqrt{\frac{2}{\tilde{r}_a(\tilde{r}_a+1)}}.$$

Thus the minimal relative velocity impulse required for rotation of the elliptic orbit plane through the angle κ is

$$\Delta\bar{V}=2\sqrt{\frac{1-\cos\varkappa}{\bar{r}_a(\bar{r}_a+1)}}=2\sin\frac{\varkappa}{2}\sqrt{\frac{2}{\bar{r}_a(\bar{r}_a+1)}}.$$

The relation $\Delta\bar{V}=f(\varkappa;\ \bar{r}_a)$ is shown in Figure 4.2.5. We see that the energy expenditures required to rotate the elliptic orbit plane decrease significantly with increase of the apocenter radius r_α.

SINGLF-IMPULSE ROTATION OF ELLIPTIC ORBIT AXIS OF APSIDES /118

This maneuver is used to shape the APS orbit.

Let the axes of the coplanar elliptic orbits 1 and 2 be separated by the angle ω (Figure 4.2.6) Single-impulse transfer between these orbits is possible at the two points of intersection I and II.

The true anomaly of the points of intersection of the ellipses is:

for transfer at point I

$$v_I^1=2\pi-\frac{\omega}{2}\quad\text{or}\quad v_I^2=\frac{\omega}{2};$$

for transfer at point II

$$v_{II}^1=\pi-\frac{\omega}{2}\quad\text{or}\quad v_{II}^2=\pi+\frac{\omega}{2}.$$

Let us examine transfer at point I. The normal velocity components at this point are

$$V_{n1}=\sqrt{\frac{\mu_{pl}}{p}}\left[1+e\cos\left(-\frac{\omega}{2}\right)\right]=\sqrt{\frac{\mu_{pl}}{p}}\left(1+e\cos\frac{\omega}{2}\right);$$

$$V_{n2}=\sqrt{\frac{\mu_{pl}}{p}}\left(1+e\cos\frac{\omega}{2}\right),$$

i.e., they are equal.

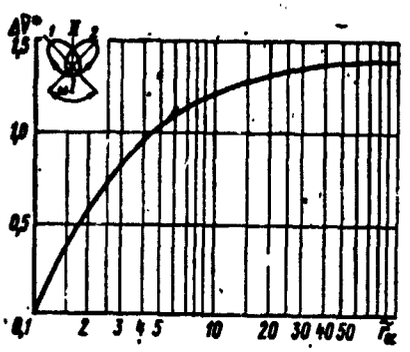

Figure 4.2.6. Characteristics of single-impulse axis of apsides rotation maneuver.

The radial velocity components are equal but opposite in direction /119

$$V_{r1}=\sqrt{\frac{\mu_{pl}}{p}}e\sin\left(-\frac{\omega}{2}\right)=-\sqrt{\frac{\mu_{pl}}{p}}e\sin\frac{\omega}{2};$$

$$V_{r2}=\sqrt{\frac{\mu_{pl}}{p}}e\sin\frac{\omega}{2}.$$

The impulse for transfer between the orbits is

$$\Delta V=2|V_{r1}|=2\sqrt{\frac{\mu_{pl}}{p}}e\sin\frac{\omega}{2}$$

and is directed radially from the attracting center. The normal velocity components are also equal at point II. The radial components are also equal and opposite in sign. The transfer impulse $\Delta V = 2|V_r|$ and is directed radially but along the direction toward the attracting center. We refer the velocities to the circular velocity ($V_{circ\pi} = \sqrt{\mu_{pl}/r_\pi}$) of the orbit with r_π and the distances to r_π. Then, considering that

$$\tilde{p}=\frac{2\tilde{r}_\alpha}{\tilde{r}_\alpha+1};\quad e=\frac{\tilde{r}_\alpha-1}{\tilde{r}_\alpha+1},$$

we obtain

$$\Delta\tilde{V}=\frac{\sqrt{2}(\tilde{r}_\alpha-1)}{\sqrt{\tilde{r}_\alpha}(\tilde{r}_\alpha+1)}\sin\frac{\omega}{2}=\Delta\tilde{V}^*\sin\frac{\omega}{2},$$

where $\tilde{r}_\alpha$ is the relative ellipse apocenter radius. The values of $\Delta V^* = f(\tilde{r}_\alpha)$ are shown in Figure 4.2.6. For $\tilde{r}_\alpha \to \infty$

$$\Delta\tilde{V}\to\sqrt{2}\cdot\sin\frac{\omega}{2}.$$

TWO-IMPULSE ROTATION OF ELLIPTIC ORBIT AXIS OF APSIDES

A schematic of such transfer between two elliptic orbits is shown in Figure 4.2.7. At point 1, the vehicle transitions to a transfer ellipse and then at point 2, to an elliptic orbit

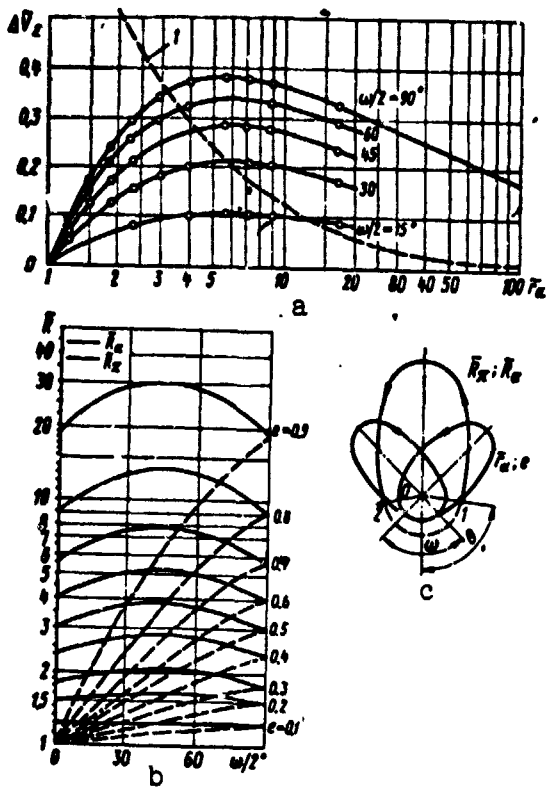

Figure 4.2.7. Characteristics of two-impulse axis of apsides rotation maneuver: a- total velocity impulse $\Delta\tilde{V}_\Sigma$ as function of apocenter radius r_α and apside axis rotation angle ω; b- transfer ellipse apocenter radius $\tilde{R}_\alpha$ and pericenter radius $\tilde{R}_\pi$ as function of angle ω; c- transfer scheme

rotated through the angle ω relative to the original orbit. Transfers of this type were examined in [36] (article by Lawden entitled "Impulsive Transfer between Elliptic Orbits"). Based on the data of this article, Figure 4.2.7 shows the basic characteristics of such a transfer: $\tilde{R}_\pi$ and $\tilde{R}_\alpha$ are the transfer orbit pericenter and apocenter radii referred to r_π of the original ellipse. $\Delta\tilde{V}_\Sigma$ is the total velocity impulse required for the transfer (referred to $V_{circ\pi}$ with $r = r_\pi$).

The largest energy expenditures occur in transfers with relative original ellipse apocenter radius $\tilde{r}_\alpha \approx 5 - 7$. The angle $\omega = 180°$ corresponds to transfer with maximal values of ΔV. In this case, the transfer orbit will be circular with $\tilde{R} = \tilde{r}_\alpha$. In this case, rotation of the apside axis takes place as follows. At the apocenter of the original orbit, the vehicle is imparted the first impulse ΔV, transferring it to a circular orbit with $r = r_\alpha$ of the ellipse. After rotation through the required angle, the vehicle is transferred to the final ellipse by a second impulse ΔV. The velocity impulse

/120

$$\Delta V = V_{cir\alpha} - V_{\alpha},$$

where

$$V_{cir\alpha} = \sqrt{\mu_{pl}/r_{\alpha}},\ V_{\alpha} = V_{cir\alpha}\sqrt{1-e}.$$

Converting to dimensionless quantities /121

$$\tilde{V} = \frac{V}{V_{cir\pi}} \text{ and } \tilde{r} = \frac{r}{r_{\pi}},$$

we obtain

$$\Delta\tilde{V} = \frac{1}{\sqrt{\tilde{r}_{\alpha}}} - \sqrt{\frac{1-e}{\tilde{r}_{\alpha}}}.$$

Substituting the value

$$e = \frac{r_{\alpha}-r_{\pi}}{r_{\alpha}+r_{\pi}} = \frac{\tilde{r}_{\alpha}-1}{\tilde{r}_{\alpha}+1},$$

we obtain

$$\tilde{V}_{\pi} = \sqrt{\frac{2}{\tilde{r}_{\alpha}(\tilde{r}_{\alpha}+1)}} \text{ and } \Delta\tilde{V} = \frac{1}{\sqrt{\tilde{r}_{\alpha}}}\left(1-\sqrt{\frac{2}{\tilde{r}_{\alpha}+1}}\right).$$

In this case, the transfer energetics are independent of the apside axis rotation angle. For $r_{\alpha}\to\infty$, the quantity $\Delta\tilde{V}_{\pi}\to 0$.

GRAVITY MANEUVER DURING PLANET FLYBY

For several interplanetary flight schemes, it is advisable to utilize a maneuver in the gravity field of a planet in order to alter the heliocentric velocity vector direction and magnitude.

Let us examine the gravity maneuver scheme in the sphere of action of a planet (Figure 4.2.8). The velocity vector $\bar{V}_{\infty 1}$ of entry into the planet's sphere of action is found as the difference between the helicentric velocity vector of approach to the planet $\bar{V}_1$ and the planet velocity vector $\bar{V}_{pl}$. In the process of the gravity maneuver in the planet sphere of action, the vector $\bar{V}_{\infty 1}$

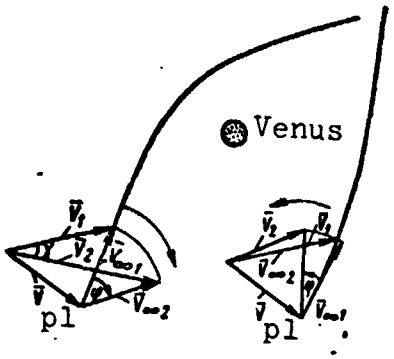

Figure 4.2.8. Scheme of gravity maneuver during planet flyby

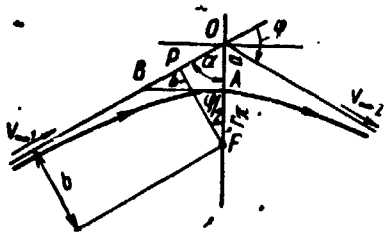

Figure 4.2.9. Scheme of flight along flyby hyperbola

is rotated through the angle φ without change in modulus and is transformed into the departure velocity vector from the planet's sphere of action $\bar{V}_{\infty 2}$. The heliocentric departure velocity vector $\bar{V}_2$ will be the sum of the vectors $\bar{V}_{\infty 2}$ and $\bar{V}_{pl}$. We see that the heliocentric vectors $\bar{V}_1$ and $\bar{V}_2$ are different in both modulus and direction.

The angle of rotation of the vector $\bar{V}_{\infty 1}$ is found as the angle between the asymptotes of the flyby hyperbola (Figure 4.2.9)

$$\sin\frac{\varphi}{2}=\frac{OP}{OF}=\frac{AO}{OF}=\frac{a}{a+r_\pi}=\frac{1}{1+\frac{r_\pi}{a}}.$$

Since $a=\frac{\mu}{V_\infty^2}$, then $\sin\frac{\varphi}{2}=\frac{1}{1+\frac{r_\pi V_\infty^2}{\mu}}$.

Rotation of the vector $\bar{V}_\infty$ through the angle φ leads to rotation of the SC heliocentric velocity vector through the angle γ (see Figure 4.2.8). The extremal values of the modulus of the rotation angle γ for given value of the angle φ will correspond to the case when $V_1 = V_2 = V$ (Figure 4.2.10). For circular planetary orbits, when $V_{pl} = V_{cir}$, the angle γ is found from the relation

/123

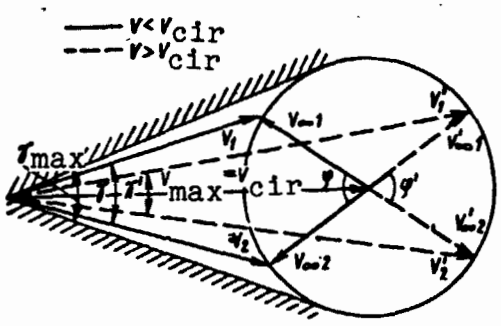

Figure 4.2.10. Scheme for determining largest heliocentric velocity vector rotation angle γ

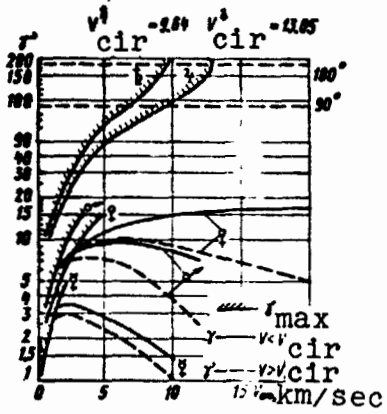

Figure 4.2.11. Angle γ as function of V_∞ for various planets

$$\frac{\sin\frac{\gamma}{2}}{\sin\frac{\varphi}{2}}=\frac{V_-}{V},$$

where

$$V^2 = V_{cir}^2 + V_\infty^2 \pm 2V_\infty V_{cir}\cos\frac{\varphi}{2},$$

hence,

$$\sin\frac{\gamma}{2}=\frac{V_-\sin\frac{\varphi}{2}}{\sqrt{V_{cir}^2 + V_\infty^2 \pm 2V_\infty V_{cir}\cos\frac{\varphi}{2}}}.$$

Here, the plus sign corresponds to $V > V_{cir}$, the minus sign to $V < V_{cir}$.

The magnitude of the angle γ cannot exceed the limiting values γ_{max} (see Figure 4.2.10), when

$$\sin\frac{\gamma_{max}}{2}=\frac{V_\infty}{V_{cir}}.$$

The magnitudes of the angle γ as a function of V_∞ for the limiting maneuvers, when $r_\pi = R_{per}$ (R_{per} is no less than the

radius of the planet and height of its dense atmosphere layers), for various planets are shown in Figure 4.2.11.

We see that, for the planets of the Earth group, there exist values of V_∞ which maximize the angles γ. For flights to the inner planets $V > V_{cir}$ and the maximal γ will be $\gamma_{max} \approx 10°$ for Venus flyby and $\gamma_{max} \approx 3°$ for Mercury flyby. For flights to the outer planets, $V < V_{cir}$ and for flight to Mars $\gamma_{max} \approx 9.5°$. Thus, the maximal possible values of the angle γ for maneuvers in the gravity field of Mars and Venus are approximately the same.

The gravity maneuver capabilities in the gravity fields of the large planets (Jupiter and Saturn) practically always correspond to γ_{lim} and for values $V_\infty = V_{cir}$ provide rotation of the heliocentric velocity vector through 180°. Rotation of the heliocentric velocity vector through the angle $\gamma = 90°$ in the gravity field of Jupiter or Saturn provides for flight to the Sun along a degenerate rectilinear hyperbola. However, this is possible only with $V_\infty \geq 9.5$ km/sec for Jupiter and with $V_\infty \geq 7.3$ km/sec for Saturn, which indicates that such flights at close distance to the Sun are possible for values of V_∞ at the planet larger than for the minimal energy flight trajectories to Jupiter or Saturn (see Tables 5.4 and 5.8). /124

ACTIVE-GRAVITY MANEUVER DURING PLANET FLYBY

The passive gravity maneuver capabilities in the gravisphere of the Earth group planets are constrained by the limit of flyby hyperbola pericenter altitude reduction to values $r_\pi < R_{per}$. Therefore, in many cases, an active-gravity maneuver with additional impulsive velocity change in the planet approach-hyperbola departure-hyperbola flyby segment becomes advantageous.

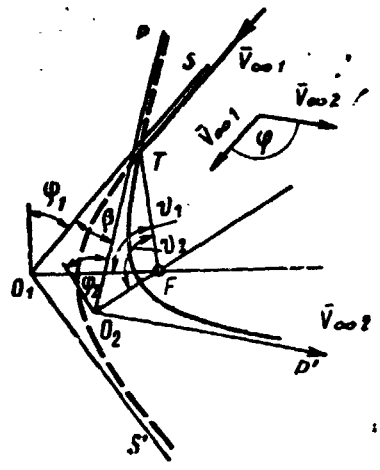

Figure 4.2.12. General scheme of single-impulse hyperbola-hyperbola transfer (F is the hyperbola focus)

A quite complete exposition of this problem is given in [63].

The general scheme of such a planar single-impulse transfer is shown in Figure 4.2.12. At the point T, the vehicle transitions from the incoming branch S of the approach hyperbola to the incoming branch P of the departure hyperbola. Four possible hyperbola-hyperbola transfer variants are shown in Figure 4.2.13. The hyperbola asymptote turning angle is (see Figure 4.2.12):

$$\varphi=\beta+2\psi_2, \tag{4.2.1}$$

where β is the angle between the incoming hyperbola asymptotes; $\psi=\frac{\pi}{2}-\alpha$ is the complement of the hyperbola asymptote declination angle α.

The following relation is valid for transfers of this type

$$\beta=(\psi_1-\psi_2)+(v_2-v_1), \tag{4.2.2}$$

where v_i is the true anomaly of the impulse application point (positive for clockwise turning from the apside axis).

Combining (4.2.1) and (4.2.2), we obtain, regardless of the transfer type, /125

$$\varphi=(\psi_1+\psi_2)+(v_2-v_1). \tag{4.2.3}$$

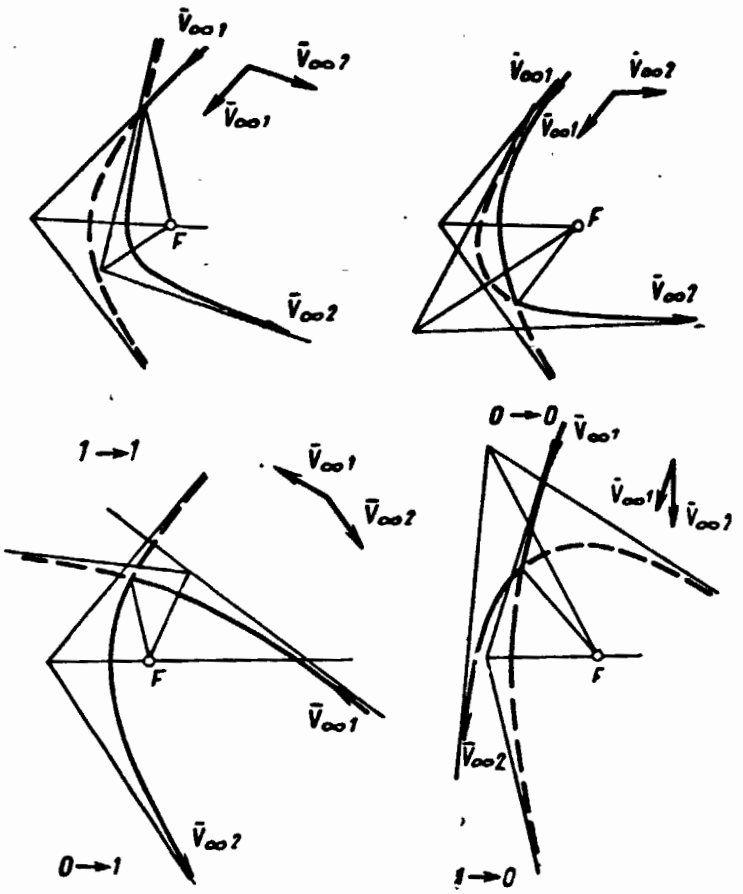

Figure 4.2.13. Possible variants of transfer between hyperbolas

We can find the impulse magnitude from the velocity triangle at the point of impulse application

$$\Delta V=(V_1^2+V_2^2-2V_1V_2\cos\varkappa)^{1/2}, \qquad (4.2.4)$$

where

$$\varkappa=\theta_2-\theta_1,$$

θ is the angle with the local horizon.

As was shown in [63], if we take ψ_1 and ψ_2 as the independent variables and consider that $a=\frac{\mu}{V_\infty^2}$, we can express the angles θ and ν in the form /126

$$\theta = \pm \cos^{-1}\left(\frac{1}{\operatorname{tg}\psi\left[\frac{rV_\infty^2}{\mu}\left(2+\frac{rV_\infty^2}{\mu}\right)\right]^{1/2}}\right). \qquad (4.2.5)$$

$$\upsilon = \pm \cos^{-1}\left[\sin\psi\left(\frac{1}{\frac{rV_\infty^2}{\mu}\operatorname{tg}^2\psi}-1\right)\right]. \qquad (4.2.6)$$

The velocity on the conic section trajectory

$$V=\left[\mu\left(\frac{2}{r}+\frac{1}{a}\right)\right]^{1/2}. \qquad (4.2.7)$$

Excluding from (4.2.3) and (4.2.4) — (4.2.7) all the variables other than ψ_1 and ψ_2, we obtain

$$\Delta V=\left(\frac{\mu}{a_1}\right)^{1/2}\left[1+\frac{a_1}{a_2}+\frac{\nu 4}{r/a_1}-\frac{2\,(a_2/a_1)^{7/2}}{(r/a_1)^2\operatorname{tg}\psi_1\operatorname{tg}\psi_2}\times\right.$$
$$\left.\times\left(1+\left\{\left[\frac{r}{a_1}\left(2+\frac{r}{a_1}\right)\operatorname{tg}^2\psi_1-1\right]\left[\frac{r}{a_2}\left(2+\frac{r}{a_2}\right)\operatorname{tg}^2\psi_2-1\right]\right\}^{1/2}\right)\right]^{1/2}; \qquad (4.2.8)$$

$$A(r/a_1)^2+B(r/a_1)+C=0, \qquad (4.2.9)$$

where

$$\left.\begin{aligned}
A&=[\cos(\varphi-\psi_1-\psi_2)-\sin\psi_1\sin\psi_2]^2-\cos^2\psi_1\cos^2\psi_2;\\
B&=2\left[\cos(\varphi-\psi_1+\psi_2)\frac{\cos\psi_1\cos\psi_2}{\operatorname{tg}\psi_1\operatorname{tg}\psi_2}\left(\frac{a_2}{a_1}\operatorname{tg}^2\psi_1+\operatorname{tg}^2\psi_2\right)-\right.\\
&\qquad\left.-\left(\frac{a_2}{a_1}\cos^2\psi_2-\cos^2\psi_1\right)\right];\\
C&=\frac{\cos\psi_1\cos\psi_2}{\operatorname{tg}\psi_1\operatorname{tg}\psi_2}\left[\frac{\sin\psi_1}{\sin\psi_2}\left(\frac{a_2\cos\psi_2}{a_1\cos\psi_1}\right)^2+\frac{\sin\psi_2}{\sin\psi_1}\left(\frac{\cos\psi_1}{\cos\psi_2}\right)^2-\right.\\
&\qquad\left.-2\,\frac{a_2}{a_1}\cos(\varphi-\psi_1-\psi_2)\right].
\end{aligned}\right\} \qquad (4.2.10)$$

If we solve (4.2.9) for r/a_1, the problem of finding the minimum ΔV reduces to finding the minimum with respect to two parameters: ψ_1 and ψ_2. If ΔV is referred to $V_{\infty 1}$, /127

$$\frac{\Delta V}{V_{\infty 1}}=\left(\frac{a_1\Delta V^2}{\mu}\right)^{1/2}$$

and we consider that

$$\frac{rV_{\infty 1}^2}{\mu}=\frac{r}{a_1},$$

the solution can be expressed through only two parameters: a_2/a_1 $\left[\text{or } \left(\frac{V_{\infty 1}}{V_{\infty 2}}\right)^2\right]$ and φ. Thus, the impulse optimizing problem becomes independent of the gravitational constant of the planet and the velocity $V_{\infty 1}$.

Let us examine the particular transfer case when the impulse is applied at the pericenters of the hyperbolas. For such pericentral transfer $v_1=v_2=0$. For this case [63],

$$\frac{r}{a_1}=\frac{\frac{a_2}{a_1}\cdot\frac{\sin\psi_2}{\sin\psi_1}\cdot\frac{\operatorname{tg}^2\psi_1}{\operatorname{tg}^2\psi_2}-1}{\operatorname{tg}^2\psi_1\left(\frac{\sin\psi_2}{\sin\psi_1}-1\right)}; \tag{4.2.11}$$

$$\varphi=\psi_1+\psi_2; \tag{4.2.12}$$

$$\sin\psi_1\left(\frac{1}{\frac{r}{a_1}\operatorname{tg}\psi_1}-1\right)=1. \tag{4.2.13}$$

Excluding r/a_1 from (4.2.11) and (4.2.13), we obtain an expression connecting ψ_1 and ψ_2:

$$\sin\psi_1=\frac{\sin\psi_2}{\frac{a_2}{a_1}+\left(1-\frac{a_2}{a_1}\right)\sin\psi_2}. \tag{4.2.14}$$

Since, for pericentral transfer, the impulse is directed along the transversal, $\cos\theta_1=\cos\theta_2$ and the formula for $\Delta V/V_{\infty 1}$ can be written as

$$\frac{\Delta V}{V_{\infty 1}}=\left(1+\frac{a_1}{a_2}+\frac{2}{r/a_1}\left[2-\left\{\left(2+\frac{r}{a_1}\right)\cdot\left(2+\frac{a_1}{a_2}\frac{r}{a_1}\right)\right\}^{1/2}\right]\right)^{1/2}. \tag{4.2.15}$$

We obtain from (4.2.12) and (4.2.14) the coupling equation

$$\sin(\varphi-\psi_2)=\frac{\sin\psi_2}{\frac{a_2}{a_1}+\left(1-\frac{a_2}{a_1}\right)\sin\psi_2}. \tag{4.2.16}$$

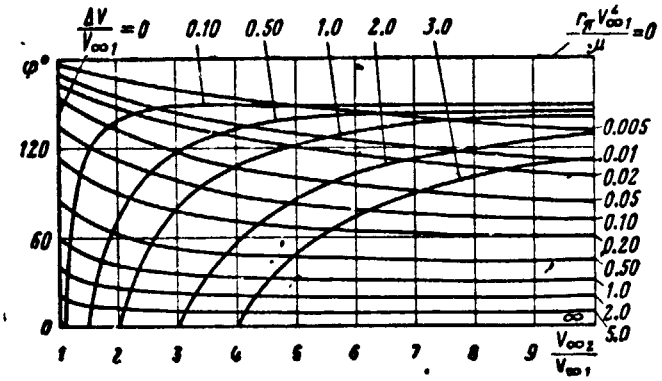

Figure 4.2.14. Summary graph of characteristics of pericentral transfer between hyperbolas

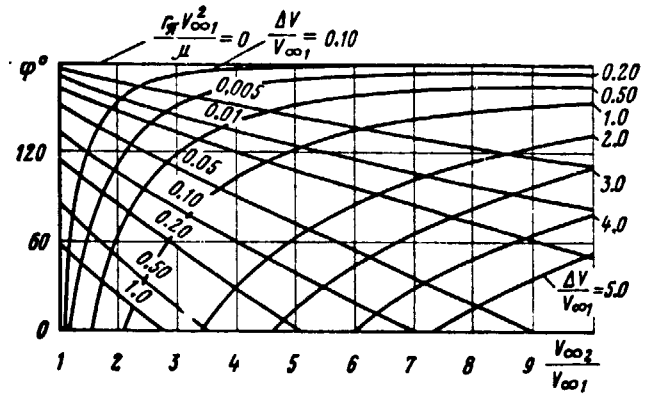

Figure 4.2.15. Characteristics of optimal nonpericentral transfers between hyperbolas

Summary graphs of the characteristics for pericentral and optimal nonpericentral transfers are shown in Figures 4.2.14 and 4.2.15. "Mirror" solutions with the same values of the required characteristic velocity ΔV apply for the inverse velocity ratios $V_{\infty 2}/V_{\infty 1}$. Therefore, the values of the characteristics are shown only for $V_{\infty 2}/V_{\infty 1} \geqslant 1$. /128

The pericentral transfer characteristic curves in Figure 4.2.14 are bounded by straight lines on the left and also above and below. The limitation on the left $V_{\infty 2}/V_{\infty 1}=1$ corresponds to the passive gravity maneuver case examined above. In this case, $\psi_1=\psi_2=\frac{\varphi}{2}$.

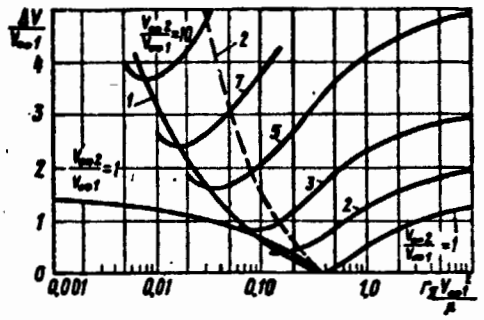

Figure 4.2.16. Characteristics of nonpericentral transfers between hyperbolas for $\varphi = 90°$:

1- optimal transfers; 2- pericentral transfers

The lower bound $\varphi = 0$ represents the degenerate unperturbed rectilinear trajectory case, when the impulse is applied outside the planet's sphere of action and the velocity vector changes impulsively in magnitude only and not in direction. /129

The upper bound $\varphi=\pi\,(r_\pi V_{\infty 1}^2/\mu=0$ and $\Delta V/V_{\infty 1}=0)$ also corresponds to the degenerate rectilinear hyperbola passing through the focus and not requiring impulse application. This case is not realized in practice because of the limitation $r_\pi \geq R_{per}$.

The graph for optimal nonpericentral transfer characteristics in Figure 4.2.15 is in general analogous to the graph of Figure 4.2.14. However, optimal transfers are realized for a smaller value of ΔV, which is seen from comparison of the curves of constant $\Delta V/V_{\infty 1}$ values. Differences are noted in the characteristics for $\varphi = 0$, where the pericentral transfers take place at infinity, while for the optimal nonpericentral transfers, the parameter $r_\pi V_{\infty 1}^2/\mu$ does not tend to infinity but varies as a function of the $V_{\infty 2}/V_{\infty 1}$ value. We note that, on the boundary $V_{\infty 2}/V_{\infty 1}=1$, the $r_\pi V_{\infty 1}^2/\mu$ curves in Figures 4.2.14 and 4.2.15 begin at the same values of φ.

For practical cases, the parameter $r_\pi V_{\infty 1}^2/\mu$ is bounded because of the condition that the transfer must be realized with a minimal value of $r_\pi \geq R_{per}$. In this case, it is convenient to represent the transfer characteristics in the form shown in Figure 4.2.16.

The curve $V_{\infty 2}/V_{\infty 1}=\text{const}$ has a horizontal asymptote as $r_* V_{\infty 1}^2/\mu \to \infty$, for which

$$\frac{\Delta V}{V_{\infty 1}}=\left[\left(\frac{V_{\infty 2}}{V_{\infty 1}}\right)^2+1-2\frac{V_{\infty 2}}{V_{\infty 1}}\cos\varphi\right]^{1/2}.$$

With approach to the planet $\Delta V/V_{\infty 1}$ decreases, reaching a minimum with smaller $\Delta V/V_{\infty 1}$ than for the pericentral transfers. Then the $\Delta V/V_{\infty 1}$ values again increase, approaching the second horizontal asymptote as $r_* V_{\infty 1}^2/\mu \to 0$ (degenerate rectilinear hyperbola passing through the focus), for which /130

$$\frac{\Delta V}{V_{\infty 1}}=\left[\left(\frac{V_{\infty 2}}{V_{\infty 1}}\right)^3+1+2\frac{V_{\infty 2}}{V_{\infty 1}}\cos\varphi\right]^{1/2}.$$

Transfers in the region to the right of the pericentral transfers correspond to type 0 — 0 transfer (in Figure 4.2.13), i.e., the SC approaches the planet along the inc g branch of the hyperbola and transfers to the second hyperbo. only after passing the pericenter of the first hyperbola.

Transfers in the region to the left of the pericentral transfers, including the optimal transfers, correspond to type 1 — 1 transfers in Figure 4.2.13, i.e., the SC transfers to the second hyperbola on the incoming branch of the first hyperbola prior to its pericenter. The minimal distance corresponds to the pericenter radius of the second hyperbola. Thus, the optimal transfers correspond to type 1 — 1 if $V_{\infty 2}/V_{\infty 1}>1$. For $V_{\infty 2}/V_{\infty 1}<1$, the regions change places and the optimal transfers correspond to type 0 — 0.

The curve for $V_{\infty 2}/V_{\infty 1}=1$ has a minimal point with $\Delta V/V_{\infty 1}=0$ and coincides with the pericentral transfer point. In this case, a passive gravity maneuver is accomplished during planet flyby.

In the relations of the type shown in Figure 4.2.16, it is easy to take into account the limitation on the parameter $r_* V_{\infty 1}^2/\mu$

from the condition $r_\pi \geq R_{per}$.

Since the optimal nonpericentral transfers lie in the vicinity of the pericentral transfers, we can use the following ΔV extremum search algorithm. First, for the given $V_{\infty 1}$, $V_{\infty 2}$ and φ, we find ΔV and the parameters ψ_1^* and ψ_2^* for pericentral transfers. Then, from these values of ψ_1^* and ψ_2^*, we seek the minimal ΔV for nonpericentral transfers with respect to the parameters ψ_1 and ψ_2. This algorithm ensures unimodality of the search region and permits using the direct extremum search methods (gradient, for example).

§ 3. SELECTION OF INJECTION SCHEME AND ROCKET STAGE PARAMETERS FOR ASCENT FROM MARS SURFACE

Analysis of the flight schemes to Mars (see Chapter 8) shows that, for launch from the surface of Mars, payload injection into the following orbits is possible:

circular with H_{cir} = 500 — 2000 km;

elliptic with H_π = 500 — 2000 km and H_α = 20 — 30 thousand km; /131

hyperbolic orbits with H_π = 500 — 2000 km.

The two-impulse or dual-burn injection scheme is rational for injection into these high orbits.

In this case, the SC is initially injected into an elliptic transfer orbit. The apocenter of this transfer ellipse corresponds to the desired orbit pericenter height. At the apocenter of this ellipse, the engine is relighted and acceleration to entry into the desired orbit takes place (Figure 4.3.1).

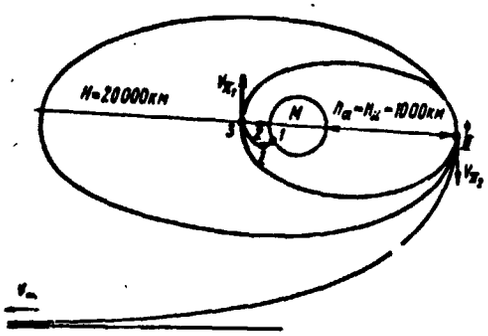

Figure 4.3.1. Scheme of ascent from surface of Mars:

I- first burn; II- second burn; 1- launch; 1 — 2- vertical ascent; 2 — 3- programmed turn; 3 — 4- passive flight; 4- acceleration to $V_f = V_{\pi_2}$

The magnitude of the useful load depends on the pitch program in the first and second injection segments and on the parameters of the transfer ellipse. Since the rarefied atmosphere of Mars is quite extensive, marked influence of drag on the flight trajectory is possible during flight along the transfer ellipse.

Examining the first active flight segment in the rarefied Mars atmosphere (p_0 = 5 — 20 mbar), we can assume that the aerodynamic loads and drag losses will be small. Therefore, we can assume that aerodynamic lift forces are not present and the drag coefficient is independent of flight speed. Ignoring the questions of control about the center of mass, we examine the motion of the rocket as a variable mass point. This formulation of the problem for estimating the energy expenditures and payload weight in design studies is quite legitimate and is used in preliminary calculations of booster injection trajectories during launch from the Earth.

The equations of booster motion in the velocity coordinate system with account for the assumptions adopted have the form /132

$$\dot{V} = \frac{g_0 E\left(\bar{P}_0 - \frac{p}{p_0}\Delta P_0\right)}{1 - \frac{\bar{P}_0}{P_{sp}}t}\cos\alpha - \frac{g_0 E c_x}{1 - \frac{\bar{P}_0}{P_{sp}}t}q - \frac{\mu_{pl}}{r^2}\sin\theta;$$

$$\dot{\theta} = \frac{1}{V}\left[\frac{g_0 E\left(\bar{P}_0 - \frac{p}{p_0}\Delta P_0\right)}{1 - \frac{\bar{P}_0}{P_{sp}}t}\sin\alpha + \left(\frac{V^2}{r} - \frac{\mu_{pl}}{r^2}\right)\cos\theta\right];$$

$$\dot{r} = V\sin\theta;$$

$$\dot{\lambda} = \frac{V}{r}\cos\theta,$$

where $g_{0\,E} = 9.81$ m/sec^2; q is the dynamic head $\left(q=\frac{\rho V^2}{2}\right)$; $\rho=\rho(h)$ and $p=p(h)$ are the density and pressure (specified by the planetary atmosphere models); $h = r - r_{pl}$ is flight altitude; r_{pl} is the radius of the planet; $\sigma_x = (c_x S_{fr})/G_0$ is the ballistic coefficient, S_{fr} is the frontal area; $\bar{P}_0=\frac{P}{G_0}$ is the booster thrust-weight ratio $\left(\Delta\bar{P}_0=\frac{S_a p_0}{G_0}\right)$; p_0 is the pressure at the surface of the planet; S_a is the nozzle area; G_0 is the launch weight; V is the flight speed, θ is the inclination angle of the vector to the local horizon; r is the distance from the planet center of mass; λ is the angular flight range; μ_{pl} is the gravitational constant of the planet; P_{sp} is the specific thrust; α is the angle of attack.

The pitch angle $\varphi=\theta+\alpha-\lambda$. It is known that, in the absence of aerodynamic losses, the optimal pitch program is nearly linear. Theoretical estimates show that the aerodynamic losses are actually small in the rarefied Martian atmosphere. Therefore, we assume that the pitch program varies linearly with time, i.e., $\varphi=\varphi_0-\dot{\varphi}(t-t_0)$. Calculations show that this injection program differs with regard to characteristic boost velocity by no more than 2 — 3% from the more complicated optimal injection programs. /133

We assume that the booster starts vertically from the surface. Then, we can take as the initial conditions the parameters at the end of the vertical active segment:*

$$V(t_0)=V_0,\ \theta(t_0)=\frac{\pi}{2},\ r(t_0)=r_0,\ \lambda(t_0)=0.$$

*The duration of the vertical segment was taken to reach V_0 = 60 m/sec.

The final conditions are determined by the parameters at a specified point of the transfer ellipse. If the transfer ellipse apocenter height h_a and the injection point true anomaly ν_f are specified, the final conditions are represented in the form

$$r_f = \frac{a(1 - e^2)}{1 + e \cos \nu_f};$$

$$V_f = \sqrt{\mu_{pl}\left(\frac{2}{r_f} - \frac{1}{a}\right)};$$

$$\theta_f = \text{arc tg} \frac{e \sin \nu_f}{1 + e \cos \nu_f};$$

where

$$a = \frac{r_a + r_n}{2};$$

$$e = \frac{r_a - r_n}{r_a + r_n}.$$

The presence of free parameters (parameters of the transfer ellipse) make it possible to satisfy these initial and final conditions.

For the linear pitch program in the first active segment, we investigated the influence of the transfer ellipse parameters on the total characteristic velocity required for injection into the specified orbit

$$V_x = V_{x1} + V_{x2} + \Delta V_{comp},$$

where V_{x1} and V_{x2} are the characteristic velocities required for injection into the transfer ellipse and from the transfer ellipse into the specified orbit; ΔV_{comp} is the characteristic velocity required to compensate for the aerodynamic losses during motion along the transfer ellipse.

With change of the transfer ellipse pericenter altitude, for /134
example, with increase of this altitude, the gravitational losses in the first active segment increase but the required characteristic velocity V_{x2} and compensating impulse decrease. Therefore, there is a transfer impulse altitude for which the overall energy expenditures required are minimal.

Study of the influence of the second active trajectory segment duration for injection from the transfer ellipse to the specified orbit (for thrust vector orientation selected to minimize the required characteristic velocity V_{x2}) showed that because of the smallness of the gravitational losses V_{x2} can be determined approximately as the geometric difference of the velocities in the transfer ellipse and in the specified orbit at the transfer point.

In the case of flight along the transfer ellipse at low pericenter altitudes, the transfer orbit distorts because of the atmospheric drag influence (the apocenter height decreases and additional energy expenditures are required to compensate for the effect of the atmosphere). Therefore, an additional velocity impulse ΔV_{comp} must be imparted at some point of the transfer ellipse. For example, at h_{π} = 60 and 70 km, the transfer ellipse apocenter height decreases from 1000 to 609 and 858 km, respectively (for the maximal atmosphere model), because of the atmosphere effect.

Calculations have shown that it is best to impart the additional velocity impulse (for minimal required energy expenditures) in the transfer ellipse pericenter region, i.e., the velocity at the end of the first injection segment must be increased somewhat.

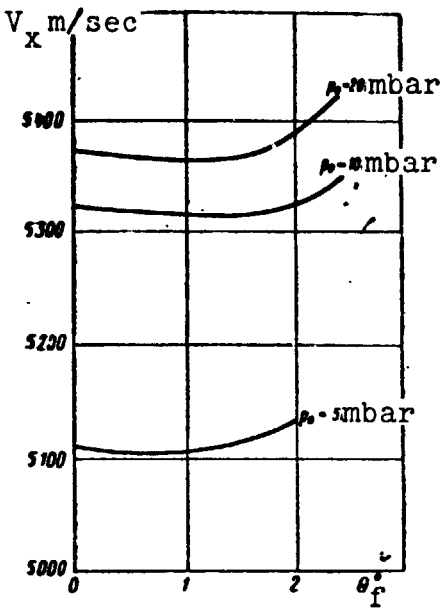

Figure 4.3.2. V_x as a function of angle θ_f for H_α = 1000 km and H_α = 20,000 km:

p_0, mbar	20	10	5
$\bar{p}_0$	1.2	1.2	1.2
h_π, km	65	45	40

The energy expenditures required to compensate for atmospheric influence may reach ΔV_{comp} = 200 m/sec.

Figure 4.3.2 shows the required characteristic velocity V_x values as a function of the velocity vector inclination θ_f to the local horizon at the end of the first active segment. We see that this relation has a very flat optimum for θ_f = 0.5 — 1.5°. /136

We also examined the influence of location of the transition point from the transfer ellipse to the desired orbit. The calculation results showed that the magnitude of the second-burn impulse has a minimum for true anomaly of the transition point to the desired orbit differing somewhat from the apocenter point. However, the overall energy expenditures in this case do not differ essentially from those for the schemes with injection at the apocenter. Therefore, we adopted the following injection scheme:

— launch from the surface of Mars and injection to the transfer ellipse pericenter with velocity ensuring compensation for the aerodynamic losses in the transfer ellipse; /137

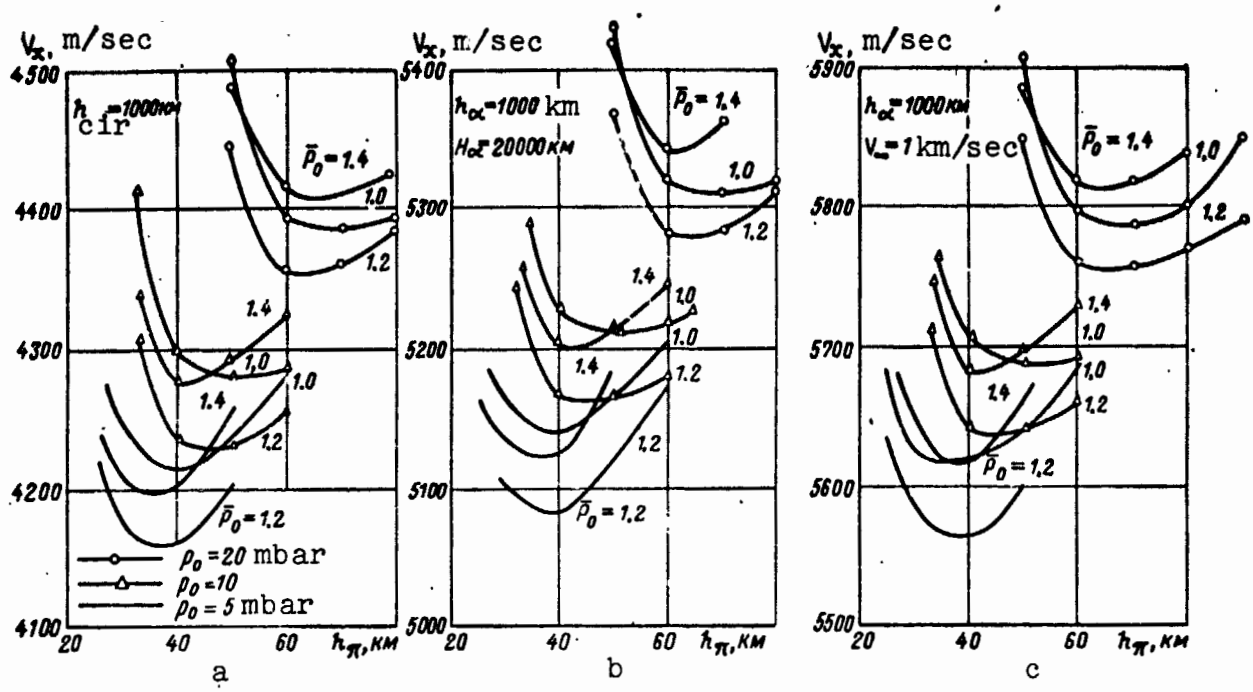

Figure 4.3.3. Influence of transfer ellipse pericenter height h_π on V_x for different final orbits

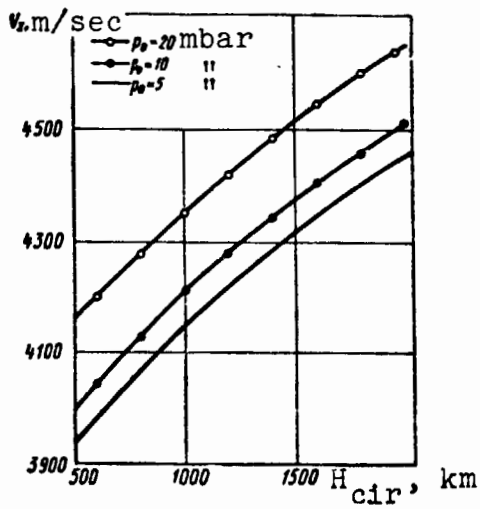

Figure 4.3.4. Influence of circular orbit height H_{cir} on V_x for $\bar{p}_0$ = 1.2:

p_2, mbar	20	10	5
h_π, km	60	45	35

— passive flight to the apocenter and acceleration at the apocenter to injection into the desired orbit (in this case, the transfer ellipse apocenter height is equal to the final specified orbit pericenter height).

For this injection scheme, we stucied the influence of transfer ellipse pericenter height h_π on the energy expenditures required for injection into various final orbits. The

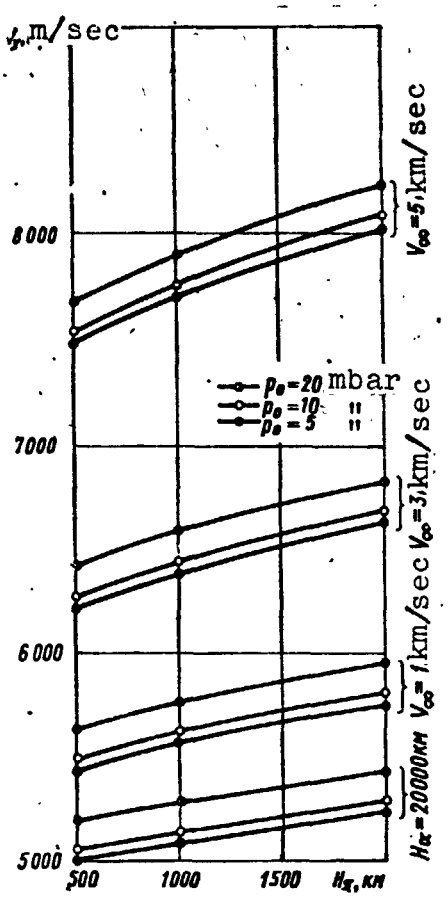

Figure 4.3.5. Influence of final elliptical and hyperbolic orbit pericenter heights on V_x for $\bar{p}_0$ = 1.2:

p_0, mbar	20	10	5
h_π, km	65	50	40

calculation results are shown in Figure 4.3.3. We see from the calculations that there is an optimal transfer ellipse pericenter height value h_π which makes it possible to obtain the minimal required energy expenditures. In this case, the optimal pericenter height value is determined basically by the atmosphere model and is h_π = 35 — 40 km for the minimal model with p_0 = 5 mbar, 40 — 50 km for the intermediate model with p_0 = 10 mbar, and 60 — 70 km for the maximal model with p_0 = 20 mbar, varying only slightly with change of the transfer orbit apocenter height.

The optimal thrust-weight r ·› is $p_0 \approx 1.2$.

Figure 4.3.4 shows the influence of final circular orbit height H_{cir} on the total characteristic velocity. Increase of the circular orbit height from H_{cir} = 500 km to H_{cir} = 2000 km leads to increase of V_x by approximately 500 m/sec.

Figure 4.3.5 shows the influence of final elliptic and hyperbolic orbit pericenter height H_π on V_x. Increase of the pericenter height H_π by 500 km leads to increase of V_x by approximately 250 — 500 m/sec, depending on the final orbit type.

CHAPTER 5. FLYBY AND IMPACTING INTERPLANETARY TRAJECTORIES

§ 1. CALENDAR OF FLIGHTS TO THE PLANETS

Exact determination of interplanetary flight trajectory characteristics involves solution of a three-dimensional problem, requiring quite laborious calculations. Preliminary estimates of the basic trajectory characteristics and nominal launch dates for optimal flight cycles to the planets can be carried out under the following assumptions: /138

— the Earth and planet orbits are circular and all lie in the same plane;

— flight is accomplished along minimal energy trajectories.

The minimal energy trajectories for this case have been examined by Hohmann [51] and are ellipses (Figure 5.1.1a) tangent at the apsidal points of the circular planetary orbits.

This problem formulation is not exact, but it permits obtaining simple approximate relations which can be used as the zero approximation characteristics. /139

FLIGHT TIME

The period of revolution in this ellipse is

$$T=\frac{2\pi}{\sqrt{\mu_\odot}}a^{\frac{3}{2}},$$

where a is the semimajor axis of the vehicle flight orbit; $\mu_\odot$ is the gravitational constant of the Sun.

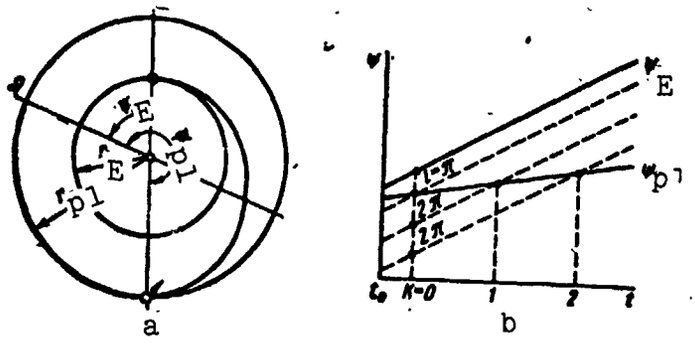

Figure 5.1.1. Transfer schemes
a- Hohmann ellipse; b- determination of difference of Earth and planet longitudes

For circular Earth and planet orbits

$$a = \frac{r_E + r_{pl}}{2},$$

where r_E, r_{pl} are the mean radii of the Earth and planet orbits, respectively.

We shall express distances in astronomic units ($r_E = 1$) and time in Earth sidereal periods ($T_E = 1$); then

$$T = \sqrt{\tilde{a}^3}.$$

The flight time from the Earth to the planet $\Delta t_f = T/2$. Substituting the quantity $\tilde{a} = (1 + \tilde{r}_{pl})/2$, we obtain

$$\Delta t_f = \frac{1}{2}\sqrt{\left(\frac{1 + \tilde{r}_{pl}}{2}\right)^3} = 0.177\sqrt{(1 + \tilde{r}_{pl})^3}.$$

The flight time to the planets from the Earth is shown in Table 5.1 and Figure 5.1.2. The flight time to the asteroid belt (97% of the asteroids have orbits in the range $\tilde{r}_{av} = 2.2$ to 3.6) is equal to $\Delta t_f^{E-A} = 1.01$ — 1.74 years. For the case of /140

TABLE 5.1.

Planet		Sun	Mercury	Venus	Mars	Asteroids
Δt_f	Years	0.177	0.288	0.401	0.710	1.01 — 1.74
	Days	65	105	146	259	369 — 636
Planet		Jupiter	Saturn	Uranus	Neptune	Pluto
Δt_f	Years	2.745	5..980	16.0	30.65	45.80
	Days	1,000	2,180	5,840	11,200	16,800

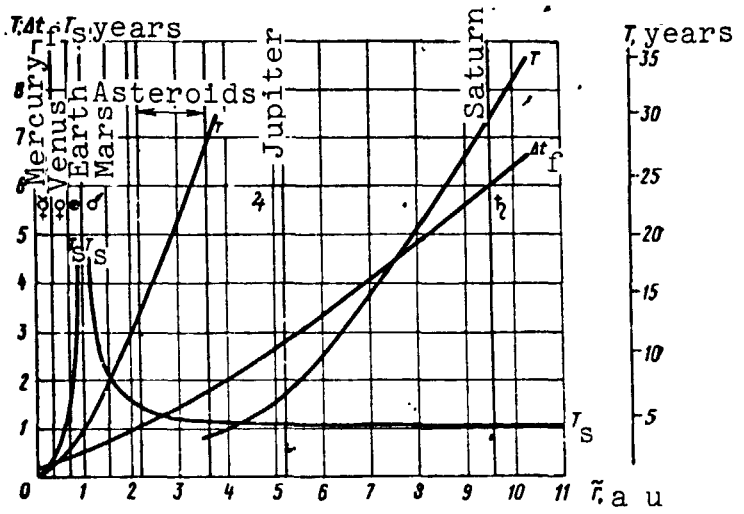

Figure 5.1.2. Planet revolution period T, flight time Δt_f, and synodic period T_s as functions of distance r from the Sun.

flight from planet to planet

$$\Delta t_f = \frac{1}{2}\sqrt{\left(\frac{\tilde{r}_1 + \tilde{r}_2}{2}\right)^3}.$$

where $\tilde{r}_1$ and $\tilde{r}_2$ are the mean planet orbit radii.

Thus, the flight time from Venus to Mercury is $\Delta t_f = 0.207$ years or about 76 days, and for flight from Mars to the asteroids, $\Delta t_f = 1.27$ -- 2.05, Mars to Jupiter $\Delta t_f = 3.08$, Mars to Saturn $\Delta t_f = 6.53$, Jupiter to Saturn $\Delta t_f = 10$, Jupiter to Uranus $\Delta t_f = 21.4$ years.

TABLE 5.2.

Planet		Mercury	Venus	Mars	Jupiter	Saturn	Uranus	Neptune	Pluto
$\Delta t_{f\ min}$	Years	0.260	0.390	0.644	2.550	5.36	15.0	30.2	38.5
	Days	95	138	234	935	1,955	5,475	11,040	11,060
$\Delta t_{f\ max}$	Years	0.320	0.412	0.780	2.910	6.600	17.1	30.8	57.3
	Days	115	150	283	1,070	2,408	6,240	11,250	20,950

The values of Δt_f presented above were calculated for circular orbits. To evaluate the influence of orbit eccentricity on flight time, we determine

$$\Delta t_{f\ max} = \frac{1}{2}\sqrt{\left(\frac{\tilde{r}_{E\ max} + \tilde{r}_{pl\ max}}{2}\right)^3};$$

$$\Delta t_{f\ min} = \frac{1}{2}\sqrt{\left(\frac{\tilde{r}_{E\ min} + \tilde{r}_{pl\ min}}{2}\right)^3}.$$

This orbit combination is unlikely, but values of Δt_f close to $\Delta t_{f\ max}$ and $\Delta t_{f\ min}$ are possible at great opposition times. The values of $\Delta t_{f\ max}$ and $\Delta t_{f\ min}$ are shown in Table 5.2.

LAUNCH DATES /141

Flight from Earth to a planet. The launch date can be determined from the condition that the difference of the heliocentric longitudes of the Earth at the launch time and the planet at the arrival time (transfer angle) is $l = \pi$.

The longitude of the Earth at the launch time

$$\psi_E = \psi_{Eo} + \omega_E t_{st\ E},$$

where ψ_{Eo} is the longitude of the Earth at zero time in rad; $\omega_E = \frac{2\pi}{T_E} = 2\pi$ is the angular rate of revolution of the Earth around the Sun in rad/year; $t_{st\ E}$ is the launch date from the Earth to the planet from zero time in years.

The longitude of the planet at the arrival time

$$\psi_{pl} = \psi_{pl\ 0} + \omega_{pl}(t_{st\ E} + \Delta t_f),$$

where $\psi_{pl\ 0}$ is the longitude of the planet at zero time; $\omega_{pl} = 2\pi/T_{pl}$ is the angular rate of revolution of the planet around the Sun.

The difference of the Earth and planet longitudes may differ by 2π (Figure 5.1.1b)

$$\psi_E - \psi_{pl} = \pm\pi + k2\pi; \quad (k=0; \pm 1; \pm 2; \pm 3),$$

where k is the number of cycles from zero time.

On the other hand, the longitude difference

$$\psi_E - \psi_{pl} = (\psi_{E\ 0} - \psi_{pl\ 0}) + (\omega_E - \omega_{pl})t_{st\ E} - \omega_{pl}\Delta t_f,$$

hence, the launch date from the Earth to the planet /142

$$t_{st\ E} = \frac{\pm\pi + k2\pi - \Delta\psi_0 + \omega_{pl}\Delta t_f}{\omega_E - \omega_{pl}} = t^0_{st\ E} + kT_s,$$

where

$$\Delta\psi_0 = \psi_{E\ 0} - \psi_{pl\ 0};$$

$t^0_{st\ E}$ is the launch date for the zero cycle; T_s is the time period between cycles.

The time period between cycles is

$$T_s = \frac{2\pi}{\omega_E - \omega_{pl}} = \frac{1}{1 - \frac{1}{T_{pl}}} = \frac{T_{pl}}{T_{pl} - 1},$$

i.e., the synodic period of revolution of the planet.

The synodic periods for the planets are presented in a table in the Appendix and in Figure 5.1.2. The synodic period of revolution and the time period between cycles for flights to an asteroid is

$$T_s = 1.44 \text{ — } 1.15$$

(the period of revolution $T_{ast} = \sqrt{\tilde{r}_{ast}^3} = \sqrt{(2.2 \text{ — } 3.6)^3} = 3.26 \text{ — } 6.85$).

For flight from planet to planet, the synodic period is

$$T_s = \frac{1}{\left|\frac{1}{T_1} - \frac{1}{T_2}\right|} = \frac{T_1 \cdot T_2}{|T_2 - T_1|}.$$

The launch date from the Earth for the zero cycle from the time origin is

$$T_{st\ E} = \frac{\pm \pi - \Delta\psi_0 + \omega_{pl}\Delta t_f}{\omega_E - \omega_{pl}} = \frac{(\pm \frac{1}{2} - \Delta\tilde{\varphi}_0) + T_{pl}\Delta t_f}{T_{pl} - 1}$$

where

$$\Delta\tilde{\psi} = \frac{\Delta\psi_0}{2\pi}.$$

To determine the launch date, it is necessary to know the heliocentric longitudes of the planets at the initial instant of time.

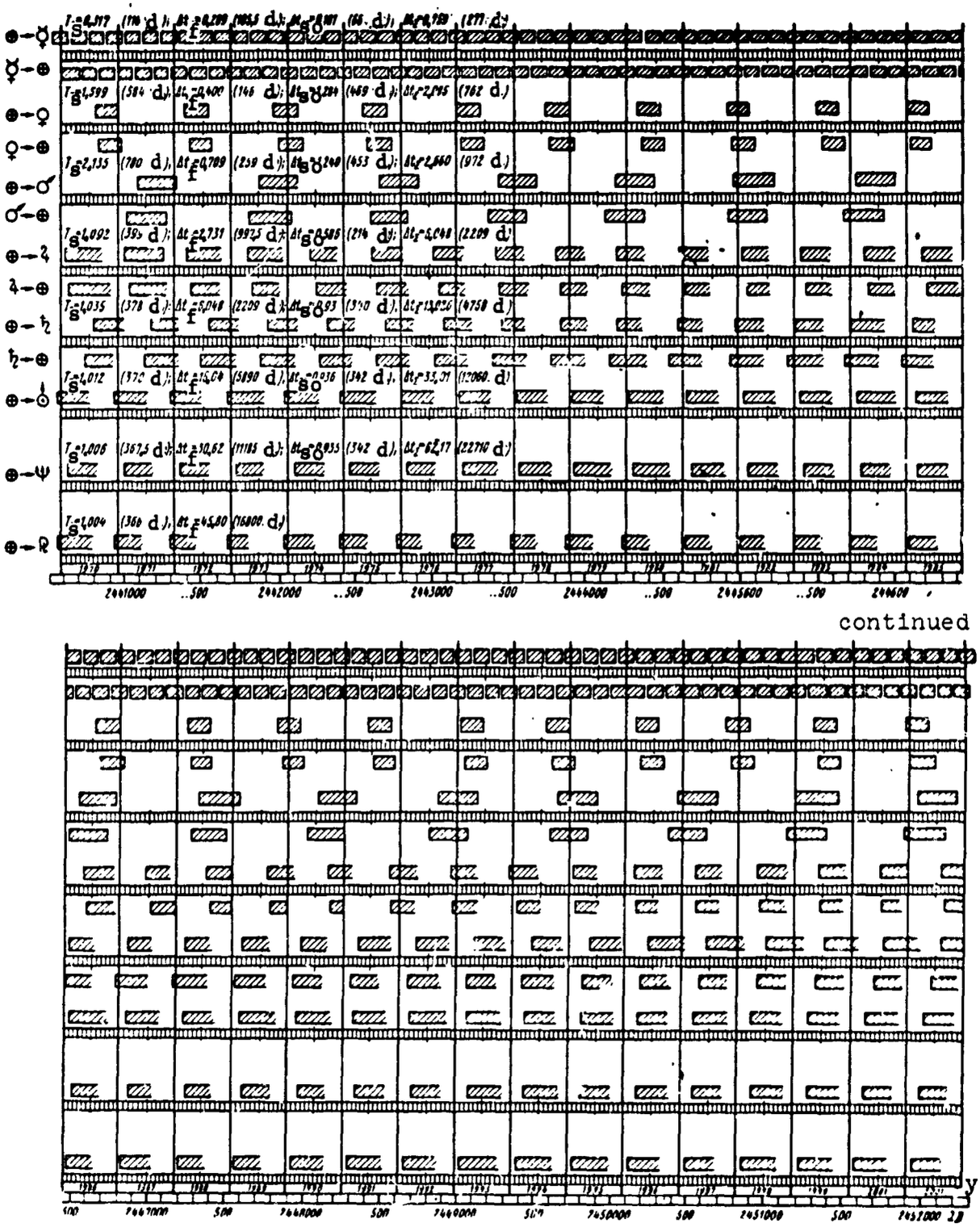

Figure 5.1.3. Calendar of flights to the planets: T_s- time between flight cycles in years; Δt_f- flight time in years; Δt_{so}- stopover time at the planet in years; $\Delta t_\Sigma = \Delta t_f + \Delta t_{so} + \Delta t_f$- total expedition cycle time in years

A calendar of flights to the planets is shown in Figure 5.1.3.

Flight from planet to the Earth. The planet longitude at the launch time is $\psi_{pl} = \psi_{pl\,0} + \omega_{pl} t_{st\,pl}$. The Earth longitude at the arrival time is $\psi_E = \psi_{E\,0} + \omega_E(t_{st\,E} + \Delta t_f)$. The longitude difference is $\psi_E - \psi_{pl} = \pm \pi + k2\pi$, or

$$\psi_E - \psi_{pl} = (\psi_{E\,o} - \psi_{pl\,0}) + (\omega_E - \omega_{pl}) t_{st\,pl} + \omega_E \Delta t_f.$$

The launch date from the planet to the Earth /143

$$t_{st\,pl} = \frac{\pm \pi + k2\pi - \Delta\psi_0 - \omega_E \Delta t_f}{\omega_E - \omega_{pl}} = t^0_{st\,pl} + kT_s.$$

The time period between cycles

$$T_s = \frac{2\pi}{\omega_E - \omega_{pl}} = \frac{T_{pl}}{T_{pl} - 1}$$

is the same as for flights from the Earth to the planet.

The launch date of the zero cycle from zero time is

$$t^0_{st\,pl} = \frac{\pm \pi - \Delta\psi_0 + \omega_E \Delta t_f}{\omega_E - \omega_{pl}} = \frac{(\pm \frac{1}{2} - \Delta\tilde{\psi}_0) + \Delta t_f}{T_{pl} - 1}$$

Knowing the heliocentric longitudes of the planets at zero time, we can determine $t^0_{st\,pl}$ and the zero cycle launch date.

Knowing the launch date and the flight time, we can determine the stopover time Δt_{so} at the planet and the time required for the complete cycle Δt_Σ: flight to the planet, stopover, and flight to the Earth (Table 5.3 and Figure 5.1.3), where

$$\Delta t_{so} = t_{st\,pl} - (t_{st\,E} + \Delta t_f);$$

$$\Delta t_\Sigma = 2\Delta t_f + \Delta t_{so}.$$

TABLE 5.3.

Planet	Δt_{so}		Δt_{Σ}	
	Years	Days	Years	Days
Mercury	0.18	66	0.76	277
Venus	1.284	469	2.085	762
Mars	1.234	453	2.666	972
Jupiter	0.56	214	6.48	2,209
Saturn	0.93	40	13.026	4,758
Uranus	0.936	--	33.01	12,060
Neptune	0.935	--	62.17	22,710

REQUIRED LAUNCH VELOCITIES AND PLANET APPROACH VELOCITIES /146

The velocity of a body in orbit

$$V^2 = 2\mu_\odot\left(\frac{1}{r} - \frac{1}{2a}\right).$$

The circular velocity at the distance r from a central body

$$V_{cir}^2 = \frac{\mu_\odot}{r}.$$

Substituting V_{cir} into the expression for V, we obtain

$$V = V_{cir}\sqrt{2\left(1 - \frac{r}{2a}\right)}.$$

We examine the moment of launch from the Earth, i.e., the moment of escape from the Earth's sphere of action. In this case, the velocity required for transfer to an elliptic orbit tangent to the orbits of the Earth and planet

$$V_{stE} = V_{cirE}\sqrt{2\left(1 - \frac{\tilde{r}_E}{2\tilde{a}}\right)} = V_{cirE}\sqrt{\frac{2\tilde{r}_{pl}}{1 + \tilde{r}_{pl}}};$$

$$2\tilde{a} = \tilde{r}_E + \tilde{r}_{pl}; \quad 1 + \tilde{r}_{pl}; \quad \tilde{r}_E = 1.$$

The relative launch velocity (approximately the velocity $V_\infty^\oplus$) at the planet sphere of action

$$V_\infty^\oplus = \Delta V^\infty_{st\ E} = V_{st\ E} - V_{cir\ E}.$$

The values of these velocities are presented in Table 5.4 and Figure 5.1.4. For flight to the asteroids ($\tilde{r}$ = 2.2 — 3.6), the relative launch velocity

$$V_\infty^\oplus = 5.14 \text{ — } 7.52 \text{ km/sec.}$$

For the case of launch from a planet to the Earth

$$V_{st\,pl} = V_{cir\,pl}\sqrt{2\left(1-\frac{r_{pl}}{2a}\right)} = V_{cir\,pl}\sqrt{\frac{2}{1+\tilde{r}_{pl}}}.$$

The relative launch velocity

$$V_\infty^{pl} = \Delta V^\infty_{st\ pl} = V_{st\ pl} - V_{cir\ pl}.$$

It is easy to see that the relative launch velocity from the planet $\Delta V^\infty_{st\ pl}$ is equal to the arrival velocity at the planet $\Delta V^\infty_{ar\ pl}$ for flight from the Earth and the relative velocity of launch from the Earth $\Delta V^\infty_{st\ E}$ is equal to the arrival velocity at the Earth $\Delta V^\infty_{ar\ E}$ for flight from the planet.

Using the energy integral, we obtain

$$(V'_{st\ pl})^2 - \frac{2\mu_{pl}}{R_{pl}} = (V_\infty^{pl})^2 - \frac{2\mu_{pl}}{R_{sp\ a\ pl}} \approx (V_\infty^{pl})^2$$

for $R_{sp\ a\ pl} \to \infty$;

$$V^2_{par} = \frac{2\mu_{pl}}{R_{pl}},$$

where $V'_{st\ pl} = V_{en\ pl}$ is the launch velocity from the planet surface, equal to the velocity of approach to the surface of the

TABLE 5.4.*

Planet	$v_{\infty}^{\oplus} - \Delta v_{ar\ E}^{\infty}$	$v'_{st\ E} - v_{en\ E}$	$\Delta v_{st}^{\oplus} - \Delta v_{b\ AES}^{\oplus}$	$v_{\infty}^{pl} - \Delta v_{ar\ pl}^{\infty}$	$v_{enp} - v'_{stp}$	$\Delta v_{st}^{pl} - \Delta v_{b\ APS}^{pl}$
Sun	−29,8	31,7	23,8		—	—
Mercury	−7,50 (−6,04 / −9,38)	13,7	5,8	9,56	10,25	7,71
Venus	−2,53	11,5	3,6	2,80	10,56	3,36
Mars	2,98 (3,50 / 2,32)	11,6 (11,75 / 11,45)	3,7 (3,85 / 3,55)	−2,65 (−3,24 / −1,92)	5,65 (5,95 / 5,35)	2,11 (2,43 / 1,83)
Asteroids	5,14—7,52	12,35—13,5	4,45—5,6	—	—	—
Jupiter	8,70	14,2	6,3	−5,65	60,01	17,51
Saturn	10,30	15,2	7,3	5,49	36,45	10,85
Uranus	11,30	15,9	8,0	−4,56	21,5	6,7
Neptune	11,66	16,2	8,3	3,94	23,35	7,05
Pluto	11,85 (11,92 / 11,65)	16,3	8,4	4,88	—	—
∞	12,31	15,68	8,78	0	—	—

* Translator's Note: Commas in numbers represent decimal points.

planet without account for gravitation and atmospheric drag losses; V_{par} is the parabolic velocity at the planet surface; R_{pl} is the radius of the planet; $R_{sp\ a\ pl}$ is the radius of the planet's sphere of action.

Using these two expressions, we obtain

$$V_{en\ pl} = V'_{st\ pl} = \sqrt{V_{par}^2 + (V_{pl}^{\infty})^2}\ .$$

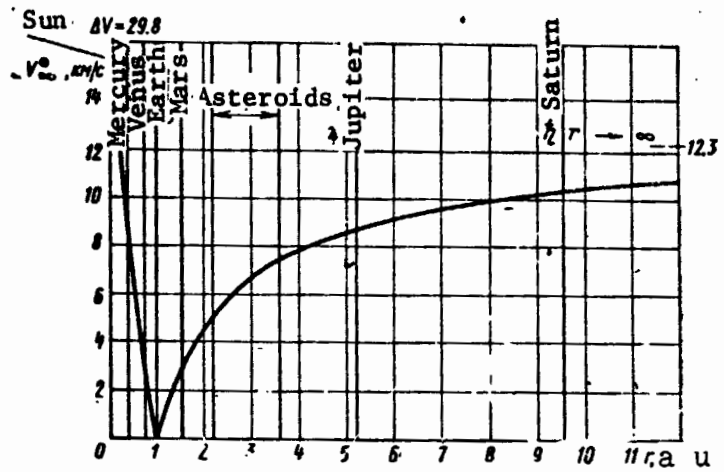

Figure 5.1.4. Velocity of launch from Earth's sphere of action for flights to planets.

The calculation results are shown in Table 5.4. For flight from planet to planet

$$V_{st2} = V_{cir2}\sqrt{\frac{2\tilde{r}_1}{\tilde{r}_2 + \tilde{r}_1}} \text{ and } V_{st1} = V_{cir1}\sqrt{\frac{2\tilde{r}_2}{\tilde{r}_1 + \tilde{r}_2}}.$$

Thus, for flight from Venus to Mercury, $\Delta V^{\infty}_{st} = 5.6$; Mercury to Venus — 7.15; Mars to the asteroids — 2.16 — 4.58; Mars to Jupiter — 5.98; Mars to Saturn — 8.20; Jupiter to Saturn — 1.79; Jupiter to Uranus — 3.28 km/sec.

For the estimate of planet orbit eccentricity influence, we obtain /149

$$V_{st\ E\ max} = V_{cir\ E}\sqrt{\frac{2\tilde{r}_{pl\ min}}{1 + \tilde{r}_{pl\ max}}};$$

$$V_{st\ E\ min} = V_{cir\ E}\sqrt{\frac{2\tilde{r}_{pl\ min}}{1 + \tilde{r}_{pl\ max}}}$$

The values of $\Delta V^{\infty}_{st\ E\ max}$ and $\Delta V^{\infty}_{st\ E\ min}$ for the planets with large eccentricity are shown in Table 5.4 (numerals in parentheses).

The launch velocity from circular APS orbit of radius $R_{cir} = R_{pl}$

$$\Delta V_{st}^{pl} = V'_{st\ pl} - V_{cir},$$

where

$$V_{cir} = \sqrt{\frac{\mu_{pl}}{R_{pl}}} .$$

The launch velocity ΔV_{st}^{pl} from APS orbit is equal to the velocity ΔV_{b}^{pl} of braking into APS orbit. The values of ΔV_{st}^{pl} and ΔV_{b}^{pl} for AES and APS are presented in Table 5.4.

The characteristics of the Hohmann interplanetary trajectories presented above give an approximate idea of the real values of these characteristics. Thus, the flight time along the Hohmann ellipse lies approximately between the real flight times along the optimal first and second semiorbit trajectories. The energy experditures of the Hohmann trajectories correspond approximately to the energy expenditures of the real flights in the best cycles. The start dates along these trajectories lie approximately between the real launch dates of flight along the optimal first and second semiorbit trajectories. These launch dates can be used as nominal dates in calculating the actual trajectories.

ACCELERATED TRAJECTORIES

Flights to the distant planets along minimal energy trajectories require a long time. It is interesting to evaluate how much energy expenditure increase is required to shorten the flight time.

For a preliminary analysis of the possibility of accelerating flights to the planets, we shall estimate the characteristics of such flight trajectories under the following assumptions.

1. We consider that the solar system planet orbits are circular and lie in the ecliptic plane.

2. The SC flight trajectories also lie in the ecliptic plane. SC launch is accomplished in the direction of the Earth's velocity along its orbit, i.e., the launch point is an apsidal point of the SC transfer orbit (tangential launch). Tangential launch provides flight along trajectories close to the minimal energy trajectories for fixed flight time Δt ("accelerated trajectories"). /150

In this case, the magnitude of the heliocentric launch velocity V_0 defines the flight trajectory.

The flight trajectory parameter

$$p=\frac{V_0^2 r_0^2}{\mu_\odot}=\frac{V_0^2}{V_{\text{cir}}^2} r_0;$$

the eccentricity

$$e=\sqrt{1+\frac{p}{\mu_\odot}\left(V_0^2-\frac{2\mu_\odot}{r}\right)}=\sqrt{1+\left(\frac{V_0}{V_{\text{cir}}^2}\right)^2 (V_0^2-2V_{\text{cir}}^2)};$$

the radius

$$r=\frac{p}{1+e\cos v}.$$

The flight time for elliptic trajectories

$$\Delta t_{\text{el}} = \frac{a^{3/2}}{\sqrt{\mu_\odot}}(E-e\sin E),$$

where

$$a=\frac{p}{1-e^2};\ \operatorname{tg}\frac{E}{2}=\operatorname{tg}\frac{v}{2}\sqrt{\frac{1-e}{1+e}};$$

for the parabolic trajectory

$$\Delta t_{par} = \frac{a^{3/2}}{2\sqrt{\mu_\odot}}\left(\operatorname{tg}\frac{v}{2}+\frac{1}{3}\operatorname{tg}^3\frac{v}{2}\right)$$

and for the hyperbolic trajectory

$$\Delta t_h = \frac{a^{3/2}}{\sqrt{\mu_\odot}}(e\operatorname{sh}H - H),$$

where

$$a=\frac{p}{e^2-1};\ \operatorname{tg}\frac{H}{2}=\operatorname{tg}\frac{v}{2}\sqrt{\frac{e-1}{e+1}}.$$

We shall convert to dimensionless quantities, referring linear dimensions to the launch point radius r_0 and velocities to the launch point circular velocity $V_{cir} = \sqrt{\mu_{pl}/r_0}$. In this case, /151

$$\tilde{p}=\tilde{V}_0^2;\quad e=\sqrt{1+\tilde{V}_0^2(\tilde{V}_0^2-2)};$$

$$\tilde{r}=\frac{\tilde{p}}{1+e\cos v},$$

$$\tilde{a}=\frac{\tilde{p}}{1-e^2}$$ — for the ellipse

$$\tilde{a}=\frac{\tilde{p}}{e^2-1}$$ — for the hyperbola.

We refer the flight time to the revolution period in the launch orbit

$$T_{cir} = 2\pi\frac{r_{cir}^{3/2}}{\sqrt{\mu_{pl}}}.$$

Then the relative flight time for the ellipse

$$\Delta\tilde{t}_{el} = \frac{\tilde{a}^{3/2}}{2\pi}(E - e\sin E);$$

for the parabola

$$\Delta\tilde{t}_{par} = \frac{\tilde{a}^{3/2}}{4\pi}\left(\operatorname{tg}\frac{v}{2} + \frac{1}{3}\operatorname{tg}^3\frac{v}{2}\right);$$

for the hyperbola

$$\Delta\tilde{t}_h = \frac{\tilde{a}^{3/2}}{2\pi}(e\operatorname{sh}H - H).$$

Figure 5.1.5 shows curves of the departure velocity $V_\infty^\oplus$ from the Earth's sphere of action and entry velocity V_∞^{pl} into the planet sphere of action for accelerated flight trajectories. Although such trajectories are of most interest for flights to the distant outer planets, it is interesting to determine the possibilities of shortening the flight time to the nearby planets as well.

The reduction of the flight time Δt_f with increase of the departure velocity from the Earth's sphere of action by $\Delta V_\infty^\oplus$ = = 0.5 km/sec in comparison with the minimal value is shown in Table 5.5.

We see that a not very large increase of the trajectory energy expenditures reduces the flight time to the nearby planets significantly.

For flights to the distant planets, increase of the energy expenditures by ΔV_∞ = 0.5 km/sec makes it possible to shorten the flight time Δt_f by a factor of 1.5 — 2, which is explained by the quite flat optimum of the $V_\infty^\oplus = f(\Delta t_f)$ curves. However, this sharp flight time reduction leads to significant increase of the SC planet encounter velocity V_∞^{pl}, which may cause difficulties for SC entering the planet atmosphere. Thus, for flights along accelerated trajectories to Venus the velocity V_∞^φ increases from 2.7 to 5.6 km/sec, which leads to increase of the entry

/153

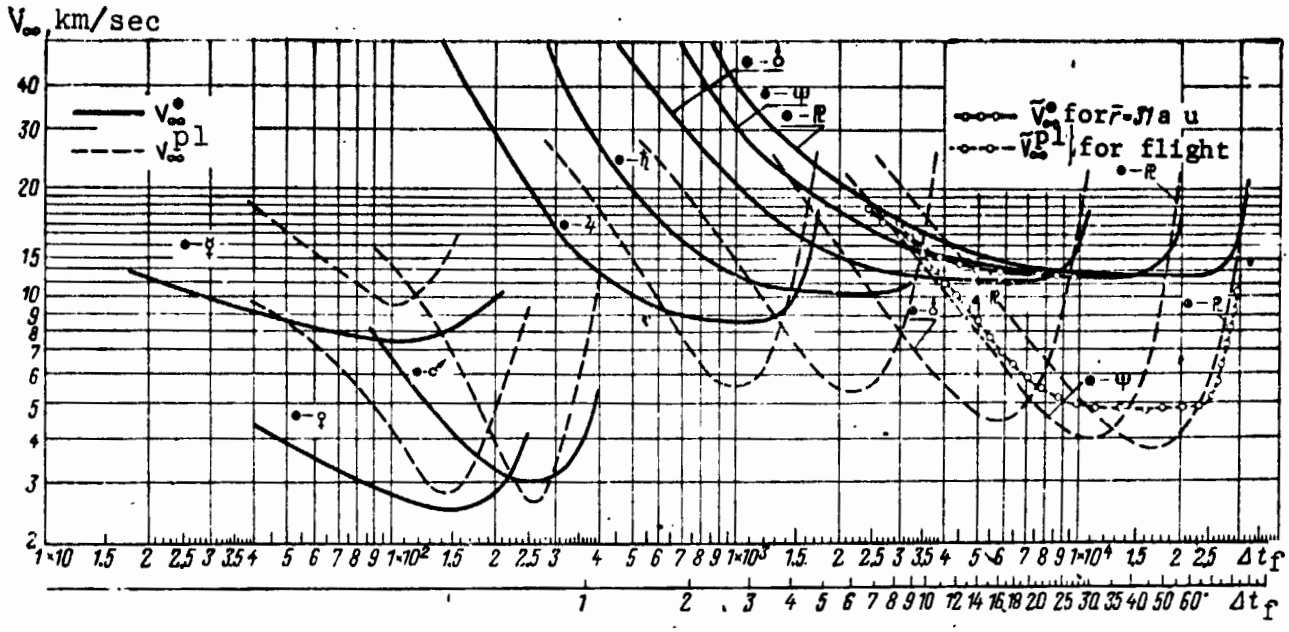

Figure 5.1.5. Characteristics of accelerated trajectories

TABLE 5.5.

Trajectory form	Characteristic	Planet							
		Mercury	Venus	Mars	Jupiter	Saturn	Uranus	Neptune	Pluto*
Optimal	$V_\infty^\odot$ km/sec	7.5	2.5	3.0	8.7	10.3	11.3	11.7	11.8
	Δt_f, days	106	146	259	2.73 year	6.05 year	16.04 year	30.6 year	33 year
Accelerated	$V_\infty^\odot$ km/sec	8.0	3.0	3.5	9.3	10.8	11.9	12.1	12.3
	Δt_f, days	65	81	180	1.75 year	3.7 year	8.0 year	16.0 year	14 year

*For flights in 1970 — 1980 period.

velocity V_{en}^{φ} into the planet atmosphere from 10.4 to 11.5 km/sec. For accelerated flights to Mars, the values of V_∞^σ increase from 2.6 to 5.5 km/sec, which leads to entry velocity increase from 5.55 to 7.4 km/sec. This may be of significant importance for SC landing in the rarefied atmosphere of Mars.

For accelerated flights to Jupiter, the velocity V_{∞}^{4} increases from 5.7 to 9.3 km/sec, which, because of the high parabolic velocity of Jupiter, causes increase of the entry velocity into Jupiter's atmosphere from 60 to 61 km/sec.

We see from this discussion that, even on the basis of the estimated values, the accelerated flight trajectories are quite interesting for realization of automatic interplanetary vehicle flight.

§ 2. OPTIMIZATION OF INTERPLANETARY FLIGHT TRAJECTORY HELIOCENTRIC SEGMENTS ON ISOLINE FIELDS

The flight trajectories of the flyby, landing, and some forms of combined flight schemes are of the single-impulse type.

It is convenient to represent the single-impulse flight trajectory characterstics in the form of isolines of the characteristic launch velocity $\Delta V_{st}^{\oplus}$ from AES orbit (or V_{∞}^{2}) in the coordinates: launch date $t_{st}^{\oplus}$ and flight time Δt_f. Such a typical isoline field for the flight cycle to Mars is shown in Figure 5.2.1. The $V_{\infty}^{\oplus}$ velocity field is divided by a "ridge" with large values of $V_{\infty}^{\oplus}$ (for transfer angles $L \approx 180°$) into two regions: /154

— transfer along the first semiorbit (lower region with $L<180°$);

— transfers along the second semiorbit (upper region with $L>180°$).

Points with minimal V_{∞}^{2} value exist for each region. Realization of a trajectory near these points naturally maximizes the payload weight injected into the flight trajectory to the

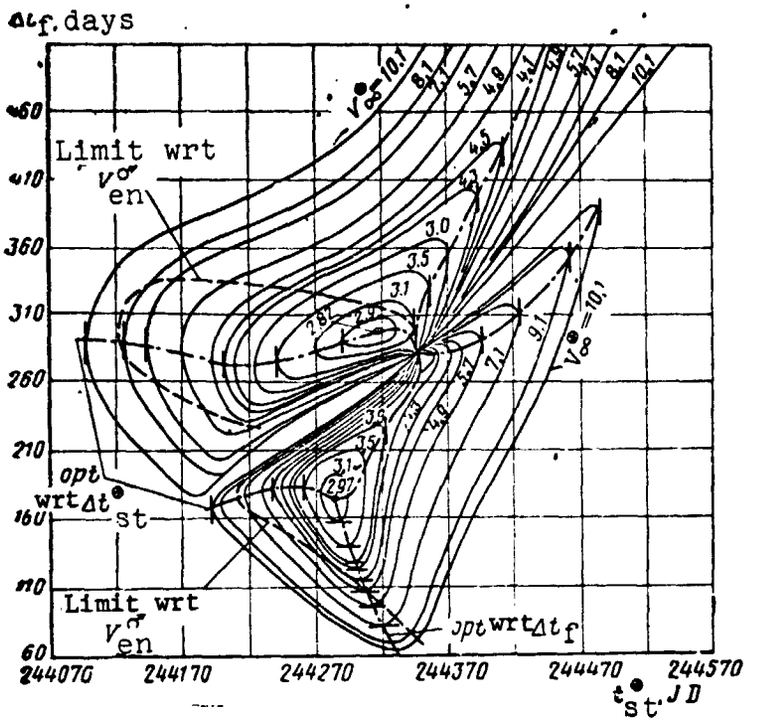

Figure 5.2.1. V_∞ isoline field for flight to Mars

planet. In addition, on this isoline field, we can optimize trajectories in two versions:

— trajectories which minimize $V_\infty^\oplus$ for the largest range of launch dates $t_{st}^\oplus$ (maximum launch date "window");

— trajectories which minimize $V_\infty^\oplus$ for a given flight time Δt_f ("accelerated" trajectories).

The first class of trajectories can be realized for flights /155 to the nearby planets (Mars and Venus) and the distant inner planet (Mercury), when there are no limitations on the flight time. On the $V_\infty^\oplus$ isoline field, these trajectories lie on the curve connecting the point of tangency of the straight lines $t_{st}^\oplus$ = const with the isolines $V_\infty^\oplus$.

Trajectories of the second class can be realized for flights to the distant outer planets (Jupiter, Saturn, and so on), when limitation of the flight time is essential. On the $V_{\infty}^{\odot}$ isoline field, these trajectories lie on the curve connecting the points of tangency of the straight lines Δt_f = const with the $V_{\infty}^{\odot}$ isolines. Naturally, in this class, the first semiorbit trajectories lying below the minimum point on the $V_{\infty}^{\odot}$ isoline field, are of greatest interest.

The flight velocity around the planet or the velocity of encounter with the planet can be characterized by the entry (encounter) velocity V_{∞}^{pl} into the planet's sphere of action. In the presence of limitations on V_{∞}^{pl} (for example, limitation of the entry velocity $V_{en} \approx V_{\pi}$ into the planet's atmosphere because of parachute braking system entry conditions, limitation of the planet flyby velocity because of mapping resolution, and so on) we can draw on the isoline field the limiting V_{∞}^{pl} isoline and optimize in the trajectory classes indicated above with account for the limitation on V_{∞}^{pl}.

The V_{∞}^{σ} isolines are drawn in Figure 5.2.2, and on the $V_{\infty}^{\odot}$ isoline field for the first semiorbit trajectories. The trajectories which optimize $V_{\infty}^{\odot}$ and V_{∞}^{σ} correspond to points of tangency* of these isolines. Such a route is shown in Figure 5.2.2. It obviously must pass through the $V_{\infty}^{\odot}$ and V_{∞}^{σ} minimum points. We see that, in this case, the $V_{\infty}^{\odot}$ minimum point limits the launch dates on the left. On the segment to the right of this point (up to the min V_{∞}^{σ} point), the launch date points are close to the path of trajectories which are optimal with respect to maximum launch date "window." To the right of the min V_{∞}^{σ} point, the V_{∞}^{σ} points deviate sharply downward from the path of trajectories which are optimal with respect to the launch date "window."

* We differentiate trajectories with $\min V_{\infty}^{\sigma}$ and $\max V_{\infty}^{\sigma}$ for a given value of $V_{\infty}^{\odot}$ (see Figure 5.2.2).

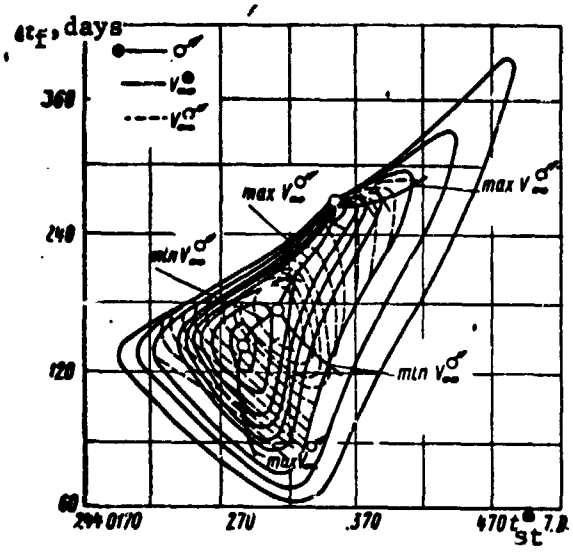

Figure 5.2.2. Optimization by minimum Mars encounter velocity $\overline{V}_\infty^\sigma$

Let us consider other trajectory optimization examples. Isoline fields for flight trajectories to Venus are plotted in Figure 5.2.3. On the launch velocity $V_{st}^\oplus$ from AES orbit isoline field, there is plotted the Earth sphere of action escape velocity vector $V_\infty^\oplus$ declination angle $\delta_\infty^\oplus$ isoline field. This angle characterizes SC visibility conditions in the initial segment of the flight trajectory. For stations located in the northern hemisphere, the best visibility conditions correspond to the maximal $\delta_{st}^\oplus$ value. /156 In Figure 5.2.3, such a route is plotted on the $V_{st}^\oplus$ isoline field. The largest $\delta_{st}^\oplus$ for given energy expenditures ($V_{st}^\oplus$) lie to the left of the min $V_{st}^\oplus$ point. Also shown is the route corresponding to trajectory optimization by launch date $t_{st}^\oplus$. The route which minimizes V_∞^δ (and consequently the minimum entry velocity into the planet's atmosphere) is also shown in Figure 5.2.3. The route of these optimal trajectories is close to that of the trajectories optimized by launch date.

We have examined some cases of trajectory optimization on the isoline fields. It is possible to construct isolines of other criteria, for example, payload weight or other combined criteria. Optimization on the isoline fields permits determining not only the optimal trajectories but also the behavior of the criterion in the vicinity of the optimal values. This makes it possible to deviate from the optimal routes in the ballistic design process, taking into account additional considerations.

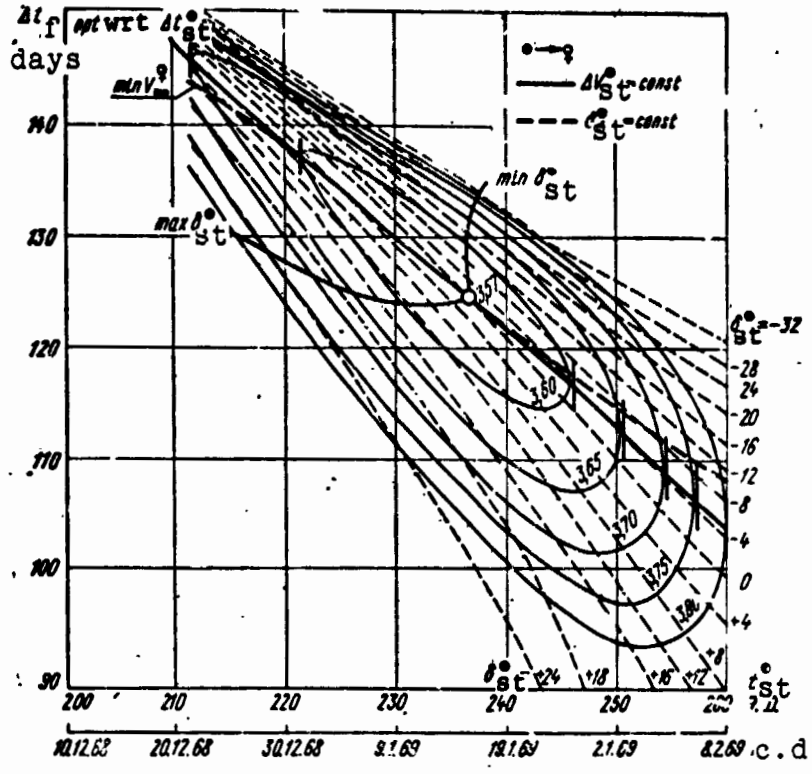

Figure 5.2.3. Optimization by minimum declination angle $\delta^{\oplus}_{st}$

The trajectory characteristics for different optimization conditions can be obtained from the isoline field. However, it is more convenient to obtain these characteristics separately. For example, trajectory optimization by launch date "window" can be made with the aid of a digital computer, determining for a given launch date $t^{\oplus}_{st}$, the optimal flight time to provide $V^{\oplus}_{st}$. In this case, to ensure unimodality of the search region (region with a single extremum), it is necessary to divide the trajectories into groups: /157

— trajectories of the first semiorbit with $0<L<180°$;

— trajectories of the second semiorbit with $180°<L<360°$.

In order to exclude nodal points* and characteristics in the energy ridge region, it is necessary to restrict the transfer angle L:

— $0<L\leqslant\pi-(i+\varepsilon)$ for the first semiorbit trajectory;

— $\pi+(i+\varepsilon)\leqslant L\leqslant 2\pi$ for the second semiorbit trajectory.

Here i is the angle between the planes of the planets. The value $\varepsilon \approx 0.5 — 1°$ ensures exclusion of the nodal points.

Tables 5.6 — 5.8 present the minimum energy expenditure trajectory characteristics for flight to Mars, Venus, and Jupiter in 1970 — 1990.

During the 1970 — 1980 period (Table 5.6), the minimum energy expenditure for flights to Venus along the first semiorbit trajectories occurs in 1975 ($V_\infty^\oplus$ = 2.5 km/sec). /161

The launch date "window" $\Delta t_{st}^{\odot}$ for margin $\Delta V_1 \approx 0.5$ km/sec is $\Delta t_{st} \approx 2 — 3$ months.

For flight to Mars (Table 5.7), the flight cycles from 1979 to 1986 ($V_\infty^\oplus$ = 3 km/sec) will be optimal for the first semiorbit trajectories. The launch "window" is $\Delta t_{st}^{\odot} \approx 1 — 1.5$ months for the first semiorbit trajectories and $\Delta t_{st}^{\odot} = 3 — 4$ months for the second.

For flights to Jupiter (Table 5.8), the optimal year was 1970 with required velocity $\Delta V_{st}^{\odot} = 6.24$ km/sec. Automatic SC flights with duration 2 — 3 years present serious difficulties in regard to ensuring operating life of the onboard systems and the vehicle as a whole. Therefore, energetically optimal "accelerated" flight trajectories are of interest for flights to the distant planets.

* Flight from Earth orbit node to planet orbit node.

TABLE 5.6. CHARACTERISTICS OF SINGLE-IMPULSE FLIGHT TRAJECTORIES TO VENUS*

Years	Semi-orbit	$t^{\oplus}_{st}$	Δt_f	$v^{\oplus}_{st}$	v^{φ}_{∞}
		date	days	km/sec	
1970	1	18.08.70	117	3,60	5,40
	2	16.09.70	167	3,70	6,35
1972	1	28.03.72	112	3,77	6,06
	2	07.04.72	117	3,59	5,42
1973	1	10.11.73	107	3,82	4,80
	2	09.11.73	156	3,55	4,29
1975	1	10.06.75	143	3,51	3,61
	2	31.05.75	154	3,49	3,69
1977	1	10.01.77	128	3,56	4,39
	2	09.12.76	157	3,73	4,45
1978	1	16.08.78	118	3,60	5,33
	2	15.09.78	167	3,70	6,38
1980	1	26.03.80	112	3,76	6,05
	2	05.04.80	171	3,60	5,47
1981	1	08.11.81	107	3,82	4,92
	2	07.11.81	157	3,56	4,36
1983	1	10.06.83	143	3,52	3,53
	2	28.05.83	155	3,49	3,66
1985	1	07.01.85	129	3,56	4,29
	2	08.12.84	157	3,71	3,73
1986	1	13.08.86	119	3,59	5,26
	2	13.09.86	167	3,71	6,44
1988	1	24.03.88	112	3,76	6,05
	2	03.04.88	171	3,60	5,51
1989	1	05.11.89	107	3,82	5,04
	2	07.11.89	156	3,56	4,42
1991	1	10.06.91	142	3,54	3,54
	2	26.05.91	156	3,49	3,60

*Translator's Note. Commas in numbers indicate decimal points.

TABLE 5.7. CHARACTERISTICS OF SINGLE-IMPULSE FLIGHT TRAJECTORIES TO MARS

Year	Semi-orbit	$t^{\oplus}_{st}$	Δt_f	$v^{\oplus}_{st}$	v^{σ}_{∞}
		date	days	km/sec	
1971	1	24.05.71	210	3,43	2,84
	2	03.05.71	249	3,56	3,14
1973	1	30.07.73	193	3,72	3,00
	2	28.08.73	408	3,91	3,68
1975	1	15.09.75	207	3,91	3,75
	2	17.09.75	373	3,66	2,89
1977	1	19.10.77	224	3,83	4,04
	2	09.10.77	333	3,55	2,45
1979	1	03.11.79	286	3,48	2,87
	2	03.11.79	287	3,48	2,84
1981	1	18.12.81	214	3,48	5,19
	2	16.12.81	327	3,47	3,85
1984	1	08.02.84	185	3,47	5,49
	2	07.03.84	313	3,42	5,28
1986	1	22.04.86	187	3,43	3,35
	2	06.05.86	259	3,41	3,89
1988	1	05.07.88	192	3,59	2,77
	2	19.08.88	414	3,83	3,96
1990	1	30.08.90	201	3,77	3,46
	2	10.09.90	388	3,711	3,17

*Translator's Note. Commas in the numbers indicate decimal points.

TABLE 5.8. CHARACTERISTICS OF SINGLE-IMPULSE FLIGHT TRAJECTORIES TO JUPITER (FIRST SEMIORBIT)*

Year	$t^{\oplus}_{st}$	Δt_f	$v^{\oplus}_{st}$	$v^{\downarrow}_{\infty}$
	date	days	km/sec	
1970	03.01.70	805	6,24	5,69
1971	30.01.71	836	6,30	6,47
1972	04.03.72	749	6,42	7,05
1973	09.04.73	721	6,53	7,12
1974	18.05.74	742	6,56	6,66
1975	30.06.75	909	6,45	5,71
1976	29.07.76	820	6,47	5,97
1977	03.09.77	774	6,65	6,48
1978	06.10.78	716	6,78	6,86
1979	07.11.79	787	6,77	6,79
1980	07.12.90	848	6,60	6,21
1982	04.01.82	1002	6,23	5,69
1983	03.02.83	819	6,32	6,59
1984	03.04.84	743	6,44	7,08
1985	15.04.85	721	6,54	7,09
1986	23.05.86	749	6,56	6,58
1987	05.07.87	1029	6,37	5,73
1988	30.08.88	810	6,49	6,03
1989	07.09.89	770	6,68	6,55
1990	11.10.90	767	6,78	6,84

*Translator's Note: Commas in numbers indicate decimal points.

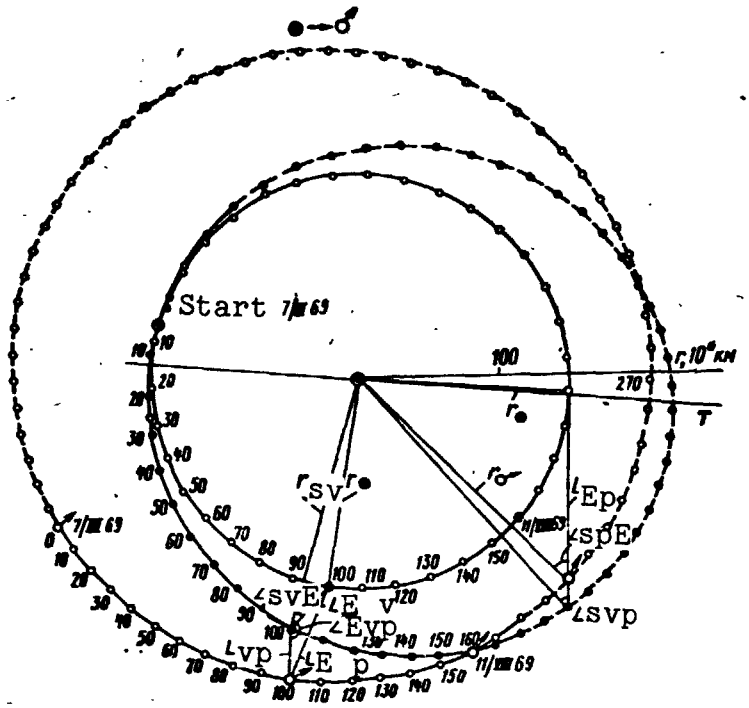

Figure 5.2.4. Earth-Mars flight trajectory (1969 cycle)

Figure 5.2.4 shows in the projection on the ecliptic plane a nearly optimal SC trajectory to Mars for one flight cycle. The flight trajectory is in the first semiorbit trajectory group. At /162 the launch time, the distance between the Earth and Mars is $L_{E\,p} \approx 165$ million kilometers. Mars opposition occurs at $\Delta t_f \approx 90$ days with distance $L_{E\,p} \approx 73$ million km. The SC passes near Mars on the $160^{\underline{th}}$ day of the flight. At this time, its distance from the Earth is $L_{E\,p} \approx 100$ million km. After Mars flyby (flyby outside the planet's activity sphere), the SC distance from the Sun increases, reaching the maximum $r_{s\,v} \approx 228$ million km on the $270^{\underline{th}}$ day of flight. The SC reaches the greatest distance from the Earth at $\Delta t_f \approx 380$ days, where the distance is $L_{E\,v} \approx 318$ million km. The SC distance $L_{s\,v}$ from the Sun determines the power of the solar batteries, the distance

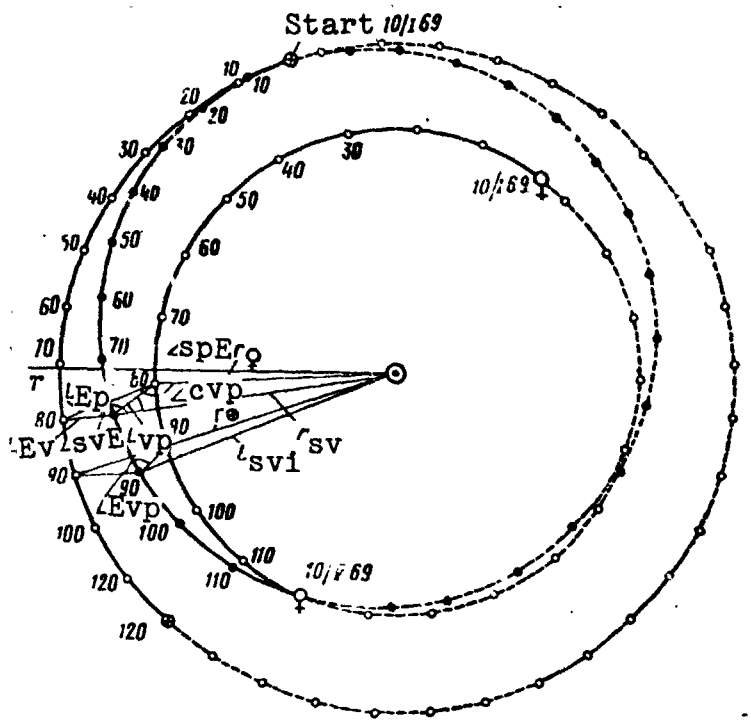

Figure 5.2.5. Earth-Venus flight trajectory (1969 cycle)

$L_{E\ v}$ from the Earth to the SC determines the radio communication link range.

Figure 5.2.5 shows the geometric characteristics of the flight trajectory to Venus. The vehicle starts from the Earth along a trajectory which is close with respect to energy expenditures to the optimal first semiorbit trajectory. The SC arrives at Venus in exactly four months. The minimal distance $L_{E\ p} \approx$ /163
42 million km between the Earth and Venus occurs on the $90^{\underline{th}}$ day of the flight. At the time of approach to Venus, the distance to the latter is $L_{E\ p} \approx 67$ million km.

Figure 5.2.6 shows the geometric charactersitics of the optimal accelerated flight trajectory to Jupiter with flight time

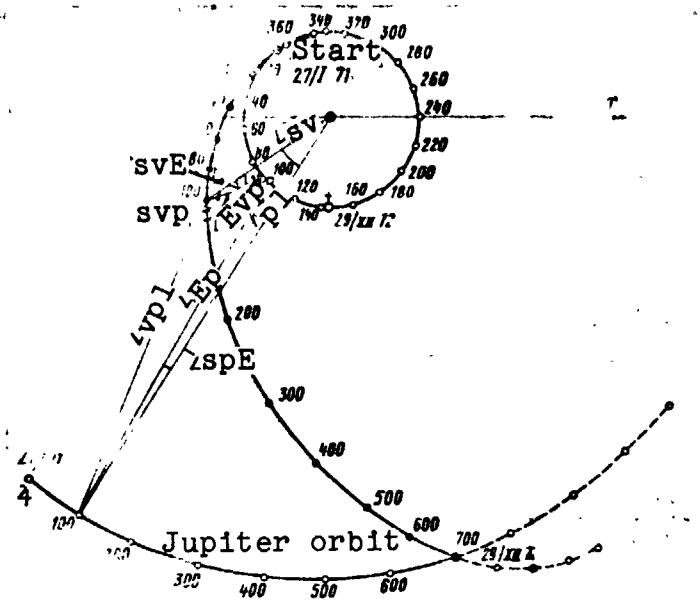

Figure 5.2.6. Earth-Jupiter flight trajectory (1971 cycle)

Δt_f = 700 days. The maximal distance from the Earth to the SC corresponds approximately to the moment of SC arrival at Jupiter and is $L_{E\,v} \approx 925$ million km. It is interesting that this distance does not vary monotonically, in contrast with flight to the nearest planets. Thus, the local maximum of $L_{E\,v}$ occurs on the $350^{\underline{th}}$ day of flight and the local minimum occurs on the $500^{\underline{th}}$ day.

§ 3. VARIATION OF OPTIMAL TRAJECTORY CHARACTERISTICS BETWEEN FLIGHT CYCLES

It was noted above that the flight cycles to a planet along the minimal energy trajectories repeat after periods close to the planet synodic period T_s. It is also known that the minimal energy trajectory characteristics are different in the different flight cycles. Analyzing the results of extensive optimal trajectory characteristic calculations for different flight cycles,

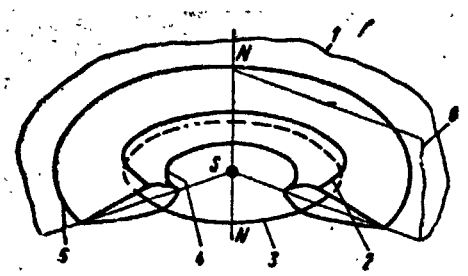

Figure 5.3.1. Reachable region and its section:

1- initial circular orbit plane; 2- line of maximal deviation from initial circular orbit plane; 3- initial circular orbit; 4- line of minimal distance from attracting center; 5- line of maximal distance from attracting center; 6- secant plane P

we can note some patterns of their variation between cycles. However, this approach is quite tedious and does not always disclose the complex variations of the characteristics between cycles, particularly for flights to the inner planets. /164

The present section, based on the data of [6], is devoted to determining the dynamics of the variation of these characteristics for various flight cycles. The "reachable region" concept is used. The essence of this method lies in the fact that, for a given characteristic launch velocity from circular orbit, the boundary of the maximal reachable region of space is determined. The minimal energy flight trajectory is realized if the target planet is located on the boundary of the maximal reachable region.

The reachable region is a body of revolution about the N — N axis passing through the attracting center S perpendicular to the initial circular orbit plane (Figure 5.3.1). Therefore, it is sufficient to determine the section of the reachable region by the secant plane P passing through the axis of revolution N — N.

The salient feature of the proposed method is that it permits separating the problem of determining the optimal lauch dates from the problem of determining the geometric and kinematic characteristics of the optimal trajectories. Moreover, by this method, the discrete process of characteristic variation between

flight cycles can be reduced to a periodic continuous process. In place of the graphical or numerical extremum search methods usually used, it reduces the problem to finding the solution of the equation trajectory family envelopes in the plane P. For certain cases, an analytic solution of this equation can be obtained. This reduces considerably the labor involved in calculating optimal trajectory characteristics and makes it possible to identify the quite complex pattern of variation of these characteristics between flight cycles.

We shall use the following assumptions:

1. As a consequence of its small eccentricity, the Earth's orbit is taken to be circular.

2. The planet orbital elements do not undergo significant changes in the next 20 — 30 years as a result of secular perturbations and are taken to be constant in the calculations.

3. The planet spheres of action are considered to be points, as is assumed in approximate interplanetary trajectory calculations. /165

4. The velocity changes impulsively during launch from orbit.

DETERMINATION OF REACHABLE REGION SECTION CONTOUR

A spacecraft in AES orbit is imparted the velocity impulse $\Delta V_{st}^{\oplus}$, which provides the required velocity $V_{\infty}^{\oplus}$ at departure from the Earth's sphere of action. The SC heliocentric velocity

$$V = V_{cir}^{\oplus} + V_{\infty}^{\oplus},$$

where $V_{cir}^{\oplus}$ is the Earth's velocity in circular orbit.

The optimal position of the vector $V_{\infty}^{\oplus}$ in space is defined by two angles α and β (Figure 5.3.2). Let us examine the particular case when the velocity triangle lies in the plane tangent to the Earth's orbit ($\beta = 0$, $\theta = 0$, and $\nu_0 = 0$). In

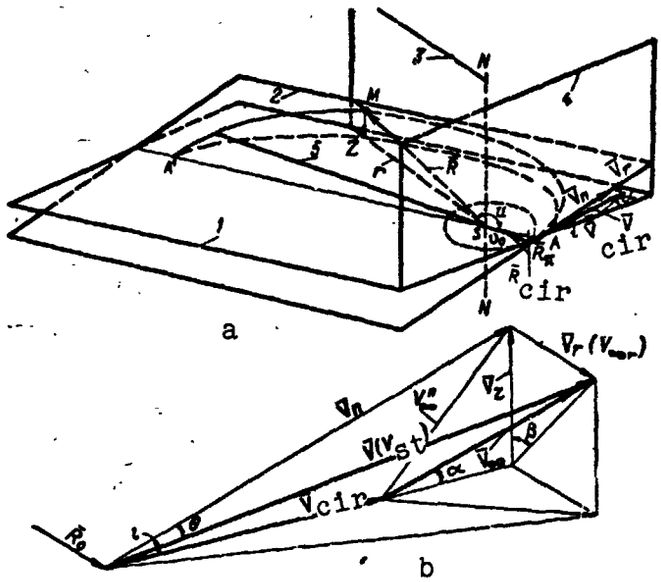

Figure 5.3.2. Transfer trajectory scheme:
a- relative position of basic planes; b- launch velocity triangle; 1- Earth's orbit plane; 2- transfer orbit plane; 3- secant plane F; 4- tangent plane ($\perp \bar{R}_0$); 5- line of apsides

this case, the position of the vector in space is defined by the single angle α. This case ("tangential launch") yields solutions close to optimal for the basic flight trajectory characteristics.

Determination of reachable region section contour for tangential launch. We shall examine a heliocentric trajectory (see Figure 5.3.2) along which the SC travels. /166

Isolines (contours of reachable region) for Δt_f = const

Figure 5.3.3a. Reachable region section contour for tangential launch with $V_{\infty}^{\oplus}$ = 2.5 km/sec

The plane P of the reachable region section passes through the attracting center perpendicular to the ecliptic plane and rotates about the N — N axis. For fixed modulus of the vector $|V_{\infty}^{\oplus}|$ and direction α of the vector $V_{\infty}^{\oplus}$, the SC flight trajectory trace remains in the plane P as it rotates about the N — N axis. We construct the trajectory trace envelope for various α varying in the interval 0 — 180° (Figure 5.3.3a). This envelope will then be the maximal reachable region section contour or the velocity isoline $V_{\infty}^{\oplus}$ = const. The SC heliocentric velocity at launch

$$V^2 = \left(V_{cir}^{\oplus}\right)^2 + 2V_{cir}^{\oplus} V_{\infty}^{\oplus} \cos\alpha + (V_{\infty}^{\oplus})^2. \qquad (5.3.1)$$

The distance R from the attracting center S to the point M on the trajectory is

$$R = \frac{p}{1 + e\cos\nu}, \qquad (5.3.2)$$

where p is the parameter, $e = (p/p_{cir}) - 1$ the eccentricity of the trajectory; ν is the true anomaly.

The distance z of the point M from the ecliptic plane (see Figure 5.3.2) is

$$z = R \sin u \sin i, \qquad (5.3.3)$$

where i is the trajectory inclination to the ecliptic [illegible] and

$$\sin i=\frac{V_{\infty}^{\oplus}\sin\alpha}{V}. \qquad (5.3.4)$$

It is obvious that, for $\alpha>0$, z will have both positive (for $v<180^{\circ}$) and negative (for $v>180^{\circ}$) values. This will correspond to flight along the first and second transfer trajectory semi- /167
orbits. If z and α have the same signs, flight takes place along the first semiorbit; if they have unlike signs, flight takes place along the second semiorbit.

Excluding the quantity ν from (5.3.2) and (5.3.3), after transformations, we obtain the equation of the trajectory trace family in the plane P:

$$\frac{\left(\frac{P}{R}-1\right)^2}{\left(\frac{P}{R_{cir}}-1\right)^2}+\frac{z^2V^2}{R^2(V_{\infty}^{\oplus})^2\sin^2\alpha}=1. \qquad (5.3.5)$$

We convert to relative quantities

$$\tilde{V}=\frac{V}{V_{cir}^{\oplus}};\quad \tilde{V}_{\infty}=\frac{V_{\infty}^{\oplus}}{V_{cir}^{\oplus}};\ \tilde{\varrho}=\frac{R}{R_{cir}};\ \tilde{\zeta}=\frac{z}{R_{cir}}. \qquad (5.3.6)$$

After some transformations (5.3.5) can be written in the form

$$(1-\gamma^2)(1-\tilde{\varrho})[(1+\tilde{\varrho})(1+\tilde{V}_{\infty}^2+2\tilde{V}_{\infty}\gamma)-2\tilde{\varrho}]+\tilde{\zeta}^2(\tilde{V}_{\infty}+2\gamma)^2=0, \qquad (5.3.7)$$

where $\gamma=\cos\alpha$.

This equation for fixed $\tilde{V}_{\infty}$ defines a one-parameter (parameter α) family of curves, each of which is the trace on the plane P of an SC flight trajectory.

Differentiating (5.3.7) with respect to the parameter γ, we obtain

$$\begin{aligned}\tilde{V}_-(1-\gamma^2)(1-\tilde{Q})(1+\tilde{Q})-\gamma(1-\tilde{Q})[(1+\tilde{Q})(1+2\tilde{V}_-\gamma+\tilde{V}_-^2)-\\-2\tilde{Q}]+2\tilde{C}^2(\tilde{V}_-+2\gamma)=0.\end{aligned} \tag{5.3.8}$$

Solving the system of equations (5.3.7) and (5.3.8), we obtain the following formulas for determining the envelopes

$$\tilde{Q}=\frac{2+\tilde{V}_-\gamma+\tilde{V}_-(\tilde{V}_-+2\gamma)(1+\tilde{V}_-\gamma+\gamma^2)}{2+\tilde{V}_-\gamma-\tilde{V}_-(\tilde{V}_-+2\gamma)(1+\tilde{V}_-\gamma+\gamma^2)}; \tag{5.3.9}$$

$$\tilde{\zeta}=\frac{\pm 2\tilde{V}_-(-\gamma^2)\sqrt{1+\tilde{V}_-\gamma+\gamma^2}}{2+\tilde{V}_-\gamma-\tilde{V}_-(\tilde{V}_-+2\gamma)(1+\tilde{V}_-\gamma+\gamma^2)}. \tag{5.3.10}$$

Determination of reachable region contour for two-parameter problem (nonplanar launch). Let the velocity vector at departure from the Earth's sphere of action be oriented arbitrarily in space and its position be defined by two angles α and β (figure 5.3.2b). The magnitude of the launch heliocentric velocity for this choice of parameters is a function of α and independent of β /168

$$V^2=(V^{\oplus}_{cir})^2+2V^{\oplus}_{cir}V^{\oplus}_{\infty}\cos\alpha+(V^{\oplus}_{\infty})^2.$$

The launch velocity components are: the velocity component along the normal to the radius vector at the launch point, lying in the flight trajectory plane

$$V_n^2=(V^{\oplus}_{cir}+V^{\oplus}_{\infty}\cos\alpha)^2+(V^{\oplus}_{\infty})^2\sin^2\alpha\cos^2\beta;$$

the radial component

$$V_r=V^{\oplus}_{\infty}\sin\alpha\sin\beta;$$

the projection of the launch velocity on the plane perpendicular to the circular velocity vector

$$V_s=V^{\oplus}_{\infty}\sin\alpha\cos\beta.$$

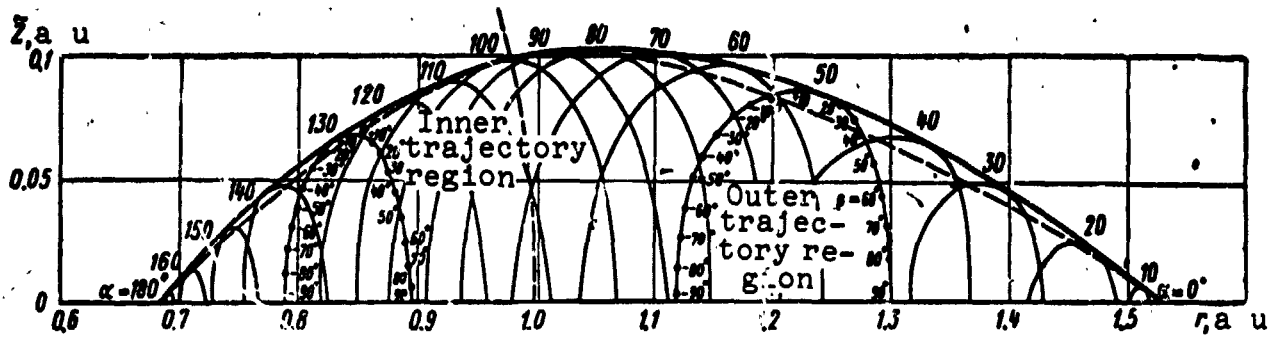

Figure 5.3.3b. Reachable region section contour for nonplanar launch with $V_{\odot} = 0.1$:*

α°	180	170	160	150	140	130	120	110	100	92°51′	90	80	70	60	50	40	30	20	10	0
β°_{opt}	0	−8,5	−16,3	−17,5	−15,6	−13,7	−10,6	−7,4	−3	0	0,3	5,7	11,1	14,5	17,6	19,7	21	22,2	22,25	0

*Translator's Note: Commas in the numbers indicate decimal points.

The distance from the attracting center is found from the expression

$$R = \frac{p}{1 + e\cos(u - \omega)}, \tag{5.3.11}$$

where ω is the argument of the pericenter.

The deviation from the ecliptic plane

$$z = R\sin i \sin u, \tag{5.3.12}$$

where

$$\sin i = \frac{V_z}{V_a}. \tag{5.3.13}$$

We convert to relative quantities using (5.3.6). Substituting (5.3.13) into (5.3.12), we obtain

$$\sin u = \frac{\bar{z}\bar{V}_a}{\bar{r}\bar{V}_z}. \tag{5.3.14}$$

Excluding ν from (5.3.14) and (5.3.11), after transformation, we obtain

$$V_n^2(1+\tilde{\zeta}\operatorname{tg}\beta-\tilde{Q})[V_n^2(1+\tilde{\zeta}\operatorname{tg}\beta+\tilde{Q})-2\tilde{Q}]+\tilde{\zeta}^2(\tilde{V}_n^2-1)=0, \qquad (5.3.15)$$

where

$$\operatorname{tg}\beta=\frac{\tilde{V}_r}{\tilde{V}_z}.$$

For fixed V_∞, the relation obtained defines a two-parameter family of curves, each of which is the trace of an SC flight trajectory on the plane P.

The envelope of the two-parameter family is found from a system of the type /169

$$\left.\begin{aligned} &F(\tilde{Q},\tilde{\zeta},\alpha,\beta)=0;\\ &\frac{\partial F}{\partial\alpha}(\tilde{Q},\tilde{\zeta},\alpha,\beta)=0;\\ &\frac{\partial F}{\partial\beta}(\tilde{Q},\tilde{\zeta},\alpha,\beta)=0. \end{aligned}\right\} \qquad (5.3.16)$$

For the first two equations of this system, we can obtain an analytic solution in the form

$$\tilde{Q}=\frac{AK}{2B-A}; \qquad (5.3.17)$$

$$\tilde{\zeta}=\frac{-L\operatorname{tg}\beta\pm\sqrt{-LM}}{L\operatorname{tg}\beta+M}, \qquad (5.3.18)$$

where $A=(\tilde{V}_n^2-1)(\tilde{V}_z^2\tilde{V}_n'+\tilde{V}_n^2\tilde{V}_z')-2\tilde{V}_n^2\tilde{V}_z^2\tilde{V}_n'$;

$$B=(\tilde{V}_n^2-1)\tilde{V}_n'-2\tilde{V}_z^2\tilde{V}_n';$$

$$\tilde{V}_n'=\frac{\partial\tilde{V}_n}{\partial\alpha};\quad \tilde{V}_z'=\frac{\partial\tilde{V}_z}{\partial\alpha};$$

$$L=\tilde{V}_z^2\tilde{V}_n^2(1+K);\ M=(\tilde{V}_n^2-1);\ K=1+\tilde{\zeta}\operatorname{tg}\beta.$$

However, it was not possible to obtain a sufficiently simple analytic solution for the complete system (5.3.16), and therefore, in order to construct the envelope of the two-parameter family of curves, we developed a digital computer algorithm using the analytic solution of the system consisting of the first two equations (5.3.17), (5.3.18).

The two-parameter envelope yields a somewhat larger reachable region than for tangential launch (see Figure 5.3.3b). The angle β vanishes at three points: for $\alpha_1=0$, $\alpha_2=180°$ (corresponds to outer and inner Hohmann transfers) and

$$\alpha_3=2\arcsin\frac{V_-^{\oplus}}{2V_{\text{cir}}^{\oplus}}$$

(corresponds to the maximal rotation of the circular orbit launch plane). The value α_3 separates the outer and inner transfer regions.

The reachable region section field can be constructed using the method described above by varying the modulus of the velocity vector at departure from Earth's sphere of action $V_-^{\oplus}$. Such a field for the range of coordinates $\tilde{r}$ and $\tilde{z}$ corresponding to flights to Mercury, Venus, and Mars is shown in Figure 5.3.4 and the field for flight to Jupiter, Saturn, Uranus, and Neptune is shown in Figure 5.3.5. These fields show flight time Δt_f isolines and planet position lines — traces of the planetary orbits on the plane P.

The planetary orbit traces on the plane P are closed curves /173
corresponding to all possible positions of the planets after their sidereal period of revolution. For a given planet position at the time of arrival, we can determine from such isoline fields the optimal trajectory characteristics. Examining all positions

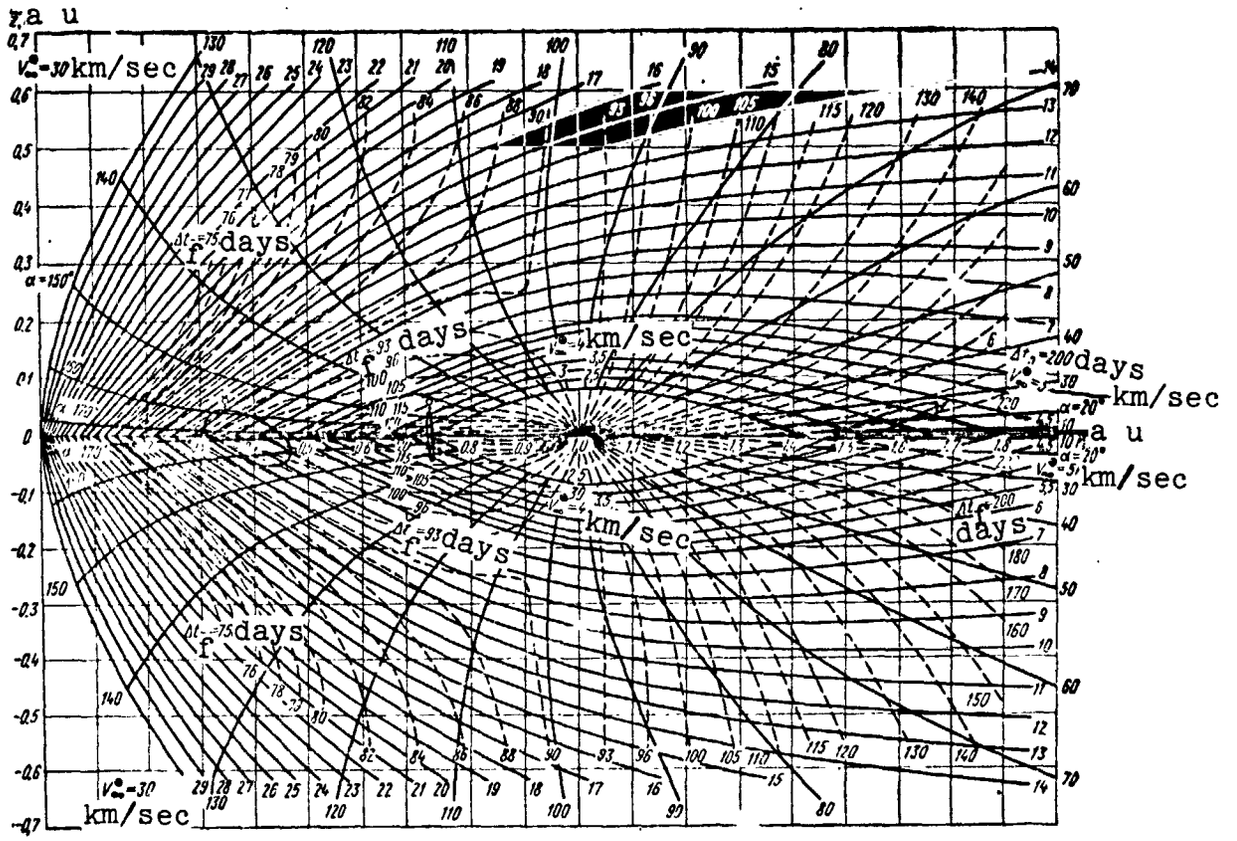

Figure 5.3.4. Reachable region contours for flights to Mercury, Venus, and Mars

of the planet on its orbit, we obtain all possible values of the trajectory characteristics.

Figure 5.3.6 shows the variation of the velocity $V_{\infty}^{\oplus}$ at departure from the Earth's sphere of action as a function of planet position in orbit. This position characterizes the dependence of the nominal arrival date t_{ar}^{nom} on the following quantities:

— radius $\tilde{r}$ of planet orbit projection on ecliptic plane;

— distance $\tilde{z}$ of planet from this plane.

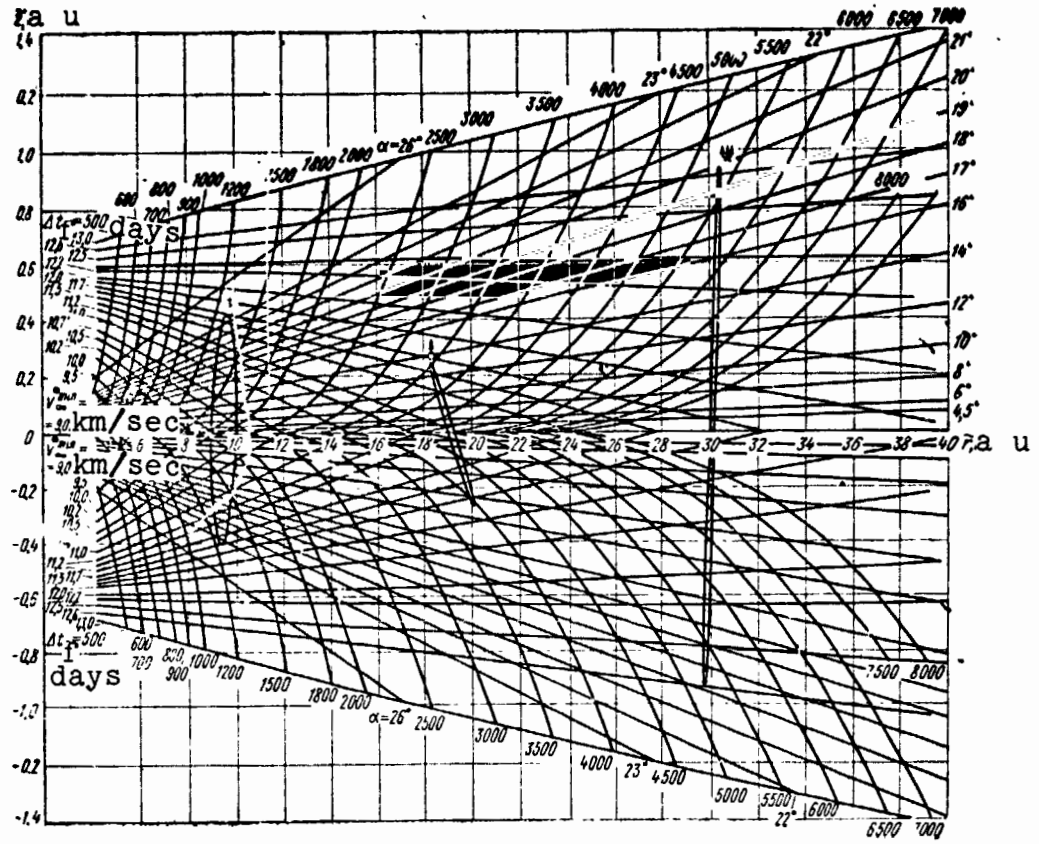

Figure 5.3.5. Reachable region contours for flights to Jupiter, Saturn, Uranus, and Neptune

We see that the deviation of $V_{\infty}^{\odot}$ from the average values (planar circular planet orbits) correlates with the deviation of the radius $\tilde{r}^{pl}$ from the average value and the variation of the modulus $\tilde{z}$. Increase of the planet radius $\tilde{r}^{pl}$ requires increase of the energy expenditures ($V_{\infty}^{\odot}$). "Departure" of the planet from the ecliptic plane also requires increase of the energy expenditures. The influence of ellipticity and noncoplanarity shows up most markedly for Mercury. For Mars, the influence of both factors is about the same. For the other planets, the influence of noncoplanarity of their orbits shows up more strongly. This indicates that account for planet orbit

/174

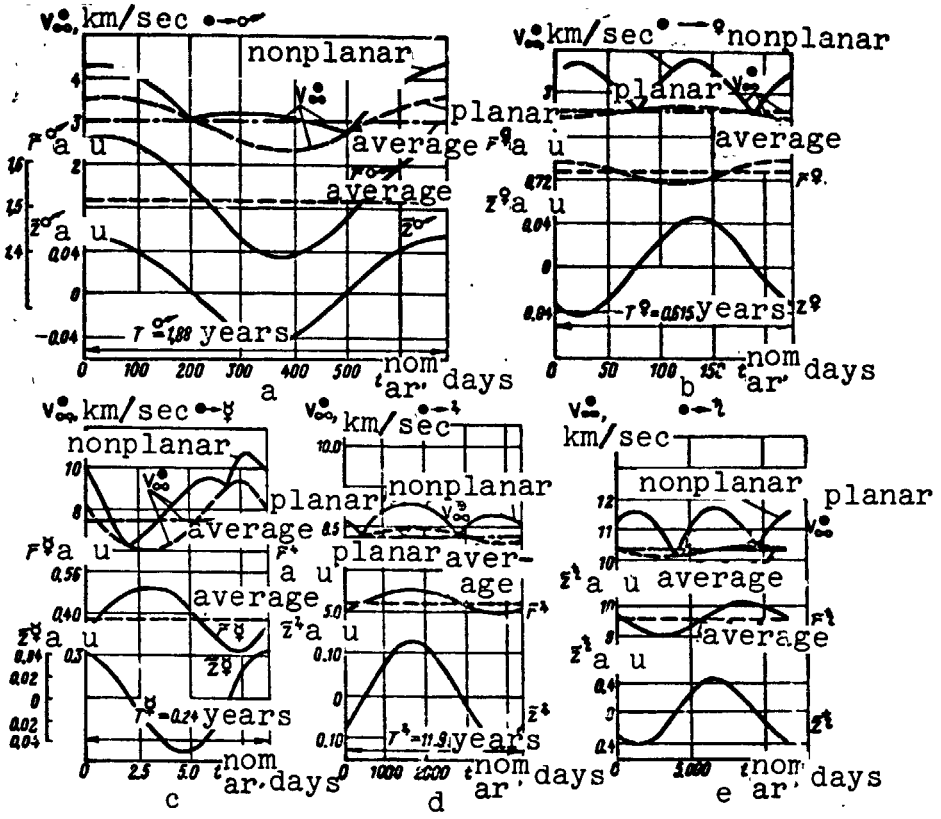

Figure 5.3.6. Velocity at departure from Earth's sphere of action required for flight to various planets — planar and nonplanar transfers

noncoplanarity is an essential factor in determining the dynamics of orbit characteristic variation between flight cycles.

DETERMINATION OF FLIGHT TRAJECTORY CHARACTERISTICS FROM NOMINAL LAUNCH DATES

The expressions obtained above for determining the reachable region section contour (trajectory trace envelope) permit finding the basic flight trajectory characteristics. The three-dimensional problem reduces to a problem on the plane P: through a given point of space, defined by the coordinates $\tilde{r}$ and $\tilde{z}$, draw the maximal reachable region section. To do this, it is necessary

to select values of the parameters α_{opt} and β_{opt}, defining the minimal energy trajectory, which will be tangent at the given point to the maximal reachable region section contour.

In order to determine $V_\infty^\oplus$ and α for the tangential launch case, we use the solution for $\tilde{V}_\infty$ and γ of the envelope equations (5.3.9) and (5.3.10) in dimensionless form. The solution of these equations for $\tilde{V}_\infty$ can be obtained analytically

$$\tilde{V}_\infty = \frac{4\tilde{V}_\infty^2\gamma\left[\tilde{V}_\infty^2(\tilde{\varrho}-1)^2-(\tilde{\varrho}^2-1)\right]}{\tilde{\zeta}^2(\tilde{\varrho}^2-1)(3-\gamma^2)-(\tilde{\varrho}^2-1)^2(1-\gamma^2)^2-2\tilde{\zeta}^4}. \qquad (5.3.19)$$

Substituting the value of $\tilde{V}_\infty$ into (5.3.8), we obtain a sixth degree equation in γ. An algorithm for determining $\tilde{V}_\infty$ and γ on a digital computer was formulated from (5.3.9) — (5.3.10) and use of this algorithm made it possible to determine the values of $V_\infty^\oplus$ and α for any planet position for flight along the minimal energy trajectory. These values of $V_\infty^\oplus$ and α were used as the zero approximation for calculating the three-dimensional launch trajectory when solving the system (5.3.16).

By specifying the planet position in orbit in the course of the sidereal period of planet revolution, we can determine the minimal energy trajectory characteristics for flight along the first and second semiorbits. These characteristics can be represented in the form of continuous curves versus nominal launch dates as follows. We specify the "zero" arrival date at the planet (0.01.1965), from which the nominal arrival dates t_{pl}^{nom} are reckoned. The nominal launch date /175

$$t_{st}^{nom} = t_{pl}^{nom} - \Delta t_f,$$

where the flight time along the first semiorbit

$$\Delta t_{f1} = \frac{a\sqrt{a}}{2\pi}\left[E-\left(1-\frac{1}{a}\right)\sin E\right],$$

where

$$a=\frac{1}{2-\tilde{V}^2}$$

is the flight trajectory semimajor axis; $\tilde{V}$ is the dimensionless launch velocity.

The flight time along the second semiorbit

$$\Delta t_{f2} = \frac{a\sqrt{a}}{2\pi} - \Delta t_{f1}.$$

For negative values of t_{st}^{nom}, the planet sidereal period T^{pl} is added. By varying the nominal arrival date from zero to the magnitude of the sidereal period T^{pl} with the required interval, we examine all possible planet positions in orbit and obtain all possible minimal energy trajectory characteristics.

This technique was used to obtain the minimal energy trajectory characteristics for tangential ($\beta=0$) and nonplanar (β_{opt}) launch, which are shown in Figures 5.3.7 — 5.3.10.

The values of $V_{\infty}^{\oplus}$ and Δt_f for the optimal nonplanar launch trajectories (velocity $V_{\infty}^{\oplus}$ at departure from the Earth's sphere of action and flight time Δt_f) differ very little from the same values for the tangential launch trajectories.

The relative velocity (entry velocity into the planet's sphere of action) vector

$$\bar{V}_{\infty\ en} = \bar{V}_{pl} - \bar{V}_{SC}.$$

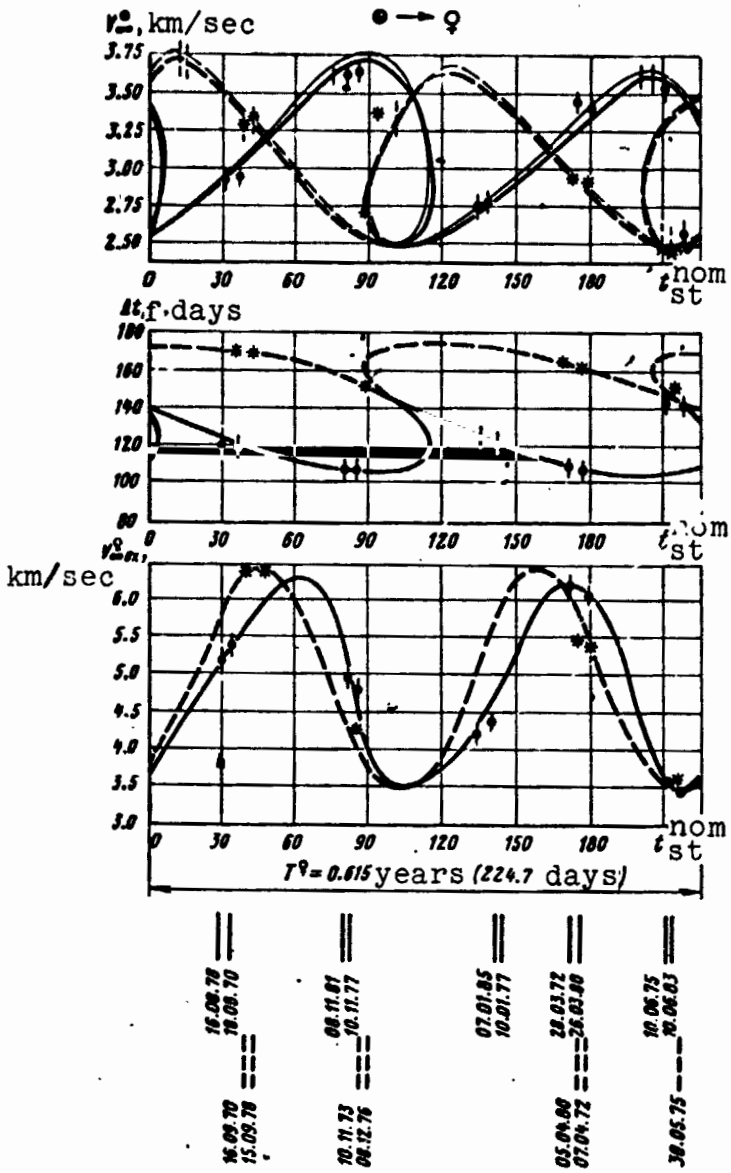

Figure 5.3.7. Dynamics of optimal Venus flight trajectory characteristics:

T_{go} = 8 years; i = 3°23'40"; a = 0.7233; e = 0.00685; T_s = 1.599 years; ●×- points calculated using Lambert-Euler method with optimization wrt $t^{\oplus}_{st}$ and Δt_f; ------ first semiorbit, β = 0, tangential launch; - - -- second semiorbit, β = 0, tangential launch; ---- first semiorbit, $\beta = \beta_{opt}$, nonplanar launch; —— second semiorbit, $\beta = \beta_{opt}$, nonplanar launch.

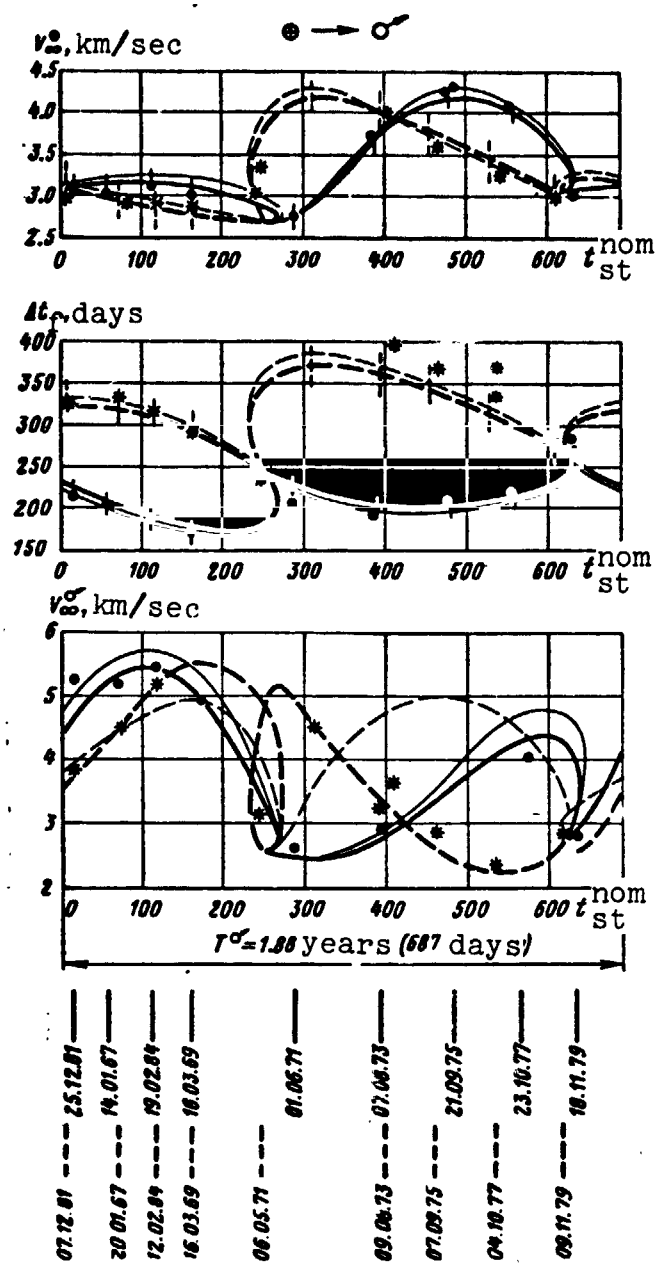

Figure 5.3.8. Dynamics of optimal Mars flight trajectory characteristics:

T_{go} = 15.83 years; a = 1.5327 a u; e - 0.0934; i = 1°51'03";
T_s = 2.135 years

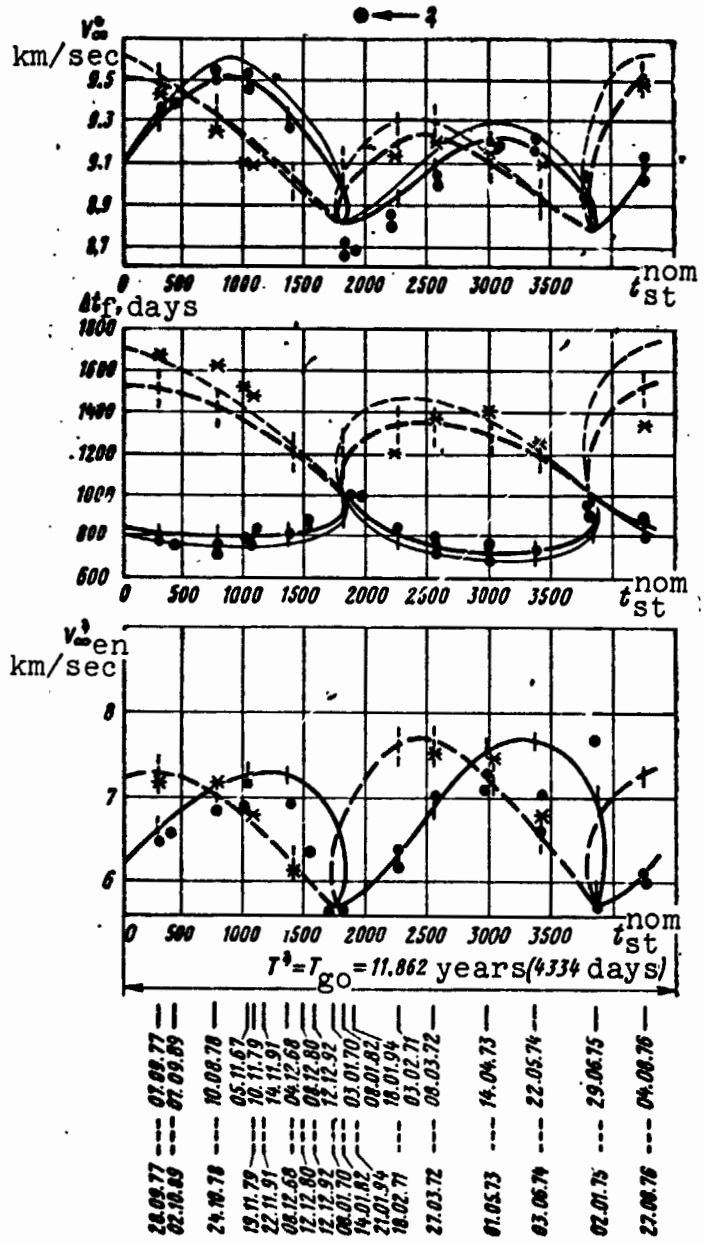

Figure 5.3.9. Dynamics of optimal Jupiter trajectory characteristics:

T_s = 1.092 years; i = 1°18'22"; a = 5.2025 a u; e = 0.0482

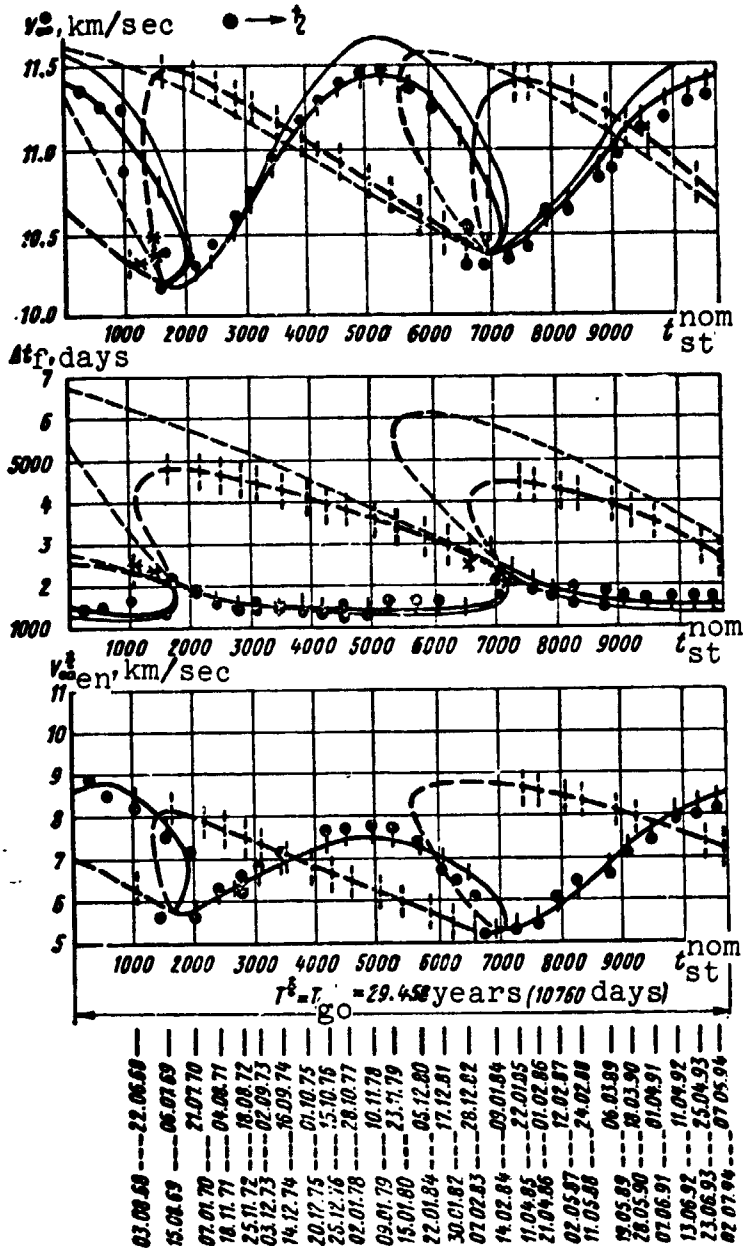

Figure 5.3.10. Dynamics of optimal Saturn flight trajectory characteristics:

i = 2°29'19"; a - 9.545 a u; e - 0.0552; T_s = 1.065 years

The moduli of the destination planet sphere of action entry velocity V_∞^{pl} are shown in Figures 5.3.7 — 5.3.10. The difference between the V_∞^{pl} curves for tangential and nonplanar launch is significant. Therefore, the V_∞^{pl} values must be determined using a more exact computational scheme for nonplanar launch from Earth orbit.

In Figures 5.3.7 — 5.3.10, the points indicate the trajectory characteristic values determined by optimization on the $V_\infty^\oplus$ isoline fields. The $V_\infty^\oplus$ (optimization criterion) points fit the curves well. The Δt_f and $V_{\infty en}$ points have considerable scatter, since their exact determination on the isoline fields is difficult because of the flatness of the $V_\infty^\oplus$ minimum. /180

We can also examine the energy expenditure variation with account for planet orbit ellipticity and noncoplanarity on the basis of these characteristics.

LAUNCH DATE DETERMINATION (PHASING PROBLEM)

The technique outlined above was used to determine the trajectory geometric parameters P_{SC} and e_{SC} and the trajectory inclination i_{SC} to the ecliptic plane. The longitude of the SC trajectory ascending node coincides with the launch point

$$\Omega_{SC} = \lambda_{pl}^{pl} - \Delta\lambda_f$$

where λ_{pl}^{pl} is the planet heliocentric longitude at the time of SC arrival; $\Delta\lambda_f$ is the projection of the arrival angle on the ecliptic plane.

The destination planet heliocentric longitude

$$\lambda_{ar}^{pl} = \Omega_{pl} + \text{Arc tg}\,[\text{tg}(\omega_{pl} + \nu_{ar}^{pl})\cos i_{pl}] = \lambda_{ar}^{pl}(t_{ar}^{pl}),$$

*Computation of the trajectories on a digital computer using the Lambert-Euler method (see § 1, Chapter 2) with optimization with respect to the parameters t_{st}^* and Δt_f.

where Ω_{pl} is the planet node longitude; ω_{pl} is the argument of planet perihelion latitude.

At the launch time, the Earth occupies a position characterized by the heliocentric longitude

$$\lambda^{\oplus}_{st}=\lambda^{\oplus}_{0}+n^{\oplus}t^{\oplus}_{st}=\lambda^{\oplus}_{st}(t^{\oplus}_{st}),$$

where $\lambda^{\oplus}_{0}$ is the heliocentric longitude of the Earth at the initial time; $n^{\oplus}$ is the diurnal motion of the Earth.

The difference of the heliocentric longitudes of the planet at the time of arrival and the Earth at the time of SC launch is $\lambda^{pl}_{ar} - \lambda^{\oplus}_{st}=\Delta\lambda$.

At the time of arrival at the destination planet, the projection of the SC flight angle on the ecliptic plane is γ_{SC} and the difference of the heliocentric longitudes of the planet at the arrival time and the Earth at the launch time must be

$$\Delta\lambda_f = \Delta\lambda. \qquad (5.3.20)$$

Knowing at this instant the arrival date and flight time, we find the date of SC launch from the Earth

$$t_{st} = t_{ar} - \Delta t_f.$$

Therefore, the process of determining launch dates for flight along optimal trajectories reduces to varying the arrival time in the specified range and finding the roots of the synchronization equation (5.3.20) (Figure 5.3.11). /181

In Figures 5.3.7 — 5.3.10, the bars indicate the launch dates $t^{\oplus}_{st}$ from the Earth, determined from solution of the synchronization equations.

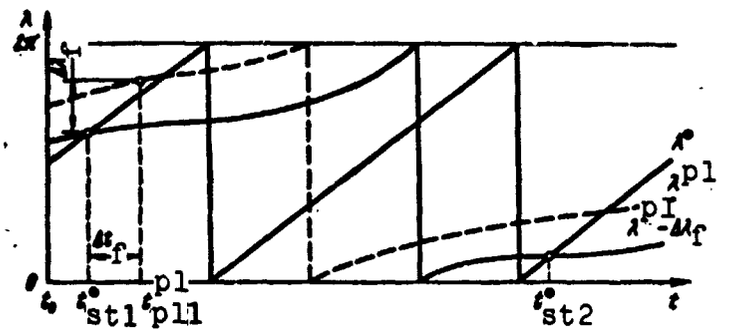

Figure 5.3.11. Diagram for determining the roots of the synchronization equation

VARIATION OF OPTIMAL TRAJECTORY CHARACTERISTICS FOR VARIOUS FLIGHT CYCLES

It is well known that SC flight cycles to the planets along minimal energy trajectories lie in the region of launch dates from the Earth close to the dates for flight along Hohmann trajectories for the case of planar circular planet orbits. For these trajectories, the flight cycles repeat after the time T_s — the synodic period of planet revolution relative to the Earth $\frac{1}{T_s} = \left|\frac{1}{T^{\oplus}} - \frac{1}{T^{pl}}\right|$.

For the actual (elliptic and noncoplanar) planet orbits in these cycles, the target-planet occupies different positions in its orbit. However, these positions will repeat after approximately the period T_{go} — the period of great oppositions of the planet.* Consequently, the characteristics of the optimal flight trajectories will also repeat after approximately T_{go} for the case of launch from any position in Earth orbit.

*$T_{go} \approx k_1 T^{\oplus} \approx k_2 T^{pl} \approx |k_2 - k_1| T_s$ is the approximate least common multiple of $T^{\oplus}$, T^{pl}, and T_s (see § 1, Chapter 9).

The technique outlined above makes it possible to determine the dynamics of the minimal energy trajectory characteristics for various flight cycles. Figures 5.3.7 — 5.3.10 present information on the characteristics of the optimal trajectories to the planets for any flight cycles. Each point of these curves will correspond (or has corresponded) to a definite real flight cycle, therefore these curves can be considered continuous /182
relations. These relations have a quite complex nature, which could scarcely be shown by calculating using the existing trajectory optimization methods for the individual discrete characteristic values even for a quite large number of flight cycles. We see that the values of the characteristics for certain cycles are ambiguous, which is reflected on the $V_{\infty}^{\oplus}$ isoline fields in the coordinates $t_{st}^{\oplus}$ and Δt_f (region with several local $V_{\infty}^{\oplus}$ minima). The characteristic points at the juncture of the first and second semiorbit trajectory curves correspond to flight along trajectories in the ecliptic plane to a point when the target-planet is at its orbital node.

However, for practical purposes, it is convenient to represent the dependence of the optimal trajectory characteristics on the actual launch dates $t_{st}^{\oplus}$* rather than the nominal dates. Figures 5.3.12 — 5.3.15 show such relations for flights to Mars, Jupiter, Venus, and Mercury, arbitrarily represented in the form of continuous curves with bars denoting the actual launch dates from the Earth.

Figure 5.3.12 shows characteristics of the optimal flight trajectories to Mars:

*Sample of the corresponding characteristics with period approximately equal to T_s form the periodic variations of these characteristics with period T_{pl}.

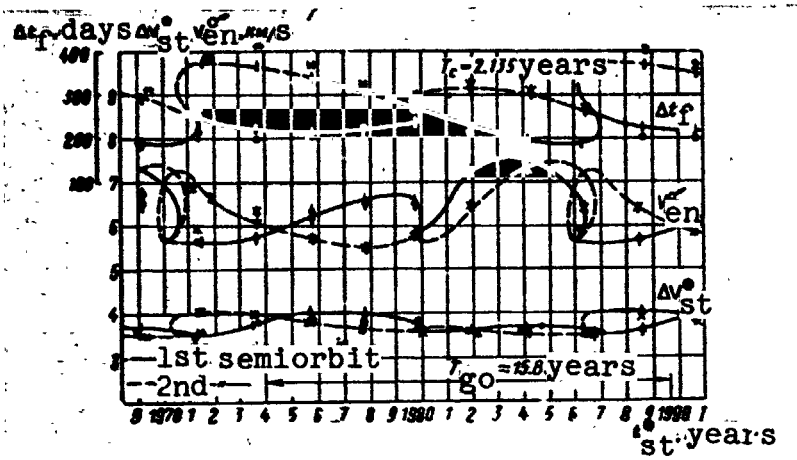

Figure 5.3.12. Characteristics of optimal flight trajectories to Mars

$\Delta V^{\oplus}_{st}$ is the velocity required for launch from circular AES orbit ($h_{cir} \simeq 200$ km); Δt_f is the flight time; V^{σ}_{en} is the velocity of SC entry into the planet atmosphere.

The curves of these characteristics have a period equal to the great opposition period: T_{go} is approximately 15.8 years. The flight cycles to Mars repeat approximately after the synodic period: T_s = 2.135 years. The points show the values of the corresponding characteristics calculated on the basis of optimization on the isoline fields. /183

The 1971, 1979, and 1986 flight cycles along the first smiorbit trajectories lie in the region of minimal flight energy expenditures (launch velocity $\Delta V^{\oplus}_{st}$). The flight cycles to Mars in the 1970s correspond to the largest variation of the optimal characteristics. The largest values of $\Delta V^{\oplus}_{st}$ occur in the 1975 and 1977 flight cycles along the first semiorbit trajectories. The increase of V^{σ}_{st} in comparison with the 1971 "best" cycle

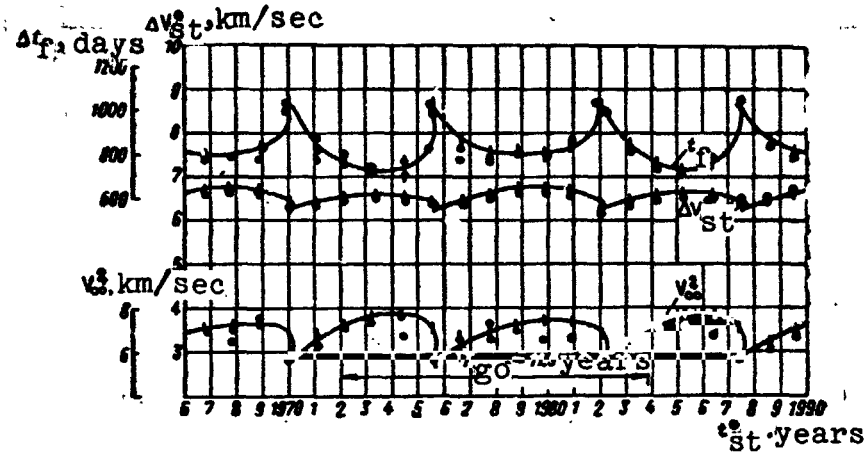

Figure 5.3.13. Characteristics of optimal flight trajectories to Jupiter (first semiorbit)

amounts to about 500 — 1000 m/sec. Transition to the more economical (for these flight cycles) second semiorbit trajectories is possible in these "poor" flight cycles along the first semiorbit trajectories. However, as we see from Figure 5.3.16, this leads to flight time increase from $\Delta t_f \approx 210$ — 220 days to $\Delta t_f = 300$ — 400 days. /184

The flight cycles to Mars in the 1980s, just as the past flight cycles in the 1960s, are more stable in regard to flight energy expenditure variation. An important characteristic for Mars landers is the entry velocity V^{σ}_{en} into the planet atmosphere.* The smallest values of V^{σ}_{en} occur in the 1971 and 1973 flight cycles for the first semiorbit trajectories. These flight cycles are obviously more favorable for the design of Mars landers.

Figure 5.3.13 shows the characteristics of optimal flight trajectories to Jupiter. The great opposition period T_{go} of this planet is approximately equal to its sidereal period (T_{go} =

*Defined in terms of the entry velocity V^{σ}_{∞} into the planet sphere of action.

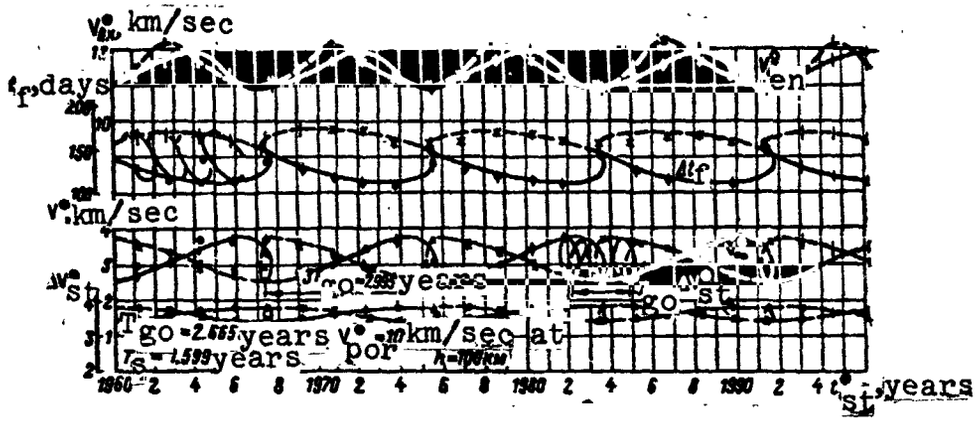

Figure 5.3.14. Characteristics of optimal flight trajectories to Venus.

11.09 years). The flight cycles to Jupiter repeat every $T_s \approx 1.09$ years. In the first half of the 1970s, there are cycles with smaller energy expenditure variation (difference $\Delta V^{\odot}_{st} \approx 300$ m/sec between the "best" and "worst" flight cycles). The best flight cycles are in 1970 and 1975. However, they correspond to a long flight time $t_f = 800 — 850$ days (flight nearly toward the nodes of Jupiter's orbit). Flight along other trajectories in these cycles leads to increase of $\Delta V^{\odot}_{st}$ by 200 m/sec but permits shortening the flight time to $\Delta t_f = 720 — 730$ days. The dynamics of flights to Saturn, because of the long opposition period of this planet ($T_{go} \sim T^{pl} \approx 29.5$ years), can be examined using the curves of trajectory characteristics as a function of nominal launch date (see Figure 5.3.10). /185

The smallest energy expenditures correspond to the flight cycles in 1970 and 1985. The worst in this sense are the flight cycles close to 1980. However, these cycles correspond to the shortest flight time $\Delta t_f = 1300$ days, in comparison with the "best" cycles, where $\Delta t_f = 1600 — 1800$ days. The energy

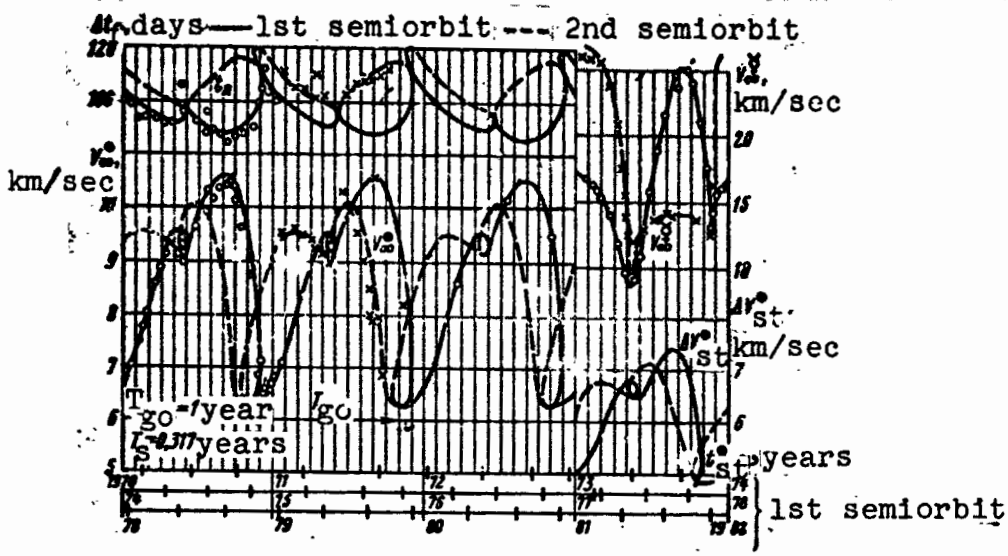

Figure 5.3.15. Characteristics of optimal flight trajectories to Mercury

requirements for flights to Saturn are considerably larger (range $\Delta V^{\oplus}_{st}$ = 7.2 — 8 km/sec) than for flights to Jupiter.

The dynamics of the characteristics of flight trajectories to Venus is shown in Figure 5.3.14. The great oppositions of this planet occur every $T_{go} \approx 8$ years (see § 1, Chapter 9). The synodic period is T_s = 1.598 years. The range of $\Delta V^{\oplus}_{st}$ variation for the various flight cycles is about 400 m/sec. The best flight cycles in regard to energy expenditure were those of 1967 — 1969 (first semiorbit trajectories) and will repeat in 1975 — 1977. The entry velocity into the Venus atmosphere varies in the limits V^{σ}_{en} = 10.9 — 12.2 km/sec.

The optimal flight cycles to Mercury occur three times a year (T_s = 0.317 years). The great opposition period of this planet is short — $T_{go} \approx 1$ year. The dynamics of the characteristics have a rapidly varying and complex nature (see Figure

5.3.15). The energy expenditures for flights to Mercury are considerably greater (range of variation $\Delta V^{\oplus}_{st}$ = 4.9 — 7.5 km/sec), than to Venus. Practically every year, we can find, among the optimal first or second semiorbit trajectories, one with energy expenditures close to the minimal values ($\Delta V^{\oplus}_{st} \approx 5$ km/sec).

SCHEME FOR DETERMINING OPTIMAL ACCELERATED TRAJECTORY CHARACTERISTICS BY THE REACHABLE REGION METHOD

For flights along minimal energy trajectories, the flight time along first semiorbit trajectories (transfer angle $L<180°$) to the outer planets varies in wide limits and may reach large values. The range of optimal flight time to these planets is: to Mars Δt_f = 190 — 250 days, to Jupiter Δt_f = 700 — 1000 days, and to Saturn Δt_f = 1200 — 2500 days.

At the present time, SC with operating life of about one year have been constructed (SC for flights to Venus and Mars and communications satellites). Increase of the operating life of automatic SC presents a serious design problem. Therefore, finding accelerated trajectories which are optimal in regard to energy expenditures is an urgent problem.

Trajectory optimization by the reachable region method makes /186 it possible to obtain the characteristics of the optimal accelerated trajectories for all possible flight cycles (in the limits of the assumption of planet orbital parameter stability for a time interval of about 20 — 30 years).

The problem is formulated as follows: for Earth orbit launch, determine the minimal energy trajectories for flight to any point of the solar system with flight time less than or equal to the specified value $\Delta t_f \leq \Delta t_{f\,giv}$.

We examine the general case when the launch velocity vector does not lie in the plane perpendicular to the ecliptic plane and tangent to the circular Earth orbit ("nonplanar launch"). Trajectory optimization on the characteristic velocity isoline fields yields similar values of the optimal trajectory characteristics.

To each point of the flight trajectory trace on the reachable region contour envelope (Figure 5.3.16), there corresponds a definite flight time, which can be found from the Kepler equation

$$\Delta t_f = \frac{a\sqrt{a}}{2\pi}[(E-E_0)-e(\sin E-\sin E_0)],$$

where $a=\frac{1}{2-\tilde{V}^2}$ is the flight trajectory semimajor axis; $\tilde{V}=\frac{V}{V^{\oplus}_{cir}}$ is the dimensionless geocentric launch velocity; $e=1-\frac{1}{a}$ is the flight trajectory eccentricity; $E=2\operatorname{arctg}\left(\sqrt{\frac{1-e}{1+e}}\operatorname{tg}\frac{\nu}{2}\right)$ is the eccentric anomaly; ν is the true anomaly.

We limit the reachable region by lines of fixed flight time Δt_f for $|V^{\oplus}_{\infty}|$ =const.

Specifying the parameters α and ν_0, we find the flight trajectory (parameters p, e, and a) as follows.

Knowing the quantity a and the flight time Δt_f, we determine from the formula for Δt_f the eccentric anomaly E and consequently, the true anomaly ν. After this, we use the formulas

$$e=\left(\frac{V^2}{\mu/R_{cir}}-1\right),\quad R=\frac{p}{1+e\cos(\upsilon-\upsilon_0)},\quad z=R\sin i\sin(\upsilon-\upsilon_0),$$

$$\sin i=\frac{V^{\oplus}_{\infty}\sin\alpha\cos\beta^*}{V_a},\quad r=\sqrt{R^2-z^2}$$

*β is determined in terms of ϑ (see Figure 5.3.2b), which depends on ν_0.

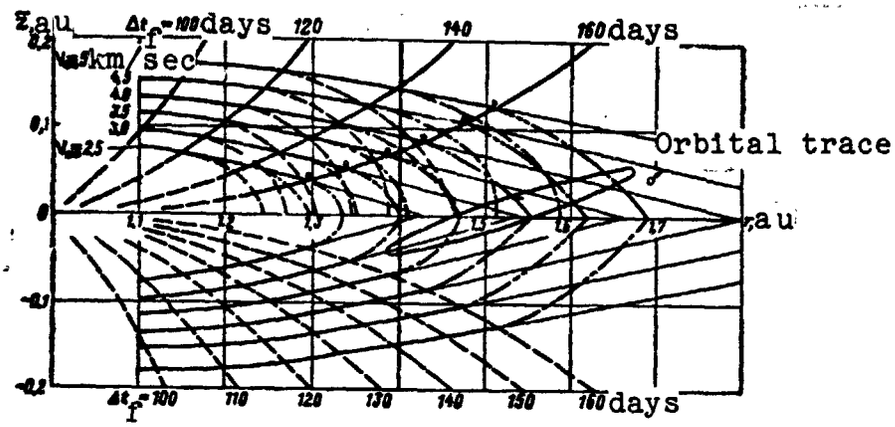

Figure 5.3.16. Reachable region contours for trajectories with fixed flight time (accelerated trajectories)

to determine the values of the coordinates r and z in the plane P.

Neglecting the parameters α and ν_0, we obtain the reachable region contour envelope for fixed flight time Δt_f. The isolines of the fixed time Δt_f (for $|V_\infty^\oplus| = \text{const}$) are tangent to the maximal reachable region isolines for free flight time. Thus, the reachable region contour for $\Delta t_f \leq \Delta t_{giv}$ will consist of a segment of the isoline with free flight time up to the point where $\Delta t_f = \Delta t_{giv}$ and the fixed flight time Δt_{giv} isoline. /187

Taking various values of the modulus $|V_\infty^\oplus| = \text{const}$, we can construct the reachable region field for free and fixed flight time. Figure 5.3.16 shows the field of such isolines for the coordinates $\tilde{r}$ and $\tilde{z}$ corresponding to flights to Mars. Knowing the target-planet orbital elements, taking ν_{pl} in the range from 0 to 2π and using the same formulas for R and z, we can calculate the planet orbit trace in the plane P. The Mars orbit trace is plotted in this way in Figure 5.3.16. A definite flight time t_{ar} to the planet corresponds to each point on the planet

orbit trace. We introduce, as before, the nominal arrival time t_{ar}^{nom}, varying from zero to T^{pl} (sidereal period of planet revolution). Taking a fixed flight time Δt_f and varying $|V_{\infty}^{\oplus}|$, we can construct the relation $|V_{\infty}^{\oplus}| = f(t_{st}^{nom})$. The nominal launch time t_{st}^{nom} from the Earth

$$t_{st}^{nom} = t_{ar}^{nom} - \Delta t_f.$$

Thus, we obtain the relation $|V_{\infty}^{\oplus}| = f(t_{st}^{nom})$ for fixed flight times Δt_f. Curves of the departure velocity $V_{\infty}^{\oplus}$ from the Earth's sphere of action and entry velocity V_{∞}^{pl} into the planet sphere of action are shown in Figures 5.3.17 — 5.3.19 for fixed Δt_f as functions of the nominal launch dates T_{st}^{nom} for flights to Mars, Jupiter, and Saturn. /191

DYNAMICS OF OPTIMAL ACCELERATED FLIGHT TRAJECTORY CHARACTERISTICS

Trajectory acceleration is of interest for flight to the distant outer planets (Jupiter and Saturn). The flight time to these planets along minimal energy trajectories is quite long (2 — 3 years to Jupiter and 3.5 — 6 years to Saturn).

Examination of accelerated flight trajectories to more distant planets (beyond Saturn) in the impulsive formulation is not advisable. Because of the comparatively high energy expenditures, the flights to these planets will probably utilize low-thrust power plants.

Although the flight time along the optimal energy trajectories to Mars does not exceed one year, this time is quite long (from six to nine months). Therefore, it is advisable to

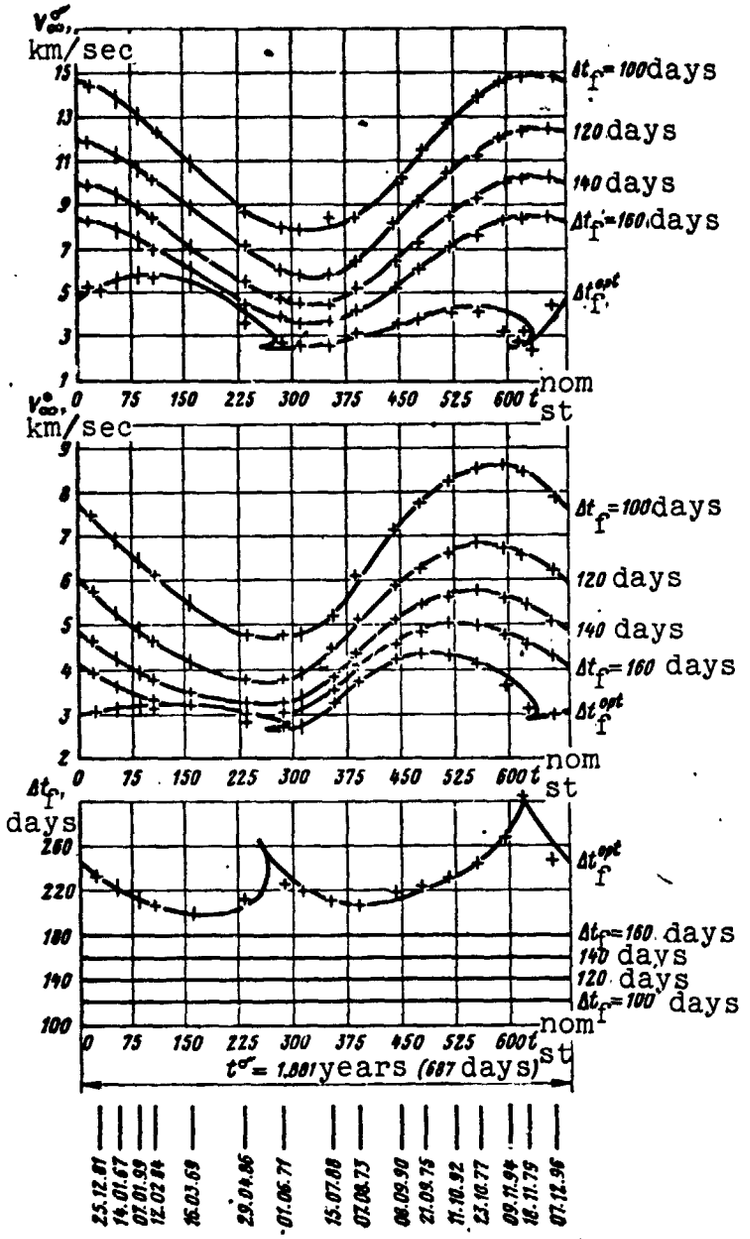

Figure 5.3.17. Characteristics of accelerated flight trajectories to Mars:

T_{go} = 15.8 years (5771 days); i = 1°51'03"; e = 0.0934; a = 1.5237 a u

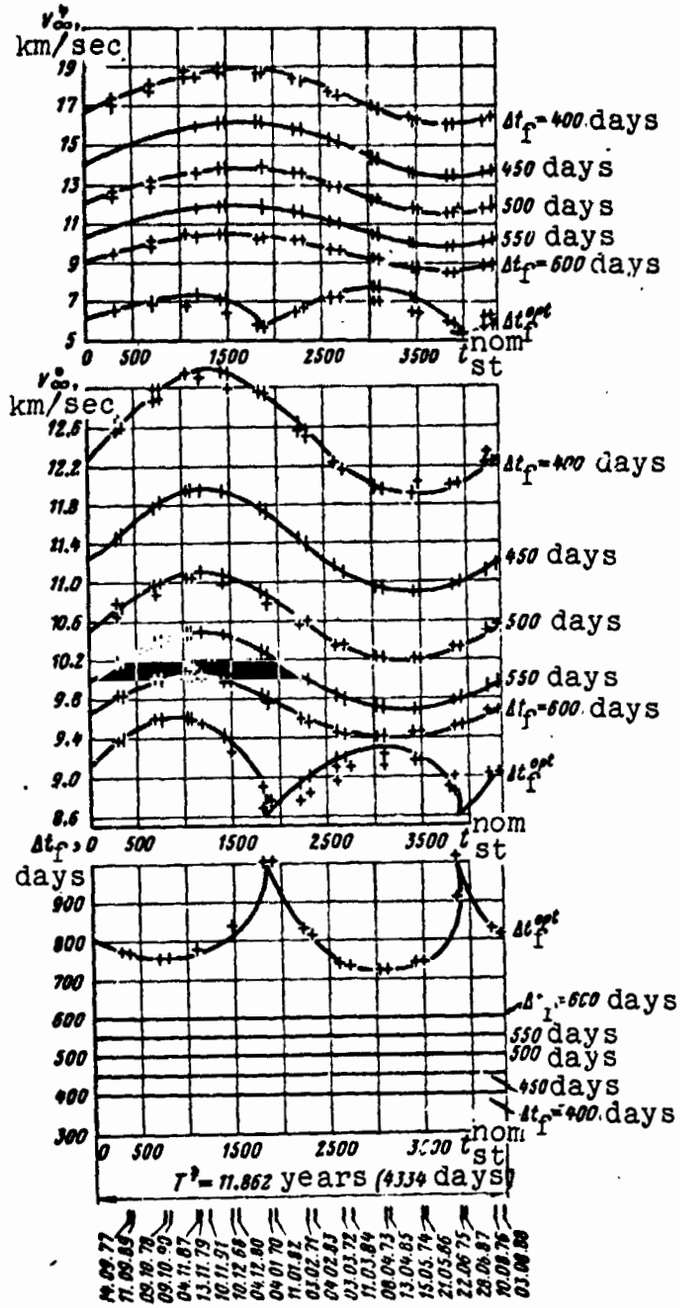

Figure 5.3.18. Characteristics of accelerated flight trajectories to Jupiter:

T_{go} = 11.8622 years (433[illegible] days); i = 1°18'22"; e = 0.0482;
a = 5.2025 a u

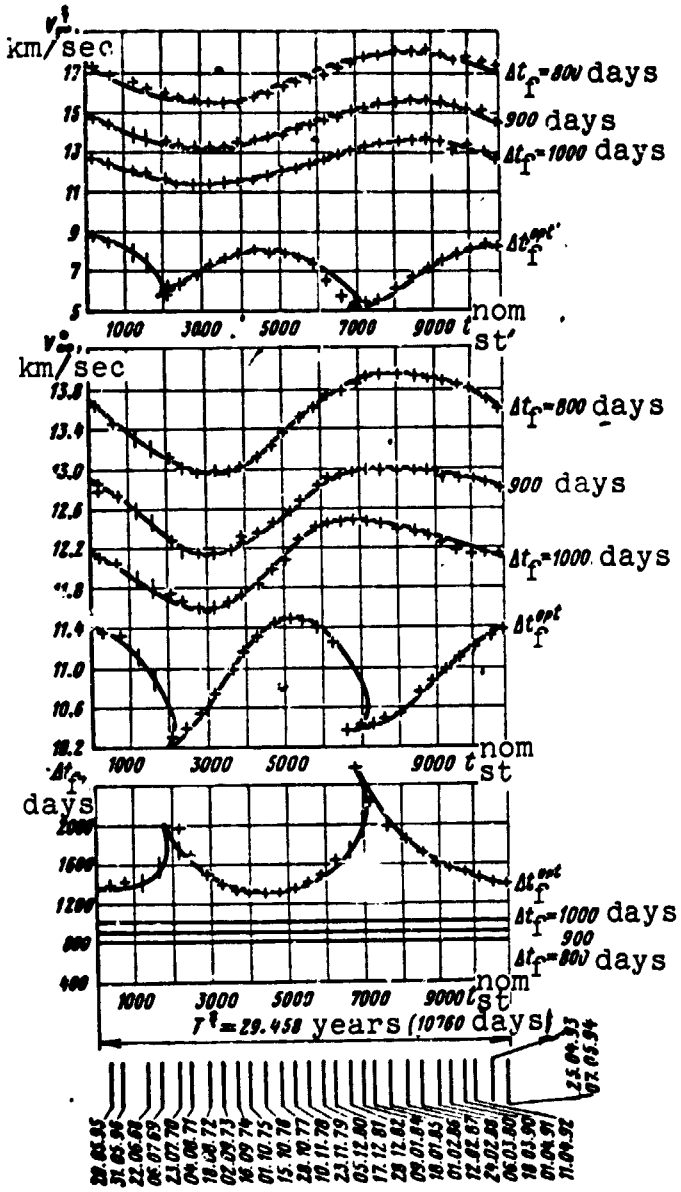

Figure 5.3.19. Characteristics of accelerated flight trajectories to Saturn:

T_{go} = 29.458 years (10,750 days); i = 2°29'19"; e = 0.0552; a = 9.545 a u

examine the possibility of shortening the flight time to this planet as well.

Figure 5.3.17 shows the characteristics of accelerated flight trajectories to Mars:

$V_{\infty}^{\oplus}$ is the departure velocity from the Earth's sphere of action required for flight to Mars; Δt_f is the flight time from the Earth to Mars; V_{∞}^{φ} is the entry velocity into the Mars sphere of action; as functions of the nominal launch date t_{st}^{nom}. In this figure, the bars denote the optimal launch dates for the flight cycles from 1967 to 2000.

The claculations showed that the launch dates for the "accelerated" flight trajectories differ very little from the launch dates for free flight trajectories ($\Delta t_{st}^{\oplus}$ = 10 — 15 days).

We see from these curves that, with reduction of the flight time, the energy expenditures for the flight to Mars ($V_{\infty}^{\oplus}$) and also the entry velocity (V_{∞}^{φ}) into the planet sphere of action increase. These flight trajectory characteristic curves can be expanded for the calendar launch dates (as was done above for the minimal energy trajectories.

The cyclicity of all the characteristics will correspond to the Mars great opposition period of $T_{go} \approx 15.8$ years. Flight cycles along the accelerated trajectories with energy expenditures close to the minimal values will occur in 1971, 1973, 1981, 1986, and 1988. The flight cycles with lowest energy expenditures also correspond approximately to the smallest values of entry velocity into the Mars sphere of action.

In Figure 5.3.17, the crosses indicate the values of the corresponding flight trajectory characteristics determined from optimization on the $V_{\infty}^{\oplus}$ isoline fields. /192

Figure 5.3.18 shows the characteristics of accelerated flight trajectories to Jupiter. The curves of the trajectory characteristics as functions of launch date also have a cyclic nature with period equal to $T_{go} \approx T4 \approx 11.9$ years. The flight cycles to Jupiter along accelerated trajectories with energy expenditures close to the optimal values occurred in 1970 and 1971 and will occur in 1982 and 1983.

Figure 5.3.19 shows the characteristics of accelerated flight trajectories to Saturn. The curves of the trajectory characteristics as functions of launch date also have a cyclic nature with period $T_{go} \approx T4 \approx 29.5$ years.

The trajectory characteristics obtained by optimization on the $V_{\infty}^{\oplus}$ isoline fields differ somewhat from those obtained by the reachable region method. However, this difference does not exceed the errors associated with the reachable region method approximations (circular Earth orbit, tangential launch), which introduce errors in determining $V_{\infty}^{\oplus}$ no greater than 200 to 300 m/sec.

CHAPTER 6. INTERPLANETARY FLIGHT TRAJECTORIES WITH INSERTION INTO PLANETARY ORBIT

§ 1. OPTIMIZATION OF INTERPLANETARY TRAJECTORIES WITH INSERTION INTO ORBIT AROUND TARGET PLANET

The optimization of artificial planet satellite (APS) SC trajectories is based on maximum payload weight. /193

For APS with aerodynamic braking, the useful payload

$$G_{APS} = G_{ul}^{I} - G_{ab},$$

where G_{ul}^{I} is the payload of the stage launched from AES orbit; G_{ab} is the weight of the aerodynamic braking equipment in APS orbit.

As is known, $G_{ul}^{I} = f(V_{st}^{\oplus})$ and its maximum corresponds to minimum AES launch characteristic velocity $V_{st}^{\oplus}$ or velocity $V_{\infty}^{\oplus}$ at departure from the Earth's sphere of action. The weight G_{ab} depends on the aerodynamic parameters of the SC braking system and the atmosphere entry conditions (entry velocity V_{en}^{pl} and entry angle). Of these parameters, only V_{en} influences the trajectory selection. Therefore, in the general case, the optimization criterion for such a mission is

$$J = f(V_{\infty}^{\oplus}; V_{\infty}^{pl}),$$

since

$$V_{en}^{pl} \approx V_{\pi h}^{pl} = \sqrt{(V_{par}^{pl})^2 + (V_{\infty}^{pl})^2} .$$

However, in most cases, $G_{ab} \ll G_{ul}^{I}$ and, in practice, trajectory optimization for such a flight mission reduces to finding the optimum for the one-impulse scheme. For the given value of $V_{st}^{\oplus}$, we select on the isoline fields the region with smallest value of V_{∞}^{pl}.

For the scheme with active braking, the trajectory is optimized wrt the maximum of $G_{ul} = G_{ul}^{I} G_{ul}^{II}$. For rocket stages of the same type, the maximum of G_{ul} corresponds to minimum total characteristic velocity $V_{x\Sigma}$. This is also approximately valid for stages with characteristics which do not differ markedly. /194

Usually $V_{x\Sigma}$ is divided between the first and second stages as required by the actual distribution of $V_{x.\Sigma}$ along the trajectory. However, cases may occur when optimal division of $V_{x\Sigma}$ into components which do not correspond to the actual impulse distribution is advisable. In this case, one of the stages operates with a discontinuity — two active segments separated by the trip time from the Earth to the planet.

For flights to certain planets, it is possible that the first stage (launch from AES) or the second stage (braking into APS) requires splitting into two stages. For example, two launch stages from the Earth using liquid rocket engines for propulsion provide high useful load for flight to Jupiter.

However, in most practical cases, the trajectory is optimized wrt minimum load characteristic velocity

$$V_{x\Sigma} = \Delta V^{\oplus}_{st} + \Delta V^{pl}_{b}.$$

where $\Delta V^{\oplus}_{st}$ is the characteristic velocity of launch from AES orbit; ΔV^{pl}_{b} is the characteristic velocity of braking into APS orbit.

Optimization can also be carried out in two variants:

— wrt maximum launch date window, i.e., when we seek $\min V_{xz}$ for given launch time $t^{\oplus}_{st}$ from AES orbit (vertical tangents on the V_{xz} isoline field in the coordinates $t^{\oplus}_{st}$; Δt_f;

— for accelerated trajectories, when we seek $\min V_{xz}$ for given flight time Δt_f (horizontal tangents on the V_{xz} field).

The characteristics of the two-impulse trajectories are examined for two APS orbit variants:

— extremely low circular APS orbit;

— energetically more favorable extremely elongated elliptic APS orbit with minimal pericenter height h_π.

For Mars satellites, we can take as such orbits, for example, orbits with the following parameters:

— circular orbit with h_{cir} = 1000 km;

— elliptic orbit with h_π = 1000 km and h_α = 20,000 km.

For Venus satellites:

— circular orbit with h_{cir} = 500 km;

— elliptic orbit with h_{π} = 500 km and h_{α} = 50,000 km.

This circular orbit altitude ensures long (on the order of a year) APS lifetime because of braking in the upper layers of the atmosphere while the parameters of the elliptic orbits with extremely low height h_{π} are close wrt energy characteristics to the minimal possible (insertion into parabolic orbit). /197

Table 6.1 shows the characteristics of the optimal first and second semiorbit flight trajectories to AMS orbit in the 1970s and 1980s.

Comparing the optimal launch dates of the two-impulse and single-impulse trajectories (see Table 5.7), we note that they differ by no more than 10 — 15 days. The minimal energy expenditures correspond to the flight cycles in 1971 and 1979.

Table 6.2 shows the characteristics of the optimal trajectories to Venus. The minimal energy expenditures occur in the flight cycles in 1975 and 1983.

§ 2. SELECTION OF PLANETARY SATELLITE ORBITAL PARAMETERS

Selection of artificial planet satellite (APS) orbit parameters is made to ensure minimal energy expenditures for injecting the SC into orbit and satisfy the requirements associated with the SC mission.

TABLE 6.1. CHARACTERISTICS OF TWO-IMPULSE FLIGHT TRAJECTORIES TO MARS (CIRCULAR AMS [ARTIFICIAL MARS SATELLITE] ORBIT)*

Year	Semi-orbit	$t^{\oplus}_{st}$	Δt_f	v_{∞}	v^{σ}_{b}
		Date	days	km/sec	
1971	1	23.05.71	205	5,61	2,19
	2	13.05.71	245	5,81	2,29
1973	1	08.08.73	211	5,85	2,07
	2	29.07.73	344	6,18	2,27
1975	1	28.09.75	242	6,14	2,06
	2	05.09.75	345	5,76	2,05
1977	1	01.11.77	270	6,00	2,05
	2	07.10.77	327	5,55	2,00
1979	1	15.11.79	260	5,96	2,45
	2	04.11.79	310	5,57	2,09
1982	1	07.01.82	228	6,52	2,79
	2	28.11.81	299	5,80	2,31
1984	1	28.02.84	208	6,42	2,75
	2	02.01.84	280	6,18	2,61
1986	1	28.04.86	201	5,97	2,36
	2	09.05.86	250	6,05	2,74
1988	1	12.07.88	202	5,99	2,08
	2	28.05.88	264	6,25	2,15
1990	1	11.09.90	230	6,07	2,06
	2	24.08.90	348	5,90	2,12
1992	1	20.10.92	259	6,12	2,04
	2	25.09.92	335	5,61	2,00

*[Translator's Note: Commas in numbers indicate decimal points.]

TABLE 6.2. CHARACTERISTICS OF TWO-IMPULSE FLIGHT TRAJECTORY TO VENUS (CIRCULAR AVS [ARTIFICIAL VENUS SATELLITE] ORBIT)*

Year	Semi-orbit	$t^{\oplus}_{st}$	Δt_f	v_{∞}	v^{φ}_b
		Date	Days	km/sec	
1970	1	04.09.70	110	7,69	3,97
	2	15.06.70	191	7,41	3,38
1972	1	17.04.72	110	7,77	3,75
	2	28.02.72	185	7,73	3,94
1973	1	25.11.73	113	7,30	3,37
	2	14.11.73	154	7,34	3,78
1975	1	09.06.75	142	6,88	3,31
	2	06.06.75	150	6,91	3,38
1977	1	11.01.77	127	7,40	3,84
	2	09.12.76	170	7,11	3,28
1978	1	01.09.78	111	7,68	3,98
	2	15.06.78	190	7,39	3,38
1980	1	14.04.80	110	7,78	3,77
	2	21.02.80	188	7,73	3,87
1981	1	23.11.81	112	7,34	3,38
	2	12.11.81	154	7,37	3,81
1983	1	09.06.83	143	6,92	3,35
	2	07.06.83	148	6,90	3,40
1985	1	10.01.85	128	7,38	3,82
	2	08.12.84	168	7,08	3,28
1986	1	29.08.86	111	7,67	3,98
	2	15.06.86	188	7,36	3,37
1988	1	12.04.88	110	7,80	3,79
	2	18.02.88	192	7,73	3,75
1989	1	21.11.89	111	7,37	3,40
	2	10.11.89	155	7,41	3,85
1991	1	10.06.91	139	6,94	3,33
	2	09.06.91	141	6,94	3,35

*[Translator's Note: Commas in numbers indicate decimal points.]

The problem can be examined in the following formulation. We consider that the entry velocity into the planet sphere of action $\bar{V}_\infty^{pl}$ is specified, i.e., the velocity modulus $|\bar{V}_\infty^{pl}|$ and its orientation angles in the equatorial planetocentric coordinate system: declination angle δ_{pl} and right ascension angle α_{pl} are given.

We first examine the APS orbit parameters in the approach hyperbola plane. Departure from the approach hyperbola plane is usually associated with large energy expenditures.

For approximate determination of the energy expenditures of launch from an elliptic orbit into a hyperbola and braking from the latter into an ellipse, we can consider that the transfers between these orbits take place impulsively. In this case, planar transfers with mating of the trajectories at their pericenters, examined in § 2 of Chapter 4, will be optimal. The characteristics of these transfers are shown in Figures 4.2.1 and 4.2.2. The angle α_h between the hyperbola asymptote and the ellipse line of apsides is

$$\cos \alpha_h = \frac{1}{e_h} . \qquad (6.2.1)$$

The position of the point of transition from the hyperbola to the ellipse relative to the vector $\bar{V}_\infty^{pl}$ is defined in terms of this angle.

We see from the discussion in § 2 of Chapter 4 that the energetically optimal APS orbit will have the minimal admissible pericenter radius r_π and the maximal admissible apocenter radius r_α. /198

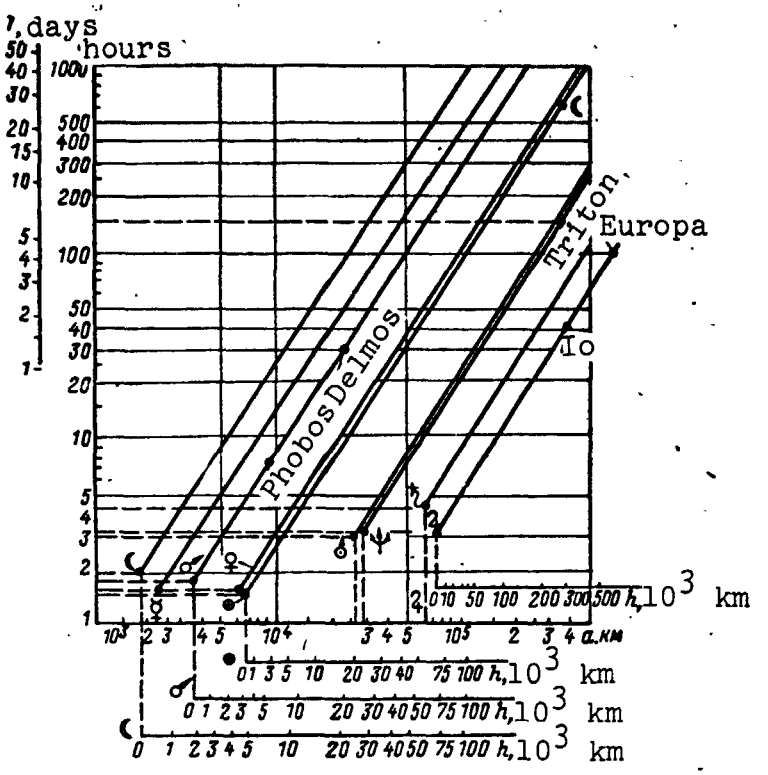

Figure 6.2.1. Planet satellite revolution period.

The period of revolution in such an orbit is

$$T = 2\pi \frac{a^{3/2}}{\sqrt{\mu_{pl}}},$$

where $a = \frac{r_a + r_\pi}{2}$ is the orbit semimajor axis.

Figure 6.2.1 shows the values of T for satellites of various planets.

Selection of the period T may influence the APS orbit radius r_α. With selection of T which is a multiple of the planet revolution period, the APS will travel along the same paths over the surface of the planet, which may not satisfy the planet mapping requirements. Selection of a period T which is a multiple of Earth days ensures communication seances with the SC at /199 the same time.

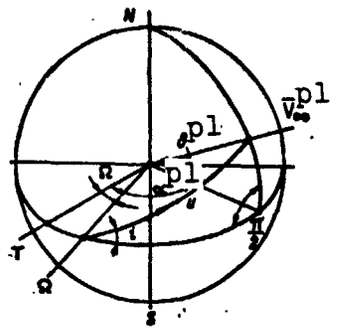

Figure 6.2.2. Determination of planet satellite orbit nodal longitude Ω.

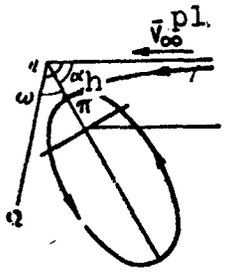

Figure 6.2.3. Determination of planet satellite argument of latitude ω

Let us examine the characteristics which determine the APS orbit plane position.

If the APS orbit inclination angle i to the equator (Figure 6.2.2) is given the longitude Ω of the line of nodes from the direction ♈ (the origin is the direction to the Earth's vernal equinox point) is found from the relation

$$\sin(\alpha_{pl} - \Omega) = \frac{\operatorname{tg}\delta_{pl}}{\operatorname{tg} i}. \qquad (6.2.2)$$

The angle between the vector $\bar{V}_\infty^{pl}$ and the line of nodes is found from the equality

$$\sin u = \frac{\sin\delta}{\sin i}, \qquad (6.2.3)$$

and the angular distance ω of the pericenter π from the line of nodes Ω (Figure 6.2.3) is

$$\omega = u - \alpha_h. \qquad (6.2.4)$$

It follows from Figure 6.2.2 and Formula (6.2.2) that the APS orbit inclination i cannot be less than the angle δ_{pl}, i.e.,

$$i \geqslant \delta_{pl} \qquad (6.2.5)$$

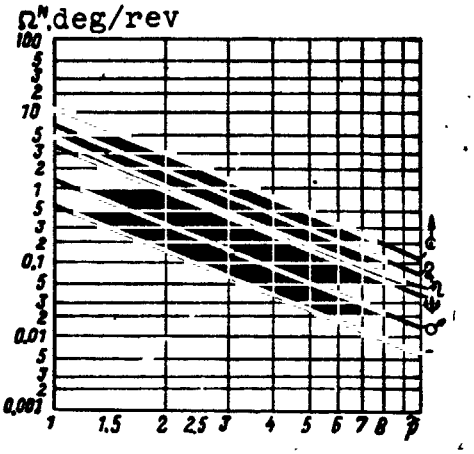

Figure 6.2.4. Characteristics of satellite orbit evolution resulting from planet gravity field noncentrality

for planar transfer from the approach hyperbola to elliptic APS orbit.

The APS orbit is subjected to various perturbations. Noncentrality of the planet's gravity field has the strongest influence on the orbit parameters. Account for the effect of planet flattening leads to changes of the satellite orbit nodal longitude Ω and orbit pericenter angular position ω. The following formulas were presented in § 3 of Chapter 1 for determining the variation of Ω and ω during a single satellite revolution /200

$$\left.\begin{aligned}\frac{d\Omega}{dN}&=-\frac{2\pi\varepsilon}{\mu_{pl}p^2}\cos i;\\ \frac{d\omega}{dN}&=\frac{\pi\varepsilon}{\mu_{pl}p^2}(5\cos^2 i-1).\end{aligned}\right\} \qquad (6.2.6)$$

Figure 6.2.4 presents curves for determining the characteristics of APS orbit parameter evolution resulting from planet flattening

$$\left.\begin{aligned}\frac{d\Omega}{dN}&=-\Omega^N\cos i;\\ \frac{d\omega}{dN}&=\frac{1}{2}\Omega^N(5\cos^2 i-1);\\ \tilde{p}&=\frac{p}{a_{eq}},\end{aligned}\right\} \qquad (6.2.7)$$

where a_{eq} is the planet equatorial radius.

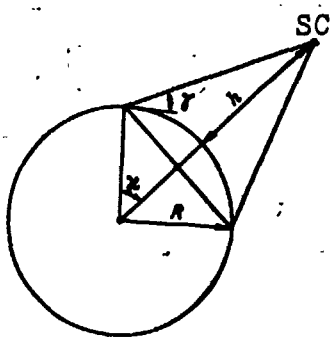

Figure 6.2.5. Determination of visibility zone boundaries

The magnitudes of the planet flattening α_{pl}^{ob} and angular velocity ω_{pl} and a_{eq} are given in the Appendix.

The variation of the quantities Ω and ω will be largest for orbits with inclination i close to zero. The APS orbit with $i \approx 63.4°$ has no perturbations of the orbit pericenter latitude argument. The polar orbit $i = 90°$ has no drift of the orbital line of nodes. The resistance of the upper layers of the planet's atmosphere may have a significant influence on the orbit parameters of an APS with relatively small pericenter radius. The technique for taking into account this influence on satellite motion is presented in [50]. However, adequately reliable data on the characteristics of the upper layers of the planetary atmosphere are not available at the present time. For a Mars satellite, we can consider tentatively that an acceptable lifetime (on the order of a year) can be obtained with $r_\pi \geq 1{,}000$ km, and for a Venus satellite with $r_\pi \geq 500$ km. /201

The ratio of planet satellite mass to planet mass is considerably smaller than the Moon-Earth mass ratio. Therefore, the influence of planet satellites on APS orbit parameters will be weaker than the influence of the Moon on AES orbits.

The influence of the Sun and other planets on APS parameters will be still smaller. The order of magnitude of this influence can be judged on the basis of the influence of the Sun and planets on AES parameters (see, for example, [50]).

The influence of the Sun and other planets on APS orbit parameters will be noticeable for long APS lifetime (on the order of several months or years). Methods for calculating the APS orbit evolution resulting from these factors were presented in [10, 50].

Let us examine the questions of calculating APS track and visibility zones from its orbit.

For problems of photographing the surface of the planet during flyby and mapping the surface from APS orbit, it is necessary to know the SC track over the surface of the planet and the visibility zone boundaries.

The angular range κ of the visibility zone boundary (Figure 6.2.5) is determined from the formula

$$\varkappa = \arccos\left(\frac{R_{pl}}{R_{pl}+h}\cos\gamma\right)-\gamma, \qquad (6.2.8)$$

where R_{pl} is the radius of the planet; h is the APS height above the planet surface; γ is the APS elevation angle above the horizon.

The APS track or projection of the satellite orbit on the surface of the planet is found from the relations

$$\left.\begin{aligned}\psi &= \arcsin(\sin u \sin i);\\ \lambda &= \Omega + \operatorname{arctg}(\operatorname{tg} u \cos i) - \omega_{pl}(t-\tau)+\Delta\Omega,\end{aligned}\right\} \qquad (6.2.9)$$

where ψ is the latitude of a point of the track; λ is the longitude of a point of the track; $u=\omega+v+\Delta\omega$ is the argument of the latitude of a point on the APS orbit; Ω is the longitude of the ascending node of the orbit; ω is the argument of the orbit pericenter latitude; i is the APS orbit inclination to the plane of the equator; τ is the pericenter passage time; v is the true /202

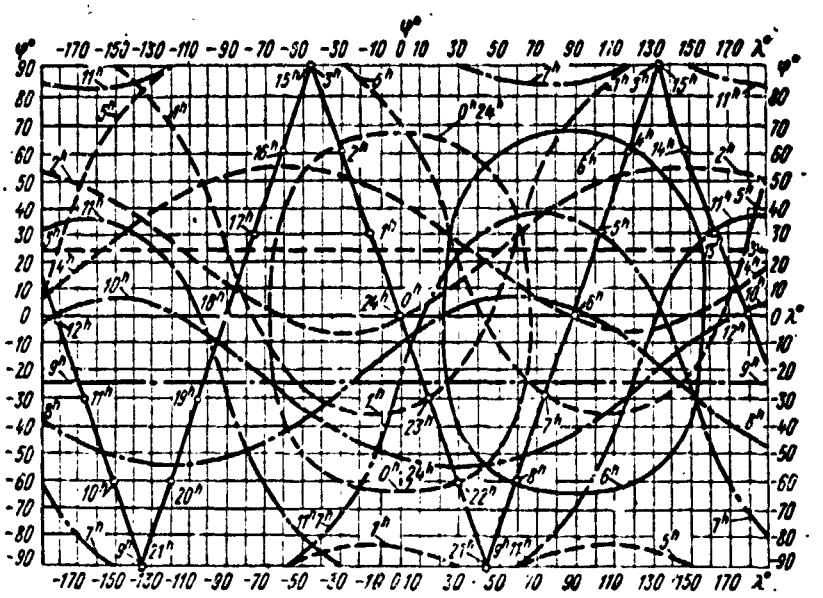

Figure 6.2.6. Track and visibility zones from circular polar satellite with revolution period T equal to the planet revolution period T_{pl}

anomaly; $\Delta\omega = \frac{d\omega}{dt}\frac{t-\tau}{T}$ is the change of ω from planet flattening; $\Delta\Omega = \frac{d\Omega}{dt}\frac{t-\tau}{T}$ is the change of Ω from planet flattening; T is the APS revolution period; t is time corresponding to the APS anomaly θ.

The visibility zone boundary is found from the relations

$$\left.\begin{aligned}\psi_\gamma &= \arcsin(\sin\psi\cos\varkappa + \cos\psi\sin\varkappa\cos\varphi);\\ \lambda_\gamma &= \lambda \pm \arccos\left(\frac{\cos\varkappa - \cos\psi\sin\varphi}{\cos\psi\cos\psi}\right),\end{aligned}\right\} \qquad (6.2.10)$$

where ψ_γ and λ_γ are the latitude and longitude of points on the visibility zone boundary; φ is the angle from a point of the track to a point on the visibility zone boundary (varies from 0 to 2π in determining the visibility zone boundary).

Figures 6.2.6 — 6.2.7 show the tracks and visibility zone boundaries of circular polar satellites with revolution period T equal to the planet revolution period T_{pl} and one half the

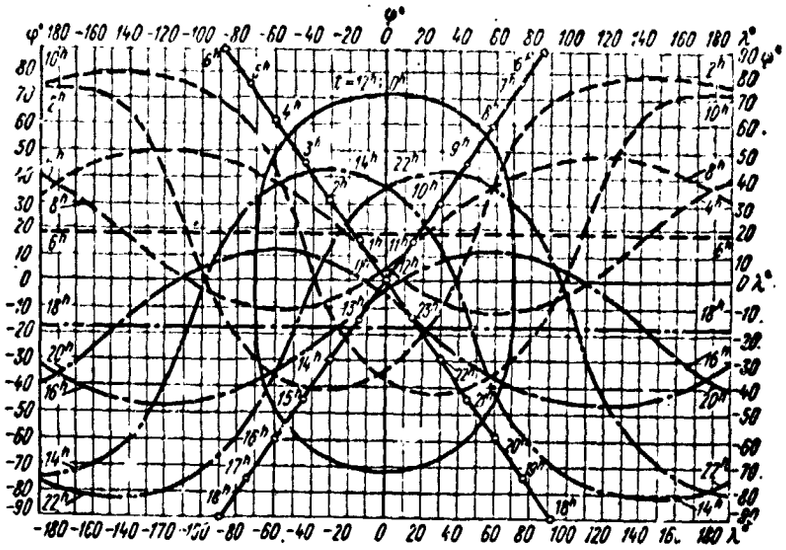

Figure 6.2.7. Track and visibility zones from circular polar satellite with period $T = (1/2)T_{pl}$

period T_{pl}. The tracks of these satellites are closed, i.e., they pass through the same surface points. The fields of view from such orbits are quite broad and make it possible to view the entire surface of the planet. /205

It is interesting to note that the circular Mars satellite orbit with $T \approx T_{pl}$ provides minimal energy expenditures for SC insertion into this orbit (in the class of circular orbits).

As was noted above, a SC with inclination $i = 63.4°$ does not have perturbations of the pericenter latitude argument ω resulting from planet flattening. The tracks and visibility zones of such APS in elliptic orbits with $h_{\pi} \approx 0.05\ R_{pl}$ and with revolution periods $T = (1/3)T_{pl}$; $(1/2)T_{pl}$, and T_{pl} are shown in Figures 6.2.8 — 6.2.10. Since the APS revolution period is a multiple of the planet revolution period T_{pl}, the

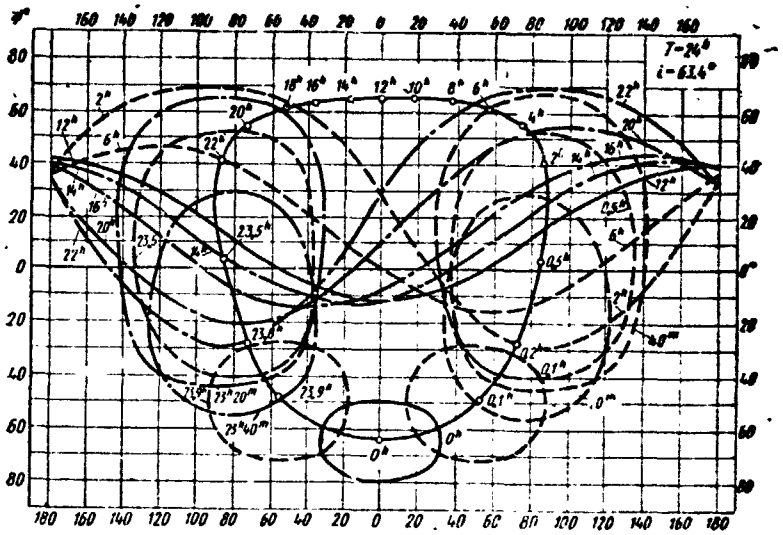

Figure 6.2.8. Track and visibility zones from elliptic satellite with $T = T_{pl}$, orbit inclination $i = 63.4°$

satellite tracks are closed. In the APS orbit apogee region, the visibility zones are very broad (for the APS with $T = T_{pl}$ the visibility zone encompasses nearly half the surface of the planet).

§ 3. CHARACTERISTICS OF OPTIMAL TRAJECTORIES FOR VARIOUS FLIGHT CYCLES

We can determine the dynamics of optimal two-impulse trajectory characteristic variation between flight cycles by accumulating the data of calculations of such trajectories for various flight cycles. However, just as in the case of the solution of this problem for the single-impulse trajectories, it is better to solve this problem by the reachable region method. The problem was solved under the same assumptions used in § 3 of Chapter 5.

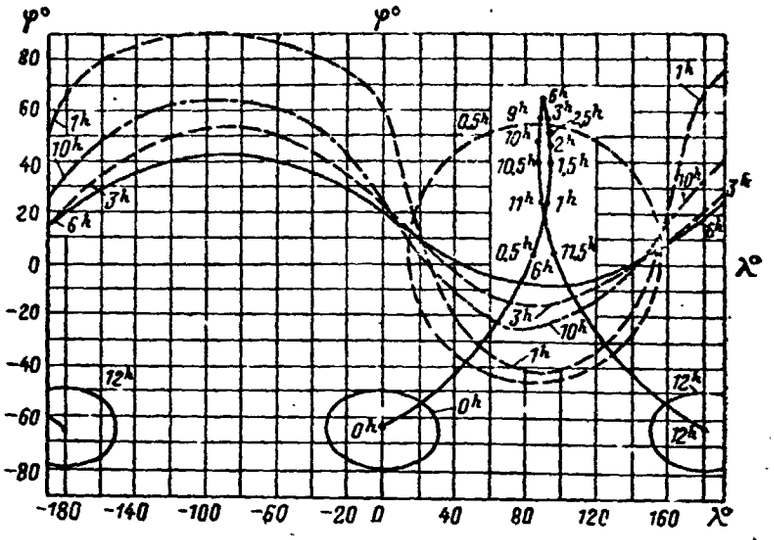

Figure 6.2.9. Track and visibility zones from elliptic satellite with $T = (1/2)T_{pl}$, $i = 63.4°$

TRAJECTORY OPTIMIZATION

The optimal trajectory must minimize the optimization criterion — the total characteristic velocity V_Σ, equal to

$$V_{x\Sigma} = \Delta V_{st}^{\oplus} + \Delta V_b^{pl},$$

where $\Delta V_{st} = \sqrt{(V_{par})^2 + (V_\infty^{\oplus})^2} - V_{c.r}^{\oplus}$ is the launch velocity from AES orbit; $V_{par}^{\oplus} = \sqrt{2\mu_\oplus / r_{cir}}$ is the hyperbolic velocity in launch orbit; $V_{cir}^{\oplus} = \sqrt{\mu_\oplus / r_{cir}}$ is the circular velocity in AES launch orbit; $V_\infty^{\oplus}$ is the velocity at departure from the Earth's sphere of action; $r_{cir} = R_\oplus + h_{cir}$ is the radius of the circular launch /206 orbit (h_{cir} = 200 km); $R_\oplus$ is the radius of the Earth; $\mu_\oplus$ is the gravitational constant of the Earth

$$\Delta V_b^{pl} = \sqrt{(V_{par}^{pl})^2 + (V_\infty^{pl})^2} - V_\pi^{pl};$$

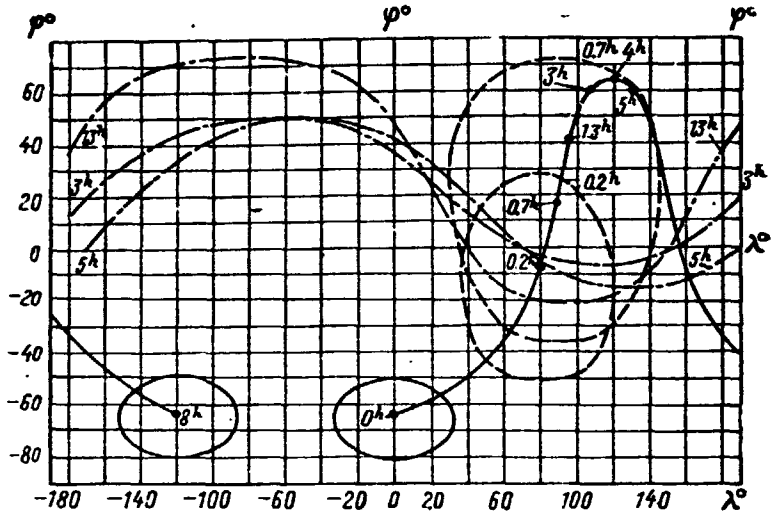

Figure 6.2.10. Track and visibility zones from elliptic satellite with $T = (1/3)T_{pl}$, $i = 63.4°$

$V_{par} = \sqrt{2\mu_{pl}/r_{\pi el}}$ is the parabolic velocity at the planet; $V_{\pi} = \sqrt{[2\mu_{pl}r_{\alpha}]/[r_{\pi}(r_{\pi} + r_{\alpha})]}$ is the velocity at the elliptic APS orbit pericenter; V_{∞}^{pl} is the entry velocity into the planet sphere of action;

$$r_{\pi} = R_{pl} + h_{\pi}; \; r_{\alpha} = R_{pl} + h_{\alpha};$$

R_{pl} is the radius of the planet; h_{π} and h_{α} are the APS orbit pericenter and apocenter heights, respectively.

The basic characteristic of the "reachable region" method is separation of the problem of determining the optimal trajectory characteristics from the problem of determining the launch date. Following the ideas of the "reachable region" method (see § 3, Chapter 5), we specify the position of the target planet at the moment of arrival (see Figure 5.3.2). In this case, we will know the planet radius R, its deviation z from the ecliptic

plane, and the planet velocity vector $\bar{V}_{pl}$. The problem of finding the optimal trajectory is a two-parameter problem. We take as the optimization parameters: λ — the projection of the transfer angle on the ecliptic plane, and ν_0 — the true anomaly of the transfer orbit at the launch point. The quantities z and R define the arriv-l point heliocentric latitude φ

$$\sin\varphi=\frac{z}{R};$$

and the sign of z determines the sign of φ. We determine the transfer angle from the right spherical triangle A_1BC (Figure 6.3.1a)

$$\cos L=\cos\lambda\cos\varphi.$$

Since the quantities λ and L are similar, the value of L can be determined from cos L.

The transfer trajectory inclination i is defined as

$$\operatorname{tg} i=\frac{\operatorname{tg}\varphi}{\sin\lambda};$$

and the sign of i corresponds to the sign of z for the fir·. /207
semiorbit trajectories $(0<L<\pi)$ and reverses for the second semiorbit trajectories $(\pi<L<2\pi)$.

The transfer trajectory parameter for given ν_0 will be

$$p=R_0(1+e\cos v_0).$$

The transfer trajectory eccentricity is found from the relations

$$R_0=\frac{p}{1+e\cos v_0};\quad R=\frac{p}{1+e\cos(L+v_0)},$$

and will be /208

$$e=\frac{R-R_0}{R_0\cos v_0-R\cos(L+v_0)}.$$

The trajectory parameters obtained above define the heliocentric velocities of launch from the Earth $\bar{V}_{st}$ and arrival at the planet $\bar{V}_1$:

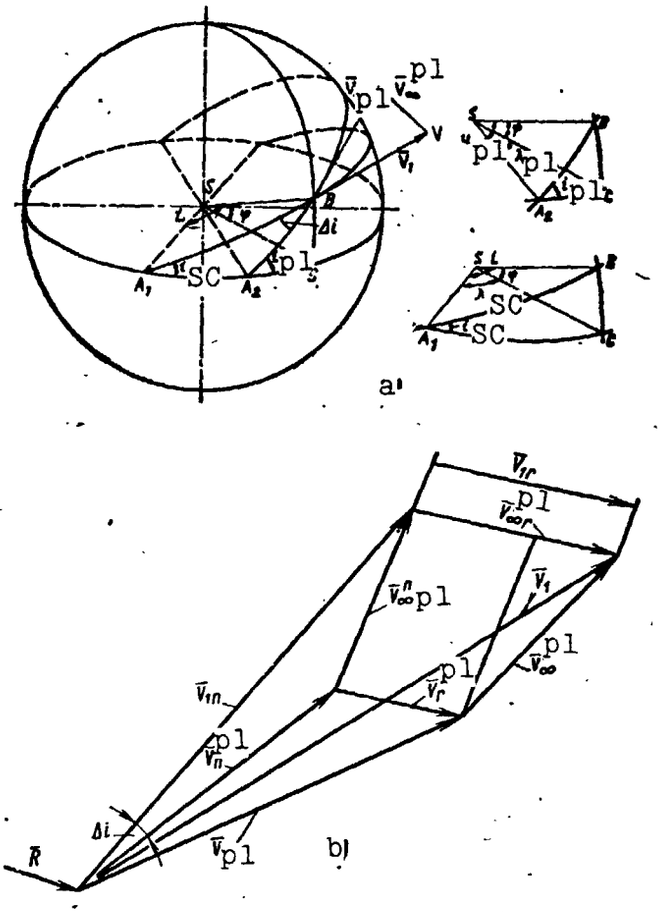

Figure 6.3.1. Determination of velocity of encounter with planet.

$V_n = \sqrt{\frac{\mu}{p}}(1 + e\cos v)$ is the transversal component;

$V_r = \sqrt{\frac{\mu}{p}} e \sin v$ is the radial component;

$V = \sqrt{V_n^2 + V_r^2}$ is the velocity vector modulus,

where $v=v_0$ at the launch time and $v=L+v_0$ at the arrival time.

The components of the departure velocity $V_\infty^\oplus$ from the Earth's sphere of action and its modulus are determined from the launch velocity triangle (see Figure 5.3.2)*

$$V_{\infty n}^\oplus = \sqrt{V_{st\ n}^2 + V_{cir}^2 - 2V_{st}V_{cir}\cos i};$$

$$V_{\infty r}^\oplus = V_{1r};\quad V_\infty^\oplus = \sqrt{(V_{\infty n}^\oplus)^2 + (V_{\infty r}^\oplus)^2}.$$

The velocity vector $\bar{V}_{pl}$ and its components $\bar{V}_n^{pl}$ and $\bar{V}_r^{pl}$ are determined by the planet position at the SC arrival time. The components of the entry velocity into the planet sphere of action and its modulus are (see Figure 6.3.1b)

$$V_{\infty n}^{pl} = \sqrt{V_{1n}^2 + (V_n^{pl})^2 - 2V_{1n}V_n^{pl}\cos\Delta i};$$

$$V_{\infty r}^{pl} = V_{1r} - V_r^{pl};\quad V_\infty^{pl} = \sqrt{(V_{\infty n}^{pl})^2 + (V_{\infty r}^{pl})^2}.$$

Here, only the angle Δi between the flight trajectory plane and the destination planet orbit plane is unknown. We find from the spherical triangle A_1BA_2 (see Figure 6.4.1a)

$$\operatorname{ctg}\Delta i = \frac{\sin L \operatorname{ctg}(\lambda - \lambda_{pl}) - \cos L\cos i}{\sin i},$$

where λ_{pl} is the longitude of the planet from the node of its orbit.

For actual flight trajectories, the angle Δi is small $\left(|\Delta i| < \frac{\pi}{2}\right)$, therefore $\cos\Delta i$ is always positive. Knowing the quantities $V_\infty^\oplus$ and V_∞^{pl}, we can find the AES orbit launch velocity $V_{st}^\oplus$ and the /209
APS orbit braking velocity V_b^{pl} and consequently, the total characteristic velocity V_{Σ}.

*The index $\oplus$ on the vector $\bar{V}_\infty^\oplus$ is omitted in Figure 5.3.2.

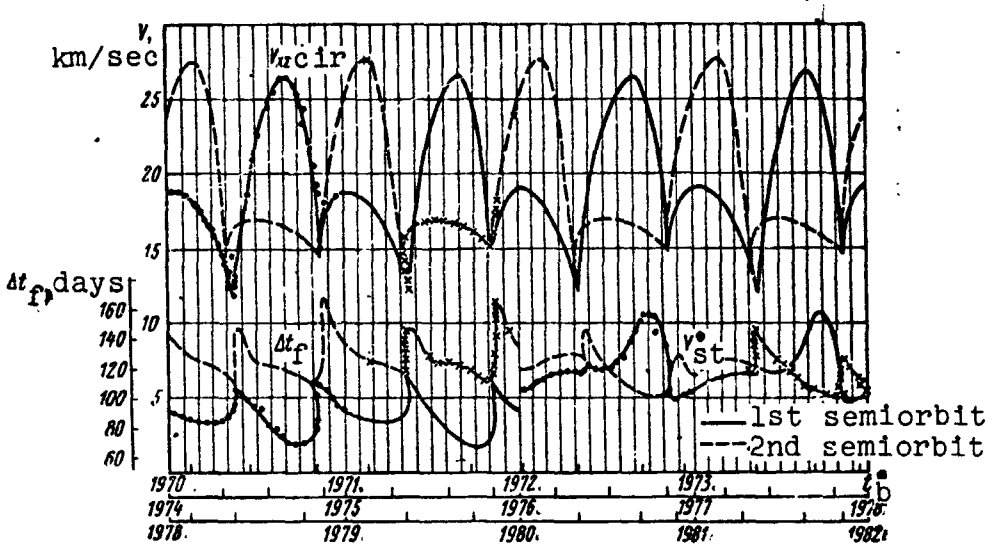

Figure 6.3.2. Characteristics of optimal flight trajectories to artificial satellite orbit of Mercury

The trajectory optimization minimizing V_{xx} wrt the parameters λ and ν_0 was accomplished using the Gauss-Seidel (coordinate descent) method. As the zero approximation, we used the optimal single-impulse trajectories (see § 3, Chapter 5). Division of the trajectories with respect to transfer angle L into first and second semiorbit trajectories ensures the identification of a region with a single extremum.

DYNAMICS OF OPTIMAL CHARACTERISTICS OF TWO-IMPULSE FLIGHT TRAJECTORIES TO MERCURY, VENUS, MARS, AND JUPITER

Figures 6.3.2 — 6.3.5 show the dynamics of the characteristics of two-impulse flight trajectories to the solar system planets. The relations shown in Figure 6.3.2 determine the dynamics of the basic characteristics of flight trajectories to Mercury (Δt_f is the flight time, $V^{\oplus}_{st}$ is the characteristic launch velocity from orbit, and $V_{x\Sigma}$ is the total characteristic velocity).

In calculating the two-impulse flight trajectories to Mercury with insertion into artificial planet satellite orbit, we selected a circular APS orbit with h_{cir} = 1000 km. For flight to artificial Mercury satellite orbit, the basic characteristics of the flight trajectory vary in the following limits: /210

— flight time Δt_{f1} = 70 — 110 days for first semiorbit trajectories and Δt_{f2} = 110 — 160 days for second semiorbit trajectories;

— launch characteristic velocity $\Delta V^{\oplus}_{st}$ = 4.9 — 10.5 km/sec;

— braking velocity in satellite orbit $\Delta V^{\mathbin{\overset{\circ}{\curlyvee}}}_{st}$ = 5.5 — 17.5 km/sec;

— total characteristic velocity $V_{x\Sigma}$ = 12.3 — 28 km/sec.

The characteristics Δt_f, $\Delta V^{\oplus}_{st}$, and $V_{x\Sigma}$ are shown as functions of launch date. Bars indicate the launch calendar dates for the various flight cycles (first semiorbit trajectories). The optimal flight cycles to Mercury satellite orbit repeat about every one-third year (the synodic period of Mercury $T^{\mathbin{\overset{\circ}{\curlyvee}}}_{s}$ = 0.317 year) for the trajectories of each semiorbit. As a rule, of the six possible flight cycles per year along the first and second semiorbit trajectories, there is one which falls in the minimal energy expenditure launch date region. The large variation range of the Mercury flight characteristics is explained by the large eccentricity and inclination of the planet's orbital plane. The periodicity of the characteristics corresponds approximately to Mercury's great opposition period

$$T^{\mathbin{\overset{\circ}{\curlyvee}}}_{go} \approx 1 \text{ year}.$$

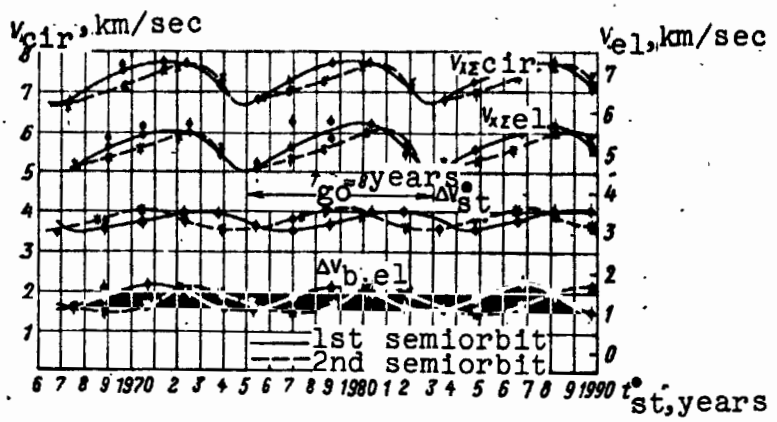
V_{cir}, km/sec
V_{el}, km/sec
$V_{\infty cir}$
$V_{\infty el}$
T_{go} = 8 years
ΔV_{st}
$\Delta V_{b.el}$
1st semiorbit
2nd semiorbit
6 7 8 9 1970 2 3 4 5 6 7 8 9 1980 1 2 3 4 5 6 7 8 9 1990
t°_{st}, years

Figure 6.3.3. Dynamics of characteristics of flight trajectories to Venus satellite orbit

For flight to Venus, we selected for the calculations a circular orbit with h_{cir} = 500 km and elongated elliptic APS orbit with the parameters: h_{π} = 500 km, h_{α} = 50,000 km.

Figure 6.3.3 shows the dynamics of the minimal V_{∞} values for flight cycles to APS orbit.

Just as for the single-impulse trajectories, the energy expenditure variation period of the two-impulse trajectories $T^{\circ}_{go} \approx 8$ years. The flight cycle in 1975 is optimal for SC insertion into artificial Venus satellite (AVS) orbit.

For the Mars satellite, we selected a circular orbit with parameter h_{cir} = 1000 km and elliptic orbit with parameters h_{π} = 1000 km, h_{α} = 20,000 km.

Figure 6.3.4 shows the dynamics of the minimal total characteristic velocity $V_{x\Sigma}$ for flight cycles to artificial Mars satellite (AMS) orbit. We see that, just as for the single-impulse trajectories, the period of the minimum-energy two-impulse

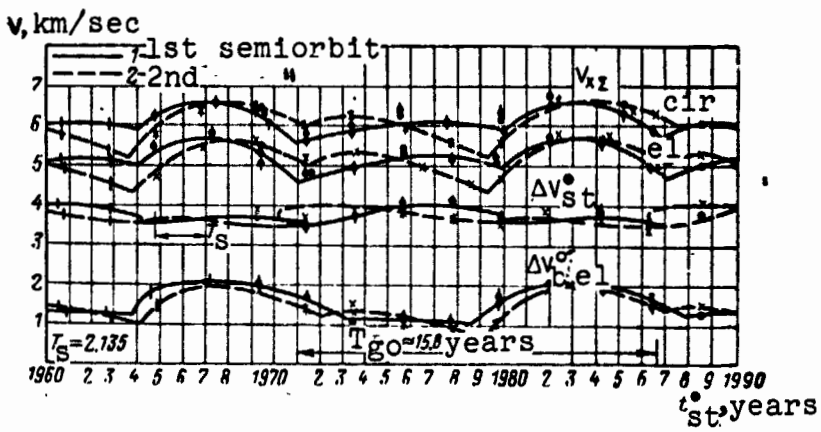

Figure 6.3.4. Dynamics of characteristics of flight trajectories to Mars satellite orbit

flight trajectories corresponds to the planet's great opposition period $T^{\sigma}_{go} \approx 15.8$ years. Thus, the best flight cycle from the energy expenditure viewpoint for flight to AMS orbit was that in 1971 along the first semiorbit and will be those in 1977 and 1979 along the second semiorbit. In general, the flight cycles of the 1970s are favorable for flights to AMS orbit. The energy expenditure maximum corresponded to the flight cycles in 1967 and 1969, and will occur again in 1982 and 1984. /211

Figure 6.3.5 shows the basic characteristics of the optimal flight trajectories to Jupiter (first semiorbit). For Jupiter, we selected satellite orbits with the parameters: circular with h_{cir} = 1000 km and elliptic with h_{π} = 1000 km, h_{α} = 1 million km. The flight time range Δt_f = 760 — 1025 days.

The launch impulse varies in the limits $\Delta V^{\oplus}_{st}$ = 6.3 — 6.8 km/sec, the braking impulse (for the elliptic orbit) is in the range $\Delta V^{\downarrow}_{b}$ = 2.3 — 2.5 km/sec. The total characteristic velocity $V_{x\Sigma}$ = 8.6 — 9.3 km/sec. /212

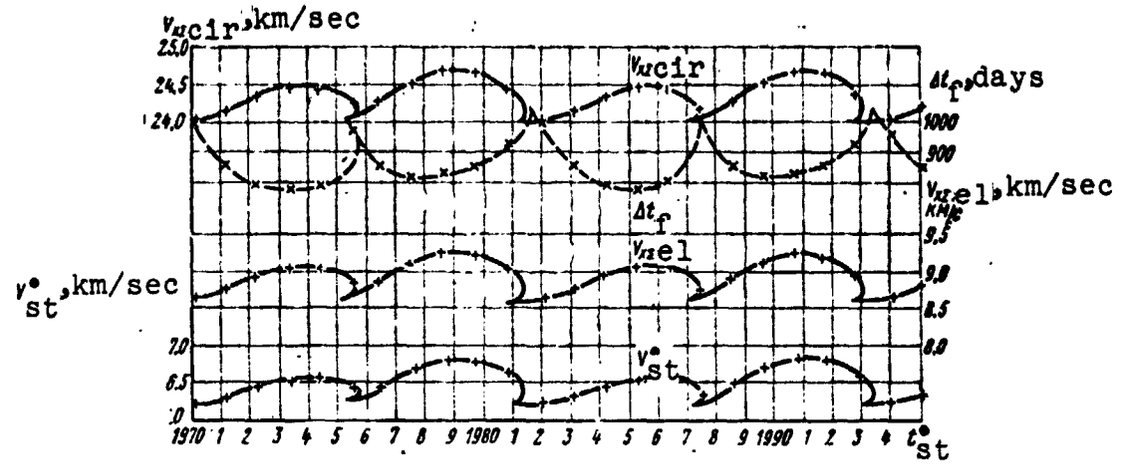

Figure 6.3.5. Characteristics of optimal flight trajectories to Jupiter satellite orbit (first semiorbit) trajectories

The flight cycles to Jupiter occur approximately every $T^{4}_{s} \approx 1.092$ years. The great opposition period of this planet is $T^{4}_{go} \approx 11.9$ years.

The optimal transfer trajectory characteristics change very little with change of the planet satellite orbit parameters. The braking impulse can be scaled for any satellite orbit with known value of the planet sphere of action entry velocity V^{pl}_{∞}.

CHAPTER 7. OPTIMIZATION OF INTERPLANETARY VEHICLE BALLISTIC DESIGN CHARACTERISTICS WITH ACCOUNT FOR ACTIVE FLIGHT SEGMENT LENGTH

§ 1. OPTIMIZATION OF INTERPLANETARY VEHICLE BASIC DESIGN PARAMETERS AND PLANETOCENTRIC FLIGHT SEGMENTS

The introduction of the patched conic ballistic flight /213
trajectory approximation makes it possible to create, examining vehicle motion in planetocentric coordinates, methods for selecting the basic design parameters and calculating the powered acceleration or deceleration segment of the required interplanetary vehicle hyperbolic departure or arrival orbit for known characteristics of the interorbital trajectory heliocentric segment. Here, the primary requirement is patching of the heliocentric segment with the hyperbolic departure and arrival orbits. The solution of the patching problem depends to a considerable degree on the method and accuracy of heliocentric segment determination. If it is calculated without account for the perturbing influence of the Earth and the destination planet and the extent of the planet gravispheres, when the point of SC departure from the Earth's gravisphere and the point of SC entry into the planet gravisphere are made to coincide, respectively, with the points at which the SC interorbital transfer orbit crosses the orbits of the Earth and destination planet, then solution of the segment patching problem is obtained with satisfaction of the equality

$$\bar{V}_{\infty 0}=\bar{V}_0-\bar{V}_\oplus,\quad \bar{V}_{\infty f}=\bar{V}_f-\bar{V}_{pl}. \qquad (7.1.1)$$

Here $\bar{V}_{\infty 0}$, $\bar{V}_{\infty f}$ are the hyperbolic excess velocities of the departure and arrival orbits, respectively, achieved by the SC during motion in the planetocentric coordinates. This solution technique is simplest and basically satisfies the SC design analysis accuracy requirements.

In the other technique for calculating the interplanetary trajectory heliocentric segment, when the extent of the planet gravispheres is taken into account, the magnitudes of the vectors $(\bar{V}_0-\bar{V}_\oplus)$ and $(\bar{V}_f - \bar{V}_{pl})$ will depend on the point of SC departure /214 from and entry into the planet gravispheres. In this case, a satisfactory solution of the inner and outer problems can be found only by joint examination of both problems.

We shall initially solve the problem of selecting the basic SC design parameters, optimizing these parameters, and calculating the powered flight segment and hyperbolic orbits in the planet gravisphere under the assumption that patching of the heliocentric segment with the hyperbolic departure and arrival orbits is obtained by satisfaction of the equalities (7.1.1). Satisfaction of (7.1.1) corresponds to the conditions

$$V_{\infty 0}=|\bar{V}_0-\bar{V}_\oplus|, \quad \bar{V}^0_{\infty 0}=(\bar{V}_0-\bar{V}_\oplus)/V_{\infty 0}, \tag{7.1.2}$$

$$V_{\infty f} = |\bar{V}_f - \bar{V}_{pl}|; \quad \bar{V}^0_{\infty f} = (\bar{V}_f - \bar{V}_{pl})/V_{\infty f}, \tag{7.1.3}$$

where $V_{\infty 0}$, $|\bar{V}_0 - \bar{V}_\infty|$, $V_{\infty f}$, $|\bar{V}_f - \bar{V}_{pl}|$ are scalar values of the vectors; $\bar{V}^0_{\infty 0}$, $\bar{V}^0_{\infty f}$ are unit vectors.

We assume that the scalar values of $V_{\infty 0}$, $V_{\infty f}$ and the unit vectors $\bar{V}^0_{\infty 0}$, $\bar{V}^0_{\infty f}$ are known from determination of the heliocentric segment. Therefore, we must select the basic SC design parameters μ_f and n_0 and determine the powered boost or braking

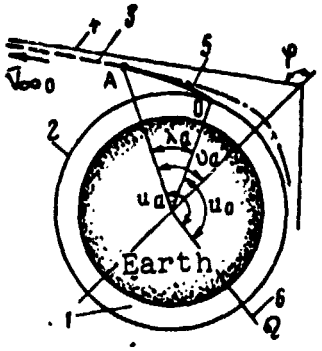

Figure 7.1.1. Boost segment: A- end of powered boost segment; O- beginning of powered boost segment; 1- parking orbit plane; 2- parking orbit; 3- departure hyperbola; 4- asymptote; 5- boost segment; 6- line of ascending node of departure orbit plane

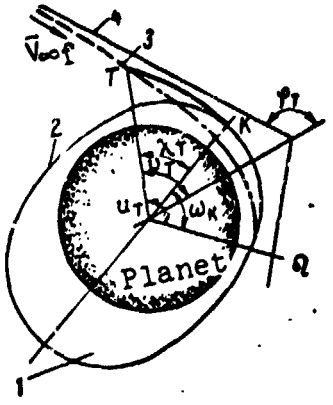

Figure 7.1.2. Braking segment: T- beginning of powered braking segment; K- end of powered braking segment; 1- final orbit plane; 2- final orbit; 3- arrival hyperbola; 4- asymptote

segment and the hyperbolic departure or arrival orbit so that the specified values of $V_{\infty 0}$ and $\bar{V}^0_{\infty 0}$ or $V_{\infty f}$ and $\bar{V}^0_{\infty f}$ will be satisfied. In solving the posed problem, we shall assume that the powered boost and braking segments and the hyperbolic departure and arrival orbits lie in the parking and final orbit planes, respectively (Figures 7.1.1 and 7.1.2), which must be defined. This satisfies the requirement for obtaining minimal energy expenditures, since there are no expenditures on a nonplanar maneuver. /215

Let satisfaction of the requirements (7.1.2) be imposed on the interplanetary vehicle boost module and the requirements (7.1.3) be imposed on the retro module. We turn to the problems of ballistic design of the boost and entry modules, i.e., selection of the ballistic design characteristics of the boost and retro modules.

INTERPLANETARY VEHICLE BOOST MODULE

The boost module design problem involves selecting those ballistic design characteristics for which the specified $V_{\infty 0}$ and $\bar{V}^0_{\infty 0}$ values will be obtained. It is important to find a solution in which the relative useful load μ_{ul} reaches the maximal value (max μ_{ul}). We shall term the ballistic design characteristics corresponding to max μ_{ul} the optimal boost module ballistic design characteristics. Search for the optimal ballistic design characteristics constitutes the principal problem of boost module ballistic design. The salient feature of this problem is that the $V_{\infty 0}$ and $\bar{V}^0_{\infty 0}$ values found from the outer problem solution are constant and independent of the ballistic design characteristics. This feature makes it possible to break the entire ballistic design problem down into two problems: ballistic design and ballistic navigation.

The subject matter of the ballistic design problem is selection of the basic module design parameters μ_f and n_0, and also determineation of the powered flight segment and the hyperbolic departure orbit Keplerian elements, which characterize its shape and dimensions for which the specified V_{∞} value is satisfied. Optimization of the ballistic design characteristics involves the solution of this problem only.

The solution of the ballistic navigation problem involves locating the parking orbit plane (in which, by assumption, the powered boost segment and hyperbolic departure orbit are located) in the geocentric coordinate system and the point of SC launch from the parking orbit which satisfy the condition for $\bar{V}^0_{\infty 0}$. This problem must obviously be solved with account for the requirements on parking orbit plane selection for booster rocket insertion of maximal useful load into orbit.

BALLISTIC DESIGN PROBLEM

/216

The primary difficulty in solving the ballistic design problem lies in correct representation and evaluation of the boost module powered flight segment. In the general case, relatively exact controlled flight characteristics can be obtained only by numerical integration of the system of differential equations of motion (see §§ 2 and 3 of Chapter 1). In this case, it is necessary to resort to the mathematical theory of optimal flight vehicle design (see, for example, [43]) in order to solve the main problem, which is selection of the optimal motion regime and optimal basic design parameters. Although the solutions obtained using this approach are exact, they are difficult and expensive to obtain. We must face each time the "curse" of iteration process convergence and evaluation of the boundary and other criterial condition satisfaction accuracy. Therefore, every designer cannot always permit himself the "luxury" of using such time-consuming optimization algorithms. (It is obvious that it may be difficult to avoid using such algorithms in many cases and at certain SC design analysis stages.)

In this connection, the usefulness of approximate methods for calculating SC ballistic design characteristics becomes understandable. The approximate method for calculating the powered segment and selecting the basic SC design parameters can be used to evaluate the powered segment kinematic parameters and select the basic boost module design parameters which satisfy the specified value of $V_{\infty 0}$ quickly and without resort to large digital computers. Such a method is that described in detail in § 3 of Chapter 2. Another advantage of this method is that it makes it possible to determine approximately the optimal values of the principal design parameters.

Bearing in mind that tangential control of the thrust vector, as was shown in § 3 of Chapter 2, is closest to optimal control, we utilize approximate integration of the system of differential equations of the controlled motion for such control. Then, in accord with (2.3.19), (2.3.23), and (2.3.28), (2.3.32), we have

$$\tilde{v}_a = v_{\text{id.a}} - \frac{1-1/\tilde{r}_a}{v_{ea}}; \tag{7.1.4}$$

$$\cos\theta_a = \frac{v_{ea}v_{ma}}{\tilde{r}_a[v_{ea}v_{ma}-(1-1/\tilde{r}_a)]}; \tag{7.1.5}$$

$$\tilde{r}_a = 1+\sin^2\frac{\sigma}{n_0}I_{ra}; \tag{7.1.6}$$

$$\chi_a = -\frac{d}{n_0}\int_1^{\mu_f}\frac{v_{\text{id}}}{\left(1+\sin^2\frac{\sigma}{n_0}I_r\right)}d\mu \tag{7.1.7a}$$

/217

or

$$\chi_a = \frac{d}{n_0}\left[(1+w)(1-\mu_f)+\mu_f w\ln\mu_f - 2\left(\frac{\sigma}{n_0}\right)^2 I_{\chi 2}+\right.$$
$$\left.+3\left(\frac{\sigma}{n_0}\right)^4 I_{\chi 4}-4\left(\frac{\sigma}{n_0}\right)^6 I_{\chi 6}+5\left(\frac{\sigma}{n_0}\right)^8 I_{\chi 8}\right], \tag{7.1.7b}$$

where

$$v_{\text{id.a}} = 1-w\ln\mu_f,\quad v_{ea}=1-0.5w\ln\mu_f,\quad v_{ma}=1-0.64w\ln\mu_f. \tag{7.1.8}$$

Since the departure orbit hyperbolic excess velocity

$$V_{\infty 0}=\frac{fm_\oplus}{a},$$

the energy integral constant at the end of the powered segment must be

$$h_{uf}=V_{\infty 0}^2 \qquad (7.1.9a)$$

or, in relative quantities

$$h=\tilde{v}_\infty^2, \qquad (7.1.9b)$$

where

$$h = \frac{h_{u\ f}}{V_{cir\ o}^2};\quad \tilde{v}_\infty=\frac{V_{\infty 0}}{V_{cir\ o}};$$

$V_{cir\ o}=\sqrt{\frac{fm_\oplus}{r_0}}$ is the circular velocity of the circular parking orbit with radius r_0.

In accord with the energy integral, the following equality must be satisfied at the end of the powered boost segment

$$\tilde{v}_a^2-\frac{2}{\tilde{r}_a}=\tilde{v}_\infty^2.$$

Substituting into this equation the values of $\tilde{v}_a$ and $\tilde{r}_a$ from (7.1.4) and (7.1.6), we find

$$\tilde{v}_\infty^2=\frac{\left[\left(1+\sin^2\frac{\sigma}{n_0}I_{ra}\right)-\frac{\sin^2\frac{\sigma}{n_0}I_{ra}}{v_{ea}v_{ic}}\right]^2}{\left(1+\sin^2\frac{\sigma}{n_0}I_{ra}\right)^2}v_{id_a}-\frac{2}{1+\sin^2\frac{\sigma}{n_0}I_{ra}}. \qquad (7.1.10)$$

Thus, the requirement on satisfaction of the specified hyperbolic excess velocity $V_{\infty 0}$ can be associated with satisfaction of (7.1.10). /218

For given circular parking orbit height and known powerplant propellant characteristics, the right side of (7.1.10) depends only on the basic design parameters μ_f and n_0. Therefore, selection of the basic design parameters is associated with solution of (7.1.10) for μ_f or n_0. Moreover, (7.1.10) makes it possible to determine the dependence of n_0 on μ_f or μ_f on n_0, satisfaction of which when selecting μ_f makes it possible to speak of satisfaction of the first equality (7.1.2). Solving (7.1.10) for n_0, we obtain

$$n_0 = \frac{w I_{ra}}{\tilde{r}_0^2 \sqrt{2} \arcsin q}, \tag{7.1.11}$$

where

$$q = \left[\frac{\sqrt{\frac{1}{v_{ea}^2}\left(\tilde{v}_\infty^2 - p_1^2\right) + (1-p_2)^2} - (1-p_2)}{\tilde{v}_\infty^2 - p_1^2} - 1 \right]^{1/2}; \tag{7.1.12}$$

$$p_1 = \frac{v_{ea} v_{id_a} - 1}{v_{ea}}, \quad p_2 = \frac{p_1}{v_{ea}}. \tag{7.1.13}$$

We write (7.1.11) in different form as

$$n_0 = \frac{N}{\tilde{r}_0^2}, \tag{7.1.14}$$

where

$$N = \frac{w I_{ra}}{\sqrt{2} \arcsin q}. \tag{7.1.15}$$

Equation (7.1.11) or (7.1.14) for a given $\tilde{v}_\infty$ and known values of $\tilde{r}_0$ and w permits calculating n_0 as a function of μ_f.

It is true that we must bear in mind that the choice of μ_f for given $\tilde{v}_\infty$ is constrained by upper μ_{fu} and lower μ_{fl} limits. The upper limit μ_{fu} corresponds to impulsive velocity change, which corresponds to the equality $\sin^3 \frac{\sigma}{n_0} I_r = 0$ as a consequence of $n_0 \to \infty$ and in accord with (7.1.10) leads to the condition

$$v_{id.a} = \sqrt{2+\tilde{v}_\infty^2}$$

and, consequently, in accord with (7.1.8), to the equality

$$\mu_{fu} = \exp\left[-\frac{\sqrt{2+\tilde{v}_\infty^2}-1}{w}\right]. \qquad (7.1.16)$$

The lower limit μ_{fl} is determined by values of $n_0 \approx 0.1$ or values of the radicands in (7.1.12) close to zero. /219

Calculation of n_0 using (7.1.14) can be simplified considerably if the function N is tabulated as a function of $\tilde{v}_\infty, w$ and μ_f in the limits $\mu_{fl} < \mu_f < \mu_{fu}$, varying as a function of $\tilde{v}_\infty$ and w.

OPTIMIZATION OF BOOST MODULE BASIC DESIGN PARAMETERS μ_f AND n_0

Arbitrary selection of μ_f in the previously indicated limits may lead to values of n_0 for which SC acceleration to the specified value $h_{u\,f} = V_{\infty 0}^2$ leads to significantly reduced values of the relative useful load μ_{ul}. Consequently, we need to select those values of μ_f and n_0 for which the specified value is achieved with maximal relative useful load μ_{ul}.

The relative useful load can be expressed in the form of the following relation or design equation (see, for example, [42, Appendix])

$$\mu_{ul} = f_{des}(\mu_f, n_0, \gamma_i), \qquad (7.1.17)$$

where γ_i are design weight coefficients, whose values are determined from statistical data.

The problem is formulated as follows: find the optimal μ_f and n_0 values for which the specified $\tilde{v}_\infty$ value is achieved with maximal μ_{ul}, expressed by the relation (7.1.17). Since we are required to satisfy the specified $\tilde{v}_\infty$, the n_0 values are connected with μ_f by (7.1.11) or (7.1.14). Then the necessary max μ_{ul} condition is the equation

$$\frac{\partial \mu_{fl}}{\partial \mu_f} = \left(\frac{\partial f_{des}}{\partial \mu_f}\right)_{n_0} + \left(\frac{\partial f_{des}}{\partial n_0}\right)_{\mu_f} \frac{\partial n_0}{\partial \mu_f} = 0.$$

If f_{des} depends linearly on μ_f and n_0, then $A_\mu = (\partial f_{des}/\partial \mu_f)$ and $A_n = -(\partial f_{des}/\partial n_0)$ are independent of them and the maximum condition is expressed in the form

$$\frac{A_\mu}{A_n} = \frac{\partial n_0}{\partial \mu_f}. \qquad (7.1.18)$$

Bearing (7.1.14) and (7.1.15) in mind, we represent the max μ_{ul} condition (7.1.18) as follows

$$\frac{A_\mu}{A_n} = \frac{1}{\tilde{r}_0^2} \frac{\partial N}{\partial \mu_f} \qquad (7.1.19a)$$

or

$$\frac{A_\mu}{A_n}-\frac{N}{\tilde{r}_0^2}\left(\frac{\frac{\partial I_{ra}}{\partial\mu_f}}{I_{ra}}-\frac{\frac{\partial q}{\partial\mu_f}}{\sqrt{1-q^2}\arcsin q}\right)=0. \qquad (7.1.19b)$$

Considering the expressions for q (7.1.12) and I_{ra} (2.3.29), /220 we write this last equation in the form

$$\frac{A_\mu}{A_n}-\frac{N}{\tilde{r}_0^2}\left[\frac{v_{id_a}}{I_{ra}}\left(1-\frac{1}{v_{ea}v_{ma}}\right)^{1/2}-\frac{\frac{\partial m}{\partial\mu_f}}{2\sqrt{(m-1)(2-m)}\arcsin\sqrt{m-1}}\right]=0, \qquad (7.1.19c)$$

where

$$m=\frac{p_3+p_2-1}{\tilde{v}_\infty^2-p_1^2},\quad p_3=\left[\frac{1}{v_{ea}^2}(\tilde{v}_\infty^2-p_1^2)+(p_2-1)^2\right]^{1/2}, \qquad (7.1.20a)$$

$$\frac{\partial m}{\partial\mu_f}=-\frac{w}{\mu_f(\tilde{v}_\infty^2-p_1^2)}\left\{\left(1+\frac{0,5}{v_{ea}^2}\right)\left(2mp_1-\frac{1/p_3-1}{v_{ea}}\right)+\right.$$
$$\left.+\frac{0,5}{v_{ea}^2}\left[(1/p_3-1)p_1-\frac{\tilde{v}_\infty^2}{v_{ea}p_3}\right]\right\}. \qquad (7.1.20b)$$

Equations (7.1.19) permit determining for given $\tilde{v}_\infty$ the optimal value μ_f^{opt}. We note that a finite value of the derivative $\partial n_0/\partial\mu_f$ exists for $1 < m < 2$ [see (7.1.19c)]. This makes it possible to determine to some degree the μ_f range in which μ_f^{opt} exists. Analysis showed that, for $m = 1$ $\mu_f = \mu_{fu}$, while for $m = 2$ μ_f, equal to its lower value μ_{fl}, satisfies the equation

$$\ln\mu_{fl}=-\frac{(v_\infty^2+1)^{1/2}+\sqrt{[(v_\infty^2+1)^{1/2}+1]^2+4}-3}{2w}.$$

Thus, the algorithm for solving the principal ballistic design problem amounts to the following: by solution for given $\bar{v}_\infty$ of the transcendental equation (7.1.19), we determine the optimal value μ_f^{opt}, then we use (7.1.14) with the calculated μ_f^{opt} to determine the optimal thrust-weight ratio n_0^{opt}. The problem solution is simplified considerably if the quantity $\partial N/\partial \mu_f$ is tabulated as a function of $\bar{v}_\infty$, ω, and μ_f.

The algorithm obtained for optimizing the basic design parameters is quite simple and permits calculating μ_f^{opt} and n_0^{opt} rapidly and efficiently. It is worthy of note that it avoids numerical integration of the system of differential equations of controlled SC motion and solution of the variational problem, which makes it possible to avoid the boundary value problem. Moreover, the simplicity of the algorithm fits in well with the required μ_f^{opt} and n_0^{opt} calculation accuracy. Thus, the errors in μ_f^{opt} and n_0^{opt} calculation for given $\bar{v}_\infty$ do not exceed 0.3 and 4%, respectively, and for the upper values of the μ_f^{opt} and n_0^{opt} errors, the errors in μ_{fl} calculation do not exceed 0.4%. /221

Note. When calculating μ_{ul}, the design equation (7.1.17) is usually expressed in the form [42]

$$\mu_{ul} = \frac{1 + a_{fc}}{1 - \mu_{str}} \mu_f - \frac{\gamma_{pp}}{1 - \mu_{str}} n_0 - \frac{a_{fc} + \mu_{str}}{1 - \mu_{str}}, \quad (7.1.21)$$

where a_{fc} is the fuel compartment relative weight; μ_{str} is the structural element relative weight; γ_{pp} is the powerplant relative weight.

In the assumed engine thrust variation range, the powerplant weight G_{pp} can be represented with good accuracy in the form of a

linear dependence on the thrust P

$$G_{pp} = \frac{\partial G_{pp}}{\partial P} P + \left(G_{pp}^{0} - \frac{\partial G_{pp}}{\partial P} P^{0} \right),$$

where G_{pp}^{0}, P^{0} are the values of G_{pp} and P at the beginning of the examined trust variation range.

Hence,

$$\frac{G_{pp}}{P} = \gamma_{pp} = \gamma_{p} + \frac{G_{pp}^{0} + \gamma_{p} P^{0}}{n_{0} G_{0}},$$

where

$$\gamma_{p} = \frac{\partial G_{pp}}{\partial P} .$$

Considering the relationships adopted, we obtain

$$\frac{A_{\mu}}{A_{n}} = \frac{1 + a_{fc}}{\gamma_{p}} .$$

Sometimes in the first approximation we take G_{pp}^{0} and P^{0} equal to zero, which leads to the equality $\gamma_{pp} = \gamma p = (\partial G_{pp})/\partial P$.

Figures 7.1.3 — 7.1.6 present curves of the derivative $\partial n_{0}/\partial \mu_{f}$, determined numerically as a result of integrating the differential equations of motion on a digital computer, as a function of n_{0} and μ_{f} for various values of V_{∞} . It is interesting that the curves of $\partial n_{0}/\partial \mu_{f}$ as a function of n_{0} for P_{sp} = 450 s form a quite narrow bundle, which broadens somewhat for P_{sp} = 1000 s. Therefore, the optimal values of n_{0} for the characteristic quantities γ_{pp} and a_{fc} are located for P_{sp} = 450 s in a small range, although the range of V_{∞} variation is quite large — from 2 to 16 km/sec. For example, for γ_{pp} =

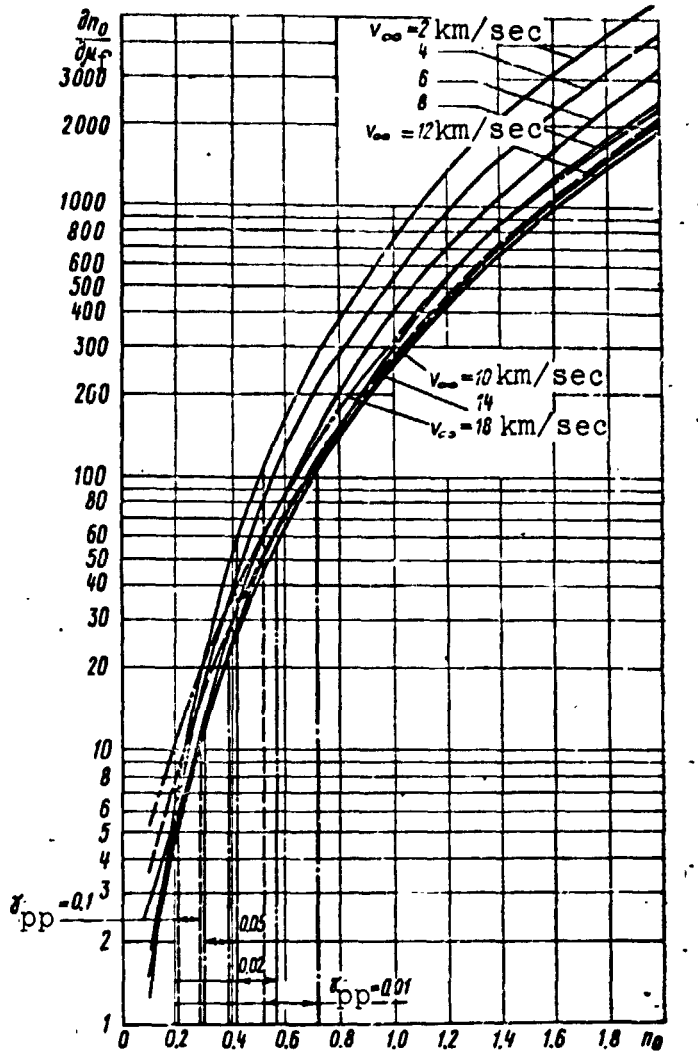

Figure 7.1.3. Derivative $\partial n_0/\partial \mu_f$ as function of thrust-weight ratio for various values of the hyperbolic excess velocity and P_{sp} = 450 sec.

0.05 — 0.02, the optimal values n_0^{opt} lie in the range n_0^{opt} = 0.3 — 0.5 with variation of V_{∞} = 2 — 16 km/sec. If, in the future, increase of P_{sp} to 800 — 1000 sec is not accompanied by /225 change of the possible range of $\gamma_p = \gamma_{pp}$ values, the upper limit of the optimal values n_0^{opt} will advance to n_0 = 1.0.

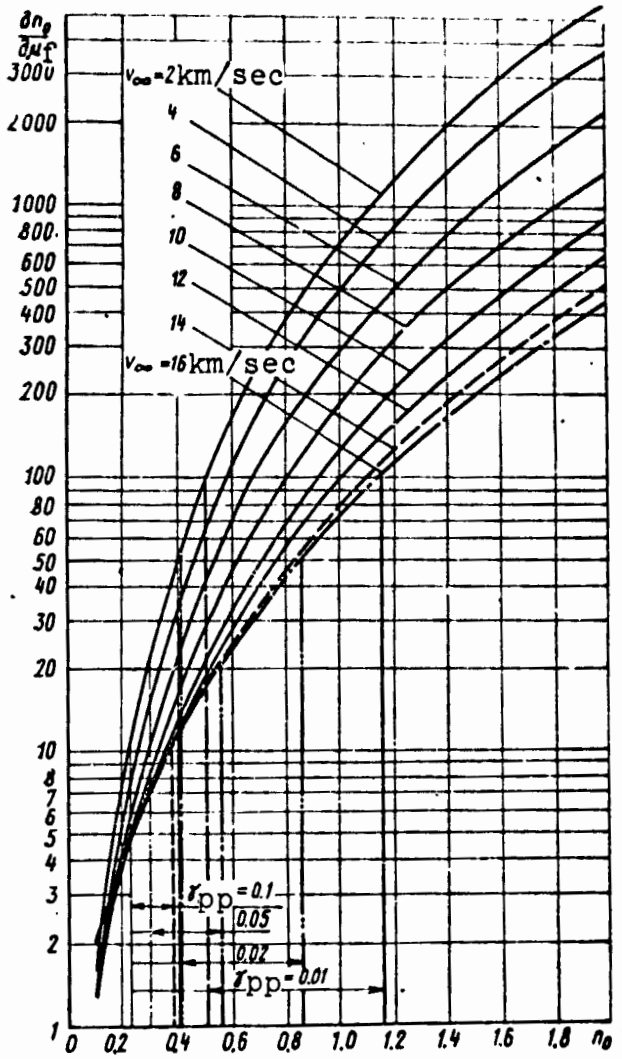

Figure 7.1.4. Derivative $\partial n_0/\partial \mu_f$ as a function of thrust-weight ratio for various values of the hyperbolic excess velocity and P_{sp} = 1000 sec.

After calculating μ_f and n_0 or μ_f^{opt} and n_0^{opt}, we use the relations (7.1.4 -- 7.1.7) to determine the kinematic parameters $\tilde{v}_a, \theta_a, \tilde{r}_a$ and χ_a of the end of the powered segment. As a result, we can find the hyperbolic departure orbit Keplerian elements a_{hd}, p_{hd}, and e_{hd} from the formulas:

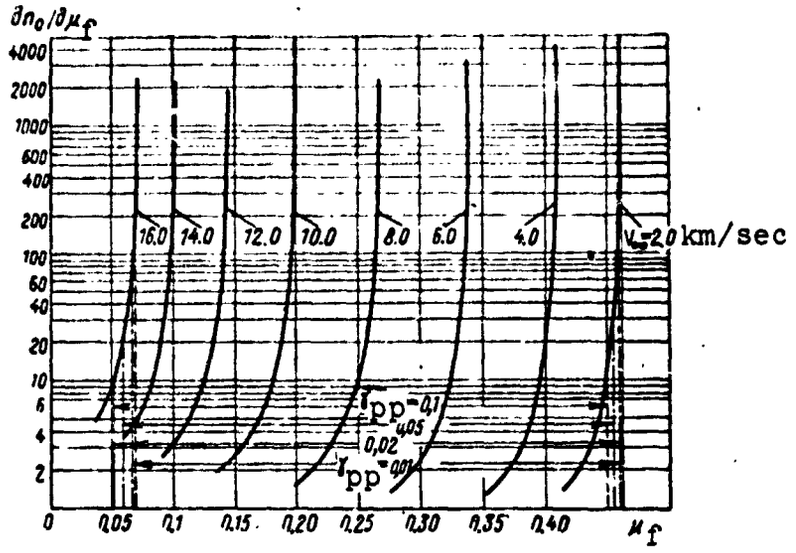

Figure 7.1.5. Derivative $\partial n_0/\partial \mu_f$ as a function oi relative final weight for various values of the hyperbolic excess velocity and P_{sp} = 450 sec.

$$\left.\begin{aligned} \tilde{a}_{hd} &= \frac{1}{\tilde{v}_\infty^2}, \qquad \tilde{p}_{hd} = (\tilde{v}_a \tilde{r}_a \cos\theta_a)^2, \\ e_{hd} &= [1+(\tilde{v}_\infty \tilde{v}_a \tilde{r}_a \cos\theta_a)^2]^{1/2}, \end{aligned}\right\} \tag{7.1.22}$$

where $a_{hd} = a_{hd}/r_0$, $\tilde{p}_{hd} = p_{hd}/r_0$. (7.1.23)

Then, the asymptote angle is found from the equation

$$\cos\varphi = -[1+(\tilde{v}_\infty \tilde{v}_a \tilde{r}_a \cos\theta_a)^2]^{-1/2}. \tag{7.1.24}$$

Thus, the ballistic design problem is completely solved.

BALLISTIC NAVIGATION PROBLEM

After solving the ballistic design problem, we determine the departure orbit plane, coinciding by assumption with the parking orbit plane, and the point of departure on the parking

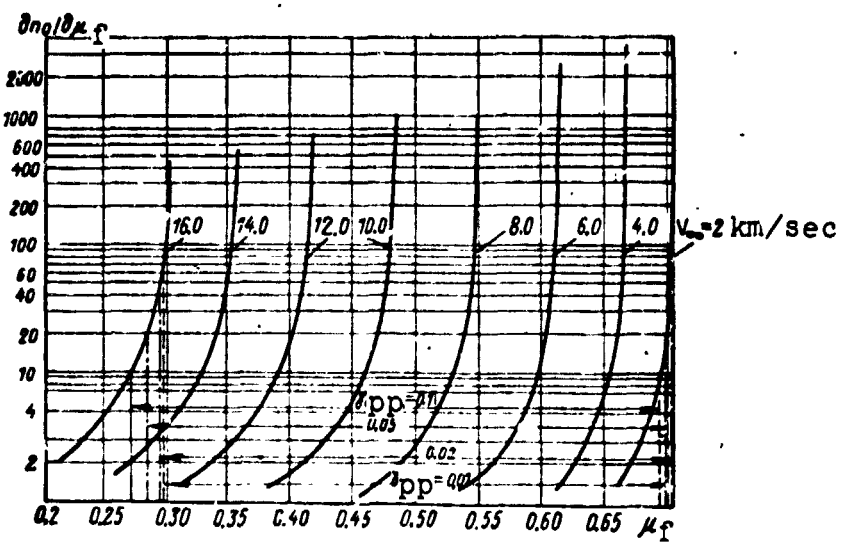

Figure 7.1.6. Derivative $\partial n_0/\partial \mu_f$ as a fu. ction of relative final weight for various values of the hyperbolic excess velocity and P_{sp} = 1000 sec.

orbit for which satisfaction of the following condition is possible

$$\bar{V}^0_{\infty 0} = (\bar{V}_0 - \bar{V}_\oplus)/V_{\infty 0}.$$

This is the subject of the ballistic navigation problem.

Hereafter, we shall call the unit vector $\bar{V}^0_{\infty 0}$ the target vector. It is the input value for the ballistic navigation problem. Using (1.3.52), we write the target vector realization condition

$$\bar{V}^0_{\infty 0} = \left[1 - \frac{r_a}{p_{hd}}[1 - \cos(\varphi - v_a)]\right]\frac{v_a}{V_{\infty 0}}\bar{V}^0_a - \left[\sqrt{\frac{fm_\oplus}{p_{hd}}}\sin(\varphi - v_a) - \right. \quad (7.1.25)$$

$$\left. - \frac{r_a v_a \sin\theta_a}{p_{hd}}[1 - \cos(\varphi - v_a)]\right]\frac{\bar{r}^0_a}{V_{\infty 0}}.$$

Converting to relative quantities, we represent the target vector realization condition (7.1.25) in the form /226

$$\overline{V}^0_{\infty 0}=\left[1-\frac{\tilde{r}_a}{\tilde{p}_{hd}}\cdot(1-\cos\beta)\right]\frac{\tilde{v}_a}{\tilde{v}_\infty}\overline{V}^0_a- \\ -[\sin\beta-\operatorname{tg}\theta_a(1-\cos\beta)]\frac{\overline{r}^0_a}{\tilde{v}_\infty\sqrt{\tilde{p}_{hd}}}, \tag{7.1.26}$$

where

$$\beta=\varphi-v_a,\quad \cos v_a=\left(\frac{\tilde{p}_{hd}}{\tilde{r}_a}-1\right)\frac{1}{e_{hd}}. \tag{7.1.27}$$

Consequently, the ballistic navigation problem solution amounts to selection of the unit vectors $\overline{V}^0_a$ and $\overline{r}^0_a$, satisfying the vector equation (7.1.26).

The direction of the boost module powered segment termination point radius vector in the equatorial geocentric coordinate system will be determined by the departure orbit Keplerian angular elements: Ω ascending node longitude; i orbit plane inclination; ω pericenter angular distance, and u_a argument of the latitude (see § 3, Chapter 1). Consequently, we have

$$\overline{r}^0_a=(\cos u_a\cos\Omega-\sin u_a\sin\Omega\cos i)\overline{i}_x+(\cos u_a\sin\Omega+ \\ +\sin u_a\cos\Omega\cos i)\overline{i}_y+(\sin u_a\sin i)\overline{i}_z, \tag{7.1.28}$$

where $\overline{i}_x$, $\overline{i}_y$, $\overline{i}_z$ are the geocentric equatorial system unit vectors. After differentiating (7.1.28) with respect to time and some transformations, we find

$$\overline{V}^0_a=-[\sin(u_a-\theta_a)\cos\Omega+\cos(u_a-\theta_a)\sin\Omega\cos i]\overline{i}_x- \\ -[\sin(u_a-\theta_a)\sin\Omega-\cos(u_a-\theta_a)\cos\Omega\cos i]\overline{i}_y+ \\ +[\cos(u_a-\theta_a)\sin i]\overline{i}_z. \tag{7.1.29}$$

We represent the hyperbolic excess velocity unit vector in the form

$$\overline{V}^0_{\infty 0}=(\cos\alpha_0\cos\delta_0)\bar{i}_x+(\sin\alpha_0\cos\delta_0)\bar{i}_y+\sin\delta_0\bar{i}_z, \qquad (7.1.30)$$

where α_0 is the right ascension of the target vector; δ_0 is the declination of the target vector (see § 1, Chapter 4).

Considering (7.1.28) — (7.1.30), we express the vector equation (7.1.26) in the form of the following three scalar equations /227

$$\cos\alpha_0\cos\delta_0=-A_v\{[\sin(u_a-\theta_a)+B_r\cos u_a]\cos\Omega+ \\ +[\cos(u_a-\theta_a)-B_r\sin u_a]\sin\Omega\cos i\}; \qquad (7.1.31)$$

$$\sin\alpha_0\cos\delta_0=-A_v\{[\sin(u_a-\theta_a)+B_r\cos u_a]\sin\Omega- \\ -[\cos(u_a-\theta_a)-B_r\sin u_a]\cos\Omega\cos i\}, \qquad (7.1.32)$$

$$\sin\delta_0=A_v[\cos(u_a-\theta_a)-B_r\sin u_a]\sin i \qquad (7.1.33a)$$

or

$$\sin i=\frac{\sin\delta_0}{A_v[\cos(u_a-\theta_a)-B_r\sin u_a]}, \qquad (7.1.33b)$$

where

$$\left.\begin{aligned} A_v&=\left[1-\frac{\tilde{r}_a}{\tilde{p}_{r.o}}(1-\cos\beta)\right]\frac{\tilde{v}_a}{\tilde{v}_\infty},\\ A_r&=[\sin\beta-\operatorname{tg}\theta_a(1-\cos\beta)]\frac{1}{\tilde{v}_\infty\sqrt{\tilde{p}_{hd}}},\\ B_r&=A_r/A_v. \end{aligned}\right\} \qquad (7.1.33c)$$

Equations (7.1.31) — (7.1.33) are the target vector realization condition in scalar form. The solution of the ballistic navigation problem is now concretized: it amounts to satisfaction of the scalar target vector realization condition.

Multiplying (7.1.31) and (7.1.32) by cos Ω and by sin Ω, respectively, and combining, after transformations, we obtain

$$\cos(\Omega-\alpha_0)=-\frac{A_v}{\cos\delta_0}[\sin(u_a-\theta_a)+B_r\cos u_a]. \qquad (7.1.34)$$

After multiplying (7.1.31) and (7.1.32) by -sin Ω and by cos Ω, respectively, and combining, as a result of transformations, we find

$$\sin(\Omega-\alpha_0)=-\frac{A_v\cos i}{\cos\delta_0}\cdot[\cos(u_a-\theta_a)-B_r\sin u_a] \qquad (7.1.35a)$$

or with account for (7.1.33),

$$\sin(\Omega-\alpha_0)=-\operatorname{tg}\delta_0\operatorname{ctg} i. \qquad (7.1.35b)$$

Solving (7.1.33) for sin u_a and cos u_a, we obtain the formulas /228

$$\left.\begin{aligned}\sin u_a&=\frac{b\cdot c\pm\sqrt{1+b^2-c^2}}{1+b^2},\\ \cos u_a&=\frac{c\mp b\sqrt{1+b^2-c^2}}{1+b^2},\end{aligned}\right\} \qquad (7.1.36a)$$

where

$$b=\frac{\sin\theta_a-B_r}{\cos\theta_a},\quad c=\frac{\sin\delta_0}{A_v\sin i\cos\theta_a}. \qquad (7.1.36b)$$

In accordance with the definition of u_a (see Figure 7.1.1), the angular distance of the module parking orbit departure point from the ascending node line

$$u_0=u_a-\chi_a. \qquad (7.1.37)$$

Thus, for known powered boost segment end kinematic parameters, the relations (7.1.35) — (7.1.37) make it possible to determine as a function of the parking orbit (or departure orbit) plane inclination angle i and the specified $\bar{v}_\infty$, α_0, δ_0 the ascending node longitude Ω and module departure point from the parking orbit. It would appear that the ballistic navigation problem has been solved. However, the question of parking orbit plane inclination angle i selection remains open.

Generally speaking, the parking plane inclination angle i choice is constrained by various requirements on the rocket boosted SC insertion segment. In order to reduce the energy losses on a nonplanar maneuver, the booster rocket powered SC insertion segment is usually performed so that this segment lies in the parking orbit plane. In this case, the choice of the angle i may be constrained by admissible safe azimuth values and by kinematic constraints arising from the requirement that the booster rocket powered SC insertion segment, the powered boost module segment, and the departure orbit be located in the departure orbit plane. The kinematic constraints are expressed by the following inequalities (see § 1, Chapter 4)

$$\left.\begin{aligned} \cos i &\leqslant \pm \cos \delta_0; \\ \cos i &\leqslant \pm \cos \varphi_{st}, \end{aligned}\right\} \qquad (7.1.38)$$

where φ_{st} is the launch point (cosmodrome) geographic latitude.

For full utilization of the Earth's rotational velocity when inserting the SC into the parking orbit by the booster rocket, the angle i should be as small as possible. Depending on the values of φ_{st} and δ_0, the angle i takes a different minimal value. If the target declination δ_0 is greater than the launch point geographic latitude φ_{st}, i.e., $\delta_0 \geq \varphi_{st}$, then with account for the conditions (7.1.38), we obtain

$$\cos i_{min} = \pm \cos \delta_0. \qquad (7.1.39a)$$

However, if the target declination δ_0 is less than the launch point geographic latitude φ_{st}, i.e., $\delta_0 < \varphi_{st}$, then with account for the conditions (7.1.38), we have /229

$$\cos i_{min} = \pm \cos \varphi_{st}. \qquad (7.1.39b)$$

The azimuth A, the angle between the launch point meridional plane and the parking orbit plane at the booster rocket launch time, measured in the easterly direction, can be found from the relation (see § 1, Chapter 4)

$$\sin A = \frac{\pm \cos i}{\cos \varphi_{st}}.$$

Therefore, if there is a constraint on choice of the azimuth A, expressed by the limiting azimuth A_{lim}, in the presence of the inequality

$$\sin A_{lim} < \frac{\pm \cos i_{min}}{\cos \varphi_{st}},$$

the angle i is determined from the equation

$$\cos i_{lim} = \pm \cos \varphi_{st} \sin A_{lim}. \qquad (7.1.40)$$

Thus, the formulas (7.1.39) and (7.1.39a) make it possible to select uniquely the parking plane inclination angle i and, using the relations (7.1.35) — (7.1.37), complete the solution of the ballistic navigation problem.

Of interest is the case $\delta_0 \geq \varphi_{st}$, when in accord with (7.1.40), we can take $\cos i_{min} = \pm \cos \delta_0$, i.e.,

$$i_{min} = |\delta_0| \text{ or } i_{min} = \pi - |\delta_0|.$$

By virtue of the relations (7.1.33) — (7.1.35), these equalities lead to the following equations

$$\begin{aligned}&\sin(\Omega-\alpha_0)=-\operatorname{sign}(\operatorname{tg}\delta_0\operatorname{ctg}i),\\&\sin(u_a-\theta_a)+B_r\cos u_a=0,\\&A_v[\cos(u_a-\theta_a)-B_r\sin u_a]=\operatorname{sign}(\sin\delta_0).\end{aligned}\qquad(7.1.41)$$

Solving the last two equations jointly, we obtain*

$$\cos u_a=\operatorname{sign}(\sin\delta_0)\sin\beta.\qquad(7.1.42)$$

Consequently, in the case $\delta_0 \geq \varphi_{st}$, the location of the parking plane orbit and boost module departure point are found from the equalities (7.1.39), (7.1.41), and (7.1.42) very simply.

INTERPLANETARY VEHICLE RETRO MODULE /230

The retro module must provide for interplanetary vehicle insertion into the final orbit around the destination planet, when the hyperbolic arrival orbit is predetermined by the conditions (7.1.3). Therefore, the retro module ballistic design problem breaks down into two problems: the ballistic design and ballistic navigation problems.

Ballistic Design Problem

The subject of the ballistic design problem is selection of the basic retro module design parameters μ_f and n_0, determination of the arrival orbit Keplerian elements, which characterize its shape and dimensions, and determination of the retro powerplant activation point in this orbit to insert the module into the final orbit. We assume that the module launches the interplanetary vehicle to the pericenter of the final orbit.

* We can say that the solution (7.1.42) is compatible with the two indicated equations.

To solve the posed problem, we use the approximate method to integrate the differential equations of motion with tangential control (see § 3, Chapter 2), bearing in mind what we have said previously about this method. Then, in accord with (2.3.39) — (2.3.41) and (2.3.43), we have

$$\tilde{v}_b = v_{id\ b} - \frac{(1 - \frac{1}{\tilde{r}_b})\tilde{v}^2_{cir\ f}}{v_{e\ b}}; \tag{7.1.43}$$

$$\cos\theta_b = \frac{v_{m\ b}v_{e\ b}}{\tilde{r}_b[v_{m\ b}v_{e\ b} - \tilde{v}^2_{cir\ f}(1 - \frac{1}{\tilde{r}_b})]}; \tag{7.1.44}$$

$$\tilde{r}_b = 1 + \sin^2\frac{\sigma}{n_0^*} I_{r\,b}; \tag{7.1.45}$$

$$\chi_b = -\frac{d_b}{n_0^*}\int_1^{\mu_f}\frac{v_{id}}{(1 + \sin^2\frac{\sigma}{n_0^*} I_r)^2}\,d\mu$$

or

$$\chi_b = \frac{d}{n_0^*}[(1 + w)(1 - \mu_f) + \mu_f w \ln\mu_f - 2(\frac{\sigma}{n_0^*})^2 I_{\chi b^2} + 3(\frac{\sigma}{n_0^*})^4 I_{\chi b^4} - 4(\frac{\sigma}{n_0^*})^6 I_{\chi b^6} + 5(\frac{\sigma}{n_0^*})^8 I_{\chi b^8}], \tag{7.1.46}$$

where

$$w = \frac{W}{V_{cir\ f}} \cdot \frac{V_{cir\ f}}{V_{f\pi}} = w_{cir} \cdot \tilde{v}_{cir\ f};\ \tilde{r}_b = \frac{r_b}{r_{f\pi}};$$

$$I_{r\ b} = -\int_1^{\mu_f} v_{id}\left(1 - \frac{\tilde{v}^2_{cir\ f}}{v_e v_m}\right)^{1/2} d\mu.$$

At the initial point of the powered retro segment, the energy integral /231

$$V_b^2 = -\frac{2\,fm_{pl}}{r_b} = V^2_{\infty f}.$$

Considering (7.1.43) and (7.1.45), we write this integral in relative quantities as follows

$$\tilde{\nu}_{\infty f}^2 = \left[\frac{\nu_{id\ b}\nu_{e\ b} - \tilde{\nu}_{cir\ f}^2}{\nu_{e\ b}} + \frac{\tilde{\nu}_{cir\ f}^2}{\nu_{e\ b}(1 + \sin^2\frac{\sigma}{n_0^*}I_{r\ b})}\right]^2 \frac{1}{\tilde{\nu}_{cir\ f}^2} - \frac{2}{1 + \sin^2\frac{\sigma}{n_0^*}I_{r\ b}} \tag{7.1.47}$$

where

$$\tilde{\nu}_{\omega f} = V_{\omega f}/\sqrt{f(m_{pl})/(r_{f\pi})}.$$

Taking

$$p_{1b} = \frac{\nu_{id\ b}\nu_{e\ b} - \tilde{\nu}_{cir\ f}^2}{\nu_{e\ b}},\ p_{2b} = \frac{p_{1b}}{\nu_{e\ b}},$$

$$q_b = \left\{\left[\sqrt{(1 - p_{2h})^2 + (1/\nu_{e\ b}^2)(\tilde{\nu}_{\infty f}^2\tilde{\nu}_{cir\ f}^2 - p_{1b}^2)} - (1 - p_{2b}\right] \times \frac{\tilde{\nu}_{cir\ f}^2}{\tilde{\nu}_{\infty f}^2\tilde{\nu}_{cir\ f}^2 - p_{1b}^2} - 1\right\}^{1/2}, \tag{7.1.48a}$$

after solving the last equation for n_0^*, we obtain

$$n_0^* = \frac{\nu_f{}^2 w I_{r\ b}}{\tilde{r}_f{}^2\sqrt{2}\ \text{arc sin}\ q_b} \tag{7.1.48b}$$

or

$$n_0^* = \frac{N_b}{r_f{}^2}\nu_f{}^2, \tag{7.1.49a}$$

where

$$N_b = \frac{w I_{r\ b}}{\sqrt{2}\ \text{arc sin}\ q_b}. \tag{7.1.49b}$$

The values of N_b can be tabulated as a function of μ_f for various values of $\tilde{v}_{\infty f}$, $\tilde{v}_{cir\ f}$, or $\nu_f = 1/\tilde{v}_{cir\ f}$ and w.

Here, as in the preceding problem, the choice of μ_f is bounded by upper μ_{fu} and lower μ_{fl} values. The upper bound of the values is determined from the equation

$$\mu_{fu} = \exp\left(-\frac{\sqrt{2 + \tilde{v}_{\infty f}^2} - \nu_f}{w\nu_f}\right).$$

Equations (7.1.48) or (7.1.49) make it possible to determine as a function of μ_f the initial thrust-weight ratio n_0 values which permit the retro module for a given $\tilde{v}_{\infty f}$ value to reach the final orbit pericenter with tangential thrust control. Bearing in mind the relations (7.1.43) — (7.1.46), we can speak in a certain sense of ballistic design problem solution. However, optimization of the ballistic design solutions still remains the principal problem. /232

OPTIMIZATION OF RETRO MODULE BASIC DESIGN PARAMETERS μ_f AND n_0

The design weight equation for the retro module can also be represented in the form (7.1.17). Then the max μ_{ul} condition will be the equation

$$\frac{\partial \mu_{ul}}{\partial \mu_f} = A_\mu - \frac{A_n^* \nu_f^2 \partial N_b}{\tilde{r}_f^2 \partial \mu_f} = 0$$

or

$$\frac{A_\mu}{A_n^*} = \frac{\nu_f^2}{\tilde{r}_f^2} \frac{\partial N_b}{\partial \mu_f}.$$

Here, in accordance with (7.1.49), we have

$$A_n^* = \frac{g_{0\ pl}}{g_{0\oplus}} A_n, \tag{7.1.50a}$$

$$\frac{\partial N_b}{\partial \mu_f} = N_b\left[\frac{\nu_{id\ b}}{I_{r\ b}}\left(1 - \frac{\tilde{v}^2_{cir\ f}}{\nu_{e\ b}\nu_{m\ b}}\right)^{1/2} - \frac{\frac{\partial m_b}{\partial \mu_f}}{2\sqrt{(m_1 - 1)(2 - m_b)}\ \text{arc sin}\ \sqrt{m_b - 1}}\right], \tag{7.1.50b}$$

$$m_b = \frac{\tilde{v}^2_{cir\ f}(p_{3b} - p_{2b} - 1)}{\tilde{v}^2_{cir\ f}\tilde{v}^2_{\infty f} - p^2_{1b}}, \tag{7.1.50c}$$

$$P_{1b} = \frac{\nu_{e\ b}\nu_{id\ b} - \tilde{v}^2_{cir\ f}}{\nu_{e\ b}}, \quad p_{2b} = \frac{p_{1b}}{\nu_{e\ b}}, \tag{7.1.50d}$$

$$p_{3b} = \left[\frac{1}{\nu^2_{e\ b}}(\tilde{v}^2_{cir\ f}\tilde{v}^2_{\infty f} - p^2_{1b}) + (p_{2b} - 1)^2\right]^{1/2},$$

$$\frac{\partial m_b}{\partial \mu_f} = -\frac{w}{\mu_f(\tilde{v}^2_{cir\ f}\tilde{v}^2_{\infty f} - p^2_{1b})}\left\{\left(1 + \frac{0.5\tilde{v}^2_{cir\ f}}{\nu^2_{e\ b}}\right)\left(\frac{2m_b p_{1b}}{\tilde{v}^2_{cir\ f}} - \frac{1/p_{3b} - 1}{\nu_{e\ b}}\right) + \right. \tag{7.1.50e}$$

$$\left. \frac{0.5}{\nu^2_{e\ b}}\left[\left(\frac{1}{p_{3b}} - 1\right)p_{1b} - \frac{\tilde{v}^2_{cir\ f}\tilde{v}^2_{\infty f}}{\nu_{e\ b}p_{3b}}\right]\right\}.$$

Solving (7.1.49) and (7.1.50) jointly, we can determine uniquely the optimal values of the retro module basic design parameters μ_f^{opt} and n_0^{opt} for which the retro maneuver will be performed with the maximal value $\mu_{ul\ max}$. Then, using (7.1.43) — (7.1.46), we find the powered retro segment initial point kinematic parameters which permit the module to reach the pericenter of the final orbit with specified pericenter radius $r_{f\pi}$ and apocenter radius r_{fa} (or a_f and e_f). /233

The values of $\partial N_b/\partial \mu_f$ can be tabulated as a function of μ_f for fixed values of $\tilde{v}_{\infty f}$, $\tilde{v}_{cir\ f}$ and w.

BALLISTIC NAVIGATION PROBLEM

The solution of the ballistic navigation problem depends on the final orbit specification condition. If the final orbit position is not fixed, the required location of its plane may be obtained by suitable choice of the retro powerplant activation point. Bearing in mind the method for solving the boost ballistic navigation problem, we represent the dependence of the final orbit plane inclination angle i_f and ascending node longitude Ω_f on the retro powerplant activation point latitude argument u_b as follows:

$$\sin i_f = \frac{\sin \delta_f}{A_b[\cos (u_b - \theta_b) - B_b \sin u_b]}; \quad (7.1.51)$$

$$\sin (\Omega_f - \alpha_f) = -\operatorname{tg} \delta_f \operatorname{ctg} i_f; \quad (7.1.52a)$$

$$\cos(\Omega_f - \alpha_f) = -\frac{A_b}{\cos \delta_f}[\sin (u_b - \theta_b) + B_b \cos u_b], \quad (7.1.52b)$$

where α_f and δ_f are the target vector $\bar{V}^0_{\infty f}$ right ascension and declination in the planetocentric coordinate system

$$A_b = [1 - \frac{\tilde{r}_b}{\tilde{p}_{ha}}(1 - \cos \beta_b)]\frac{\tilde{v}_b}{\tilde{v}_{\infty f}},$$

$$B_b = [\sin \beta_b - \operatorname{tg} \theta_b(1 - \cos \beta_b)]/[1 - \frac{\tilde{r}_b}{\tilde{p}_{ha}}(1 - \cos \beta_b)]\tilde{v}_b\sqrt{\tilde{p}_{ha}},$$

$\tilde{p}_{ha} = \frac{p_{ha}}{r_{f\pi}}$ is the relative focal parameter of the hyperbolic arrival orbit.

Since the following equality holds (see Figure 7.1.2)

$$u_b = \chi_b + \omega_f, \qquad (7.1.53)$$

by suitable selection of the final orbit pericenter angular distance ω_f using the relations (7.1.51) and (7.1.52), we can find the desired value of i_f or Ω_f. Thus, the ballistic navigation problem will be solved.

§ 2. METHOD OF INTERPLANETARY VEHICLE BALLISTIC DESIGN CHARACTERISTIC CALCULATION AND OPTIMIZATION WITH ACCOUNT FOR PATCHING OF HELIOCENTRIC SEGMENT WITH PLANETOCENTRIC TRAJECTORY SEGMENTS

In the preceding section, we solved the problem of optimizing the basic design parameters and active flight segment of an interplanetary vehicle in a planet sphere of action for given hyperbolic excess velocity vector $\bar{V}_\infty$. We assumed that the heliocentric trajectory segment was calculated without account for the disturbing influence of the Earth, destination planet, and the extent of the planet activity spheres, when the point of SC departure from the Earth's sphere of acti[illegible]nd the point of SC entry into the planet's sphere of the a[illegible]oincide, respectively, with the points where the SC interorbita[illegible]jectory crosses the orbits of the Earth and the destination pla[illegible]is assumption satisfies SC preliminary design accuracy re[illegible]nts and permits solving quite simply the problem of patchin[illegible] heliocentric segment with the hyperbolic departure and arrival orbits by satisfying the conditions (7.1.1). /234

It is significant that the solutions obtained in § 1 were based on the assumption that the SC basic design parameters and boost and retro segments do not influence the determination of the interorbital trajectory heliocentric segment. However, t[illegible]

assumption is not always legitimate. On the other hand, the method for calculating and optimizing the ballistic design characteristics of multistage interplanetary vehicles in which the departure and capture problems (inner problems) and the problem of determining the interorbital trajectory heliocentric segment are examined together and with account for their mutual influence is of interest and very useful and convenient in practice. The present section is devoted to the development and discussion of just such a method. We shall present an algorithm for determining both the optimal "single" interplanetary transfer trajectory from the parking orbit to the final orbit around the planet and the optimal multistage interplanetary vehicle basic design parameters $\mu_{f\,i}$ and $n_{0\,i}$ $(i = 1, \ldots, n)$.

We arbitrarily break the general problem of determining the "single" interplanetary flight trajectory and the multistage interplanetary vehicle basic design parameters into three problems: the problem of ballistic calculation of the interplanetary transfer heliocentric segment, the design problem, and the navigation problem.*

BALLISTIC CALCULATION OF HELIOCENTRIC SEGMENT /235

The objective of ballistic calculation of the interplanetary flight heliocentric segment is determination of the kinematic parameters at the beginning (point P_0 in Figure 7.2.1) and end point P_f) points of the transfer orbit, the transfer time Δt, and the hyperbolic excess velocities $V_{\infty 0}$ and $V_{\infty f}$, which are the initial values for solution of the design problem.

* Here, as in § 1, the term "navigation problem" is to be taken in a restricted sense. It applies only to the SC ballistic design analysis stage.

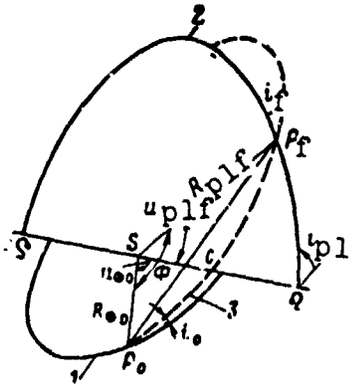

Figure 7.2.1. Kinematics of interplanetary flight heliocentric segment:

1- departure planet (Earth) orbit; 2- destination planet orbit; 3- heliocentric segment

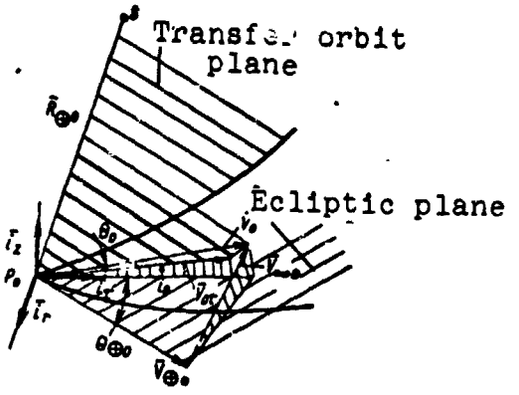

Figure 7.2.2. Velocity triangle at point P_0

In the rectangular coordinate system with origin coinciding with the position of the Earth at the initial time (point P_0), the SC heliocentric velocity vector $\bar{V}_0$ can be expressed in the form

$$\bar{V}_0 = V_{0r}\cdot\bar{i}_r + V_{0\tau}\cos i_0\cdot\bar{i}_\tau + V_{0\tau}\sin i_0\bar{i}_z.$$

Here V_{0r}, $V_{0\tau}$ are, respectively, the projections of the SC heliocentric velocity V_0 on the radius $R_{\oplus 0}$ and on the normal to the radius in the transfer orbit plane; $\bar{i}_r$, $\bar{i}_\tau$, $\bar{i}_z$ are unit vectors (Figure 7.2.2); $\bar{i}_r$ is parallel to the radius vector $R_{\oplus 0}$ of point P_0 and directed away from the Sun; $\bar{i}_z$ is parallel to the Z axis of the heliocentric ecliptic system and coincides with its positive direction; $\bar{i}_\tau$ forms the right-hand system; i_0 is the transfer orbit plane inclination to the ecliptic plane.

DETERMINATION OF HYPERBOLIC EXCESS VELOCITIES $V_{\infty 0}$ AND $V_{\infty f}$ /236

Considering the velocity triangle at the point P_0 (see Figure 7.2.2), we represent the hyperbolic excess velocity vector $V_{\infty 0}$ as:

$$\bar{V}_{\infty 0}=(V_{0r}-V_{\oplus r})\bar{i}_r+(V_{0\tau}\cos i_0-V_{\oplus\tau})\bar{i}_\tau+V_{0\tau}\cdot\sin i_0\bar{i}_z. \qquad (7.2.1)$$

Hence, we obtain

$$\tilde{v}_{\infty 0}=x_0[(\tilde{V}_{0r}-\tilde{V}_{\oplus r})^2+(\tilde{V}_{0\tau}\cos i_0-\tilde{V}_{\oplus\tau})^2+(\tilde{V}_{0\tau}\sin i_0)^2]^{1/2}, \qquad (7.2.2)$$

where

$$\tilde{v}_{\infty 0}=\frac{V_{\infty 0}}{\sqrt{\frac{fm_\oplus}{r_0}}} \quad \text{(see § 1, p. 254);}$$

$$x_0=\sqrt{\frac{m_\odot r_0}{m_\oplus a_\oplus}};$$

$$\tilde{V}_{0r}=\frac{V_{0r}}{\sqrt{\frac{fm_\odot}{a_\oplus}}}, \quad \tilde{V}_{0\tau}=\frac{V_{0\tau}}{\sqrt{\frac{fm_\odot}{a_\oplus}}},$$

$$\tilde{V}_{\oplus r}=\frac{V_{\oplus r}}{\sqrt{fm_\odot/a_\oplus}}, \quad \tilde{V}_{\oplus\tau}=\frac{V_{\oplus\tau}}{\sqrt{fm_\odot/a_\oplus}};^*$$

$a_\oplus$ is the Earth's orbit semimajor axis; r_0 is the circular parking orbit radius.

Considering the expressions

$$\left.\begin{aligned}&\tilde{V}_{0r}=\tilde{V}_0\sin\theta_0, \quad \tilde{V}_{0\tau}=\tilde{V}_0\cos\theta_0,\\&\tilde{V}_0=\sqrt{\left(2-\frac{R_0}{a}\right)\frac{1}{R_0}},\end{aligned}\right\} \qquad (7.2.3)$$

where $R_0=R_{\oplus 0}/a_\oplus$; θ_0 is the transfer orbit trajectory angle at the point P_0 and a is the transfer orbit semimajor axis, we transform (7.2.2) to the form

$$\tilde{v}_{\infty 0}=\frac{x_0}{\sqrt{R_0}}\left[4-\frac{R_0}{a}\left(1+\frac{a}{a_\oplus}\right)-\frac{2}{R_0}\sqrt{p_\oplus p}\,(\cos i_0+\operatorname{tg}\theta_0\operatorname{tg}\theta_{\oplus 0})\right]^{1/2}, \qquad (7.2.4a)$$

where p is the transfer orbit focal parameter.

*For calculation of planetary motion kinematic parameters, see Appendix.

a.4

In view of the fact that $e_{\oplus} = 0.01657 \ll 1$, in the first approximation we can assume the Earth's orbit to be circular, i.e., $e_{\oplus 0}=0$, which permits writing (7.2.4a) as /237

$$\tilde{v}_{\infty 0}=\dot{x}_0\left(3-\frac{1}{a}-2\sqrt{p}\cos i_0\right)^{1/2}. \qquad (7.2.4b)$$

We express the hyperbolic excess velocity $\tilde{v}_{\infty f}$ at the point P_f similarly in the form of the relation

$$\tilde{v}_{\infty f} = \kappa_f[(\tilde{V}_{f\ r} - \tilde{V}_{pl\ r})^2 + (\tilde{V}_{f\tau}\cos i_f - \tilde{V}_{pl\tau})^2 + (\tilde{V}_{f\tau}\sin i_f)^2]^{1/2}. \qquad (7.2.5)$$

Here

$$\tilde{v}_{\infty f} = \frac{V_{\infty f}}{\sqrt{fm_{pl}/r_{f\pi}}} \text{ (see § 1, p. 273);}$$

$$\tilde{V}_{f\ r} = \frac{V_{f\ r}}{\sqrt{\frac{fm_{\odot}}{a_{\oplus}}}},\ \tilde{V}_{f\tau} = \frac{V_{\tau f}}{\sqrt{\frac{fm_{\odot}}{a_{\oplus}}}},\ \tilde{V}_{pl\ r} = \frac{V_{pl\ r}}{\sqrt{\frac{fm_{\odot}}{a_{\oplus}}}},\ \tilde{V}_{pl\tau} = \frac{V_{pl\tau}}{\sqrt{\frac{fm_{\odot}}{a_{\oplus}}}};$$

$V_{f\ r}$ and $V_{f\tau}$ are, respectively, the projections of the SC heliocentric velocity V_f on the radius $R_{pl\ f}$ and on the normal to the radius in the transfer orbit plane;

$$\kappa_f = \sqrt{\frac{m_{\odot} r_{f\pi}}{m_{pl} a_{\oplus}}};$$

$r_{f\pi}$ is the pericenter radius of the final orbit around the planet; i_f is the transfer orbit plane inclination to the destination planet orbit plane (see Figure 7.2.1).

Considering the equalities

$$\tilde{V}_{f\,r} = \tilde{V}_f \sin\theta_f,\ \tilde{V}_{f\tau} = \tilde{V}_f \cos\theta_f,$$
$$\tilde{V}_f = \sqrt{\frac{1}{R_f}\left(2 - \frac{R_f}{a}\right)}, \tag{7.2.6}$$

where $R_f = \frac{R_{pl\,f}}{R_{\oplus 0}}$ and θ_f is the transfer orbit trajectory angle at the point P_f, we write (7.2.5) in the form

$$\tilde{v}_{\infty f} = \frac{x_f}{\sqrt{R_f}}\left[4 - \frac{R_f}{a}\left(1 + \frac{a}{a_{pl}}\right) - 2\frac{\sqrt{p_{pl}p}}{R_f}\left(\cos i_f + \operatorname{tg}\theta_f \operatorname{tg}\theta_{pl\,f}\right)\right]^{1/2}, \tag{7.2.7a}$$

Since $e_{pl} < 0.095$ for the planets (except for Mercury and Pluto, <u>/238</u> see Appendix), assuming in the first approximation that the destination planet orbits are circular, we obtain

$$\tilde{v}_{\infty f} = \frac{x_f}{\sqrt{R_f}}\left(3 - \frac{R_f}{a} - 2\sqrt{\frac{p}{R_f}}\cos i_f\right)^{1/2}. \tag{7.2.7b}$$

DETERMINATION OF ANGULAR VARIABLES Φ, i_0, i_f

An important parameter which determines to a considerable degree the interplanetary trajectory heliocentric segment kinematic characteristics is the trajectory angle Φ — the angular distance from the point P_0 to the point P_f in the transfer orbit plane (see Figure 7.2.1). Using the spherical trigonometry cosine theorem, we find from the spherical triangle $\Omega P_f' P_0'$ (see Figure 7.2.1)

$$\cos\Phi = \cos u_{\oplus 0}\cos u_{pl\,f} - \sin u_{\oplus 0}\sin u_{pl\,f}\cos i_{pl},^{*} \tag{7.2.8a}$$

where $$u_{\oplus 0} = 2\pi - (\tilde{u}_{\oplus 0} - \Omega_{pl\,f});$$

* For algorithm to calculate $\tilde{u}_{\oplus 0}$ and $u_{pl\,f}$, see Appendix.

P_0' and P_f' are the projections of the points P_0 and P_f on the unit sphere.

Since $\Phi < (u_{pl\ f} + u_{\oplus 0})$, the quadrant of the angle Φ is determined basically by the quadrant of the angle $(u_{pl\ f} + u_{\oplus 0})$, i.e.,

$$\sin\Phi = \operatorname{sign}[\sin(u_{pl\ f} + u_{\oplus 0})]\sqrt{1-\cos^2\Phi}. \qquad (7.2.8b)$$

It is not difficult to show that, for $u_{pl\ f} + u_{\oplus 0} = \pi$, the inequality $(\pi - i_{pl}) < \Phi < \pi$ holds. Using the sine and cosine theorems, we obtain from the spherical triangle $\Omega P_f' P_0'$

$$\sin i_0 = \sin i_{pl}\frac{\sin u_{pl\ f}}{\sin\Phi};$$
$$\cos i_0 = \frac{\cos u_{pl\ f} - \cos u_{\oplus 0}\cos\Phi}{\sin u_{\oplus 0}\sin\Phi}; \qquad (7.2.9)$$

$$\sin i_f = \sin i_{pl}\frac{\sin u_{\oplus 0}}{\sin\Phi};$$
$$\cos i_f = \frac{\cos u_{\oplus 0} - \cos u_{pl\ f}\cos\Phi}{\sin u_{pl\ f}\sin\Phi}. \qquad (7.2.10)$$

DETERMINATION OF INTERPLANETARY FLIGHT HELIOCENTRIC SEGMENT TIME Δt AND TRANSFER ORBIT FOCAL PARAMETER p

In the present case, it is simpler and easier to determine the flight time Δt from point P_0 to point P_f and the transfer orbit focal parameter p using the Lambert method (see § 1, Chapter 2). Depending on the transfer orbit type, the flight time Δt and focal parameter p are expressed by the following relations: /239

elliptic transfer orbit

$$\left.\begin{aligned}
\Delta t &= \frac{a^{3/2}}{2}\left\{2N + 1 + \frac{1}{\pi}\left[\operatorname{sign}(\Delta t_m - \Delta t)(\varepsilon - \sin\varepsilon - \pi) - \right.\right. \\
&\quad \left.\left. - \operatorname{sign}(\sin\Phi)(\delta - \sin\delta)\right]\right\}, \\
\sin\frac{\varepsilon}{2} &= \left(\frac{s}{2a}\right)^{1/2}, \quad \sin\frac{\delta}{2} = \left(\frac{s-c}{2a}\right)^{1/2}, \\
c^2 &= R_0^2 + R_f^2 - 2R_0 R_f \cos\Phi, \quad s = \frac{1}{2}(R_0 + R_f + c), \\
\Delta t_m &= \frac{s^{3/2}}{4\sqrt{2}}\left[2N + 1 - \frac{\operatorname{sign}\sin\Phi}{\pi}(\delta_m - \sin\delta_m)\right], \\
\sin\frac{\delta_m}{2} &= \left(\frac{s-c}{s}\right)^{1/2},
\end{aligned}\right\} \qquad (7.2.11e)$$

$$\left.\begin{aligned}
p &= \frac{R_0 R_f (1 - \cos\Phi)}{2a \cdot \sin^2\frac{1}{2}(\varepsilon - \gamma)}, \\
\gamma &= \delta\left[\operatorname{sign}(\Delta t_m - \Delta t)\operatorname{sign}(\sin\Phi)\right];
\end{aligned}\right\} \qquad (7.2.12e)$$

parabolic transfer orbit*

$$\Delta t_{par} = \frac{\sqrt{2}}{6\pi}\left[s^{3/2} - (s-c)^{3/2}\operatorname{sign}(\sin\Phi)\right], \qquad (7.2.11p)$$

$$p = \frac{2(s-r_0)(s-r_f)}{c^2}\left[s^{1/2} + \operatorname{sign}(\sin\Phi)(s-c)^{1/2}\right]^2; \qquad (7.2.12p)$$

hyperbolic transfer orbit*

$$\left.\begin{aligned}
\Delta t &= \frac{\sqrt{(-a)^3}}{2}\left[(\operatorname{sh}\alpha - \alpha) - (\operatorname{sh}\beta - \beta)\operatorname{sign}(\sin\Phi)\right], \\
\operatorname{sh}\frac{\alpha}{2} &= \left(-\frac{s}{2a}\right)^{1/2}, \quad \operatorname{sh}\frac{\beta}{2} = \left(-\frac{s-c}{2a}\right)^{1/2},
\end{aligned}\right\} \qquad (7.2.11h)$$

$$\left.\begin{aligned}
p &= -\frac{R_0 R_f (1 - \cos\Phi)}{2a\operatorname{sh}^2\frac{1}{2}(\alpha - \gamma)}, \\
\gamma &= \beta\operatorname{sign}(\sin\Phi).
\end{aligned}\right\} \qquad (7.2.12h)$$

---

* The real solutions are associated with elliptic transfer orbits. Examination of parabolic and hyperbolic transfer orbits is dictated by the search for the required solutions.

DETERMINATION OF TRANSFER ORBIT TRAJECTORY ANGLES θ_0 AND θ_f

Using (2.1.25), we obtain /240

$$\operatorname{tg}\theta_0=\operatorname{ctg}\frac{1}{2}\Phi-\sqrt{\frac{R_0}{R_k}}\operatorname{cosec}\frac{1}{2}\Phi\cos\frac{\Delta}{2}, \qquad (7.2.13)$$

$$\operatorname{tg}\theta_f=\sqrt{\frac{R_k}{R_0}}\operatorname{cosec}\frac{1}{2}\Phi\cos\frac{\Delta}{2}-\operatorname{ctg}\frac{1}{2}\Phi. \qquad (7.2.14)$$

Here, for elliptic transfer orbits

$$\Delta=(2N+1)\pi+(\varepsilon-\pi)\operatorname{sign}(\Delta t_m-\Delta t)-\delta\operatorname{sign}(\sin\Phi), \qquad (7.2.15e)$$

for hyperbolic transfer orbits

$$\Delta=\alpha-\beta\operatorname{sign}(\sin\Phi). \qquad (7.2.15h)$$

DESIGN PROBLEM

The objective of the design problem is to optimize the basic design parameters $n_{0\,i}$ and $\mu_{f\,i}$ of the interplanetary vehicle boost and retro modules. The solution of this problem involves specification of the initial conditions. If we are considering interplanetary SC flights from parking orbit around the Earth prior to final orbit around the destination planet, we usually examine as the initial conditions the nominal launch date t_0 — the initial time (point P_0) of the heliocentric trajectory segment, or the nominal arrival date t_f — the final time (point P_f) of the heliocentric segment. However, in the general case, these dates are not among the initial conditions and the flight time Δt and the dates t_0 and t_f are sought parameters.

In the case when the date t_0 or t_f and the flight time Δt are specified, the design problem reduces to optimizing the basic design parameters of the boost and retro modules for known hyperbolic excess velocities $V_{\infty 0}$ and $V_{\infty f}$, whose solution was presented in § 1 of the present chapter. This conclusion is a consequence of the unique determination of the values of $V_{\infty 0}$ and $V_{\infty f}$ as a result of solving the problem of ballistic calculation of the interplanetary flight heliocentric segment for specified date t_0 or t_f and given flight time Δt.

However, in the case when only the date t_0 (or t_f) is specified, the design problem solution will be associated with the mutual influence of the multistage interplanetary vehicle basic design parameters and the heliocentric segment kinematic parameters.

OPTIMIZATION OF $\mu_{f\ i}$ AND $n_{0\ i}$ ($i = 1.2$) FOR GIVEN t_0 OR t_f AND FLIGHT TIME Δt

If the design problem initial values are t_0 or t_f ard Δt, /241 then as a consequence of the equality

$$t_f = t_0 + \Delta t \qquad (7.2.16)$$

this is equivalent to specification of the nominal launch and arrival dates. Therefore, bearing in mind the application in which the algorithm for calculating planet location as a function of T is given, we can consider R_0, R_f, $u_{\oplus 0}$, $u_{pl\ f}$, i_{pl}, $\theta_{\oplus 0}$, $\theta_{pl\ f}$, and $p_{\oplus}$, p_{pl} to be known.

Now, using (7.2.8) — (7.2.10), we find Φ, i_0, and i_f. Then, after solving (7.2.11), we find the transfer orbit semimajor

axis a, which permits calculating on the basis of (7.2.12) the transfer orbit focal parameter p and, with the aid of (7.2.13) — (7.2.14), the trajectory angles θ_0 and θ_f. Moreover, (7.2.3) and (7.2.6) make it possible to find the SC heliocentric velocities at the transfer orbit beginning ($\tilde{V}_0$) and end ($\tilde{V}_f$) points.

The values obtained are completely sufficient for unique determination from (7.2.4) and (7.2.7) of the hyperbolic excess velocities $\tilde{v}_{\infty 0}$ and $\tilde{v}_{\infty f}$.

Thus, after determining the transfer orbit Keplerian elements i_0, p, and a, its kinematic parameters V_0, θ_0, and V_f, θ_f at the points P_0 and P_f, and the hyperbolic excess velocities $\tilde{v}_{\infty 0}$ and $\tilde{v}_{\infty f}$, the design problem for given date t_0 or t_f and flight time Δt reduces to optimizing the basic design parameters of the boost and retro modules, which was solved in detail in § 1 of the present chapter. The block diagram for solution of the subject design problem is shown in Figure 7.2.3.

It is quite clear that, if we are considering interplanetary SC flight from parking orbit around the Earth to the destination planet with flyby near the latter for given t_0 or t_f and Δt, the design problem after using the described method (Figure 7.3.2) to determine the transfer orbit Keplerian elements i_0, p, and a, its kinematic parameters $\tilde{v}_0, \theta_0$ at the point P_0, and the hyperbolic excess velocity $\tilde{v}_{\infty 0}$ also reduces to the problem of optimizing the boost module basic design parameters for known $\tilde{v}_{\infty 0}$, which was examined in § 1.

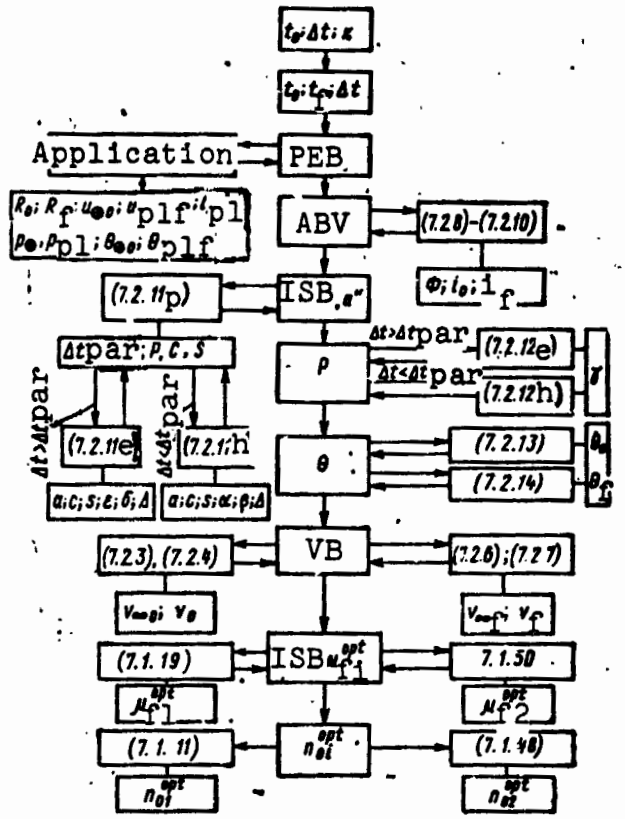

Figure 7.2.3. Block diagram of design problem solution for given Δt (DPBΔt):

PEB- planet element calculation block; AVB- angular variable calculation block; ISB"a"- iteration select block for transfer orbit semimajor axis "a"; VB- block for calculation of heliocentric velocities V_0 and $\tilde{V}_f$ and hyperbolic excess velocities $\tilde{v}_{\infty 0}$ and $\tilde{v}_{\infty f}$; ISB μ_{fi}^{opt}- iteration select block for optimal values μ_{f1}^{opt} and μ_{f2}^{opt}

OPTIMIZATION OF BASIC DESIGN PARAMETERS $\mu_{f\,i}$ AND n_{0i} (i = 1.2), AND FLIGHT TIME Δt FOR GIVEN t_0 AND t_f

In the preceding design problem formulation, the basic design parameters did not influence the results of the ballistic calculation of the interplanetary journey heliocentric segment. A characteristic of this design problem is absence of specification of the flight time Δt, which does not permit unambiguous /242

determination of the heliocentric segment and solution of the design problem. The freedom in selection of the flight time Δt and, therefore, of the heliocentric segment and basic design parameters n_{0i} and $\mu_{f\ i}$ makes it possible to impose a requirement on determining these parameters so that the relative useful load μ_{ul} will reach a maximal value. We shall call such an interplanetary flight heliocentric segment and such values of the flight time Δt and basic design parameters $\mu_{f\ i}$ and n_{0i} optimal. Finding them involves solution of the max μ_{ul} problem in the presence of constraints in the form of the design weight and kinematic equations. We shall discuss these constraints and note several of their peculiarities. /243

The design weight equation of the two-stage interplanetary vehicle is expressed in the form

$$\mu_{ul} = \mu_{0I} \cdot \mu_{0II},$$

where the relative useful weights of the boost $\mu_{0I}=G_{0\,II}/G_0$ and retro $\mu_{0\,II}= G_{ul}/G_{0\ II}$ modules depend on the relative values of the weight coefficients γ_{ji} and the basic design parameters n_{0i} and $\mu_{f\ i}$, i.e.,

$$\mu_{0I}=\mu_{0I}(\mu_{f1}, n_{0I}, \gamma_{jI}) \qquad \text{and} \qquad \mu_{0II}=\mu_{0II}(\mu_{f2}, n_{0II}, \gamma_{jII}).$$

Using the energy integral and the dependences of $\tilde{v}_a$ and $\tilde{r}_a$ on μ_{f1} and n_{01} and $\tilde{v}_b$ and $\tilde{r}_b$ on μ_{f2} and n_{02}, in accordance with (7.1.10) and (7.1.47), we have

$$\tilde{v}_{-l}=\tilde{v}_{-l}(n_{0l}, \mu_{f\ i}) \quad (l=0, k;\ i=1, 2).$$

Considering (7.2.8) and (7.2.11) along with the relations (7.2.9), (7.2.10) and (7.2.12) — (7.2.15), we can speak of the existence of dependence of Φ and a on the flight time Δt. Therefore, in accord with (7.2.4) and (7.2.7), we can write

$$\tilde{v}_{\infty l}=\varphi_l(\Delta t) \quad (l=0,\ k).$$

Now the max μ_{ul} problem is formulated as follows: find those values of Δt, $\mu_{f\,i}$, and n_{0i} for which the condition is satisfied

$$\mu_{ul\,\max} = \max_{n_{0i},\ \mu_{f\,i}} \mu_{0i}\mu_{0ii}$$

with constraints in the form

$$F_1=\tilde{v}_{\infty 0}(n_{01},\ \mu_{f1})-\varphi_0(\Delta t)=0,$$
$$F_2=\tilde{v}_{\infty k}(n_{02},\ \mu_{f2})-\varphi_k(\Delta t)=0.$$

To solve this problem, we formulate with use of the Lagrange coefficients λ_j $(j=1, 2)$ a new function J as follows

$$J=\mu_{0i}\mu_{0ii}+\sum_{j=1}^{2}\lambda_j F_j.$$

The necessary condition for max J (or μ_{ul}) are the equations /244

$$\frac{\partial J}{\partial \mu_{f1}}=\mu_{0ii}\frac{\partial \mu_{0i}}{\partial \mu_{f1}}+\lambda_1\frac{\partial \tilde{v}_{\infty 0}}{\partial \mu_{f1}}=0,$$
$$\frac{\partial J}{\partial n_{0i}}=\mu_{0ii}\frac{\partial \mu_{0i}}{\partial n_{0i}}+\lambda_1\frac{\partial \tilde{v}_{\infty 0}}{\partial n_{0i}}=0,$$
$$\frac{\partial J}{\partial \mu_{f2}}=\mu_{0i}\frac{\partial \mu_{0ii}}{\partial \mu_{f2}}+\lambda_2\frac{\partial \tilde{v}_{\infty f}}{\partial \mu_{f2}}=0,$$
$$\frac{\partial J}{\partial n_{02}}=\mu_{0i}\frac{\partial \mu_{0ii}}{\partial n_{02}}+\lambda_2\frac{\partial \tilde{v}_{\infty f}}{\partial n_{02}}=0,$$
$$\frac{\partial J}{\partial \Delta t}=\lambda_1\frac{\partial \varphi_0}{\partial \Delta t}+\lambda_2\frac{\partial \varphi_f}{\partial \Delta t}=0.$$

Excluding the Lagrange coefficients λ_1 and λ_2 from this system of equations, we find

$$\frac{\partial\mu_{01}/\partial\mu_{f1}}{\partial\mu_{01}/\partial n_{01}} + \frac{\partial\tilde{v}_{\infty 0}/\partial\mu_{f1}}{\partial\tilde{v}_{\infty 0}/\partial n_{01}} = 0,$$

$$\frac{\partial\mu_{011}/\partial\mu_{f2}}{\partial\mu_{011}/\partial n_{02}} + \frac{\partial\tilde{v}_{\infty f}/\partial\mu_{f2}}{\partial\tilde{v}_{\infty f}/\partial n_{02}} = 0, \qquad (7.2.17)$$

$$\mu_{011}\frac{\partial\mu_{01}}{\partial\mu_{x1}}\frac{\partial\varphi_1/\partial\Delta t}{\partial\tilde{v}^2_{\infty 0}/\partial\mu_{f1}} + \mu_{01}\frac{\partial\mu_{011}}{\partial\mu_{f2}}\frac{\partial\varphi_2/\partial\Delta t}{\partial\tilde{v}^2_{\infty f}/\partial\mu_{f2}} = 0$$

or, in a different form

$$\frac{\partial\mu_{01}/\partial\mu_{f1}}{\partial\mu_{01}/\partial n_{01}} + \left(\frac{\partial n_{01}}{\partial\mu_{f1}}\right)_{\tilde{v}_{\infty 0}} = 0, \qquad (7.2.18)$$

$$\frac{\partial\mu_{011}/\partial\mu_{f2}}{\partial\mu_{011}/\partial n_{02}} + \left(\frac{\partial n_{02}}{\partial\mu_{f2}}\right)_{\tilde{v}_{\infty f}} = 0, \qquad (7.2.19)$$

$$\mu_{011}\frac{\partial\mu_{01}}{\partial\mu_{f1}}\frac{\partial\mu_{f1}}{\partial\Delta t} + \mu_{01}\frac{\partial\mu_{011}}{\partial\mu_{f2}}\frac{\partial\mu_{f2}}{\partial\Delta t} = 0. \qquad (7.2.20)$$

Equations (7.2.18) and (7.2.19), with account for the equalities (7.1.11) and (7.1.49), are, respectively, the n_{01}, μ_{f1}, and n_{02}, μ_{f2} optimization conditions for constant values of $\tilde{v}_{\infty 0}$ and $\tilde{v}_{\infty f}$. It is interesting to note that they are identical to the optimization conditions for the basic design parameters of the boost and retro modules for given values of $\tilde{v}_{\infty 0}$ and $\tilde{v}_{\infty f}$ (7.1.18) and (7.1.50), found in § 1.

Equation (7.2.20) is the flight time Δt optimization condition and its satisfaction depends to a considerable degree on the basic design parameters $\mu_{f\,i}$ and n_{01} of the multistage interplanetary vehicle. This is the fundamental difference between it and the well-known Δt optimization condition, when we take as /245

the optimality criterion the sum of the characteristic velocities (or the sum of the absolute values of the hyperbolic excess velocities $\bar{v}_{\infty 0}$ and $\bar{v}_{\infty f}$) necessary for interplanetary flight from the parking orbit to the final orbit around the destination planet.

The design problem with specification of only the date t_0 or t_f is solved as follows. We first specify (arbitrarily) the flight time Δt in the heliocentric segment of the interplanetary flight. Then, the calculation is made using the algorithm described above and shown in Figure 7.2.3. After determining the transfer orbit elements $\bar{v}_{\infty 0}$ and $\bar{v}_{\infty f}$ and the basic design parameters n_{0i} and $\mu_{f\,i}$, we must check for satisfaction of the condition (7.2.20). If this condition is not satisfied, we repeat the problem solution procedure, specifying a new value of Δt in a definite fashion. The cycle is terminated when the flight time Δt optimization condition (7.2.20) is satisfied. The block diagram of this design problem solution procedure is shown in Figure 7.2.4.

Only the design problem associated with finding the optimal design solutions which determine the optimal values of the multistage interplanetary vehicle and basic design parameters n_{0i} and $\mu_{f\,i}$ flight time Δt corresponds to the basic SC design requirement — achievement of max μ_{ul}. In this case, there is an interconnection between the optimal interplanetary trajectory heliocentric segment and the optimal basic design parameters $\mu_{f\,i}$ and n_{0i}; this connection is manifested through (7.2.20) and influences the fuel mass distribution and powerplant thrust distribution between the interplanetary vehicle boost and retro modules, which effects directly the energy level of the powered

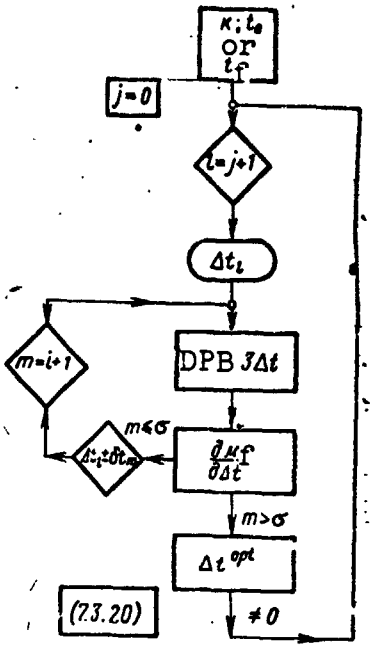

Figure 7.2.4. Block diagram of design problem solution when optimizing Δt, $\mu_{f\,i}$, and n_{0i} (DPB Δt^{opt})

boost and retro segments. Therefore, we should examine carefully both the results of optimizing the flight time Δt and interplanetary flight trajectories with injection into orbit around the destination planet and the results of multistage interplanetary vehicle ballistic design characteristic selection when the sum of the characteristic velocities $V_{x\Sigma} = V_{x1} + V_{x2}$ is taken as the optimality criterion. /246

In accordance with (7.2.17), the solution of the design problem for flyby interplanetary trajectories, when the SC only performs close flyby of the destination planet, involves in addition to (7.2.18), the following optimization condition

$$\frac{\partial \tilde{v}_{\infty 0}}{\partial \Delta t} = 0.$$

This condition permits complete solution of the interplanetary flight heliocentric segment ballistic calculation problem with specification of only t_0 or t_f and finding the transfer orbit Keplerian elements i_0, a, p, and the flight time Δt, and the hyperbolic excess velocity $\tilde{v}_{\infty 0}$. Thus, this design problem with specification of only t_0 or t_f reduces to the problem of optimizing the basic design parameters of the boost module for known $\tilde{v}_{\infty 0}$, which was solved in § 1 of the present chapter.

OPTIMIZATION OF BASIC DESIGN PARAMETERS $\mu_{f\,i}$ AND n_{0i}, HELIOCENTRIC LAUNCH DATE t_0, AND FLIGHT TIME Δt

The problem arises of determining in a given calendar range the heliocentric launch date t_0 or final date t_f and SC ballistic design characteristics which permit achieving max μ_{ul} with account for maneuvering at the destination planet. The difference between this and the preceding problem lies in optimizing (in addition to the flight time Δt and basic design parameters n_{0i} and $\mu_{f\,i}$) the heliocentric launch date t_0 or final date t_f in the given calendar range, which may encompass part of a synodic period, one synodic period, or several synodic periods.

We can use as the basis for solving this problem the algorithm for solving the preceding problem, which permits optimizing t_0 (or t_f) using one of the methods for finding the extremum of a function wrt a single variable [46]. In this case, the problem solution scheme is expressed as

$$\mu_{ul\,max} = \max_{t_{0min} < t_0 < t_{0max}} \left\{ \max_{\Delta t} \left[\max_{n_{0i}, \mu_{fi}} (\mu_{ul})^{\Delta t = const} \right]_{t_0 = const} \right\} \qquad (7.2.21a)$$

or, if the range of calendar heliocentric arrival dates t_f is specified,

$$\mu_{ul\,max} = \max_{t_{f\,min} < t_f < t_{f\,max}} \left\{ \max_{\Delta t} \left[\max_{n_{0i}, \mu_{f\,i}} (\mu_{ul})^{\Delta t = const} \right]_{t_f = const} \right\}. \qquad (7.2.21b)$$

(OUTER) NAVIGATION PROBLEM /247

The solution of the navigation problem involves determination of the SC heliocentric velocity vectors at the beginning and end points of the heliocentric segment and the hyperbolic

excess velocity vectors $\bar{V}^0_{\infty 0}$ and $\bar{V}^0_{\infty f}$, which permits obtaining the initial values for solution of the departure and capture problem: the spherical coordinates of the target vectors in the equatorial planetocentric coordinate system.

The SC heliocentric velocity vectors at the initial and final points of the heliocentric segment may be found from the relations (2.1.21) and (2.1.22) expressed in the present case as follows:

$$\left.\begin{aligned} \bar{V}_0 &= A\bar{R}_f - B_1\bar{R}_0, \\ \bar{V}_f &= B_2\bar{R}_f - C\bar{R}_0. \end{aligned}\right\} \qquad (7.2.22)$$

Here,

$$\left.\begin{aligned} A &= [\Delta t - a^{3/2}(\Delta - \sin\Delta)]^{-1}, \\ B_1 &= A\left[1 - \frac{a}{R_0}(1-\cos\Delta)\right], \quad B_2 = A\left[1 - \frac{a}{R_f}(1-\cos\Delta)\right], \\ C &= \frac{\sqrt{a}\sin\Delta}{R_0 R_f} + B_1\left[1 - \frac{a}{R_f}(1-\cos\Delta)\right]. \end{aligned}\right\} \qquad (7.2.23)$$

However, when determining the angles Φ, θ_0, θ_f and the location of the Earth and the destination planet, it is clearer and simpler to express the components of the vectors $\bar{V}_0$ and $\bar{V}_f$ in the ecliptic heliocentric system and the components of the vectors $\bar{V}_{\infty 0}$, $\bar{V}_{\infty f}$ in the second equatorial geocentric system and in the equatorial planetocentric system for finding the spherical coordinates of the target vector with the aid of some transformations, utilizing the kinematic schemes of Figures 7.2.5 — 7.2.7.

Let us determine the components of the unit vector $\bar{V}_0^0$ in the XYZ ecliptic heliocentric coordinate system (see Figure 7.2.5). Using the cosine theorem of spherical trigonometry, we

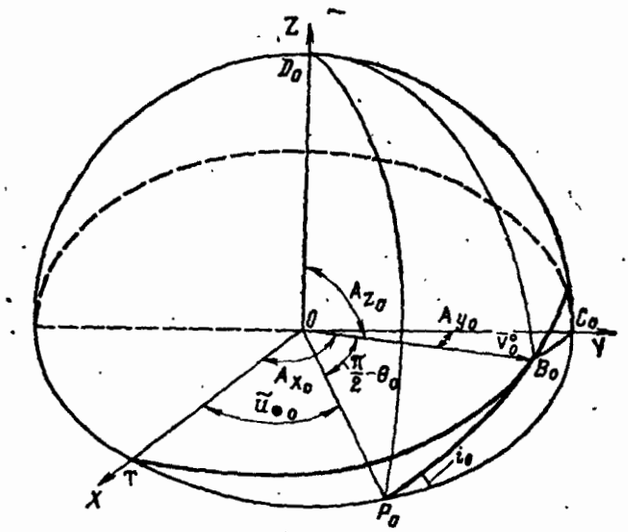

Figure 7.2.5. Kinematic scheme for determining the components of the unit vector $\bar{V}_0^0$

find from the spherical triangles $P_0B_0\Upsilon$, $P_0B_0C_0$ and $P_0B_0D_0$, respectively, on the unit celestial sphere

$$\left.\begin{aligned} V_{x0}^0 &= \cos A_{x0} = \cos \tilde{u}_{\odot 0} \sin \theta_0 - \sin \tilde{u}_{\odot 0} \cos \theta_0 \cos i_0, \\ V_{y0}^0 &= \cos A_{y0} = \sin \tilde{u}_{\odot 0} \sin \theta_0 + \cos \tilde{u}_{\odot 0} \cos \theta_0 \cos i_0; \\ V_{z0}^0 &= \cos A_{z0} = \cos \theta_0 \sin i_0, \end{aligned}\right\} \qquad (7.2.24)$$

where $\tilde{u}_{\odot 0}$ is the argument of the Earth's latitude in the ecliptic heliocentric coordinate system at the time t_0.

Now let us determine the components of the unit vector $\bar{V}_f^0$ /249 in the XYZ ecliptic heliocentric coordinate system (see Figure 7.2.6). Using the cosine theorem again, we obtain from the spherical trianges $P_0B_f\Upsilon$, $P_0B_fC_f$, and $P_0B_0D_f$ on the unit celestial sphere

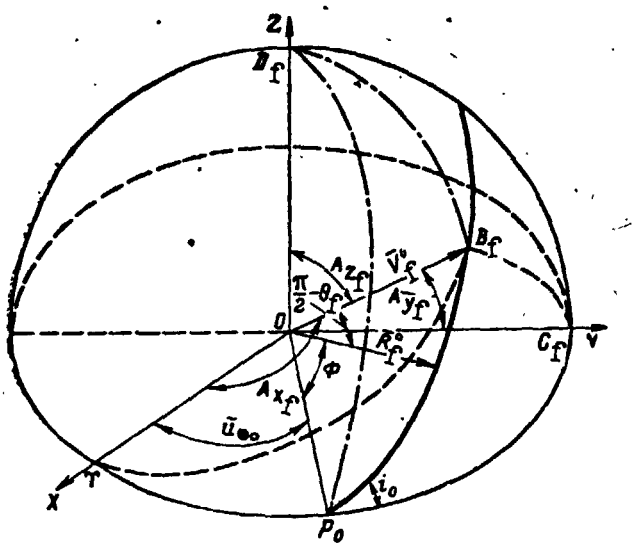

Figure 7.2.6. Kinematic scheme for determining the components of the unit vector $\bar{V}_f^0$

$$
\begin{aligned}
V^0_{x\,f} &= \cos A_{x\,f} = -[\cos \tilde{u}_{\oplus 0} \sin(\Phi-\theta_f)+ \\
&\quad + \sin \tilde{u}_{\oplus 0} \cos(\Phi-\theta_f)\cos i_0], \\
V^0_{y\,f} &= \cos A_{y\,f} = -\sin \tilde{u}_{\oplus 0} \sin(\Phi-\theta_f)+ \\
&\quad + \cos \tilde{u}_{\oplus 0} \cos(\Phi-\theta_f)\cos i_0, \\
V^0_{z\,f} &= \cos A_{z\,f} = \cos(\Phi-\theta_f)\sin i_0.
\end{aligned}
\tag{7.2.25}
$$

We represent the components of the unit vectors $\bar{V}^0_{\infty 0}$ and $\bar{V}^0_{\infty f}$ in the second equatorial geocentric coordinate system as follows:

$$
\left.
\begin{aligned}
V^0_{\infty x0} &= \frac{\varkappa_0}{\tilde{v}_{\infty 0}}(\tilde{V}_{x0}-\tilde{V}_{\oplus x}), \\
V^0_{\infty y0} &= \frac{\varkappa_0}{\tilde{v}_{\infty 0}}[(\tilde{V}_{y0}-\tilde{V}_{\oplus y})\cos\varepsilon-\tilde{V}_{z0}\sin\varepsilon], \\
V^0_{\infty z0} &= \frac{\varkappa_0}{\tilde{v}_{\infty 0}}[(\tilde{V}_{y0}-\tilde{V}_{\oplus y})\sin\varepsilon+\tilde{V}_{z0}\cos\varepsilon],
\end{aligned}
\right\}
\tag{7.2.26}
$$

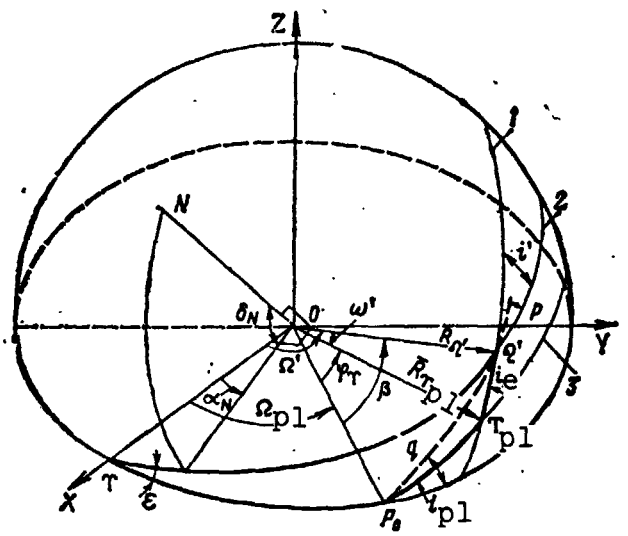

Figure 7.2.7. Geometric interpretation of ccordinate transformation:

1- destination planet equatorial plane; 2- Earth's equatorial plane; 3- destination planet orbital plane

/250

$$\left.\begin{aligned}
\hat{V}^0_{\infty xf} &= \frac{-x_f}{\tilde{v}_{\infty f}}(\tilde{V}_{pl^x} - \tilde{V}_{xf}),\\
\hat{V}^0_{\infty yf} &= \frac{-x_f}{\tilde{v}_{\infty f}}[(\tilde{V}_{pl^y} - \tilde{V}_{yf})\cos\varepsilon - (\tilde{V}_{pl^z} - \tilde{V}_{zf})\sin\varepsilon],\\
\hat{V}^0_{\infty zf} &= \frac{-x_f}{\tilde{v}_{\infty f}}[(\tilde{V}_{pl^y} - \tilde{V}_{yf})\sin\varepsilon + (\tilde{V}_{pl^z} - \tilde{V}_{zf})\cos\varepsilon].
\end{aligned}\right\} \qquad (7.2.27)$$

Here

$$\tilde{V}_{x0} = \tilde{V}_0 \cos A_{x0},\ \tilde{V}_{y0} = \tilde{V}_0 \cos A_{y0},\ \tilde{V}_{z0} = \tilde{V}_0 \cos A_{z0};$$

$$\tilde{V}_{x\,f} = \tilde{V}_f \cos A_{x\,f},\ \tilde{V}_{y\,f} = \tilde{V}_f \cos A_{y\,f},\ \tilde{V}_{z\,f} = \tilde{V}_f \cos A_{z\,f}.$$

$V_{\oplus x}$, $V_{\oplus y}$ and $V_{pl\ x}$, $V_{pl\ y}$, and $V_{pl\ z}$ are the Earth and destination planet velocity vector components, respectively, in the ecliptic heliocentric coordinate system

$$\left.\begin{aligned}
\tilde{V}_{\oplus x} &= -\tilde{V}_{\oplus 0}\sin(\tilde{u}_{\oplus 0} - \theta_{\oplus 0}),\\
\tilde{V}_{\oplus y} &= \tilde{V}_{\oplus 0}\cos(\tilde{u}_{\oplus 0} - \theta_{\oplus 0}),\\
\tilde{V}_{\oplus z} &= 0;
\end{aligned}\right\} \qquad (7.2.28)$$

$$\tilde{V}_{pl\,x} = \tilde{V}_{pl\,f}[\sin(u_{pl\,f} - \theta_{pl\,f})\cos\Omega_{pl} + \cos(u_{pl\,f} - \theta_{pl\,f})\sin\Omega_{pl}\cos i_{pl}],$$

$$\tilde{V}_{pl\,y} = \tilde{V}_{pl\,f}[-\sin(u_{pl\,f} - \theta_{pl\,f})\sin\Omega_{pl} + \cos(u_{pl\,f} - \theta_{pl\,f})\cos\Omega_{pl}\cos i_{pl}], \quad (7.2.29)$$

$$\tilde{V}_{pl\,z} = \tilde{V}_{pl\,f}\cos(u_{pl\,f} - \theta_{pl\,f})\sin i_{pl}.$$

Considering these relations, we represent the spherical coordinates of the target vectors $\bar{V}^0_{\infty 0}$ and $\bar{V}^0_{\infty f}$ in the second equatorial system in the form

$$\operatorname{tg}\delta_0 = \frac{V^0_{\infty x0}}{\sqrt{(V^0_{\infty x0})^2 + (V^0_{\infty y0})^2}} \quad \left(-\frac{\pi}{2} \leqslant \delta_0 \leqslant \frac{\pi}{2}\right), \quad (7.2.30)$$

$$\left.\begin{aligned} \sin\alpha_0 &= \frac{V^0_{\infty y0}}{\sqrt{(V^0_{\infty x0})^2 + (V_{\infty y0})^2}} \quad (0 \leqslant \alpha_0 \leqslant 2\pi), \\ \cos\alpha_0 &= \frac{V^0_{\infty x0}}{\sqrt{(V^0_{\infty x0})^2 + (V^0_{\infty y0})^2}}. \end{aligned}\right\} \quad (7.2.31)$$

/251

$$\operatorname{tg}\tilde{\delta}_f = \frac{\hat{V}^0_{\infty zf}}{\sqrt{(\hat{V}^0_{\infty xf})^2 + (\hat{V}^0_{\infty yf})^2}} \quad \left(-\frac{\pi}{2} \leqslant \tilde{\delta}_f \leqslant \frac{\pi}{2}\right); \quad (7.2.32)$$

$$\left.\begin{aligned} \sin\tilde{\alpha}_f &= \frac{\hat{V}^0_{\infty yf}}{\sqrt{(\hat{V}^0_{\infty xf})^2 + (\hat{V}^0_{\infty yf})^2}} \quad (0 \leqslant \tilde{\alpha}_f \leqslant 2\pi), \\ \cos\tilde{\alpha}_f &= \frac{\hat{V}^0_{\infty xf}}{\sqrt{(\hat{V}^0_{\infty xf})^2 + (\hat{V}^0_{\infty yf})^2}}. \end{aligned}\right\} \quad (7.2.33)$$

Several transformations must be performed to determine the spherical coordinates of the target vector $\bar{V}^0_{\infty f}$ in the equatorial planetocentric coordinate system. Let Ω' be the angular distance from the Earth's vernal equinox point to the ascending node Ω of the target planet equator on the Earth's equator (see Figure 7.2.7); $\omega' = \bar{R}_{\gamma_{pl}} \bar{R}_{\Omega'}$ is the angle between the radius vector $\bar{R}_{\gamma_{pl}}$ of the destination planet vernal equinox point and the radius vector $\bar{R}_{\Omega'}$ of the ascending node point of the nodal line of the equatorial planes of the Earth and destination planet; i' is the inclination of the target planet equatorial plane to the Earth's equatorial plane. If α_N and δ_N are the mean spherical coordinates of the target planet north pole in the equatorial geocentric system,* then (see Figure 7.2.7)

$$\left.\begin{aligned} \Omega' &= \frac{\pi}{2} + \alpha_N, \\ i' &= \frac{\pi}{2} - \delta_N. \end{aligned}\right\} \qquad (7.2.34)$$

Performing the usual rotation transformation with account for the angles introduced above, we find the components of the unit vector $\bar{V}^0_{\infty f}$ in the equatorial planetocentric system from the relation

$$\begin{bmatrix} V^0_{\infty x f} \\ V^0_{\infty y f} \\ V^0_{\infty z f} \end{bmatrix} = \begin{bmatrix} \hat{P}_x \hat{P}_y \hat{P}_z \\ \hat{Q}_x \hat{Q}_y \hat{Q}_z \\ \hat{W}_x \hat{W}_y \hat{W}_z \end{bmatrix} \begin{bmatrix} \hat{V}^0_{\infty x f} \\ \hat{V}^0_{\infty y f} \\ \hat{V}^0_{\infty z f} \end{bmatrix}, \qquad (7.2.35)$$

where, with account for (7.2.34) /252

* The values of α_N and δ_N for the planets are given in the Appendix.

$$
\left.
\begin{aligned}
\hat{P}_x &= -(\cos\omega' \sin\alpha_N + \sin\omega' \cos\alpha_N \sin\delta_N),\\
\hat{P}_y &= \cos\omega' \cos\alpha_N - \sin\omega' \sin\alpha_N \sin\delta_N,\\
\hat{P}_z &= \sin\omega' \cos\delta_N;\\
\hat{Q}_x &= \sin\omega' \sin\alpha_N - \cos\omega' \cos\alpha_N \sin\delta_N,\\
\hat{Q}_y &= -(\sin\omega' \cos\alpha_N + \cos\omega' \sin\alpha_N \sin\delta_N),\\
\hat{Q}_z &= \cos\omega' \cos\delta_N,\\
\hat{W}_x &= \cos\alpha_N \cos\delta_N,\\
\hat{W}_y &= \sin\alpha_N \cos\delta_N,\\
\hat{W}_z &= \sin\delta_N.
\end{aligned}
\right\} \qquad (7.2.36)
$$

As a result of determining $V^0_{\infty x\,f}$, $V^0_{\infty y\,f}$, and $V^0_{\infty z\,f}$, the spherical coordinates of the target vector $\bar{V}^0_{\infty\,f}$ in the equatorial planetocentric system may be written as

$$
\operatorname{tg}\delta_f = \frac{V^0_{\infty z f}}{\sqrt{(V^0_{\infty x f})^2 + (V^0_{\infty y f})^2}} \cdot \left(-\frac{\pi}{2} \leqslant \delta_f \leqslant \frac{\pi}{2}\right); \qquad (7.2.37)
$$

$$
\left.
\begin{aligned}
\sin\alpha_f &= \frac{V^0_{\infty y f}}{\sqrt{(V^0_{\infty x f})^2 + (V^0_{\infty y f})^2}} \quad (0 \leqslant \alpha_f \leqslant 2\pi);\\
\cos\alpha_f &= \frac{V^0_{\infty x f}}{\sqrt{(V^0_{\infty x f})^2 + (V^0_{\infty y f})^2}}.
\end{aligned}
\right\} \qquad (7.2.38)
$$

In order to use (7.2.35), we must find the dependence of ω' on the known mean angular planetary elements Ω_{pl}, i_{pl}, α_N and δ_N. Using the cosine and sine theorems, we obtain from the spherical triangle $P_0 \Upsilon_{pl} \Omega'$ (see Figure 7.2.7)

$$
\cos\omega' = \cos\beta \cos\varphi_\Upsilon + \sin\beta \sin\varphi_\Upsilon \cos(q - i_{pl}), \qquad (7.2.39)
$$

$$
\sin\omega' = \frac{\sin(q - i_{pl}) \sin\beta}{\sin i_E}, \qquad (7.2.40a)
$$

where $\beta = \bar{R}_{\Omega} \cdot \bar{R}_P$ is the angular distance from the heliocentric point P_0 to the ascending node Ω'; q is the inclination of the $P_0 O \Omega'$ plane to the ecliptic plane; $\varphi_\Upsilon = \bar{R}_{\oplus R} \cdot \bar{R}_{\Upsilon_{pl}}$ is the angular

distance from the point P_0 to the target planet vernal equinox point; i_e is the inclination of the target planet equatorial plane to its orbital plane.

From the same spherical triangle /253

$$\sin\varphi_\Upsilon = \frac{\sin\beta\cos(p+\delta_N)}{\sin i_e}, \qquad (7.2.41a)$$
$$\cos\varphi_\Upsilon = \cos\omega'\cos\beta + \sin\omega'\sin\beta\sin(p+\delta_N).$$

Solving this equation, together with (7.2.39), we obtain

$$\cos\omega' = [\cos\beta\sin(q - i_{pl})\sin(p+\delta_N) + \cos(q - i_{pl})\cos(p+\delta_N)]\frac{1}{\sin i_e}, \qquad (7.2.40b)$$

$$\cos\varphi_\Upsilon = [\sin(q - i_{pl})\sin(p+\delta_N) + \cos(q - i_{pl})\cos(p+\delta_N)]\frac{1}{\sin i_e}. \qquad (7.2.41b)$$

Consequently, in order to determine ω' and φ_Υ as functions of the target planet angular elements Ω_{pl}, i_{pl}, α_N and δ_N, we must find the dependence of β, q, p and i_e on these elements. To do this, we turn to the spherical triangle $P_0\Omega'\Upsilon$, from which we find

$$\cos\beta = -\sin\alpha_N\cos\Omega_{pl} + \cos\alpha_N\sin\Omega_{pl}\cos\varepsilon,$$
$$\sin\beta = \frac{\sin\varepsilon\cos\alpha_N}{\sin q}. \qquad (7.2.42a)$$

or, since $\frac{\sin\varepsilon}{\sin q} > 0$,

$$\sin\beta = \operatorname{sign}(\cos\alpha_N)\sqrt{1-\cos^2\beta}. \qquad (7.2.42b)$$

Examining this same spherical triangle $P_0\Omega'\Upsilon$, we obtain

$$-\sin\alpha_N=\cos\Omega_{pl}\cos\beta-\sin\Omega_{pl}\sin\beta\cos q$$

or, with account for (7.2.42),

$$\cos q=\frac{\sin\alpha_N\sin\Omega_{pl}+\cos\alpha_N\cos\Omega_{pl}\cos\varepsilon}{\sin\beta}, \qquad (7.2.43a)$$

$$\sin q=\frac{\sin\varepsilon\cos\alpha_N}{\sin\beta}. \qquad (7.2.43b)$$

Moreover, from this triangle, we also have

$$\left.\begin{aligned}\sin p&=\frac{\sin\varepsilon\sin\Omega_{pl}}{\sin\beta},\\ \cos p&=\frac{\cos\alpha_N\cos\Omega_{pl}+\sin\alpha_N\sin\Omega_{pl}\cos\varepsilon}{\sin\beta}.\end{aligned}\right\} \qquad (7.2.44)$$

Let us express the angle i_e. Using the cosine theorem (second form), we find from the spherical triangle $P_0\Upsilon\Omega'$ /254

$$\cos i_e=\cos(q-i_{pl})\sin(p+\delta_N)-\sin(q-i_{pl})\cos(p+\delta_N)\cos\beta. \qquad (7.2.45)$$

The relations (7.2.42) — (7.2.45) define the dependence of ω' on the known target planet angular elements Ω_{pl}, i_{pl}, α_N, and δ_N. Thus, the (outer) navigation problem is solved.

§ 3. OPTIMIZATION OF INTERPLANETARY VEHICLE DESIGN SOLUTIONS WITH ACCOUNT FOR PLANETARY GRAVISPHERE DIMENSIONS

In the preceding sections, the interplanetary trajectory heliocentric segment was determined without account for the planetary gravisphere dimensions, i.e., the Earth and the destination planet were considered nongravitating centers. This

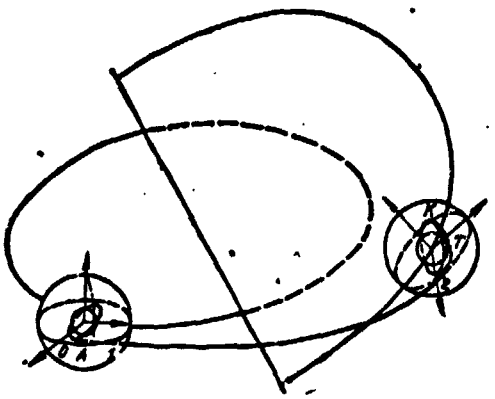

Figure 7.3.1. Schematic of patched conic interplanetary flight trajectory with account for planetary gravisphere dimensions:

O-A- active boost segment; A-1- passive flight segment in Earth's gravisphere; 1-2- heliocentric flight segment; 2-T- passive flight segment in destination planet gravisphere; T-K- active braking segment

is the traditional way to evaluate the heliocentric segments. However, with increase of the requirements on design analysis accuracy, it may become necessary to take into account the gravitational fields of the planets, which are significant at least within the limits of their gravispheres. This factor may even become obligatory for the Jupiter group planets because of the large dimensions of their gravispheres.

EVALUATION OF PLANETARY GRAVISPHERE SIZE INFLUENCE

In fact, taking as the initial conditions the heliocentric launch date t_1 and the flight time $\Delta t_{1,2}$ (or the heliocentric arrival date t_2), which determine the Earth and target planet positions, as a consequence of the difference between $\bar{R}_1$ and $\bar{R}_{\oplus 0}$ and $\bar{R}_2$ and $\bar{R}_{pl\,f}$ (Figure 7.3.1), we have the difference (Figures 7.3.2 and 7.3.3) /255

$$\delta\bar{V}_0 = \bar{V}_0 - \bar{V}_1 = \delta\bar{V}_{\infty 0} = \bar{V}_{\infty 0} - \bar{v}_1,$$
$$\delta\bar{V}_f = \bar{V}_f - \bar{V}_2 = \delta\bar{V}_{\infty f} = \bar{V}_{\infty f} - \bar{v}_2,$$

where $\bar{v}_1, \bar{v}_2$ are the SC geocentric and planetocentric velocity vectors at the gravispheres; $\bar{V}_1, \bar{V}_2$ are the heliocentric velocity vectors at the beginning and end of the heliocentric segment, represented with account for the planetary gravisphere dimensions; $\bar{V}_{\infty 0}$, $\bar{V}_{\infty f}$, $\bar{V}_0$, $\bar{V}_f$ are the hyperbolic excess velocity and heliocentric velocity vectors at the beginning and end of the

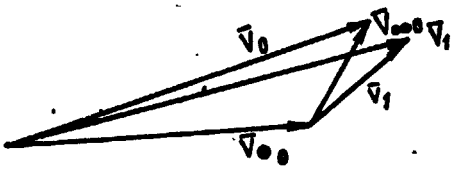

Figure 7.3.2. Velocity triangle at instant of heliocentric launch without $(\bar{V}_{\oplus 0}, \bar{V}_0, \bar{V}_{\infty 0})$ and with account $(\bar{V}_{\oplus 0}, \bar{V}_1, \bar{v}_1)$ for Earth's gravisphere dimensions

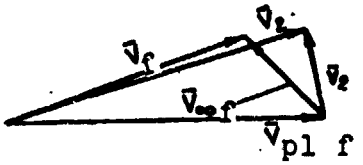

Figure 7.3.3. Velocity triangle at instant of heliocentric arrival without $(\bar{V}_{pl\ f}, \bar{V}_f, \bar{V}_{\infty f})$ and with account $(\bar{V}_{pl\ f}, V_2, v_2)$ for destination planet gravisphere dimensions

heliocentric segment, represented without account for the gravisphere dimensions; $\bar{R}_{\oplus 0}$, $\bar{R}_{pl\ f}$, $\bar{R}_1$, $\bar{R}_2$ are the radii vectors of the initial and final points of the heliocentric trajectory calculated without and with account for the planetary gravisphere dimensions, respectively.

Since, in accord with (7.2.22), the heliocentric velocity vectors at the initial and final points of the heliocentric segment are

$$\bar{V}_0 = A_0\bar{R}_{pl\ f} - B_{01}\bar{R}_{\oplus 0},\quad \bar{V}_f = B_{02}\bar{R}_{pl\ f} - C_0\bar{R}_{\oplus 0};$$

$$\bar{V}_1 = A_1\bar{R}_2 - B_1\bar{R}_1,\qquad \bar{V}_2 = B_2\bar{R}_2 - C_1\bar{R}_1,$$

then, representing $\bar{R}_1 = \bar{R}_{\oplus 0} - \bar{r}_1$ and $\bar{R}_2 = \bar{R}_{pl\ f} + \bar{r}_2$, we find the vectors $\delta\bar{V}_0$ and $\delta\bar{V}_f$, $\delta\bar{V}_{\infty 0}$ and $\delta\bar{V}_{\infty f}$ from the relations

$$\delta\bar{V}_0 = \delta\bar{V}_{\infty 0} = (A_0 - A_1)\bar{R}_{pl\ f} - (B_{01} - B_1)\bar{R}_{\oplus 0} - (A_1\bar{r}_2 - B_1\bar{r}_1), \qquad (7.3.1)$$

$$\delta\bar{V}_f = \delta\bar{V}_{\infty f} = (B_{02} - B_2)\bar{R}_{pl\ f} - (C_0 - C_1)\bar{R}_{\oplus 0} - (B_2\bar{r}_2 - C_1\bar{r}_1). \qquad (7.3.2)$$

Here the coefficients A_0, B_{01}, B_{02}, C_0 and A_1, B_1, B_2, C_1 are expressed by (7.2.23) for the heliocentric segments, calculated, respectively, without and with account for the planetary gravisphere dimensions and $r_1 = \Delta_\oplus$, $r_2 = \Delta_{pl}$. /256

The expressions presented abov. confirm that account for the planetary gravisphere dimensions leads to difference between the vectors $\bar{V}_1$ and $\bar{v}_1$, $\bar{V}_2$ and $\bar{v}_2$ and the vectors $\bar{V}_0$ and $\bar{V}_{\infty 0}$, $\bar{V}_f$ and $\bar{V}_{\infty f}$, respectively, and the difference becomes more marked for planets with large gravisphere radius Δ_{pl}.

Also of interest are the differences

$$\Delta V_{\infty 0} = V_{\infty 0} - v_1, \quad \Delta V_{\infty f} = V_{\infty f} - v_2,$$

which influence directly the differences in the magnitudes of the basic SC design parameters $\mu_{f\,1}$ and n_{0i}. We can assume with good approximation that $\bar{v}_1 \cdot \bar{r}_1 = v_1 \Delta_\oplus$ and $\bar{v}_2 \cdot \bar{r}_2 = v_2 \Delta_{pl}$. Then we obtain

$$\Delta V_{\infty 0} = V_{\infty 0} - \frac{(\bar{V}_1 - \bar{V}_{\oplus 0}) \cdot (\bar{R}_1 - \bar{R}_{\oplus 0})}{\Delta_\oplus}, \qquad (7.3.3)$$

$$\Delta V_{\infty f} = V_{\infty f} - \frac{(\bar{V}_2 - \bar{V}_{pl\,f}) \cdot (\bar{R}_2 - \bar{R}_{pl\,f})}{\Delta_{pl}} \qquad (7.3.4)$$

These relations show the inevitability of the existence of the differences $\Delta V_{\infty 0}$ and $\Delta V_{\infty f}$, whose values increase significantly for the planets with large gravisphere radii.

Table 7.1* shows the exact values of $\Delta V_{\infty 0}$ and $\Delta V_{\infty f}$ and the components δV_0 and δV_f for flights to Mars and Jupiter and their approximate values calculated using the formulas presented above.

NATURE OF PROBLEM FORMULATION FOR GIVEN t_1 AND $\Delta t_{1,2}$ /257

Turning to the problem of determining the ballistic characteristics of an interplanetary trajectory whose heliocentric segment is calculated with account for the planetary gravisphere

* For flights to Mars $t_1 = 2441903.5$, $t_2 = 2442093.5$; for flights to Jupiter $t_1 = 2441375.5$, $t_2 = 2442005.5$.

TABLE 7.1

Planet	δV_{x0}	δV_{y0}	δV_{z0}	$\Delta V_{\infty 0}$	δV_{xf}	δV_{yf}	δV_{zf}	$\Delta V_{\infty f}$
Mars $r_1 = \Delta_{L\sigma}$	0.0661	0.001	-0.1129	0.0246 (0.0261)	0.0526	0.1263	0.0615	0.0931 (0.943) km/sec
Jupiter $r_1 = \Delta_{L\Psi}$	-0.1393	-0.3059	0.8349	0.1667 (0.171)*	0.5601	-1.3214	-0.1664	1.3463 (1.363)* km/sec

* Approximate values from (7.3.3), (7.3.4).

dimensions, we shall discuss the peculiarities of this problem. The principal feature is that specification of the heliocentric launch date and flight time or heliocentric arrival date does not permit direct solution of the heliocentric segment ballistic calculation problem, since this formulation permits direct determination of only $\bar{R}_{\infty 0}$ and $\bar{R}_{pl\ f}$ and does not permit finding the heliocentric vectors of its initial and final points. Determination of $\bar{R}_1$ and $\bar{R}_2$ involves finding the values of $\bar{r}_1$ and $\bar{r}_2$ for which it is possible to calculate for the given flight time the heliocentric segment from the Earth's gravisphere surface to the destination planet's gravisphere surface. This process requires the solution of a boundary value problem. In order to rationalize the calculations, it is advisable to combine the process of solving the boundary value problem with the design problem — finding the optimal values of the basic design parameters $\mu_{f\ i}$ and n_{0i}. This becomes possible if we take as the independent variables the components of the vector $\bar{v}_1 : v_1$ and its right ascension α_1 and declination δ_1. As a result of the solution, we also find those values for v_1, α_1, and δ_1 for which the SC transfer from the parking orbit around the Earth to the final orbit around the destination planet will be performed with maximal relative useful load μ_{ul} and with the specified heliocentric launch date and flight time $\Delta t_{1,2}$ in the heliocentric

segment, which can be calculated with account for the planetary gravisphere dimensions. Thus, the position in space of the circular parking and final elliptic orbits will be defined.

ALGORITHM FOR SOLUTION OF DESIGN AND BOUNDARY VALUE PROBLEM

The construction of the algorithm for solving the formulated problem can be based on the relations obtained in § 1 of Chapter 4 and in §§ 1 and 2 of Chapter 7.

GEOCENTRIC BOOST SEGMENT

Let the zero solution be known: ν_1, α_1, and δ_1. Then, after determining the value of $\tilde{v}_{\infty 1}^2$ from the formula

$$\tilde{v}_{\infty 1}^2 = \tilde{v}_1^2 - \frac{2}{\tilde{\Delta}_\oplus}, \tag{7.3.5}$$

we find, with the aid of (7.1.19), (7.1.20), and (7.1.11), the optimal values of μ_{f1} and n_{01}. Then we use (7.1.4) — (7.1.6) to calculate the values of $\tilde{v}_a$, θ_a, and $\tilde{r}_a$, which makes it possible to find the trajectory angle θ_1 at the point of departure from the gravisphere at the moment t_1 /258

$$\theta_1 = \arccos \frac{\tilde{v}_a \tilde{r}_a \cos \theta_a}{\tilde{v}_1 \tilde{\Delta}_\oplus} \tag{7.3.6}$$

and using (7.1.22), the elements $\tilde{a}_{hd}$, $\tilde{p}_{hd}$, and $\tilde{e}_{hd}$ of the hyperbolic departure orbit. Use of the conditions (7.1.39) and (7.1.40) makes it possible to determine the inclination i_{hd} of the departure plane and thereby the parking orbit:

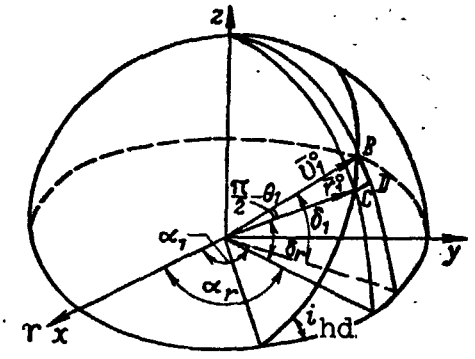

Figure 7.3.4. Kinematic vector of SC departure from Earth's gravisphere

for $\delta_1 \geq \varphi_{st}$

$$i_{hd} = |\delta_1| \quad \text{or} \quad i_{hd} = \pi - |\delta_1|,$$

for $\delta_1 < \varphi_{st}$

$$i_{hd} = |\varphi_{st}| \quad \text{or} \quad i_{hd} = \pi - |\varphi_{st}|, \qquad (7.3.7)$$

for $\sin A_{lim} < \pm \dfrac{\cos i_{hd}}{\cos \varphi_{st}}$

$$\cos(i_{hd})_{lim} = \pm \cos \varphi_{st} \sin A_{lim}.*$$

We find from the right spherical triangle CDB (Figure 7.3.4) the right ascension α_r and declination δ_r of the radius vector of the SC departure point on the Earth's gravisphere surface $\bar{r}_1$ /259

$$\operatorname{tg}(\alpha_1 - \alpha_r) = \operatorname{ctg} \theta_1 \sin i_{hd}$$

$$\sin(\delta_1 - \delta_r) = \cos \theta_1 \cos i_{hd}$$

* We note that, in practice, the parking orbit inclination equal to i_{hd} is determined by the actual track.

or

$$\left.\begin{aligned}\delta_r &= \delta_1 - \arcsin(\cos\theta_1 \sin i_{hd}\\ \alpha_r &= \alpha_1 - \operatorname{arctg}(\operatorname{ctg}\theta_1 \cos i_{hd}\end{aligned}\right\} \qquad (7.3.8)$$

HELIOCENTRIC FLIGHT SEGMENT

The initial values and the relations obtained make it possible to determine the heliocentric segment initial point kinematic parameters — the heliocentric velocity vector components V_{x1}, V_{y1}, V_{z1} and the heliocentric radius vector components X_1, Y_1, and Z_1 in the ecliptic coordinate system from the equations

$$\left.\begin{aligned}V_{x1} &= V_{\oplus x} + v_1 \cos\alpha_1 \cos\delta_1,\\ V_{y1} &= V_{\oplus y} + v_1(\sin\alpha_1 \cos\delta_1 \cos\varepsilon + \sin\delta_1 \sin\varepsilon),\\ V_{z1} &= v_1(-\sin\alpha_1 \cos\delta_1 \sin\varepsilon + \sin\delta_1 \cos\varepsilon);\end{aligned}\right\} \qquad (7.3.9)$$

$$\left.\begin{aligned}X_1 &= X_{\oplus 0} + \Delta_\oplus \cos\alpha_r \cos\delta_r,\\ Y_1 &= Y_{\oplus 1} + \Delta_\oplus(\sin\alpha_r \cos\delta_r \cos\varepsilon + \sin\delta_r \sin\varepsilon),\\ Z_1 &= \Delta_\oplus(-\sin\alpha_r \cos\delta_r \sin\varepsilon + \sin\delta_r \cos\varepsilon),\end{aligned}\right\} \qquad (7.3.10)$$

where

$$V_{\oplus x} = -V_{\oplus 0}\sin(\tilde{u}_{\oplus 0} - \theta_{\oplus 0}),\ V_{\oplus y} = V_{\oplus 0}\cos(\tilde{u}_{\oplus 0} - \theta_{\oplus 0}),$$
$$X_{\oplus 0} = R_\oplus \cos\tilde{u}_{\oplus 0},\ Y_\odot = R_{\oplus 0}\sin\tilde{u}_{\oplus 0}.$$

The values of V_1 and R_1 are given by the formulas

$$V_1 = (V_{x1}^2 + V_{y1}^2 + V_{z1}^2)^{1/2} \qquad (7.3.11)$$

$$R_1 = (X_1^2 + Y_1^2 + Z_1^2)^{1/2}. \qquad (7.3.12)$$

After finding the heliocentric segment orbital elements from the expressions

$$\left.\begin{aligned} a&=-\frac{fm_\odot}{V_1^2-\frac{2fm_\odot}{R_1}},\\ p&=\frac{(R_1V_1)^2-(\bar{R}_1\cdot\bar{V}_1)^2}{fm_\oplus},\quad e=\left(1-\frac{p}{a}\right)^{1/2}. \end{aligned}\right\} \qquad (7.3.13)$$

the true anomaly of the heliocentric segment initial point will be /260

$$\left.\begin{aligned} \cos v_1&=\left(\frac{p}{R_1}-1\right)\frac{1}{e},\\ \sin v_1&=\sqrt{\frac{p}{fm_\oplus}}\,\frac{(\bar{R}_1\cdot\bar{V}_1)}{eR_1}. \end{aligned}\right\} \qquad (7.3.14)$$

After determining for e < 1 the value of the eccentric anomaly E_2 from the Kepler equation [see (1.3.35)]

$$\frac{\Delta t_{1,2}}{a^{3/2}\sqrt{fm_\odot}}+E_1-e\sin E_1=E_2-e\sin E_2 \qquad (7.3.15e)$$

or for e > 1 the value of H_2 from the equation [see (1.3.37)]

$$\frac{\Delta t_{1,2}}{a^{3/2}\sqrt{fm_\odot}}+e\,\mathrm{sh}\,H_1-H_1=e\,\mathrm{sh}\,H_2-H_2, \qquad (7.3.15h)$$

where

$$E_1=2\mathrm{arctg}\left(\sqrt{\frac{1-e}{1+e}}\,\mathrm{tg}\,\frac{v_1}{2}\right), \qquad (7.3.16e)$$

$$H_1=2\mathrm{Arth}\left(\sqrt{\frac{e-1}{e+1}}\,\mathrm{th}\,\frac{v_1}{2}\right), \qquad (7.3.16h)$$

we find

$$v_2=2\mathrm{arctg}\left(\sqrt{\frac{1+e}{1-e}}\,\mathrm{tg}\,\frac{E_2}{2}\right)\ \text{or}\ \ v_2=2\mathrm{Arth}\left(\sqrt{\frac{e+1}{e-1}}\,\mathrm{th}\,\frac{H_2}{2}\right)$$

(for $E_2>2\pi$ we must add 2π to this value of ν_2)

$$\Phi=v_2-v_1, \quad R_2=\frac{p}{1+e\cos v_2},$$

$$V_2=\left(\frac{2fm_\odot}{R_2}-\frac{fm_\odot}{a}\right)^{1/2}.$$

As a result, the kinematic parameters of the heliocentric segment end can be determined from the vector equations [see (1.3.51) and (1.3.52)]:

$$\left.\begin{aligned}\bar{R}_2&=\left[1-\frac{R_2}{p}(1-\cos\Phi)\right]\bar{R}_1+\frac{R_2R_1}{\sqrt{fm_\odot p}}\sin\Phi\cdot\bar{V}_1,\\ \bar{V}_2&=\left[\frac{(\bar{R}_1\cdot\bar{V}_1)}{pR_1}(1-\cos\Phi)-\sqrt{\frac{fm_\odot}{p}}\frac{\sin\Phi}{R_1}\right]\bar{R}_1+\\ &\quad+\left[1-\frac{R_1}{p}(1-\cos\Phi)\right]\bar{V}_1.\end{aligned}\right\} \qquad (7.3.17)$$

PLANETOCENTRIC BRAKING SEGMENT /261

The solution of the posed problem will be associated with satisfaction of the equality

$$F_\Delta = \Delta_{pl} - |\bar{R}_2 - \bar{R}_{pl\ f}| = 0, \qquad (7.3.18)$$

indicating SC impact on the destination planet gravisphere surface. After this, we find the values of the kinematic parameters at the entry point on the destination planet gravisphere surface

$$\left.\begin{aligned}\bar{v}_2&=\bar{V}_2-\bar{V}_{pl\ f}\\ \bar{r}_2&=\bar{R}_2-\bar{R}_{pl\ f}\end{aligned}\right\} \qquad (7.3.19)$$

The hyperbolic arrival orbit elements are expressed by the relations:

$$a_{ha} = \frac{fm_{pl}}{\nu_2^2 - \frac{2fm_{pl}}{\Delta_{pl}}},$$

$$p_{ha} = \frac{(\Delta_{pl}\nu_2)^2 - (\bar{r}_2\bar{v}_2)^2}{fm_{pl}}, \quad e_{ha} = \left(\frac{p_{ha}}{a_{ha}} - 1\right)^{1/2}. \tag{7.3.20}$$

Satisfaction of the equalities

$$\nu_b^2 - \frac{2}{\tilde{r}_b} = \frac{1}{\tilde{a}_{ha}}, \tag{7.3.21}$$

$$F_p = \tilde{p}_{ha} - (\tilde{v}_b\tilde{r}_b \cos\theta_b)^2 = 0 \tag{7.3.22}$$

meets the requirement that the retro module enter a final orbit of specified form. If the module is assumed to be freely oriented, the final maneuver conditions are met.

The first condition (7.3.21) is satisfied automatically with optimization of μ_{f2} and n_{02}, when the equations (7.1.50) are realized with account for (7.1.48), in which in place of $\tilde{v}_{\infty f}^2$ we substitute

$$\tilde{v}_{\infty 2}^2 = \frac{1}{\tilde{a}_{ha}}.$$

Satisfaction of the second condition (7.3.22) terminates the solution of the posed problem, i.e., selection of those ν_1, α_1, and δ_1 values for which the conditions of basic design parameter n_{0i} and $\mu_{f\,i}$ (i = 1, 2) optimization and interplanetary vehicle transition from the Earth parking orbit to the final orbit around the destination planet for the given heliocentric launch date and flight time in the heliocentric segment are satisfied.

However, satisfaction of the boundary conditions (7.3.18) and (7.3.22) for different, although similar values of $\bar{v}_i$ is theoretically possible. Therefore, satisfaction of the boundary conditions (7.3.18) and (7.3.22), achievable according to the algorithm presented above with simultaneous optimization of n_{0i} and $\mu_{f\ i}$, may not lead to unambiguous determination of μ_{ul}. Consequently, the process of satisfaction of the conditions (7.3.18) and (7.3.22) simultaneously with optimization of n_{0i} and $\mu_{f\ i}$ must be organized so that, as a result of the attained solution, a real maximum of μ_{ul} will be obtained by corresponding selection of $\bar{v}_i$. Organization of the algorithm for solution of the boundary value and design problems with account for this requirement makes it possible to represent the solution in the form of the expression

/262

$$\mu_{ul\ max} = \inf_{\bar{v}_i=(v_i,\varkappa_i,\delta_i)} \{k_\mu(1-\mu_{ul}) + k_\Delta abs\, F_\Delta + k_p abs\, F_p : \forall \mu_{ul} \in \max_{n_{0i},\,\mu_{f\ i}} \mu_{ul} \}^*_{\substack{t_i=const \\ \Delta t_{1,2}=const}} \quad (7.3.23)$$

Here k_μ, k_Δ, and k_p are constant weighting coefficinets of the functional whose lower bound is being determined.

An important condition for convergence of the described process, regardless of the mathematical method for finding inf, is the determination of the zero solution. The heliocentric segment ballistic characteristics determined with and without account for the planetary gravisphere dimensions are not significantly different. Therefore, we take as the zero solution

/263

* The symbol : indicates the property which μ_{ul} must have and the symbol $\forall$ denotes "for all."

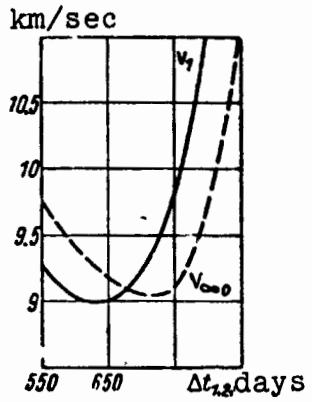

Figure 7.3.5. Variation of hyperbolic excess velocity $V_{\infty 0}$ and velocity v_1 at surface of the Earth's sphere of action t_1 = 2441348.5

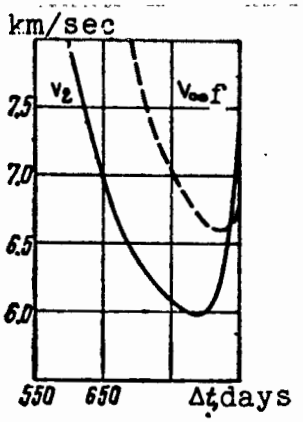

Figure 7.3.6. Variation of hyperbolic excess velocity $V_{\infty f}$ and velocity v_2 at surface of Jupiter's sphere of action t_1 = 2441348.5

of the posed problem the ballistic characteristics, the values of $\tilde{v}_{\infty 0}, \alpha_0$ and δ_0, determined by solving the ballistic and navigation problem presented in the preceding section (see § 2, Chapter 7), when the planets were taken to be nongravitating centers. The algorithm for determining the heliocentric segment ballistic characteristics and the values of $\tilde{v}_{\infty 0}, \alpha_0$ and δ_0 for given t_0 and Δt without account for the planetary gravisphere dimensions is very simple and rapidly realized. Therefore, it makes sense when seeking the zero solution to include this algorithm in the algorithm for calculating $\mu_{ul\ max}$ using (7.3.23).

Figures 7.3.5 and 7.3.6 present the results of calculation of the heliocentric flight segments to Jupiter [t_1 = 2441348.5 (1 Mar 1972)], carried out with and without account for the planetary gravisphere dimensions, in which we took the planetary spheres of action to be Laplace gravispheres. The values of the hyperbolic excess velocity $V_{\infty 0}$ and the velocity v_1 as functions of flight time are shown in Figure 7.3.5 and the values of $V_{\infty f}$

and ν_2 are shown in Figure 7.3.6. The shift of the V_{∞} and ν_1, V_{∞_f} and ν_2 isolines is significant.

OPTIMIZATION OF THE FLIGHT TIME $\Delta t_{1,2}$

So far we have examined the problem of determining the interplanetary vehicle ballistic design characteristics when the heliocentric trajectory segment is calculated with account for the planetary gravisphere dimensions for given heliocentric launch date and heliocentric transfer time. However, the heliocentric flight time $\Delta t_{1,2}$ influences markedly the quantity μ_{ul} and therefore, it is frequently taken as an optimizable parameter. Generally speaking, the three-parameter v_1, α_1, and δ_1 problem formulated above can be formally reduced to a four-parameter problem: v_1, α_1, δ_1 and $\Delta t_{1,2}$, while retaining the mathematical solution method used previously. However, if we start from the requirement for improvement of the iteration process convergence, we find that the algorithm for optimizing μ_{ul}, a component part of which is the preceding algorithm expressed by (7.3.23), is more effective. The scheme of this algorithm may be represented as follows

$$\mu_{ul\,max} = \max_{\Delta t_{1,2}\in\Delta T}\{\mu_{ul} : \forall \mu_{ul} \in \inf_{\bar{v}_\Delta}\{k_\mu(1-\mu_{ul}) + k_\Delta abs F_\Delta + k_p abs F_p : \forall \mu_{ul} \in \max_{n_{0i},\mu_{f\,i}} \mu_{ul}\Big|_{\Delta t_{1,2}=const}\Big|_{t_\Delta=const}\}, \tag{7.3.24}$$

where ΔT is a bounded set of $\Delta t_{1,2}$ values.

Thus, search for $\mu_{ul\,max}$ is made on the curve $\mu_{ul} = \varphi(\Delta t_{1,2})$ /264 at each point of which the solution (7.2.23) is satisfied. Correct definition of the zero solution is important for convergence of this iterative process, just as in the preceding

example. The zero solution may be found on the basis of the algorithm for optimizing the ballistic design characteristics and flight time, examined in the preceding section, when the planetary gravisphere dimensions were not taken into account in calculating the heliocentric segment. In order to accelerate the series of calculations, this algorithm must be included in the algorithm realizing (7.3.24). This algorithm also permits determining the ΔT region to some extent.

OPTIMIZATION OF THE HELIOCENTRIC LAUNCH DATE t_1

The question arises of whether or not the optimal heliocentric launch dates in the planetary synodic periods change if the heliocentric segment is determined with account for the planetary gravisphere dimensions. The answer to this question is fundamental. The possible launch "windows" on the optimal dates are also associated with this question. Therefore, it is of interest to optimize the heliocentric launch date t_1 along with the optimization of the basic design parameters n_{0i} and $\mu_{f\,i}$ and heliocentric flight time $\Delta t_{1,2}$. Thus, the problem reduces to finding $\mu_{ul\,max}$ with the limitations (7.3.18) and (7.3.22) wrt nine variables: n_{0i}, $\mu_{f\,i}$ $(i = 1, 2)$, v_1, α_1, and δ_1, $\Delta t_{1,2}$, and t_1. Using the solution of the design problem of n_{0i} and $\mu_{f\,i}$ optimization for given v_1 and v_2 values (see § 1, Chapter 7), the solution of the formulated problem can be reduced to finding max μ_{ul} with the indicated limitations wrt the five variables v_1, α_1, δ_1, $\Delta t_{1,2}$ and t_1. In constructing the algorithm for solving this problem, on the basis of the requirements for rapid convergence of the iteration process, we should use the previously presented algorithm for optimizing $\Delta t_{1,2}$, expressed

by (7.3.24). Then, the t_1 optimization algorithm can be represented by the formula

$$\mu_{ul\ max} = \max_{t_1 \in T_1} \{\mu_{ul} : \forall\, \mu_{ul} \in \max_{\Delta t_{1,2} \in \Delta T} \{\mu_{ul} : \forall\, \mu_{ul} \in \inf_{\bar{v}_1} \{k_\Phi (1 - \mu_{ul} + k_\Delta abs\, F_\Delta + k_\beta abs F_\beta : \forall \mu_{ul} \in \max \mu_{ul} \}_{t_1 = const}_{\Delta t_{1,2} = const}\}_{t_1 = const}\}, \tag{7.3.25}$$

$$\mu_{0l}, \mu_{fl}$$

where T_1 is a bounded set of t_1 values.

The zero solution, near which the actual solution of the posed problem is determined, should be found on the basis of the μ_{ul} optimization algorithm, expressed by (7.2.21a). It also permits determining T_1.

CHAPTER 8. FLIGHT TRAJECTORY TO A SINGLE PLANET WITH RETURN TO THE EARTH

§ 1. OPTIMIZATION OF HELIOCENTRIC SEGMENTS

The optimal flight cycles to a single planet with return to the Earth repeat, just as to a planet without return, i.e., after the synodic period T_s. Approximate repeatability of the flight cycles also takes place with the planetary great opposition period T_{go}. We shall examine the methods for optimizing trajectories to a single planet with return to the Earth for the example of flight trajectories to Mars with return to the Earth. /265

OPTIMIZATION OF ROUNDTRIP FLIGHT TRAJECTORIES

It is more convenient to optimize the interplanetary segments of the roundtrip flight trajectories on the isoline field of the velocity impulse components V_1, V_2, and so on in launch date versus planet arrival date coordinates. The isoline field for flight cycles to Mars in 1975 for the two-impulse flight scheme is shown in Figure 8.1.1 (aerobraking into Artificial Mars Satellite [AMS] orbit).

The launch dates from the Earth $t_1 = t^{\oplus}_{st}$ and the arrival dates at the Earth $t_4 = t^{\oplus}_{ar}$ are plotted along the abscissa axis, the Mars arrival dates $t_2 = t^{\sigma}_{ar}$ and Mars departure dates $t_3 = t^{\sigma}_{st}$ are plotted along the ordinate axis.

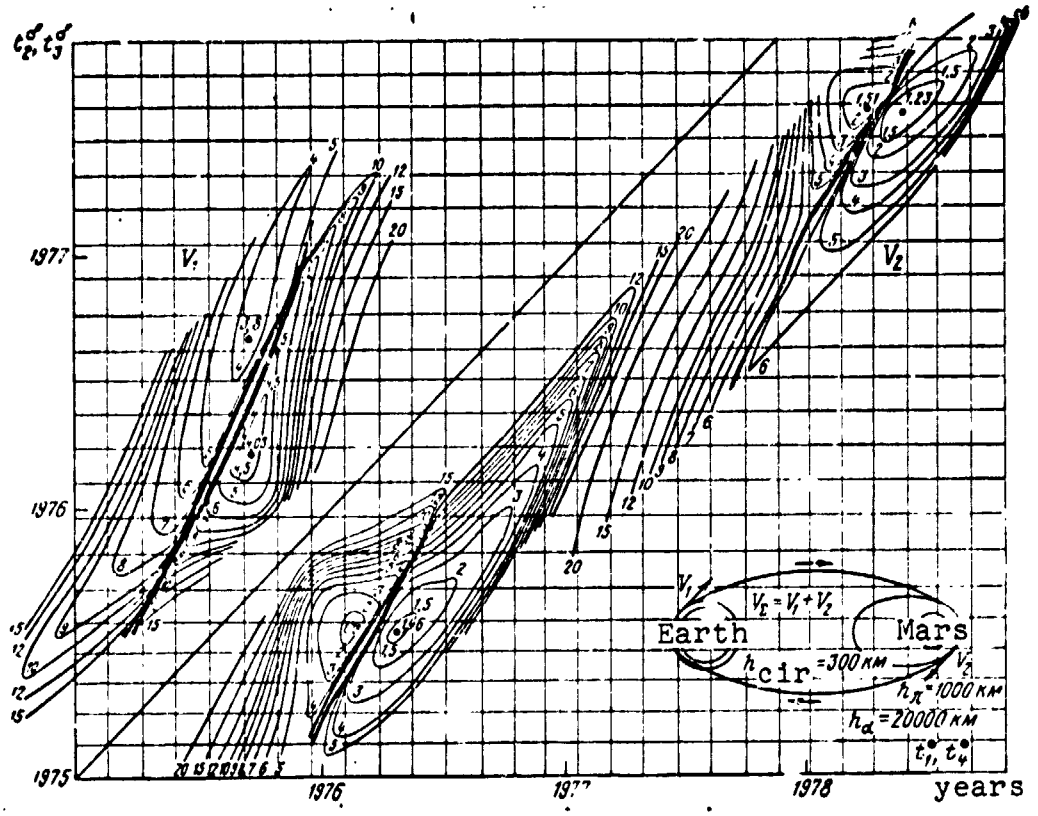

Figure 8.1.1. Characteristic velocity isoline field for two-impulse Mars roundtrip for 1975 flight cycle

The AES orbit launch velocity $V_1 = V_{st}^{\oplus}$ isolines are plotted above the coordinate system bisector (region of Earth-Mars flights) and the isolines of launch velocity $V_2 = V_{st}^{\sigma}$ from elliptic Mars satellite orbit are plotted below the bisector (region of Mars-Earth flights).

The distance from any point on the velocity V_1 isoline field to the bisector (in the direction of the coordinate axes) determines the flight time from Earth to Mars

$$\Delta t_f^{\oplus - \sigma} = t_2 - t_1;$$

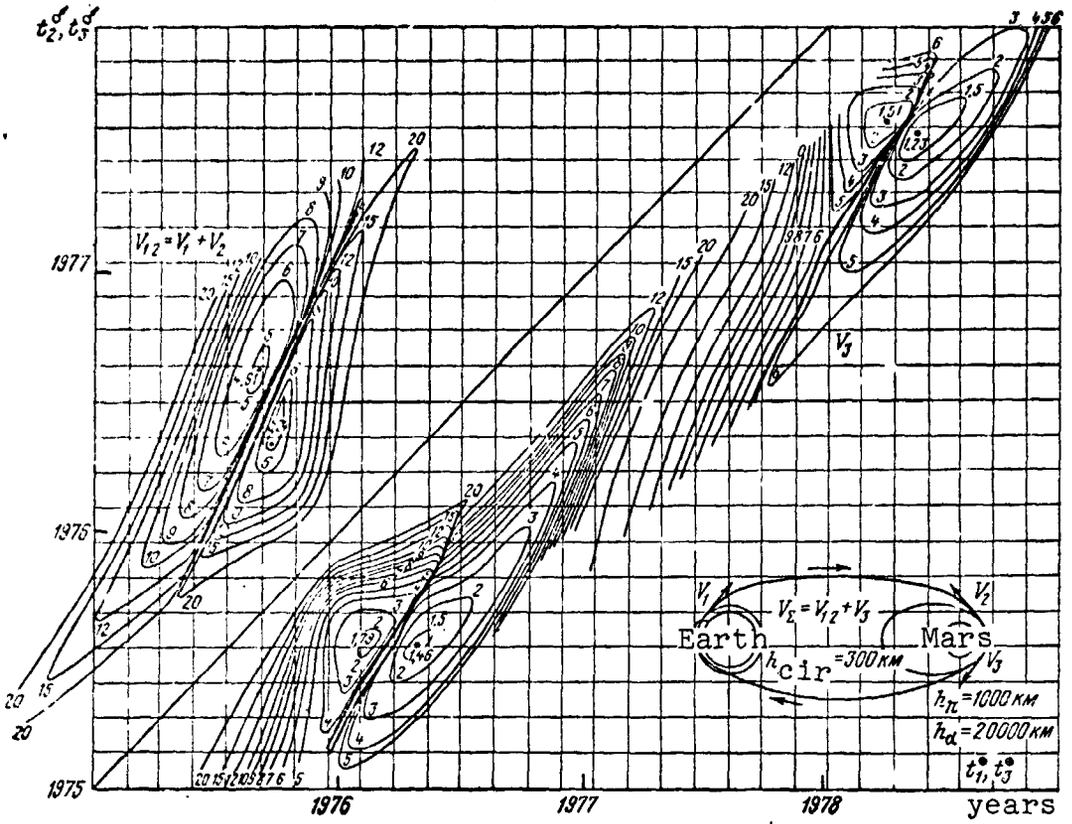

Figure 8.1.2. Characteristic velocity isoline field for three-impulse Mars roundtrip for 1975 flight cycle

and the analogous distance for a point on the V_2 isoline field /267 determines the Mars-Earth flight time:

$$\Delta t_f^{\sigma\to\oplus} = t_4 - t_3.$$

The stopover time on Mars (or in Mars satellite orbit)

$$\Delta t_{so} = t_3 - t_2.$$

The total roundtrip vehicle flight time

$$\Delta t_\Sigma = \Delta t_f^{\oplus\to\sigma} + \Delta t_{so} + \Delta t_f^{\sigma\to\oplus} = t_4 - t_1$$

Figure 8.1.2 shows the isoline field for three-impulse flights to Mars in 1975.

For fixed Earth launch t_1 and Mars arrival t_2 dates, there is a unique correspondence between the velocity V_1 (launch from AES orbit) and the velocity V_2 (braking into AMS orbit). Therefore, in the Earth-Mars flight region (above the bisector) the total velocity isoline field is plotted

$$V_{12}=V_1+V_2.$$

In the Mars-Earth flight region (below the bisector), the AMS orbit launch velocity V_3 isoline field is plotted.

The flight times $\Delta t_f^{\oplus-\sigma}$ and $\Delta t_f^{\sigma-\oplus}$, the stopover time Δt_{so}, and the total roundtrip flight time Δt_Σ are defined as described above.

Figure 8.1.3 shows the isoline field for the four-impulse scheme (accelerated trajectories) for the case of Earth's atmosphere entry velocity $V_{en}^{\oplus}$ prebraking to $V_{en}^{\oplus}$ = 15.5 km/sec. In this case,

$$V_{34}=V_3+V_4,$$

where $V_4 = V_{en}^{\oplus} - 15.5$.

Thus, for any flight scheme, we need to find on the isoline field the trajectories which minimize the total velocity, made up from two components:

$V_{\Sigma}=V_1+V_2$ for the two-impulse scheme;
$V_{\Sigma}=V_{12}+V_3$ for the three-impulse scheme;
$V_{\Sigma}=V_{12}+V_{34}$ for the four-impulse scheme.

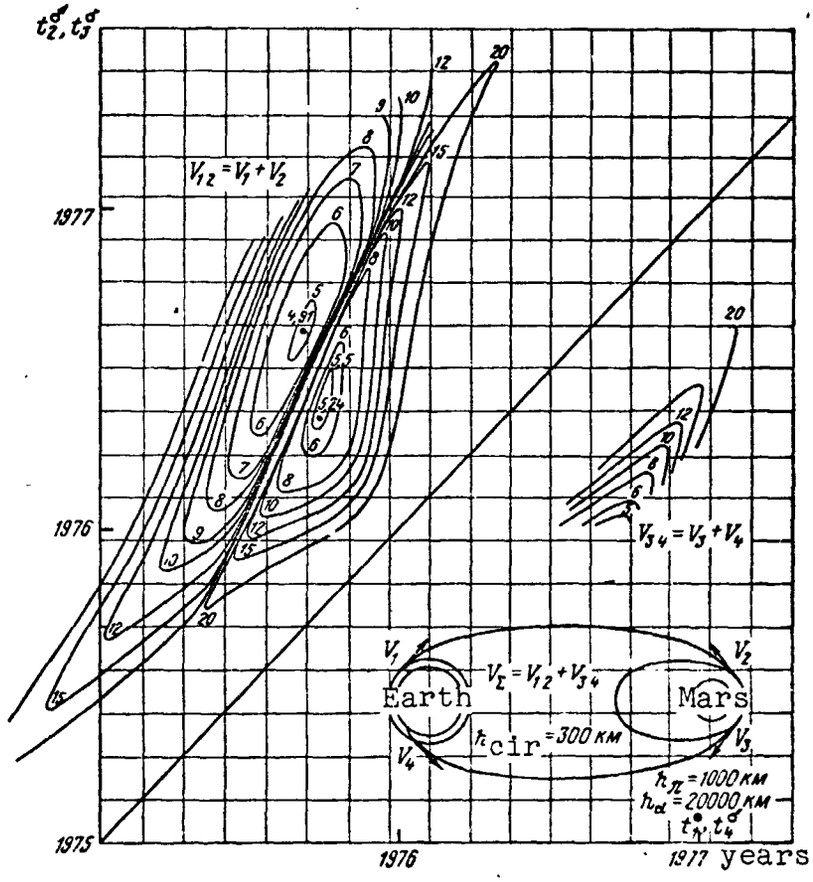

Figure 8.1.3. Characteristic velocity isoline field for four-impulse Mars roundtrip for 1975 flight cycle (braking to $V_{en}^{\oplus}$ = 15.5 km/sec)

Isolines of the velocity components for flights along botn the first semiorbit (region of isolines close to the bisector) and second semiorbit (region of isolines more distant from the bisector) trajectories are plotted on all the fields. These regions are separated from one another by an "energy ridge" — a narrow zone of high velocity values.

In order for the V_{Σ} optimization problem to be unambiguous, /269 all possible roundtrip flight trajectories can be broken down into the following four groups:

Group	⊕→♂	♂→⊕
I-I	Trajectory of first semiorbit	Trajectory of first semiorbit
II-II	Trajectory of second "	Trajectory of second "
I-II	Trajectory of first "	Trajectory of second "
II-I	Trajectory of second "	Trajectory of first "

Let us examine the flight trajectory optimization case when /270 there are no limitations on either the total flight time Δt_Σ or the stopover time Δt_{so}. In this case, the value of $V_{\infty\Sigma}$ will be smallest for each trajectory group for flights along trajectories with minimal velocity components (V_1 and V_2; V_{12} and V_3, and so on). The Earth launch date t_1 and Mars arrival date t_2 are determined as the coordinate corresponding to a minimum of the velocity V_1 or V_{12} (Mars launch date t_3 and Earth arrival date t_4 corresponding to minimum of V_3 or V_{34}). The velocity $V_{\infty\Sigma}$ values obtained must be the lowest of all possible values for the selected trajectory group.

This is the first energy minimum, corresponding to long duration flights with $\Delta t_\Sigma \approx 3$ years and $\Delta t_{so} \approx 1$ year.

The various trajectory groups will yield four different values of $V_{\infty\Sigma}$ and Δt_Σ, from which we can select the best combination of trajectory grouping wrt the semiorbits for the given flight cycle.

Let us examine the case when the total roundtrip flight time Δt_Σ is given. We shall find the trajectory which minimizes $V_{\infty\Sigma}$. We fix some Earth launch date t_1, which in turn determines the Earth return date:

$$t_4 = t_1 + \Delta t_\Sigma.$$

For fixed values of t_1 and t_4, we can plot the relations

$$V_1 = f_1(t_2) \text{ and } V_2 = f_2(t_2)$$

for two-impulse flight

$$V_{12} = f_{12}(t_2) \text{ and } V_3 = f_3(t_3)$$

for three-impulse flight and

$$V_{12} = f_{22}(t_2) \text{ and } V_{34} = f_{34}(t_2)$$

for four-impulse flight.

From these relations, we find the Mars arrival date t_2 and the Mars departure date t_3, which minimize V_{Σ} and the stopover time

$$\Delta t_{so} = t_3 - t_2.$$

With reduction of the time Δt_2, the optimal time Δt_{so} decreases and may even become negative. In this case, it is necessary to impose an additional limitation on

$$\Delta t_{so} \geq \Delta t_{so\ per}.$$

For $\Delta t_{so} = \Delta t_{so\ per}$, the optimization scheme for fixed t_1 and t_4 remains the same; however, now

$$V_1 = f_1'(V_2),\ V_{12} = f_{12}'(V_3) \text{ and } V_{12} = f_{34}'(V_{34}),$$

since $t_3 = t_2 + \Delta t_{so\ per}$.

Then, varying the Earth departure date t_1, we find for both of the examined variants that date which minimizes V_{Σ}. /271

A digital computer program was compiled in order to determine the optimal roundtrip SC interplanetary flight trajectory characteristics. The problem in the two variants described is formulated as follows (for the two-impulse flight scheme).

Variant 1. Find the values of t_1, t_2, and t_3 which provide $\min V_{x\Sigma}=V_1+V_2$ for given $\Delta t_2=t_4-t_1$.

Variant 2. Find the values of t_1 and t_2 which provide $\min V_{x\Sigma}=V_1+V_2$ for given values of

$$\Delta t_2=t_4-t_1;$$
$$\Delta t_{so}=t_3-t_2.$$

The search for the optimal t_1, t_2, and t_3 values was made by the coordinate descent method. With reduction of the time Δt_2, when the time Δt_{so} became $\Delta t_{so} \leq \Delta t_{so\ per}$, transition from variant 1 to variant 2 was provided.

The flight trajectory (trajectory group) semiorbit combination is specified. We select the best of the four possible flight trajectory group variants.

Figures 8.1.4 and 8.1.5 show curves of minimal values of $V_{x\Sigma}=f(\Delta t_2)$ for the 1975 cycle roundtrip flight trajectories for the /272 different trajectory groups. We see that, for each trajectory group, there are two minima:

— for Δt_Σ = 900 — 1000 days (long duration flights);

— for Δt_Σ = 350 — 550 days (accelerated flights).

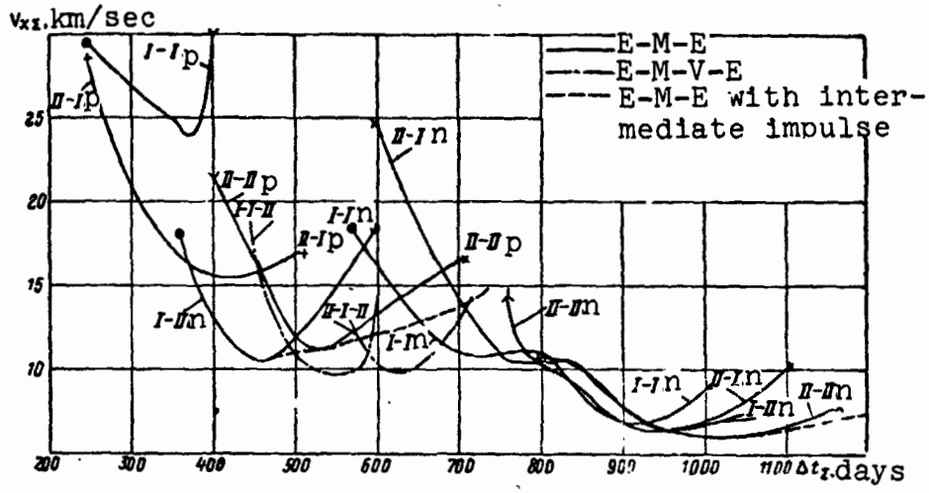

Figure 8.1.4. Total characteristic velocity for 1975 Mars cycle three-impulse roundtrip (n indicates natural cycle, p indicates preceding cycle)

The accelerated flight minimum corresponds to the case with limited stopover time (Δt_{so} = 30 days).

The V_{xz} minima differ very little for the different long duration flight trajectory groups. The shortest time Δt_z corresponds to trajectory group I-I (combination of first semi-orbit trajectories). The stopover time is not limited and is $\Delta t_{so} \approx$ 1 year.

We shall term trajectories of this type "natural cycle" trajectories. For such trajectories, Δt_z increases with reduction of the time V_{xz} . For certain trajectory groups, there is a "shelf" of nearly constant V_{xz} values in the Δt_z =700—800 days region, after which there is sharp increase of the V_{xz} values. As a rule, this V_{xz} increase takes place as a result of the Mars-Earth flight trajectory velocity components. When changing from the long duration trajectories to the accelerated trajectories, there is transition through the "energy ridge" separating the region of 1975 cycle ("natural cycle") return trajectories into the region of 1973 cycle return trajectories (we term them the "preceding cycle" trajectories).

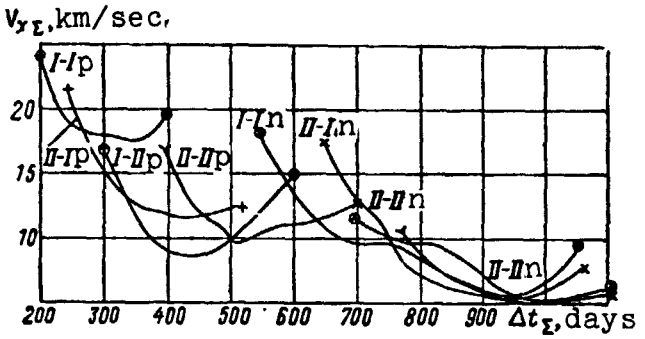

Figure 8.1.5. Total characteristic velocity for 1975 Mars cycle two-impulse roundtrip (n indicates natural cycle, p indicates preceding cycle)

This is explained by the fact that the Earth-Mars flight velocity component minimum regions have "steeper slopes" than the return trajectory velocity component minimum regions. For the accelerated trajectories, the lowest $V_{x\Sigma}$ occur for the I-IIp trajectory group (Earth-Mars trajectory of the first semiorbit, return flight trajectory of the second semiorbit) with total roundtrip flight time Δt_Σ = 430 — 460 days (with stopover time /273 Δt_{so} = 30 days). In this case, we obtain high Earth atmosphere entry speeds

$$V_{en}^{\oplus} = 20 — 23 \text{ km/sec.}$$

Figure 8.1.6 shows the influence of stopover time Δt_{so} on the accelerated flight trajectory characteristics. We see that, with increase of Δt_{so}, the total flight energy expenditures ($V_{x\Sigma}$ is the total characteristic velocity, the Earth atmosphere entry velocity $V_{en}^{\oplus} \approx V_{\pi}^{\oplus}$) and the total flight time Δt_Σ increase.

Let us see how the roundtrip flight trajectory characteristics change when using heliocentric trajectory segments with intermediate impulse application.

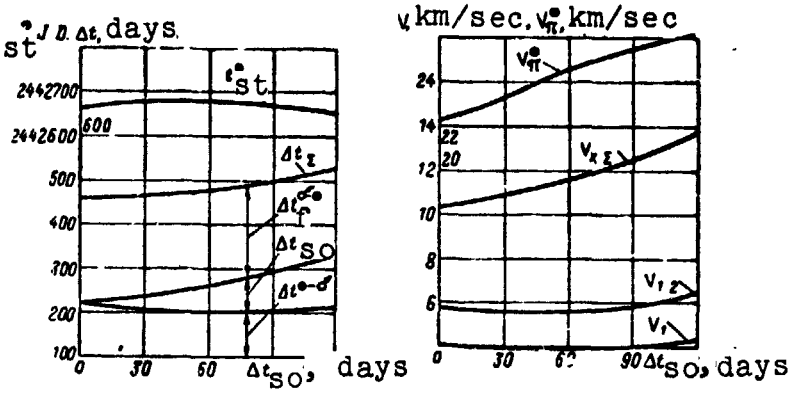

Figure 8.1.6. Influence of stopover time on accelerated trajectory characteristics. Three-impulse E-M-E flight scheme (1975 cycle), group I-II (elliptic AMS)

Figure 8.1.7 shows the impulse component isoline field

$$V_{12} = V_1 + V_2 + \Delta V_{in} \text{ and } V_3 + \Delta V_{in}$$

(ΔV_{in} is the intermediate impulse on the corresponding heliocentric trajectory segment) for the three-impulse Mars flight scheme in 1975. We compare this isoline field with the isoline field for the analogous scheme without intermediate impulse in Figure 8.1.2. We see that the energy expenditures in the region of the "energy ridges" separating the first and second semiorbit trajectories decreased markedly for both the Earth-Mars and Mars-Earth flights. For the two-impulse Earth-Mars trajectory segment (when defining the segments, we consider only impulses in the planetospheres), the isoline field became single-extremal. On the single-impulse Mars-Earth flight segment, the isoline field remained two-extremal, but with significantly leveled energy ridge. /274

The energy expenditures on both flight segments in the second semiorbit trajectory region also decreased markedly for large flight times, which reduced significantly the energy expenditures

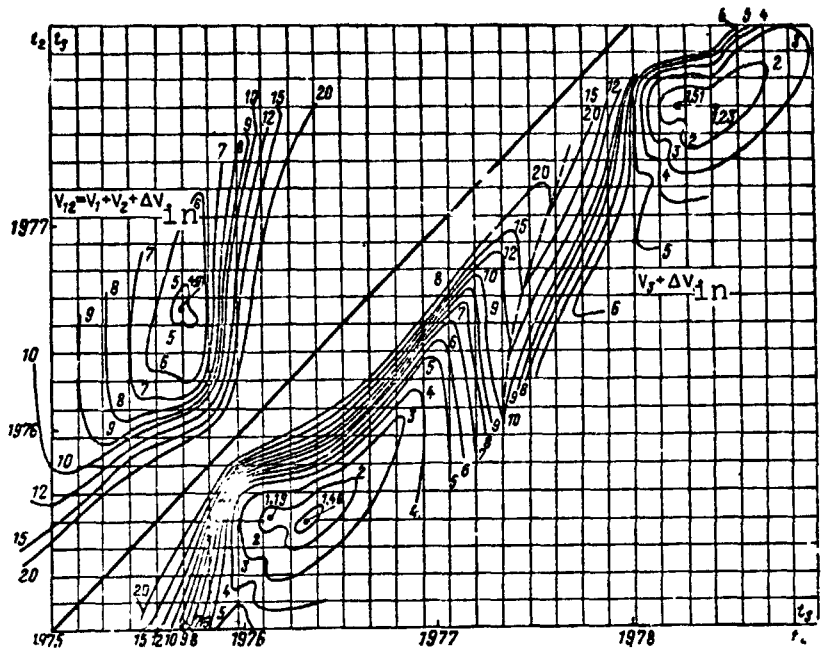

Figure 8.1.7. Characteristic velocity isoline field for three-impulse trajectories with intermediate impulse (1975 cycle)

in the region where the Mars-Earth trajectories for the "natural" and "preceding" cycles join. All this led (see Figure 8.1.4) to reduction of the energy expenditures for the "accelerated" trajectories to the left of the minima for the I-IIp and II-IIp semiorbit combination. For the "long duration" flight trajectories, the energy expenditures decreased for the semiorbit combination II-IIn for large values of $\Delta t_2 > 1000$ days.

Thus, the use of flight trajectories with intermediate impulse in the heliocentric segments makes it possible to reduce the energy expenditures for Δt_2 values between the "accelerated" and "long duration" trajectories.

Figure 8.1.4 also shows V_{∞} curves for flight trajectories to Mars with a maneuver in the gravity field of Venus, examined in § 2, Chapter 9. We see that use of the flight scheme along

the Earth-Mars-Venus-Earth route makes it possible to reduce still further the energy expenditures for Δt_2 values between the "long duration" and "accelerated" trajectories, as a result of which we obtain energy characteristics with $\Delta t_2 = 450-800$ days, which vary little. /275

OPTIMIZATION OF MARS FLYBY TRAJECTORIES WITH RETURN TO EARTH

Mars flyby trajectories using the single-impulse scheme (launch impulse from AES orbit) with passive planet flyby both outside the sphere of action ("distant flyby") and in the sphere of action ("close flyby") were examined in [5].

For trajectories of this class, the trajectories which are optimal wrt launch impulse lie in the vicinity of the so-called two-year flight trajectories (total flight time 730 days). We term trajectories of this type "long duration Mars flyby" trajectories. However, if we change over to the two-impulse Mars flyby scheme (second impulse in the planet's sphere of action), we can in most cases improve significantly the characteristics of the "long duration flyby" trajectories ($\Delta t_2 \approx 2$ years) and obtain a new class of "accelerated Mars flyby" trajectories with significantly shorter flight time $\Delta t_2 \approx 450-500$ days. In this case, the trajectory optimization criterion will be the total characteristic velocity

$$V_{x\Sigma} = V_{st}^{\oplus} + \Delta V_m^{\sigma},$$

where $V_{st}^{\oplus}$ is the launch characteristic velocity from AES orbit ($H_{cir} \approx 300$ km); ΔV_m^{σ} is the maneuver impulse in the Mars sphere of action for transfer from the planetocentric approach hyperbola to the return hyperbola.

The optimization parameters for such a flyby trajectory are:

1) Earth launch date $t^{\oplus}_{st}$;

2) Mars arrival date t^{σ}_{ar};

3) total flight time Δt_2 .

In order to find the unimodal search region, the trajectories are broken down into four groups of semiorbit combinations in the individual flight stages: I-II, I-I, II-II, and II-I. The flight trajectories are further broken down into long duration with $\Delta t_2 = 600-800$ days, and accelerated with $\Delta t_2 = 400-500$ days. This makes it possible to use the gradient search methods to find the optimal trajectories. The configuration method of [46] was used to obtain the optimal accelerated Mars flyby trajectories.

§ 2. CHARACTERISTICS OF INTERPLANETARY SC TRAJECTORIES WITH RETURN TO THE EARTH

CHARACTERISTICS OF MARS FLYBY TRAJECTORIES WITH RETURN TO THE EARTH

Two types of Mars flyby trajectories are possible — long duration (flight time about two years) and "accelerated" (flight time ~ 450 — 500 days). /276

The "long" flyby trajectories take place with essentially zero maneuver impulse in the Mars sphere of action. The energy expenditures of these trajectories for the best semiorbit combinations exceed only slightly the energy expenditures required for flights to Mars without return (see points ⊕ in Figure 8.2.1).

The "accelerated" Mars flyby trajectories require the application of a significant impulse ($\Delta V_m \approx 1$ — 4 km/sec) during Mars swingby in its sphere of action.

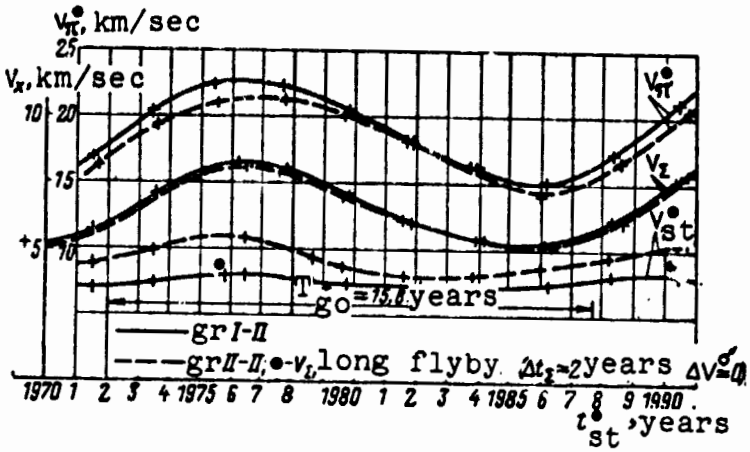

Figure 8.2.1. Energy expenditures for accelerated Mars flyby trajectories.

In the 1975 cycle, the flight trajectory semiorbit combination I-I yields a very high value of the $V_{\infty\Sigma}$ optimum for the accelerated trajectories. The optimal $V_{\infty\Sigma}$ value for the "long" trajectories of this semiorbit combination is $V_{\infty\Sigma} \approx 6$ km/sec for total flight time $\Delta t_\Sigma = 620$ days. The trajectory characteristics for the I-II combination are considerably better. For the accelerated trajectories, the minimum of $V_{\infty\Sigma} \approx 8$ km/sec for $\Delta t_\Sigma = 450$ days. The Earth launch and Mars maneuver impulses amount to about 4 km/sec.

For the long duration flyby trajectories, the minimum of $V_{\infty\Sigma} = 4.4$ km/sec for $\Delta t_\Sigma = 700-750$ days. The maneuver impulse in the Mars sphere of action $\Delta V_m^\sigma < 100$ m/sec, i.e., it reduces to the magnitude of a correcting impulse. The entry velocity into the Earth's atmosphere for the accelerated trajectories $V_\infty^\oplus = 22.5$ km/sec, for the long duration trajectories $V_\infty^\oplus = 12$ km/sec. /277

The group II-II accelerated trajectories also have good characteristics for the 1975 cycle. The quantity $V_{\infty\Sigma} = 8$ km/sec for $V_{\infty\Sigma} = 520$ days and the Earth atmosphere entry velocity $V_\infty^\oplus = 21$ km/sec. The optimum of the long duration trajectories for this

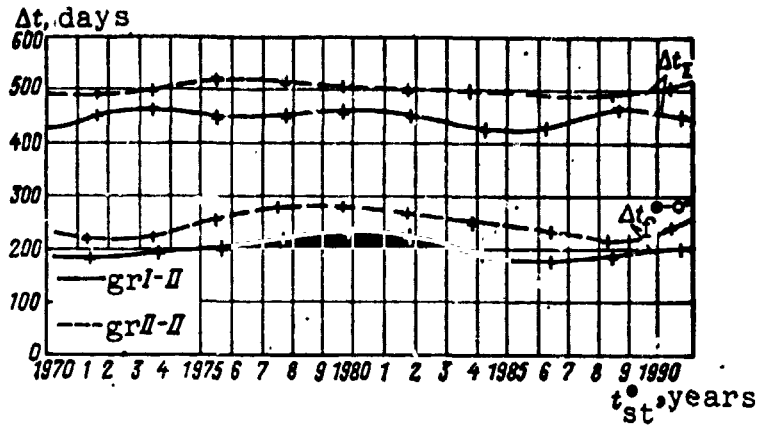

Figure 8.2.2. Flight time for accelerated Mars flyby trajectories

semiorbit group corresponds to the total time $\Delta t_\Sigma = 800$ days. The flight trajectories for the semiorbit combination II-I have the poorest characteristics for both the accelerated and long duration flight trajectories.

The flight cycle to Mars in 1975 is the worst. Check calculations showed that the qualitative picture of the optimal accelerated trajectory characteristics is approximately the same for the best flight cycle in 1986. The trajectory groups I-II and II-II are best. Figures 8.2.1 and 8.2.2 show, for these "best" trajectory combinations, the variations of the characteristics for the different flight cycles. The nominal curves connecting points of the characteristics of the different cycles have a periodicity approximately equal to the Mars great opposition period $T_{go} \approx 15.8$ years. This makes it possible to extrapolate the characteristics to cycles extending beyond the limits of the calculated characteristics, from 1970 to 1990. The "best" Mars flight cycle was in 1969 and will occur again in 1986. The 1975 and 1977 cycles are the worst.

For the best cycles $V_{\infty} = 5.1-5.2$ km/sec, $\Delta t_\Sigma = 425$ days for group I-II, $\Delta t_\Sigma = 490$ days for group II-II, $V_\infty = 14.5$ and 15.1 km/sec. /278

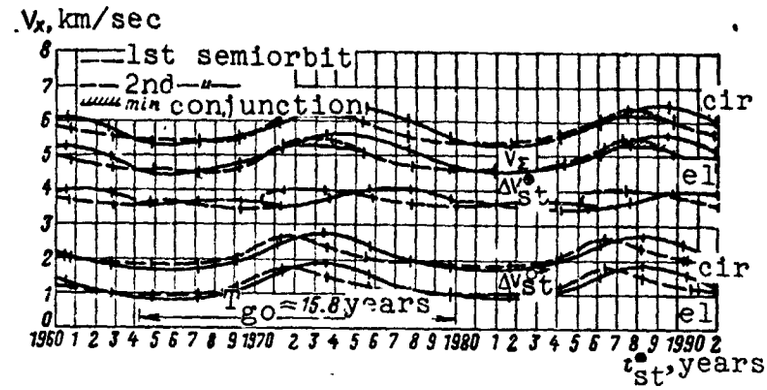

Figure 8.2.3. Characteristics of long duration two-impulse Mars roundtrips (circular and elliptic AMS)

For the worst cycles $V_{x\Sigma}$ = 8.2 — 8.3 km/sec, Δt_Σ = 450 days for group I-II, Δt_Σ = 520 days for group II-II, $V^{\odot}_{\infty}$ = 21.5 and 23 km/sec.

The large energy expenditures and high Earth atmosphere entry speeds for the worst flight cycles may be an obstacle when using accelerated direct Mars flyby trajectories in these flight cycles.

CHARACTERISTICS OF OPTIMAL TRAJECTORIES FOR VARIOUS MARS ROUNDTRIP FLIGHT SCHEMES

Calculations were made using the technique described above of the optimal trajectories for various Mars roundtrip schemes in 1970 — 1980.

Figures 8.2.3 and 8.2.4 show curves of the total velocity $V_{x\Sigma}$ and its components for long duration two-impulse and three-impulse Mars roundtrip schemes. The points denoted by bars correspond to the optimal launch dates, which repeat at approximately T_s = 2.135 years. These points are connected by smooth curves. The variation of $V_{x\Sigma}$ and its components for all the

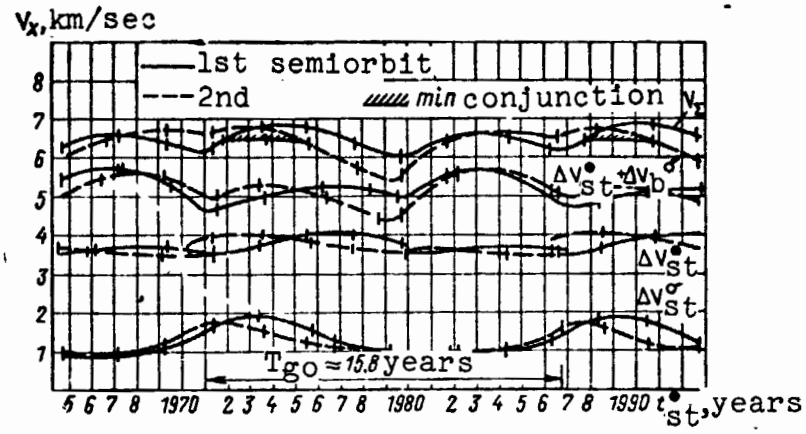

Figure 8.2.4. Characteristics of long duration three-impulse Mars roundtrips (elliptic AMS)

flight schemes is periodic with period equal to approximately the Mars great opposition period T_{go} = 15.8 years. The $V_{x\Sigma}$ range is approximately 500 — 800 m/sec for the best trajectory semiorbit combinations. For the two-impulse flight scheme, the values of $V_{x\Sigma}$ and its components are presented for insertion into circular AMS orbit with h_{cir} = 1000 km and elliptic orbit with h_{π} = 1000 km and h_{α} = 20,000 km. The values of $V_{x\Sigma}$ for insertion into elliptic orbit are approximately 1 km/sec less in comparison with insertion into circular orbit. The selected elliptic orbit provides energy expenditures close to the minimal possible value (insertion to a parabola reduces $V_{x\Sigma}$ by only 250 m/sec). For the three-impulse flight scheme $V_{x\Sigma}$ for insertion to an ellipse is about 2 km/sec less than for insertion into circular orbit. The total flight time of the long duration roundtrips lies in the range Δt_{Σ} = 900 — 1100 days. The Earth atmosphere entry velocity $V^{\oplus}_{*}$ = 11.5 — 12.3 km/sec. The stopover time at Mars $\Delta t_{so} \approx$ 330 — 450 days. /279

The characteristics of the optimal two- and three-impulse accelerated roundtrip schemes are also periodic. This period is

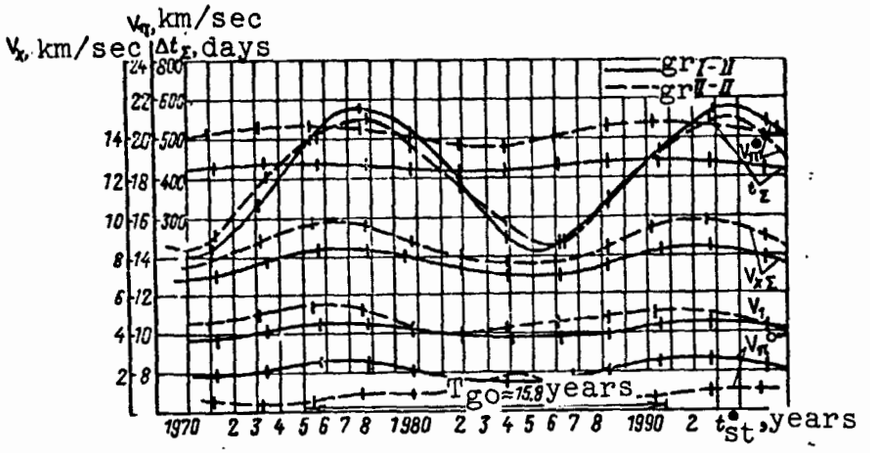
V_{π}, km/sec
V_{χ}, km/sec
Δt_{Σ}, days
gr I-II
gr II-II
$T_{go} \approx 15.8$ years
1970 2 3 4 5 6 7 8 1980 2 3 4 5 6 7 8 1990 2 $t^{\oplus}_{st}$, years

Figure 8.2.5. Characteristics of accelerated two-impulse Mars roundtrips (elliptic AMS, h_{π} = 1000 km, h_{α} = 20,000 km, Δt_{so} = 30 days.

approximately equal to the Mars great opposition period (Figures 8.2.5 and 8.2.6).

The total characteristic velocity $V_{x\Sigma}$ for the accelerated flights is significantly higher than for the long duration flights. The range of $V_{x\Sigma}$ variation for the various flight cycles is also significantly greater and equal to 1.5 — 2 km/sec. The Earth atmosphere entry velocity $V_{*}^{\oplus}$ (from 14 to 23 km/sec) changes particularly markedly. The minimal $V_{*}^{\oplus}$ value corresponds approximately to minimum $V_{x\Sigma}$. However, the total flight time is quite stable and amounts to Δt_{Σ} = 430 — 530 days with variation range for trajectories of one semiorbit combination of no more than 50 days. The Mars atmosphere entry velocity for the two-impulse flight scheme is approximately $V_{*} \approx 6.5$ — 8.5 km/sec. The AES orbit launch velocity for the trajectories with semiorbit combination I-II is quite stable and is $V^{\oplus}_{st}$ = 3.5 — 4 km/sec for the three-impulse scheme and $V^{\oplus}_{st} \approx$ 3.8 — 4.3 km/sec for the two-impulse scheme. /280

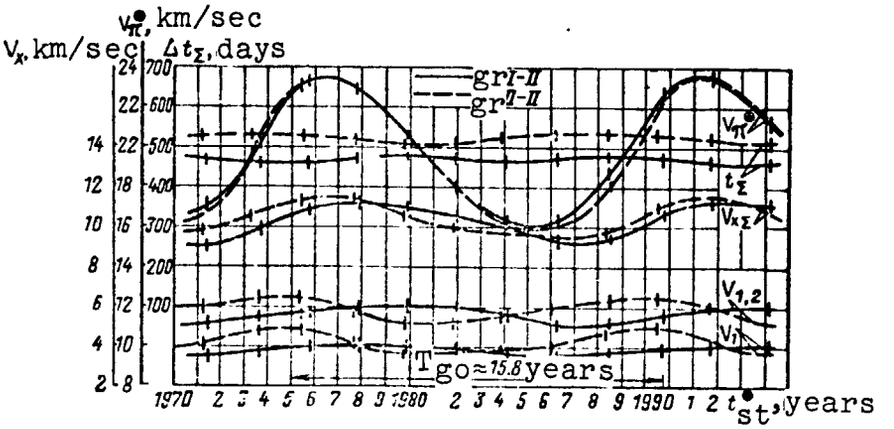

Figure 8.2.6. Characteristics of accelerated three-impulse Mars roundtrips (conditions same as in legend of Figure 8.2.5)

The large variation of the Mars flight trajectory characteristics for the various flight cycles leads to a situation in which there are "good" (1984, 1986) and poor (1975, 1977) flight cycles. In the "good" flight cycles, the energy expenditures (total velocity $V_{\infty\Sigma}$) and the Earth atmosphere entry velocity $V_{\pi}^{\bullet}$ are minimal, which makes them favorable for realizing direct flights to Mars. /281

CHARACTERISTICS OF VENUS FLYBY TRAJECTORIES WITH RETURN TO THE EARTH

Such trajectories may be of interest for both the automatic vehicle returning to the Earth and the piloted vehicle during the first flights to the planet. The long duration Venus flyby trajectories with total flight time $\Delta t_{\Sigma} \approx 2$ years have energy characteristics close to the flight trajectories to Venus without return. The maneuver impulse in the Venus sphere of action is equal to zero.

Accelerated Venus flyby trajectories with return to the Earth with total flight time $\Delta t_{\Sigma} \approx$ 350 — 500 days are possible. The trajectories with semiorbit combinations I-II and II-II have

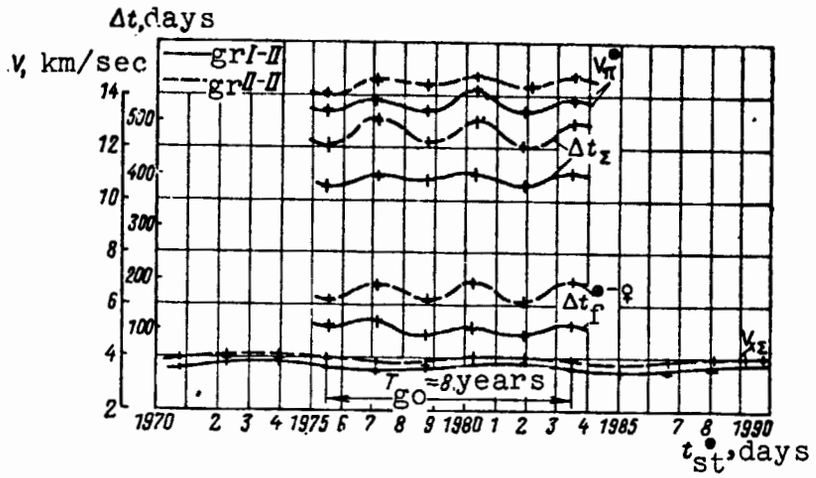

Figure 8.2.7. Characteristics of accelerated Venus flyby trajectory (ΔV^{φ}_{m} < 100 m/sec)

the best characteristics. The semiorbit combinations I-I and II-I yield values of the total characteristic velocity which are higher by 1 — 2 km/sec.

The Venus flyby trajectory characteristics have a small range of variation (Figure 8.2.7). Thus, for V_{∞} the range of variation for the various flight cycles is ΔV_{∞} = 300 m/sec. The optimal trajectories correspond to small values of the velocity impulse in the Venus sphere of action ($\Delta V^{\varphi}_{m} \leqslant 100$ m/sec). The total flight time along the Venus flyby trajectories is also quite stable and amounts to $\Delta t_{\Sigma} \approx$ 380 — 400 days for trajectories with the semiorbit combination I-II and Δt_{Σ} = 450 — 500 days /282 for the combination II-II. We note that the Venus flyby V_{∞} (V_{∞} = 3.6 — 4 km/sec for the semiorbit combination I-II) exceeds only slightly the velocity 3.4 — 3.8 km/sec required for flights to Venus without return. The vehicle entry velocity into the Earth's atmosphere $V_{\pi}^{\oplus}$ = 14 — 14.8 km/sec for the semiorbit combination II-II and $V_{\pi}^{\oplus}$ = 13 — 14.2 km/sec for I-II. The optimal Venus flyby cycles repeat at approximately the Venusian synodic period $T_s \approx$ 1.6 years. The optimal trajectory cycles repeat at

approximately the Venusian great opposition period $T_{go} \approx 8$ years. Considering this, we can extrapolate approximately the optimal trajectory characteristics to other flight cycles.

§ 3. SELECTION OF PLANET PARKING ORBIT SHAPING SCHEME

In most published works, both Soviet and foreign, on optimization of roundtrip vehicle flight trajectories to a planet, it is assumed that the braking maneuver from the approach hyperbola to parking orbit around the planet and the launch from this orbit into the departure hyperbola takes place at the pericenter points of these trajectories. In the real situation, this case cannot usually be realized. The requirement naturally arises to find the maneuver which can actually be realized to shape the parking orbit at the planet with minimal energy expenditures. In the present section, we compare three orbit shaping maneuver variants, combined from a maneuver in the elliptic parking orbit plane (rotation of the elliptic orbit axis of apsides, nonpericentral ellipse-hyperbola transfers) and elliptic orbit plane rotation at its apocenter (see § 2, Chapter 4). This comparison does not pretend to provide strict optimization of the parking orbit shaping maneuver. However, the resulting minimal energy maneuver varient, based on nonpericentral ellipse-hyperbola transfers, is apparently close in energy expenditures to the minimal scheme.

We examine cases of parking orbit shaping both in the plane of the planet approach vector and advanced planet launch vector (base plane) and in a plane of arbitrary inclination to the base plane.

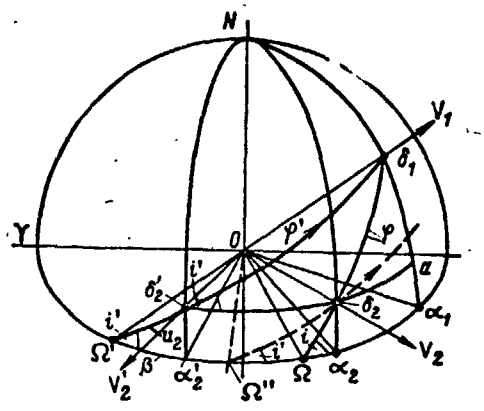

Figure 8.3.1. Schematic for determining parking orbit inclination i

ORBIT IN PLANE OF PLANET APPROACH AND DEPARTURE VECTORS

Let the directions of the velocity vectors on the asymptotes of the approach and departure hyperbolas (V_1 and V_2 in Figure 8.3.1) be given. The directions of these vectors are characterized in the equatorial planetocentric coordinate system by the angles α_1 and α_2 — right ascension, δ_1 and δ_2 — declination. /283

In this case, it is natural to shape the parking orbit in the plane of the vectors V_1 and V_2. The inclination of this orbit to the equator is i and the ascending node longitude is Ω. The angle φ between the vectors V_1 and V_2 is found from the spherical triangle $\delta_2 a \delta_1$

$$\cos\varphi = \cos(\alpha_1 - \alpha_2)\cos(\delta_1 - \delta_2).$$

During the stopover time Δt_{so} at the planet, the parking orbit node longitude changes by the amount*

$$\Delta\Omega = -\frac{2\pi\varepsilon}{\mu_{pl} p^2}\cos i\,\frac{\Delta t_{so}}{T},$$

and the axis of apsides turns through the angle

$$\Delta\omega = \frac{\pi\varepsilon}{\mu_{pl} p^2}(5\cos i - 1)\,\frac{\Delta t_{so}}{T}.$$

* See § 1, Chapter 2.

Here ε is the coefficient characterizing planet flattening; μ_{pl} is the gravitational constant of the planet; p is the parking orbit parameter; $T = 2\pi(a^{3/2}/\sqrt{\mu_m})$ is the period of revolution in the parking orbit; a is the parking orbit semimajor axis.

In this case, the parking orbit plane will pass through the vector $\bar{V}_1$ and the advanced vector $\bar{V}_2$, (base plane). The direction of the vector $\bar{V}_2$, is characterized by the angles $\alpha_2' = \alpha_2 + \Delta\Omega'$, $\delta_2' = \delta_2$. /284 In this case, the parking orbit inclination will be i_1' and the nodal longitude will be Ω'. The angle between the vectors V_1 and V_2' is equal to φ' (see Figure 8.3.1). During the stopover time Δt_{so}, the orbital inclination i_1' does not change but the nodal longitude becomes

$$\Omega'' = \Omega' + \Delta\Omega',$$

where

$$\Delta\Omega' = \frac{2\pi\varepsilon}{\mu_{pl}p^2} \cos i' \frac{\Delta t_{so}}{T}.$$

In this case, at the end of the stopover time, the parking orbit plane will pass through the launch velocity vector V_2. We find from the spherical triangle $\delta_2' a \delta_1$

$$\operatorname{tg}(\delta_1 - \delta_2) = \sin(\alpha_1 - \alpha_2 - \Delta\Omega')\operatorname{tg} i'.$$

After transformation of this expression, we have

$$\frac{\operatorname{tg}(\delta_1 - \delta_2)}{\operatorname{tg} i'} = \sin(\alpha_1 - \alpha_2)\cos\Delta\Omega' - \cos(\alpha_1 - \alpha_2)\sin\Delta\Omega'.$$

This transcendental equation defines the angle i'. The angle φ' between the vectors V_1 and V_2 (from the spherical triangle $\delta_2' a \delta_1$.)

$$\cos\varphi' = \cos(\alpha_1 - \alpha_2 - \Delta\Omega')\cos(\delta_1 - \delta_2).$$

The angular distance u_2 of the vector V_2' from the line of nodes Ω' is found from the spherical triangle $\Omega'\alpha_2'\delta_2'$

$$\sin u_2 = \frac{\sin \delta_2}{\sin i'}.$$

From the spherical triangle $\Omega'\alpha_2'\delta_2'$, we obtain

$$\sin \beta = \frac{\operatorname{tg} \delta_2}{\operatorname{tg} i'}.$$

The nodal longitude Ω' will be

$$\Omega' = \alpha_2 + \Delta\Omega' - \beta = \alpha_2 + \Delta\Omega' - \arcsin \frac{\operatorname{tg} \delta_2}{\operatorname{tg} i'}.$$

When determining i on a digital computer, it is advisable to determine i' by successive approximations from the following recurrence relations without solving the transcendental equation

$$\operatorname{tg} i^{(k)} = \frac{\operatorname{tg} (\delta_1 - \delta_2)}{\sin \left(\alpha_1 - \alpha_2^{(k)}\right)},$$

$$\Delta\Omega^{(k)} = -\frac{2\pi\varepsilon}{\mu_{pl} p^2} \cos i^{(k)} \frac{\Delta t_{so}}{T},$$

$$\alpha_2^{(k+1)} = \alpha_2 + \Delta\Omega^{(k)}.$$

Taking into account the axis of apsides rotation resulting from planet flattening, we find the angle $\varphi'' = \varphi' - \Delta\omega$ between the asymptotes of the hyperbolas, which is necessary for calculating the transfer maneuver in the plane of the vectors V_1, V_2. /285

We shall examine several variants of the transfer maneuver between the hyperbolic arrival orbit, elliptic parking orbit, and departure hyperbola. The parking orbit pericenter radius r_π and the apocenter radius r_α are given. All these transfer variants are based on a series of elementary maneuvers, the technique for calculating which was described in § 2, Chapter 4.

COMPARISON OF VARIOUS PARKING ORBIT SHAPING MANEUVER VARIANTS IN THE BASE PLANE

The following variants of coplanar transfer maneuver from the approach hyperbola to the parking orbit and launch from the parking orbit into the planet departure hyperbola are possible.

1. Pericentral transfers between the hyperbolas and the elliptic orbit with rotation of the ellipse axis of apsides;

a) with single-impulse rotation of the elliptic orbit apsidal axis.

b) with two-impulse rotation of the elliptic orbit apsidal axis.

2. Nonpericentral transfer between the hyperbolic and elliptic orbits.

Let the angle between the velocity vectors $\bar{V}_\infty^b$ and $\bar{V}_\infty^{st}$ on the asymptotes of the hyperbolas be φ (Figure 8.3.2). Two transfer modes and two parking orbit positions are possible. The first transfer mode (solid lines in Figure 8.3.2) yields larger rotation Δv_2* of the apsidal axes of the hyperbolas than the second mode (dashed lines). The angle between the apsidal axes of the hyperbolas (transfer points)

$$\Delta v_2 = \pi \pm \varphi - (\alpha_b + \alpha_{st}).$$

The "+" sign is for the first transfer mode; the "-" sign is for the second mode.

---

* We note that, in the nonpericentral transfer variant, the points of transfer from the hyperbola to the ellipse coincide with the pericenter of the hyperbola.

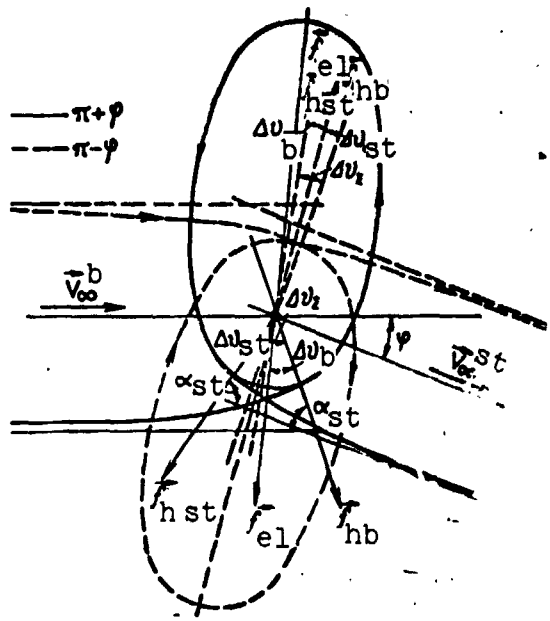

Figure 8.3.2. Planar ellipse-hyperbola-ellipse transfer

For pericentral transfers, the angle Δv_1 is equal to the required ellipse apsidal axis rotation angle. For nonpericentral transfer, the angles Δv are equal to the anomaly of the braking point on the ellipse or point of launch from the ellipse. In the general case, when the approach and departure hyperbola velocity moduli V_∞ are not equal, the relation holds

$$\Delta v_b + \Delta v_{st} = \pi \pm \varphi - (\alpha_b + \alpha_{st}) \quad (\Delta v_b \neq \Delta v_{st}).$$

The optimal redistribution of v_b and v_{st} minimizes /286

$$\Delta \tilde{V}_{x\Sigma} = \Delta \tilde{V}_b + \Delta \tilde{V}_{st},$$

where $\Delta \tilde{V}_b$ and $\Delta \tilde{V}_{st}$ are the velocity impulses in braking (or launching) from the hyperbola to the ellipse. Figure 8.3.3 shows for $r_*=5$ the additional energy expenditures on the transfer maneuver with noncoinciding apsidal axes of the braking and launching hyperbolas in comparison with pericentral transfers with coinciding apsidal axes of the hyperbolas. The quantity

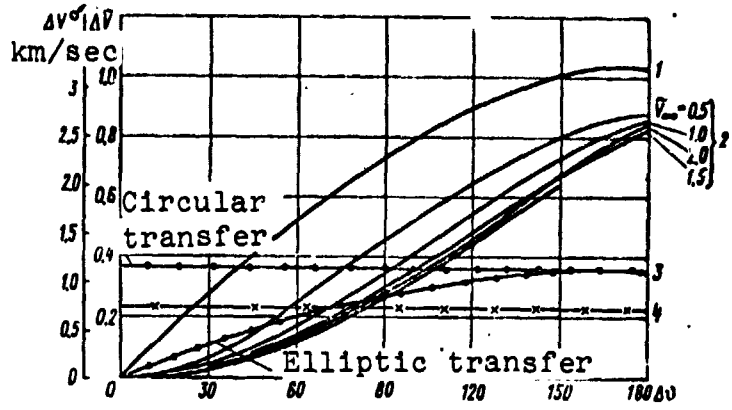

Figure 8.3.3. Characteristic of different planar ellipse-hyperbola-ellipse transfer variants for $\bar{r}_a=5$:

1- one-impulse rotation of axis of apsides; 2- nonpericentral transfer; 3- two-impulse rotation of axis of apsides; 4- two-impulse parabolic transfer

$$\Delta\tilde{V} = \tilde{V}_{x\Sigma} - (\Delta\tilde{V}_{\pi}^{b} + \Delta\tilde{V}_{\pi}^{st}),$$

where $\tilde{V}_{x\Sigma}$ are the total expenditures on the transfer maneuver for noncoinciding apsidal axes of the hyperbolas; $\Delta\tilde{V}_{\pi}^{b}$, $\Delta\tilde{V}_{\pi}^{st}$ are the expenditures on pericentral braking (launch) from the hyperbola to the ellipse.

We see that the transfer maneuver with single-impulse rotation of the apsidal axis of the ellipse corresponds to the largest energy expenditures. The transfer maneuver with two-impulse rotation of the apsidal axis becomes advantageous in comparison with the nonpericentral transfer variant only for large apsidal axis rotation angles Δv_2. Moreover, its advantages /287 show up at smaller values of Δv_2 with increase of the elliptic parking orbit relative radius r_α. However, for realistic values of $v_\infty \approx 1-2$ and $\Delta v_2 < 60°$, the most economical variant is nonpericentral transfer between the hyperbolas and the ellipse. Figure 8.3.4 shows the relation $\Delta\tilde{V}_{x\Sigma}=f(\bar{r}_a)$ for the different transfer

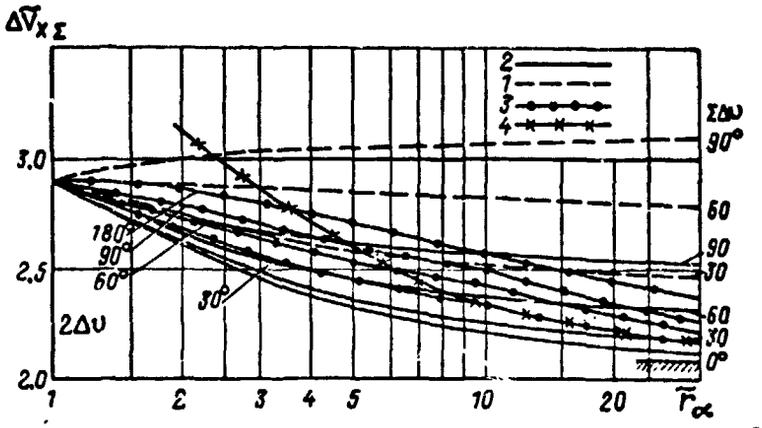

Figure 8.3.4. Comparison of different planar ellipse-hyperbola-ellipse transfer variants for $\tilde{r}_{\pi 2}$ (notations same as in Figure 8.3.3)

variants. We see that, in most cases, the transfer energy expenditures diminish with increase of $\tilde{r}_\alpha$.

ORBIT OF ARBITRARY INCLINATION TO THE BASE PLANE

As the base plane we take that in which the arrival velocity /288 vector $\bar{V}_\infty^b$ and the launch vector velocity vector $\bar{V}_\infty^{st}$ lie (velocities on the asymptotes of the hyperbola bundle at the entrance to and departure from the planet sphere of action).

We consider the inclination i_b of the approach hyperbolic orbit plane to the reference plane to be given. The values of r_π and r_α of the elliptic parking orbit are also given. We examine the following variants of the parking orbit shaping maneuver and launch from this orbit:

Variant I — maneuver with two pericentral ellipse-hyperbola transfers and various variants of two-impulse ellipse apsidal axis rotations;

Variant II — maneuver with two pericentral ellipse-hyperbola transfers and two single-impulse ellipse apsidal axis rotations;

Variant III — maneuver with two nonpericentral ellipse-hyperbola transfers.

In all variants, elliptic orbit plane rotation is required.

We shall examine the individual stages and variants of the maneuvers for shaping a parking orbit of arbitrary inclination to the base plane.

MANEUVERS WITH PERICENTRAL TRANSFERS BETWEEN ELLIPSE AND HYPERBOLA

In this case, the maneuver of parking orbit shaping and launch from this orbit consists of the following stages:

— two pericentral transfers between the ellipse and the approach and departure hyperbolas;

— rotation of the ellipse apsidal axis;

— rotation of the elliptical orbit plane.

As before, two variants of ellipse absidal axis rotation are possible — single-impulse and two-impulse.

Maneuver with two-impulse circular rotation of apsidal axis and rotation of the elliptical orbit plane (variant Ia). The inclination i_b of the approach hyperbola plane to the reference plane is given (Figure 8.3.5). Initially, at point 1, a planar pericentral transfer maneuver from the approach hyperbola to an

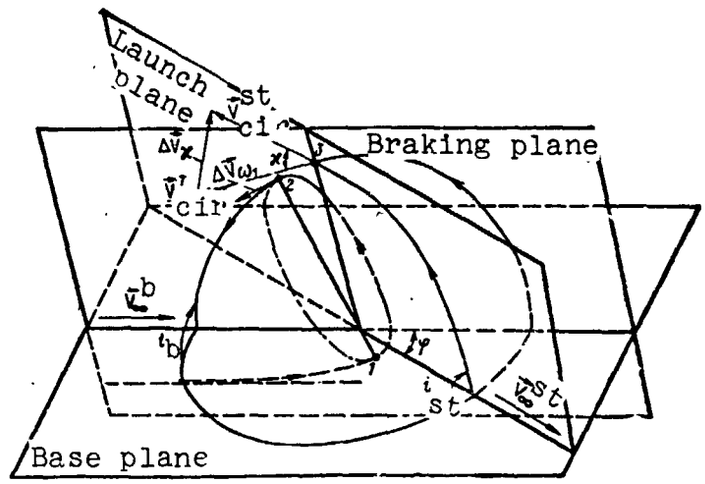

Figure 8.3.5. Schematic of nonplanar ellipse-hyperbola-ellipse transfer with two-impulse rotation of apsidal axis (variant Ia)

ellipse with given values of r_π and r_α is performed, then at the point 2, a planar transfer maneuver to a circular intermediate orbit with radius r_α is performed. Then, at point 3, follows rotation of the plane of this circular orbit through the angle κ, then transfer from the circular orbit to the launch ellipse. The final stage is the pericentral launch maneuver from the ellipse into the departure hyperbola.* The inclination i_{st} of the launch ellipse orbit plane is selected to be optimal wrt minimizing the energy expenditures on the overall maneuver. Let the angle between the planetary sphere of action entry vector $\bar{V}_\infty^b$ and departure vector $\bar{V}_\infty^{st}$ be φ. The angle of rotation of the velocity vector in the circular intermediate orbit is κ. It follows from the spherical triangle that

/289

$$\cos(\pi - \kappa) = -\cos i_b \cos i_{st} + \sin i_b \sin i_{st} \cos(\pi - \varphi),$$

* The last two stages are not shown in Figure 8.3.5.

hence

$$\cos \kappa = \cos i_b \cos i_{st} + \sin i_b \sin i_{st} \cos \varphi .$$

For given r_π and r_α of the elliptic parking orbit, the minimum total impulse will occur for minimum intermediate orbit plane rotation impulse ΔV_*. For given i_b and φ, this corresponds to a maximum of $\cos \kappa$. Therefore,

$$\frac{\partial(\cos \kappa)}{\partial i_{st}} = -\cos i_b \sin i_{st} + \sin i_b \cos i_{st} \cos \varphi =$$

or

$$\sin^2 i_b \cos^2 \varphi (1 - \sin^2 i_{st}) = \cos^2 i_b \sin^2 i_{st}.$$

The optimal value $i_{st\ opt}$ is found from

$$\sin^2 i_{st} = \frac{\sin^2 i_b \cos^2 \varphi}{\cos^2 i_b + \sin^2 i_b \cos^2 \varphi}$$

The total relative impulse for two-impulse rotation of the apsidal axis (impulse $\Delta \tilde{V}_\omega$) and rotation of the plane through the angle κ (impulse $\Delta \tilde{V}_\kappa$) /290

$$\Delta \tilde{V}_{\Sigma} = \Delta \tilde{V}_\omega + \Delta \tilde{V}_\kappa .$$

The total relative impulse $\Delta \tilde{V}_{\Sigma}$ as a function of the angle φ for various approach orbit inclinations i_b and $\tilde{r}_a = 5$ is shown in Figure 8.3.6. The largest ΔV_{Σ} values correspond to braking plane inclination $i_b = \pm 90^\circ$. The transfer maneuvers are symmetric relative to the base plane. The energy expenditures of this transfer variant (Ia) depend crucially on the elliptic parking orbit apocenter radius $\tilde{r}_a$.

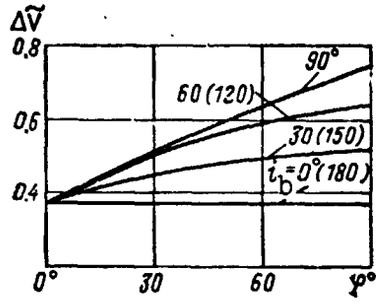

Figure 8.3.6. Total impulse $\Delta\tilde{V}_\Sigma$ versus angles φ and i for variant Ia ($\bar{r}_a$=5)

Maneuver with single-impulse rotation of apsidal axis and rotation of elliptic orbit plane (variant II). The transfer maneuver to the parking orbit and departure from this orbit takes place as follows (Figure 8.3.7). At point 1 (pericenter of approach hyperbola and ellipse), the vehicle transitions to the first elliptic orbit. At point 2, the radial impulse $\Delta V_{\omega b}$ is used to transfer the vehicle to the second elliptic orbit, rotated relative to the first through the angle ω_b. Then, at point 3, the impulse ΔV_κ rotates the plane of the ellipse relative to the apsidal axis through the angle κ. The launch plane is shaped by this maneuver. In this plane, the apsidal axis of the ellipse is rotated through the angle ω_{st} and from the pericenter of this rotated ellipse, pericentral transfer to the departure hyperbola is accomplished (the last stages of the maneuver are not shown in Figure 8.3.7). The required characteristics of this maneuver are found from the relations

$$\cos\kappa = \cos i_b \cos i_{st} + \sin i_b \sin i_{st} \cos\varphi;$$

$$\cos\gamma_{st} = -\cos\gamma_b \cos\varphi + \sin\gamma_b \sin\varphi \cos i_b;$$

$$\sin i_{st} = \sin i_b \frac{\sin\gamma_b}{\sin\gamma_{st}};$$

$$\omega_{st} = \gamma_{st} - \alpha_{st} \text{ and } \omega_b = \gamma_b = \alpha_b.$$

For given relative elliptic parking orbit apocenter height $\tilde{r}_a$, /291
angle φ between the vectors $\bar{V}_\infty^b$ and $\bar{V}_\infty^{st}$, and braking hyperbola plane inclination i_b, the calculation is made as follows. By

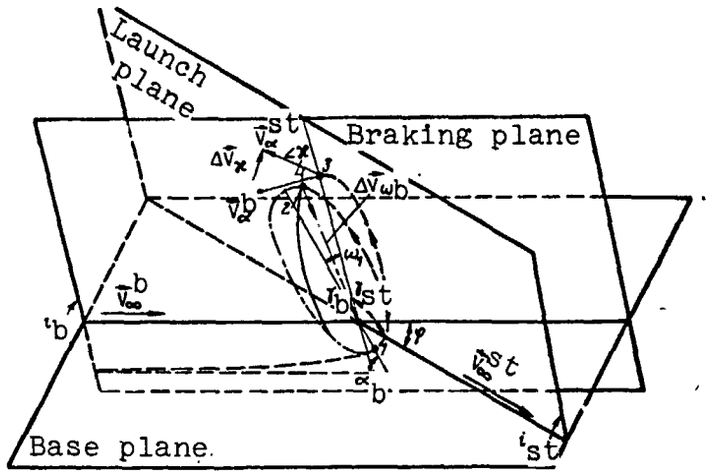

Figure 8.3.7. Schematic of nonplanar hyperbola-ellipse-hyperbola transfer with single-impulse rotation of the apsidal axis (variant II)

selecting various values of γ_b, we determine its optimal value which minimizes the energy expenditures

$$\Delta\tilde{V}_{x\Sigma} = \Delta\tilde{V}_{\omega b} + \Delta\tilde{V}_{\omega st} + \Delta\tilde{V}_{x},$$

where

$$\Delta\tilde{V}_{\omega} = \Delta\tilde{V}\sin\frac{\omega}{2};$$
$$\Delta\tilde{V}_{x} = 2\tilde{V}_{a}\sin\frac{\varkappa}{2}$$

The values of $\Delta\tilde{V}_{\omega} = f(\tilde{r}_a)$ and $\Delta\tilde{V}_{x} = f(\varkappa, \tilde{r}_a)$ are shown in Figures 4.2.1 and 4.2.2. The optimal departure hyperbola inclination i_{st} corresponds to the optimal γ_b. The optimal value $\omega_b^{opt} = 0$. Of interest is the degenerate transfer case, when $\omega_b = \omega_{st} = 0$. In this case,

$$\cos i_b^* = \frac{\cos\alpha_{st} + \cos\alpha_b + \cos\varphi}{\sin\alpha_b \sin\varphi};$$

$$\sin i_{st}^* = \sin i_b \frac{\sin\alpha_b}{\sin\alpha_{st}};$$

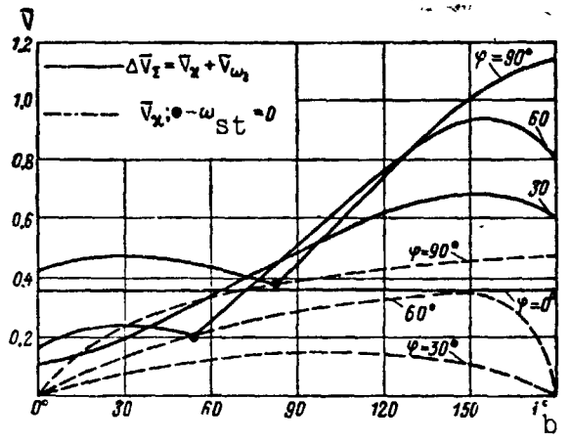

Figure 8.3.8. Total impulse ΔV_Σ as function of i_b and φ (variant II) for $\tilde{r}_\alpha = 5$, $\tilde{V}_\infty^b = 1$, $\tilde{V}_\infty^{st} = 2$ and $\omega_{b\ opt} = 0$

$$\cos\kappa^* = \cos i_b \sqrt{1 - \sin^2 i_b \left(\frac{\sin\alpha_b}{\sin\alpha_{st}}\right)^2} + \sin i_b^2 \frac{\sin\alpha_b}{\sin\alpha_{st}}.$$

And, if in addition $\tilde{V}_\infty^b = \tilde{V}_\infty^{st} (\alpha_b = \alpha_{st} = \alpha)$, then /292

$$\cos i_b = \frac{\cos\alpha(1-\cos\varphi)}{\sin\alpha\sin\varphi} = \frac{\operatorname{tg}\frac{\varphi}{2}}{\operatorname{tg}\alpha};$$

$$\cos\kappa = \cos^2 i_b + \sin^2 i_b \cos\varphi.$$

Figure 8.3.8 shows the dependence of the total impulse $\Delta\tilde{V}_{x\Sigma}$ and its components on launch orbit inclination i_b for various φ. The relation $\Delta\tilde{V}_{x\Sigma} = f(i_b)$ has a quite complex nature. We see points (for φ=60 and 90°) at which $\omega_{st} = 0$. The characteristics of this transfer maneuver are symmetric relative to the base plane. The largest values of $\Delta\tilde{V}_{x\Sigma}$ correspond to inclination i_b close to 180°.

Maneuver with two-impulse elliptic rotation of apsidal axis and rotation of the transfer ellipse plane (variant Ib). The maneuver is accomplished as follows (Figure 8.3.9). From the

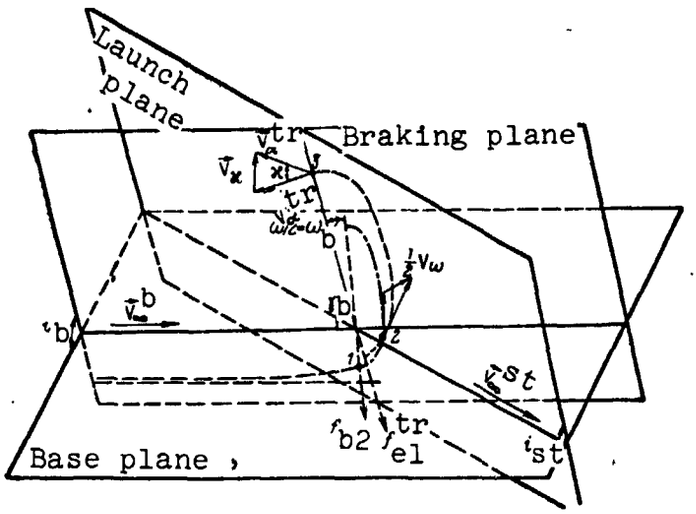

Figure 8.3.9. Schematic of nonplanar elliptic transfer with two-impulse rotation of apsidal axis (variant Ib)

braking hyperbola at point 1, pericentral transfer is made to the elliptic parking orbit, at point 2, transfer is made to an intermediate ellipse, rotating the apsidal axis through the angle ω. At the apocenter point 3 of the intermediate ellipse, the plane is rotated through the angle κ. Transfer from the intermediate ellipse to the parking orbit and pericentral departure from this orbit to the departure hyperbola are accomplished in this (launch) plane (the second stage of the maneuver is not shown in Figure 8.3.9).

Symmetry of the elliptic rotation of the axis of apsides /293 requires that

$$\omega_{st} = \omega_b = \omega/2.$$

In this case,

$$\gamma_b = \alpha_b + \omega/2; \quad \gamma_{st} = \alpha_{st} + \omega/2.$$

From the basic relation

$$\cos \gamma_{st} = -\cos \gamma_b \cos \varphi + \sin \gamma_b \sin \varphi \cos i_b$$

after transformations we obtain

$$\operatorname{tg} \frac{\omega}{2} = \frac{\cos \alpha_{st} + \cos \alpha_b \cos \varphi - \sin \alpha_b \sin \varphi \cos i_b}{\sin \alpha_{st} + \sin \alpha_b \cos \varphi + \cos \alpha_b \sin \varphi \cos i_b} .$$

The rotation angle of the intermediate ellipse velocity V_α

$$\cos \kappa = \cos i_b \cos i_{st} + \sin i_b \sin i_{st} \cos \varphi ,$$

where

$$\sin i_{st} = \sin i_b \frac{\sin \gamma_b}{\sin \gamma_{st}} .$$

Using these values of ω and κ, we find the total maneuver impulse

$$\Delta\tilde{V}_{\Sigma} = \Delta\tilde{V}_{\omega} + \Delta\tilde{V}_{\kappa},$$

where $\Delta\tilde{V}_{\omega}$ is the total impulse of apsidal axis rotation through the angle ω (see Figure 4.1.5, elliptic two-impulse transfer); $\Delta\tilde{V}_{\kappa}$ is the impulse of orbit plane rotation at its apocenter through the angle κ (see Figure 4.1.3).

Figure 8.3.10 shows the total impulse $\Delta\tilde{V}_{\Sigma}$ as a function of braking orbit inclination i_b for various values of the angle φ with $\tilde{r}_\alpha = 5$ and $\tilde{V}_\infty^b = 1$, $V_\infty^{st} = 2$. The largest values of $\tilde{V}_{\Sigma}$ occur at $i_{st} = 120 — 130°$. Here again there are points where $\Delta\tilde{V}_{\omega}=0$. Figure 8.3.11 shows the values of $\tilde{R}_a$ and $\tilde{R}_\pi$ of the intermediate ellipse. For points where $\Delta\tilde{V}_{\omega}=0$, $\tilde{R}_\pi=1$ and $\tilde{R}_a=5$. In the general case, the values of R_π and R_a are larger than $\tilde{r}_\pi$ and $\tilde{r}_a$ for the parking orbit. /294

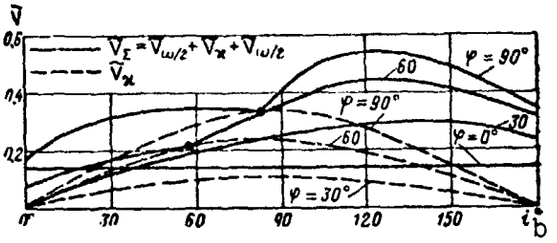

Figure 8.3.10. Total impulse ΔV_Σ as function of i_b and φ for elliptic transfer (variant Ib) with $\tilde{r}_\alpha = 5$, $\tilde{V}_\infty^b = 1$, and $\tilde{V}_\infty^{st} = 2$.

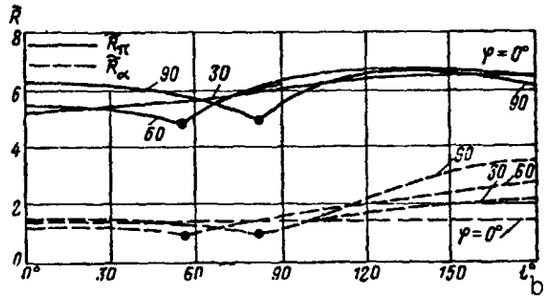

Figure 8.3.11. $\tilde{R}_\pi$ and $\tilde{R}_\alpha$ of intermediate ellipse (variant Ib)

MANEUVER WITH NONPERICENTRAL TRANSFER BETWEEN ELLIPSE AND HYPERBOLA (VARIANT III)

In this case, the maneuver of parking orbit shaping and departure from this orbit consists of two nonpericentral transfers between the hyperbola and ellipse (points 1 and 3 in Figure 8.3.12) and rotation of the ellipse plane through the angle κ at point 2. The characteristic calculation scheme is the same as in /295 the variant II case. For given $\tilde{r}_\alpha$, i_b, and φ, we seek the optimal value of γ_b which minimizes

$$\Delta\tilde{V}_{\Sigma\Sigma} = \Delta\tilde{V}_b + \Delta\tilde{V}_{st} + \Delta\tilde{V}_\varkappa,$$

where $\Delta\tilde{V}_b$ and $\Delta\tilde{V}_{st}$ are the differences of the velocity impulses between the nonpericentral and pericentral transfer maneuvers between the ellipse and the hyperbola,

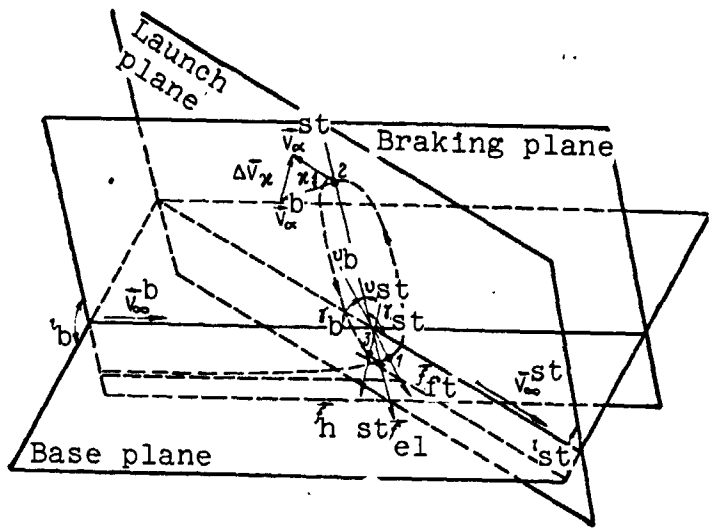

Figure 8.3.12. Schematic of nonplanar nonpericentral hyperbola-ellipse-hyperbola transfer (variant III)

$$\Delta\tilde{V}_1 = 2\tilde{V}_\infty \sin\frac{\varkappa}{2}.$$

The dependence of the impulse components on departure orbit inclination i_b and the angle φ between the vectors $\tilde{V}_\infty^b$ and V_∞^{st} is shown in Figure 8.3.13. The curves have the same nature as for the maneuver cases with single-impulse rotation of the apsidal axis, however, $\Delta\tilde{V}_1$ is significantly smaller. The relation $\Delta\tilde{V}_1 = f(i_b)$ is also symmetric about the base plane. However, in this case, as a rule, $\omega_b^{opt} \neq 0$. In Figure 8.3.13, the points corresponding to $\omega_b = \omega_{st} = 0$ are noted.

INSERTION INTO ORBIT OF ARBITRARY INCLINATION FOR SMALL VALUES OF THE ANGLE φ

If the angle φ between the approach velocity vector $\bar{V}_\infty^b$ and the departure velocity vector $\bar{V}_\infty^{st}$ is equal to zero, the parking orbit inclination can be selected arbitrarily. This mutual positioning of the vectors $\bar{V}_\infty^b$ and $\bar{V}_\infty^{st}$ can, in principle, be

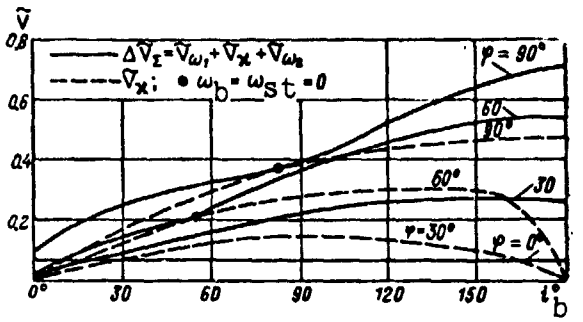

Figure 8.3.13. Dependence of ΔV_Σ on i_b and φ for nonpericentral transfer (variant III) with $\tilde{r}_\alpha = 5$, $\tilde{V}_\infty^b = 1$, $\tilde{V}_\infty^{st} = 2$

assured by varying the parameters of the heliocentric trajectory segments adjacent to the planet. However, calculations have shown that, in this case, the energy expenditures along the flight trajectory increase significantly. This is explained by the fact that, for alignment of the vectors $\bar{V}_\infty^b$ and $\bar{V}_\infty^{st}$, it is necessary, in addition to variation of the trajectory configuration in their planes, to align the orbit planes on the segments adjacent to the planet.

The vectors can also be aligned by rotating one of the vectors $\bar{V}_\infty^b$ or $\bar{V}_\infty^{st}$ through the angle φ. Naturally, the vector with smaller modulus should be rotated. In this case, trajectory optimization is based on the total velocity V_Σ with addition of the rotation impulse

$$\Delta V_\varphi = 2V_\infty^{b(st)} \sin\frac{\varphi}{2}.$$

The energy expenditures required for the case $\tilde{V}_\infty^b = 1$ and $\tilde{V}_\infty^{st} = 2$ are shown as a function of φ in Figure 8.3.14. We see that, for $\varphi > 0$, the energy expenditures of this maneuver variant will be larger than for variants II and III. However, for small values of φ, its application does not lead to significant increase of the energy expenditures and makes it possible to select an orbit of arbitrary inclination i_b for the same energy expenditures.

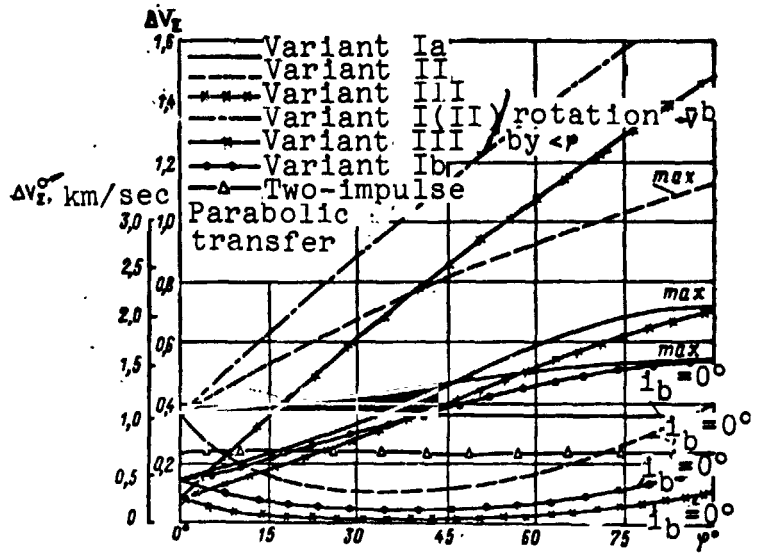

Figure 8.3.14. Comparison of different nonplanar hyperbola-ellipse-hyperbola transfer variants for $\tilde{r}_a = 5$, $\tilde{V}_\infty^b = 1$, $\tilde{V}_\infty^{st} = 2$

COMPARISON OF DIFFERENT ARBITRARY INCLINATION PARKING ORBIT SHAPING MANEUVER VARIANTS

Figure 8.3.14 shows the values of the additional characteristic velocity $\Delta\tilde{V}_\Sigma$ expenditures in comparison with the pericentral maneuver for different parking orbit shaping maneuver variants as a function of the angle φ between the approach $\bar{V}_\infty^b$ and departure $\bar{V}_\infty^{st}$ vectors. The values of $\Delta\tilde{V}_\Sigma$ are shown for braking orbit inclination $i_b = 0$ and i_b for maximal energy expenditure. For maneuver variant I, this corresponds to $i_b = 90°$, for variant III, $i_b = 180°$. The calculations were made for the typical transfer case with $\tilde{V}_\infty^b = 1$ and $\tilde{V}_\infty^{st} = 2$ for the relative elliptic orbit apocenter height $\tilde{r}_a = 5$. For all the parking orbit shaping maneuver variants, the smallest energy expenditures correspond to the braking orbit inclination $i_b = 0$. /298 In this case, the best shaping variant is III.

Variant III will be best for insertion into an orbit of arbitrary inclination (maximum energy expenditures) for $\varphi<40°$, while for $\varphi>40°$, variant Ib will be best. Figure 8.3.14 also shows the energy expenditures which provide insertion into an orbit of arbitrary inclination by prerotation of the vector $\bar{V}_\infty^b$ through the angle φ. As noted before, this transfer case yields larger energy expenditures for variants II and III in comparison with the previously examined parking orbit formation cases. For arbitrary incli..ation (maximum energy expenditures), variant Ib provides values of ΔV_2 close to variant III.

CHAPTER 9. INTERPLANETARY FLIGHT VEHICLE FLIGHT TRAJECTORIES TO SEVERAL PLANETS

§ 1. EVALUATION OF FLIGHT CYCLICITY TO SEVERAL PLANETS

We shall examine the case (Figure 9.1.1) when the planet orbits are circular and lie in the same plane. Planet 1 is the launch planet and planet n is the last planet in the flyby chain. In the case when flyby of several planets takes place with return to the Earth, planet n corresponds to planet 1. For generality, we examine the case of flight with stopover at each planet for some time Δt_i (stopover time at the planet). /299

The heliocentric longitude of planet 1 at the instant of launch from it /300

$$\varphi_1^{st} = \varphi_1^0 + \omega_1 t_1,$$

where φ_1^0 is the longitude of planet 1 at zero time; ω_1 is the angular velocity of planet 1; t_1 is the time of launch from planet 1;

The heliocentric longitude of planet 2 at the instant of arrival at it

$$\varphi_2^{ar} = \varphi_2^0 + \omega_2 (t_1 + \Delta t_{12}),$$

where φ_2^0 and ω_2 are the initial longitude and angular velocity of planet 2; Δt_{12} is the flight time between planets 1 and 2.

The same for planet 3

$$\varphi_3^{ar} = \varphi_3^0 + \omega_3 (t_1 + \Delta t_{12} + \Delta t_2 + \Delta t_{23}).$$

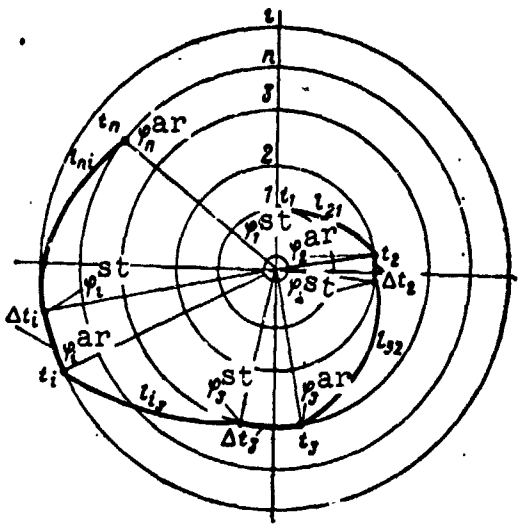

Figure 9.1.1. Schematic of flight route to several planets

where Δt_2 is the stopover time at planet 2, and so on.

We shall examine the flight segment from planet 1 to 2.

The difference of the heliocentric longitudes

$$\varphi_2^{ar} - \varphi_1^{st} = l_{21} + k_{21} \cdot 2\pi$$

for the k$^{\underline{th}}$ flight cycle may differ from the zero cycle (transfer angle l_{21}) by multiples of 2π. Substituting the values of φ_2^{ar} and φ_1^{st}, we obtain

$$\Delta\varphi_{21}^0 + \omega_2(t_1 + \Delta t_{12}) - \omega_1 t_1 = l_{21} + k_{21} \cdot 2\pi,$$

where $\Delta\varphi_{21}^0 = \varphi_2^0 - \varphi_1^0$. Hence, the launch date from planet 1

$$t_1 = \frac{-\Delta\varphi_{21}^0 - \omega_2 \Delta t_{12} + l_{21}}{\omega_2 - \omega_1} + k_{21}\frac{2\pi}{\omega_2 - \omega_1} = t_1^0 + T_s^{21} \cdot k_{21},$$

where T_s^{21} is the synodic period of planet 2 relative to planet 1; t_1^0 is the zero flight cycle launch data.

Similarly for planets 1 and 3

$$t_1 = \frac{-\Delta\varphi_{31}^0 - \omega_3(\Delta t_{12} + \Delta t_2 + \Delta t_{32}) + (l_{21} + \Delta\varphi_2 + l_{32})}{\omega_3 - \omega_1} +$$

$$+ k_{31}\frac{2\pi}{\omega_3 - \omega_1} = t_1^0 + T_s^{31} k_{31},$$

where $\Delta\varphi_2 = \omega_2 \Delta t_2$, and so on for all possible combinations of transfer segments between all the planets. /301

For the selected n planet flyby route, the moments of time t_1 and t_1^0, determined on each transfer segment, are equal. Consequently,

$$T_s^{21}k_{21} = T_s^{31}k_{31} = T_s^{32}k_{32} = \ldots = T_s^{n1}k_{n1} =$$

$$T_s^{n2}k_{n2} = \ldots = T_s^{n(n-1)}k_{n(n-1)} = T_s^{\Sigma}.$$

Thus, the overall synodic period T_s^{Σ} is equal to the least common multiple of all the mutual synodic periods T_s of these planets. Since no limitations are imposed on the mutual configurations of the trajectories and the planet flyby sequence (including the stopover time at the planet, the period T_s^{Σ} will be the repetition period of any planet flyby configuration and sequence.

But the real synodic periods T_s^{Σ} of the planets are not exact multiples of one another. However, for sufficiently high accuracy of T_s multiplicity, we can guarantee repetition after the period T_s^{Σ} of configurations which differ sufficiently little. For the real solar system with elliptic and noncoplanar orbits, the trajectory characteristics will differ somewhat after the period T_s^{Σ}.

The relative planet location configuration (for circular planetary orbits) repeats after the period T_s^{Σ}. Repetition of the planet position configuration in space is possible. As is known, for two planets, this "absolute configuration" repeats after the great opposition period T_{go}. In this case, each planet occupies the original places

$$\left.\begin{aligned}
&\varphi_1^{k1} - \varphi_1^0 = k_1 2\pi = \omega_1 T_{go}^{\Sigma};\\
&\varphi_2^{k2} - \psi_2^0 = k_2 2\pi = \omega_2 T_{go}^{\Sigma};\\
&\cdots\cdots\cdots\cdots\\
&\varphi_n^{kn} - \varphi_n^0 = k_n 2\pi = \omega_n T_{go}^{\Sigma},
\end{aligned}\right\} \qquad (9.1.1)$$

where φ_n^{kn} is the longitude of the $k^{\underline{th}}$ planet at n revolutions after the zero flight cycle; φ_n^0 is the longitude of the $k^{\underline{th}}$ planet at the zero flight cycle time. Hence,

$$T_{go}^{\Sigma} = k_1 \frac{2\pi}{\omega_1} = k_2 \frac{2\pi}{\omega_2} = \ldots k_n \frac{2\pi}{\omega_n}$$

or

$$T_{go}^{\Sigma} = k_1 T_1 = k_2 T_2 = \ldots = k_n T_n,$$

where T_k is the sidereal period of the $k^{\underline{th}}$ planet. Comparing in (9.1.1) each succeeding and preceding relation (first and second, for example), we obtain /302

$$T_{go}^{\Sigma} = k_{21} T_s^{21} = k_{31} T_s^{31} = k_{32} T_s^{32} = \ldots = k_{n1} T_s^{n1} = \ldots k_{n(n-1)} T_s^{n(n-1)}.$$

Thus, "absolute repetition" of the planet place configuration will take place after the overall great opposition period T_{go}^{Σ}, equal to the least common multiple of the sidereal and all the mutual synodic planet periods T_s. The periodicity of cycle repetition after T_{go}^{Σ} is also valid for noncoplanar and elliptic planet orbits.

It should be noted that the synodic and sidereal period multiplicity in the general case may be only approximate. Therefore, depending on the degree of approximation, there will be different values of T_s^{Σ} and T_{go}^{Σ} — coarse and more exact. For flight schemes with return to the departure planet (the Earth), the return segment has no influence on flight cycle

periodicity. Moreover, the planet flyby sequence has no influence on the cyclicity (it is sufficient to know simply the listing of the planets along the route).

In order to determine the flight cyclicity to different planet combinations, it is necessary to know the planet synodic revolution periods T_s. It is clear from the above that T_s for two planets is the repetition period of their mutual position relative configuration or the revolution period of the planets relative to one another.

The synodic period of planet 1 relative to planet 2 (or vice versa

$$T_s = \left|\frac{T_1 T_2}{T_2 - T_1}\right|,$$

where T_1 and T_2 are the planet sidereal revolution periods. The values of T_s for various mutual combinations of two planets are tabulated in the Appendix.

The great opposition period of two planets is the repetition period of the absolute configuration of their mutual positioning. In Chapters 5 and 6, the values of T_{go} for the Earth and the various planets were presented when the approximate repetition /303 periods of the optimal trajectory characteristics with respect to the flight cycles were indicated.

For the case of flight from planet 1 to planet 2 (flight from the Earth to a planet), the great opposition period

$$T_{go} = k_1 T_1 = k_2 T_2 = k_{21} T_s.$$

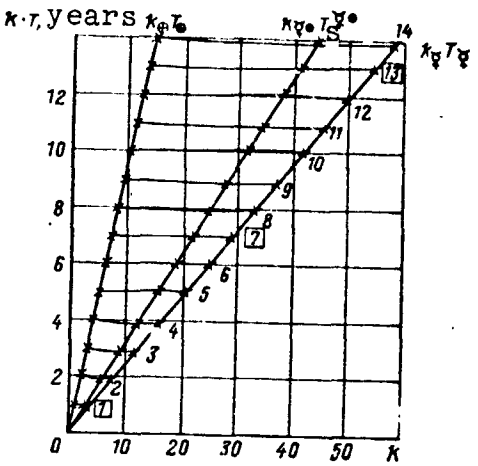

Figure 9.1.2. Schematic of graphical determination of T_{go} (flight to Mercury)

For approximate determination of T_{go}, it is necessary to find those k_1, k_2, and k_{21} which minimize the error

$$\Delta = |k_{21} T_s - k_1 T_1|$$

or

$$\Delta = |k_2 T_2 - k_1 T_1|.$$

In this case, the T_{go} values will be whole periods T_1 (the Earth period $T \approx 1.00004 \approx 1$ year). It is convenient to solve the system of equations for determining T_{go} graphically (Figure 9.1.2). The error Δ varies as a function of k in a pulsating fashion. The values of the integer k corresponding to the minimal errors are easily found from the graph. After this, the quantity Δ is refined by computation. Thus, for flights to Mercury, the T_{go} values with minimal errors will be (see Figure 9.1.2):

for T_{go} = 1 $\Delta = 0.048$, $k_{\oplus} = 1$, $k_{\breve{\varphi}\oplus} = 3$ and $k_{\breve{\varphi}} = 4$;

for T_{go} = 7 $\Delta = 0.02$, $k_{\oplus} = 7$, $k_{\breve{\varphi}\oplus} = 22$ and $k_{\breve{\varphi}} = 29$, etc.

Table 9.1 presents T_{go} values of differing order of multiplicity accuracy for flights from the Earth to the planets. It is better to convert the error Δ into the trajectory angle error $\Delta l = 2\pi\Delta$ for flight to the inner planets and to $\Delta l = 2\pi \frac{\Delta}{T_{pl}}$ for flight to the outer planets (i.e., for flights to the inner planets Δl corresponds to the shift of the Earth, while for flight to the outer planets, it corresponds to the shift of the planet). In this demarcation variant, Δl will be the smallest

TABLE 9.1*

Flight trajectory	T_s years	T_{go}, years/$\Delta l°$
Earth — Mercury	0,317	$\frac{1}{17,3'}$ $\frac{7}{7,2'}$ $\frac{13}{28'}$ $\frac{19}{13'}$ $\frac{25}{23'}$ ...
Earth — Venus	1,599	$\frac{3}{4,5'}$ $\frac{5}{4,7'}$ $\frac{8}{1,35'}$ $\frac{11}{4,4'}$ $\frac{13}{5,4'}$ $\frac{16}{2,7'}$ ...
Earth — Mars	2,135	$\frac{17}{5,5'}$ $\frac{32}{14,6'}$ $\frac{47}{4,2'}$ $\frac{64}{12,8'}$ $\frac{79}{1,8'}$ ...
Earth — Jupiter	1,092	$\frac{12}{4,2'}$ $\frac{71}{5,1'}$ ...
Earth — Saturn	1,035	$\frac{29}{5,6'}$ ...
Earth — Uranus	1,012	$\frac{84}{0,07'}$ ...
Earth — Neptune	1,006	$\frac{165}{0,43'}$ ...
Earth — Pluto	1,004	$\frac{248}{0,29'}$ ...

*[Translator's Note: Commas in numbers indicate decimal points.]

change of the flight trajectory characteristics. Usually, the first period T_{go} is most characteristic. Thus, for flights to Mercury, it is equal to one year. It would appear that the multiplicity corresponding to $\Delta l = 17.3°$ is not very exact. However, as was shown in § 3 of Chapter 5, the repeatability of the flight characteristics to Mercury after one year is quite exact. This is explained by the fact that the optimum of the characteristic velocity $V^{\oplus}_{st}$ as a function of flight time Δt_f (or as a function of trajectory angle l) is quite flat. Therefore, the increase of the error Δl in the course of the first three or four years from the original position (see Figure 9.1.2) does not influence optimal characteristics very strongly. Then the error Δ decreases, reaching a second minimum at $T_{go} = 7$ years. Then it again increases in the course of three or four years, reaches a third minimum at $T_{go} = 13$ years, and so on. /304

For flights to Mars (Table 9.1), the first period $T_{go} \approx 17$ years with quite small error Δl, the second period $T_{go} = 32$ years with still smaller Δl, and so on. The third multiplicity period $T_{go} = 8$ years for flights to Venus is very exact and is clearly seen on the flight characteristics to Venus in § 3, Chapter 5.

For flights to the distant outer planets, the first multiplicity period is equal to the planet's sidereal period T rounded to the nearest year. The periods T_{go} of higher multiplicity are too long to have any practical value. We recall that addition of the Earth return segment to all the flight routes to the planets does not disrupt the cyclicity.

We can also determine the period of great oppositions between two planets as follows. After one synodic period T_s, the difference in the heliocentric longitudes of the planets will be /305

$$\Delta\varphi = |\omega_{pl} T_s - k2\pi|.$$

For repetition of the absolute position of the planets, the quantity $\Delta\varphi$ must repeat n (in the general case, n is not an integer) times per revolution, i.e., $n = \frac{2\pi}{\Delta\varphi}$. In this case, the great opposition period

$$T_{go}^{pl} = nT_s = \frac{2\pi T_s}{|\omega_{pl} T_s - k2\pi|} = \frac{T_s}{\left|\frac{T_s}{T_{pl}} - k\right|}.$$

For flights to Mercury,

$$T_{go}^{\mathrm{☿}} = 1.005 \text{ years with } k = 1;$$

to Venus

$$T_{go}^{\mathrm{♀}} = 2.667 \text{ years with } k = 2;$$

to Mars

$$T_{go}^{\sigma} = 15.83 \text{ years with } k = 1.$$

The quantity k is equal to the rounded whole number of complete planet revolutions during the period T_s. For flights to the distant outer planets, for which $T_{pl} \gg T_s$, the quantity $k = 0$. In this case, $T_{go}^{pl} = T_{pl}$. Such values of the period correspond to the repetition period of the flight trajectory characteristics on the nominal curves of the characteristics versus Earth launch date (see § 3 of Chapter 5, § 3 of Chapter 6, and § 2 of Chapter 8) for the Earth-planet and Earth-planet-Earth flight routes. For flights to Venus, the repeatability of the characteristics corresponds to $T_{go}^{\varphi} = 2.667$ years and for the more highly smoothed relations with $T_{go} = 3T_{go}^{\varphi} \approx 8$ years. The values of the periods T_{go}^{pl} rounded to a whole number are equal to the first T_{go} values from Table 9.1.

For flights to several planets, the total synodic period T_s^{Σ} and the total great opposition period T_{go}^{Σ} are determined graphically. Table 9.2 presents the values of T_s^{Σ} and T_{go}^{Σ} of the first harmonic for a series of flight routes to several planets.

Most interesting at the present time are the following routes:

— flight to Mercury via Venus with a maneuver in its gravity field ($T_s^{\Sigma} = 1.6$);

— flight to Mars via Venus (maneuver in its gravity field) with return to the Earth ($T_s^{\Sigma} = 6.5$ years);

— flights to the distant planets with maneuver in the gravity field of Jupiter.

TABLE 9.2*

Flight Trajectory	$\frac{T_s}{\Delta}$, years	$\frac{T^{\Sigma}_{go}}{\Delta}$, years
Earth-Venus-Mercury	$\frac{1,6}{0,015}$	$\frac{3}{0,176}$, $\frac{5}{0,136}$, $\frac{8}{0,052}$, $\frac{11}{0,079}$, $\frac{13}{0,086}$, $\frac{16}{0,104}$, $\frac{19}{0,072}$, $\frac{21}{0,072}$, $\frac{24}{0,085}$, $\frac{27}{0,041}$, $\frac{32}{0,033}$, $\frac{35}{0,077}$, $\frac{38}{0,145}$, $\frac{40}{0,019}$, ...
Earth-Venus-Mars	$\frac{6,4}{0,01}$	$\frac{17}{0,225}$, $\frac{32}{0,075}$, $\frac{49}{0,217}$, $\frac{64}{0,060}$, $\frac{77}{0,116}$, ...
Earth-Mars-Venus-Mercury	$\frac{6,37}{0,053}$	$\frac{13}{0,18}$, $\frac{19}{0,19}$, $\frac{32}{0,033}$, ...
Earth-Venus-Jupiter	$\frac{3,24}{0,076}$	$\frac{12}{0,3}$, ...
Earth-Venus-Mars-Jupiter	$\frac{6,55}{0,3}$	$\frac{12}{0,42}$, ...
Earth-Jupiter-Mercury	$\frac{1,02}{0,14}$	$\frac{12}{0,14}$, ...
Earth-Mercury-Venus-Jupiter	$\frac{3,25}{0,1}$	$\frac{12}{0,3}$, ...
Earth-Mercury-Venus-Mars-Jupiter	$\frac{6,45}{0,3}$	$\frac{12}{0,42}$, ...
Earth-Mars-Jupiter	$\frac{2,2}{0,14}$	$\frac{12}{0,42}$, ...
Earth-Mars-Jupiter-Saturn	$\frac{19,7}{0,3}$	$\frac{59}{0,6}$, ...
Earth-Jupiter-Saturn	$\frac{19,75}{0,11}$	$\frac{59}{0,2}$, ...
Earth-Jupiter-Uranus	$\frac{14}{0,2}$	$\frac{84}{1,0}$, ...
Earth-Jupiter-Saturn-Uranus	$\frac{138}{1,9}$	
Earth-Jupiter-Neptune	$\frac{12,9}{0,15}$	$\frac{165}{1,0}$, ...
Earth-Jupiter-Pluto	[illegible]	$\frac{249}{0,6}$, ...

CONTINUED

TABLE 9.2*

(Continued)

Flight Trajectory	$\frac{T_s}{\Delta}$, years	$\frac{T^{\Sigma}_{go}}{\Delta}$, years
Earth-Jupiter-Saturn-Uranus-Neptune	$\frac{177}{0,5}$	
Earth-Jupiter-Saturn-Pluto	$\frac{170}{0,6}$	Grand tour variants
Earth-Jupiter-Uranus-Neptune	$\frac{168}{3,4}$	
Earth-Jupiter-Saturn-Neptune	$\frac{103}{4,8}$	
Earth-Jupiter-Saturn-Uranus-Neptune-Pluto	$\frac{500}{13}$	

* Translator's Note: Commas in numbers indicate decimal points.

The latter group includes the flight schemes using three Grand Tour program variants. However, flights along this route are a unique phenomenon ($T_s \approx 170$ — 180 years). More realistic are the flights along routes of the Earth-Jupiter-destination planet type. Thus, flight to Saturn via Jupiter with $T_s \approx 20$ years, to Uranus via Jupiter with $T_s \approx 14$ years, and to the more distant planets (Neptune and Pluto) via Jupiter with $T_s \approx 13$ years. /307

§ 2. FLIGHT TRAJECTORIES TO MARS WITH RETURN TO EARTH AND UTILIZING VENUS'S GRAVITY FIELD

Spacecraft flights to Mars with return to the Earth and Venus flyby are possible along two routes:

Earth-Mars-Venus-Earth (E-M-V-E);

Earth-Venus-Mars-Earth (E-V-M-E).

One of the basic difficulties in optimizing flight trajectories to several planets is identification of the unimodal extremum search region (in the terminology of [46] unimodality means having a single-valued extremum). The first means for identifying this region on the basis of Earth launch dates $t^{\oplus}_{st}$ is determination of the cyclicity of optimal flights to the planets.

For direct roundtrips to Mars, the synodic period T_s = 2.135 years and the great opposition period T_{go} = 17 years (the same as for flights to Mars without return to the Earth). For any of the flight route variants to Mars via Venus (E-M-V-E or E-V-M-E), the synodic period T_s = 6.4 years and the great opposition period $T_{go} \approx 32$ years. /308

Thus, after finding the set of optimal routes and schemes for the time interval T^{Σ}_s, we can find the entire sequence of launch dates for these schemes in terms of the period T^{Σ}_s.

OPTIMIZATION OF FLIGHT TRAJECTORIES "VIA VENUS"

The optimization criterion for the subject problem will be the total velocity $V_{x\Sigma}$

$$V_{x\Sigma} = V^{\oplus}_{st} + V^{\sigma}_{b} + V^{\sigma}_{st} + V^{\varphi}_{m}$$

(st indicates launch, b indicates braking, m indicates maneuver) for the three-impulse scheme or

$$V_{x\Sigma} = V^{\oplus}_{st} + V^{\sigma}_{st} + \Delta V^{\varphi}_{m}$$

for the two-impulse scheme.

The function V_{Σ} is a function of five parameters. For the E-M-V-E route, these parameters will be: launch date from the Earth $t_{st}^{\oplus}$; flight time from the Earth to Mars Δt_f^{σ}; stopover time in AMS orbit Δt_{so}; flight time from Mars to Venus $\Delta t_f^{\varphi-\sigma}$; total roundtrip time Δt_{Σ}.

Only the order of the flight time segment components changes for the E-V-M-E route.

In order to localize the extremum search region, we break the flight trajectory down into groups based on semiorbit combination. In our three-planet flyby case, the number of groups $N = 2^n = 8$. In addition, we also break the flight trajectory down on the basis of overall flight time into long duration and accelerated. This narrows the extremum search region markedly; however, for the subject problem, it still does not ensure identification of the unimodal region.

The impossibility of a priori identification of the unimodal search region in the three-planet flyby problem precludes direct utilization of the gradient extremum search methods. Therefore, the search for a minimum of the function V_{Σ} is made sequentially, in two stages.

The first stage is finding the initial approximation of the minimal value of the function V_{Σ} for the simplified problem by parameter variation with large step.

The second stage is final optimization of the function V_{Σ} by the gradient methods (in our case, the configuration method, see [46]).

We break the multiparameter problem down into to separate problems (trajectory segments) with a smaller number of parameters. We represent the flight trajectory in the form of two segments: the first segment is the trajectory near Venus (M-V-E or E-V-M), the second is the E-M segment for the E-M-V-E route or the M-E segment for the E-V-M-E route. /309

Calculations showed that the $V_{x\Sigma}$ optimum differs very little from the optima of the $V_{x\Sigma}$ components on each segment. Therefore, for the first approximation stage, we can optimize each segment with respect to its independent criterion ($V'_{x\Sigma}$ for the first segment and $V''_{x\Sigma}$ for the second).

If Venus flyby takes place on the E-V-M trajectory segment prior to encounter with Mars (route E-V-M-E), then $V'_{x\Sigma}$ has the form:

$$V'_{x\Sigma} = V^{\oplus}_{st} + \Delta V^{\varphi}_{m} + V^{\sigma}_{b} \text{ for the three-impulse scheme;}$$

$$V'_{x\Sigma} = V^{\oplus}_{st} + V^{\varphi}_{m} \text{ for the two-impulse scheme.}$$

If Venus flyby takes place on the Earth return trajectory (route E-M-V-E), then V'_{Σ} has the same for both the two-impulse and three-impulse schemes, namely

$$V'_{\Sigma} = V^{\sigma}_{st} + \Delta V^{\varphi}_{m}.$$

The magnitude of the energy expenditures on this segment is very sensitive to the time of Venus flyby. In most cases, deviation of the Venus flyby time t^{φ}_{ar} by 5 — 10 days leads to considerable losses in the total energy expenditures. As a rule, the energy expenditure minimum lies in the region of small Venus maneuver impulses ($\Delta V^{\varphi}_{m} \approx 0$ — 300 m/sec). Since, in the parameter variation intervals in question, the function $V'_{x\Sigma}$

has several extremal points, we find the minimum of the function V'_{Σ} by variation of its three parameters — one launch date and two flight times. Reduction of the number of parameters from five to three makes it possible to use the parameter variation method. Moreover, the approximate nature of the first search stage makes it possible to thin out the parameter variation grid. No less than four V'_{Σ} optima are possible (four semiorbit combination groups). From these optima, we select that which yields the smallest value of V'_{Σ}. In the case of similar values of the V'_{Σ} optima, we select that which yields a significant gain in flight time $\Delta t_f^{\sigma-\varphi} + \Delta t_f^{\varphi}$ (or $\Delta t_f^{\varphi-\varphi} + \Delta t_f^{\varphi-\sigma}$). However, if the flight times are also similar, all the variants enter into the second approximation optimization cycle.

Optimization of the second segment wrt the criterion V'_{Σ} reduces to the single-parameter problem of determining the Earth lauch date $t^{\oplus}_{st}$ (for the E-M-V-E route) or the Earth arrival date (E-V-M-E route). The V'_{Σ} minimum for this restricted problem (fixed Mars flyby time) does not correspond to the minimum point of the two-parameter problem of independent optimization of this segment (E-M and/or V-E trajectories) but is close to the minimum point. /310

Preliminary optimization using the technique described above was carried out for the "accelerated flight" trajectory class in the total flight time range $400 \leqslant \Delta t_{\Sigma} \leqslant 700$ days for fixed minimal stopover time at Mars $\Delta t_{so} = 15$ days.

As a result of these calculations, we obtain an approximate but global pattern of the optimal trajectory characteristic variation for a single flight cycle in the Earth launch date range $\Delta t^{\oplus}_{st} \approx 6.4$ years. A similar configuration of the three planets — Earth, Mars, and Venus — repeats approximately after the total syncdic period $T^{\Sigma}_{s} = 6.4$ years.

On this basis, we found the optimal trajectory cycles and corresponding flight groups for the time intervals from 1970 to 1992. A refined search for the optimal trajectories was made by the configuration method for the points corresponding to the approximate optima. Use of the preliminary optimization points ensures unimodality of the search region.

CHARACTERISTICS OF ROUNDTRIP TRAJECTORIES FOR 1970 — 1990 FLIGHT CYCLES

In order to find the Mars roundtrip spacecraft flight cycles in which the Venus gravity field can be used, we made trajectory calculations for flights from 1970 to 1992 along the E-M-V-E and E-V-M-E routes. In the process of the calculations, we found that for the E-M-V-E routes, the Earth launch dates are close to the dates for flights along the E-M route, while for the E-V-M-E route, they are close to the launch dates for the E-V route. Of all the local V_{∞} optima, we selected only those which yield $V_{\infty} < 30$ km/sec. As a result, for the 23 years from 1970 to 1992, of the 14 possible optima for the E-V-M-E route (E-V flight synodic period T_c = 1.6 years) and the 11 optima for the E-M-V-E route (E-M flight synodic period T_s = 2.135 years), we found the optimal cycles for both routes.

The calculation results for the cycles with small energy expenditures are shown in Tables 9.3 and 9.4.

The calculations showed that there are two semiorbit combination groups for the minimal trajectories. One minimizes V_{∞} for the E-M-V-E route trajectories and corresponds to flight from the Earth to Mars along the first semiorbit trajectories; the second minimizes V_{∞} for flight from the Earth to Mars along the second semiorbit trajectories. In the different cycles, the

C-5-1

TABLE 9.3. CHARACTERISTICS OF TWO-IMPULSE FLIGHT TRAJECTORIES*

Stopover Time at Mars 15 Days

Route E-M-V-E, Group I-X-Y

Year	v_Σ	$v^{\oplus}_{st}$	v^{σ}_{st}	Δv^{φ}_{m}	$v^{\oplus}_{\infty}$	v^{σ}_{∞}	$t^{\oplus}_{st}$	t^{σ}_{st}	t^{φ}_{st}	R_{pa}	τ_Σ	Group
	km/sec						J. D.		—	км	days	
1973	12,06	7,09	4,83	0,13	15,1	11,4	.2441810	2441960	2442150	70901	550	I—II—I
1975	6,95	4,24	2,68	0,028	13,7	7,6	...2673	...2848	...3048	609524	500	I—I—II
1977	10,51	5,21	5,19	0,108	13,6	11,5	...3425	...3585	...3755	6393	460	I—I—II
1984	6,60	3,68	2,82	0,091	12,3	8,5	...5740	...5915	...6080	14417	450	I—I—I
1988	6,81	3,77	3,02	0,018	13,00	5,6	...7335	...7530	...7740	11368	540	I—I—II
1990	9,27	4,74	4,17	0,35	13,00	9,2	...8130	...8275	...8490	239723	420	I—II—I

Route E-M-V-E, Group II-X-Y

1973	11,29	6,32	4,83	0,13	15,1	7,8	2441750	2441960	2442150	70901	620	II—II—I
1975	8,27	5,56	2,68	0,028	13,7	6,00	...2593	...2848	...3048	609524	580	II—I—II
1977	11,75	6,79	4,78	0,172	13,6	7,9	...3345	...3580	...3755	6941	540	II—I—I
1984	7,24	4,27	3,00	0,054	12,3	7,1	...5670	...5920	...6080	13822	520	II—I—I
1988	7,45	4,36	3,05	0,044	12,1	5,4	...7280	...7525	...7740	10605	640	II—I—I
1990	10,66	5,89	4,46	0,30	13,00	6,4	...8050	...8280	...8490	265270	500	II—II—I

Continued

TABLE 9.3*

(Continued)

Route E-V-M-E, Group X-Y-I

Year	v_∞	$v^{\oplus}_{st}$	v^{σ}_{st}	Δv^{φ}_{m}	$v^{\oplus}_{*}$	v^{σ}_{*}	$t^{\oplus}_{st}$	t^{φ}_{st}	t^{σ}_{st}	R_{pa}	t_∞	Group
	km/sec						J. D.		–	km	days	
1970	5,84	4,09	1,67	0,085	11,8	9,9	2440818	2440908	2441103	47065	470	I—II—I
1972	5,77	4,05	1,65	0,068	11,5	7,5	...1470	...1640	...1835	949037	570	II—I—I
1977	11,03	4,08	6,89	0,052	14,00	6,8	...3175	...3300	...3480	38656	510	I—I—I
1978	5,21	4,09	1,11	0,009	12,60	13,8	...3811	...3981	...4096	45283	560	II—I—I
1983	9,16	5,02	4,09	0,052	14,2	7,5	...5510	...5374	...5815	193698	500	I—II—II
1985	4,96	3,89	1,01	0,048	14,6	12,9	...6141	...6311	...6456	106204	540	II—I—I
1989	7,08	4,67	2,38	0,029	11,7	8,00	...7842	...7912	...8107	13623	460	I—II—I
1991	6,05	4,15	1,87	0,023	13,2	8,1	...8500	...8667	...8817	12684	550	II—I—I

Route E-V-M-E, Group X-Y-II

1970	5,75	3,91	1,80	0 039	12,5	9,2	2440828	2440913	2441113	359630	535	I—II—II
1972	5,958	4,05	1,83	0,068	11,6	7,5	...1470	...1640	...1835	94957	635	II—I—II
1977	6,42	4,08	2,18	0,052	16,3	6,8	...3175	...3300	...3480	38656	620	I—I—II
1978	5,27	4,13	1,13	0,001	11,7	13,2	...3824	...3984	...4099	43738	620	II—I—II
1983	7,07	5,02	1,99	0,05	14,5	7,5	...5510	...5574	...5815	193708	570	I—II—II
1985	4,99	3,86	1,06	0,057	11,9	13,5	...6131	...6306	...6451	24227	600	II—I—II
1989	6,47	4,67	1,78	0,029	12,1	8,00	...7842	...7912	...8107	13623	570	I—II—II
1991	5,57	4,14	1,35	0,081	11,3	8,00	...8505	...8667	...8817	12566	595	II—I—II

*[Translator's Note: Commas in numbers indicate decimal points.]

TABLE 9.4. CHARACTERISTICS OF THREE-IMPULSE FLIGHT TRAJECTORIES*

Stopover Time at Mars 15 Days

Route E-M-V-E, Group I-X-Y

Year	V_Σ	$V^{\oplus}_{st}$	V^{σ}_{b}	V^{σ}_{st}	ΔV^{φ}_{m}	$V^{\oplus}_{\infty}$	$t^{\oplus}_{st}$	t^{σ}_{st}	t^{φ}_{st}	R_{pa}	t_Σ	Group
	km/sec						J. D.			км	days	
1973	17,20	6,30	4,65	6,18	0,051	15,3	2441795	2441975	2442150	2446921	570	I—II—I
1975	9,30	6,04	2,12	3,12	0,012	12,7	...2668	...2878	...3050	566355	520	I—I—II
1977	16,91	5,60	5,58	5,64	0,082	13,5	...3395	...3590	...3755	457785	490	I—I—II
1984	10,05	3,60	3,09	3,31	0,029	13,3	...5740	...5935	...6090	13659	440	I—I—I
1988	8,24	3,80	1,40	3,02	0,018	12,9	...7330	...7530	...7740	11378	545	I—I—II
1990	13,07	4,96	3,54	4,46	0,099	12,8	...8092	...8280	...8490	503099	460	I—II—I

Route E-M-V-E, Group II-X-Y

1973	14,08	6,14	2,65	5,24	0,046	15,2	2441725	2441965	2442150	608292	645	II—II—I
1975	9,62	5,15	1,33	3,12	0,012	12,6	...2598	...2878	...3053	566355	590	II—I—II
1977	14,80	6,96	2,11	5,64	0,082	13,5	...3315	...3590	...3755	457785	570	II—I—II
1982	8,63	3,63	1,34	3,57	0,086	12,3	...4938	...5238	...5388	11003	600	II—I—II
1984	9,76	4,21	2,20	3,31	0,029	13,4	...5660	...5935	...6090	13659	520	II—I—I
1988	8,57	4,30	1,23	3,02	0,018	13,6	...7285	...7530	...7740	11368	590	II—I—II
1990	12,38	5,74	1,87	4,46	0,20	13,0	...8040	...8280	...8490	265270	510	II—II—I

Continued

TABLE 9.4*

(Continued)

Route E-V-M-E, Group X-Y-I

Year	v_∞	$v^{\oplus}_{st}$	v^{σ}_{b}	Δv^{σ}_{st}	v^{φ}_{m}	$v^{\oplus}_{\infty}$	$t^{\oplus}_{st}$	t^{φ}_{st}	t^{σ}_{st}	R_{pa}	t_Σ	Group
	km/sec						J. D.			km	days	
1970	10,26	3,75	3,58	2,90	0,029	12,2	2440818	2440918	2441138	25325,7	490	I—II—I
1972	9,12	4,05	3,37	1,61	0,07	11,5	...1470	...1649	...1840	79570	570	II—I—I
1977	13,85	4,18	2,72	6,89	0,05	13,9	...3175	...3300	...3480	38656	510	I—I—I
1978	9,40	4,32	2,94	2,08	0,063	13,2	...3834	...3999	...4164	66947	515	II—I—I
1983	12,47	5,02	3,30	4,08	0,052	14,2	...5510	...5574	...5815	19369,8	500	I—II—I
1985	8,00	3,95	2,83	1,16	0,051	11,8	...6146	...6317	...6516	13426	600	II—I—I
1990	11,04	4,67	3,97	2,37	0,029	11,7	...7842	...7912	...8107	13623	460	I—II—I
1991	9,60	4,17	3,51	1,72	0,18	12,2	...8509	...8667	...8827	12404.9	545	II—I—I

Route E-V-M-E, Group X-Y-II

1970	9,04	3,69	3,15	2,16	0,037	12,8	2440830	2440925	2441152	23215	5735	I—II—II
1972	9,35	4,05	3,39	1,83	0,0688	11,6	...1470	...1640	...1835	94957	630	II—I—II
1977	9,69	4,52	2,72	2,35	0,09	15,5	...3192	...3307	...3482	616540	590	I—I—II
1977	9,49	4,66	2,30	2,41	0,12	17,0	...3196	...3308	...3518	168318	611	I—I—II
1978	8,65	4,35	2,86	1,40	0,043	12,8	...3841	...3999	...4166	122407	635	II—I—II
1983	10,37	5,02	3,31	1,99	0,052	14,8	...5510	...5574	...5815	193698	570	I—II—II
1985	8,13	3,95	2,83	1,29	0,05	12,1	...6146	...6317	...6516	134268	620	II—I—II
1990	10,45	4,67	3,97	1,78	0,029	12,0	...7842	...7912	...8107	13623	570	I—II—II
1991	9,21	4,21	3,61	1,32	0,061	11,4	...8512	...8667	...822	124416	590	II—I—II

*[Translator's Note: Commas in numbers indicate decimal points.]

trajectories in the segments adjacent to Venus have different semiorbit combinations.

If the flight is accomplished along the E-V-M-E route trajectory, the first combination which minimizes $V_{\infty\Sigma}$ corresponds to flight from Mars to the Earth along the first semiorbit trajectory and the second corresponds to flight along the second semiorbit trajectory. /315

The tables present the impulse application point radius R_{pa} for Venus flyby.

Figures 9.2.1 and 9.2.2 show the optimal $V_{\infty\Sigma}$ values for the two- and three-impulse schemes versus Earth launch date for the E-M-V-E and E-V-M-E routes. The relations are periodic. The energy minima of the optimal "via Venus" flight trajectories occur for each route approximately after the total synodic period $T_S^{\Sigma} = 6.4$ years. Since these minima overlap one another, flight along a minimal energy trajectory of one of the routes is possible approximately every 3.2 years. The Earth atmosphere entry velocity $V_*^{\oplus}$ for all the optimal flight trajectories does not exceed 16 km/sec (Figures 9.2.3 and 9.2.4), and the Mars atmosphere entry velocity $V_*^{\sigma} = 9$ km/sec.

Let us compare the energetically optimal accelerated "via Venus" flight trajectories (for the two- and three-impulse schemes) with the optimal flight trajectories along the E-M-E route.

The energy expenditures required for realization of the direct Mars flight trajectories are greater than the minimal values for the "via Venus" flights. The characteristic velocity components for these variants are also unstable in certain flight

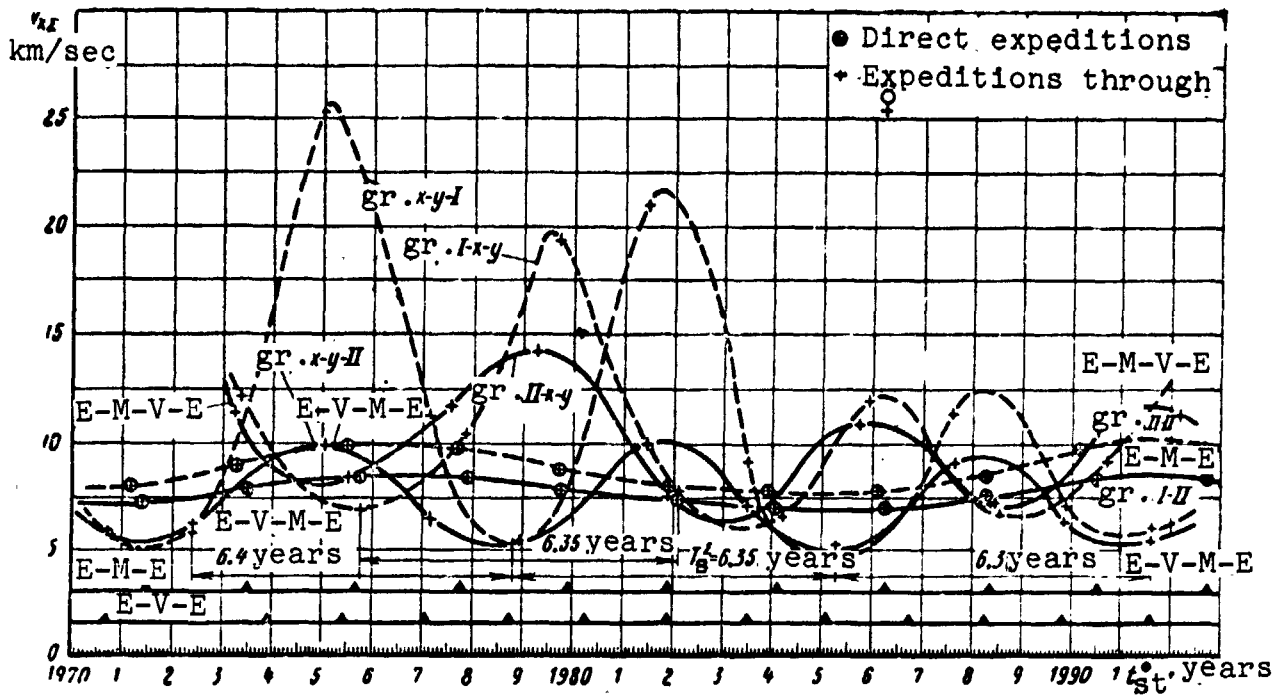

Figure 9.2.1. Energy characteristics of various two-impulse Mars roundtrip flight versions

stages. The energy expenditures are most stable for launch from ARS orbit $V_{st}^{\oplus} \approx 4 \pm 0.5$ km/sec.

When analyzing the Mars spacecraft roundtrip flight trajectories, we usually examine trajectories with limitation of the Earth atmosphere entry velocity to $V_*^{\oplus} < 15.5$ km/sec. In this case, the energy expenditures for realization of the E-M-E route trajectories are significantly higher than for the flight trajectories "via Venus." For most cycles, the direct Mars flight trajectories have an Earth atmosphere entry velocity $V_*^{\oplus} \geq 15.5$ km/sec. A braking impulse (four-impulse flight scheme) is applied prior to entry into the atmosphere in order to reduce the excess velocity. Thus, for the 1975 four-impulse flight cycle scheme along the E-M-E route trajectory (see Figure 9.2.2), the total energy expenditures $V_{\Sigma} = 17$ km/sec, while for the

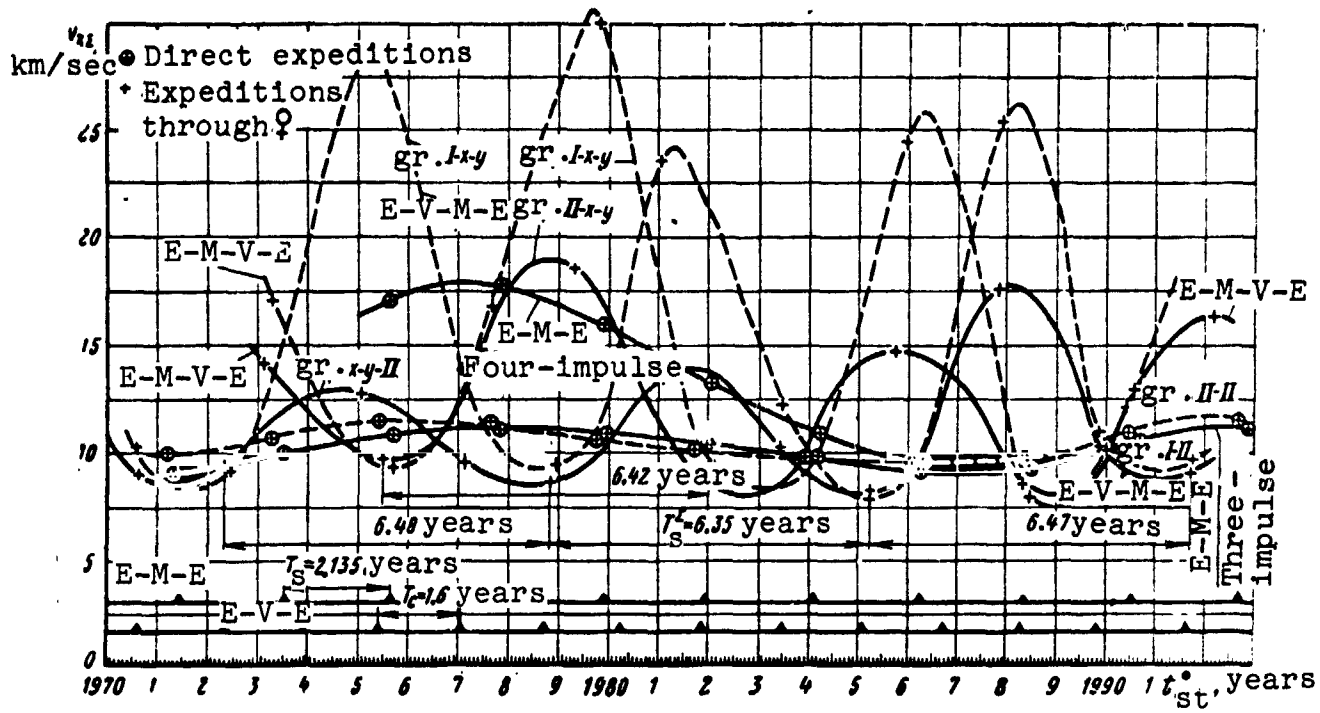

Figure 9.2.2. Energy characteristics of various three-impulse Mars roundtrip flight versions

optimal E-M-V-E route trajectory $V_{\infty} = 9.3$ km/sec. Here the difference in the total roundtrip flight time of these routes is $\Delta t_{\Sigma} = 60$ days. The 1975 cycle for direct flights to Mars corresponds to the largest energy expenditures and highest Earth approach velocity.

In the best direct Mars flight cycles (cycles near 1985), prebraking is not required and the four-impulse flight energy expenditures are close to those for the three-impulse scheme. /320

As a rule, the function V_{∞} reaches a minimal value for $\Delta t_{so} = 0$ except for the 1982 flight cycle, where the optimal stopover time $\Delta t_{so} = 35$ days. In this connection, the calculations of the optimal trajectories, except for 1982, were made for fixed minimal stopover time $\Delta t_{so} = 15$ days.

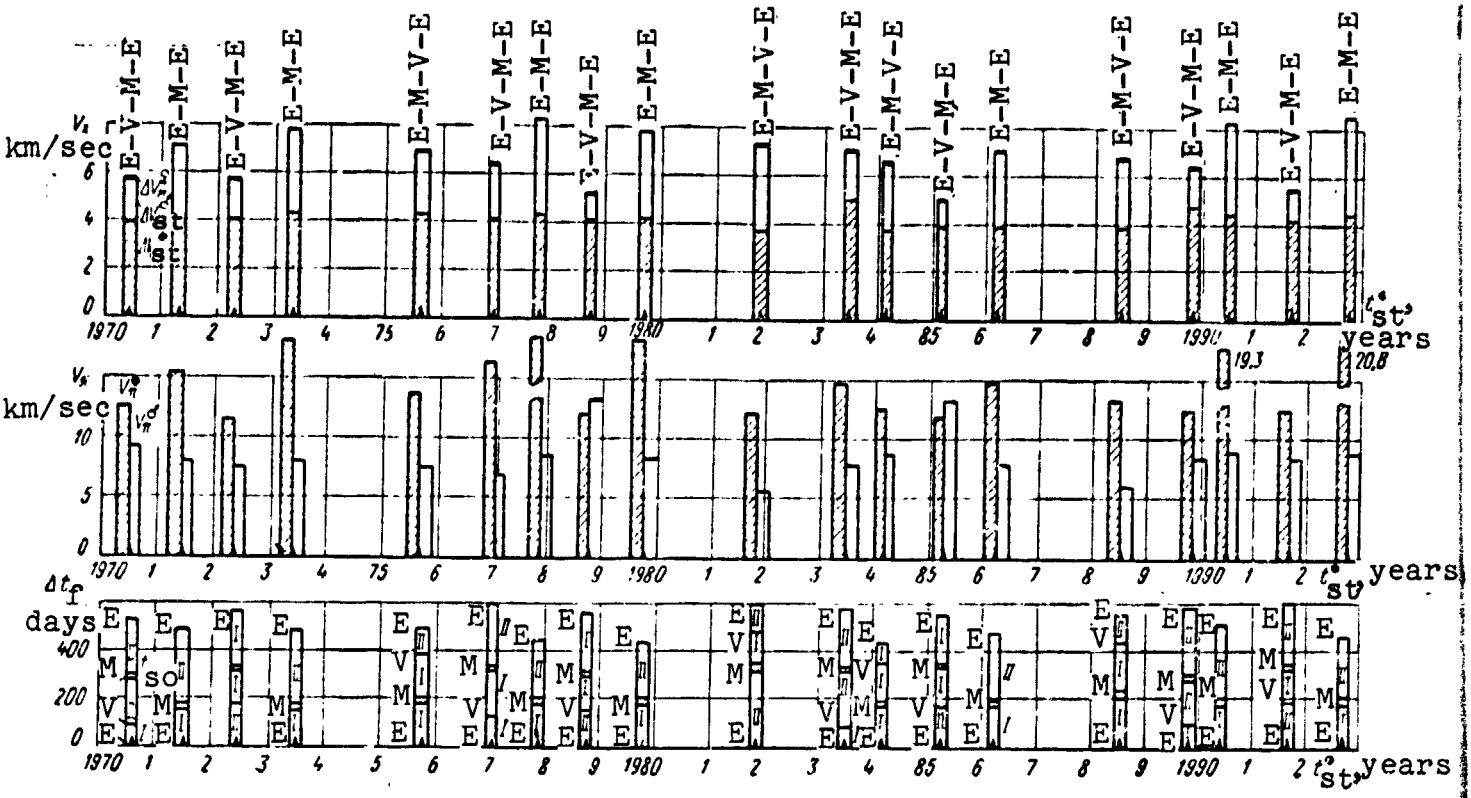

Figure 9.2.3. Characteristics of various two-impulse Mars roundtrip flight versions

CHARACTERISTICS OF OPTIMAL MARS AND VENUS FLYBY TRAJECTORIES FOR 1970 — 1980 FLIGHT CYCLES

With respect to geometric and kinematic characteristics, the trajectories of joint Mars and Venus flyby are very similar to the roundtrip trajectories to Mars by way of Venus.

Table 9.5 and Figures 9.2.5 and 9.2.6 show the characteristics of the optimal Mars and Venus flyby trajectories in the flight cycles from 1979 to 1992.

The nominal curves connecting the V_{∞} points for the optimal trajectories have a nature analogous to the same curves for the Mars roundtrip by way of Venus. The low values of V_{∞} for each

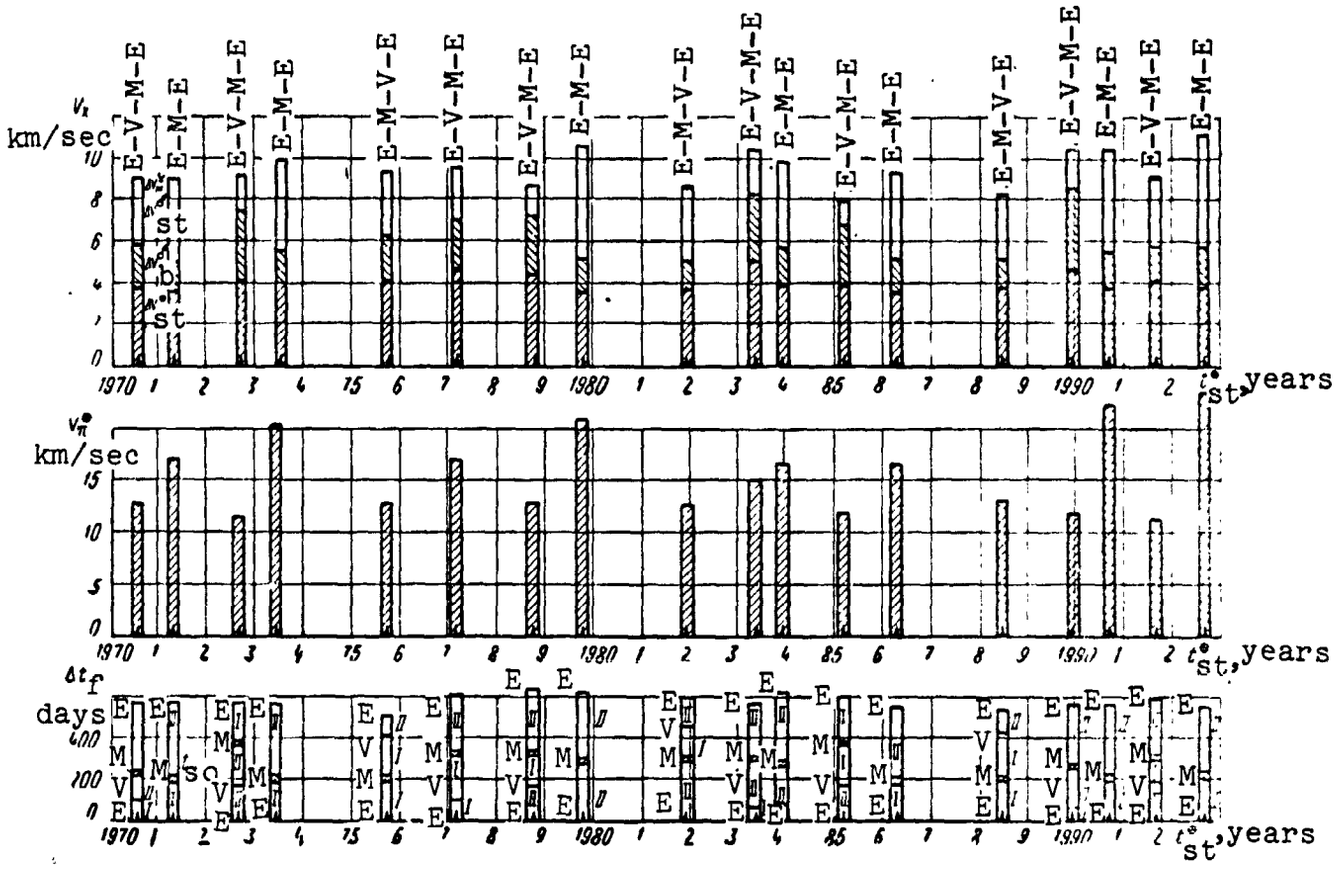

Figure 9.2.4. Characteristics of various three-impulse Mars roundtrip flight versions

of the two flight routes (E-V-M-E or E-M-V-E) repeat with the total synodic period T_s^{Σ} = 6.4 years. In the cycles with large V_{∞} for one of the routes, there are smaller V_{∞} along the other route. Thus, the cycles with low values of V_{∞} repeat approximately every 3.2 years.

The optimal trajectory characteristics of the different routes are also combined with respect to trajectory semiorbit grouping, just as for the roundtrip trajectories.

Figure 9.2.5 also shows the characteristics of Mars flyby trajectories without Venus swingby (direct flyby). We see that the direct flyby trajectories, as a rule, yield larger values of

TABLE 9.5. FLYBY TRAJECTORY CHARACTERISTICS*

Route E-M-V-E, Group I-X-Y

Year	V_Σ	$V^{\oplus}_{st}$	ΔV^{σ}_{M}	R^{σ}_{pa}	ΔV^{φ}_{M}	R^{φ}_{pa}	$V^{\oplus}_{\infty}$	$t^{\oplus}_{st}$	t^{σ}_{st}	t^{φ}_{st}	t_Σ	Group
	km/sec			km	km/sec	km	km/sec	J. D.			days	
1975	7,97	4,10	3,85	56992	0,02	7108	14,2	2442659	2442866	2443048	510	I—I—II
1982	5,29	3,67	1,62	7058	0,002	8242	12,3	...4963	...5155	...5371	560	I—I—II
1984	0,04	3,88	2,88	513556	0,28	227496	18,00	...5710	...5900	...6125	455	I—II—I
1988	5,54	3,72	1,80	4403	0,018	11367	12,9	...7345	...7530	...7740	530	I—I—II

Route E-M-V-E, Group II-X-Y

1973	8,30	6,86	0,17	4814	1,27	7486	12,9	2441660	2441904	2442080	670	II—I—I
1975	6,38	5,40	0,96	5847	0,02	6176	12,1	...2593	...2843	...3053	610	II—I—II
1982	6,07	4,58	1,42	4935	0,05	10770	12,2	...4963	...5238	...5388	580	II—I—II
1984	5,01	4,79	0,20	6396	0,028	6628	15,6	...5635	...5897	...6102	535	II—I—II
1985	8,98	7,8	1,02	65327	0,19	8524	12,7	...6310	...6580	...6750	640	II—I—II
1988	5,99	4,14	1,78	4515	0,065	10244	12,0	...7300	...7515	...7540	580	II—I—II
1990	9,56	5,98	3,28	5176	0,30	265270	13,0	...8020	...8280	...8499	530	II—II—I

Continued

TABLE 9.5*

(Continued)

Route E-V-M-E, Group X-Y-II

Year	V_∞	$V^{\odot}_{st}$	ΔV^{φ}_{M}	R^{φ}_{pa}	ΔV^{σ}_{M}	R^{σ}_{pa}	$V^{\odot}_{\infty}$	$t^{\odot}_{st}$	t^{φ}_{st}	t^{σ}_{st}	t_∞	Group
	km/sec			km	km/sec	km	km/sec	J. D.			days	
1970	3,90	3,65	0,23	16768	0,017	5195	13,8	2440825	2440925	2441148	615	I—II—II
1970	4,31	3,65	0,13	7953	0,53	544757	12,7	...0808	...0908	...1158	570	I—II—II
1972	5,69	4,20	0,074	16039	1,41	6147	11,6	...1485	...1640	...1815	590	I—II—II
1972	4,67	3,96	0,29	15030	0,41	4558	12,6	...1465	...1635	...1800	670	I—II—II
1975	7,16	5,84	0,032	616931	1,28	5099	20,0	...2418	...2633	...2817	680	II—I—II
1977	6,93	4,68	0,44	108304	1,81	159811	15,5	...3200	...3310	...3500	580	I—I—II
1977	4,71	4,60	0,079	7193	0,028	217980	16,5	...3192	...3310	...3500	605	I—I—II
1978	4,86	4,70	0,032	611584	0,13	428399	15,11	...3840	...4014	...4260	570	II—I—II
1982	8,01	5,08	1,96	81308	0,96	7568	19,5	...4748	...4968	...5138	660	II—I—II
1983	6,97	5,08	1,78	381732	0,106	9067	14,5	...5520	...5579	...5835	539	I—II—II
1983	5,59	5,13	0,330	11568	0,13	5927	15,7	...5525	...5583	...5840	590	I—II—II
1985	4,90	4,05	0,28	7359	0,57	5348	12,5	...6167	...6317	...6547	610	II—I—II
1985	4,54	4,19	0,043	618041	0,31	7609	13,5	...6165	...6320	...6540	670	II—I—II
1988	7,98	7,47	0,11	6681	0,40	5949	17,7	...7083	...7273	...7538	700	I—II—II
1990	6,97	5,75	0,006	16492	0,26	70794	12,7	...7895	...7990	...8170	535	I—I—II
1990	5,45	4,55	0,88	17194	0,02	9278	14,5	...7880	...8000	...8215	590	I—I—II
1991	5,31	4,18	0,62	8571	0,51	52777	13,5	...8507	...8662	...8797	680	II—I—II

Route E-V-M-E, Group X-Y-I

1970	6,88	3,91	0,11	12112	2,86	519173	13,5	2440823	2440913	2441158	510	I—II—I
1972	4,29	4,20	0,074	16033	0,02	59886	14,5	...1485	...1640	...1815	485	II—I—I
1978	6,85	4,31	0,036	619937	2,48	395121	12,1	...3839	...4004	...4199	580	II—I—I
1978	5,26	4,28	0,044	8238	0,93	174290	17,8	...3839	...3999	...4154	470	II—I—I
1985	5,16	3,99	0,07	7647	1,10	5342	11,5	...6152	...6320	...6547	565	II—I—I
1985	4,97	3,98	0,04	344498	0,95	381217	15,0	...6150	...6320	...6540	490	II—I—I
1991	4,46	4,38	0,08	7354	0,005	593147	17,8	...8527	...8682	...8887	475	II—I—I
1991	5,57	4,21	0,043	9057	1,32	8624	12,8	...8512	...8667	...8807	550	II—I—I

*[Translator's Note: Commas in numbers indicate decimal points.]

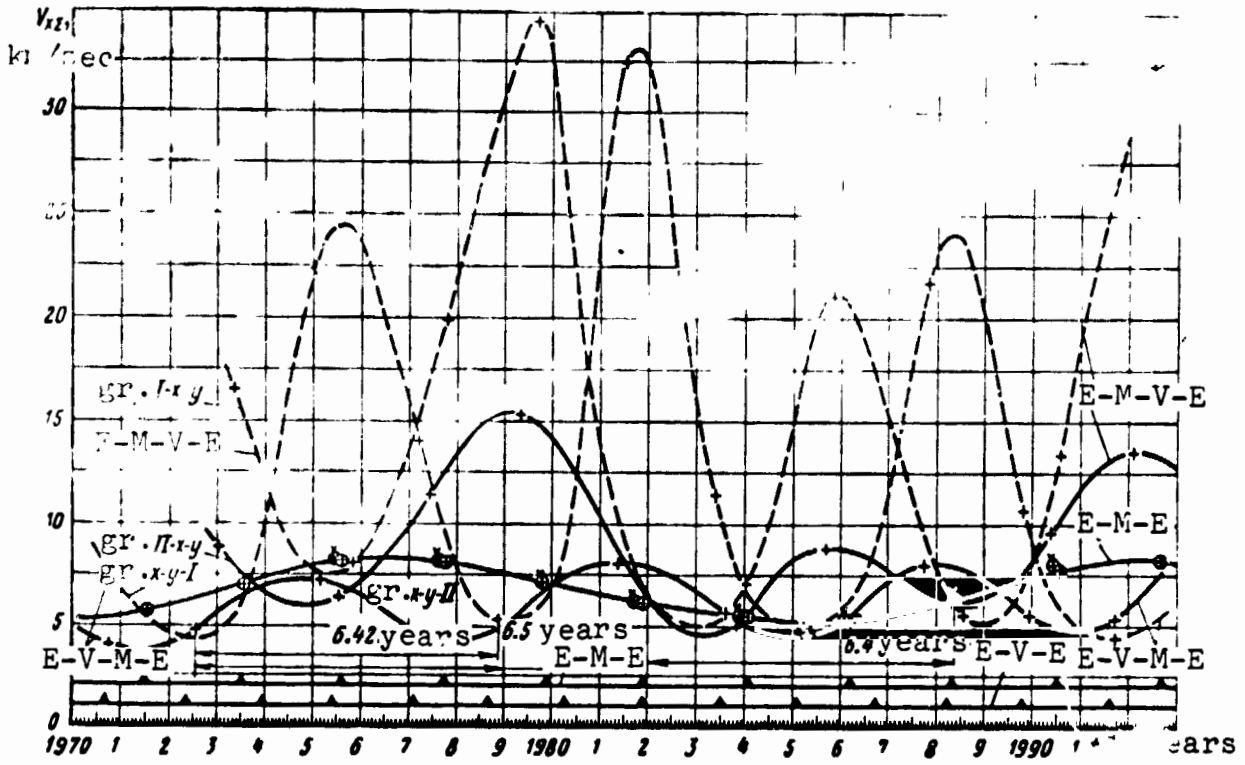

Figure 9.2.5. Energy expenditures for various Mars flyby trajectory variants

V_{xI} than the dual flyby trajectories. Moreover, for such trajectories, the Earth atmosphere entry velocity is significantly higher, just as in the case of the analogous Mars round-trip trajectories.

Use of dual and direct flyby trajectories makes it possible to perform Mars flybys along one route or another practically every year.

We see from this discussion that the flight trajectories to Mars using the gravity field of Venus are of definite interest and may serve as the basic working trajectories for future piloted flights to Mars. In most cycles, they provide lower energy expenditures and Earth atmosphere entry velocities less than 16 km/sec.

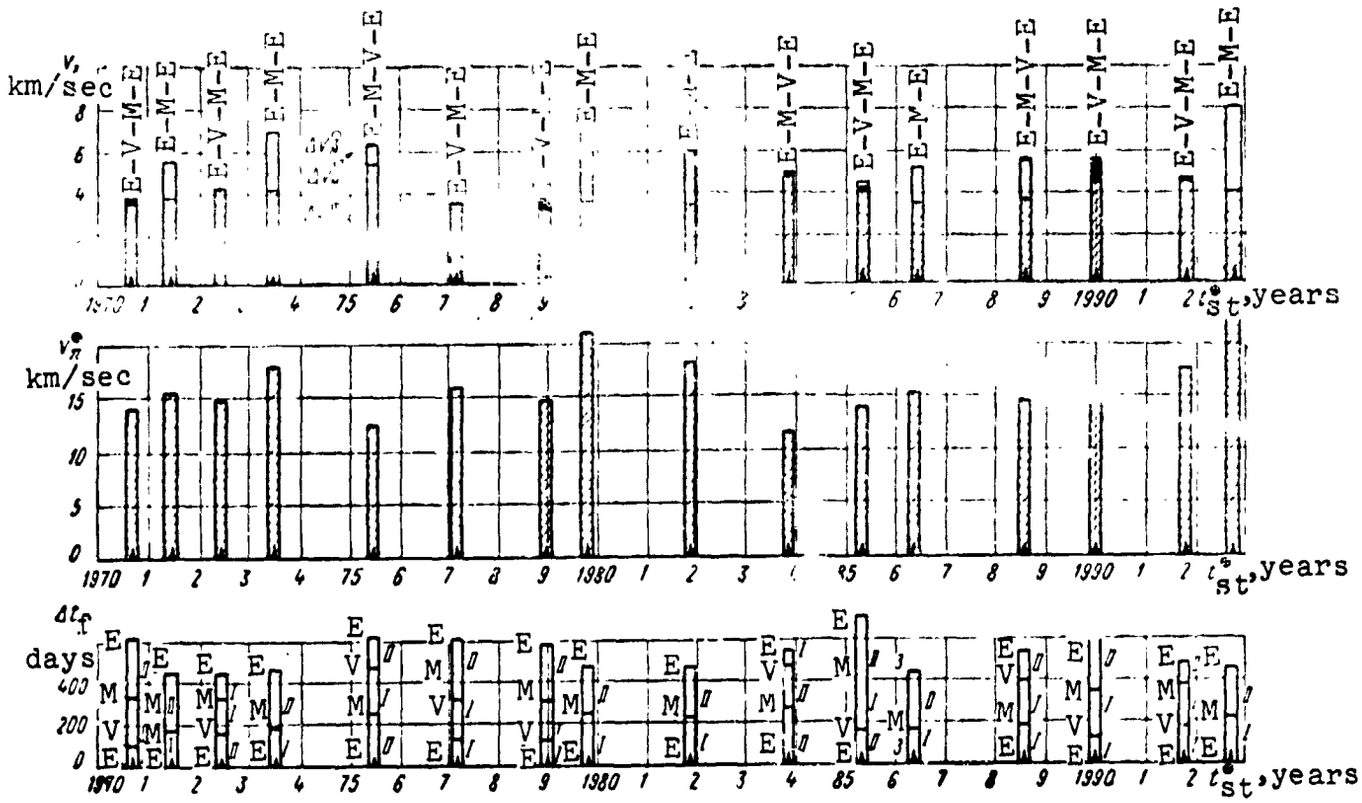

Figure 9.2.6. Characteristics of various Mars flyby variants

Use for roundtrip spacecraft flight to Mars of the "direct flight" and "Venus swingby" flight trajectories increases significantly the number of possible flight variants and shortens the time between the optimal flight cycles. /325

§ 3. FLIGHT TO MERCURY USING THE GRAVITY FIELD OF VENUS

The direct interplanetary flight trajectories to Mercury — swingby interplanetary Earth-Mercury trajectories and interplanetary Earth-Mercury trajectories with entry into orbit around the destination planet — were examined in principle in Chapters 5 and 6. The analysis made there showed that direct interplanetary Earth-Mercury flights require large energy expenditures for their realization. In the best case, the required

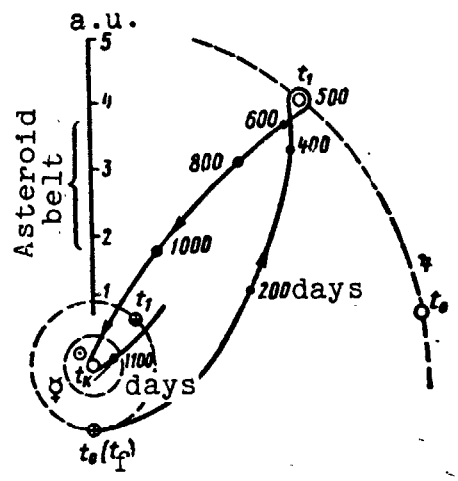

Figure 9.3.1. Projection of Earth-Jupiter-Sun interplanetary SC trajectory on ecliptic (in principle, launch is possible every year):
V_{x1} = 16.5 km/sec; $i_{\pi 1}$ = 5.3 R_4; $R_{\pi\odot}$ = 0.02 a.u.; $V_{\pi\odot}$ = 298 km/sec

launch characteristic velocity for Mercury flyby is 25% greater than the analogous velocity for Mars flyby. Spacecraft entry into final orbit around Mercury requires far larger energy expenditures in comparison with the same operation around Mars. Moreover, direct Earth-Mercury swingby trajectories are characterized by large hyperbolic planetary flyby speeds, which are not always acceptable for normal conduct of experimental studies.

Increase of the energetic efficiency of interplanetary flights to Mercury is an important factor in planning such flights for the near future. Here the characteristic feature of the solar system structure which makes it possible to utilize the gravity fields of Venus or Jupiter may play a decisive role.

In fact, using Jupiter's gravity field to alter SC energy and flight direction, we can obtain many heliocentric segment versions passing near the Sun and intersecting the orbit of Mercury (Figure 9.3.1). It is true that such flights have long duration (up to three years), but when using conventional powerplants (liquid rocket engines), the use of Jupiter's gravity field is practically the only way to accomplish SC flyby near the Sun at distances no more than 0.1 a.u. and intersect Mercury's orbit (Figure 9.3.2). However, the planning of flights directly to Mercury using the planet Jupiter is not advisable because of the long duration and the very small gain in flight energy expenditure.

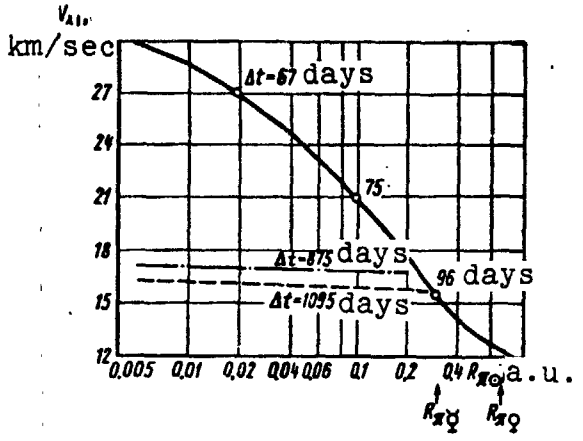

Figure 9.3.2. Values of characteristic launch velocity for flights to the Sun as function of transfer orbit perigee:

--- direct Earth-Sun flight;
-·-·- flight using Jupiter's gravity field

A quite promising technique for solving this problem is the use of Venus's gravity field. There are, in principle, several schemes for flight to Mercury using Venus flyby. While ballistic Venus flyby with a constant value of $V_{\infty 1}$ makes it possible to alter the direction and magnitude of the SC heliocentric velocity by utilizing the Venus gravity field alone, in the powered flyby case, both the direction and the hyperbolic excess velocity at departure are altered as a result of the correction. /326

The Venus flyby trajectory characteristics depend to a considerable degree on the purpose of the SC maneuver near Mercury. Therefore, the flyby scheme choice may, in many cases, be predetermined by the type of interplanetary flight trajectory. /327

MERCURY SWINGBY TRAJECTORIES

The interplanetary Mercury swingby trajectory energy expenditures are defined by the launch characteristic velocity. This means that Venus flyby is only effective when it reduces this velocity. In this connection, we would expect that ballistic Venus flyby may, in principle, lead to larger gains in comparison with other flyby schemes. The limitation here is the required pericenter altitude of the planetocentric Venus flyby orbit, since this height cannot be less than the height of the upper atmosphere, approximately 200 — 150 km. This difficulty can

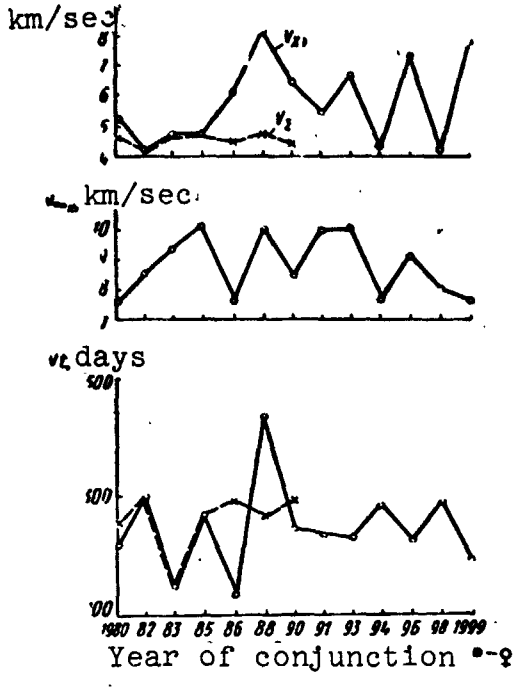

Figure 9.3.3. Characteristics of interplanetary flight trajectory to Mercury with active and ballistic Venus flyby:
—— ballistic; ---- active

be avoided with the aid of a planetocentric flyby trajectory pericenter altitude correction maneuver. The correction, usually requiring a small velocity increment, makes it possible to obtain the desired minimal value of the subsequent flyby trajectory pericenter altitude. Although the energetic characteristics of the flyby schemes with pericenter height correction are not always better than for ballistic flyby, the launch windows become wider.

The kinematics of Earth-Mercury interplanetary flights with Venus flyby are such that they correspond to every Earth-Venus conjunction, which occurs approximately every 17 months. This, then, determines the calendar year of possible launch for SC flight to Mercury with Venus flyby. Now it remains to find the transfer orbit to Mercury with account for active and ballistic Venus flyby with minimal launch characteristic velocity. The technique for finding such transfer orbits is analogous to that described in § 2.

The required minimal launch V_{x1} and total V_{Σ} (in the active flyby case) characteristic velocities, hyperbolic Mercury arrival velocity $V_{\infty f}$, and flight time Δt as functions of the Earth-Venus conjunction calendar year are shown in Figure 9.3.3. Comparison of the minimal launch characteristic velocities for direct SC flight to Mercury and for flight with account for ballistic Venus

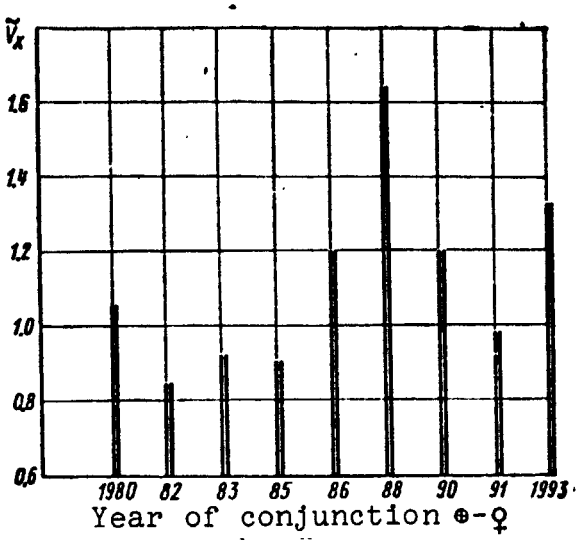

Figure 9.3.4. Comparison of launch characteristic velocities for direct flight to Mercury and with account for ballistic Venus flyby

flyby is shown in Figure 9.3.4.* Analysis of the calculation results makes it possible to draw several conclusions. Flight of an interplanetary vehicle to Mercury with ballistic Venus flyby and launch in the Earth-Venus conjunction years 1982, 1983, and 1985 is energetically more effective (see Figure 9.3.4) in comparison with /329 direct flight. In 1982, the launch characteristic velocity will be the lowest in the 1980 — 1990 decade and equal to about 4 km/sec and 16% lower than for the comparable direct trajectory. Flight to Mercury with active Venus flyby permits significant reduction of the energy expenditures in 1988 — 1990 in comparison with ballistic flyby. Such flights are also possible in 1975, 1977, and 1978 with required values of $V_\infty = 4.08$ km/sec, $\Delta t = 172$ days, and $V_\infty = 4.47$ km/sec, $\Delta t = 119$ days, $\tilde{V}_\infty = 4.44$ km/sec, respectively. The flight time increases by more than double in all cases in comparison with the direct transfers.

The hyperbolic arrival velocity at Mercury is on the average 10 km/sec and is considerably lower in the direct flight case. For the interplanetary Mercury swingby trajectory with ballistic Venus flyby, the design problem reduces to optimizing the basic design parameters of the boost module for given hyperbolic excess velocity. Figures 9.3.5 and 9.3.6 show the optimal

* In Figure 9.3.4, the value of $\tilde{V}_x$ is equal to the ratio of the launch characteristic velocities for ballistic Venus flyby and for direct flight.

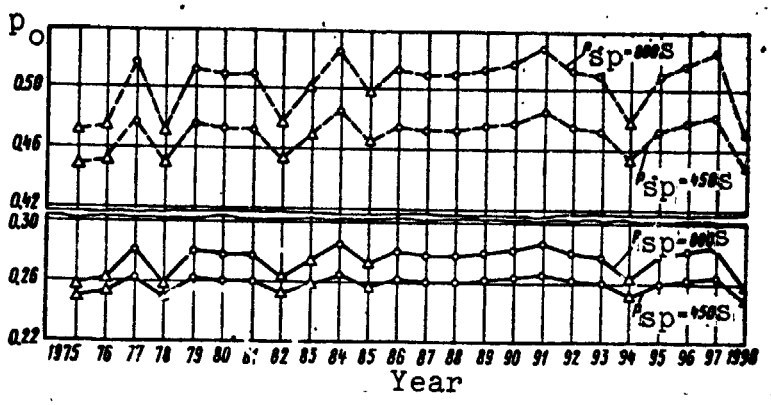

Figure 9.3.5. Optimal values of boost module thrust-weight ratio of interplanetary vehicle swinging by Mercury:
0- direct flight; Δ- flight with Venus flyby; —— $\gamma_{pp} = 0.1$; --- $\gamma_{pp} = 0.02$

values of n_0 and μ_f for the module of an interplanetary vehicle intended for Mercury swingby with and without ballistic Venus flyby for launch in 1975 — 1998. Here the departure hyperbolic excess velocities (corresponding to V_{x1}) are taken from Figure 9.3.4.

FLIGHT TRAJECTORIES WITH SC ENTRY INTO ORBIT AROUND MERCURY

For such a maneuver near Mercury, the Venus flyby will reduce the total characteristic velocity V_Σ, which depends on both the launch and braking characteristic velocities. Thus, /330 Venus flyby is energetically more effective when it leads to change of the characteristic launch and braking velocities such that V_Σ decreases. Decrease of V_Σ is not always associated with reduction of the braking characteristic velocity. Most often, it may be caused by reduction of the departure hyperbolic excess velocity (launch characteristic velocity). The reason is that choice of the Earth-Venus transfer orbit is more flexible. However, selection of the departure hyperbolic excess velocity is limited by its minimal value, below which the SC arrival

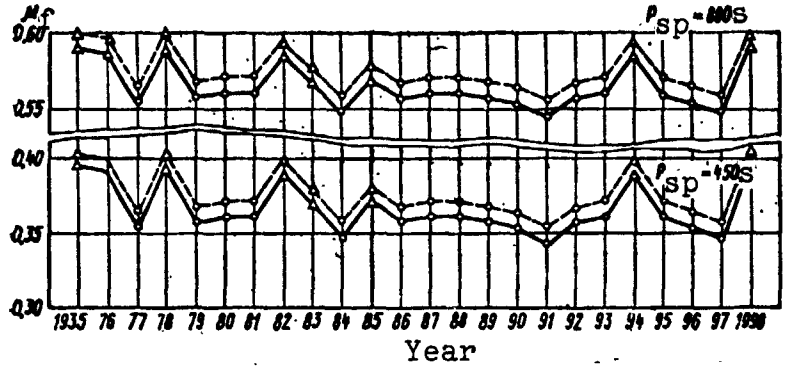

Figure 9.3.6. Optimal values of relative final weight of boost module of interplanetary vehicle swinging by Mercury:
0- direct flight; Δ- flight with Venus flyby; —— γ_{pp} = 0.1; --- γ_{pp} = 0.02

velocity at Venus will be very low, which does not permit using the gravity field of the planet for flight to Mercury. Because of this limitation, it is not possible to utilize the minimal characteristic velocity ellipse for the Earth-Venus trajectory and reach Mercury as a result of ballistic Venus flyby.

The calculations showed that transfer orbits with ballistic Venus flyby and entry into orbit around Mercury are characterized by the same kinematic parameters as the previously examined swingby transfer orbits. Figure 9.3.7 shows the minimal values of the total characteristic velocity versus Earth-Venus conjunction year with ballistic Venus flyby. The smallest value V_Σ = 11.8 m/sec [t_0=2449650 J. D. (24/X 1994); Δt = 290 days], which is 9% less than the minimal total characteristic direct flight velocity [t_0=2446562 J.D. (11/V 1986); Δt = 95 days]. Comparison of the minimal values of the total characteristic velocity for the direct and indirect (ballistic Venus flyby) interplanetary flights with entry into orbit around Mercury is given in Figure 9.3.8.* /331

* In Figure 9.3.8, the value of $\tilde{V}_\Sigma$ is equal to the ratio of V_Σ for ballistic flyby to V_Σ for direct flight.

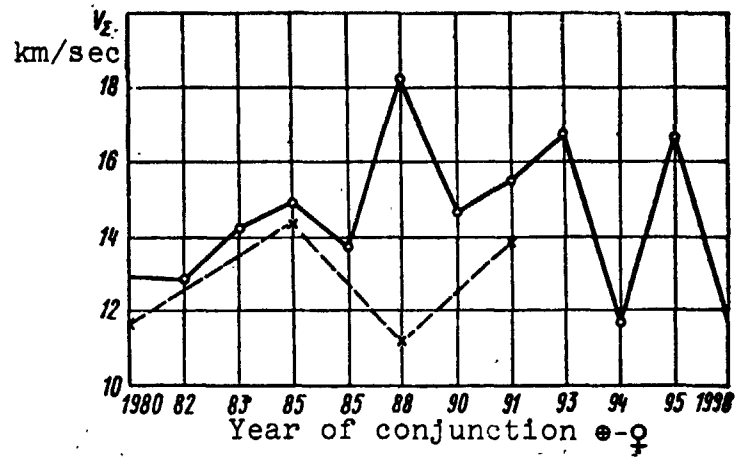

Figure 9.3.7. Minimal values of the total characteristic velocity of interplanetary flight with entry into orbit around Mercury as function of launch year (years of ⊕ — ♀ conjunction). Final orbit is circular, H_f = 1000 km; --- scheme with flyby orbit pericenter altitude correction

Ballistic Venus flyby for entry into orbit around Mercury is more effective than direct flights only in 1980, 1982, 1983, and 1994, 1998.

The minimal V_Σ can be achieved only within 20 days from the Earth-Venus conjunction date. Deviation from these limits leads to marked increase of V_Σ.

It is interesting to note that the trajectories with ballistic Venus flyby lead to encounter with Mercury near the descending node region — aphelion of Mercury's orbit. Therefore, the characteristic braking velocity for transfer orbits with ballistic Venus flyby is basically larger than its values for direct flights. In this connection, ballistic Venus flyby effectiveness is achieved only by reducing the launch characteristic velocity in comparison with the direct flights. This result makes it possible to seek reserves for reducing V_Σ by regulating the longitude of the point of encounter with Mercury

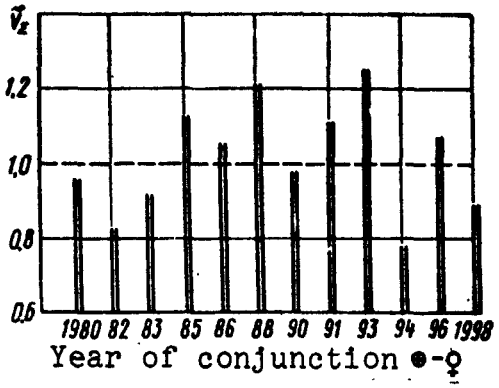

Figure 9.3.8. Comparison of minimal total characteristic velocity for direct and indirect (ballistic Venus flyby) flights with entry into orbit around Mercury. Final orbit is circular, H_f = 1000 km

by means of active Venus flyby. If this leads to encounter with Mercury's orbit — then we can postulate reduction of V_Σ.

However, calculations show that this reduction is not achieved because of the large energy expenditures in the vicinity of Venus, the characteristic velocity of which reaches 3 km/sec. In this sense, the Venus flyby scheme with flyby orbit pericenter altitude correction is more promising. /332

In Figure 9.3.7, the dashed line connects points with minimal V_Σ for this Venus flyby scheme. We see that V_Σ decreases to 11.2 km/sec for launch date t_0=2447330 J. D. (17/VI 1988) and Δt = 300 days.

If we take the total characteristic velocity as the optimality criterion, the solution of the design problem in which ballistic Venus flyby is taken into account will reduce to optimizing the basic design parameters of the boost and retro modules for known hyperbolic excess velocities. Of the two interplanetary flight types — direct and indirect (ballistic Venus flyby) — we selected transfer orbits with minimal V_Σ, on the basis of which by solving the design problem, we determined the optimal basic design parameters of the boost and retro modules of the interplanetary vehicle intended for flight to Mercury with entry into a terminal orbit. The solution results are shown in Figures 9.3.9 and 9.3.10.

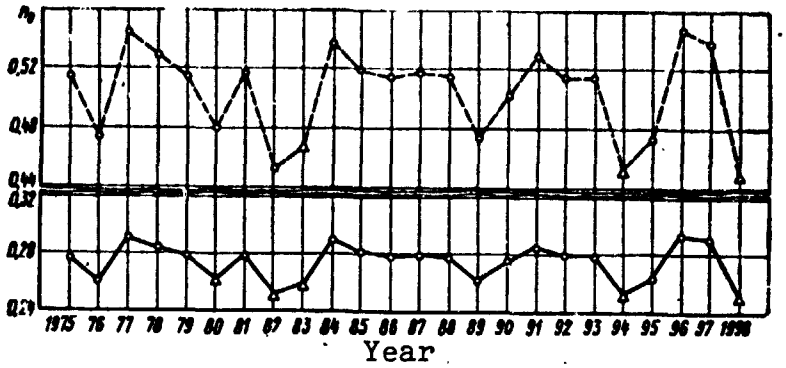

Figure 9.3.9. Optimal thrust-weight ratio of boost module (entry into orbit around Mercury):
0- direct flight; Δ- flight with Venus flyby; —— $\gamma_{pp} = 0.1$; --- $\gamma_{pp} = 0.02$; $P_{sp} = 450$ sec

The influence of Venus flyby on the energy characteristics of the interplanetary flight trajectories to Mercury with return to the Earth may show up differently for the return trajectories. The calculation results show that, for return trajectories, only a small reduction of V_Σ (less than 10%) is possible as a result of Venus flyby, but this involves a large mission duration increase (by 50 — 100%) [72]. For this reason, we shall not examine here the Mercury-Earth return trajectories with Venus flyby, although in many cases they may lead to lower Earth atmosphere entry velocities.

The criterion for use of the Venus flyby schemes to solve Mercury flight problems should not be related only with the energy expenditure level. Other important characteristics are the launch "window" width and sensitivity of the nominal interplanetary trajectory to the magnitudes of the deviations. /333

In the case of ballistic Venus flyby for transfer orbits with minimal characteristic velocity, the launch "window" size depends on the minimal pericenter height limitations. For example,

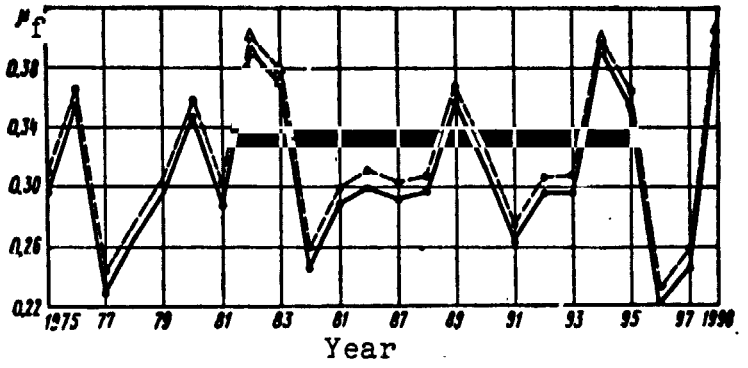

Figure 9.3.10. Optimal relative final weight of boost module (entry into orbit around Mercury):

0- direct flight; Δ-flight with Venus flyby; —— γ_{pp} = 0.1; --- γ_{pp} = 0.02; P_{sp} = 450 sec

for the 1980 conjunction, the launch "window" narrows in comparison with direct flight by nearly a factor of three and amounts to only seven days [72]. In the case of low pericenter altitudes with ballistic Venus flyby, changeover to the flyby scheme with altitude correction yields large advantages. For the same conjunction year (1980), changeover to pericenter height correction of the flyby orbit with 5% V_Σ margin broadens the launch "window" to 42 days [72]. If the flyby orbit pericenter height is already quite high, ballistic flyby also makes it possible to broaden the launch "window" significantly. For example, for the 1982 conjunction, ballistic Venus flyby (pericenter height 1980 km) permits for 5% V_Σ margin broadening the launch "window" to 50 days [72]. Thus, depending on the flyby orbit, pericenter height selection of the proper Venus flyby scheme makes it possible to broaden considerably the launch "window" of the interplanetary vehicle to Mercury. Therefore, even if the rational Venus flyby scheme does not yield an appreciable gain in energetics, an even greater advantage is the launch interval broadening. /334

Realization of the interplanetary flight trajectory to Mercury with Venus flyby depends to a considerable degree on the nominal trajectory sensitivity to deviations of the kinematic parameters from the theoretical values. Control of the indirect Earth-Venus-Mercury flight trajectory is a more difficult problem than for direct flight. In fact, even very small errors in realization of the theoretical pericenter altitude may cause marked errors in the direction of the altered hyperbolic flyby orbit asymptote. Judging by the results of approximate calculations and numerical integration, the fuel supply available for correction should supplement the average total required fuel supply by $(2.3 — 3.5)\sigma$ (σ is the mean square deviation of the correction realization error), which for indirect flights with Mercury swingby during the 1970 and 1973 Earth-Venus conjunctions correspond to a characteristic velocity of about 250 m/sec.

Thus, the above results of preliminary analysis of indirect flight trajectories to Mercury make it possible to look optimistically at technical realization of interplanetary flights to Mercury with Venus flyby.

§ 4. SC MANEUVERS UTILIZING JUPITER'S GRAVITY FIELD

The gravity field of Jupiter, the largest planet, is a good "assistant" in laying out space routes to inaccessible and distant regions of the solar system. These include regions near the Sun, regions above and below the ecliptic plane, the outer planets from Saturn to Pluto, and the deep space regions. The location of Jupiter's orbit and its mass are such that these problems can be successfully solved with lower energy expenditures by using /335 the gravity field of Jupiter to alter the SC-planet encounter geometry.

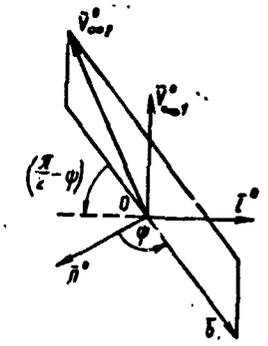

Figure 9.4.1. Kinematics of flyby orbit vectors: $\bar{n}^\circ = \bar{i}^\circ \times \bar{V}^\circ_{\infty 1}$; $\bar{i}^\circ \cdot \bar{K}_4 = 0$; $\bar{n}^\circ$ is positive

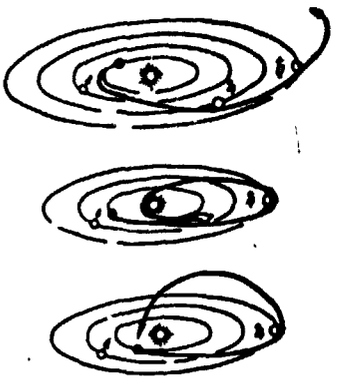

Figure 9.4.2. Promising schemes of SC space maneuvers with Jupiter flyby

It was shown previously that the magnitudes of the target range $\bar{b}$ (or pericenter height) and the angle ψ for unchanged $V_{\infty 1}$ determine completely the SC-planet encounter geometry and characterize the planetocentric flyby orbit (Figure 9.4.1). By altering $\bar{b}$ and the angle ψ, we can obtain many flight variants in view of the change after flyby of the magnitude and direction of the SC heliocentric flight velocity. Some promising SC flight schemes with Jupiter flyby are shown in Figure 9.4.2. We shall examine the SC ballistic design characteristics for such flight schemes.

FLIGHT TRAJECTORIES TO THE SUN

Flyby orbits with values of ψ close to zero can be used for SC flights to the Sun (solar probes) since the SC heliocentric velocity decreases markedly after flyby, which leads to nearly rectilinear heliocentric trajectories and in certain cases, even to Sun "impact" trajectories. Direct flight from the Earth to the vicinity of the Sun requires large energy expenditures (Figure 9.3.2). Among the possible flight schemes to the Sun ($R_\odot \leqslant 0.2$), the flight scheme using the gravity field of Jupiter requires the

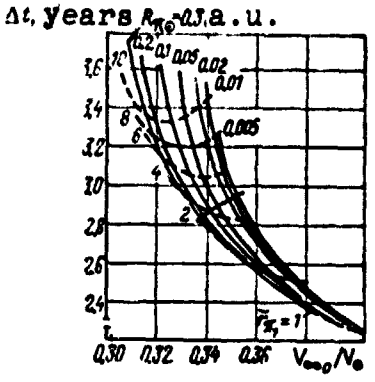

Figure 9.4.3. Required flight time to the Sun versus departure orbit hyperbolic excess velocity

smallest energy expenditures and is therefore the most promising. Figure 9.4.3 shows the required flight times Δt of SC performing flight to the Sun with Jupiter flyby as a function of the hyperbolic excess velocity $V_{\infty\odot}$, perihelion radius /336 $R_{*\odot}$ of the transfer orbit after Jupiter flyby, and pericenter radius $\bar{r}_{*1}$ of the planetocentric flyby orbit, represented in Jupiter radius units. The other ballistic design characteristics coincide with the direct Earth-Jupiter flight values.

FLIGHT TRAJECTORIES OUT OF THE ECLIPTIC

Probing of the regions above and below the ecliptic plane is of great scientific interest because of the possibility of studying the Sun from "below" ("above") and investigating the characteristics of the interstellar medium and the possible asymmetry of conditions in space (distribution of meteoritic bodies, solar phenomena, and so on). Heliocentric SC flight trajectories in planes with large inclination angles (close to 90°) make it possible to solve this problem

Direct flights from the Earth to the regions above the ecliptic require large energy expenditures. Figure 9.4.4 shows the values of the departure orbit hyperbolic excess velocity as a function of heliocentric orbit inclination to the ecliptic plane and perihelion radius [73]. In view of the large values of $V_{\infty\odot}$, we can hardly expect realization of such flight schemes to distant regions above the ecliptic plane.

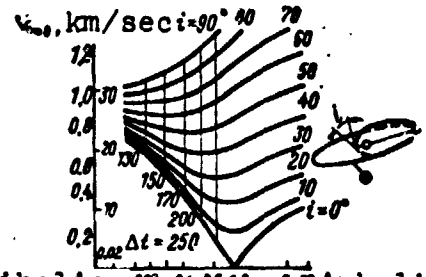

Figure 9.4.4. Variation of hyperbolic excess velocity of departure orbit from transfer orbit perigee for direct flights from the Earth to regions above the ecliptic plane

The use of Jupiter's gravity field makes it possible to deflect the SC heliocentric orbit for values of ψ close to 90° (see Figure 9.4.1) in order to achieve large ecliptic latitudes. Two flight schemes are possible, depending on the problem formulation. The first flight scheme involves rotation of the transfer orbit plane after Jupiter flyby to 90° to the ecliptic plane and permits the SC to pass above (below) the Sun. This scheme flight is shown in Figure 9.4.5. /337

The second flight scheme meets the requirement for maximizing the SC heliocentric velocity components after Jupiter flyby normal to the ecliptic plane. This scheme makes it possible to achieve the greatest distance between the SC and the ecliptic plane at the point of its maximal heliocentric latitude. Figure 9.4.6 shows the maximal deviation H_e from the ecliptic plane as a function of launch characteristic velocity for the two flight schemes [40].

INTERPLANETARY FLIGHT TRAJECTORIES TO THE OUTER PLANETS

After accomplishment of interplanetary vehicle flights to Jupiter, the requirement will inevitably arise for studying the more distant planets — Saturn, Uranus, Neptune, and Pluto. However, direct flights to these planets require still greater energy expenditures with excessively long flight time required (see § 3, Chapter 5). Reduction of the flight time to acceptable magnitudes can be accomplished only at the expense of further energy expenditure increase (Figure 9.4.7). /338

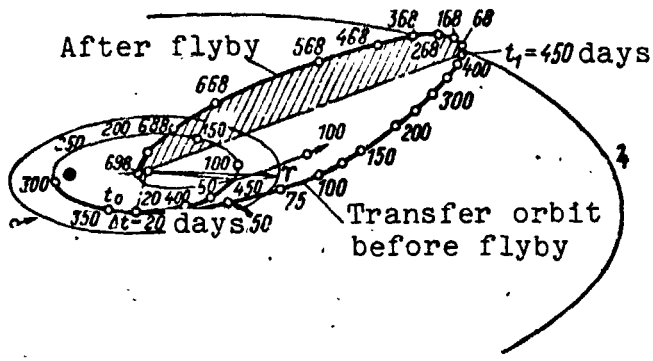

Figure 9.4.5. Jupiter flyby with transfer orbit plane rotation to 90° to the ecliptic plane (first scheme):

t_0=2442590.5 J. D.; $V_{\infty 0}$=0.37 $V_\oplus$; i=90°; $R_{\pm\odot}$=0.045 a.u.; $\tilde{r}_\pi$=7

The solution of the problem of flight to the outer planets with energy characteristics and flight times which are acceptable for SC with high-thrust engines (liquid rocket engines and nuclear rocket engines) becomes feasible when using Jupiter's gravity field. If flyby takes place with angles ψ close to 180° (see Figure 9.4.1), the interplanetary vehicle can acquire sufficient energy from Jupiter so that, after flyby, it can travel along a hyperbolic orbit and thereby overcome the gravitational force of the solar system. Such a flight scheme with proper positioning of the planets makes it possible to reach the next planet quite quickly. Sequential utilization of the gravity fields of the outer planets can permit interplanetary vehicle flight to many planets after Jupiter. In recent years, several studies have been made of interplanetary flights to the outer planets with use of Jupiter's gravity field or the gravity fields of several planets.*

It is of interest that the possibilities for studying the outer planets of the solar system (Saturn, Uranus, Neptune, and Pluto) utilizing Jupiter flyby are being brought to light in the present decade. Interplanetary trajectories with flyby of

*An analysis of some such studies in the U.S. is given in [40].

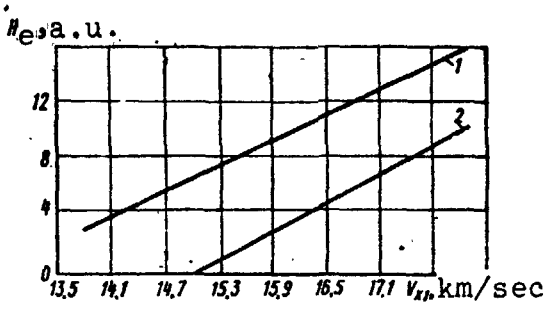

Figure 9.4.6. SC distance from ecliptic plane at time of its passage above Sun for two flight schemes:

1- scheme with maximization of normal velocity component;
2- scheme with 90° rotation to the ecliptic plane

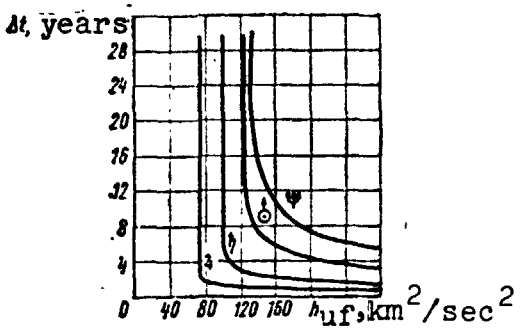

Figure 9.4.7. Minimal time of direct flights to the outer planets as function of launch energy

two, three, or even four outer planets for moderate values of the launch characteristic velocity (from 14.5 to 16.5 km/sec) and flight times are also possible. The following three fundamental planet swingby schemes are usually considered:

1) two-planet swingby scheme along the routes: Jupiter-Saturn (J-S); Jupiter-Uranus (J-U); Jupiter-Neptune (J-N); and Jupiter-Pluto (J-P);

2) three-planet swingby scheme along the routes: Jupiter-Saturn-Pluto (J-S-P); Jupiter-Uranus-Neptune (J-U-N);

3) four-planet swingby scheme along the Jupiter-Saturn-Uranus-Neptune (J-S-U-N) route.

An important characteristic of these flight schemes is that Jupiter is the first planet on each route. Therefore, the minimal energy expenditures will be determined primarily by the Earth-Jupiter flight conditions. /339

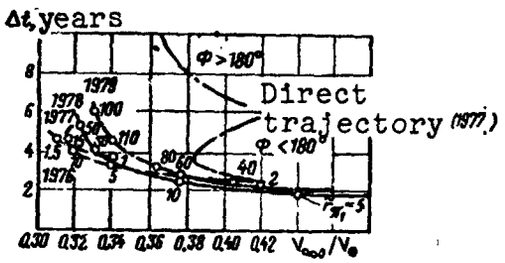

Figure 9.4.8. Flight time as function of departure orbit hyperbolic excess velocity for the E-J-S route

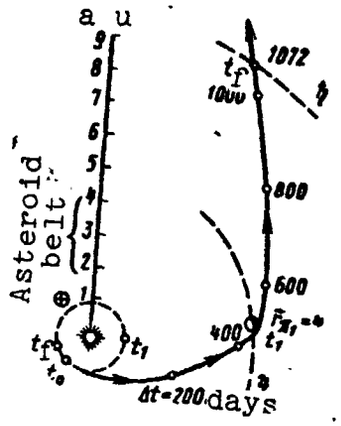

Figure 9.4.9. Interplanetary flight trajectory to Saturn with Jupiter flyby:
t_0 - September 1977; $V_{\infty 0}=0.35\,V_\oplus$

Let us examine each swingby scheme.

Two-Planet Swingby Scheme

(Earth)-Jupiter-Saturn. The dependence of the flight time to Saturn on the departure orbit hyperbolic excess velocity $V_{\infty 0}$ for various launch dates and various planetocentric flyby orbit pericenter radii $\tilde{r}_{\pi 1}$ (in Jupiter radii) is shown in Figure 9.4.8 [73]. We see that the best possibilities for flight to Saturn with Jupiter flyby occur with launch in 1977 — 1978, when the smallest $V_{\infty 0}$ with practically minimal Δt and acceptable $\tilde{r}_{\pi 1}$ can be achieved. If we select the launch date in 1977, then $V_{\infty 0}=0.32\,V_\oplus$ with $\tilde{r}_{\pi 1}=10$, while for direct flight, its minimal value is $0.385\,V_{\infty 0}$. However, for flights to the outer planets, reduction of the flight time may be a more important factor than reduction of $V_{\infty 0}$. In this sense, the flight characteristics to Saturn with Jupiter flyby become still better, the flight time decreases from four years to 2.75 years. The shortest flight time for launch in 1977, 1978, and 1979 is two years.

Figure 9.4.9 [73] shows the projection on the ecliptic plane of the interplanetary flight trajectory to Saturn with Jupiter flyby for launch on 6 September 1977. A similar

TABLE 9.6. OPTIMAL SC BALLISTIC DESIGN CHARACTERISTICS FOR FLIGHTS TO THE OUTER PLANETS WITH JUPITER FLYBY*

Trajectory	Start date	$V_{\infty 0}$ km/sec	Δt_{Σ} days	n_0^{opt}	μ_f^{opt}	γ_{pp}	s_{pp} s
Earth-Jupiter-Saturn	September 1977	10,41	1072	0,38 0,72 0,5 0,93	0,174 0,183 0,456 0,468	0,05 0,01 0,05 0,01	450 1000
Earth-Jupiter-Uranus	October 1978	10,41	2080	0,38 0,72 0,5 0,93	0,174 0,183 0,456 0,468	0,05 0,01 0,05 0,01	450 1000
Earth-Jupiter-Neptune	November 1979	11,01	2920	0,38 0,72 0,51 0,95	0,162 0,169 0,437 0,449	0,05 0,01 0,05 0,01	450 1000
Earth-Jupiter-Pluto	1977	10,12	3650	0,38 0,72 0,49 0,92	0,185 0,194 0,467 0,476	0,05 0,01 0,05 0,01	450 1000

*[Translator's Note: Commas in numbers indicate decimal points.]

interplanetary trajectory is possible with launch in October, 1978. The next optimal launch dates are possible only after the total synodic period (20 years) in 1997 — 1998. Table 9.6 shows the optimal boost module basic design parameters n_0 and μ_f for the September, 1977, launch date.

(Earth)-Jupiter-Uranus. The ballistic characteristics of /340
the interplanetary flight trajectory to Uranus using Jupiter's gravity field are shown in Figure 9.4.10 [73]. The most acceptable flight characteristics occur for launch dates in 1978 — 1979. Thus, for $V_{\infty 0}=0.34\,V_{\oplus}$, the flight time is 6.5 years and $\tilde{r}_{s1}=2$ (1978) or $\tilde{r}_{s1}=12$ (1979), while the minimal flight duration is about five years but with $V_{\infty 0}=0.38-0.4\,V_{\oplus}$.

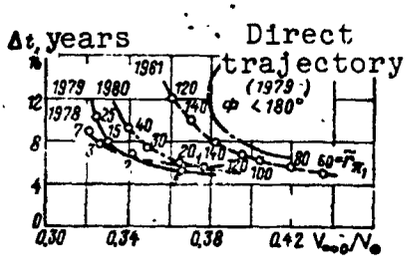

Figure 9.4.10. Flight time as function of departure orbit hyperbolic excess velocity for E-J-U route

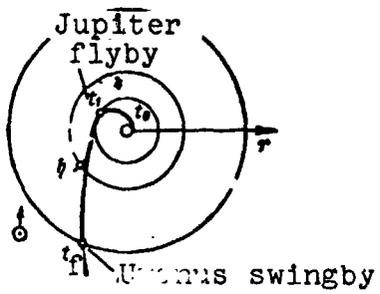

Figure 9.4.11. Interplanetary flight trajectory to Uranus with Jupiter flyby:
t_0- October, 1978; $V_{\infty 0}=0.35\,V_\oplus$

The direct flight with launch in 1979 will last 12 years with minimal hyperbolic excess velocity $V_{\infty 0}$ equal to 0.38 $V_\oplus$. While the direct flight duration will be 6.5 years, it requires $V_{\infty 0}$= 0.42 $V_\oplus$. In the first case, Jupiter flyby makes it possible to reduce the flight time by a factor of 1.8 with some reduction of $V_{\infty 0}$, in the second case for the same flight time $V_{\infty 0}$ is less by 2.4 km/sec or nearly 30%.

Figure 9.4.11 shows the projection of the E-J-U interplanetary flight trajectory on the ecliptic plane for the October, 1978, launch date and $V_{\infty 0}=0.35\,V_\oplus$ [73]. Table 9.6 shows the optimal boost module basic design parameters n_0 and μ_f for the October, 1979, launch date.

The next optimal launch dates are possible only in 1992 — 1993.

(Earth)-Jupiter-Neptune. Among the ballistic characteristics of the flight trajectories to Neptune using the gravity field of Jupiter shown in Figure 9.4.12, the most acceptable are those for launch dates in 1979 — 1980 [73]. Thus, for the November, 1979, launch date, interplanetary SC flight to Neptune with Jupiter

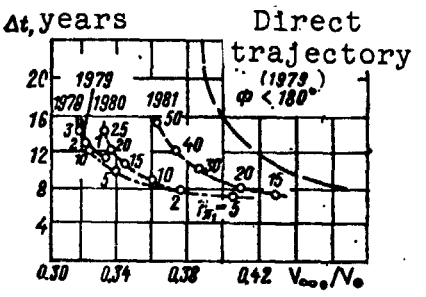

Figure 9.4.12. Flight time versus departure orbit hyperbolic excess velocity for E-J-N route

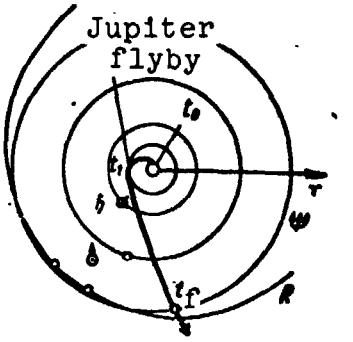

Figure 9.4.13. Interplanetary flight trajectory to Neptune with Jupiter flyby:
t_0 - November, 1979; $V_{\infty 0}=0.37\,V_\oplus$

flyby can be realized with hyperbolic excess velocity $V_{\infty 0}=0.37\,V_\oplus$ and Δt = 8 years, close to the minimal value, and $\bar{r}_{x1}=3$. The interplanetary flight trajectory with launch in 1980, when $\bar{r}_{x1}=9$ /341 has similar characteristics.

The interplanetary flight trajectories to Neptune with Jupiter flyby have qualitatively better ballistic characteristics in comparison with direct flight (see Figure 9.4.12). /342 Thus, for launch in 1979 and flight time eight years $V_{\infty 0}=0.48\,V_\oplus$, which is 3.3 km/sec higher than $V_{\infty 0}$ for flight using the gravity field of Jupiter. While direct flight is realized with minimal $V_{\infty 0}=0.39\,V_\oplus$ (close to $V_{\infty 0}$ for flight with Jupiter flyby), the flight time increases by nearly 17 years.

Figure 9.4.13 shows the projection on the ecliptic plane of the interplanetary flight trajectory to Neptune with Jupiter flyby for launch on 10 November 1979, $V_{\infty 0}=0.37\,V_\oplus$ and Δt = 8 years. Table 9.6 shows the optimal boost module basic design parameters n_0 and μ_f corresponding to this trajectory. The next optimal launch dates are possible only in 1992 — 1993.

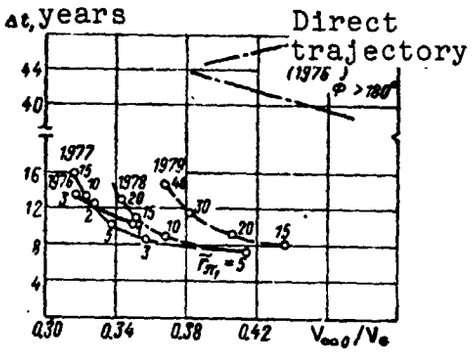

Figure 9.4.14. Flight time versus departure orbit hyperbolic excess velocity for the E-J-P route

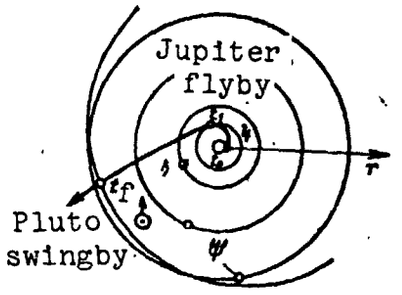

Figure 9.4.15. Interplanetary flight trajectory to Pluto with Jupiter flyby:

t_0 - January, 1977; $V_{\infty 0} = 0.34\ V_\oplus$

(Earth)-Jupiter-Pluto. The ballistic characteristics of the interplanetary flight trajectory to Pluto using Jupiter's gravity field are shown in Figure 9.4.14 [73]. We see that 1977 — 1978 are the most acceptable years for launch, when relatively short flight time can be achieved with relative low $V_{\infty 0}$ values and convenient $\tilde{r}_{\pi 1}$. Thus, in 1977, flight to Pluto with Jupiter flyby can be realized for $V_{\infty 0} = 0.34\, V_\oplus$ with $\tilde{r}_{\pi 1} = 5$ and Δt = 10 years.

The ballistic characteristics deteriorate considerably for direct flight with optimal launch date in 1976: in the case of flight with the minimal value of $V_{\infty 0} = 0.38\, V_\oplus$, we have Δt = 44 years, while flight with minimal time Δt = 38 years is possible with $V_{\infty 0} = 0.48\, V_\oplus$.

Figure 9.4.15 shows the projection on the eclip ic plane of the interplanetary flight trajectory to Pluto with Jupiter flyby for launch in 1977 and $V_{\infty 0} = 0.34\, V_\oplus$. At the time of interplanetary vehicle swingby, Pluto will be at the perihelion of its orbit, having R_π = 30 a.u. This is the reason for the relatively low energy expenditures for flight to Pluto. /343

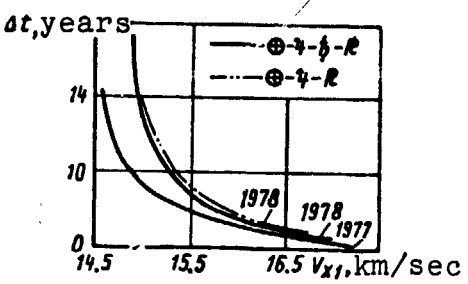

Figure 9.4.16. Flight time to Pluto versus characteristic launch velocity for various swingby schemes

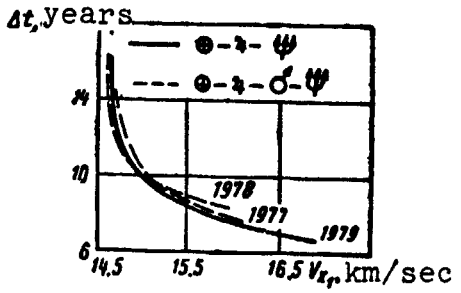

Figure 9.4.17. Flight time to Neptune versus characteristic launch velocity for various swingby schemes

Table 9.6 presents the optimal boost module basic design parameters n_0 and μ_f corresponding to this flight trajectory. The next optimal launch dates are possible only in 1989 — 1990.

Three-Planet Swingby Scheme

To demonstrate the capabilities for reducing the energy expenditures and flight time to the most distant planets of the solar system, Neptune and Pluto, it is interesting to examine the three-planet swingby schemes along the E-J-S-P* and E-J-U-N routes. Figures 9.4.16 and 9.4.17 show the relationships between the minimal characteristic launch velocity and flight duration along these routes [75]. We see that the ballistic characteristics of the two- and three-planet swingby schemes are quite similar. The similarity of the energy expenditures is explained by the fact that the first flyby planet on each route is Jupiter and the energy requirements are determined primarily by the Earth-Jupiter trajectory. The similarity of the flight time values means that the primary factor determining the transfer time is the heliocentric distance of the final destination planet, and that the number of intermediate flyby planets is not of

* Flight scheme following program which has been termed the "Grand Tour."

significant importance. We also note that the flight times to Neptune and Pluto are quite similar because of the similarity of /344 their heliocentric distances in 1980 and 1990, when SC swingby is expected.*

A favorable launch period for the E-J-S-P route occurs in 1977 — 1978 and for the E-J-U-N route, in 1978 — 1980. The next favorable periods will occur only in 2076 — 2077 and 2155 — 2156, respectively. This is one of the hazards in planning for the three-planet swingby schemes, the other hazard is the greater sensitivity of the nominal trajectory to deviations in comparison with the two-planet scheme. Moreover, for the E-J-S-P route, although the SC does not cross Saturn's rings, unfavorable conditions for Saturn observation are created. Therefore the advisability of planning for the three-planet swingby schemes is questionable at the moment.

Four-Planet Swingby Scheme

The interplanetary flight trajectory following the E-J-S-U-N route** is attractive because of the possibility of solving certain fundamental scientific problems in study of the outer planets and distant regions of the solar system using a small number of interplanetary vehicles. The uniqueness of this route (since the next favorable period occurs only after 180 years) imposes special requirements on analysis of the ballistic design characteristics of the interplanetary vehicle intended for this critical flight. It is still difficult at this time to analyze all aspects of the project because of the absence of reliable information on the outer planets. The limitations on the choice of the interplanetary trajectory, which will be dictated by the space conditions near the planets, may influence the energetics

* This is associated with the fact that, at the time of interplanetary vehicle swingby, Pluto will be located near the perihelion of its orbit.

** Variant of the Grand Tour flight scheme.

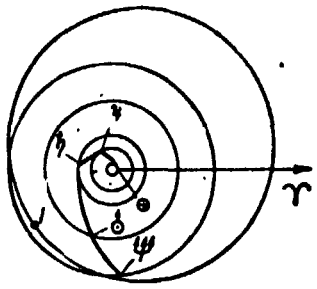

Figure 9.4.18. Four-planet flyby scheme

and flight time markedly. However, on the basis of the existing information on the outer planets, we can identify rational Grand Tour mission interplanetary flight trajectories. Let us examine some characteristics of this mission.

Since the Grand Tour mission can be realized only with strictly defined position of the outer planets relative to one another, favorable periods for SC launch are very rare. The favorable launch capability periodicity is determined primarily by the synodic period of Uranus and Neptune (171.4 years) and repeats with an interval of about 13 months from 1976 to 1979. The energetic requirements become excessively high for launches after 1979, since Jupiter flyby does not yield the necessary effect because of its position. For the scheme with flyby of /345 several planets, there is an energy expenditure limit, exceeding which does not lead to further shortening of the time. This limitation is caused by the kinematics of the planet flyby schemes. For flyby of several planets, the trajectory must "reflect" at some angle from each intermediate planet (Figure 9.4.18). However, it is not possible in practice to realize the planet flyby scheme with large reflection angles, since this requires excessively low planetocentric flyby orbit pericenter heights which cannot be achieved because of the planet's atmosphere. Consequently, the required flight times are limited from below by the minimal allowable flyby orbit pericenter altitudes. This analysis is confirmed by the calculation results. Figures 9.4.19 and 9.4.20 show the flight time as a function of nominal launch date for various values of the launch energy $H_{u\,f}$ and flyby orbit nominal pericenter altitude H_{π_1}, respectively.

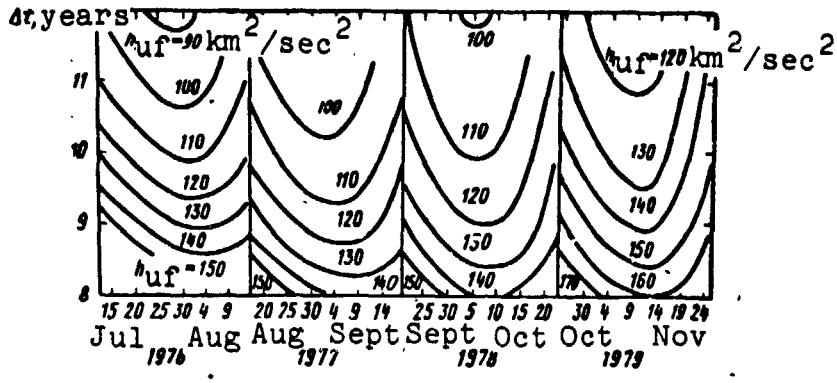

Figure 9.4.19. Grand Tour mission duration as function of launch date (for 1976 — 1979) and launch energy

Saturn is the most critical planet for realization of the Grand Tour mission. First, the minimal mission duration is directly related with the closest approach of the SC to Saturn. Second, additional limitations on the flyby orbit pericenter radius choice arise because of the existence of Saturn's rings, encounter with which must be avoided. The orientation of Saturn and its rings in the assumed flyby period (1979 — 1983) /346 permits SC flyby both outside of the rings and between the inner side of the rings and the surface of the planet. It is true that the duration of the entire mission for flyby outside of the rings increases two years in comparison with flyby along the inner side of Saturn's rings.

The ballistic characteristics of the Grand Tour mission interplanetary flight trajectory are shown in Figure 9.4.21 as a function of Saturn flyby orbit planetocentric pericenter radius $\tilde{r}_{\pi\hat{\eta}}$. Analysis of the relations shown makes it possible to develop definite recommendations on choice of the nominal Grand Tour mission interplanetary flight trajectory. First, the scientific value of the mission will depend to a considerable degree on the closeness of SC passage around each flyby planet. Second, the trajectories corresponding to Saturn flyby orbit pericenter

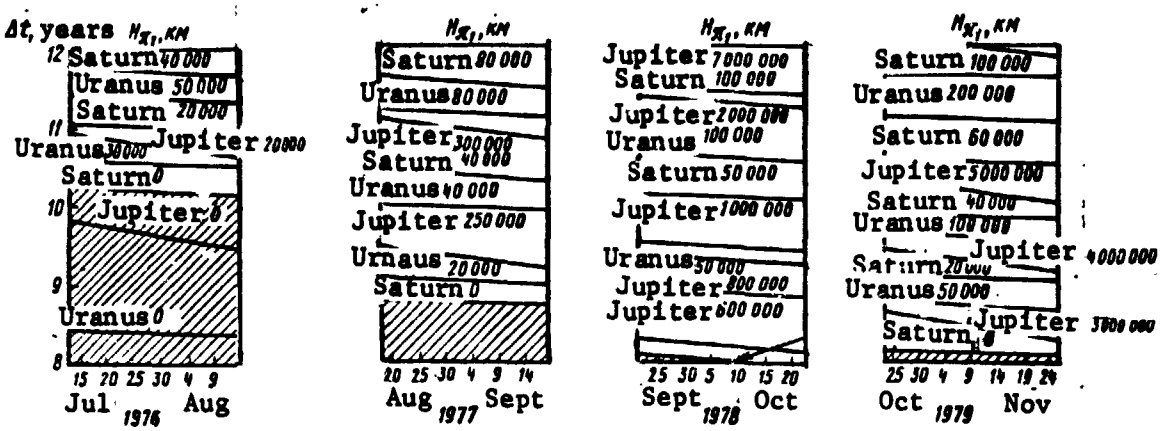

Figure 9.4.20. Influence of planetocentric flyby orbit nominal pericenter height $H_{\pi 1}$ on Grand Tour mission duration (unrealizable trajectories in shaded region)

distances equal to $\tilde{r}_{\pi\hbar} = 1.2-2.4$ planet radii should be excluded at once, since this space is occupied by Saturn's rings. Considering these remarks, trajectories with the following launch dates can be considered the best Grand Tour mission interplanetary flight trajectories: ($\tilde{r}_{\pi\hbar} = 2.4$); 1977 ($\tilde{r}_{\pi\hbar} = 1.2$); 1977 ($\tilde{r}_{\pi\hbar} = 2,4$) and 1978 ($\tilde{r}_{\pi\hbar} = 1.2$) However, taking into account the propellant and time expenditures and the definite risk associated with Saturn flyby along the inner side of the rings, the preferable nominal interplanetary trajectory is that characterized by launch in 1977 and Saturn flyby outside of the rings. The ballistic design characteristics /347 of the corresponding interplanetary vehicle are shown in Table 9.7.*

Performance of the Grand Tour mission imposes severe requirements on interplanetary trajectory realization accuracy. An error in position of a few kilometers in flyby of one planet may lead to errors of thousands of kilometers in reaching another planet. The success of the Grand Tour mission will be largely determined by proper determination of the correcting impulse points of application and magnitudes, which depend on the nominal

* See "Design of Unmanned Automatic Vehicle for the Grand Tour Mission," A.R., No. 14, 1970, ref. 187-188.

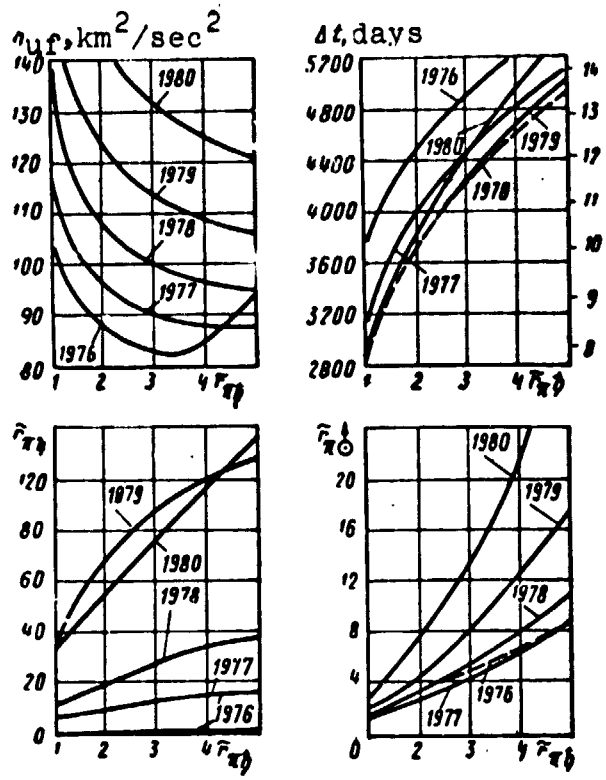

Figure 9.4.21. Ballistic characteristics of Grand Tour mission interplanetary flight trajectory as function of relative Saturn flyby orbit pericenter radius

trajectory sensitivity to errors in the initial conditions of the heliocentric segments and the planetocentric planet flyby orbits. /349 The principal error sources are inaccuracy of SC insertion into the nominal trajectory, inaccuracy of realization of the correcting maneuvers and determination of the actual trajectory.

For the planet flyby planetocentric segments, errors in determining the trajectory may lead to disruption of the flight plan or to marked increase of the correction requirements. Errors in determining the trajectory in the planet approach segments are made up of the tracking errors and inaccurate knowledge of the ephemeris of the flyby planets. Estimates of the possibilities of refining the ephemeris of the planets by the end of the 1970's indicate that the celestial longitudes and latitudes of

TABLE 9.7. BALLISTIC DESIGN CHAPACTERISTICS OF THE GRAND TOUR MISSION*

Characteristic	Flight segment			
	Earth Jupiter	Jupiter Saturn	Saturn Uranus	Uranus Neptune
Launch date	1 Sept. 1977	—	—	—
Thrust-weight ratio n_o^{opt} ($\gamma_{pp} = 0.05$, $P_{sp} = 450$ sec)	0,38	—	—	—
Relative final weight μ_f^{opt}	0,206	—	—	—
Hyperbolic excess velocity at departure from planet sphere of action in km/sec	$V_{\infty_0}=9,5$	$V_{\infty_2}^{♃}=8,1$	$V_{\infty_2}^{♄}=11,3$	$V_{\infty_2}^{☉}=15,4$
Target declination at departure from planet sphere of action in degrees	$\delta_0=30$	$\delta_2^{♃}=5,9$	$\delta_2^{♄}=-28,4$	$\delta_2^{☉}=-51,8$
Right ascension at departure from planet sphere of action in degrees	$\alpha_0=64,9$	$\alpha_2^{♃}=55,7$	$\alpha_2^{♄}=288,9$	$\delta_2^{☉}=4,5$
Hyperbolic excess velocity of arrival orbit in km/sec	$V_{\infty_1}^{♃}=8,1$	$V_{\infty_1}^{♄}=11,3$	$V_{\infty_1}^{☉}=15,4$	$V_{\infty_1}^{♅}=17,4$
Target declination at entry into planet sphere of action in degrees	$\delta_1^{♃}=-4,8$	$\delta_1^{♄}=-9,6$	$\delta_1^{☉}=-72,7$	$\delta_1^{♅}=29,7$
Right ascension at entry into planetsphere of action in degrees	$\alpha_1^{♃}=318,0$	$\alpha_1^{♄}=200$	$\delta_1^{☉}=31$	$\alpha_1^{♅}=109$
Flyby orbit pericenter radius in km	$r_{\pi_1}^{♃}=63500$	$r_{\pi_1}^{♄}=144000$	$r_{\pi_1}^{☉}=98600$	—
Flyby orbit inclination to planet equatorial plane in degrees	$i^{♃}=17,2$	$i^{♄}=29,3$	$i^{☉}=101,8$	—
Miss parameter b in km	$1,7\cdot10^6$	$3,3\cdot10^5$	$1,2\cdot10^5$	—
Angular miss parameter ψ in degrees	5,2	—27,7	—133,5	—
Hyperbolic excess velocity vector turning angle during flyby in degrees	98	84	24	—

Continued

TABLE 9.7*

(Continued)

Characteristic	Flight segment			
	Earth Jupiter	Jupiter Saturn	Saturn Uranus	Uranu Neptune
Date of departure from planet sphere of action	2.IX 1977	28.VIII 1979	9.IX 1981	6.XII 1985
Date of entry into planet sphere of action	4.V 1979	16.VI 1981	21.IX 1985	20.II 1989
Date of flyby orbit pericenter passage	I.VII 1979	29.VII 1981	30.X 1985	—
Transfer orbit plane inclination i_0 relative to ecliptic plane in degrees	2,1	2,6	2,7	2,5
Transfer segment angular range Φ in degrees	158,1	54,4	66,8	22,8
Transfer orbit perihelion radius $R_{\odot}$ in degrees	1.01	5,0	9,6	14,6
Transfer orbit aphelion radius $R_{\odot}$ in a.u.	6,5	Hyperbola		
Transfer segment orbit eccentricity e	0,73	1,4	3,71	6,35
Flight time Δt_f on segment in days	668	759	1554	1210
Total flight time Δt_{Σ} in days	668	1427	2981	4191

*[Translator's Note: Commas in numbers indicate decimal points.]

the outer planets will be determined to within 0.2 arc-sec. At the distance of Uranus (about 19 a.u.) this angular indeterminacy is equivalent to a distance error of about 3000 km. If this error is not determined and corrected in the Uranus approach segment, such an error will lead to a miss distance of about a million kilometers during Neptune flyby. A careful study must be made of the capabilities of the Doppler tracking equipment,

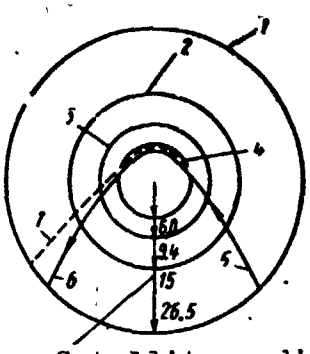

Figure 9.4.22. Typical scheme of SC rendezvous with Jupiter and positioning of the Galilean satellites:

1- orbit of Callisto; 2- orbit of Ganymede; 3- orbit of Europa; 4- orbit of Io; 5- planet approach trajectory; 6- unperturbed trajectory; 7- perturbed trajectory

distance determination methods, stellar navigation, and so on, and their connection with the SC ballistic design characteristics in order to select an optimal scheme for controlling the SC trajectory. In examining the questions of SC design, we should use the improved estimates of the trajectory parameters, which /350 permits taking a required characteristic velocity of 250 m/sec for realization of the correction maneuvers.

Influence of Galilean Satellites on Heliocentric Segments after Jupiter Swingby

The Galilean satellites of Jupiter: Io

$$\left(\frac{m}{m_\oplus}=0.012 \text{ and } \frac{R}{R_\oplus}=0.255\right),$$

Europa

$$\left(\frac{m}{m_\oplus}=0.0079 \text{ and } \frac{R}{R_\oplus}=0.226\right),$$

Ganymede

$$\left(\frac{m}{m_\oplus}=0.026 \text{ and } \frac{R}{R_\oplus}=0.394\right)$$

and Callisto

$$\left(\frac{m}{m_\oplus}=0.016 \text{ and } \frac{R}{R_\oplus}=0.35\right)$$

are very significant objects of the solar system. Therefore, their influence may show up in evaluating the results of study of the ballistic characteristics of interplanetary SC flights with utilization of Jupiter's gravity field. Figure 9.4.22 shows a typical scheme of SC rendezvous with Jupiter and arrangement of the Galilean satellite orbits.

The interplanetary flight trajectory analysis made in [67] showed marked influence of Galilean satellite perturbing action on SC swingby around Jupiter if the SC is required to reach a given point of space. Therefore, the heliocentric flight segments to the outer planets after Jupiter swingby may differ markedly from the theoretical segment if the Galilean satellite perturbing action is not taken into consideration. The Galilean satellite perturbing action can be ignored for any other flights whose objective is simply to cover definite distances, reach large inclinations to the ecliptic plane, and so on.

This conclusion is well illustrated by Table 9.8 [67]. The results of Galilean satellite perturbing action influence on the elements and parameters of the heliocentric segment after Jupiter /352
swingby are represented in the table in the form of the difference between the elements and parameters calculated with account for the perturbing action of the Sun alone and with account for the combined perturbation from the Sun and the Galilean satellites. It is interesting to determine the relative magnitude of changes presented in the table.

In many cases, the Δa reach large magnitudes. However, the dimension a is large in itself. Therefore, the relative perturbation magnitude Δa does not reach more than 4%. The perturbations of the other elements of the heliocentric segment do not exceed the usual bounds.

TABLE 9.8. INFLUENCE OF PERTURBING ACTION OF JUPITER'S GALILEAN SATELLITES ON HELIOCENTRIC ORBIT ELEMENTS*

No. in sequence	Target distance	Flight time	φ	Δe	Δa	Δi	$\Delta\Phi$	$\Delta\Omega$	$\Delta\omega$	ΔR	ΔV	Total position deviation at departure from gravisphere	Total velocity deviation at departure from gravisphere	Difference of time in gravisphere	Difference of time to reach distance 10 a.u.	Flight distance out of ecliptic plane	Distance of closest approach to Sun
	km	days	deg		km	deg.				km	km/sec	km	km/sec	days		a.u.	km
1	1,25·10⁶	450	0	0,0001	310000	0,01	0	0,560	0,52	100000	0,027	107000	0,0317	0,001	—	—	—
2	1,25·10⁶	450	90	0,0033	713000	0,086	0,135	0,081	0,20	50000	0,024	110000	0,0358	0.002	2,84	0,590 0,008	—
3	1,25·10⁶	450	180	0,0056	2510000	0,001	0,148	0,004	0,16	40000	0,020	122000	0,0375	0,006	0,18	—	—
4	1,25·10⁶	450	270	0,0036	104700000	0,089	0,141	0,040	0,12	40000	0,024	110000	0,0356	0,002	2,75	0,827 0,010	—
5	1,25·10⁶	500	0	0	540000	0,175	0	0,730	0,22	80000	0,189	76400	0,0194	0,004	—	—	Impact
6	1,25·10⁶	550	0	0,0013	1730000	0,046	0,021	0,155	0,33	370000	0,093	416800	0,0938	0,020	—	—	656000
7	1,0·10⁶	450	180	0,0081	2030000	0,001	0,182	0,0049	0,20	90600	0,026	176800	0,0546	0,004	0,06	—	—
8	1,5·10⁶	450	180	0,0040	2990000	0,001	0,127	0,0032	0,13	30000	0,016	92000	0,0276	0,005	0,21	—	—

*[Translator's Note: Commas in numbers indicate decimal points.]

An important factor is the radius vector magnitude change. Since the SC is at a distance of about 5 a.u. from the Sun at this point, these changes are in general small. However, if the flight objective is to reach some definite point of space, for example, subsequent flight to one or more planets, then any, even small, deviations must be carefully taken into account. In this connection, it is advisable to examine the general SC velocity and position deviations at the time of its departure from Jupiter's gravisphere (planetocentric coordinate system). Such deviations are defined in Table 9.8 (columns 13 and 14) as the square roots of the sum of the squares of the individual component deviations. These data show that, depending on the swingby type being examined, additional requirements may be imposed on the guidance system in the heliocentric trajectory segment after contact with Jupiter.

Table 9.8 also presents data on Galilean satellite influence on the trajectory parameters for flight schemes in which guidance accuracy does not play a significant role. Columns 15 and 16 show the difference of the time the SC is in the gravisphere of Jupiter and the difference of the time at which the SC reaches a distance of 10 a.u. from the Sun.

For cases 2 and 4 of Table 9.8, the difference in the distances which the SC can cover traveling outside the ecliptic plane reaches large magnitudes. However, the realistically achievable distances amount to at least 25 a.u. for both cases, which indicates the relatively small influence of the perturbations.

The influence of the Galilean satellite perturbing action on flight to the Sun is illustrated by cases 5 and 6. In case 5, the trajectory leads to impact on the Sun regardless of whether the satellite influence is taken into account or not. In case

6, the perturbation influence leads to deviation by only $0.6 \cdot 10^6$ km. Therefore, in this flight scheme, as in the preceding schemes, the influence of the Galilean satellite perturbing action can be neglected without introducing significant errors into the parameters of the flight trajectory to the Sun.

CHAPTER 10. DESCENT TRAJECTORIES IN PLANETARY ATMOSPHERES

§ 1. DESCENT FROM AES ORBIT

A schematic of flight along a descent trajectory from /353
orbit is shown in Figure 10.1.1. The descent trajectory from orbit may be broken down into the following segments:

1. Braking segment — operation of the retro powerplant (RPP). In this trajectory segment, the velocity is reduced from the satellite orbit flight velocity V_0 to the velocity V_1 required for transition into an ellipse which intersects the dense layers of the atmosphere.

2. Transfer ellipse — the passive flight segment in practically airless space from the time of RPP cutoff up to entry into the dense layers of the atmosphere (in the present study, we take the boundary of the dense layers of the atmosphere to be the height h_0 = 100 km).

3. Vehicle descent trajectory in the atmosphere — the /354
primary portion of the descent trajectory during which the vehicle reduces its velocity from nearly the satellite velocity to the velocity of steady fall or glide. In this segment, the vehicle is subjected to the action of high temperatures and load factors.

4. Landing segment — this includes steady-state vertical descent or glide and vehicle landing touchdown.

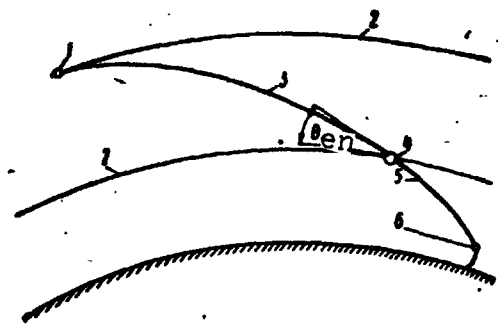

Figure 10.1.1. Schematic of descent from satellite orbit: 1- braking; 2- satellite orbit; 3- transfer ellipse; 4- entry into the atmopshere; 5- descent trajectory in the atmosphere; 6- landing trajectory segment; 7- edge of atmosphere

Usually the satellite orbit height has a lower limit determined by the required satellite lifetime. For stationary objects in orbit (satellite station, spacecraft assembly, and so on), we can take $h_{cir} \approx 200 — 300$ km as the lower limit of orbit height. The upper limit of manned satellite orbit height is selected so that the vehicle will be below the radiation belts of the Earth and is $h_{cir} \approx 500 — 600$ km.

VEHICLE BRAKING AND FLIGHT ALONG TRANSFER ELLIPSE

To determine the parameters of the transfer ellipse, we need to know the vehicle motion characteristics at the end of the braking segment.

The braking time

$$t=\frac{\Delta V}{g_0 n}, \qquad (10.1.1)$$

where ΔV is the velocity loss during braking

$$g_0=9.81 \text{ m/sec}^2;$$

$n = P/G$ is the load factor during braking.

In the general case, when the braking impulse is applied at the angle α to the velocity vector in orbit, the velocity at the end of the braking segment

$$V_1=\sqrt{V_0^2+\Delta V^2-2V_0\Delta V\cos\alpha}\approx V_0-\Delta V\cos\alpha, \qquad (10.1.2)$$

and the trajectory inclination to the horizon

$$\theta_1=\theta_0+\operatorname{arctg}\frac{\Delta V\sin\alpha}{V_0-\Delta V\cos\alpha}\approx\theta_0+\frac{\Delta V}{V_0}\sin\alpha, \qquad (10.1.3)$$

where V_0 is the flight velocity in orbit; θ_0 is the trajectory (orbit) inclination at the instant of braking impulse application.

Knowing the transfer ellipse initial parameters (V_1 and θ_1), we can, from the known relations of elliptic motion theory, determine the vehicle trajectory characteristics (V_{en}, θ_{en}, L_{en}, and t_{en}) at entry into the atmosphere.

For the case of practical interest — descent from a circular orbit ($\theta_0=0$) with braking impulse application at the angle $\alpha = 0$ — we can obtain simple approximate formulas. /355

The entry velocity V_{en} into the atmosphere is found from the energy integral

$$V_1^2-\frac{2\mu}{r_1}=V_{en}^2-\frac{2\mu}{r_{en}},$$

where r_1 is the orbit radius at the point of braking impulse application; r_{en} is the atmosphere boundary radius; μ is the gravitational constant.

We introduce relative velocities and heights

$$\tilde{V}=\frac{V}{V_0} \text{ and } \tilde{h}=\frac{h}{r_{en}}, \qquad (10.1.4)$$

where

$$V_0 = \sqrt{\frac{\mu}{r_1}}.$$

After transformation, we obtain

$$\tilde{V}_{en} = \sqrt{(1-\Delta\tilde{V})^2 + 2\tilde{h}_a} \approx \sqrt{1-2(\Delta\tilde{V}-\tilde{h}_a)}, \qquad (10.1.5)$$

where

$$\Delta\tilde{V} = \frac{\Delta V}{V_0} \text{ and } \tilde{h}_a = \frac{r_1 - r_{en}}{r_{en}},$$

The entry angle into the atmosphere is found from the angular momentum conservation law

$$\cos\theta_1 r_1 V_1 = \cos\theta_{en} r_{en} V_{en}$$

or for our case $\theta_1 = 0$

$$\cos\theta_{en} = \frac{r_1}{r_{en}} \frac{V_1}{V_{en}}.$$

Since the entry angle is usually small, it is more convenient to calculate $\sin\theta_{en}$ rather than $\cos\theta_{en}$:

$$\sin^2\theta_{en} = 1 - \left(\frac{r_1}{r_{en}} \frac{V_1}{V_{en}}\right)^2.$$

After transformations and introducing relative magnitudes, we obtain

$$\sin^2\theta_{en} = \frac{\tilde{h}_a(4\Delta\tilde{V}-\tilde{h}_a) - \Delta\tilde{V}\tilde{h}_a[\tilde{h}_a\Delta\tilde{V} + 2(\Delta\tilde{V}-\tilde{h}_a)]}{1-2(\Delta\tilde{V}-\tilde{h}_a)+\Delta\tilde{V}^2}$$

or

$$\theta_{en} \approx \sqrt{\frac{\tilde{h}_a(4\Delta\tilde{V}-\tilde{h}_a)}{1-2(\Delta\tilde{V}-\tilde{h}_a)}} \approx \sqrt{\tilde{h}_a(4\Delta\tilde{V}-\tilde{h}_a)}. \qquad (10.1.6)$$

The flight range along the transfer ellipse can be obtained from the equation of the elliptic trajectory /356

$$r=\frac{p}{1+e\cos v},$$

where $p=rk\cos\theta$ is the parameter of the ellipse $\left(k=\frac{rV^2}{\mu}\right)$; $e=1-k$ is the eccentricity of the ellipse; ν is the true anomaly (measured from the perigee).

In our case, $\theta_1=0$ and $v_1\approx 2\pi$ (braking impulse at the apogee).

The flight range along the transfer ellipse

$$L=R\beta=R(2\pi-v_{en}), \qquad (10.1.7)$$

where β is the angular range, R is the radius of the planet,

The true anomaly of the atmospheric entry point

$$\cos \nu_{en} = \frac{\tilde{h}_a(1-\Delta\tilde{V})^2}{\Delta\tilde{V}(2-\Delta\tilde{V})}-1. \qquad (10.1.8)$$

These formulas in relative magnitudes of the velocity $\tilde{V}$ and orbit height $\tilde{h}_a$ above the top of the atmosphere are valid for any planets.

FLIGHT TRAJECTORIES IN THE ATMOSPHERE

Marked heating and deceleration of the vehicle in the atmosphere begin at an altitude $h\approx 100$ km. The following external forces (Figure 10.1.2) act on a vehicle flying in the atmosphere at altitude with the velocity V: drag force X directed along the tangent to the trajectory opposite the direction of flight, lift Y along the direction perpendicular to the trajectory, and /357 gravity force G along the direction of the local vertical. These forces are balanced by the forces of inertia. We project these forces on the x and y velocity axes. The sum of the projections

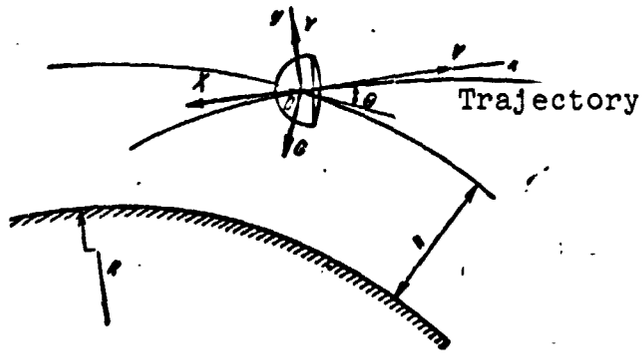

Figure 10.1.2. Diagram of forces acting on descent vehicle

of all the forces on the x axis

$$-m\frac{dV}{dt}-X-G\sin\theta=0,$$

where $m=\frac{G_0}{g_0}$ is the vehicle mass (G_0 and g_0 are the weight and gravity force acceleration for h = 0); t is the flight time; θ is the trajectory inclination to the horizon; G is the vehicle weight. The sum of the projections on the y axis

$$-m\frac{V^2}{r_{cur}}-G\cos\theta+Y=0,$$

where r_{cur} is the radius of curvature of the trajectory. We replace

$$\frac{V^2}{r_{cur}}=\frac{\omega r_{cur}V}{r_{cur}}=\omega V,$$

where $\omega=\frac{d\theta}{dt}-\frac{d\beta}{dt}$ is the angular rate of rotation of the velocity vector relative to the Earth: $\frac{d\beta}{dt}=\frac{V\cos\theta}{R+h}$ and β is the central angle traversed by the vehicle from the time of entry into the atmosphere (angular flight range).

After transformations, we obtain the following system of equations describing vehicle planar motion during descent in the atmosphere:

$$\begin{cases} \dfrac{dV}{dt} = -g_0 \dfrac{\rho V^2}{2p_x} - g \sin\theta; \\ V \dfrac{d\theta}{dt} = g_0 \dfrac{\rho V^2}{2p_y} - g\cos\theta + \dfrac{V^2}{R+h}\cos\theta; \\ \dfrac{dh}{dt} = V\sin\theta; \\ \dfrac{d\varphi}{dt} = \dfrac{V\cos\theta}{R+h}, \end{cases} \qquad (10.1.9)$$

where $p_x = \frac{m}{c_x S}$ is the specific drag loading in kg/m^2, and $p_y = \frac{m}{c_y S}$ S is the characteristic drag to which the aerodynamic coefficients c_x and c_y are referred; $g = g_0\left(\frac{R}{R+h}\right)^2$ is the local gravity force acceleration.

The system of equations in general form is nonlinear and is solved by numerical integration using the Runge-Kutta method on a digital computer. /358

We shall examine the class of descent trajectories with constant values of the drag loading p_x and aerodynamic efficiency $K = \frac{p_x}{p_y}$, i.e., trajectories with $p_x = \text{const}$ and $p_y = \text{const}$, which are quite close to the actual case.

The major portion of the descent trajectory (i.e., the portion where aerodynamic heating occurs and load factors act) lies in the hypersonic flight region (M>3—5), where the aerodynamic characteristics are nearly independent of Mach number. Therefore, the conditions p_x = const and p_y = const correspond to vehicle descent with constant angle of attack, i.e., the most realistic case from the viewpoint of vehicle control. Specifically, these regimes include ballistic descent (K = 0).

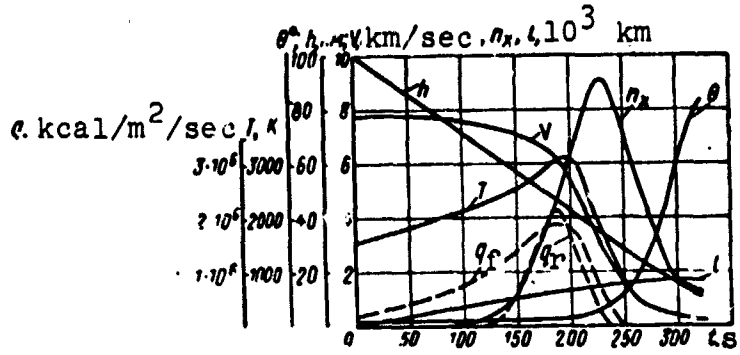

Figure 10.1.3. Ballistic descent trajectory from AES orbit with K = 0; p_x = 650 kg/km^2; V_{en} = 7.8 km/sec; θ_{en} = -2°

Figure 10.1.3 shows the ballistic descent trajectory characteristics for a vehicle entering the Earth's atmosphere with velocity V_{en} = 7.8 km/sec at the angle θ_{en} = -2° to the horizon.

Marked braking of the vehicle begins at an altitude h ≈ 70 km. The maximal longitudinal load factors reach n_x = 9 at h ≈ 35 km. We note that the zone of most marked vehicle braking lies in a relatively narrow altitude range $20<h<50$ km. The load factor peak ($n_x \approx 9$) lasts for about 10 seconds, however, the total time of high load factor ($n_x > 4$) action is relatively long $\Delta t \approx 100$ sec.

At entry into the atmosphere (h = 100 km), the temperature is already T = 1500° K (in Figure 10.1.3 and subsequent figures, the temperatures are the theoretical values at the stagnation point of a sphere of radius R = 1 m for a perfectly thermally insulated wall). The temperature "peak" $T_{max} \approx 3000°$ K is reached at h ≈ 45 km. Characteristically, the temperature peak always leads the load factor peak. The region of high temperatures $T>1000$ K extends to h = 30 km. /359

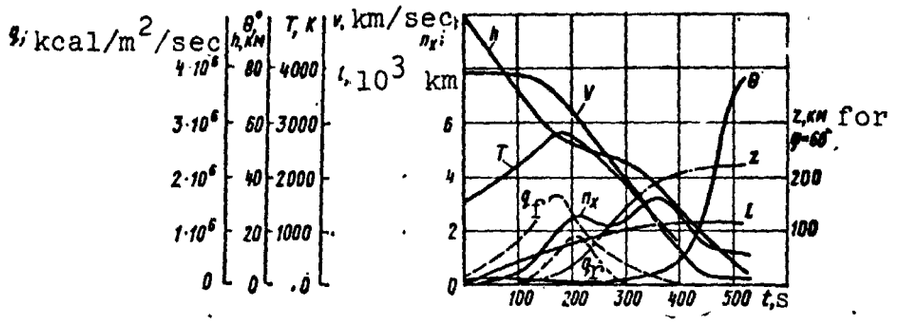

Figure 10.1.4. Gliding trajectory descent from AES orbit with $\theta_{en} = -2°$; K = 0.2, $p_x = 650$ kg/m^2; $V_{en} = 7.8$ km/sec

Heating of the vehicle during descent into the atmosphere takes place as a result of both convective q_c and radiative q_r thermal fluxes from the hot gas behind the shock wave. In the peak temperature zone, the convective and radiative fluxes are approximately the same (we recall tnat we are referring to the stagnation point of a sphere with R = 1 m).

The trajectory inclination is nearly constant for a long time and marked increase of its slope begins only for h < 40 km. The total flight range in the atmosphere L = 1750 km. The flight time to h = 10 km is t ≈ 5.5 min.

The gliding descent trajectory with vehicle aerodynamic efficiency K = 0.2 is shown in Figure 10.1.4. In comparison with the ballistic descent trajectory, the maximal load factors decrease significantly and the maximal temperature also decreases somewhat. The "peak" values of the radiative fluxes q_r decrease markedly. The skipping nature of the trajectory with two load factor peaks and increase of the flight range and time are characteristic.

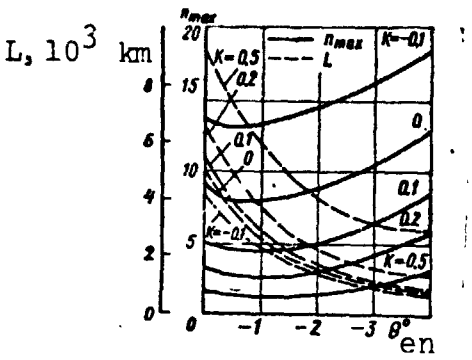

Figure 10.1.5. Influence of entry angle θ_{en} on load factor n_{max} and flight range L in the atmosphere for p_x = 650 kg/m^2, V_{en} = 7.8 km/sec

Let us examine the influence of various parameters on the descent trajectory characteristics. Figure 10.1.5 shows the influence of vehicle aerodynamic efficiency and atmosphere entry angle on the maximal load factors and flight range.

The existence of a lift force, i.e., changeover from the ballistic descent vehicle to gliding descent vehicles, is one of the radical techniques for reducing the load factors. Significant reduction of the maximal load factors to n_{max} = 3 — 4, i.e., values which man can withstand for a quite long time without any aftereffects, can be obtained with comparatively low aerodynamic efficiency K ≈ 0.2. We note that the load factors decrease most rapidly /360 for K ≤ 0.2 — 0.3.

The reduction of the load factors in the presence of lift forces is explained by the fact that, for a gliding vehicle, the trajectory is higher than for a ballistic vehicle and its deceleration takes place more gradually (extends over a longer time). This is particularly marked in comparing the trajectories of Figures 10.1.3 and 10.1.4. With increase of the entry angle θ_{en}, the maximal load factors increase (see Figure 10.1.5). This is explained by the fact that in the steep entry case, the vehicle "digs" into the dense layers of the atmosphere as a result of inertia, where it is braked strongly. The minimal load factors correspond to an entry angle θ_{en} = 0 — -2°. As we would expect, the flight range increases with increase of the

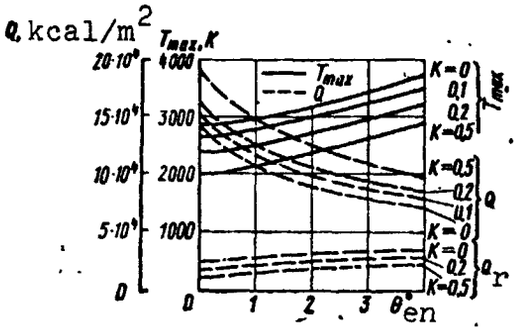

Figure 10.1.6. Influence of entry angle θ_{en} on temperature T_{max} and integral thermal flux Q for p_x = 650 kg/m^2, V_{en} = 7.8 km/sec

vehicle aerodynamic efficiency. The flight range decreases significantly with increase of the atmosphere entry angle.

The influence of aerodynamic efficiency K and entry angle θ_{en} on the maximal temperature T_{max} (at the stagnation point of a thermally insulated sphere with R = 1 m) and on the time-integral thermal fluxes Q (at the same point)* is shown in Figure 10.1.6. With increase of the aerodynamic efficiency, the maximal temperature T_{max} decreases somewhat but the time-integral thermal flux Q increases. The temperature reduction is explained by braking of the gliding vehicle in the more rarefied layers of the atmosphere in comparison with the ballistic vehicle. The increase of the integral thermal fluxes is explained by flight time increase (as a result of the convective fluxes). With increase of the aerodynamic efficiency, the integral radiative fluxes Q_r decrease markedly. With increase of the entry angle θ_{en}, the maximal temperature increases but the integral thermal fluxes decrease significantly. /361

Knowledge of the maximal temperature T_{max} makes it possible to evaluate the thermal stability of the thermal protection material (in the case of thermal protection without sublimation). The magnitude of the integral thermal fluxes Q determines the weight of the sublimating part of the thermal protection. Therefore, these quantities can serve to some degree as trajectory evaluation criteria.

* $Q = \int_0^{t_f} q\,dt$, where q are the local thermal fluxes in kcal/m^2.

Analyzing the information presented above, we can select more or less satisfactory values of the entry angle θ_{en} for the ballistic descent vehicle. Provision for minimal load factors limits the quantity $\theta_{en} \leq -2° — 2.5°$. The maximal temperature obviously does not influence trajectory selection in the sublimating thermal protection case (in the ballistic descent case, the temperature is sufficiently high for realistic values of p_x = 300 — 500 kg/m^2 to consider thermal protection without ablation). However, in order to reduce the thermal protection weight, it is desirable to have lower integral thermal fluxes Q, i.e., changeover to high entry angles, which should be taken at the upper limit considering the load factors. High entry angles are also desirable for reducing the touchdown point scatter because of possible entry angle errors, since with increase of the entry angle, the flight range and the derivative $\partial L/\partial\theta_{en}$ decrease (see Figure 10.1.5).

Considering the load factor level n = 3 — 4 to be acceptable with regard to crew comfort during descent, it hardly makes sense to increase the aerodynamic efficiency above K = 0.15 — 0.25 for a gliding descent, since with increase of K, the integral heat fluxes and consequently the thermal protection weight increase.

Let us examine the influence of the specific drag loading on the basic descent trajectory characteristics (Figures 10.1.7 and 10.1.8).

The drag loading p_x reduces the maximal load factors and flight range slightly, but decrease of p_x reduces both the maxi- /362
mal temperature T and integral heat fluxes Q significantly. Considering this, we can identify the requirements on shape of the vehicle with minimal thermal protection weight

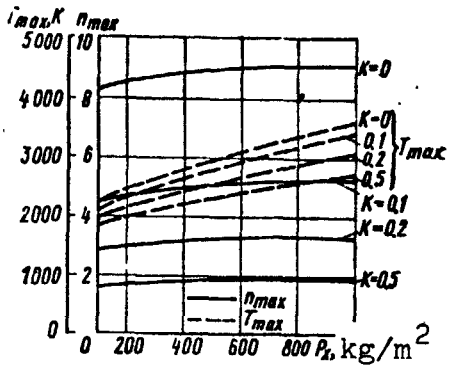

Figure 10.1.7. Influence of drag loading p_x on temperature T_{max} and load factor n_{max} for $\theta_{en} = -2°$; $V_{en} = 7.8$ km/sec

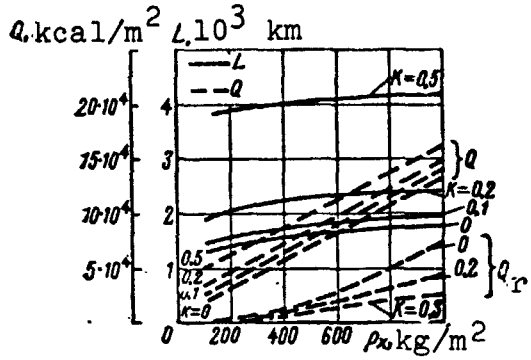

Figure 10.1.8. Influence of drag loading p_x on flight range L and integral thermal fluxes Q for $\theta_{en} = -2°$; $V_{en} = 7.8$ km/sec

Actually, the parameter $p_x = G/c_x S$. Usually the vehicle weight and dimensions (and therefore, the frontal area) are given. Consequently, the vehicle with minimal thermal protection weight will have a shape which yields the largest drag coefficient c_x. Under hypersonic flight conditions, the body with forebody which is closest to flat will have the largest c_x (headlight-type shape in Figure 10.1.2). This is valid for vehicles using both ballistic and gliding descent.

§ 2. DESCENT IN EARTH'S ATMOSPHERE WITH HYPERBOLIC VELOCITY

TRAJECTORIES WITH LARGE ATMOSPHERE ENTRY ANGLES

Let us first examine atmospheric entry trajectories with escape velocity at angles $\theta_{en} = -15$ — $-90°$. The nature of the trajectory characteristic variation is the same as for descent from AES orbit; however, the braking process takes place considerably faster. Characteristic is nearly constant trajectory inclination θ to the horizon in the basic trajectory segment. The load factor n_x and minimal temperature T_{max} are considerably higher than for descent from orbit.

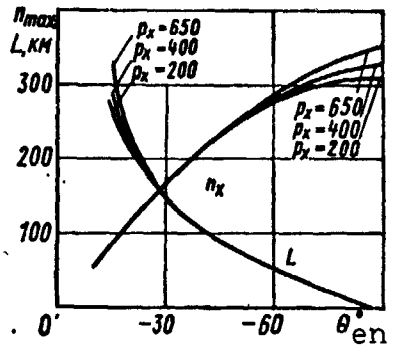

Figure 10.2.1. Influence of entry angle θ_{en} on load factor n_{max} and flight range L for K = 0; V_{en} = 11 km/sec

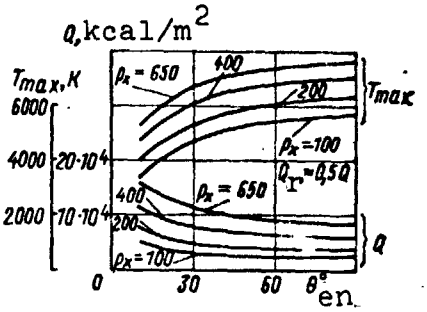

Figure 10.2.2. Influence of entry angle θ_{en} on temperature T_{max} and integral thermal fluxes Q for K = 0, V_{en} = km/sec

Figure 10.2.1 shows the influence of entry angle θ_{en} and drag loading p_x on the maximal load factor n_{max} and flight range L. The maximal load factors decrease significantly with reduction of the atmosphere entry angle, which is explained by the increase of the braking path length (increase of the flight range L). The drag loading p_x has practically no influence on the flight range L and load factor n_{max}. The spread of the n_{max} values for the angle θ_{en} = -90° is explained by the fact that, for different p_x, the maximal load factor zone occurs in different segments of the atmosphere with different values of the density gradient (in the calculations we used the Earth ISA). Just as in the descent-from-orbit case, increase of the entry angle leads to increase of the maximal temperature and reduction of the integral heat fluxes (Figure 10.2.2). /363 Decrease of the drag loading p_x reduces both the temperature T_{max} and the integral thermal fluxes Q. In the case of descent with Earth escape velocity, the radiative thermal fluxes, which constitute about 50% of the overall integral thermal fluxes, increase significantly.

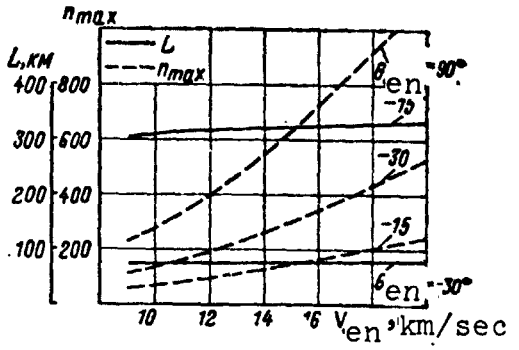

Figure 10.2.3. Influence of entry velocity V_{en} on load factor n_{max} and flight range L for K = 0; p_x = 400 kg/m^2

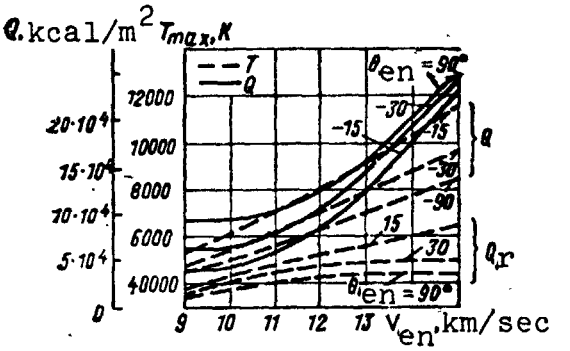

Figure 10.2.4. Influence of entry speed V_{en} on temperature T_{max} and integral thermal fluxes Q for K = 0; p_x = 400 kg/m^2

The load factor n_{max} increases as the square of the velocity. However, the flight range L increases very little (Figure 10.2.3). With increase of the atmosphere entry velocity V_{en}, the maximal temperature T_{max} and integral thermal fluxes Q increase significantly (Figure 10.2.4). Because of the large load factors n_{max}, trajectories with large entry angles are suitable only for descent of automatic vehicles returning from flight trajectories to the planets. For the case of ballistic entry into the atmosphere (K = 0) at large entry angles, when the inclination $\theta \approx \theta_{en}$ = const on most of the trajectory, an analytic solution can be obtained for the basic trajectory characteristics.

For this case, we can neglect in the first equation of the system (10.1.9) the term g sin θ, since it is considerably smaller than the term defined by the drag. Thus, the first equation of the system (10.1.9) can be written in the form /364

$$\frac{dV}{dt} = -g_0 \frac{\rho V^2}{2p_x}. \qquad (10.2.1)$$

The second equation of this system becomes meaningless for this case (θ = const, K = 0).

We represent the density variation law by the approximate relation (isothermal atmosphere)

$$\varrho = \varrho_0 e^{-\beta h}.$$

Then (10.2.1) may be written in the form

$$\frac{dV}{dt} = -kV^2\Delta, \qquad (10.2.2)$$

where

$$k = \frac{g_0 Q_0}{2p_x}; \quad \Delta = \frac{\varrho}{\varrho_0} = e^{-\beta h};$$

$\beta = \frac{\mu g}{RT}$ is the mean logarithmic atmospheric density gradient; μ is the molecular weight of the atmospheric gas; g is the gravity force acceleration; T is the mean atmospheric temperature; R is the universal gas constant.

Using still another equation of the system (10.1.9), namely the equation for determining the descent velocity vertical component

$$\frac{dh}{dt} = V \sin\theta. \qquad (10.2.3)$$

Differentiating $\Delta = e^{-\beta h}$ and using (10.2.3), we obtain

$$\frac{d\Delta}{dt} = \frac{d\Delta}{dh}\frac{dh}{dt} = -V \sin\theta \cdot \beta e^{-\beta h}. \qquad (10.2.4)$$ /365

Excluding time from (10.2.2) and (10.2.4) and separating variables, we obtain

$$\frac{dV}{V} = \frac{k}{\beta \sin\theta} d\Delta. \qquad (10.2.5)$$

Integrating (10.2.5) from h_0 to h, we obtain the velocity dependence on flight altitude

$$V=V_0 e^{-\frac{k}{\beta \sin\theta}(\Delta-\Delta_0)}.$$

As $h_0\to\infty$ (entry into the atmosphere from infinity)

$$V=V_0 e^{-\frac{K}{\beta \sin\theta}\Delta}.$$

Substituting into (10.2.2) the expression for the velocity, we obtain

$$\frac{dV}{dt}=kV_0^2 e^{-\left[\beta h+\frac{2K}{\beta \sin\theta}(\Delta-\Delta_0)\right]}.$$

The axial load factor acting on the SC

$$n_x=\frac{k}{g_0}V^2 e^{-\left(\beta n+\frac{2K}{\beta \sin\theta}\Delta\right)}.$$

We obtain the height corresponding to $n_{x\ max}$ from the equation

$$\frac{dn_x}{dh}=n_x\left(-\beta+\frac{2k}{\sin\theta}\Delta\right)=0.$$

The height corresponding to $n_{x\ max}$

$$h_{n_x\ max}=-\frac{1}{\beta}\ln\frac{\beta \sin\theta}{2k}.$$

The maximal load factor

$$n_{x\ max}=\frac{V_0^2\beta}{2g_0 e}\sin\theta. \qquad (10.2.6)$$

In addition to these solutions, we can determine from (10.2.3) the flight time from the moment of entry into the atmosphere to the height h:

$$t=-\int_{h_0}^{h}\frac{dh}{V\sin\theta}=-\int_{h_0}^{h}\frac{dh}{V_0 e^{\frac{k\Delta}{\beta \sin\theta}}\sin\theta}.$$

Substituting $dh = -\frac{d\Delta}{\beta\Delta}$, we obtain

/366

$$t = \frac{1}{V_0\beta\sin\theta}\int_{\Delta_0}^{\Delta}\frac{e^{-\frac{k}{\beta\sin\theta}}}{\Delta}d\Delta = \frac{1}{V_0\beta\sin\theta}\left[\ln\frac{\Delta}{\Delta_0} + \frac{k\Delta}{\beta\sin\theta} + \right.$$

$$\left. + \left(\frac{k\Delta}{\beta\sin\theta}\right)^2\frac{1}{3\cdot 3!} + \ldots\right] = \frac{1}{V_0\beta\sin\theta}\left[\beta(h_0 - h)\frac{k\Delta}{\beta\sin\theta} + \ldots\right].$$

Comparison of the values calculated using the formulas presented above with numerical integration of the equations of motion shows that, for atmospheric entry angles θ_{en} from -90 to -15°, the approximate formulas yield satisfactory accuracy over most of the trajectory (to h ≈ 20 — 25 km).

TRAJECTORIES WITH SMALL ENTRY ANGLES AT THE LIMIT OF VEHICLE CAPTURE BY THE ATMOSPHERE

Figure 10.2.5 shows the characteristics of a ballistic descent trajectory at escape speed for atmospheric entry angle (θ_{en} = -5°) close to the limit of vehicle capture by the atmosphere. The descent time along this trajectory is significantly longer than for large entry angles and corresponds approximately to the descent time from AES orbit, while the maximal load factor (n_{max} = 6.5) is even somewhat less than for ballistic descent from orbit, where n_{max} ≈ 8. Characteristic for the trajectories at the capture limit is the prsence of the skipping phenomenon, expressed in the form of two maximal load factor "peaks."

The maximal temperature T_{max} for descent at the escape velocity is significantly greater than for descent from AES orbit in the case of both ballistic and gliding descent. The basic characteristics of the descent regime for atmospheric entry /367

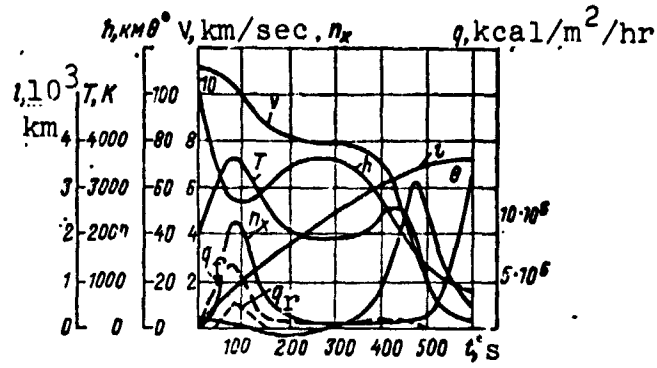

Figure 10.2.5. Gliding descent trajectory for $\theta_{en} = -5°$; K = 0.1; p_x = 650 kg/m^2; V_{en} = 11 km/sec

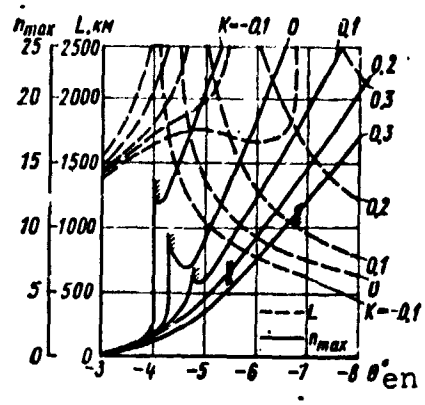

Figure 10.2 . Influence of θ_{en} and aerodynamic efficiency K on load factor n_{max} and flight range L for V_{en} = 11 km/sec; p_x = 400 kg/m^2

angles close to the capture limit* for vehicles with drag loading p_x = 400 kg/m^2 and for various values of the aerodynamic efficiency K are shown in Figures 10.2.6 and 10.2.7. Increase of K leads to decrease of the maximal load factors n_{max} for fixed atmospheric entry angle θ_{en} and to some decrease of the derivative $\frac{\partial n_{max}}{\partial \theta_{en}}$. Characteristic for the regimes with $K \leqslant 0.2$ is a minimum of the load factor n_{max} at entry angles θ_{en} close to the capture limit $\theta_{en\ lim}$ and abrupt decrease of n_{max} for $\theta_{en} < \theta_{en\ lim}$. For K > 0.2, passage through the capture limit does not cause any changes in the $n_{max} = f(\theta_{en})$ curve. Also interesting is the fact that there is a minimum of n_{max} as a function of K (for K ≈ 0.1). We see from Figure 10.2.6 that the limit of vehicle capture by the atmosphere is characterized by sharp increase of the flight range L in the atmosphere (L is determined from the moment of

* In the present study, we consider those descent trajectories for which the vehicle entering the atmosphere at h_{en} = 100 km does not again reach this height to be "captured."

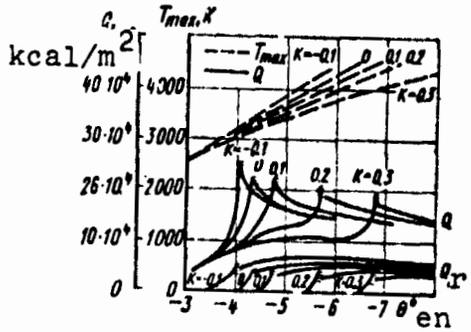

Figure 10.2.7. Influence of entry angle θ_{en} and aerodynamic efficiency K on thermal fluxes Q and temperature T_{max} for V_{en} = 11 km/sec; p_x = 400 kg/m^2

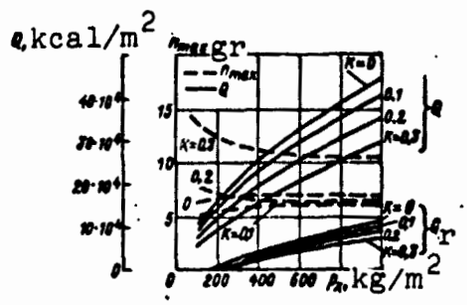

Figure 10.2.8. Influence of drag loading p_x on load factor n_{max} and thermal fluxes Q at capture limit for V_{en} = 11 km/sec

entry into the atmosphere at n_{en} = 100 km to the moment of either vehicle landing or departure from the atmosphere). With increase of the entry angle θ_{en}, there is marked increase of the maximal temperature T_{max} on the descent trajectory (see Figure 10.2.7). We note that T_{max} at the capture limit increases with increase of K. Characteristic is the presence of "peaks" of the integral thermal fluxes Q at the capture limit, and also the fact that, with increase of K, the "peak" values of Q at the capture limit decrease. The integral radiative thermal fluxes Q_r at the capture limit remain practically unchanged with variation of K.

Figures 10.2.8 and 10.2.9 show the influence of drag loading p_x on the basic descent trajectory characteristics for small atmospheric entry angles. The maximal load factors at the $n_{max} = f(\theta_{en})$ minimum point or at the capture limit for K < 0.1 depend very little on p_x, while for K > 0.2, they increase somewhat for small values of p_x. The entry angle $\theta_{en\ lim}$ corresponding to the atmospheric capture limit increases somewhat with increase

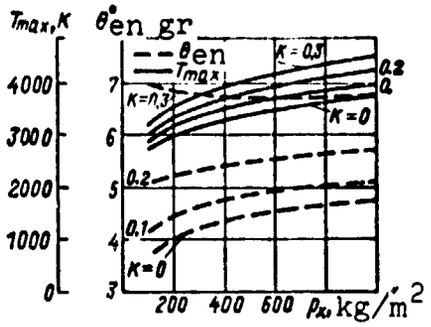

Figure 10.2.9. Influence of drag loading p_x on entry angle θ_{en} and temperature T_{max} at capture limit for V_{en} = 11 km/sec

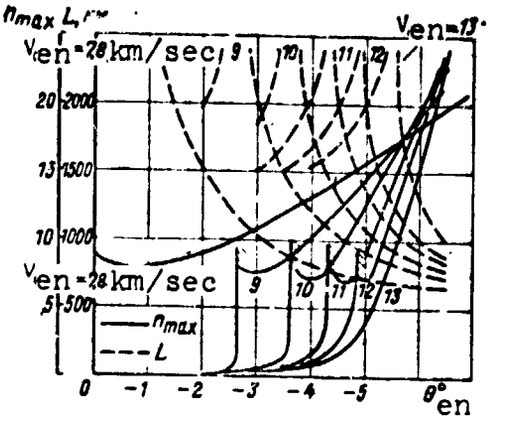

Figure 10.2.10. Influence of angle θ_{en} and entry speed V_{en} on load factors n_{max} and flight range L for K = 0, p_x = 400 kg/m^2

of p_x for $K \leq 0.3$. The maximal temperature $T_{max\ lim}$ at the capture limit and the integral thermal fluxes Q_{lim} increase with increase of p_x. The increase of T_{max} and Q_{lim} with increase of p_x is explained by the fact that, for large p_x, braking of the vehicle takes place in the more dense layers of the atmosphere.

The influence of atmospheric entry velocity on the basic ballistic descent trajectory characteristics is shown in Figures 10.2.10 and 10.2.11. The limiting entry angle $\theta_{en\ lim}$ and also /369 the derivative $\partial n_{max}/\partial\theta_{en}$ naturally increase with increase of the entry speed. We note that for $V_{en} > 12$ km/sec, the n_{max} minimum near the capture limit disappears. The maximal temperature $T_{max\ lim}$ and the integral thermal fluxes Q_{lim} at the capture limit increase significantly with increase of the atmospheric entry speed. The integral radiative fluxes Q_r also increase markedly.

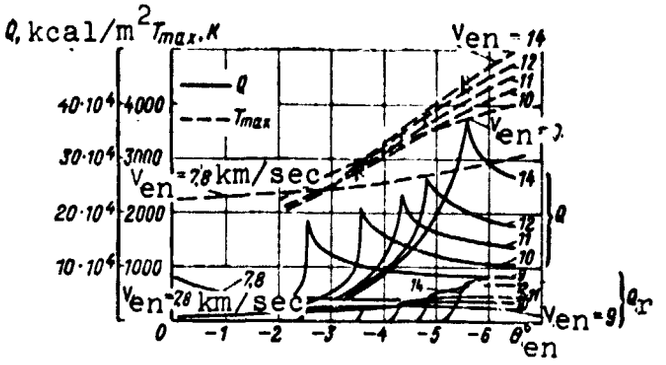

Figure 10.2.11. Influence of angle θ_{en} and entry speed V_{en} on thermal fluxes Q and temperature T_{max} for K = 0, p_x = 400 kg/m^2

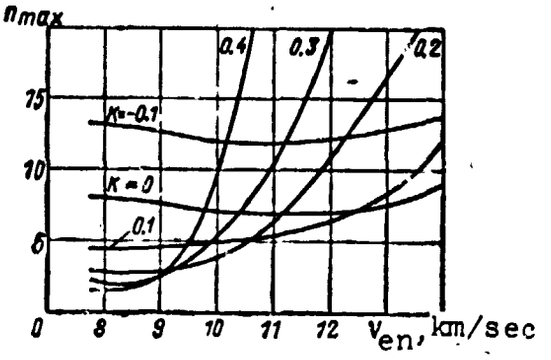

Figure 10.2.12. Influence of entry velocity V_{en} on maximal load factors n_{max} for p_x = 400 kg/m^2

We see from Figure 10.2.12 that, for each atmospheric entry velocity, there are values of the aerodynamic efficiency K corresponding to a minimum of the load factors n_{max}. While for descent from orbit (V_{en} = 7.8 km/sec) this $K_{opt} \to \infty$, even for parabolic entry velocity (V_{en} = 11 km/sec, the quantity $K_{opt} \approx$ 0.1 — 0.15, and for V_{en} = 14 km/sec, K_{opt} = 0. Figure 10.2.13 shows the influence of atmospheric entry speed V_{en} on the integral thermal fluxes Q and maximal temperature T_{max} at the capture limit. The following facts are of interest. First, the radiative fluxes Q_r at the capture limit are nearly independent of /370 the aerodynamic efficiency K and, second, for entry speed greater than V_{en} = 8.5 km/sec, increase of the efficiency leads to decrease of the integral thermal fluxes Q and increase of the temperature T_{max} at the capture limit.

Let us examine the influence of various descent vehicle parameters and its entry speed into the atmosphere on the capture limit. It is more convenient to characterize the limit of vehicle capture by the atmosphere, not by the entry angle but

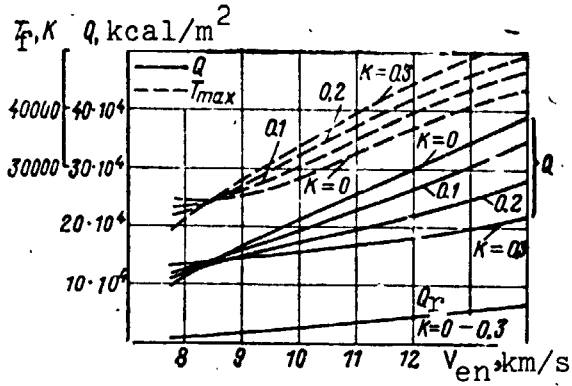

Figure 10.2.13. Influence of entry speed V_{en} on thermal fluxes Q and temperature T_{max} at the capture limit for p_x = 400 kg/m^2

rather by the vehicle trajectory perigee height h_π calculated on the basis of the atmospheric entry conditions (h_{en} = 100 km; θ_{en} and V_{en}), considering that flight takes place in airless space. This nominal perigee height h_π is more convenient for evaluating the accuracy of SC guidance systems during atmospheric entry. The nominal perigee radius r_π may be determined if we know the atmospheric entry height h_0, entry speed V_{en}, and entry angle θ_{en}. In fact, we have, from the conic section equation /371

$$r = \frac{p}{1 + e\cos v},$$

where $p = (V_{en}^2 \cos^2\theta_{en} r_{en})/\mu$ is the trajectory parameter; ν is the true anomaly; $r = R + h$; R is the radius of the Earth;

$$e = \sqrt{1 + \frac{p}{\mu}\left(V_{en}^2 - \frac{2\mu}{r}\right)}$$

is the eccentricity of the orbit.

At the normal perigee $\nu = 0$, then

$$h_\pi = \frac{p}{1+e}.$$

Figure 10.2.14 shows the influence of the specific drag loading p_x at the limit nominal perigee height $h_{\pi lim}$ for various values of K. We see that, for large p_x, the descent vehicle must

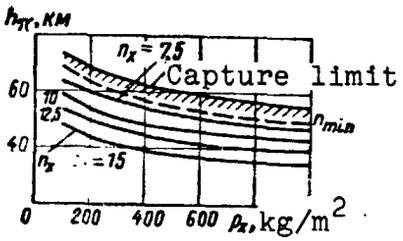

Figure 10.2.14. Dependence of nominal perigee height h_{π} on drag loading p_x and load factor n_{max} for p_x = 400 kg/m^2, K = 0

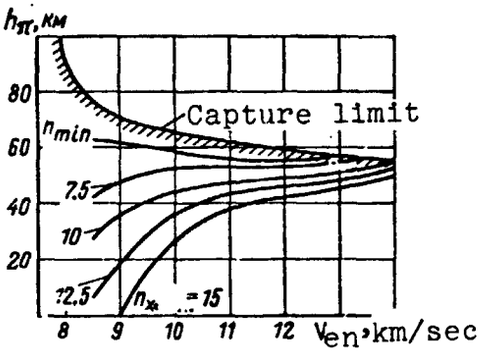

Figure 10.2.15. Dependence of nominal perigee height h_{π} on entry speed V_{en} for V_{en} = 11 km/sec, K = 0

penetrate more deeply into the atmosphere in order to be captured. With increase of the atmospheric entry speed V_{en}, the perigee height $h_{\pi lim}$ at the capture limit also decreases (Figure 10.2.13).

The "entry corridor" concept is used to evaluate SC guidance system accuracy for entry into the atmosphere. The entry corridor is bounded on one side by the limit of SC capture by the atmosphere and on the other side by the admissible load factor level. The entry corridor height can be characterized by the difference of the nominal perigee heights. The entry corridor height Δh_{π} can be found from Figure 10.2.14. The drag loading p_x has practically no influence on the entry corridor height but does shift its boundaries. With increase of the atmospheric entry speed, the entry corridor height Δh_{π} decreases. Thus, for ballistic trajectories with V_{en} = 14 km/sec and n_{max} = 10, the entry corridor vanishes (Figure 10.2.15).

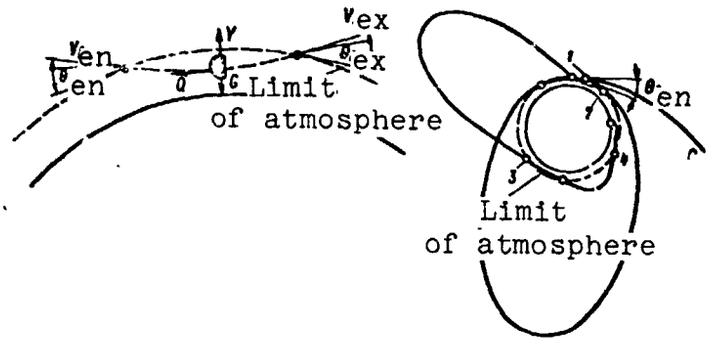

Figure 10.2.16. Diagram of skipping descent trajectory

SKIPPING DESCENT TRAJECTORIES. SC INSERTION INTO SATELLITE ORBIT WITH MANEUVER IN THE ATMOSPHERE

If an SC enters the atmosphere with entry angle θ_{en} less than the angle corresponding to the capture limit, then after partially decelerating in the atmosphere, the vehicle will leave the atmosphere. After flying for some time along an elliptic trajectory, it again enters the atmosphere but now with lower velocity. After performing several such skips, the SC finally decends to the Earth (Figure 10.2.16). Figures 10.2.17 — 10.2.18 show some characteristics of skipping descent trajectories to the Earth at escape velocity. It is characteristic that the highest load factors occur during the last entry into the atmosphere and are practically constant over a wide range of entry angles. In the ballistic descent case, these load factors correspond approximately to the minimal load factors for descent from AES orbit. The skipping trajectories are also characterized by the fact that the integral thermal fluxes Q increase significantly with increase of the number N of entries into the atmosphere. /372

Table 10.1 presents the basic characteristics of a skipping ballistic descent trajectory for V_{en} = 11 km/sec, θ_{en} = -3.8°,

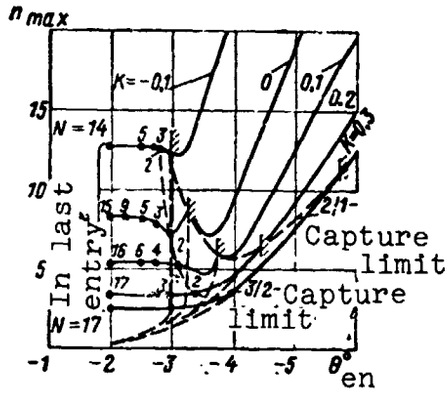

Figure 10.2.17. Dependence of n_{max} on entry angle θ_{en} for skipping trajectories with V_{en} = 11 km/sec; p_x = 400 kg/m^2

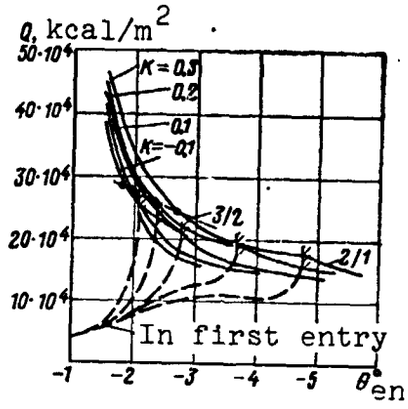

Figure 10.2.18. Thermal flux Q in skipping trajectories for V_{en} = 11 km/sec, p_x = 400 kg/m^2

and drag loading p_x = 400 kg/m^2.

It is characteristic that the temperature T_{max} is observed during the first entry into the atmosphere, while the maximal integral thermal flux is observed during the last entry. The flight along each transfer ellipse constitutes nearly a complete orbit around /373 the Earth. The vehicle descends to the Earth after making 2.2 orbits around the Earth.

The skipping trajectories are of interest because of the fact that, for fixed latitude of the point of entry into the atmosphere (or latitude at the point of nominal perigee passage), they permit landing in a given latitude zone by regulating the flight range. Trajectories of this type were used for landing on the territory of the Soviet Union of SC returning from lunar flyby trajectory, for which the nominal perigee point was in the southern latitudes. However, we note that descent along the skipping trajectories yields significantly higher integral thermal fluxes, which leads to increased thermal protection weight. The skipping trajectories make it possible to expand the atmospheric entry corridor. In fact, we see from Figure 10.2.19 that transition to trajectories with two entries into the atmosphere

TABLE 10.1.* CHARACTERISTICS OF SKIPPING DESCENT TRAJECTORIES FOR V_{en} = 11 km/sec, θ_{en} = -3.8°, AND p_x = 400 kg/m^2

	θ°_{en}	T_{max} K	Q kcal/m^2	V_{en} km/sec	L км	r_a км	n_{max}	n orbits
First flight in atmosphere	-3,8	2980	8,7·10^4	11,0	1830		1,16	0,836
Transfer ellipse					38060	32740		
Second flight in atmosphere	-2,9	2750	8,5·10^4	10,0	4050		1,07	1,03
Transfer ellipse					37340	13730		
Third flight in atmosphere	-2,55	2580	14,3·10^4	9,1	7150		8,12	0,18
Σ			31,5·10^4		88430			2,21

*[Translator's Note: Commas in numbers indicate decimal points.]

increases markedly the entry corridor Δh_x. Thus, if we limit the load factor to a value h_{max} = 10, then $\Delta h_{x max}$ for the 3/2* boundary increases by nearly a factor of two in comparison with the 2/1 boundary. Transition to trajectories with boundary 4/3 /374 and higher does not yield such a large increase of Δh_x. The maximal entry corridor width increase will occur for departure from the atmosphere with the parabolic velocity (number of entries $N \to \infty$).

Figure 10.2.20 shows for this case the upper limit of entry corridor height as a function of SC entry velocity V_{en} into the atmosphere and aerodynamic efficiency K. The lower limit

* $3/2 = \frac{N=3}{N=2}$ is the "capture" limit for two entries into the atmosphere, $2/1 = \frac{N=2}{N=1}$ is for a single entry.

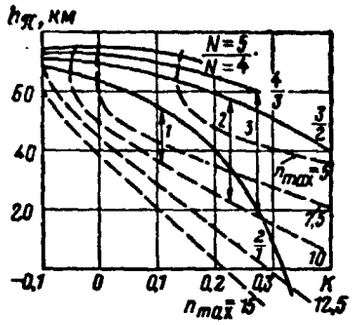

Figure 10.2.19. Capture limit on skipping trajectories for V_{en} = 11 km/sec, p_x = 400 kg/m^2:

1- $\Delta h_{п max}$ for the 2/1 limit; 2- for 3/2; 3- for 4/3

of the entry corridor is bounded by entry trajectories with n_{max} = 10. Flight along the upper limit of the corridor takes place with a negative value of the SC aerodynamic efficiency (SC inverted), while flight along the lower limit corresponds to flight with positive K. In this case, the SC enters the atmosphere with the maximal positive value of K and then transitions to an iso-load-factor trajectory with given n_{max}. For flight along this trajectory, it is necessary to vary either the drag in the ballistic descent case (controllable retro devices), or the lift force (roll angle variation), or vary both (change of SC angle of attack).

The skipping descent trajectories can be used for the /375
maneuver of SC insertion into satellite orbit around the planet with braking in the atmosphere. The "entry corridor" for these trajectories will lie between the 2/1 capture limit and the limit of departure with parabolic velocity ($N\to\infty$). In the case of entry along the upper limit of the corridor (velocity of departure from the atmosphere close to V_{par}) during departure from the atmosphere, correcting impulses (one or two) are imparted to the SC for insertion into an elongated elliptic orbit.

In the case of entry along the lower limit, the SC is transitioned into a low, nearly circular orbit by means of correcting impulses. SC landing on the surface of the planet is made from these intermediate orbits. As was shown in § 2,

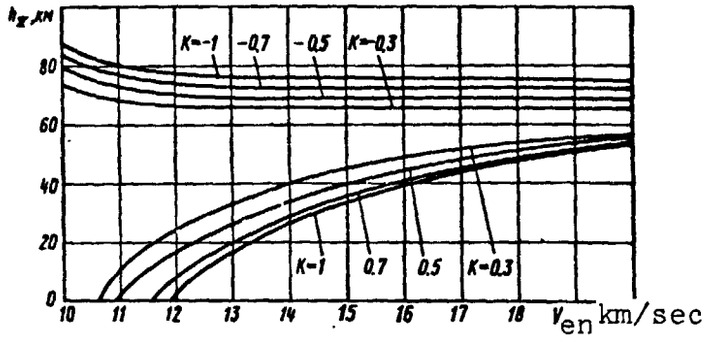

Figure 10.2.20. Dependence of entry corridor limit on entry velocity V_{en} and aerodynamic efficiency K for p_x = 500 kg/m^2; n_{max} = 10

Chapter 8, use of such a maneuver permits considerable reduction of the energy expenditure in flight schemes with insertion into APS orbit. Moreover, insertion into APS orbit facilitates considerably the problem of SC landing in a given region of the planet's surface. However, the realization of this flight scheme narrows the SC entry corridor into the planetary atmosphere, which may increase markedly the requirements on accuracy of the SC navigation and control systems both in the interplanetary flight segment and in the atmosphere.

§ 3. SC DESCENT IN PLANETARY ATMOSPHERES

Direct study of the physical conditions on the surface of the planets requires the landing of spacecraft. The first vehicles to carry out braking in the atmosphere of a planet were the SC of the Soviet Venera interplanetary stations. The first landing of a Soviet SC on the surface of Mars with braking in its atmosphere has been accomplished. Development of SC to probe the atmosphere of Jupiter is under way.

From the viewpoint of SC landing, all the planets can be broken down into two types:

— planets with dense atmosphere, in which the space velocity can be dissipated completely (the SC is braked to the equilibrium fall or gliding velocity);

— planets with rarefied atmosphere in which the space velocity can be reduced only partially.

The first type includes the Earth, Venus, and the planets of the Jupiter group (Jupiter, Saturn, Uranus, and Neptune); the second type includes Mercury and some large satellites of the planets of the Jupiter group. Mars may be considered an intermediate planet type. Its atmosphere is too rarefied to dissipate completely the space velocity of an SC with moderate drag loadings p_x = 400 — 600 kG/m^2 and large atmosphere entry angles, but permits complete braking of SC with p_x = 50 — 100 kg/m^2 (braking devices, large deflectors, and so on).

SC DESCENT IN MARS ATMOSPHERE /376

Let us examine the descent of SC entering the Mars atmosphere directly from an interplanetary flight trajectory. In this case, the vehicle may enter the atmosphere with hyperbolic velocity and entry angles from θ_{en} = -90° to small angles at the limit of vehicle capture by the atmosphere.

Figures 10.3.1 and 10.3.2 show the basic ballistic descent trajectory characteristics as functions of atmospheric entry angle θ_{en} and specific drag loading p_x. The general nature of the relations are the same as for descent in the Earth's atmosphere, however the maximal load factors n_x are considerably lower. The integral thermal fluxes Q are approximately an order of magnitude lower. The influence of Mars atmosphere entry velocity on the descent trajectory characteristics is shown in /377

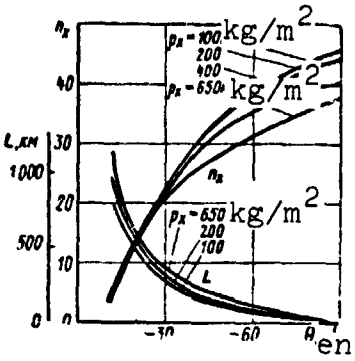

Figure 10.3.1. Maximal n_x and L versus θ_{en} for V_{en} = 6 km/sec, K = 0

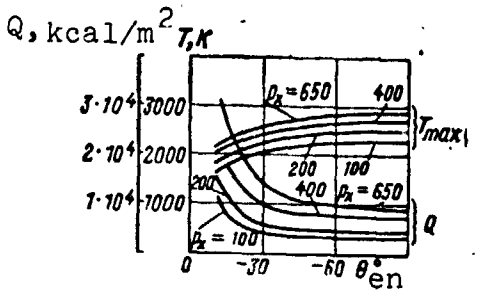

Figure 10.3.2. Q and T_{max} versus entry angle θ_{en}, K = 0

Figures 10.3.3 and 10.3.4. The general nature of the relations are the same as for descent in the Earth's atmosphere.

Figure 10.3.5 shows the influence of logarithmic density gradient $\beta = \frac{K\mu}{RT}$ (variation exponential atmopshere $\varrho = \varrho_0 e^{-\beta h}$) on the descent trajectory characteristics. The range of β variation was taken with account for the possible scatter because of

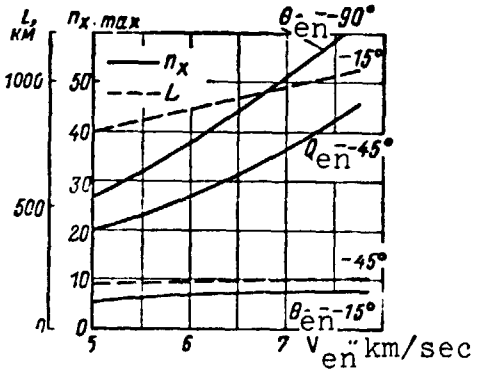

Figure 10.3.3. Influence of V_{en} on $n_{x\,max}$ and L for p_x = 650 kg/m^2, K = 0

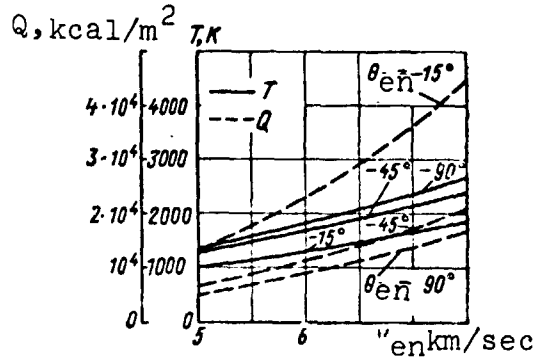

Figure 10.3.4. Influence of V_{en} on Q and T for p_x = 650 kg/m^2; K = 0

incomplete knowledge of the phsyical properties of the Mars atmosphere. Variation of β has the strongest influence on the maximal load factors n_{max}. The integral thermal fluxes Q decrease somewhat with increase of β, while the flight range L

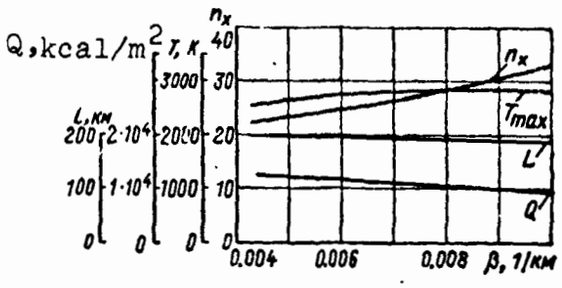

Figure 10.3.5. Influence of aerodynamic efficiency K on descent characteristics for p_x = 650 kg/m^2, K = 0, θ_{en} = -45°

and temperature T_{max} change very little. Inexact knowledge of the density ρ_0 at the surface of the planet does not affect characteristics such as n_{max}, T_{max}, and Q, but rather leads only to change of the n_{max} and T_{max} zone of action height.*

We see from analysis of the descent trajectory characteristics in the Mars atmosphere with entry velocity V_{en} close to the escape speed ($V_{par} \approx 5$ km/sec) that the conditions of SC descent to Mars are considerably less severe than in the case of /378 descent to the Earth in analogous situations. However, with respect to admissible load factor (n_{max} = 10), manned vehicle descent is possible only with small entry angles (θ_{en} = 15 — 17°). Figure 10.3.6 shows the influence of the aerodynamic efficiency K on the descent trajectory characteristics. We see that, just as for the Earth, the aerodynamic efficiency K reduces the maximal load factor n_{max} for low entry angles but has very little influence on this factor for large entry angles. The variation of the temperature T_{max} as a function of K is very slight. These are the basic characteristics in the case of descent in the Mars atmopshere from interplanetary flight trajectories.

Let us examine the descent trajectory characteristics from Mars satellite orbit. The basic descent trajectory characteristics as functions of entry angle θ_{en} into the Mars atmosphere

* With complete SC braking.

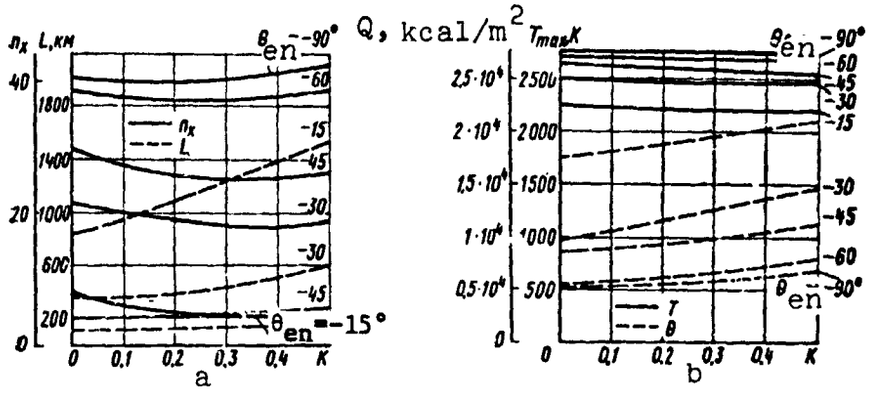

Figure 10.3.6. Influence of aerodynamic efficiency K on descent characteristics for p_x = 400 kg/m^2, V_{en} = 6 km/sec

and specific drag loading p_x are shown in Figure 10.3.7. The qualitative nature of the relations is the same as for descent from AES orbit. The minimal value of the load factor $n_{max} \approx$ 1.5, while for the Earth $n_{max} \approx 8$. The integral thermal fluxes Q for descent from Mars satellite orbit are lower by approximately a factor of 20 than from AES orbit.

SC DESCENT IN VENUS ATMOSPHERE

The velocity of entry directly into the Venus atmosphere from an interplanetary flight trajectory is V_{en} = 10.5 — 11.5 km/sec for flight from the Earth along the minimal energy trajectory. Characteristics such as the descent time t and flight range L differ very little from the same characteristics for the Earth. T_{max} and Q also differ very little. Figure 10.3.8 shows the ballistic thermal characteristics as functions of θ_{en} and drag loading p_x. Figures 10.3.9 and 10.3.10 show the basic characteristics of ballistic and gliding descent trajectories for entry angles close to the capture limit. We see that, with increase of K, the limiting angle θ_{en} increases,

/379

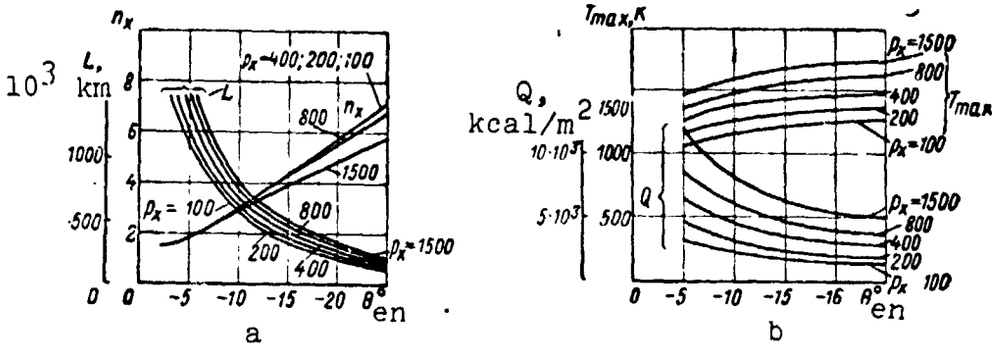

Figure 10.3.7. Dependence of descent trajectory characteristics on θ_{en} and p_x for V_{en} = 3.5 m/sec, K = 0

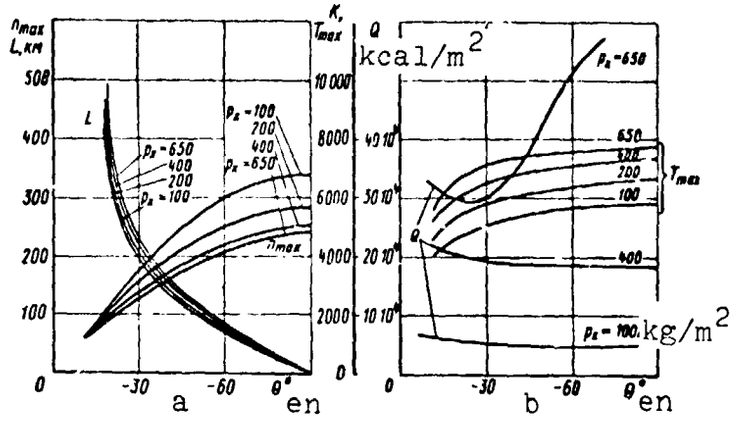

Figure 10.3.8. Influence of entry angle θ_{en} on ballistic descent trajectory characteristics for V_{en} = 10.7 km/sec, K = 0, β = 0.167 1/km

just as for the case of descent in the Earth's atmopshere. The value of Q varies in the same fashion for $\theta_{en\ lim}$ with increase of K. The influence of the specific drag loading p_x on the maximal load factors n_{max}, temperature T_{max}, and time-integral thermal fluxes Q is shown in Figure 10.3.11. We see that increase of p_x has very little effect on n_{max} but increases T_{max} and Q significantly. Figure 10.3.12 shows the influence of K on n_{max}

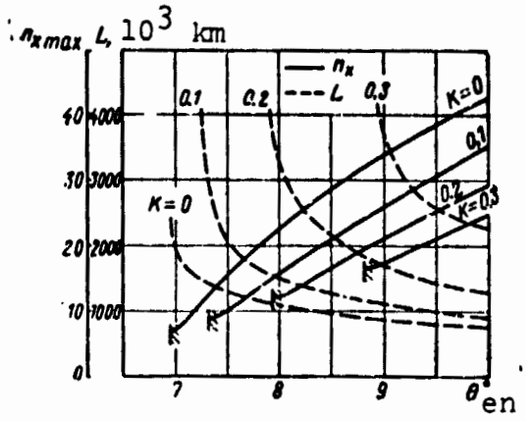

Figure 10.3.9. Influence of entry angle θ_{en} and aerodynamic efficiency K on load factor n_{max} and flight range L for V_{en} = 10.7 km/sec, p_x = 400 kg/m^2, β = 0.167 1/km

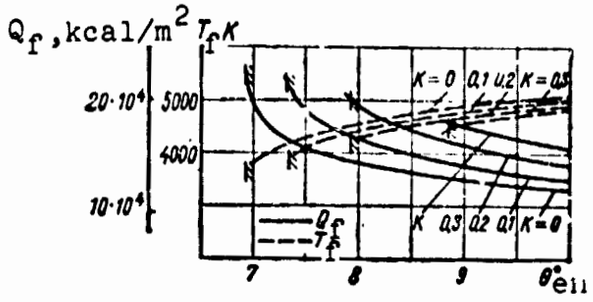

Figure 10.3.10. Influence of entry angle θ_{en} and aerodynamic efficiency K on Q and T_{max} for V_{en} = 10.7 km/sec, p_x = 400 kg/m^2, β = 0.167 1/km

and Q at the capture limit. /382

Figure 10.3.13 shows the influence of change of the atmosphere parameter β on the descent trajectory characteristics. Increase of β has very little effect on Q but alters n_{max} markedly.

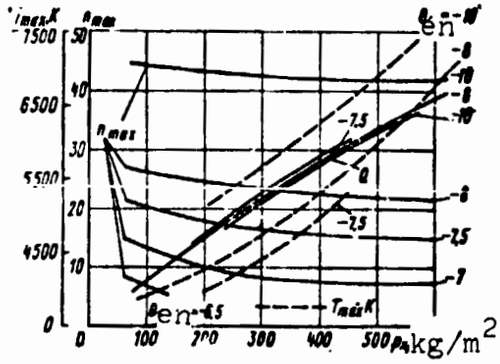

Figure 10.3.11. Influence of specific drag loading p_x on n_{max} and T_{max} for V_{en} = 10.7 km/sec, K = 0, β = 0.167 1/km

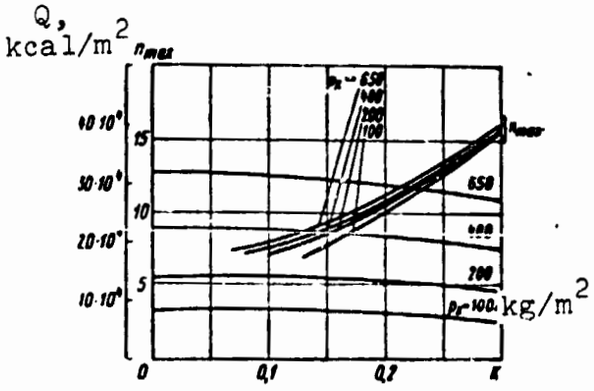

Figure 10.3.12. Dependence of load factor n_{max} and thermal flux Q on aerodynamic efficiency K and drag loading p_x for trajectories at the capture limit for V_{en} = 10.7 km/sec, β = 0.167 1/km

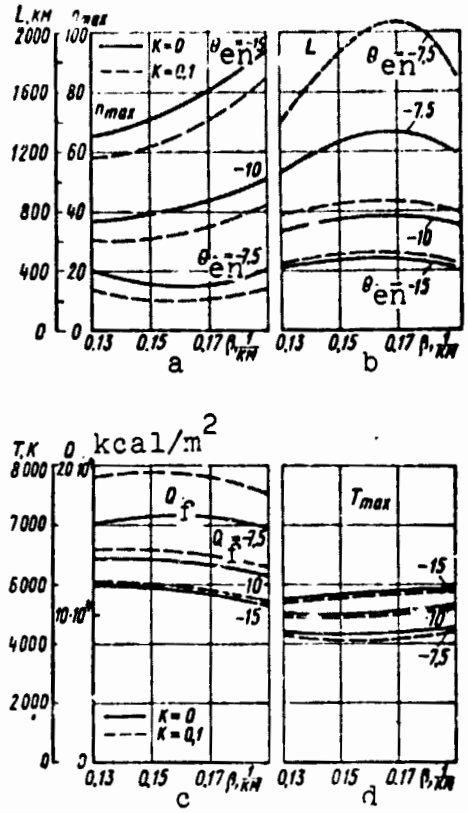

Figure 10.3.13. Influence of β on descent trajectory characteristics for V_{en} = 10.7 km/sec, p_x = 400 kg/m^2

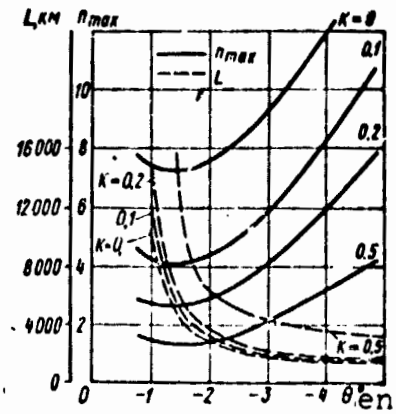

Figure 10.3.14. Dependence of load factor n_{max} and range L on entry angle θ_{en} for V_{en} = 10.7 km/sec, p_x = 400 kg/m^2

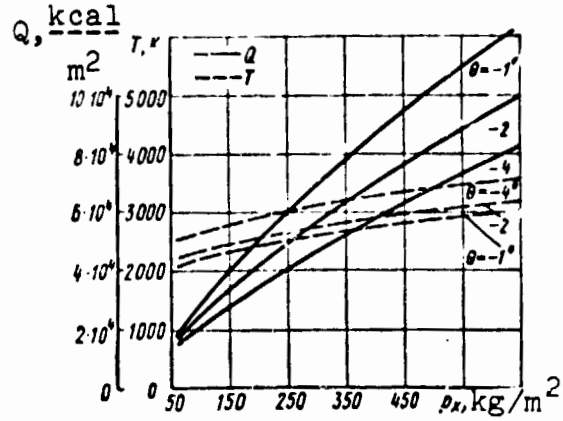

Figure 10.3.15. Dependence of thermal flux Q and T_{max} on drag loading p_x for β = 0.167 1/km, V_{en} = 7.13 km/sec, K = 0

Let us examine the trajectory characteristics during descent from Venus satellite orbit. The nature of the curves and the trajectory parameters are close to those for descent from AES orbit. Figures 10.3.14 and 10.3.15 show the basic descent trajectory characteristics as functions of atmospheric entry angle θ_{en} and specific drag loading p_x. The minimal load factors n_{max} are nearly the same as for the Earth. The integral thermal fluxes are somewhat higher.

§ 4. OPTIMIZATION OF SC SOFT LANDING SYSTEM PARAMETERS

Let us examine the final SC flight segment — the segment of contact with the surface of the planet. In the case of descent in the Earth's atmosphere, beginning at h = 15 — 20 km, the SC transitions to the steady-state vertical fall regime (ballistic descent) or to the gliding regime (gliding or "grazing" descent). The landing (touchdown) system must ensure safe SC touchdown with acceptable load factors. The possibility of maneuvering in order to select the touchdown area is also desirable. Let us examine some possible SC soft landing system variants.

PARACHUTE SYSTEM WITH IMPACT ATTENUATION

The parachute system is obviously the simplest system. In order to achieve acceptable load factors upon contact with the surface, it is necessary to use impact attenuating devices (inflatable bags, wheeled or ski landing gear with shock absorbers, and so on). In the case of cargo container or unmanned SC landing, the acceptable load factors may be quite large (n ≈ 50), and impact attentuation of the container with cargo or equipment inside the SC can be used. For manned SC landing (acceptable impact load factor no more than n = 15 — 20), it is necessary to use external attenuating devices with large travel (landing gear). The work absorbed by the gear is

/383

$$A = \frac{GV_{td}^2}{2g} + GS = nGS\eta,$$

where G is the SC weight at touchdown; V_{td} is the touchdown velocity (sink speed); S is the shock absorber travel; η is the shock absorber efficiency (η = 0.5 for spring and η = 0.6 — 0.8 for pneudralic shock absorber).

The load factor with shock absorber operation

$$n = \frac{V_{td}^2 + 2gS}{2\eta gS}$$

The relative gear weight can be calculated using the formula

$$\mu_{lg} = \frac{G_{lg}}{G} = anS.$$

The coefficient a can be taken approximately as a = 0.05 — 0.06 for S in meters. The relative parachute system weight can be found as

$$\mu_{ps} = \frac{G_{ps}}{G} = \frac{\gamma_{par}}{p_{par}},$$

where $p_{par} = G/S_{par}$ is the specific loading on the parachute canopy; $\gamma_{par} = G_{ps}/S_{par}$ is the weight of the parachute system per square meter of canopy (γ_{par} = 0.18 — 0.22 kg/m^2).

In selecting the dimensions of the individual parachute system canopies, we must consider that the dynamic load factor during canopy deployment

$$n_d = \frac{(p_{par} c_{x\ par})_{n-1}}{(p_{par} c_{x\ par})_n} k,$$

where $c_{x\ par}$ is the parachute canopy drag coefficient ($c_{x\ par}$ = 0.5 — 0.8), and k, the dynamic coefficient (k = 0.7 — 1.0) must not exceed the acceptable value.

Figure 10.4.1 shows the parachute system relative weight μ_{ps} and landing gear relative weight μ_{lg} as functions of load factor μ_{par} on the parachute. With increase of p_{par}, the gear weight increases (V_{td} increases) but the parachute system weight decreases. The total weight of the parachute touchdown landing /384

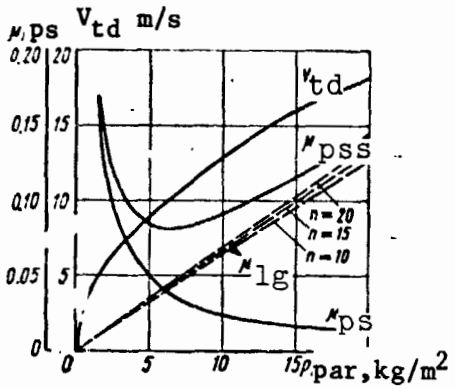

Figure 10.4.1. Characteristics of parachute system with shock absorption as a function of parachute loading p_{par}

with impact attenuation $\mu_{ps\ s} = \mu_{ps} + \mu_{lg}$ has a minimum for parachute loading $p_{par} \approx 6$ kg/m^2 which corresponds to touchdown velocity $V_{td} \approx 8$ — 10 m/sec. With gear shock absorber travel S = 0.75 m, the load factor does not exceed n = 15. The weight of the optimal parachute system with impact absorption amounts to 8 — 9% of the vehicle weight. The landing system is quite simple and lightweight, however, the impact load factors are still large for acceptable shock absorber travel values. Moreover, we should note that landing on gear (shock absorbers) with side drift owing to wind (simple impact attenuation in the form of inflatable bags) may cause the SC to overturn. However, the use of systems with airplane type shock absorbers (struts and ski footpads) leads to complication of the system.

RETRO SYSTEM

Landing using a parachute system with shock absorption is accompanied by high impact load factors at the instant of contact with the surface.

Use of a retro landing system makes it possible to achieve comfortable descent conditions, reducing the load factors to practically zero ("soft" landing). Liquid rocket, solid rocket, and turbojet engines can be used for this purpose.

The equations of motion of SC with retro-thrust landing system can be written in the following form (vertical landing)

$$\frac{dV}{dt} = -\frac{g}{p_x}\frac{\rho V^2}{2} - g\Delta\tilde{P};$$
$$\frac{dh}{dt} = V, \qquad (10.4.1)$$

where $\Delta\tilde{P} = \frac{P-G}{G} = \tilde{P} - 1$; $\tilde{P} = \frac{P}{G}$, P is the retro-engine thrust. Quite simple analytic solution of these equations can be obtained /385 under the conditions:

— constant atmospheric density (ρ=const);

— constant retro-engine thrust (P = const);

— constant vehicle weight (G = const).

All these conditions are essentially satisfied in the landing segment using retro engines. Actually, the braking segment does not exceed a few hundred meters, i.e., ρ=const . The propellant consumption is also not large, i.e., G = const. In this case,

$$dh = \frac{-d\left(\frac{V^2}{2}\right)}{\frac{\rho g}{2p_x}V^2 + g\Delta\tilde{P}}.$$

Integrating in the limits from $V = V_{par}$ to V = 0 and h from h_b to zero, we obtain

$$h_b = \frac{p_x}{\rho g}\ln\left(\frac{\Delta\tilde{P} + \frac{\rho}{2p_x}V_{par}^2}{\Delta\tilde{P}}\right).$$

Since braking takes place in the steady-state vertical descent segment (free fall, where $V_{par}^2 = 2p_x/\rho$), the expression for h_b simplifies:

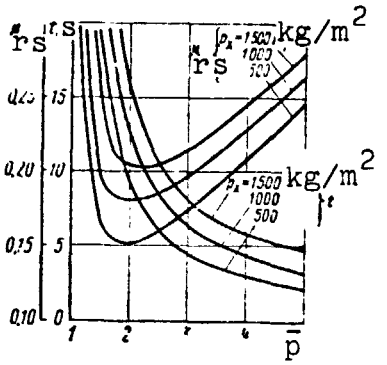

Figure 10.4.2. Characteristics of landing system with liquid rocket engine:

$\gamma_{eng} = 0.04$, $P_{sp} = 250$ sec

$$h_b = \frac{V_{ff}^2}{2g} \ln \left(\frac{\tilde{\Delta P} + 1}{\tilde{\Delta P}}\right) =$$

$$\frac{V_{ff}^2}{2g} \ln \left(\frac{\tilde{P}}{\tilde{P} - 1}\right).$$

We obtain the motion time from the equation

$$dt = \frac{-dV}{\frac{\varrho g}{2p_x} V^2 + g\tilde{\Delta P}}.$$

Integrating from t = 0 to t and from V_{ff} to V = 0, we obtain

$$t = \frac{V_{par}}{g} \frac{1}{\sqrt{\tilde{\Delta P}}} \operatorname{arc\,tg} \sqrt{\frac{1}{\tilde{\Delta P}}}.$$

A check of this solution using numerical calculation data (without the assumptions adopted above) made on a digital computer showed satisfactory accuracy both when using a turbojet engine powerplant for the landing (G varies only slightly, ρ varies somewhat more) and when using a liquid rocket engine (ρ varies little, G varies more). Figure 10.4.2. shows powerplant operating time t as a function of thrust-weight ratio $\tilde{P}$ and drag loading p_x. The relative weight of the fuel and tanks required for SC braking is /386

$$\mu_f = \frac{\tilde{P}t}{P_{sp}}(1 + a_t).$$

The relative weight of the retro engine is defined as

$$\mu_{eng} = \gamma_{eng}\tilde{P},$$

where γ_{eng} is the retro engine specific weight (kg/kg thrust).

The tank weight is proportional to the fuel weight (a_t is 5 — 10% of the fuel weight). The total system weight $\mu_{rs} + \mu_f + \mu_{eng}$. Let us evaluate the characteristics of the retro landing system with liquid rocket engine (LRE). For an LRE with thrust P = 3000 — 5000 kg, we can take $\gamma_{eng} = 0.04$. The characteristics of the LRE retro system are shown in Figure 10.4.2. With increase of the retro engine thrust-weight ratio $\tilde{R}$, the relative weight μ_{eng} increases but the fuel weight μ_f decreases because of the reduced descent time (gravitational losses in SC braking). The optimal LRE thrust-weight ratio $\tilde{P} \approx 2$. For specific drag loading $p_x = 500$ kg/m^2 and specific thrust $P_{sp} \approx 250$ s, the LRE retro system relative weight μ_{rs} is equal to 15 — 16%. Solid rocket engines (SRE) can be used for the retro landing system. The weight characteristics of such a landing system are close to those of the LRE system. A drawback of the retro landing systems using LRE and SRE is the difficulty in providing for maneuvering in the landing region, since the high fuel consumption rate limits engine operating time (additional operating time $\Delta t \approx 20$ — 30 sec when using LRE with thrust equal to SC weight requires approximately 10% of the SC weight in fuel supply). Moreover, the gas jets cause soil erosion in the case of extended SC hovering near the surface. This can be avoided by locating the landing powerplant on an extensible boom above the SC or in the parachute shroud lines.

Let us examine the characteristics of retro landing systems using turbojet engines (TJE). The short duration TJE developed for vertical takeoff airplanes have the best weight characteristics. The characteristics of a landing system with TJE with /387

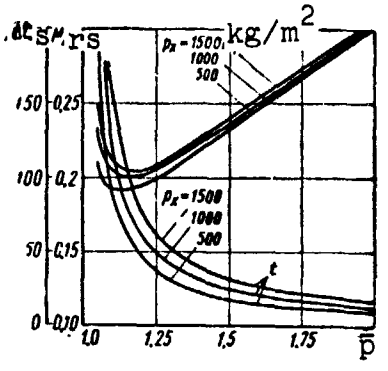

Figure 10.4.3. Characteristics of landing system with TJE γ_{eng} = 0.15, C_R = 1 kg/kg/hr

specific weight γ_{eng} = 0.15 and specific fuel consumption C_R = 1 kg fuel/kg thrust/hour are shown in Figure 10.4.3. Because of the high engine weight and lower fuel weight, the optimal thrust-weight ratio is lower than for the LRE and is equal to $\tilde{P}$ = 1.1 — 1.2. The landing system is somewhat heavier than when using the TJE. However, because of the relatively low fuel consumption, it is possible to maneuver in the landing touchdown region with only slight increase of the system weight owing to the additional fuel. Thus, for an additional fuel supply on the order of 5% of the vehicle weight, the vehicle can hover for three minutes, which permits range maneuvering with l = 2 — 3 km. The maneuver range can be increased by another 1 — 2 km by sideslipping in the braking segment (t ≈ 50 — 60 sec). The possibility of micromaneuvering in the touchdown region makes it possible to select an area convenient for landing. The TJE causes considerably less soil erosion and landing of such vehicles on grass covered soil is possible. In this regard, the use of the turbofan retro engine, in which the specific fuel consumption and propulsive jet discharge velocity are lower than for the TJE, is still more interesting.

PARACHUTE-RETRO SYSTEM

Let us examine the combined parachute-retro landing system. The system operates as follows. The SC descent velocity is reduced significantly by deployment of the parachute system, then the retro engine is activated in the immediate vicinity of the surface and the vehicle velocity is reduced to practically

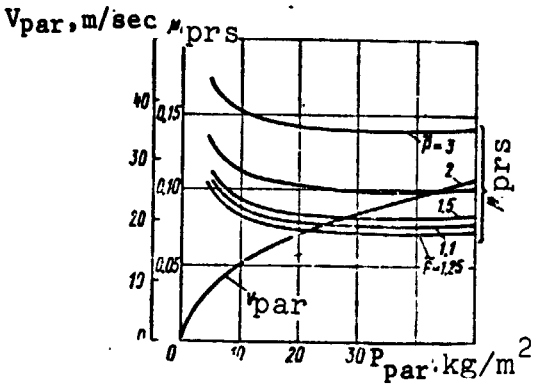

Figure 10.4.4. Characteristics of the parachute-retro landing system with LRE

zero at the instant of contact with the ground.

The primary weight component of the retro system with LRE and SRE is the fuel weight. Preliminary braking of the SC by a parachute permits significant reduction of the landing system weight. The equations of motion of a vehicle with such a system are similar to the equations of motion of the vehicle with retro system with replacement of the SC specific drag loading by the reduced loading /388

$$p_{x\ red} = \frac{G}{c_{xa}S_a + S_{x\ par}S_{par}},$$

where c_{xa}; $c_{x\ par}$ are the drag coefficients of the SC and parachute, respectively; S_a; S_{par} are the frontal areas of the SC and parachute.

The relative weight of such a landing system is

$$\mu_{prs} = \mu_{eng} + \mu_f + \mu_{ps},$$

where $\mu_{eng} = \gamma_{eng}\tilde{P}$ is the retro engine weight; $\mu_f = \tilde{P}/P_{sp}t(1 + a_t)$ is the weight of the fuel and tanks; $\mu_{ps} = \gamma_p/p_{par}$ is the parachute system weight.

The weight of the parachute-retro system with LRE is shown in Figure 10.4.4 as a function of parachute loading p_{par} and retro engine thrust-weight ratio $\tilde{P}$. We see that, in this case, there are optimal values of both p_{par} and $\tilde{P}$. The system

weight is less by nearly a factor of two than the weight of the retro system with LRE. The optimal thrust-weight ratio is considerably less than for the retro system and is close to $\tilde{P}$ = 1.2 — 1.3. The descent velocity for the optimal parachute loading p_{par} = 20 — 40 kg/m^2 is V_{par} = 18 — 25 m/sec. In regard to weight, this system is nearly equivalent to the parachute system with shock attenuation and at the same time, provides a significant advantage — soft touchdown.

The parachute retro system provides a weight advantage only for the LRE and SRE. The weight advantage in combination with the TJE is small. The parachute retro-system with SRE was used successfully on the Voskhod and Soyuz SC, providing reliable and comfortable landing for the crew.

APPENDIX

BRIEF CHARACTERISTICS OF SOLAR SYSTEM PLANETS

Astronomical Symbols and Notations /389

⊙ Sun (Helios)
☿ Mercury (Hermes)
♀ Venus (Aphrodite)
⊕ or (♁) Earth (Earth)
♂ Mars (Ares)
♃ Jupiter (Zeus)
♄ Saturn (Cronus)
♅ Uranus (Uranus)
♆ Neptune (Poseidon)
♇ Pluto (Hades)
☾ Moon (Selene)

♈ Constellation Aries, and also vernal equinox point of planet

☊ Ascending node point.

The Greek names of the planets are shown in parentheses.

Mean Elements of Planet Orbits

The mean elements of the planet orbits change with time. There are formulas for determining the mean elements of the planet orbits as functions of time, measured in Julian centuries from some selected epoch. For the planets of the Earth group, these formulas are given in the Astronomical Almanac* and for the planet Jupiter — in Michaux's book.** These formulas are

* Astronomical Almanac of the USSR for 1974, Moscow, Nauka Press, 1972.

** Michaux, C. M. Handbook of the Physical Properties of the Planet Jupiter, Mir Press, 1970.

REPRODUCIBILITY OF THE ORIGINAL PAGE IS POOR.

$$T = \frac{(\text{J.D.}) - (\text{J.D.})_0}{36525.0},$$

where $(\text{J.D.})_0$ = 2415020.0 (January 0.5, 1900) is the initial epoch; J.D. is the current Julian date; 36525.0 is the number of Julian days in a Julian century.

The mean elements of the orbits of the large planets are expressed by the relations:

ELEMENTS OF PLANET ORBITS*

Mercury

$\lambda = 178°10'44'',68 + 538106654'',80\ T + 1'',084\ T^2$;
$\pi = 75°53'58'',91 + 5599'',76\ T + 1'',061\ T^2$;
$\Omega = 47°8'45'',40 + 4266'',75\ T + 0'',626\ T^2$;
$i = 7°0'10'',37 + 6'',699\ T - 0'',066\ T^2$;
$e = 0{,}20561421 + 0{,}00002046\ T - 0{,}000000030\ T^2$;
$a = 0{,}3870984$.

Venus

$\lambda = 342°46'1'',39 + 210669162'',88\ T + 1'',1148\ T^2$;
$\pi = 130°9'19'',8 + 5068'',93\ T - 3'',515\ T^2$;
$\Omega = 75°46'46'',73 + 3239'',46\ T + 1'',476\ T^2$;
$i = 3°23'37'',07 + 3'',621\ T - 0'',0035\ T^2$;
$e = 0{,}00682069 - 0{,}00004774\ T + 0{,}000000091\ T^2$;
$a = 0{,}72333015$.

Earth

$\lambda = 99°41'48'',04 + 129602768'',13\ T + 1'',089\ T^2$;
$\pi = 101°13'15'',0 + 6189'',03\ T + 1'',63\ T^2 + 0'',012\ T^3$;
$\Omega = 0°$;
$i = 0°$;
$e = 0{,}01675104 - 0{,}00004180\ T - 0{,}000000126\ T^2$;
$a = 1{,}00000023$.

Mars

$\lambda = 293°14'51'',46 + 68910117'',33\ T + 1'',1184\ T^2$;
$\pi = 334°13'5'',53 + 6626'',73\ T + 0'',4575\ T^2 - 0'',0043\ T^3$;
$\Omega = 48°47'11'',19 + 2775'',57\ T - 0'',005\ T^2 - 0'',0192\ T^3$;
$i = 1°51'1''.20 - 2'',430\ T + 0'',0454\ T^2$;
$e = 0{,}09331290 + 0{,}000092064\ T - 0{,}000000077\ T^2$;
$a = 1{,}52368839$.

Jupiter

$\lambda = 238°2'57'',32 + 10930687'',148\ T + 1'',20486\ T^2 - 0'',005936\ T^3$;
$\pi = 12°43'15'',34 + 5795'',862\ T + 3'',60258\ T^2 - 0'',01236\ T^3$;
$\Omega = 99°26'36'',19 + 3637'',908\ T + 1'',2680\ T^2 - 0'',03064\ T^3$;
$i = 1°18'31'',45 - 20'',506\ T + 0''0{,}14\ T^2$;
$e = 0{,}04833475 + 0{,}000164180\ T - 0{,}0000004676\ T^2 - 0{,}0000000017\ T^3$;
$a = 5{,}202561$.

* [Translator's Note: Commas in the numbers indicate decimal points.]

Saturn

$\lambda = 266°33'51'',76 + 4404635'',5810\,T + 1'',16835\,T^2 - 0'',021\,T^3$;
$\pi = 91°5'53'',38 + 7050'',297\,T + 2'',9749\,T^2 + 0'',0166\,T^3$;
$\Omega = 112°47'25'',40 + 3143'',5025\,T - 0'',54785\,T^2 - 0'',0191\,T^3$;
$i = 2°29'33'',07 - 14'',108\,T - 0'',05576\,T^2 + 0'',00016\,T^3$;
$e = 0{,}05589232 - 0{,}00034550\,T - 0{,}000000728\,T^2 + 0{,}00000000074\,T^3$;
$a = 9{,}554747$.

Uranus

$\lambda = 244°11'50'',89 + 1547508'',765\,T + 1'',13774\,T^2 - 0'',002176\,T^3$;
$\pi = 171°32'55'',14 + 5343'',958\,T + 0'',8539\,T^2 - 0'',00218\,T^3$;
$\Omega = 73°28'37'',55 + 1795'',204\,T + 4'',722\,T^2$;
$i = 0°46'20'',87 + 2'',251\,T + 0'',1422\,T^2$;
$e = 0{,}0463444 - 0{,}00002658\,T + 0{,}000000077\,T^2$;
$a = 19{,}21814$.

Neptune

$\lambda = 84°27'28'',78 + 791589'',291\,T + 1'',15374\,T^2 - 0'',002176\,T^3$;
$\pi = 46°43'38'',37 + 5128'',168\,T + 1'',40694\,T^2 - 0'',002176\,T^3$;
$\Omega = 130°40'52'',89 + 3956'',166\,T + 0'',89952\,T^2 - 0'',016984\,T^3$;
$i = 1°46'45'',27 - 34'',357\,T - 0'',0328\,T^2$;
$e = 0{,}00899704 + 0{,}000006330\,T - 0{,}000000002\,T^2$;
$a = 30{,}10957$.

Pluto

$T = 1989$, октябрь 0,0344;
$\pi = 113°31'17'',72$;
$\Omega = 108°57'16'',18$;
$i = 17°8'48'',40$;
$e = 0{,}2486438$;
$a = 39{,}517738$.

/392

Here $\lambda = \Omega + \omega + M$ is the mean longitude, M is the mean anomaly.

After determining the mean elements of the planet orbit, we can calculate the mean M_{pl} and true ν_{pl} anomalies and also the planet argument of latitude u_{pl} from relations

$$M_{pl} = \lambda_{pl} - \pi_{pl}$$

$$\nu_{pl} = M_{pl} + \left(2e_{pl} - \frac{e_{pl}^2}{4} + \frac{5}{96}\,e_{pl}^5\right) \sin M \qquad e_{pl}^2 - \frac{11}{24}\,e_{pl}^4\Big) \times$$

$$\times \sin 2M_{pl};$$

$$u_{pl} = \pi_{pl} + \nu_{pl} - \Omega_{pl};$$

for Earth

$$\tilde{u}_{\oplus} = \pi_{\oplus} + \nu_{\oplus}.$$

SYNODIC PLANET REVOLUTION PERIODS

The synodic period is defined as the time interval between two successive coincidences of the heliocentric longitudes of one planet relative to another. The values of the synodic revolution periods of the planets in tropical years are given in the table.

MEAN EQUATORIAL GEOCENTRIC COORDINATES OF PLANET'S NORTH POLE

The equatorial geocentric coordinates of a planet's north pole are α_N and δ_N, the mean values of which with account for precession are defined by the following formulas [Reference 1, pages 53, 57, 58].*

Mars

$$\alpha_N = 316{,}844^\circ + 0{,}6533^\circ T_\epsilon, \quad \delta_N = +53{,}009^\circ + 0{,}3542^\circ T_\epsilon.$$

Jupiter

$$\alpha_N = 17^h52^m10{,}72^s + 24{,}7^s T_\epsilon, \quad \delta_N = +64^\circ33'10'',6 - 60'' T_\epsilon.$$

Saturn

$$\alpha_N = 2^h33^m39^s{,}93 + 1015^s{,}20 T_\epsilon + 0^s{,}18 T_\epsilon^2 + 2^s{,}55 T_\epsilon^3,$$
$$\delta_N = +83^\circ18'37{,}3'' + 1570'',4 T_\epsilon - 46'',3 T_\epsilon^2 - 3'',1 T_\epsilon^3,$$

where

$$T_\epsilon = \frac{(\text{J.D.}) - 2433282{,}4234}{36524{,}22}$$

J.D. is the current Julian date; $(\text{J.D.})_0$ = 2433282.4234 (January 0.5, 1950) is the initial epoch; 36524.22 are the ephemeris days of a tropical century.

* [Translator's Note: Commas in numbers indicate decimal points.]

SYNODIC REVOLUTION PERIODS OF THE PLANETS*

Planet	Mercury	Venus	Earth	Mars	Jupiter	Saturn	Uranus	Neptune	Pluto
Mercury	∞	0,39[illegible]	0,31726	0,27622	0,24584	0,24284	0,24154	0,24120	0,24108
Venus	0,39580	∞	1059871	0,91424	0,64886	0,62833	0,61975	0,61752	0,61674
Earth	0,31726	1,59871	∞	2,1354	1,09211	1,03518	1,01209	1,00615	1,00408
Mars	0,27622	0,91424	2,1354	∞	2,23533	2,00918	1,92396	1,90261	1,89524
Jupiter	0,24584	0,64886	1,09211	2,23533	∞	19,85931	13,81242	12,78236	12,45704
Saturn	0,24284	0,62833	1,03518	2,00918	19,85931	∞	45,36307	35,86985	33,42057
Uranus	0,24154	0,61975	1,01209	1,92396	13,81242	45,36307	∞	171,403	126,94673
Neptune	0,24120	0,61752	1,00615	1,90261	12,78236	35,86985	171,403	∞	489,4482
Pluto	0,24108	0,61674	1,00408	1,89524	12,45704	33,42058	126,94673	489,4482	∞

*[Translator's Note: Commas in numbers indicate decimal points.]

REFERENCES

1. Abalakin, V. K., Ye. P. Aksenov, et al. Spravochnoye rukovodstvo po nebesnoy mekhanike i astrodinamike (Handbook on Celestial Mechanics and Astrodynamics). Moscow, Nauka Press, 1971.

2. Alekseyev, K. B., G. G. Bebenin, and V. A. Yaroshevskiy. Manevrirovaniye kosmicheskikh apparatov (Spacecraft Maneuvering). Moscow, Mashinostroyeniye Press, 1970.

3. Andreyevskiy, V. V. Dinamika spuska kosmicheskikh apparatov na zemlyu (Dynamics of Spacecraft Landing). Moscow, Mashinostroyeniye Press, 1970.

4. Balk, M. B. Elementy dinamiki kosmicheskogo poleta (Elements of Space Flight Dynamics). Moscow, Nauka Press, 1965.

5. Bauze, V. R. E., A. A. Dashkov, and V. N. Kubasov. Planet Flyby Trajectories with Return to Earth. Kosmicheskiye Issledovaniya, Vol. 6, No. 6, 1968.

6. Bachmanov, A. A., Ts. V. Solov'yev, and V. N. Filimonov. Dynamics of Single-Impulse Interplanetary Flight Trajectory Optimal Characteristics. Kosmicheskiye Issledovaniya, Vol. 9, No. 4, 1971.

7. Battin, R. H. Navedeniye v kosmose (Astronautical Guidance). Moscow, Mashinostroyeniye Press, 1966.

8. Grodzovskiy, G. L., Yu. N. Ivanov, and V. V. Tokarev. Mekhanika kosmicheskogo poleta s maloy tyagoy (Mechanics of Low Thrust Space Flight). Moscow, Nauka Press, 1966.

9. Dashkov, A. A., and V. V. Ivashkin. On a Remarkable Property of a Bundle of Hyperbolic Trajectories. Kosmicheskiye issledovaniya, Vol. 3, No. 5, 1965.

10. Demin, V. G. Dvizheniye iskusstvennogo sputnika v netsentral'nom pole tyagoteniya (Artificial Satellite Motion in Noncentral Gravity Field). Moscow, Nauka Press, 1968.

11. Dubovskiy, S. V. Interorbital and Interplanetary Transfers. Kosmicheskiye issledovaniya, Vol. 5, No. 4, 1967.

C-6

12. Duboshin, G. N. Teoriya prityazheniya (Gravity Theory). Moscow, Fizmatgiz Press, 1961.

13. Duboshin, G. N. Nebesnaya mekhanika (Osnovnye zadachi i metody) [Celestial Mechanics (Fundamental Problems and Methods)]. Moscow, Fizmatgiz Press, 1963.

14. Duboshin, G. N., and D. Ye. Okhotsimskiy. Some Problems of Astrodynamics and Celestial Mechanics. Kosmicheskiye issledovaniya, Vol. 1, No. 2, 1963.

15. Yegorov, V. A. Some Questions of Interplanetary Space Sounding Trajectory Optimization. Avtomatika i telemekhanika, No. 5, 1970.

16. Yegorov, V. A. On the Question of Capture in the Restricted Circular Three-Body Problem. In the collection: Iskusstvennye sputniki Zemli (Artificial Earth Satellites). No. 3, 1959.

17. Yevtushenko, Yu. G., et al. Dvizheniye iskusstvennykh sputnikov v gravitatsionnom pole Zemli (Motion of Artificial Satellites in the Earth's Gravity Field). Computer Center of the Academy of Sciences of the USSR, 1967.

18. Zhukovskiy, N. Ye. Teoriya prityazheniye. Sbornik sochinenii (Gravitation Theory. Collection of Works). Vol. 5, Goztekhizdat Press, 1949.

19. Ivanov, N. M., and A. I. Martynov. On the Maximal Allowable Load on the Frontal Surface of a Vehicle Performing Aerodynamic Descent in the Mars Atmosphere. Scientific Notes of TsAGI, Vol. 2, No. 3, 1971.

20. Ivashkin, V. V., and A. P. Skorokhodov. Optimal Nonplanar Single-Impulse Transfer from Hyperbolic to Circular Orbit. Kosmicheskiye issledovaniya, Vol. 9, No. 4, 1971.

21. Il'in, V. A. Transfer to AES Orbit by Braking in the Atmosphere. Inzhenernyi zhurnal, Vol. 3, No. 2, 1963.

22. Il'in, V. A. On the Calculation of SC Transfer Trajectories between Coplanar Circular Orbits in Newtonian Gravity Field. Kosmicheskiye issledovaniya, Vol. 2, No. 5, 1964. /396

23. Kazakov, R. K., V. C. Kiselev, and A. K. Platonov, Study of the Energetics of Optimal Flight Orbits to Jupiter. Kosmicheskiye issledovaniya, Vol. 6, No. 1, 1968.

24. Kislik, M. D. Motion of Artificial Satellite in the Earth's Normal Gravity Field. In the collection: Iskusstvennye sputniki Zemli (Artificial Earth Satellites). No. 4, 1960.

25. Kislik, M. D. Analysis of the Motion Integrals of an Artificial Satellite in the Earth's Normal Gravity Field. In the collection: Iskusstvennye sputniki Zemli (Artificial Earth Satellites), No. 13, 1962.

26. Kislik, M. D. Spheres of Influence of the Large Planets and the Moon. Kosmicheskiye issledovaniya, Vol. 2, No. 5, 1964.

27. Space Trajectories. Moscow, Foreign Literature Press, 1963.

28. Kosmicheskaya Era. Prognozy na 2001 goda (The Space Era. Predictions for 2001). Moscow, Mir Press, 1970.

29. Kosmonavtika (Malen'kaya entsiklopediya) [Cosmonautics (Small Encyclopedia)]. Moscow, Sovetskaya Entsiklopediya Press, 1970.

30. Kulikov, K. A. Novaya sistema astronomicheskikh edinits (New System of Astronomical Units). Moscow, Nauka Press, 1969.

31. Levantovskiy, V. I. Mekhanika kosmicheskogo poleta (v elementarnom izlozhenii) [Space Flight Mechanics (In Elementary Presentation)]. Moscow, Nauka Press, 1970.

32. Livanov, L. B. On a Class of Optimal Impulsive Earth-Planet-Earth Transfers. Kosmicheskiye issledovaniya, Vol. 9, No. 2, 1971.

33. Lawden, D. F. Optimal'nyye trayektorii dlya kosmicheskoy navigatsii (Optimal Trajectories for Space Navigation). Moscow, Mir Press, 1966.

34. Loh, T. L. Dynamics and Thermodynamics of Planetary Entry. Moscow, Mir Press, 1966.

35. Martin, D. Atmospheric Entry. Introduction to Theory and Practice. Moscow, Mir Press, 1969.

36. Leitman, G., ed. Optimization Techniques with Application to Aerospace Systems. Moscow, Nauka Press, 1965.

37. Mekhanika v SSSR za 50 Let (Mekhanika kosmicheskogo poleta. Nebesnaya mekhanika) [Fifty Years of Mechanics in the USSR (Space Flight Mechanics. Celestial Mechanics)]. Vol. 1, Moscow, Nauka Press, 1968.

38. Osnovy teorii poleta kosmicheskikh apparatov (Fundamentals of Spacecraft Flight Theory). Moscow, Mashinostroyeniye Press, 1972.

39. Ponomarev, V. M. Teoriya upravleniya dvizheniem kosmicheskikh apparatov (Theory of Spacecraft Motion Control). Moscow, Nauka Press, 1965.

40. Sovremennoye sostoyaniye mekhaniki kosmicheskogo poleta (Present Status of Space Flight Mechanics). Edited by P. B. Richards, Moscow, Nauka Press, 1969.

41. Subbotin, M. F. Vvedeniye v teoreticheskuyu astronomiya (Introduction to Theoretical Astronomy). Moscow, Nauka Press, 1968.

42. Tarasov, Ye. V. Optimal'nye rezhimy poleta letatel'nykh apparatov (Optimal Flight Vehicle Flight Regimes). Moscow, Oborongiz Press, 1963.

43. Tarasov, Ye. V. Algoritm optimal'nogo proyektirovaniya letatel'nogo apparata (Algorithm for Optimal Flight Vehicle Design). Moscow, Mashinostroyeniye Press, 1970.

44. Tarasov, Ye. V., and A. V. Labunskiy. Optimizatsiya proyektno-ballisticheskikh kharakteristik mezhplanetnogo apparata dlya pereleta na orbitu IS planety naznacheniya (Optimization of Ballistic Design Characteristics of Interplanetary Vehicle for Transfer to Artificial Satellite Orbit of Destination Planet). Proceedings of Sixth Lecture Series on Development of the Scientific Heritage and Ideas of Tsiolkovskiy, 1972.

45. Tikhonravov, M. K. On Exact Account for the Accelerations Caused by the Influence of Celestial Bodies in the Formulas for Spacecraft Orbital Element Perturbations. Kosmicheskiye issledovaniya, Vol. 6, No. 1, 1968.

46. Wild, D. J. Optimum Seeking Methods. Moscow, Nauka Press, 1967.

47. Tsiolkovskiy, K. E. Izbrannye trudy (Selected Works). Moscow, Academy of Sciences of the USSR Press, 1962.

48. Chebotarev, G. A. Analiticheskiye i chislennye metody nebesnoy mekhaniki (Analytic and Numerical Methods of Celestial Mechanics). Moscow, Nauka Press, 1965.

49. Shternfel'd, A Ya. Vvedeniye v kosmonavtiku (Introduction to Cosmonautics). Moscow, ONTI (United Scientific and Technical Presses), 1937.

50. El'yasberg, P. Ye. Vvedeniye v teoriyu poleta iskusstvennogo sputnika Zemli (Introduction to Artificial Earth Satellite Flight Theory). Moscow, Nauka Press, 1965.

51. Ehricke, K. A. Space Flight. Vol. 1, Moscow, Fizmatgiz Press, 1963; Vol. 2, Part 1, Nauka Press, 1969; Part 2, Nauka Press, 1970. /397

52. Escobal, P. R. Methods of Orbit Determination. Moscow, Mir Press, 1970.

53. Escobal, P. R. Methods of Astrodynamics. Moscow, Mir Press, 1971.

54. Battin, R. H. A New Solution for Lambert's Problem. IAF Paper No. AD 101, 1968.

55. DeBra, D. B. Vectors and Dyadics: The Natural Tools of Space Vehicle Mechanics. Preprint. Amer. Astronaut. Soc., No. 76, 1961.

56. Bourke, R. D., and F. G. Beerer. Mariner Mission to Venus and Mercury in 1973. Astronaut. and Aeronaut. Vol. 9, No. 1, 1971.

57. Breakwell, J. V., R. W. Gillespie, and S. Ross. Research in Interplanetary Transfer. Amer. Rocket. Soc. Preprints. Nos. 954-59. No. 30, 1960.

58. Breakwell, J. V. Trajectories of Spacecraft Launches Normal to the Ecliptic. XIV Congr. Internat. Astronaut., 1963.

59. Deerwester, J. M., and S. M. D'Haem. Systematized Comparison of Venus Swingby Mode with Standard Mode of Mars Round Trips. Journal of Spacecraft and Rockets. Vol. 4, No. 7, 1967.

60. Fimple, W. R. Optimum Midcourse Plane Changes for Ballistic Interplanetary Trajectories. AIAA J., Vol. 1, No. 2, 1963.

61. Faust, N. L., and T. B. Murtagh. Manned Mars Lander Launch-to-Rendezvous Analysis for a 1981 Venus Swingby Mission. AIAA Papaer, No. 1075, 1970.

62. Gillespie, R. W., and S. Ross. The Venus Swingby Mission Mode and Its Role in the Manned Exploration of Mars. Journal of Spacecraft and Rockets, AIAA J. Vol. 5, No. 5, 1967.

63. Gobetz, F. W. Optimal Transfer Between Hyperbolic Asymptotes. AIAA J., Vol. 1, No. 9, 1963.

64. Gobetz, F. W., and J. R. Doll. A Survey of Impulsive Trajectories. Journal of Spacecraft and Rockets, Vol. 7, No. 5, 1969.

65. Greenwood, S. W. Orbits for Solar Exploration: A Review. Canad. Aeronaut. and Space J., Vol. 13, No. 10, 1967.

66.* Kornhauser, A. L., P. M. Lion, and G. A. Hazelrigg. An Analytic Solution for Constant Thrust, Optimal Cost, Minimum Propellant Space Trajectories. AIAA J., Vol. 9, July, 1971.

67. Kaufman, B. Effects of the Galilean Moons on Jupiter Flyby Trajectories. AIAA J., Vol. 8, No. 7, 1970.

68. Kellermeier, H. E., D. E. Koelle, and W. Muller. Ballistic Mechanical and Technical Problems of a Mercury Flyby Mission. Baumfahrtforschung, Vol. 4, No. 1, 1970.

69. Klopp, D. A., and J. C. Niehoff. Jupiter Gravity-Assisted Trajectories. J. Spacecraft and Rockets Vol. 6, No. 4, 1969.

70. Lascody, D. N., E. D. Thorson, et al. Analysis of Earth-Mars-Earth Mission in the 1975-1985 Period. AIAA J, Vol. 3, No. 10, 1965.

71. Lee, V. A., and S. W. Wilson, Jr. A Survey of Ballistic Mars Mission Profiles. AIAA J. Vol. 5, No. 5, 1967.

72. Manning, L. A. Trajectory Modes for Manned and Unmanned Missions to Mercury. J. Spacecraft and Rockets, Vol. 4, No. 9, 1967.

73. Mueller, W. Trajectory of the Swingby Technique of the Planet Jupiter for Interplanetary Missions. (Raumfahrtforschung, Vol. 12, No. 4, 1968.

74. Niehoff, J. C. Gravity-Assisted Trajectories to Solar System Targets. J. Spacecraft and Rockets, Vol. 3, No. 9, 1966.

*[Translator's Note: Th article is correctly cited above from English source. Foreign text is incorrect.]

75. Norman, S. M. A Comparison of Passage Conditions at the Outer Planets for Several Flyby Trajectory Modes. AIAA Paper, No. 1071, 1970.

76. Ragsac, R. V., and R. R. Titus. Optimization of Interplanetary Stopover Missions. AIAA J., Vol. 1, No. 8, 1963.

77. Silver, R. W. Grand Tours of the Jovian Planets. J. Spacecraft and Rockets, Vol. 5, No. 6, 1968.

78. Sohn, R. L. Mars-Venus Flyby Missions with Manned Mars Landers. J. Spacecraft and Rockets, Vol. 4, No. 1, 1967.

79. Titus, R. R. Powered Flybys of Mars. Astronaut. Acta, Vol. 11, No. 5, 1965.

80. TOPS: Thermoelectric Outer-Planet Spacecraft. Astronaut. and Aeronaut., Vol. 8, No. 9, 1970.

81. Vickery, J. D., and J. L. Horsewood. Mission Window Definition for Jupiter Swingbys to the Outer Planets. J. Spacecraft and Rockets, Vol. 6, No. 5, 1969.

82. Willes, E. A., Jr. New Class of Optimal Interplanetary Trajectories with Specified Trip Time. AIAA Paper 65-36, 1965.

Translated for National Aeronautics and Space Administration under Contract No. NASw 2483 by SCITRAN, P. O. Box 5456, Santa Barbara, California, 93108.